A Study of Metal-Metal Bonds and Multiconfiguration Pair-Density Functional Theory

A DISSERTATION
SUBMITTED TO THE FACULTY OF
UNIVERSITY OF MINNESOTA
BY

Rebecca Kathleen Carlson

IN PARTIAL FULFILLMENT OF THE REQUIREMENTS
FOR THE DEGREE OF
DOCTOR OF PHILOSOPHY

Laura Gagliardi, advisor

July 2017

Acknowledgements

Firstly, I would like to thank my advisor, Professor Laura Gagliardi, for all her help and support during my time as a graduate student. She has given me the chance to explore a wide variety of projects and travel to interesting conferences where I had the chance to meet many scientists in the field. She has also been there to reassure me during more than one existential crisis as a graduate student. Secondly, I would like to thank Professors Donald G. Truhlar and Connie C. Lu for their guidance on various projects and helping me see the bigger picture when I get lost in the details. I would also like to thank members of the Gagliardi Group, especially Giovanni Li Manni, Nora Planas, and Samuel Odoh for their help in learning to code and debug, understating experimental data, and their continued support and mentorship. Lastly, I would like to thank my family and friends for their encouragement over my time in graduate school. Their support through many late nights has been greatly appreciated.

Dedication

This thesis is dedicated to Grandpa Bale, who gave me my first physics textbook in elementary school, which I loved to carry around to “learn” new things.

Table of Contents

List of Tables viii
List of Figures xii
Introduction 1
Chapter 1. Role of the Metal in the Bonding and Properties of Bimetallic Complexes Involving Manganese, Iron, and Cobalt 13
1.1 Overview 14
1.2 Introduction 14
1.3 Experimental Section 17
1.4 Computational Methods 17
1.4.1 CASSCF/CASPT2 Calculations 18
1.4.2 DFT Calculations 19
1.5 Results and Discussion 20
1.5.1 Synthesis 20
1.5.2 NMR Spectroscopy 22
1.5.3 UV-vis NIR Spectroscopy 24
1.5.4 X-Ray Diffraction Studies 26
1.5.5 Electrochemistry 31
1.5.6 Mössbauer Spectroscopy 33
1.5.7 Magnetic Susceptibility 35
1.5.8 Theoretical Studies 39
1.6 Conclusions 44
Chapter 2. Influence of Copper Oxidation State on the Bonding and Electronic Structure of Cobalt-Copper Complexes 46
2.1 Overview 47
2.2 Introduction 47
2.3 Experimental Section 48
2.4 Computational Methods 48
2.5 Results and Discussion 49
2.5.1 Synthesis 49
2.5.2 NMR Spectroscopy 51
2.5.3 X-Ray Diffraction Studies 53
2.5.4 EPR Spectroscopy and Magnetic Susceptibility 58
2.5.5 Electrochemistry 59
2.5.6 Electronic Absorption Spectroscopy 61
2.5.7 Theory 62
2.6 Conclusions 64
Chapter 3. Synthesis and Redox Reactivity of a Phosphine-ligated Dichromium Paddlewheel 66
3.1 Overview 67
3.2 Introduction 67
3.3 Experimental Section 69
3.4 Computational Methods 69

3.5 Results and Discussion 70
3.5.1 Synthesis 70
3.5.2 Molecular Structures 71
3.5.3 NMR Studies 75
3.5.4 Cyclic Voltammetry 79
3.5.5 Electronic Absorption Spectroscopy 81
3.5.6 Theory 84
3.5.7 Initial Reactivity Studies 86
3.6 Conclusions 86
Chapter 4. Pushing the Limits of Delta Bonding in Metal–Chromium Complexes with Redox Changes and Metal Swapping 88
4.1 Overview 89
4.2 Introduction 89
4.3 Experimental Section 91
4.4 Computational Methods 91
4.5 Results and Discussion 94
4.5.1 Synthesis and Cyclic Voltammetry 94
4.5.2 NMR and EPR Spectroscopy 97
4.5.3 Solid-state Structures 100
4.5.4 Diamagnetic Anisotropy 105
4.5.5 Theory 107
4.5.6 Mössbauer Spectroscopy 112
4.5.7 Vis-NIR and Resonance Raman Spectroscopy 114
4.6 Conclusions 120
Chapter 5. Bimetallic cobalt dinitrogen complexes: impact of the supporting metal on N_2 activation. 122
5.1 Overview 123
5.2 Introduction 123
5.3 Experimental Section 124
5.4 Computational Methods 124
5.4.1 DFT calculations 124
5.4.2 CASSCF/CASPT2 calculations 125
5.5 Results and Discussion 126
5.5.1 Synthesis and characterization of CoTiL (1) 126
5.5.2 Electrochemistry of CoML series 129
5.5.3 Synthesis and characterization of dinitrogen adducts **2** and **3** 130
5.5.4 Theory 132
5.6 Conclusions 136
Chapter 6. Structure and bonding of group-4 nickel heterobimetallics supported by 2-(diphenylphosphino)pyrrolide ligands 138
6.1 Overview 139
6.2 Introduction 139
6.3 Experimental Methods 141
6.4 Computational Details 141

6.4.1 DFT 141
6.4.2 CASSCF calculations 141
6.5 Results and Discussion 142
6.6 Conclusions 153
Chapter 7. Multiconfiguration Pair-Density Functional Theory 155
7.1 Overview 156
7.2 Introduction 156
7.3 Theory 162
7.3.1 MC-PDFT equations 162
7.3.2 Pair-Density functionals 163
7.4 Test Cases 165
7.5 Computational Details 167
7.5.1 Basis Sets 167
7.5.2 CASSCF 167
7.5.3 CASPT2 168
7.5.4 KS-DFT 168
7.5.5 MC-PDFT 169
7.6 Results 170
7.7 Discussion 170
7.8 Concluding Remarks 177
Chapter 8. Multiconfiguration Pair-Density Functional Theory: Barrier Heights and Main Group Transition Metal Energetics 189
8.1 Overview 190
8.2 Introduction 190
8.3 Theory 195
8.4 CE56 Database and its Subdatabases 195
8.5 Computational Details 196
8.6 Multireference Diagnostics 198
8.7 Results 199
8.8 Discussion 199
8.9 Conclusions 208
Chapter 9. Multiconfigurational Pair-Density Functional Theory: A Fully Translated Gradient Approximation and its Performance for Transition Metal Dimers and the Spectroscopy of $Re_2Cl_8^{2-}$ 210
9.1 Overview 211
9.2 Introduction 211
9.3 Theory 214
9.4 Translated and Fully Translated Functionals 215
9.5 Test Systems 219
9.5.1 CE56 Database and its Subdatabases 219
9.5.2 Transition Metal Dimers and a Dinuclear Complex 219
9.6 Computational Details 220
9.7 Results 222
9.8 Discussion 222

9.8.1 CE56 Dataset 222
9.8.2 Ag_2 224
9.8.3 Cr_2 226
9.8.4 Cu_2 228
9.8.5 Os_2 230
9.8.6 $Re_2Cl_8^{2-}$ 231
9.9 Conclusions 233
Chapter 10. The Separated-Pair Approximation and Separated-Pair Pair-Density Functional Theory 235
10.1 Overview 236
10.2 Introduction 236
10.3 Theory 240
10.3.1 On-top density functionals 240
10.3.2 Separated pair approximation 241
10.4 Computational Details 246
10.4.1 Basis Sets 247
10.4.2 Symmetry 247
10.4.3 CASPT2 and CAS-PDFT 247
10.4.4 SP calculations 248
10.4.5 KS-DFT calculations 248
10.4.6 Geometries 248
10.4.7 Bond energies and atomization energies 249
10.4.8 Software 249
10.4.9 Systems Studied 249
10.5 Results and Discussion 250
10.5.1 Diatomic molecules 250
10.5.2 Equilibrium bond distances of diatomic molecules 251
10.5.3 Dissociation energies of diatomic molecules 253
10.5.4 Potential energy curves of diatomic molecules 256
10.5.5 Triatomic molecules 258
10.5.6 Methylene 259
10.5.7 Ozone 262
10.5.8 C-H bond dissociation energies in organic compounds 263
10.5.9 Barrier heights for pericyclic reactions 266
10.5.10 Open-shell singlet systems 268
10.6 Concluding remarks 270
Chapter 11. On-top Pair Density as a Measure of Left-Right Correlation in Bond Breaking 276
11.1 Overview 277
11.2 Introduction 277
11.3 Theoretical Foundations 280
11.4 Computational Details 282
11.5 Results and Discussion 282
11.5.1 Density and on-top pair density for H_2 near equilibrium 283

11.5.2 Density and on-top density at the Coulson-Fischer point.....287
11.5.3 Density and on-top density at the dissociation limit.....290
11.5.4 The on-top ratio *R*.....291
11.5.5 On-top pair density and bond breaking.....296
11.6 Conclusions.....298
Chapter 12. Can Multiconfigurational Self-Consistent Field Theory and Density Functional Theory Correctly Predict the Ground State of Metal-Metal Bonded Complexes.....299
12.1 Overview.....300
12.2 Introduction.....300
12.3 Computational Details.....304
12.3.1 Wave Function Calculations.....304
12.3.2 DFT Calculations.....305
12.4 Results and Discussion.....306
12.4.1 Multiconfigurational Calculations.....306
12.4.2 Isostructural Co-Co-Cl Complex.....313
12.4.3 Density Functional Theory Approaches.....315
12.4.4 Calculated Structural Properties.....318
12.4.5 MC-PDFT results for Fe-Fe-Cl.....319
12.5 Conclusions.....321
Bibliography.....323
Appendix 1.....338
Appendix 2.....344
Appendix 3.....348
Appendix 4.....351
Appendix 5.....360
Appendix 6.....363
Appendix 7.....367
Appendix 8.....372

List of Tables

Table 1.1. Proton NMR assignments of 1-5 with chemical shifts (ppm) and T_1 (ms).....24

Table 1.2. Geometrical parameters, including bond lengths (Å) and angles (°) for complexes 1-5.[a].....28

Table 1.3. Compositions of the metals (Co, Fe, Mn) at the unique binding sites (M_1, M_2) in the heterobimetallic complexes (2, 3, 5) as determined by X-ray anomalous scattering studies.[a].....30

Table 1.4. Reduction and oxidation potentials (V) of 1-5.[a].....32

Table 1.5. Zero-field 57Fe-Mössbauer parameters (mm/s) for **2**, **4**, and **5**.....35

Table 1.6. Magnetic couplings, anisotropy constants, and g-values of **1-5**.[a].....37

Table 1.7. Relative CASPT2 energies for the various spin states of **1-5.**.....40

Table 1.8. Effective bond order (EBO) and weight of dominant configuration in wave function.....43

Table 1.9. Calculated magnetic coupling constants *J* (in cm−1) for various functionals. 43

Table 2.1. Proton NMR chemical shifts (ppm) of **1**-OTf and **2**-CD_3CN with corresponding spin-lattice relaxation times (ms) in parentheses.....52

Table 2.2. Geometrical Parameters, Including Bond Lengths (Å) and Angles (deg), for Complexes **1**-Cl, **2**-CH_3CN, and **2**.[a].....54

Table 2.3. Relative energies (kcal/mol) for **1** and **2** for accessible spin states.....62

Table 3.1. Selected bond lengths and angles for **2** and **3**.....73

Table 3.2. Diamagnetic anisotropy ($\Delta\chi$) values for selected dichromium paddlewheels. 78

Table 3.3. Visible electronic absorption data (λ_{max}, nm; molar absorptivity in parenthesis, M^{-1} cm^{-1}) for **3**, $\mathbf{3}^{+}$, and $\mathbf{3}^{2+}$ and selected dichromium paddlewheels.....83

Table 4.1. Redox Potentials (V)[a] of **2** – **4**.....95

Table 4.2. Geometrical parameters, including bond lengths (Å) and angles (°) for 2-4..102

Table 4.3. Ultra-short Cr-Cr bond distances in selected Cr2 systems.....102

Table 4.4. Diamagnetic anisotropies ($\Delta\chi$) for multiply bonded bimetallic complexes....107

Table 4.5. Main electronic configuration of metal-chromium complexes and the formal versus effective bond orders (FBO vs. EBO).....108

Table 4.6. Percentage of Metal Character (% Cr, % M) in metal-chromium bonding orbitals of σ-, π-, and δ-symmetry from CASSCF calculations.....111

Table 4.7. DFT bond lengths for MCrL series (Å).....112

Table 4.8. Visible-NIR electronic absorbance data for **2**, $\mathbf{2}^{\mathbf{red}}$, **3**, $\mathbf{3}^{\mathbf{red}}$, **4**, $\mathbf{4}^{\mathbf{red}}$, and $\mathbf{4}^{\mathbf{ox}}$....117

Table 5.1. Geometrical parameters, including bond lengths (Å), formal shortness ratio (FSR), and angles (deg), for **1** – **3**.....128

Table 5.2. Effective oxidation state of $[(N_2)CoML^{Me}]^-$ and percent polarization of σ bond on Co.....135

Table 6.1. Relevant bond lengths (Å) and angles (°) for **4**-**6**.....145

Table 7.1. Main group atomic excitation energies (eV).....171

Table 7.2. Transition metal atomic excitation energies (eV).....172

Table 7.3. Singlet-to-singlet atomic and vertical electronic excitation energies (eV).....173

Table 7.4. Dissociation energies (eV) of diatomic molecules.....175

Table 7.5. Averaged mean absolute errors (eV).....178

Table 8.1. Descriptions of Subdatabases.....197

Table 8.2. Main-Group Average Bond Energies (kcal/mol).....200

Table 8.3 Transition-Metal-Ligand Average Bond Energies (kcal/mol).....202

Table 8.4. Proton Affinities of Small Molecules (kcal/mol).....203

Table 8.5. Alkyl Bond Dissociation Energies (kcal/mol).....204

Table 8.6. Non-covalent energy of hydrogen bonding (kcal/mol).....204

Table 8.7. Forward and reverse barrier heights for small molecules (kcal/mol).....205

Table 8.8. Reaction energies for small molecules (kcal/mol)[a].....207

Table 8.9. Average mean unsigned errors (kcal/mol).....208

Table 9.1. Average mean unsigned errors (kcal/mol) for entire database and breakdown into subdatabase containing transition metals and the rest.....223

Table 9.2. Average mean unsigned errors (kcal/mol) for subdatabases.....224

Table 9.3. Silver dimer geometries and dissociation energies with the def2-TZVP basis set.....225

Table 9.4. Chromium dimer geometries and dissociation energies with the cc-pVTZ-DK basis set 228

Table 9.5. Copper dimer geometries and dissociation energies with the def2-TZVP basis set with DKH 229

Table 9.6. Osmium dimer geometries and dissociation energies of the $^5\Pi_u$ state 230

Table 9.7. Osmium dimer geometries and relative energies of the $^7\Delta_u$ and $^5\Pi_u$ states 231

Table 9.8. $Re_2Cl_8^{2-}$ excitation energies for the δ to δ^* transition ($^1A_{1g}$ to $^1A_{2u}$) with the ANO-RCC-VTZP basis set with DKH 232

Table 10.1 The experimental dissociation energies (in parentheses below molecule) of eleven main-group diatomic molecules and the chromium dimer, Cr_2, are compared with the calculated results obtained with several levels of theory. The MAE obtained without the results for Cr_2 is labeled as MAE-11. For each theoretical method, the deviation of the calculated results from experimental values is given. A negative sign denotes underestimation of the bond energy, while a positive sign indicates overestimation (kcal/mol). 255

Table 10.2. Effect of imposing restrictions on the active space with the GAS scheme on the total electronic energies of N_2, O_2 and Cr_2 as functions of inter-nuclear distance *R*(Å). The differences in the total electronic energies obtained with CASSCF and SP, CAS-tPBE and SP-tPBE as well as CAS-ftPBE and SP-ftPBE are reported in kcal/mol, where A:B denotes the absolute value of the energy difference between A and B. 257

Table 10.3 Comparison of the calculated equilibrium bond distances (R_e), bond angles (<), and atomization energies (AE) of CH_2 and O_3 obtained at different levels of theory with experimental data. For each theoretical method, the deviation of the calculated results from experimental values is given. A negative sign denotes underestimation and a positive sign indicates overestimation of the experimental data. The calculated adiabatic singlet-triplet (S-T) gaps of CH_2 are also presented. 260

Table 10.4. The calculated C-H dissociation energies (kcal/mol) of three organic compounds obtained with different levels of theory are compared with experimental data. For each theoretical method, the deviations of the calculated results from experimental values are give. A negative sign denotes underestimation and a positive sign indicates overestimation of the experimental data. 264

Table 10.5. the calculated barriers (kcal/mol) of five pericyclic reactions computed with different methods are compared with experimental data. For each method, the deviations of the calculated results from experimental values are also given. A negative sign denotes underestimation and a positive sign indicates overestimation of the experimental data. 267

Table 10.6 The calculated energy separation (kcal/mol) of twisted and planar ethylene (**A**) and the singlet-triplet gaps of 1,4-didehydrobenzene (**B**) and α,3-didehydrotoluene (**C**). 269

Table 11.1. On-top ratio at the bond midpoint.....292

Table 12.1. Relative spin state energies (kcal/mol) of the Fe-Fe-Cl complex for various active spaces with respect to the energy of the septet state. 307

Table 12.2. EBO, weight of dominant configuration (DC) and percent distribution of d_{xz} and d_{yz} components between the Fe centers of the π symmetry molecular orbitals for the septet spin state of Fe-Fe-Cl. 308

Table 12.3: Relative spin state energies (kcal/mol) of the septet and nonet spin states of Fe-Fe-Cl obtained at the CASPT2 and RASPT2 levels of theory. 309

Table 12.4. Relative spin state energies (kcal/mol) of the Co-Co-Cl complex obtained with active spaces containing various amounts of the 4*d* shell. 314

Table 12.5. Effect of active space size on the weights of the dominant configuration (DC) and estimated EBO for the singlet spin state of the Co-Co-Cl complex. 315

Table 12.6. Mean Absolute Errors (MAE) of the structural properties (M-M, M-Cl, M-N bond distances (Å) and N-M-N bond angles (degrees)) obtained at the DFT level compared to experimental structures. 319

List of Figures

Figure 1.1 Metal pairings for the bimetallic complexes. 16

Figure 1.2. Two-step metallation reactions: (1) synthesis of K[Co(py_3tren)] and K[Fe(py_3tren)]; and (2) synthesis of M1M2Cl(py_3tren) complexes 1-5.....22

Figure 1.3. Stacked plot of the ^{1}H NMR spectra of 1-5 (500 MHz, CD_2Cl_2). Inset shows a close-up of a broad peak, assigned as the proton in 3. The residual solvent peaks are marked by the dotted line.....23

Figure 1.4. (top) UV-Vis plots of K[Co(py_3tren)] and cobalt-containing complexes 1-3. (bottom) UV-Vis plots of K[Fe(py_3tren)] and iron-containing complexes 4 and 5. Insets show the Vis-NIR region. Spectra were collected as solutions in CH_2Cl_2. The asterisk denotes artifacts from solvent subtraction. 26

Figure 1.5. Solid-state structure of 1−5. Thermal elliposids are shown at 50% probability. Protons are omitted for clarity. For the heterobimetallic species, the percentages of each metal (Co in green, Fe in red, and Mn in blue) at each binding site (as determined by X-ray anomalous dispersion) are depicted as pie charts. 27

Figure 1.6. Cyclic voltammograms of 1-5 in 0.4 M [nBu4N]PF6/THF at 300 mV/s (except for 2, 0.1 M [nBu4N]PF6/THF at 10 mV/s). 32

Figure 1.7. Zero-field Mössbauer spectra of **2** (*left*), **4** (*center*), and **5** (*right*) at 77 K. The experimental data is plotted as dots. Total fits are shown as red lines. Mössbauer parameters, δ (Δ*E*Q) in mm/s, are for **2**, 0.88 (2.62); for **4**, 0.58 (0.38) (in green) and 0.48 (1.31) (in blue); and for **5**, 0.46 (1.69) mm/s. 34

Figure 1.8. Temperature dependence of the magnetic susceptibility, plotted as $\chi_M T$, of **1** (black solid squares), **2** (red triangles), **3** (blue diamonds), **4** (purple, open squares), and 5 (green circles) at 1 Tesla, from 2 to 290 K. Solid lines represent the best fit.....35

Figure 1.9. Qualitative MO diagrams showing the natural orbitals for dicobalt **1** (*left*) and diiron **4** (*right*). Only the dominating electronic configurations are shown. 42

Figure 1.10. Plot of |J| values for compounds 1, 2, 3, and 5. 44

Figure 2.1. Synthesis of Co-Cu complexes in two oxidation states, $(CoCu)^{4+}$ and $(CoCu)^{3+}$. Two viable routes to **1**-OTf are shown. 50

Figure 2.2. Stacked ^{1}H NMR spectra of **1**-OTf and **2**-CD_3CN (300 MHz, CD_3CN).....52

Figure 2.3. Solid-state structures of **1**-Cl (a – side view, b – top view) and **2**-CH_3CN (c – side view, d – top view). Bond distances (Å) and N_{py}−Cu−N_{py} angles are provided. Thermal ellipsoids are shown at 50% probability, and protons were omitted for clarity. The pie chart indicates the metal composition in the pyridyl site as determined by X-ray anomalous scattering.....54

Figure 2.4. (a) Molecular structure of **2** with thermal ellipsoids at 50% probability. Protons omitted for clarity. Intermolecular bonds are shown in gold. (b) Space filling model of the macromolecular **2** showing its hexagonal polymeric structure. 57

Figure 2.5. X-band EPR spectra (9.65 MHz) of **2** in frozen THF (1 mM, 20 K). Experimental spectra is shown as a solid, black line, and the corresponding simulation in a red dashed line. Simulation parameters for **2**: $D = 0$, $E/D = 0.1$, $g = (4.33, 4.3, 2.002)$, W = (24.1, 38.5, 18 G), $A_z = 206$ MHz (real g-values: 2.163, 2.16, 2.002) 58

Figure 2.6. Temperature dependence of the magnetic susceptibility of **1-Cl** plotted as μ_{eff} versus T (2 to 290 K, 1 T). The data, represented by open circles, was corrected for temperature independent paramagnetism of 350 x 10^{-6} emu). The red line shows the simulation with the following parameters: $S = 1$, $g = 1.956$, $D = 64.584$ cm^{-1}. 59

Figure 2.7. Cyclic voltammagrams of **1**-OTf (top) and **2**-CH_3CN (bottom) in 0.1 M [$n$$Bu_4N$]$PF_6$/$CH_3CN$ at varying scan speeds: 2 (in black), 1, 0.5, 0.25, 0.1, 0.05 V/s (in light grey). Currents were corrected for scan speed. 60

Figure 2.8. UV-Vis plots of **1**-Cl (black), **2**-CH_3CN (solid grey), and K[Co(py_3tren)] (dashed grey). Inset shows the Vis-NIR region. Spectra were collected as solutions in CH_2Cl_2. The asterisk denotes artifacts from solvent subtraction. 61

Figure 2.9. Qualitative MO diagram and natural orbitals of **1**-Cl. Electron filling corresponds to the main configuration (42%), while the numerical value of each natural orbital is the population summed over all contributing configurations. 63

Figure 2.10. Qualitative MO diagram and natural orbitals of **2**-CH_3CN. Electron filling corresponds to the main configuration (91%), while the numerical value of each natural orbital is the population summed over all contributing configurations. 64

Figure 3.1. Dichromium paddlewheels 68

Figure 3.2. Synthesis of the ligand, H_2(PNONP) (**1**), and the dinuclear Cr complexes, **2** and **3**. [a] 1.95 $^{i}Pr_2PCH_2OH$, THF, 65 °C, 12 h; [b] *i*) 2 ^{n}BuLi, Et_2O, −196 °C to rt, 2 h; *ii*) $CrCl_3(THF)_3$, THF, −50 °C to rt, 12 h; [c] *i*) 2 ^{n}BuLi, Et_2O, −196 °C to rt, 2 h; *ii*) $CrCl_2$, THF, −50°C to rt, 12 h; [d] 2 KC_8, THF, −78°C, 3 h. 71

Figure 3.3. Solid−state structure of the core of dinuclear **2** by X−ray crystallography at 173 K. Thermal ellipsoids are shown at 50% probability for atoms in the first coordination sphere only. For clarity, only one of the two ligands is shown, and hydrogen atoms are omitted. 72

Figure 3.4. Two views of the solid-state structure of [PNONPCr]$_2$ **3** (50% probability level). View **a** is perpendicular to the Cr−Cr bond axis, and view **b** looks down the bond axis. For clarity, only one of the two ligands is fully shown. Hydrogen atoms are omitted for clarity.
.....73

Figure 3.5. Stacked ^{31}P VT−NMR plot of **3** (THF-d_8, −80° to 100°C). At each temperature, the position and integration of the peak was determined against an internal reference of 85% H_3PO_4 at temperatures above 0°C and PPh_3 in toluene at temperatures below 0°C. 76

Figure 3.6. CV of $[Cr_2(PNONP)_2]^{0/+1/+2}$ (**3**, $\mathbf{3}^+$, and $\mathbf{3}^{2+}$) in 0.1 M $[N^nBu_4]PF_6$ with a scan rate of 200 mV/s. Complexes $\mathbf{3}^+$ and $\mathbf{3}^{2+}$ were generated *in situ* by adding $[FeCp_2][BAr^F{}_4]$. Potentials were referenced to $FeCp_2^{0/+}$. 80

Figure 3.7. *In situ* oxidation of **3** with $[FeCp_2][BAr^F{}_4]$ in THF at −80°C, to produce $\mathbf{3}^+$, and $\mathbf{3}^{2+}$. The ferrocene byproduct (one and two equivalents, respectively) has a weak absorption at 440 nm, but its intensity (100 M^{-1} cm^{-1}) is very low. 82

Figure 3.8. M06-L molecular orbitals for singlet diradical **3**. 84

Figure 3.9. Natural orbitals of **3** and their electron occupation numbers. 85

Figure 4.1. Metal-chromium complexes and their (*d-d*)n counts, where the polarity of the M-Cr bonds increases as M = Cr > Mn > Fe. White boxes represent new compounds. Previously reported complexes are shown in light gray boxes. 91

Figure 4.2. From complex **1** (*left*), the syntheses of: neutral metal-chromium complexes **2** – **4** and their one-electron reduced and/or oxidized counterparts. 95

Figure 4.3. Cyclic voltammograms of 2 – 4 with [nBu4N]PF6 (0.1 to 0.4 M) in THF (vs. FeCp20/+). Scan rates and electrolyte concentrations for: 2 (black), 25 mV/s, 0.4 M; 3 (blue), 250 mV/s, 0.4 M; and 4 (red), 10 mV/s, 0.1 M. 96

Figure 4.4. Stacked plot of variable temperature 1H NMR spectra for K[$\mathbf{2}^{red}$] (THF−d_8, 500 MHz). Protons are color-matched to by the inset color figure. For clarity, only one ligand arm is labeled. 97

Figure 4.5. X-band EPR spectra (9.65 MHz) of **2** (top, 20 K) and $\mathbf{3}^{red}$ (bottom, 34 K) in frozen THF (1 mM). Experimental spectra are shown as black, solid lines with corresponding simulations in red, dashed lines. Simulation parameters: for **2**, $g_x = g_y = g_z = 1.99$; W=(11, 16, 11 G), A(3 x 31P) = 10 x 10−4 cm−1 and for $\mathbf{3}^{red}$, $g_{ave} = 1.79$, g = (1.95, 1.88, 1.52), W = (30, 200, *620*) G, A_x(55Mn) = 36 x 10^{-4} cm^{-1} 99

Figure 4.6. Solid−state structures of **1**, **2**, $\mathbf{2}^{red}$, $\mathbf{3}^{red}$, and $\mathbf{4}^{ox}$ by X−ray crystallography at 123 K for $\mathbf{4}^{ox}$ and at 173 K for the remaining compounds. Thermal ellipsoids are shown at 50% probability. Hydrogen atoms, counterions, and lattice solvent molecules have been omitted for clarity. Green, chromium; red, manganese; pink, iron; blue, nitrogen; orange, phosphorus. M−Cr bond distances are given in red, and average M-P and Cr-N bond distances are given in blue 100

Figure 4.7. Spatial zones of shielded (+) and deshielded (-) chemical shifts that arise from the diamagnetic anisotropy of the multiply bonded $[MCr]^{3+}$ cores. 106

Figure 4.8. Qualitative MO diagram of **2**$^{\mathbf{red'}}$ showing the natural orbitals of σ (d_z2), two π (d_{xz}, d_{yz}), and two δ (d_{xy}, d_x2-d_y2) symmetry for main configuration (60%) from RASSCF calculations. 109

Figure 4.9. Zero-field 57Fe Mössbauer spectra of 4ox recorded at 80 K (top) and magnetic spectrum recorded at 4.2 K with a field of 7 Tesla applied perpendicular to the γ –rays (bottom). The green line represents the best fit with δ = 0.18 mm s-1 and ΔEQ = +5.85 mm s-1 , η = 0 (85% purity) and with S = 0. There is also a high-spin Fe(II) impurity with δ = 0.83 mm s-1 and ΔEQ = 2.15 mm s-1 (dotted blue line in top panel). 113

Figure 4.10. Vis-NIR plots for **2** and **2**$^{\mathbf{red}}$ (top), **3** and **3**$^{\mathbf{red}}$ (middle), and **4**$^{\mathbf{ox}}$, **4**, and **4**$^{\mathbf{red}}$ (bottom) in THF at rt. Artifacts from solvent subtraction or light source changes appear at ~1750 nm. 116

Figure 4.11. A stack plot of the resonance Raman spectrum of **2red** (10.4 mM in THF, λex: 647.1 nm, 77 K) (top, in black) and the DFT calculated Raman spectrum of **2red'** (bottom, in red). 118

Figure 5.1. Synthesis of compound **1**.....126

Figure 5.2. Molecular structure of **1** shown at 50% thermal ellipsoid probability. Hydrogen atoms were omitted for clarity. Average bond lengths (Å) are shown. 127

Figure 5.3. Cyclic voltammograms of CoML complexes collected under an atmosphere of N_2 (colored lines) or argon (---) in 0.4 M [^{n}Bu$_4$N]PF$_6$ in THF at a scan speed of 50 mV/s. Exceptions: 10mV/s for CoCrL and Co_2L, which was dissolved in 0.1 M [^{n}Bu$_4$N]PF$_6$ in DME. Asterik (*) indicates [CoML]$^{0/-}$ redox couple. 129

Figure 5.4. Synthesis of compounds **2** and **3**. 130

Figure 5.5. Molecular structures of **2** and **3** shown at 50% thermal ellipsoid probability. Hydrogen atoms, K(crypt-222) counterion, and non-coordinating solvent molecules were omitted for clarity. Average bond lengths (Å) are shown. 131

Figure 5.6. Qualitative MO diagram showing the natural orbitals for CoTiL^{Me} (**1'**) that arise from CASSCF calculations. The dominating electronic configuration (83%) is shown. 133

Figure 5.7. Qualitative MO diagrams of the d-orbital manifold for the [(N$_2$)CoML^{Me}]$^-$ series, where M = Al, Ti, V, Cr, and Co. 135

Figure 6.1. Synthesis of mono-metallic **1**, **2**, and **3**. 143

Figure 6.2. Synthesis of bimetallic **4**, **5**, and **6**. 143

Figure 6.3. Thermal ellipsoid drawings of **4** (left), **5** (center), and **6** (right). Solvent and hydrogen atoms have been removed and phenyl groups have been reduced to the ipso

carbon for clarity. Relevant bond distances (Å) and angles (°) are presented in Table 6.1. 144

Figure 6.4. Variable temperature ^{31}P NMR spectra of **4** showing decoalescence of the 3 inequivalent Ni-bound phosphines at low temperature**.** 146

Figure 6.5. Qualitative molecular orbital diagrams taken from M06-L energies for **4**, **5**, and **6**(above) and representative molecular orbitals for **4**(below). 147

Figure 6.6. Cyclic voltammograms of **1**, **2**, and **3** (top) and **4**, **5**, and **6** (bottom). Potentials are referenced to Fc/Fc^{+}. 149

Figure 6.7. Synthesis of **7**. 151

Figure 6.8. Binding of CO to **4** to form a Ni-CO adduct **8**. 152

Figure 6.9. Structure of product (**9**) that forms when crystallizing **4** in trace amounts of H_2O. 153

Figure 7.1. Potential energy curves for H_2. (a) Part a shows the whole range of distances. At equilibrium, the Var. and WABS curves for each functional are the same, but they are different at intermediate distances. The CASPT2 minimum is just below the WABS PBE minimum. (b) Part b is a blowup of the region from 1 to 3 Å. The WABS curves are lower in energy than the Var. counterparts at intermediate distances. 181

Figure 7.2. Potential energy curves for N_2. (a) Part a shows the whole range of distances. At equilibrium, the Var. and WABS curves for each functional are the same, but they are different at intermediate distances. (b) Part b is a blowup of the region from 1.3 to 2.8 Å. 182

Figure 7.3. Potential energy curves for F_2. a) Part a shows the whole range of distances. At equilibrium, the Var. and WABS curves for each functional are the same, but they are different at intermediate distances. b) Part b is a blowup of the region from 1.6 to 2.8 Å. 183

Figure 7.4. Potential energy curves for the $^{1}\Sigma^{+}$ state of CaO. a) Part a shows the whole range of distances. The CASPT2 and tPBE curves are very close at equilibrium and so are hard to distinguish in the figure. b) Part b is a blowup of the region from 2.5 to 5.5Å. 184

Figure 7.5. Potential energy curves for Cr_2. The experimental curve (Casey and Leopold, Ref. 219) is shown for experimentally measurable distances and is shifted to a common asymptote by the experimentally determined dissociation energy. 185

Figure 7.6. Potential energy curves for the $^{2}\Pi$ state of NiCl. a) Part a shows the whole range of distances. At equilibrium, the electronic structure is ionic, with Ni^{+} having a $3d^{9}$ configuration. At dissociation, Ni is in its $3d^{8}4s^{2}$ ground state. b) Part b is a blowup of the region from 2.5 to 5.5 Å.....186

Figure 7.7. Plot of the pair density, total density, and the ratio for H_2 along the bond axis. In the plot, 0 Å is the middle of the bond between the atoms. a) Part a represents these quantities, f(z), at equilibrium. Only one atom of the dimer is represented in the plot, centered at about 0.35 Å. b) Part b represents these quantities at dissociation.....187

Figure 7.8. Plot of the pair density, total density, and the ratio for N_2 along the bond axis. In the plot, 0 Å is the middle of the bond between the atoms. The pair density and total density have been scaled in this figure by a factor of 1000 and 100, respectively. a) Part a represents these quantities, f(z), at equilibrium. Only one atom of the dimer is represented in the plot, centered at about 0.55 Å. b) Part b represents these quantities at 2Re. 188

Figure 9.1. Plot of tPBE and ftPBE approximations to χ as a function of R. In the original translation (as used in tPBE), the red curve is followed for $0<R\leq1.0$, and χ is zero beyond that. In the full translation (as used in ftPBE), the red curve is followed when $0<R<0.9$, the black curve is followed when $0.9\leq R\leq1.15$, and χ is zero beyond that; this piecewise curve is continuous with continuous first and second derivatives. 218

Figure 9.2. Silver dimer potential energy curves with def2-TZVP basis set.....225

Figure 9.3. Chromium dimer potential energy curves with cc-pVTZ-DK basis set.....226

Figure 9.4. Copper dimer potential energy curves with def2-TZVP basis set and DKH relativistic Hamiltonian.....229

Figure 10.1. The four GAS subspaces used in the SP-4 approximation for the carbon dimer, C_2. In this scheme, the 2s, $2p_z$, $2p_x$, and $2p_y$ atomic orbitals form σ_g, σ_u, $\pi(p_x)$, and $\pi(p_y)$ (which are bonding or in the case of $2\sigma_u$, GAS2, antibonding) orbitals respectively as well as their antibonding (or in the case of $2\sigma_u$, GAS2, bonding) counterparts. These pairs are shown from left to right. The orbitals with an occupation close to two are placed at the *top*, while those that are nearly empty are placed at the *bottom*. Two electrons are placed in each GAS subspace. Intra-space excitations (up to double excitations) between a bonding orbital and its antibonding pair are allowed. Inter-subspace excitations between GAS subspaces are not allowed. 243

Figure 10.2. The three GAS subspaces used in SP calculations on triplet dioxygen, O_2. In this scheme, the $2p_z$ atomic orbitals form 3σ and $3\sigma^*$ orbitals, and the $2p_x$ and $2p_y$ atomic orbitals form bonding $\pi(p_x)$, and $\pi(p_y)$ orbitals and correlating antibonding $\pi^*(px)$, and $\pi^*(py)$ orbitals. These are shown from left to right. GAS 1 contains two electrons while GAS 2 and GAS 3 each contain 3 electrons. Inter-subspace excitations between GAS spaces are not allowed 244

Figure 10.3. Mean absolute errors (MAE) with respect to experimental values of the calculated bond distances of eleven main-group diatomic molecules and Cr_2, obtained with several approaches (left). The MAE obtained without the results for Cr_2 (labeled as MAE-11) is shown on the right. The methods are grouped into three classes. The first are

based on CASSCF (CASSCF, CASPT2, CASPT2-0, CAS-tPBE, CAS-ftPBE). The second are based on the SP approximation (SP, SP-tPBE, SP-ftPBE). The third is Kohn-Sham DFT with the PBE exchange-correlation functional. All experimental data were obtained from ref. 449.....251

Figure 10.4. Illustrative descriptions of the CAS and SP active spaces used in CASSCF and SP calculations on CH_2 (left) and O_3(right). Refer to text for the full descriptions of the active spaces used in the CASSCF and SP calculations. 259

Figure 10.5. Illustrative descriptions of the CAS and SP active spaces used in CASSCF and SP calculations on: ethane)top) and the ethyl radical (bottom). Notice that the C-C- orbitals are not included in SP sub spaces as we are concerned only with C-H bond dissociation. 265

Figure 10.6. The barriers for these pericyclic reactions were calculated with SP-PDFT and other theoretical methods. 267

Figure 10.7. Illustrations of the structures of twisted ethylene, 1,4-didehydrobenzene and α,3-didehydrotoluene 269

Figure 11.1. Contour plot of on-top pair density for CASSCF(2,2) at 1.4 a_0 where the bond is along the z-axis. Part (a) has a color scale that illustrates the structure as well as possible. Part (b) uses the same color scale as Fig. 2 so that one can see the difference clearly.....284

Figure 11.2. Contour plot of on-top pair density for RHF at 1.4 a_0 where the bond is along the z-axis 284

Figure 11.3. Natural logarithm of the absolute value of the difference of the RHF on-top pair density from the CASSCF(2,2) on-top pair density at 1.4 a_0. The RHF wave function has larger values of Π everywhere except for the oval in the center of the contour plot from -0.7 to 0.7 a_0 along the x-axis.....285

Figure 11.4. Contour plots of contributions to the on-top pair density for H_2 at 1.4 a_0 for (a) RHF ionic terms, (b) RHF covalent terms (c) CASSCF(2,2) ionic terms, and (d) CASSCF(2,2) covalent terms.....286

Figure 11.5. Natural logarithm of the difference (RHF minus CASSCF(2,2)) in values of the on-top pair density at 2.5 a_0. RHF has larger values of Π everywhere. 288

Figure 11.6. Contributions to the on-top pair density at a point 0.5 a_0 from one hydrogen atom inside the bond along the internuclear axis for (a) CASSCF(2,2) and (b) RHF.....288

Figure 11.7. Contributions to the on-top pair density at a point 0.5 a_0 from one H atom inside the bond along the internuclear axis for CASSCF(2,2) and RHF near the CF point. 289

Figure 11.8. Contour plot of on-top ratio R at r_{ab} = 1.4 a_0.....291

Figure 11.9. Plots of eq 12 and a series expansion along z-axis for a) r_{ab} = 1.4 a_0 b) r_{ab} = 1.7 a_0 c) r_{ab} = 2.5 a_0 d) r_{ab} = 3.5 a_0 e) r_{ab} = 4.5 a_0 f) r_{ab} = 10 a_0 294

Figure 11.10. On-top ratio at the bond midpoint for various internuclear distances. 296

Figure 11.11. Effective bond order calculated by CASSCF(2,2) 297

Figure 12.1. Structure of the M_1-M_2-Cl series of complexes. These complexes possess a N,N,N-tri(2-(2-pyridylamino)ethyl)amine ligand scaffold and two 1st row transition metals that are labeled as M_1 (bottom metal) and M_2 (top metal). There are three nitrogen atoms in the equatorial regions of the metal atoms while M_1 also has a apical nitrogen. 303

Figure 12.2a. Mulliken spin density plot of 3*d* orbitals for Fe-Fe-Cl for the (12,15) and (12,20)/(12,10)/2 active spaces. 311

Figure 12.2b. Mulliken spin density plot of 4*d* orbitals for Fe-Fe-Cl for the (12,15) and (12,20)/(12,10)/2 active spaces. 311

Figure 12.3. Qualitative orbital diagrams for the 3*d* orbitals computed with the (12,20)/(12,10)/2 and (12,15) active spaces. The natural orbital occupation numbers obtained for these orbitals in the (12,20)/(12,10)/2 calculation are shown while those corresponding to the (12,15) active space are given in parentheses. Note that the (12,15) MO diagram shows a more localized bonding manifold, similar to the other M-M-Cl complexes, especially for the π and π* orbitals. This is in contrast to the larger (12,20)/(12,10)/2 active space which shows significant delocalization in these particular orbitals.....313

Figure 12.4. Calculated relative energies of various electronic spin states of Fe-Fe-Cl obtained with several (*left*) local and (*right*) hybrid exchange-correlation functionals. The energies of the various states are given relative to the energy of the septet state. 316

Figure 12.5. A series of π (*left* and *middle*) and σ (*right*) orbitals between the metals of Fe-Fe-Cl obtained at the PBE level of theory. The contributions to the π orbitals are 51%-Fe_1+37%-Fe_2 (*left*) and 49%-Fe_1+37%-Fe_2 (*middle*) with PBE. These orbitals become localized largely on the bottom metal when hybrid functionals are used. For example with PBE0 the contributions to the π orbitals are 56%-Fe_1+5%-Fe_2 and 71%-Fe_1+8%-Fe_2. ..318

Figure 12.6. Relative spin state energies (kcal/mol) for CASPT2 (12,12), CASPT2 (12,14), RASPT2 (12,20)/(12,10)/2, tPBE (12,12), and tPBE (12,20)/(12,10)/2 for Fe-Fe-Cl. 320

Introduction

Introduction

One of the fundamental concepts in chemistry is that of the chemical bond.[1] Across the periodic table, the valency of atoms changes, resulting in the potential ability to form of a wide variety of bonds between atoms. Of particular interest are those atoms that can form multiple bonds, which are largely found in the transition metals. A seminal discovery in 1964 by Cotton et al. was the first experimental evidence of a delta bond, which suggested the $[Re_2Cl_8]^{2-}$ molecule contained a formal quadruple bond.[2,3] Hoffman et al.[4] discussed the potential structural requirements for a quintuple bond based on point group variation and there have been complexes with formal quintuple bonds isolated[5–7] that show promise for small molecule activation[8] or cycloaddition.[9] A unique class of inorganic complexes that can contain metal-metal multiple bonds are paddlewheel complexes. Studies of these compounds have increased the fundamental understanding of magnetic exchange[10] and the nature of the metal-metal bond.[11]

A relevant application for molecules with metal-metal multiple bonds is for use as catalysts for small molecule activation, e.g. H_2, N_2, and CO_2. Bimetallic clusters that occur in metalloenzymes such hydrogenases and nitrogenases, which may contain Ni-Fe or Mo-Fe and V-Fe bonds, are able to facilely activate these small molecules.[12] However, synthetic approaches to converting small molecules into usable chemicals such as ammonia and other hydrocarbons tend to be less efficient with a large carbon footprint and often rely on catalysts that are not earth abundant.[13,14] For example, the Haber-Bosch process uses high temperatures and pressures in order to convert N_2 to ammonia and the process uses about 2% of the world's total energy expenditure for this production.[15]

Therefore, it is desirable to utilize earth abundant metals, such as first row transition metals, in such catalytic processes to produce products in an energy efficient and low cost manner.[13]

First row transition metals, however, do not tend to undergo multi-electron redox processes, and instead tend to undergo 1-electron transfer pathways.[16] One method to enhance the multi-electron transfer capabilities of a system is through the use of multi-metallic complexes that can create cooperativity between metals to undergo multiple electron transfers, mimicking what occurs in metalloenzymes.[17–19] Metal-metal multiple bonds offer a rich environment where multiple redox events may occur and their formation is a synthetic way to overcome the propensity for 1-electron transfer pathways.

A synthetic challenge for inducing the formation of metal-metal bonds is designing new ligands that can facilitate the bonding between different metals. Due to the difference in size between early and late transition metals along a row and those belonging to different rows in the periodic table, forming new bonds can be a challenge. Lu and coworkers have recently designed and synthesized new ligand scaffolds that have resulted in many new complexes with multiple bonds between first row transition metals that have shown promising reactivity for small molecule activation.[20–25] Dunn et al. have also synthesized rare examples of complexes with a direct Zr-Ni or Hf-Ni bonds.[26] (Chapters 1-6).

Useful insight into the nature of these metal-metal bonds and the properties of these systems can be gained though quantum mechanical calculations. For example, calculations on the $[Re_2Cl_8]^{2-}$ molecule suggest a triple bond, rather than a formal

quadruple bond.[27] One of the benefits of theoretical calculations is the ability to aid in the understanding of experiment results and predict new experimental outcomes. Chapters 1-6 discuss the bonding and properties of various bimetallic complexes through the lens of both theory and experiment.

Chapters 1-2 discuss a new ligand, N,N,N-tris(2-(2-pyridylamino)ethyl)amine, which is able to bind homobimetallic complexes of cobalt and iron, as well as hetero-bimetallic complexes of cobalt, with manganese, iron, and copper with minimal metal scrambling, thus allowing for a systematic study of magnetic and electronic properties as the metal-metal bond changes. Calculations on the complexes reveal their highly multiconfigurational electronic structure and explain why the homo-nuclear diiron complex is set apart from the others in the series and also help elucidate the trends in magnetic coupling.

Chapter 3 discusses the electronic structure of a dichromium paddlewheel and its unique properties relative to other similar dichromium paddlewheels due to its suppression of delta bonding in favor of localized d_{xy} and $d_{x^2-y^2}$ orbitals, revealed though calculations, which suggest a possible diradical singlet ground state.

Chapter 4 discusses a ligand variant that is able to promote multiple bonds between chromium and iron and chromium and manganese. These complexes experience multiple redox processes, which are favorable for their use in small molecule activation. Calculations on the various complexes indicate how the bonding changes as the number of *d* electrons increases across the series and suggest that new ways to calculate bond

orders may be necessary when metal-metal bonds are a mixture of covalent and dative interactions.

Chapter 5 uses the same ligand as Chapter 4, but focuses on complexes with bonds between early-late transition metals, such as cobalt with chromium, vanadium, and titanium and the change in metal pairing influences the extent of N_2 activation. Similarly to Chapter 4, as the metal pairing includes atoms that are increasingly far apart on the periodic table, the bonding becomes less covalent.

Finally, Chapter 6 discusses another series of early-late complexes of nickel with titanium, zirconium, and hafnium that use a phosphinopyrrolide ligand that has weak nitrogen π-donors to enhance metal-metal interaction. Calculations suggest that similarly to the complexes in Chapters 4-5, the early-late metal-metal bonds tend to form dative bonds.

While many applications of quantum mechanical methods, including most of the results presented here, are in good agreement with experimental data, there are cases where due to the multiconfigurational nature of the wave function, the fidelity of computational results to experimental ones is dependent on the choice of method.[28–30] Simply put, a multiconfigurational wave function is one in which a single electron configuration is not sufficient to accurately describe the system and complexes containing transition metals are common examples. In fact, the homo-nuclear diiron complex from Chapter 1 is such an example. One of the outstanding challenges for quantum mechanical methods is the proper treatment of multiconfigurational systems.

Beyond complexes with transition metals, multiconfigurational systems also may include things such as biradicals, transition states, and excited states of atoms and molecules. Any system that cannot be described by a single Slater determinant falls into this category and are often described as "strongly correlated". The errors in the energy of a multiconfigurational system when treated with a single determinant are generally referred to as "static", "nondynamic" , or "left-right" correlation energy.[31–33]

Multi-configuration self-consistent field (MCSCF) methods are able to account for the static correlation these systems contain. The complete active space self-consistent field (CASSCF)[34] variant is a popular MCSCF method where all possible configurations of n electrons are generated in a subset of the N total orbitals. While CASSCF describes static correlation well, it does not include enough dynamic correlation energy for quantitative accuracy, which is related to short-range Coulomb repulsion whereby the electrons try and maximize their distance to reduce their mutual repulsion.[35] For accurate results, dynamic correlation is added in a post-SCF method, like multireference configuration interaction (MRCI)[36] or complete-active-space second order perturbation theory (CASPT2).[37] These methods fall under the general category of wave function theory (WFT) and suffer from unfavorable scaling with system size. Even though it would be possible to obtain the correct energy (within a certain size basis set) by distributing all n electrons in all N orbitals, called full configuration interaction (FCI) , this is not practically feasible and WFT methods can only be applied on small to medium sized systems.

Since every configuration that is generated in a FCI calculation does not contribute substantially to the wave function, a way to reduce the cost of the problem is by removing, what has been termed "deadwood" configurations, to reduce the size of the CI expansion.[38,39] Such MCSCF variants include the restricted active space (RAS)[40] or generalized active space (GAS)[41] self-consistent field methods and allow for an accurate treatment of static correlation at a lower cost than CASSCF, but still require a post-SCF calculation to recover dynamic correlation energy, which keeps the cost of the calculation high.

As the cost of WFT is one of the limiting factors in practical applications, a popular, more affordable, alternative method is Kohn–Sham density functional theory (KS-DFT).[42] KS-DFT is a single determinantal method that is formally exact, if the universal density functional were known. However, only approximate exchange-correlation functionals exist and they can depend on different quantities, including the electron spin density, their gradients, and the exchange energy density to obtain accurate energies. Since KS-DFT is a single determinantal method, the energies obtained from it may result from a broken symmetry solution that does not have the proper spin and spatial symmetry of the true wave function.[43] If the true spin densities were used in an approximate exchange-correlation functional from a multideterminantal wave function, the energies from the exchange-correlation functional would not be correct. This situation is termed the "symmetry dilemma".[44]

A classic example of this is the H_2 dissociation problem, where as the molecule dissociates, the wave function can no longer be described as a single determinant. To get

the correct dissociation limit with KS-DFT, each atom contains either one alpha or beta electron. However, this is not the true density, which can only be obtained by using multiple determinants. This can cause trouble in knowing which state is being approximated, as a broken symmetry solution can be a mixture of several spin states to obtain the lowest possible energy.[35,45]

Even though this is a fundamental problem with KS-DFT, this method can still be used to obtain good results for a variety of systems, including multiconfigurational ones (many results from chapters 1-6 are examples). However, a notable exception is the diiron complex in Chapter 1 and is discussed in more detail in Chapter 12. While the electronic structure and magnetic properties of the other bimetallic analogues were in agreement between WFT and KS-DFT, this was not the case for the diiron complex. In fact, a much larger and expensive RASSCF/RASPT2 was necessary to describe the wave function, with no agreement between KS-DFT and WFT.

Is there a way to accurately treat such multiconfigurational systems but do so at an affordable cost? A new approach that attempts to do so is called multi-configuration pair-density functional theory (MC-PDFT)[46] (Chapters 7-10). MC-PDFT essentially combines the power of a wave function based method, like CASSCF, for accurately describing the multiconfigurational nature of the wave function with a low cost density functional calculation to recover the missing correlation (see Chapter 7 for details).

There have been many other attempts to combine WFT and DFT.[47–90] One variety of WFT+DFT methods attempts to split the electron-electron interaction part of the Hamiltonian into long-range and short-range contributions. The short-range

correlation effects are taken into account by a density functional and the long-range effects are dealt with using a multideterminantal wave function method where a cut-off parameter is used to define the range-separation.[65] It can be troublesome, however, when long-range and short-range effects are not cleanly separable. Gräfenstein et al. took an approach that involved adding the energy from a wave function calculation with a DFT term. Despite efforts to minimize double counting of correlation effects between the two methods by scaling part of the DFT term, for example, but it is not straightforward and uniformly applicable to all types of systems.[60]

One of the essential problems addressed by MC-PDFT is that of double counting correlation energy where in MC-PDFT, only the kinetic energy and classical Coulomb energy are calculated by a multi-configuration wave function and the rest of the energy is recovered by the density functional term. Another problem addressed by MC-PDFT is that of the symmetry dilemma. It can be avoided by using the total density ρ and on-top pair density Π, which is the probability of finding two electrons in the same point in space, as suggested by Becke et al.[91] By using these spin-free quantities in what is called the on-top functional, there is no ambiguity in which state is being approximated, as the total density ρ and on-top pair density Π are derived from a multiconfigurational wave function. A current exchange-correlation functional may depend only the total density ρ, and the spin magnetization density m and the magnitudes, $\rho' \equiv |\nabla\rho|$ and $m' \equiv |\nabla m|$, of their gradients, where

$$\rho(\mathbf{r}) = \rho_\alpha(\mathbf{r}) + \rho_\beta(\mathbf{r}) \tag{1}$$

and

$$m(\mathbf{r}) = \rho_\alpha(\mathbf{r}) - \rho_\beta(\mathbf{r}) \tag{2}$$

and where ρ_α is the density of spin-up electrons, and ρ_β is the density of spin-down electrons. As previously mentioned, these quantities can give good energies as a result of using broken symmetry determinant. For a single determinatal wave function, there is a relationship between the spin quantities in eq. 1 and 2 and the spin-free quantities of ρ and Π using

$$m(\mathbf{r}) = \rho(\mathbf{r})\left[1 - R(\mathbf{r})\right]^{1/2} \tag{3}$$

where

$$R(\mathbf{r}) = \frac{4\Pi(\mathbf{r})}{\left[\rho(\mathbf{r})\right]^2} \tag{4}$$

with $R \leq 1$ everywhere in space. A multiconfigurational wave function may result in complex values of eq. 3 as R may be greater than one. While new functionals may need to be developed that only depend on ρ and Π, currently, MC-PDFT uses existing exchange-correlation functionals, where new quantities in eq. 1 and 2 are computed from eq. 3 and 4 in a process referred to as "translating". Since current exchange-correlation functionals depend on real valued quantities, when the situation where $R > 1$ is encountered, eq. 3 (and its gradient) are set to 0 (Chapters 7-8).

A problem with this approximation is that there is a discontinuity in the functional. This may be a problem in computing gradients, for example, as would be necessary in optimizing geometries. In order to have a continuous function with continuous first and second derivatives, a new class of on-top functionals is proposed,

that allows for the complete translation of ρ, Π, and their gradients, called "fully translated" functionals (Chapters 9). Its performance is tested on a wide variety of problems including atomization energies, barrier heights, reaction energies, and spin state splittings (Chapters 9-10).

As previously mentioned, one of the goals of MC-PDFT is to accurately treat multiconfigurational systems at an affordable cost. One way to reduce the cost is to use a multiconfigurational wave function that has a smaller CI expansion than CASSCF by placing certain restrictions on the configurations that can be generated, as is done in the RASSCF method and also the GASSCF method, where further restrictions may be defined. The separated-pair (SP) approximation[92] is a particular definition of GASSCF that is designed to minimize the number of configurations, while retaining the correct physics of the wave function (Chapter 10).

While it is important to understand how changes in the wave function affect the total density ρ and on-top pair density Π in MC-PDFT, these quantities are not just specific to this method and a fundamental understanding of how they change is insightful for understanding electron correlation in general. The on-top ratio *R* in eq. 4 can be used to illuminate the differences in a single determinantal and multideterminantal wave function. When $R \neq 1$ at a point in space, the wave function can no longer be described by a single determinant. For a simple case like H_2, the analytic expressions for ρ, Π, and *R,* can be derived for both a single determinantal Hartree–Fock wave function and a multideterminantal CASSCF(2,2) wave function. Chapter 11 analyzes these quantities

for the two wave functions as the molecule dissociates to better understand left-right correlation.

Ultimately, studying the basic quantities like ρ, Π, and R will help to fundamentally understand electron correlation and hopefully lead to useful improvements to methods, like MC-PDFT, so that multiconfigurational systems can be treated accurately. For example, this may be useful in understanding why the diiron complex discussed in Chapters 1 and 12 could not accurately be described with KS-DFT and required a large WFT calculation to reproduce the experimental results. Results with MC-PDFT show good fidelity with CASPT2 (Chapter 12). An accurate description of the physics of a system is especially important when moving to large systems that cannot be validated with many different levels of theory and a method like MC-PDFT has the potential to fill this need.

Chapter 1

Role of the Metal in the Bonding and Properties of Bimetallic Complexes Involving Manganese, Iron, and Cobalt

Reproduced in part with permission from

Role of the Metal in the Bonding and Properties of Bimetallic Complexes Involving Manganese, Iron, and Cobalt, Stephen J. Tereniak, Rebecca K. Carlson, Laura J. Clouston, Victor G. Young, Jr., Eckhard Bill, Rémi Maurice, Yu-Sheng Chen, Hyun Jung Kim, Laura Gagliardi, and Connie C. Lu**,** *Journal of the American Chemical, Society,* **2014** *136* (5), 1842-1855.

1.1 Overview

A multidentate, ligand platform is introduced that enables the isolation of both homo- and heterobimetallic complexes of divalent first-row transition metal ions such as Mn(II), Fe(II), and Co(II). By using a two-step metallation strategy, five bimetallic coordination complexes were synthesized with the general formula $MMCl(py_3tren)$, where py_3tren is the triply deprotonated form of *N*,*N*,*N*-tris(2-(2- pyridylamino)ethyl)amine. The metal-metal pairings include dicobalt (**1**), cobalt-iron (**2**), cobalt- manganese (**3**), diiron (**4**), and iron-manganese (**5**). The bimetallic complexes have been investigated by X-ray diffraction and X-ray anomalous scattering studies, cyclic voltammetry, magnetometry, Mössbauer spectroscopy, UV-Vis-NIR spectroscopy, NMR spectroscopy, combustion analyses, inductively coupled plasma optical emission spectrometry, and *ab initio* quantum chemical methods. Only the diiron chloride complex in this series contains a metal-metal single bond (2.29 Å). The others show weak metal-metal interactions (2.49 to 2.53 Å). The diiron complex is also distinct with a septet ground state, while the other bimetallic species have much lower spin states from $S = 0$ to $S = 1$. We propose that the diiron system has delocalized metal-metal bonding electrons, which seems to correlate with a short metal-metal bond and a higher spin state. Multiconfigurational wave function calculations reveal that, indeed, the metal-metal bonding orbitals in the diiron complex are much more delocalized compared to the orbitals of the dicobalt analogue.

1.2 Introduction

Heterometallic clusters are used as bioinorganic cofactors to perform diverse chemical reactions. They occur in MoFe and VFe nitrogenases, [NiFe] hydrogenases, purple acid phosphatases, Ni-[3Fe-4S] CO dehydrogenases, and class Ic ribonucleotide reductases (RNRs).[93–96] Many of these heterometallic cofactors pair a mid and late first-row transition metal, e.g. Fe and Ni, to promote the heterolytic activation of small molecules, e.g. H_2 and CO_2.[12] In contrast, Class Ic RNRs uses two *similar* metals, Fe and Mn, to tune the redox properties of the cofactor.[97,98] The heterometallic cofactor is unique to this subclass, as most class I RNRs use a classical diiron(II,II) active site with a neighboring tyrosine.[99] When the diiron cofactor reacts with dioxygen, a diiron(III,III)-

tyrosyl radical (i.e. 2Fe(III)-Y•) intermediate is formed, where the reactive hole equivalent is located on the amino acid. It is proposed that since Class Ic RNRs lack this tyrosine, an iron site is swapped for manganese to store the oxidizing equivalent as the Fe(III)Mn(IV) intermediate.[100–104] To better understand the different roles of iron versus manganese, Fe-Mn complexes have been targeted, but only a few, biomimetic Fe-Mn complexes have been reported.[105–107] A key challenge is the selective preparation and/or clean isolation of the heterometallic core when the metal centers are so similar.[106]

Beyond their bioinorganic relevance, heterometallic clusters may give rise to unusual magnetic and electronic properties. Indeed, Fe-Mn complexes have been studied for elucidating magnetic exchange interactions.[108–111] Betley and co-workers have shown that the homotrimetallic clusters, Fe_3, Co_3 and Mn_3, exhibit interesting magnetic behavior and are extending their studies to mixed-metal analogues.[112–115] Also, as in the case of Class Ic RNRs, swapping of metal sites with similar transition metals could prove a versatile strategy for tuning redox potentials. In related work, Agapie *et al.* have shown that the redox potentials of Mn_3-oxide clusters can be systematically tuned over 800 mV by covalently attaching redox- inactive metal centers of varying Lewis acidities.[116,117] Systematic studies of heterobimetallic species may provide great insight into structure-property relationships, and hold promise for achieving predictable and precise control of cluster properties through metal atom substitution.

Of note, nearly all these examples contain a bridging oxo, phenoxo, or amido ligand, which can greatly attenuate the metal-metal interaction. We have been interested in configuring bonds between first- row transition metals by using ligands that facilitate

metal-metal bonding.[21,22,118] Recently, use of multidentate ligands with two distinct binding sites enabled the synthesis of a rare, iron-cobalt heterobimetallic complex.[119] The same ligand also gave access to a related dicobalt complex. Both the iron-cobalt and dicobalt species have short metal-metal bonds and are high spin. However, attempts to extend the coordination chemistry to other similar metal pairings were unsuccessful.

Herein, we report a new ligand variant where three pyridyl groups are covalently attached to tris(2-aminoethyl)amine, or tren. The ligand, *N*,*N*,*N*-tris(2-(2-pyridylamino)ethyl)amine, or $H_3(py_3tren)$, has enabled the isolation of homo- and heterobimetallic complexes of cobalt, iron, and manganese. Five bimetallic chloride complexes, $MMCl(py_3tren)$ (Figure 1.1), have been isolated and characterized by a host of physical methods.

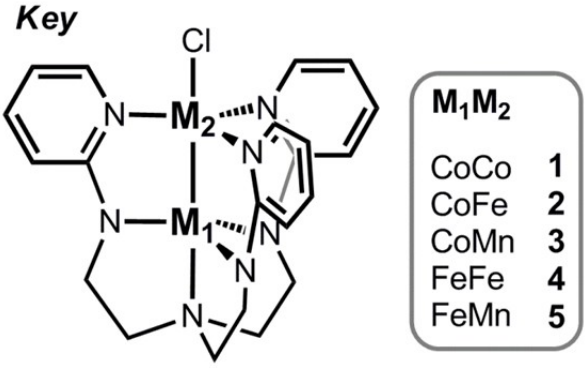

Figure 1.1 Metal pairings for the bimetallic complexes.

Since standard X-ray diffraction experiments do not differentiate between similar transition metals, the heterobimetallic species have been further examined by both X-ray anomalous scattering and inductively coupled plasma optical emission spectrometry (ICP-OES) for analysis of single crystals and the bulk material, respectively. Two of the three

heterobimetallic complexes (CoMn **3** and FeMn **5**) showed only a slight degree of metal-site mixing, while CoFe **2** is contaminated by CoCo **1** (8%). The good to high purity of these heterobimetallic complexes is remarkable given the propensity of high-spin Co(II), Fe(II), and Mn(II) ions to undergo ligand exchange and thus, effect metal scrambling.

This unprecedented family presents a unique opportunity to systematically study the effect of the metal identity on metal-metal bonding as well as on their electronic and magnetic properties. We have found that the metal-metal interactions are generally weak with the notable exception of the diiron chloride, **4**, which contains a bonafide iron-iron bond. With the exception of **4**, the electrochemical and magnetic properties of the bimetallic family can be rationalized by considering these bimetallic species as individual metals, or as localized spins that couple antiferromagnetically, giving lower spin states. In contrast, complex **4**, which has an $S = 3$ ground state, does not fit the localized description. Theoretical studies reveal delocalized metal-metal bonding in **4**, which is correlated with its different magnetic behavior. Finally, the isotropic magnetic couplings for the bimetallics were computed using density functional theory (DFT) with various exchange-correlation functionals.

1.3 Experimental Section

Details about the experimental synthesis and characterization protocol and calibration, including X-Ray crystallography, anomalous diffraction, NMR, and SQUID magnetometry can be found in Appendix 1.

1.4 Computational Methods

1.4.1 CASSCF/CASPT2 Calculations. All complete active space self-consistent field (CASSCF)[34] calculations, which were followed by perturbation theory to second order (CASPT2),[37] were performed with the MOLCAS 7.8 package[120] on experimental structures without symmetry constraints. Relativistic all-electron ANO-RCC basis sets were used for all elements.[121,122] Double-ζ quality (ANO-RCC-VDZP) basis sets were used for Co, Fe, Mn, N, and Cl atoms and minimal basis sets (ANO-RCC-MB) were used for C and H atoms. The following contractions were used: [5s4p2d1f] for the metals, [3s2p1d] for N and Cl, [2s1p] for C, and [1s] for H. To include relativistic effects in the calculation, the Douglas-Kroll-Hess Hamiltonian[123,124] was used. Resolution of identity combined with the Cholesky decomposition (RICD) was used to reduce the computational cost associated with the treatment of 2-electron integrals.[125] Lowest energy solutions were calculated for all spin states at the CASSCF level of theory and subsequent CASPT2 calculations were performed to recover more dynamical correlation, in which an imaginary level shift of 0.2 a.u. was used to prevent the occurrence of intruder states.[126]

The active spaces for the five complexes were chosen to include the ten valence 3*d* electrons plus two correlating 4*d* orbitals. The active spaces for **1**, **2**, **3** and **5** respectively, are 14 electrons in 12 orbitals or (14,12), (13,12), (12,12), and (11,12), respectively. Only twelve active orbitals were considered to obtain a reasonable level of accuracy while limiting the computational cost. Diiron **4** was a more challenging system and required the use of a larger active space. Thus, restricted active space (RAS) SCF calculations including a large configuration interaction space were performed, denoted by

(12,20)/(12,10)/2, where the first set of parenthesis corresponds to the total number of electrons in RAS1 and RAS2 and total number of orbitals in all RAS spaces. The second set of parentheses corresponds to the number of active electrons and orbitals in RAS2 and the final value of 2 indicates the number of allowed particles into RAS3.

The natural orbital occupation numbers were used for the evaluations of the effective bond order (EBO), which is calculated as the difference between the total occupancies of the bonding and anti-bonding molecular orbitals of the metal-metal bond divided by two.[27,127]

1.4.2 DFT Calculations. Density functional theory (DFT) calculations were performed to evaluate the magnitude of the isotropic magnetic couplings between the two metal centers in **1**, **2**, **3** and **5**. As proposed by Noodleman for weakly coupled systems, magnetic coupling constants in two-spin systems can be obtained from a high-spin and a spin- symmetry-broken solution within spin unrestricted formalisms.[45] The isotropic magnetic couplings are introduced via the phenomenological Heisenberg-Dirac-van-Vleck (HDVV) Hamiltonian:

$$\widehat{H}^{HDVV} = -2\sum_{ij} J_{ij}\widehat{\boldsymbol{S}}_i\widehat{\boldsymbol{S}}_j$$

where J_{ij} is the coupling constant, and $\hat{S}_i$ and $\hat{S}_j$ are the spin operators on the magnetic centers i and j. The difference in energy between the spin-broken symmetry (BS) solution and high spin (HS) solution are used to extract the coupling values. In Noodleman's approach, or the weak-coupling limit scheme, the BS solution is considered to be an ideal mixture of spin states corresponding to the appropriate Clebsch-Gordan

coefficients. This situation corresponds to the case in which there is no orbital overlap between the magnetic centers *i* and *j*. In the studied complexes, a partly covalent interaction between the (local) magnetic orbitals is possible, and thus we chose to use the intermediate coupling scheme proposed by Yamaguchi:[128]

$$(\langle S^2\rangle^{HS} - \langle S^2\rangle^{LS})J_{ij} = E_{BS} - E_{HS}$$

where $\langle S^2\rangle^{HS}$ and $\langle S^2\rangle^{BS}$ are the expectation values of the total spin squared operator coming from the spin unrestricted calculations. All DFT calculations were performed with the *Gaussian 09* program package.[129] The BS solutions have been obtained from the HS solutions by flipping the spins on one of the magnetic centers and breaking all symmetry and spin constraints up to a stable solution using the *stable=opt* keyword of *Gaussian*. Three functionals, one global hybrid (PBE0),[130,131] one range separated functional with long-range screened Hartree-Fock exchange (HSE),[132,133] and one range separated functional with a 100% of Hartree-Fock exchange at long range (LC- ωPBE)[134] were used together with the TZVP basis set on the Co, Mn, Fe Cl, and N atoms and the SVP basis set on the C and H atoms.[135,136]

1.5 Results and Discussion

1.5.1 Synthesis

The ligand, *N*,*N*,*N*-tris(2-(2-pyridylamino)ethyl)amine, or $H_3(py_3tren)$, was obtained in one step by heating tren with 2-bromopyridine (3.14 equiv.) and K_2CO_3 in DMSO (180 °C, 3 days). The slight excess of 2-bromopyridine was necessary to facilitate the work up, as the desired product is more easily separated from the tetra-substituted

byproduct than from the bis-substituted one. The reaction worked well on a 20 g scale; and, subsequent purification by column chromatography gave a moderate yield (14.2 g, 55 %) of clean $H_3(py_3tren)$ as a tan solid.

A five-membered series of homo- and heterobimetallic complexes featuring cobalt, iron, and/or manganese was then rapidly assembled using the two-step metallation strategy depicted in Figure 1.2. Deprotonation of $H_3(py_3tren)$ with 3 equiv. of benzylpotassium (abbreviated as KBn) followed by metathesis with $CoCl_2$ and $FeCl_2$ generated the mononuclear precursors, K[Co(py_3tren)] and K[Fe(py_3tren)], respectively. A crystal structure of K[Co(py_3tren)] shows that the cobalt center is exclusively coordinated by the tris(amido)amine donors, leaving the pyridine donors free to bind a second metal. Indeed, K[Co(py_3tren)] can be reacted with $CoCl_2$, $FeCl_2(THF)_{1.5}$, or $MnCl_2(THF)_2$ to form bimetallic CoCoCl(py_3tren) (**1**), CoFeCl(py_3tren) (**2**), or CoMnCl(py_3tren) (**3**), respectively. Similarly, the mononuclear iron precursor, K[Fe(py_3tren)], can be mixed with $FeCl_2(THF)_{1.5}$ or $MnCl_2(THF)_2$ to produce FeFeCl(py_3tren) (**4**) and FeMnCl(py_3tren) (**5**), respectively. The homobimetallic species **1** and **4** were synthesized at rt. On the other hand, the second metallations for the heterobimetallic complexes were conducted at much lower temperatures of −50 °C to impede metal scrambling in the two distinct binding sites (vide infra).

Of note, we did observe significant metal scrambling during the attempted synthesis of FeCoCl(py_3tren), which is a structural isomer of **2**. The metallation reaction of mono-iron with $CoCl_2$ gave a mixture of dicobalt **1**, diiron **4**, and cobalt-iron **2** (by ^{1}H NMR). In contrast, the metallation reaction of mono-cobalt with $FeCl_2(THF)_{1.5}$ proceeds

quite cleanly to **2**. Based on these results, we believe that complex **2** is the thermodynamically favored isomer, and that attempts to kinetically prepare the higher energy isomer are unsuccessful because of the lability of high-spin M(II) ions in these binding sites.

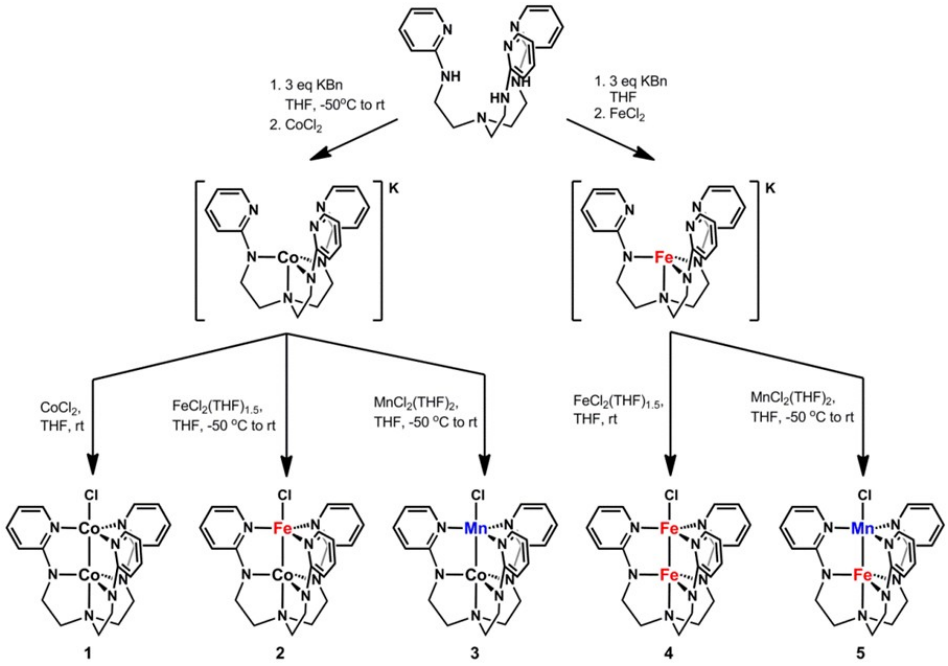

Figure 1.2. Two-step metallation reactions: (1) synthesis of K[Co(py_3tren)] and K[Fe(py_3tren)]; and (2) synthesis of M1M2Cl(py_3tren) complexes **1-5.**

1.5.2 NMR Spectroscopy

Each of the five bimetallic compounds has been characterized by NMR and UV-Vis-NIR spectroscopy. Proton NMR spectra for all the bimetallics contain six resonances, which is consistent with C_{3v} symmetry in solution (Figure 1.3). At rt, the complexes also appear to be paramagnetic based on the isotropic peak shifts. Interestingly, dicobalt **1** has the smallest range of proton chemical shifts from −1.6 to 21.7 ppm, while diiron **4** has by far the largest range from −15.7 to 168 ppm.

The protons of the tren backbone can be distinguished from those of the pyridyl ring by the relative peak integrations of ^{2}H and ^{1}H, respectively. The pyridyl protons can be further differentiated by using two-dimensional NMR techniques. Correlation spectroscopy (COSY) of dicobalt **1** showed all the major cross peaks, including $\alpha-\beta$, $\beta-\gamma$, and $\beta'-\gamma$. Unfortunately, the $\alpha-\beta$ cross peak was not observed for cobalt-iron **2** or iron-manganese **5**; and, *no* cross peaks were detected for **3** and **5**.

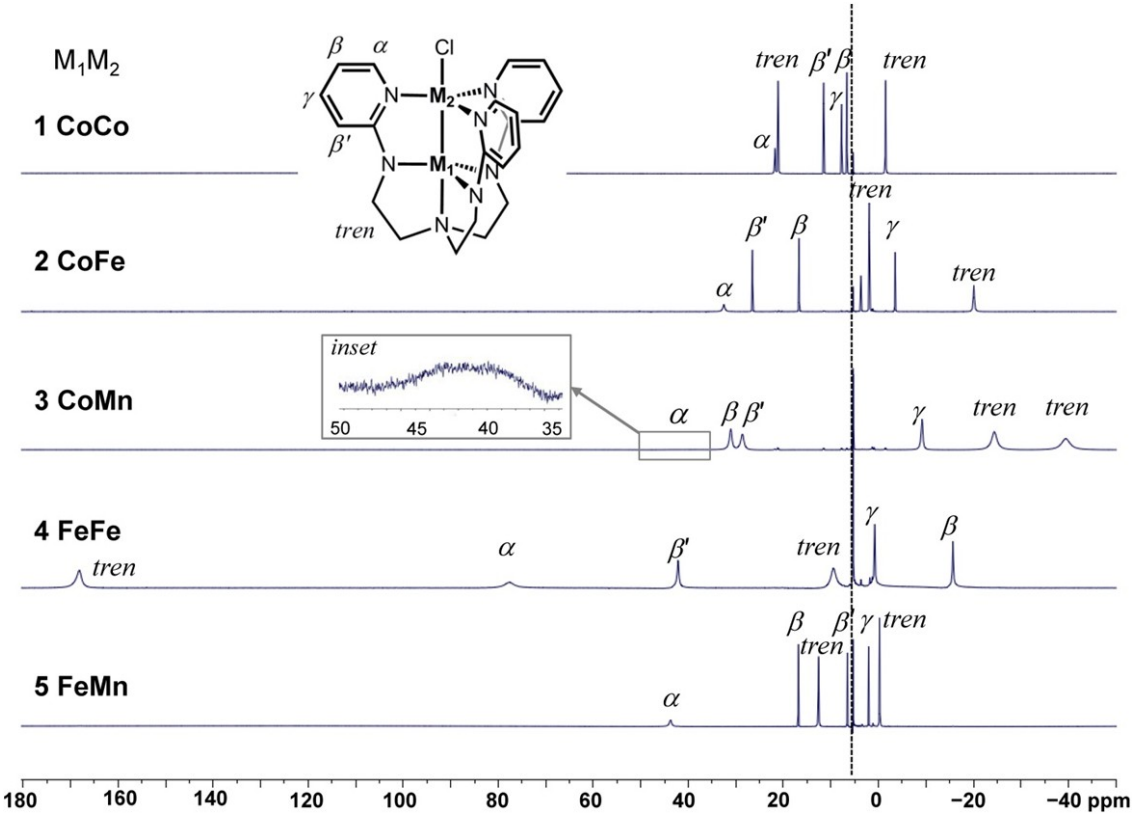

Figure 1.3. Stacked plot of the ^{1}H NMR spectra of **1-5** (500 MHz, CD_2Cl_2). Inset shows a close-up of a broad peak, assigned as the proton in **3**. The residual solvent peaks are marked by the dotted line.

Since the loss of coupling information often accompanies paramagnetic peak broadening, we performed inversion recovery experiments to measure the spin-lattice

relaxation times (T_1). The T_1 values and proton assignments are shown in Table 1.1. The α-protons of the pyridyl ring, which are the most downfield peak (except in the case of diiron **4**), have the shortest T_1 relaxation times of all the proton types. At the other extreme, the γ-protons, which are located farthest from *any* metal center, have the longest T_1 values. The specific assignments of β and β' protons are obvious only in the case of **1** (based on COSY), but they are ambiguous in the other bimetallic complexes. As the β' proton is located closer to M_1 (4.5 to 4.6 Å) than β is to M_2 (~5.0 Å), we assign the resonance with the slightly shorter T_1 to β', which is independently confirmed for **1**. Interesting, the bimetallic complexes can be subdivided into two categories based on their T_1 values: **1**, **2**, and **5** relax more slowly compared to **3** and **4**. Of interest, the faster relaxation times appear to be correlated with the overall spin state, $S_{tot} > ½$ (vide infra), rather than the identity of the metal ion(s).

Table 7.1. Proton NMR assignments of **1-5** with chemical shifts (ppm) and T_1 (ms).

Cpd.	(T_1)	(T_1)	(T_1)	′(T_1)	*tren* (T_1)
1	21.7 (5.6)	6.7 (95)	7.7 (255)	11.5 (80)	20.9 (15), −1.6 (15)
2	32.5 (1.4)	16.8 (69)	−3.6 (105)	26.6 (46)	1.7 (33), −20.3 (29)
3	40.0 (*nd*)[a]	31.1 (1.9)	−9.2 (3.7)	28.6 (1.6)	−24.4 (1.3), −39.4 (1.1)
4	79 (*nd*)[a]	−15.7 (5.1)	0.78 (8.0)	42 (2.5)	168 (0.65), 9.5 (0.67)
5	43.7 (1.0)	16.8 (57)	2.0 (67)	6.5 (30)	−0.3 (16), 12.6 (7.8)

[a] *nd* = not determined because of peak broadness.

1.5.3 UV-Vis-NIR Spectroscopy

All the coordination complexes, both mono- and dinuclear, are colorful. The mononuclear cobalt complex is bright green, and its bimetallic derivatives are green-

brown for dicobalt **1**, red for cobalt-iron **2**, and green-yellow for cobalt-manganese **3**. In the iron series, the mononuclear iron species is yellow, while diiron **4** is dark red, and iron-manganese **5** is orange.

Of interest, all complexes show intense bands in the UV-visible region and weak bands in the near-infrared region (NIR) (Figure 1.4). In the cobalt series, mononuclear cobalt and complexes **1** – **3** have an intense peak at ~315 nm ($\varepsilon > 22{,}000\ M^{-1}cm^{-1}$) with a shoulder at ~350 nm. A second shoulder is discerned in two complexes, the mono-cobalt (386 nm, $\varepsilon = 6{,}700\ M^{-1}cm^{-1}$) and cobalt-manganese (397 nm, $\varepsilon = 6{,}780\ M^{-1}cm^{-1}$). The bimetallics **1** – **3** also have a visible band at ~450 nm ($\varepsilon = 7{,}480$ to $8{,}950\ M^{-1}cm^{-1}$), which is notably absent for mono-cobalt. Of interest, this band undergoes a blueshift from **1** (450 nm) to **2** (448 nm) to **3** (435 nm). Hence, this band is proposed to correspond to a metal-to-metal intervalence charge transfer, namely $Co \rightarrow M_2$, as the energy decreases from M_2 = Co to Fe to Mn, which is consistent with the trend in the metal ions' electronegativities. Finally, mono-cobalt and complexes **1** – **3** have NIR bands of similar intensities, $\varepsilon \sim 100\ M^{-1}cm^{-1}$. The main NIR band shifts to the blue from mono-cobalt to **2** ~ **3** to **1**. The NIR band is proposed to arise from an intrametal d-d transition.

In the iron series, the UV-Vis region is remarkably similar for mono-iron and the bimetallics **4** and **5**. Of note, the intensities of the bands in the UV-Vis are practically identical for mono-iron and iron- manganese **5**, but are greater for diiron **4**, which suggest that the doubling of the intensity of the broad visible band may be due to the presence of two iron centers. The broad, visible band also detectably redshifts from mono-iron to bimetallic **4** and **5**. Unlike the cobalt series, there is no indication of any unique

absorption feature that can be attributed to a metal-metal intervalence charge transfer. Like the cobalt series, the NIR bands in iron series also undergo a blueshift from mono-iron to bimetallic **4** and **5**, with the NIR band for the homobimetallic diiron **4** gaining appreciable intensity.

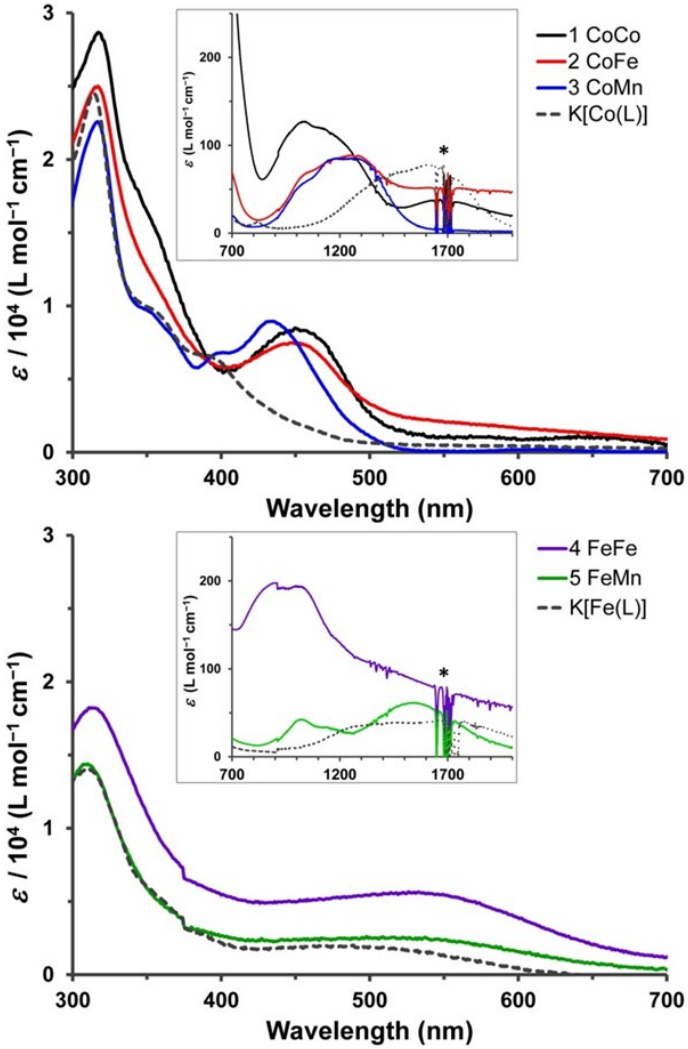

Figure 1.4. (top) UV-Vis plots of K[Co(py_3tren)] and cobalt-containing complexes **1-3**. (bottom) UV-Vis plots of K[Fe(py_3tren)] and iron-containing complexes 4 and 5. Insets show the Vis-NIR region. Spectra were collected as solutions in CH_2Cl_2. The asterisk denotes artifacts from solvent subtraction.

1.5.4 X-ray Diffraction Studies

Single crystals of **1** – **5** were examined by X-ray diffraction. Dicobalt **1** crystallized in the orthorhombic space group $P2_12_12_1$, while complexes **2** – **5** all crystallized in the monoclinic space group $P2_1/n$ with similar unit cells. The coordination geometry at each metal center is trigonal bipyramidal with an axial chloride ligand bound to the pyridine-coordinated metal, i.e. M_2 (Figure 1.5).

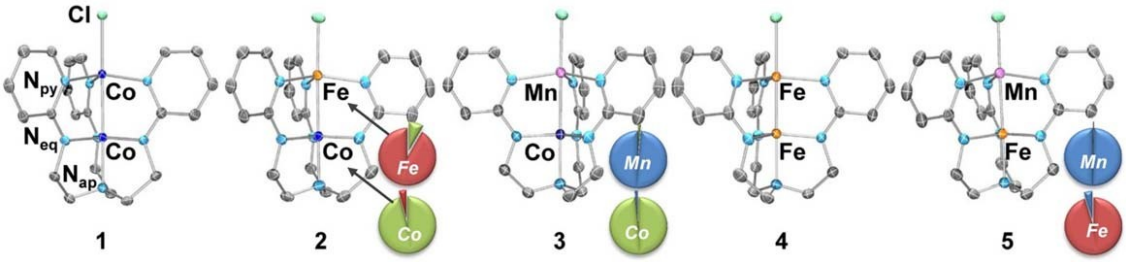

Figure 1.5. Solid-state structure of **1**−**5**. Thermal elliposids are shown at 50% probability. Protons are omitted for clarity. For the heterobimetallic species, the percentages of each metal (Co in green, Fe in red, and Mn in blue) at each binding site (as determined by X-ray anomalous dispersion) are depicted as pie charts.

Unfortunately, standard X-ray data cannot distinguish between metals of similar atomic numbers. To address the complicated issue of metal-site scrambling, we have conducted X-ray anomalous scattering experiments for the heterobimetallic complexes (vide infra). Nonetheless, some clear trends are observed in the collective geometrical data that support the metal assignments (Table 1.2). For instance, the cobalt-apical amine (N_{ap}) bond distance remains essentially unchanged at 2.01 to 2.02 Å in the cobalt series, i.e. when M_1 = Co. The iron-N_{ap} bond lengths in **4** and **5** are identical at 2.05 Å, and gratifyingly, they are slightly longer than those for Co-N_{ap}, which is consistent with the larger covalent radius of Fe(II) versus Co(II). Likewise, the bond distances between the bottom metal and the equatorial nitrogen atoms (i.e. M_1−N_{eq}) increase from 1.89 − 1.90 Å

for M_1 = Co (in **1** – **3**) to 1.93 − 1.94 Å for M_1 = Fe (in **4** and **5**). For the metal-ligand bonds lengths around the top metal center, especially M_2−Cl, no clear trend was readily discerned as M_2 can be Co, Fe or Mn. One notable finding is that when M_2 = Mn (in **3** and **5**), the M_2−N_{py} (where py = pyridine) and M_2−Cl bond distances are essentially identical.

Table 1.8. Geometrical parameters, including bond lengths (Å) and angles (°) for complexes **1-5.**[a]

	1	2	3	4	5
M_1-M_2 (Å)	2.4986(4)	2.4913(3)	2.5312(4)	2.2867(5)	2.5283(3)
r[b]	1.08	1.07	1.09	0.98	1.08
M_1-N_{ap} (Å)	2.012(1)	2.010(1)	2.018(2)	2.054(1)	2.053(1)
M_1-N_{eq} (Å)[c]	1.885±0.004	1.894±0.006	1.903±0.005	1.931±0.007	1.940±0.007
M_2-Cl (Å)	2.3487(5)	2.3455(4)	2.361(2)	2.3759(6)	2.3559(5)
M_2-N_{py} (Å)[c]	2.074±0.007	2.107±0.008	2.163±0.008	2.11±0.01	2.179±0.007
M_1-M_2-Cl (°)	177.79(2)	177.36(1)	177.92(2)	178.14(2)	177.26(2)

[a] Estimated standard deviations (esd) are provided in parentheses. [b] *r* = ratio of M_1−M_2 bond distance to the sum of M_1 and M_2 single-bond radii. [c] M_1−N_{eq} and M_2−N_{py} bond lengths are reported as averages ± standard deviations.

Of central interest, the M_1−M_2 bond lengths would give insight into the nature of the metal-metal bonding in these different metal pairs. The longest M_1−M_2 distances (2.53 Å) are observed in cobalt- manganese **3** and iron-manganese **5**. Intermediate metal-metal bond distances of 2.49 − 2.50 Å are found in dicobalt **1** and cobalt-iron **2**, while the diiron complex **4** has by far the shortest metal-metal bond distance of 2.29 Å in this series. Because the expected differences in metal covalent radii complicate any absolute comparisons, Cotton *et al.* introduced the formal shortness ratio[11] (denoted as *r* in Table 1.2), where the metal-metal bond lengths are normalized by the sum of the two metals' single-bond radii. With the notable exception of diiron **4**, the *r* values for all the other

bimetallic complexes are significantly greater than one (1.07 to 1.09), suggesting that the metal-metal covalent interactions are weak at best. In the case of diiron **4**, the *r* value of 0.98 is near the expected value of 1.0 for a single metal-metal bond. Hence, diiron **4** is outstanding in this series in that it has a bona fide metal-metal bond. Of interest, an extremely short, isolable iron-iron bond of 2.13 Å is found in a diiron(I,I) bis(guanidinate) complex by Jones *et al*.[137] The authors proposed the iron centers to be multiply bonded and reported a large magnetic moment of 7.95 μB.

The heterobimetallic species **2**, **3**, and **5** were investigated by X-ray anomalous scattering to assess the purity of each metal-binding site, and consequently, to determine the selectivity of our metallation strategy. This technique differentiates metals with similar number of electrons by exploiting the differences in the metals' K-edge energies. As the X-ray wavelength approaches the metal's K edge energies, the anomalous terms of the atomic scattering factor change rapidly (Figure A.1). Using a synchrotron source, a series of anomalous datasets are collected to span the metals K-edges, including the edge energies (λ_{edge}) as well as 50 eV above and below it ($\lambda_{edge} \pm 50$ eV).[138] In addition, an additional dataset is collected at high energy (30 keV) to determine a high-resolution structure. For reasons detailed in the experimental section, the measurements taken at lower energy ($\lambda > \lambda_{edge}$) are more reliable, and so, they were used exclusively in solving the metal occupancies at each binding site.[139] Recently, Betley *et al.* reported a similar methodology.[112] A unique aspect of our approach is that we simultaneously analyze the anomalous datasets and perform a least-square refinement[140] to determine metal occupancies.

The results of the metal occupancies are given in Table 1.3 and graphically portrayed as pie charts in Figure 1.5. Gratifyingly, very little metal-mixing is observed. For compounds **3** and **5**, both metal-binding sites are substitutionally pure (≥ 95%), and thus, we expect these complexes to be highly homogeneous.

Table 1.9. Compositions of the metals (Co, Fe, Mn) at the unique binding sites (M_1, M_2) in the heterobimetallic complexes (**2, 3, 5**) as determined by X-ray anomalous scattering studies.[a]

Compound	M_1	M_2	purity (%)	M_1:M_2
				Co:Fe
2	Co 0.957(11)	Fe 0.916(11)	88	1.04 : 0.96
	Fe 0.043(11)	Co 0.084(11)		(1.01 : 0.99)
				Co:Mn
3	Co 0.983(12)	Mn 0.985(11)	97	1.00 : 1.00
	Mn 0.017(12)	Co 0.015(11)		(0.99 : 1.01)
				Fe : Mn
5	Fe 0.952(16)	Mn 0.995(15)	95	0.96 : 1.04
	Mn 0.048(16)	Fe 0.005(15)		(0.92 : 1.08)

[a] Metal ratios of the *bulk* sample as determined by ICP-OES are given in parenthesis.

While the main component is quite clearly the expected product, $M_1M_2Cl(py_3tren)$, other related species may be present as minor impurities, including its constitutional isomer, $M_2M_1Cl(py_3tren)$, and the two homobimetallic species. If we assume statistical mixing of the M_1/M_2 populations at the two independent sites, then the overall purity of the $M_1M_2Cl(py_3tren)$ is estimated to be 97 and 95% for **3** and **5**, respectively. Using the same analysis, complex **2** has an overall purity of 88% with a significant presence of dicobalt **1** (8%). This suggests that either dicobalt **1** is carried over from the first metalation step and/or that iron and cobalt ions exchange during the second metalation. Because of the high purity of the related cobalt-containing complex **3**, we conclude it is the mixing of the similar iron and cobalt centers during the second metalation of **2** that generates the

dicobalt impurities. While these results are promising for single crystals, it does not assess the purity of the bulk material. Hence, we sought to independently verify the metal composition of the bulk using inductively coupled plasma optical emission spectrometry (ICP- OES). To our delight, the metal compositions are in excellent agreement with those determined by the anomalous measurements (Table 1.3, last column).

1.5.5 Electrochemistry

All the bimetallic coordination complexes have been characterized by cyclic voltammetry in 0.1−0.4 M [nBu$_4$N]PF$_6$/THF. To aid the interpretations of the cyclic voltammogram (CVs), we have also examined the neutral ligand and the monometallic complexes. The ligand, H$_3$(py$_3$tren), shows an irreversible oxidation at E_{pa} = 0.5 V, which shifts cathodically to 0.3 and −0.1 V in mono- iron and mono-cobalt, respectively. The mononuclear species also have an additional, quasi-reversible oxidation at −0.5 V for cobalt and −1.4 V for iron, where the mono-iron is significantly easier to oxidize than mono-cobalt by nearly 1 V. No reductive processes were observed for H$_3$(py$_3$tren) or the monometallic species.

The CVs of the bimetallic complexes are shown in Figure 1.6, with the corresponding redox potentials given in Table 1.4. Complexes **1** − **5** all show an irreversible oxidation at E_{pa} = 0.34 to 0.44 V, which is attributed to a ligand-based oxidation (not shown in figure). In the cobalt series, complexes **1**, **2**, and **3**, all have one quasi-reversible/irreversible oxidative process at $E^{\circ\prime}$ (or E_{pa}) = 0.0 V. Because of the similarity in the redox potentials of mono-cobalt and of the cobalt series, the redox reaction occurring at 0 V is likely to be Co(II)/Co(III) in nature. The iron series,

consisting of **4** and **5**, differ from the cobalt series in that two additional oxidative processes are observed at $E^{\circ\prime}$ (or E_{pa}) = −0.40 and 0.19 V. Presumably, the former redox potential corresponds to an Fe(II)/Fe(III) couple, while the latter may suggest Fe(III)/Fe(IV). In contrast, the mono-iron showed no indication of a second iron-based oxidation.

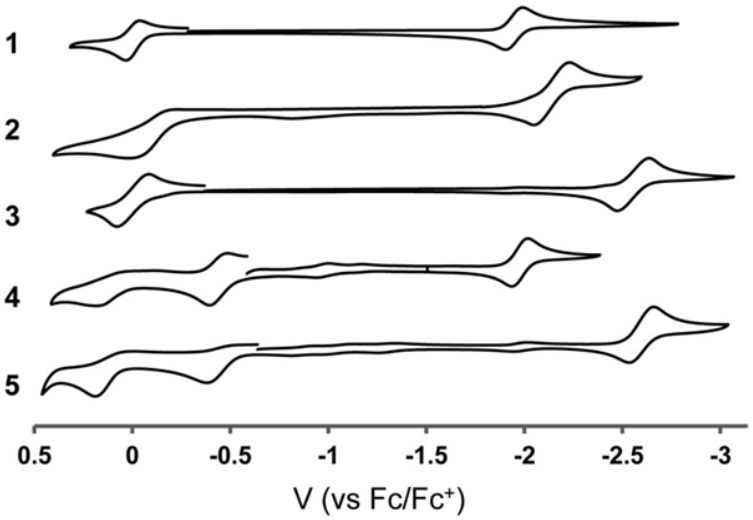

Figure 1.6. Cyclic voltammograms of **1-5** in 0.4 M [*n*Bu4N]PF6/THF at 300 mV/s (except for 2, 0.1 M [*n*Bu4N]PF6/THF at 10 mV/s).

Table 1.10. Reduction and oxidation potentials (V) of **1-5**.[a]

Cpd.	oxidations ($E^{\circ\prime}$ or E_{pa})[b]	reduction ($E^{\circ\prime}$)
1	0.01, *0.44*	−1.95
2	*0.02*, *0.34*	−2.06
3	−0.02, *0.41*	−2.55
4	−0.42, *0.19*, *0.39*	−1.98
5	*−0.38*, *0.19*, *0.43*	−2.61

[a] vs. Fc/Fc^+ [b] E_{pa} denoted in italics

Complexes **1** − **5** each exhibit a single quasi-reversible/reversible reductive process. Due to the lack of any similar processes in the monometallic species, we believe that these reductions are localized at the top metal, i.e. M_2. In support of this hypothesis,

when M_2 = Mn as in cobalt-manganese **3** and iron- manganese **5**, the reduction potentials are nearly identical at −2.6 V. Also, in the cobalt series, the reduction potentials shift as a function of M_2, from −1.95 V for **1** (M_2 = Co) to −2.06 V for **2** (M_2 = Fe) to −2.55 V for **3** (M_2 = Mn). While these potentials correspond to the one-electron M(II)/M(I) redox couples, they follow the same trend as the two-electron redox potentials for the M(II) ions, where M(II)(*aq*) + 2e → M(*s*). However, when M_2 = Fe, the reduction potentials are slightly different for **2** (−2.06 V) and **4** (−1.98 V). Perhaps, this difference arises from the dissimilarity of the metal-metal interactions in **2** versus **4**, where the latter has a more delocalized metal-metal bond compared to the former.

To summarize the CV studies, bimetallic complexes **1** − **5** can undergo multiple electron transfers, and these reactions appear to be primarily localized at the individual metal centers. Specifically, the first oxidative processes are associated with M_1; and, their potentials correspond to M_1(II)/M_1(III) redox couples. The potentials of the reductive processes, on the other hand, change with M_2 and are consistent with the M_2(II)/M_2(I) redox couple. In these complexes, the metal-metal interactions must be sufficiently weak so to exhibit similar electron-transfer behavior as their individual metal centers.

1.5.6 Mössbauer Spectroscopy

The iron-containing bimetallic complexes were further characterized by ^{57}Fe Mössbauer spectroscopy (0 T, 77 K). As expected, one major doublet was observed for the heterobimetallic compounds **2** and **5**, while two main signals were observed for diiron **4**, which is consistent with its two unique iron sites (Figure 1.7, Table 1.5). In cobalt-iron **2**, the iron center has an isomer shift (δ) of 0.88 mm/s with a quadrupole splitting (ΔE_Q) of

2.62 mm/s. As expected, these parameters are typical of high-spin Fe(II). However, in iron-manganese **5**, both δ and ΔE_Q have significantly decreased to 0.46 mm/s and 1.69 mm/s, respectively.

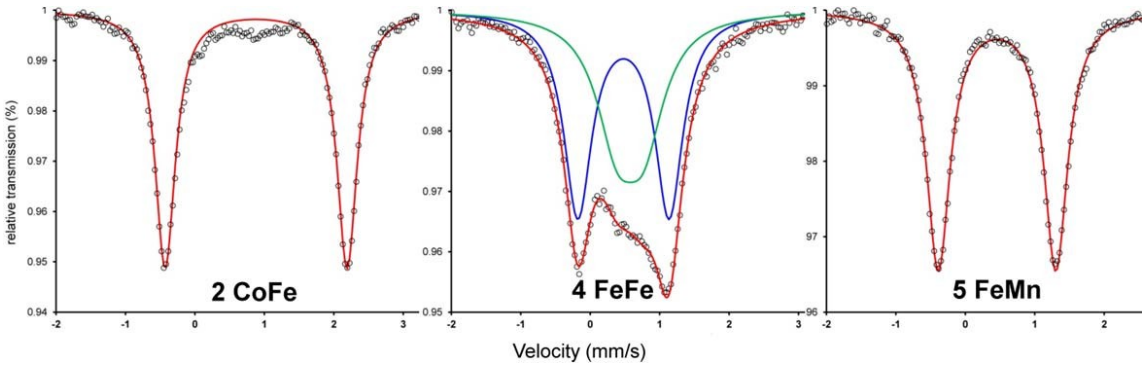

Figure 1.7. Zero-field Mössbauer spectra of **2** (*left*), **4** (*center*), and **5** (*right*) at 77 K. The experimental data is plotted as dots. Total fits are shown as red lines. Mössbauer parameters, δ (ΔEQ) in mm/s, are for **2**, 0.88 (2.62); for **4**, 0.58 (0.38) (in green) and 0.48 (1.31) (in blue); and for **5**, 0.46 (1.69) mm/s.

A similar drop in isomer shift is observed for both iron centers in diiron **4** (δ = 0.58 and 0.48 mm/s). Although these isomer shifts are atypically low for $S = 2$ Fe(II) centers, they are also unusually high for either $S = 1$ or $S = 0$ Fe(II). In the literature, decreased isomer shifts have been reported for systems where the iron center is engaged in metal-metal bonding. For example, trigonal diiron(II,II) complexes with iron-iron distances ranging from 2.58 to 2.87 Å have isomer shift values ~0.60 mm/s.[114] A tri-iron(II,II,II) system with short metal-metal bond distances of 2.30 Å (comparable to **4**) has an even lower isomer shift of 0.38 mm/s, although this could also be attributed to the overall lower spin, $S = 1$.[141]

For diiron **4**, the two Mössbauer signals can be tentatively assigned by comparing to **5**. Specifically, the doublet centered at 0.48 mm/s in complex **4** is remarkably similar to

that of **5**. Since **4** and **5** have a common iron site at M_1, we believe that this doublet for **4** corresponds to M_1, and that the other signal at 0.58 mm/s belongs to M_2. Although complexes **2** and **4** share a common iron site at the M_2 position, their isomer shift values are dramatically different, and this variation may be attributed to the significant metal-metal bonding in **4** that is not present in **2**.

Table 1.11. Zero-field ^{57}Fe-Mössbauer parameters (mm/s) for **2**, **4**, and **5**.

Cpd.	δ	ΔE_Q	line width [a]
2	0.88	2.62	0.35
4	0.58	0.38	0.72
	0.48	1.31	0.48
5	0.46	1.69	0.42

[a] Modeled as two Lorentzian lines with equal intensities and widths

1.5.7 Magnetic Susceptibility

We have conducted variable temperature magnetic susceptibility measurements of the bimetallic complexes **1** – **5** under an applied dc field of 1 Tesla. The magnetic susceptibility (χ) data are plotted as χT versus T, where T is temperature, in Figure 1.8.

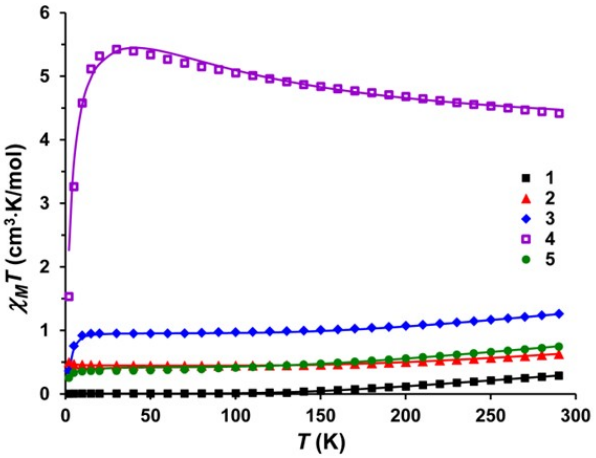

Figure 1.8. Temperature dependence of the magnetic susceptibility, plotted as $\chi_M T$, of **1** (black solid squares), **2** (red triangles), **3** (blue diamonds), **4** (purple, open squares), and 5 (green circles) at 1 Tesla, from 2 to 290 K. Solid lines represent the best fit.

All the χT plots show temperature dependence and appear to reach ground state configurations in the low temperature range of 15 to 50 K. Below 15 K, changes in χT may arise from several factors, including field saturation, magnetic anisotropy, and/or intermolecular effects. As we were primarily interested in understanding metal-metal exchange interactions, which are evident at higher T, no additional measurements were made to elucidate the factors that manifest themselves in the temperature regime below 15 K.

At low T (from 15 to 50 K) χT approaches 0 for dicobalt **1**, indicating a singlet ground state. For cobalt-iron **2** and iron-manganese **5**, χT plateaus to 0.36 and 0.45 cm^3K/mol at low T, respectively. These values are near 0.375 cm^3K/mol, the expected value for $S = ½$. For cobalt-manganese **3**, χT decreases slowly to 0.95 cm^3K/mol at low T, which is consistent with $S = 1$ (for $g = 2$, $\chi T = 1.0$ cm^3K/mol). One general explanation is that the ground spin states are the net outcome of two high-spin M(II) spins that are antiferromagnetically coupled, where the overall spin state, S_{tot}, is equivalent to $S_1 - S_2$. Thus, when the two M(II) ions are both cobalt like in **1**, a singlet state is generated. When the two M(II) ions belong to neighboring groups of the periodic table, as in **2** and **5**, a doublet spin state results. Finally, a triplet state is derived for **3**, where the group numbers of the two M(II) ions differ by two.

For **1**, **2**, **3**, and **5**, χT rises slightly with increasing temperature. The increase in χT suggests thermal population of higher spin states, which likely arise from the decoupling of the two high-spin M(II) centers. By using a two-spin Hamiltonian to simulate the magnetic data, we determined the average *g* values and antiferromagnetic exchange

coupling constants (J) for these various metal-metal interactions. These parameters are provided in Table 1.6. We find that the magnitude of the coupling constants decreases significantly (> 50 cm^{-1}) from dicobalt **1** to cobalt-iron **2** to iron-manganese **5** with a smaller decrease of 25 cm^{-1} to cobalt-manganese **3**.

Table 1.12. Magnetic couplings, anisotropy constants, and g-values of **1-5**.[a]

Cpd.	S_{tot}	S_1	S_2	J (cm^{-1})	g_1	g_2	$D_{1,2}$[b] (cm^{-1})	θ_W[b] (K)
1	0	1.5	1.5	−231	2.16	2.16	0	0
2	0.5	1.5	2.0	−184	2.00	2.09	0	0.3
3	1.0	1.5	2.5	−120	2.06	2.00	2.5[c]	0
4[d]	*3.0*	*2.0*	*1.0*	*+14*	*2.00*	*2.00*	*0*	*−3.0*
5	0.5	2.0	2.5	−145	2.00	2.06	0	−1.5

[a] Some spectra have been corrected for temperature-independent paramagnetism (TIP). See experimental section. [b] As discussed in the text, we cannot differentiate between magnetic anisotropy arising from zero-field splitting (D) or intermolecular interactions (θ_W) below 15 K, so these values are not well parameterized. [c] D_1 and D_2 were arbitrarily set to be equal. [d] Parameters are from imposing a *localized* treatment, though we propose that a *delocalized* treatment is more appropriate for **4**.

Notably, diiron **4** stands apart from the other members in that it exhibits higher χT values, peaking to 5.42 cm^3K/mol at 30 K. This value is near the spin-only value for $S = 3$ ($\chi T = 6.0$ cm^3K/mol). Coincidentally, a χT value of 6.0 cm^3K/mol is also expected for two non-interacting $S = 2$ spins, e.g. high- spin Fe(II). However, the latter interpretation is inconsistent with the temperature dependence of χT, which decreases with increasing temperature. It is further improbable that **4** should have non-interacting spins when it is the only complex in this series with a bonafide metal-metal bond. Therefore, the magnetic data suggests a very different type of magnetic interaction in **4**.

Magnetic behavior of complexes featuring multiple metal centers can be complex, as several exchange mechanisms are possible, including direct exchange (via

metal-metal), superexchange (via a bridging ligand), and double exchange. Double exchange pathways, which may occur in mixed-valent systems, are easily ruled out in these systems since the metal ions are in the same oxidation states of +2. While some of the heterobimetallic systems, e.g. cobalt-iron **2**, may superficially resemble mixed-valent systems (with a d^7-d^6 electron count), it is unreasonable for an electron to move between the metal ions as the alternate d^6-d^7 configuration would formally correspond to Co(III)-Fe(I).

In systems featuring weak metal-metal interactions, direct and super- exchange pathways can compete. With the exception of **4**, the metal ions in these bimetallic systems couple antiferromagnetically. We conclude at this stage that the primary pathway is superexchange. Our reasoning is based on the fact that metal-metal interactions in complexes **1**, **2**, **3**, and **5** are weak at best. If direct exchange was dominating, then complex **4**, which should have the best *d*-*d* orbital overlap, should strongly couple antiferromagnetically, which is not observed. Moreover, Goodenough-Kanamori rules predict that single electrons occupying *d*-orbitals of δ-symmetry (with respect to the M-M axis), would couple antiferromagnetically through the π-system of the pyridyl-amide bridge. On the other hand, it is not obvious how single electrons occupying *d*-orbitals of π-symmetry would interact (as there are no matching orbitals on the ligand), so it is possible that direct exchange via a weak metal-metal interaction may also play a significant role in the overall antiferromagnetism.

In the case of **4**, we have scrutinized similar exchange interactions but no satisfactory model has yet emerged. For instance, we have considered **4** as two localized

spins that couple ferromagnetically. To obtain a good fit of the experimental data and in order to produce S_{tot} = 3, one of the spins was set to high- spin Fe(II) while the other had to be modeled as intermediate-spin Fe(II). A weak ferromagnetic coupling of +14 cm^{-1} was thus determined (Table 1.6). The fit, however, is problematic because we cannot explain the origin of the different spins at the two Fe(II) centers. We also considered an alternative fit with two equal S = 1.5 centers; but to maintain the +4 charge of the diiron core, the oxidation states would have to be different, namely Fe(III)Fe(I). The failure of the localized models is not surprising in the light of the work by Betley *et al.* The authors have described the shortcomings in the localized description for explaining the magnetic behavior of systems with strong metal-metal interactions.[114] Instead, the authors advocated the use of a delocalized molecular orbital (MO) scheme to account for the temperature variation of χT. Basically, metal d-orbitals that engage in metal-metal bonding give rise to a delocalized d-orbital manifold, which by population according to Hund's rules yields higher-spin ground states. In the delocalized model, the decrease in χT would result from spin crossover to a lower spin state.

1.5.8 Theoretical Studies

To validate our hypothesis of delocalized metal-metal bonding in **4**, we performed multi- configurational calculations on the full experimental structures of compounds **1** – **5** using the CASSCF method, followed by CASPT2 calculations to recover additional dynamical correlation. For each compound, the active space comprised twelve orbitals, including all ten, valence *3d*-orbitals and two additional *4d* orbitals that correlated with the *3d* orbitals. The energies of various spin states were computed; and with the exception

of **4**, the calculated ground states matched the experimentally determined states (Table 1.7). To correctly predict the ground state of **4**, we investigated a much larger active space of 20 orbitals (all *3d* and *4d* orbitals) with restricted active space (RAS) SCF and PT2 calculations. While these ultimately preferred higher spin states, the energy difference between the nonet and septet states was nominal (< 0.02 kcal/mol).

Table 1.7. Relative CASPT2 energies for the various spin states of **1-5.**

System	Spin State	Rel. CASPT2 Energies (kcal/mol)
CoCoCl (**1**)	singlet	0.0
	triplet	2.0
	quintet	5.6
	septet	10.7
CoMnCl (**3**)	singlet	72.0
	triplet	0.0
	quintet	2.5
	septet	6.0
	nonet	10.6
CoFeCl (**2**)	doublet	0.0
	quartet	2.3
	sextet	5.8
	octet	9.5
FeMnCl (**5**)	doublet	0.0
	quartet	1.7
	sextet	4.3
	octet	7.9
	dectet	12.6
FeFeCl (**4**)[a]	singlet	1.5
	triplet	1.6
	quintet	-0.1
	septet	0.0
	nonet	2.0

[a] Relative RASPT2 energies

For metal-metal bonds in trigonal symmetry, the maximum overlap of the two metals' *3d*-orbitals would ideally yield a highly delocalized MO manifold with σ, π, and δ bonds, e.g. (σ)(π)(δ)(δ*)(π*)(σ*). Poor overlap of the metal orbitals, however, would cause electron density to localize at the individual metal centers. The heterobimetallic

species are expected to have greater localization than the homobimetallics because different metal centers should have worse overlap versus same metal centers. Thus, it is interesting that dicobalt **1** is low-spin and shares similar characteristics with the heterobimetallic species, whereas diiron **4** is higher spin and the lone stand out. To elucidate the physical bases of their different properties, the bonding nature of **1** and **4** were further investigated.

The main electronic configurations of **1** and **4** are compared in Figure 1.9. Of note, the MO diagram of **4** shows the idealized metal-metal bond that is fully delocalized. The main electronic configuration of **4**, which accounts for 28% of the total wave function, is $(\sigma)^2(\pi)^4(\delta)^2(\delta^*)^2(\pi^*)^2(\sigma^*)^0$. The septet state thus arises from the population of energetically close δ, δ*, and π* MOs. This configuration also corresponds to a formal double bond between the iron centers. However, the sum of all the contributing configurations yields MOs with the following natural populations, $(\sigma)^{1.27}(\pi)^{3.42}(\delta)^{2.01}(\delta^*)^{1.99}(\pi^*)^{2.52}(\sigma^*)^{0.72}$, where the increased population in anti-bonding orbitals such as π* and σ* lowers the effective bond order (EBO) to 0.73, which is reasonably close to a single bond.

In contrast, complex **1** is characterized by a more localized MO diagram, where the only, truly delocalized natural orbitals are σ and σ*. (The δ-symmetry MO's are predominantly localized at one metal center, as the ratio of the electron density of the two cobalt centers ranges from 5:1 to 9.5:1). The dominant configuration of **1**, which accounts for 19% of the wave function, is

$(\sigma)^2(Co_1\ d_{yz},d_{xz})^4(Co_2\ d_{yz},d_{xz})^4(Co_1\ d_{xy},d_{x^2-y^2})^2(Co_2\ d_{xy},d_{x^2-y^2})^2(\sigma^*)^0$. Formally, this predicts a single bond between the cobalt centers. However, the sum of all configurations, $(\sigma)^{1.22}(Co_1\ d_{yz},d_{xz})^{3.98}(Co_2\ d_{yz},d_{xz})^{3.96}(Co_1\ d_{xy},d_{x^2-y^2})^{2.08}(Co_2\ d_{xy},d_{x^2-y^2})^2(\sigma^*)^{0.78}$, provides an EBO of only 0.22, which is consistent with a metal-metal interaction that is weaker than a single bond.

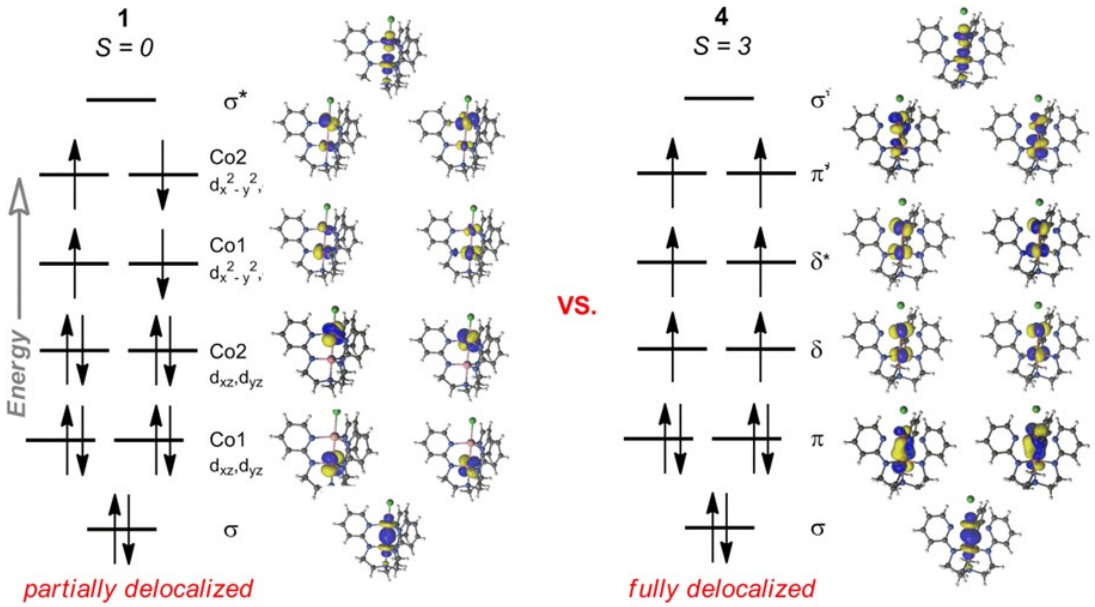

Figure 1.9. Qualitative MO diagrams showing the natural orbitals for dicobalt **1** (*left*) and diiron **4** (*right*). Only the dominating electronic configurations are shown.

For all the heterobimetallic complexes, **2**, **3**, and **5**, the ground states were predicted to be highly multiconfigurational, where the main electronic configuration accounts for only 7% or less of the total wave function (Table 1.8). Thus, the "main" configurations for the heterobimetallics are not representative of the whole bonding picture, and we do not delve further into their bonding descriptions. One important finding, however, is that the EBOs are all low, between 0.22 and 0.31 (Table 1.8), which is consistent with the long metal-metal bond lengths observed experimentally.

Table 1.8. Effective bond order (EBO) and weight of dominant configuration in wave function

	EBO	Dominant Config. Weight
FeFeCl (**4**)	0.73	28%
CoCoCl (**1**)	0.22	19%
CoFeCl (**2**)	0.22	7.0%
CoMnCl (**3**)	0.22	6.5%
FeMnCl (**5**)	0.21	2.1%

Finally, density functional theory (DFT) calculations were performed to shed light on the magnetic interactions between the metal centers within the bimetallic complexes. Magnetic coupling constants can be extracted from DFT solutions of the high-spin and broken-symmetry states, which were calculated with three different exchange-correlation functionals: PBE0, HSE, and LC-ωPBE (Table 1.9). For "purely" magnetic systems, where the magnetic electrons are localized at the individual metal centers, the HSE and LC-ωPBE functionals typically give more accurate coupling values compared to PBE0.[142,143]

Table 1.9. Calculated magnetic coupling constants J (in cm^{-1}) for various functionals.

Cpd	PBE0	HSE	LC-ωPBE	J_{exp}
1	−333	−350	−370	−231
2	−207	−244	−304	−184
3	−210	−217	−231	−120
5	−181	−187	−198	−145

For bimetallic **1**, **2**, **3**, and **5**, the calculated magnetic coupling values are fairly consistent across the functionals. In contrast, the computed magnetic couplings for diiron **4** were quite inconsistent for the various functionals, and thus, compound **4** was excluded from the present study. Although the predicted magnetic coupling constants are generally

overestimated, the *trend* in |*J*| values (Figure 1.10) shows good correspondence between theory and experiment, especially for LC-ωPBE.

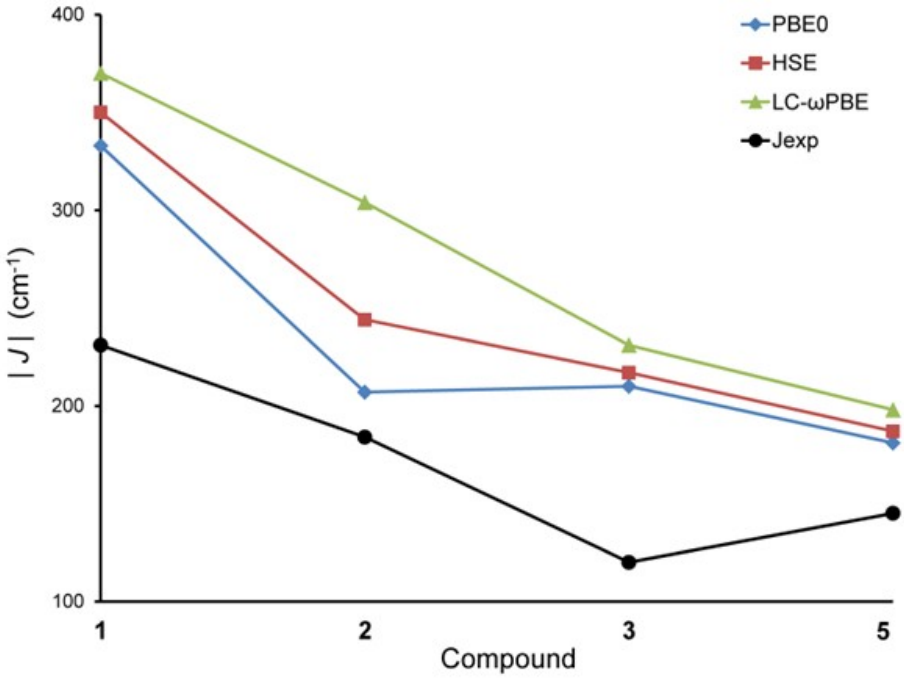

Figure 1.10. Plot of |*J*| values for compounds **1**, **2**, **3**, and **5**.

All the functionals correctly reproduce an important periodic trend for the cobalt series, namely, that the antiferromagnetic coupling decreases in the CoM complexes from M = Co to M = Fe to M = Mn. One discrepancy between theory and experiment is that a weaker coupling is predicted for **5** compared to **3**, rather than vice versa. We hypothesize that this discrepancy arises from a problem with electron correlation, which can become even more complicated when magnetic orbitals overlap. Thus, there is still room for the development of new and more generally applicable exchange-correlation functionals for computing isotropic magnetic couplings.

1.6 Conclusions

A simple ligand design allows the preparation of bimetallic complexes containing Mn(II), Fe(II), and/or Co(II) ions with high compositional purity. Gratifyingly, minute disorder resulting from metal-mixing was observed, despite the fact that these metal ions are typically substitutionally labile and share similar covalent radii. Three heterobimetallic complexes (CoMn, CoFe, and FeMn) were isolated and are highly substitutionally pure in the two metal-binding sites. With these different metal-metal pairings in hand, we were able to characterize their spectroscopic, electronic, and magnetic properties. We do not yet understand why the diiron complex is an outlier of this series, but we correlate its short metal-metal bond and higher spin state with a more delocalized electron density between the two metal centers. Future efforts will focus on exchanging the chloride ligand with more reactive groups in order to study the effects of the metal-metal bonding on reactivity.

Author Contributions

Experimental: Stephen J. Tereniak, Laura J. Clouston, Victor G. Young, Jr., Eckhard Bill, Yu-Sheng Chen, Hyun Jung Kim, Connie C. Lu

Theoretical: Rebecca K. Carlson contributed all calculations, Rémi Maurice contributed to the understanding and methodology for magnetic coupling constants, Laura Gagliardi

Chapter 2

Influence of Copper Oxidation State on the Bonding and Electronic Structure of Cobalt-Copper Complexes

Reproduced in part with permission from

Influence of Copper Oxidation State on the Bonding and Electronic Structure of Cobalt-Copper Complexes, Reed J. Eisenhart, Rebecca K. Carlson, Laura J. Clouston, Victor G. Young, Jr., Yu-Sheng Chen, Eckhard Bill, Laura Gagliardi, and Connie C. Lu, *Inorganic Chemistry,* **2015,** *54* (23), 11330-11338.

2.1 Overview

Heterobimetallic complexes that pair cobalt and copper were synthesized and characterized by a suite of physical methods, including X-ray diffraction, X-ray anomalous scattering, cyclic voltammetry, magnetometry, electronic absorption spectroscopy, electron paramagnetic resonance, as well as quantum chemical methods. Both Cu(II) and Cu(I) reagents were independently added to a Co(II) metalloligand to provide (py_3tren)CoCuCl (**1**-Cl), (py_3tren)CoCuOTf (**1**-OTf), and (py_3tren)CoCu(CH_3CN) (**2**-CH_3CN), respectively, where py_3tren is the triply deprotonated form of *N*,*N*,*N*-tris(2-(2-pyridylamino)ethyl)amine. Complex **2**-CH_3CN can lose the acetonitrile ligand to generate a coordination polymer consistent with the formula "(py_3tren)CoCu" (**2**). The Cu(II)/Cu(I) redox couple for **1**-OTf and **2**-CH_3CN is reversible at −0.56 and −0.33 V vs. Fc^+/Fc, respectively. One-electron chemical oxidation of **2**-CH_3CN with AgOTf regenerated **1**-OTf. The copper oxidation state impacts the electronic structure of the heterobimetallic core, as well as the nature of the Co−Cu interaction. Quantum chemical calculations showed modest electron delocalization in the $(CoCu)^{+4}$ state via a Co−Cu sigma bond that is weakened by partial population of the Co−Cu sigma anti-bonding orbital. By contrast, no covalent Co−Cu bonding is predicted for the $(CoCu)^{+3}$ analogue, and the d-electrons are fully localized at individual metals.

2.2 Introduction

The copper II/I redox couple is prevalent in biology and underlies a wide range of enzymatic activities including electron transfer, O_2 transport, substrate oxidation, and respiration.[144–147] In many of these enzymes, a single copper ion is coupled to a redox-active ligand, e.g. in galactose oxidase, or other transition metal(s), e.g. heme-copper oxidases, to achieve multi-electron reactivity. The diverse multimetallic cooperativity in biology has inspired synthetic efforts to engineer coordination complexes with multiple transition metals for promoting multi-electron reduction of small molecules.[148–151]

Multi-electron cooperativity may also arise from metal-metal bonded complexes, where the electronic structure is delocalized across individual metals.[152–155] The metal-metal interactions involving copper are primarily cuprophilic in nature, involving weakly interacting d^{10} Cu(I) centers.[156] Among the short (< 2.5 Å) heterometallic interactions

involving copper, iron and cobalt are common partners, but nearly all these complexes feature bridging or semi-bridging carbonyl ligands and are low spin.[157]

The heptadentate ligand, py_3tren, which is the triply deprotonated form of *N*,*N*,*N*-tris(2-(2-pyridylamino)ethyl)amine, was used previously to stabilize homo- and heterobimetallic complexes of manganese, iron, and cobalt in a wide range of spin states. Extending this series, we report cobalt-copper heterobimetallics in two redox states, Co(II)Cu(II) and Co(II)Cu(I). Both redox states are paramagnetic, $S = 1$ and $S = 3/2$, respectively, and comprise a high-spin Co(II) center. The Co-Cu distances in both redox states are less than 2.5 Å, suggesting a significant metal-metal interaction. By comparing bimetallics with two different oxidation states of Cu, we find that the unfilled Cu(II) d-valence shell is requisite for covalent bonding to Co(II) and a more delocalized electronic structure compared to d^{10} Cu(I). A visible excitation band is proposed to arise from an intermetal charge transfer in the Co(II)Cu(II) core, or Co(II)Cu(II) $\xrightarrow{h\nu}$ Co(III)Cu(I). Finally, the coordination chemistry of Cu(I) in the Co(II)Cu(I) species can toggle between 5-coordinate, distorted trigonal pyramidal and 3-coordinate T-shaped, which results from loss of a labile solvent ligand and cleavage of the Co-Cu interaction.

2.3 Experimental Section

Details about the experimental synthesis and characterization protocol and calibration, including X-Ray crystallography, anomalous diffraction, NMR, and SQUID magnetometry can be found in Appendix 2.

2.4 Computational Methods

RASSCF/RASPT2 calculations were performed on **1**-Cl and **2**-CH_3CN with the Molcas 7.8 package[120] using the experimental geometries in full and without optimization. The active space of **1**-Cl and **2**-CH_3CN are denoted by (16,20)/(16,10)/2 and (17,20)/(17,10)/2, respectively. The first set of parentheses is the total number of electrons in RAS1 and RAS2 and the total number of orbitals (20) in all of the RAS spaces, and the second set of parentheses corresponds to the number of active electrons and orbitals (10) in RAS2; the final value of 2 indicates the number of particles allowed into RAS3. Relativistic all-electron ANO-RCC basis sets were used.[121,122] Double-ζ quality (ANO-RCC-VDZP) basis sets were used for Co, Cu, N, and Cl atoms and minimal basis sets (ANO-RCC-MB) were used for C and H atoms. The follow contractions: [5s4p2d1f] for metals, [3s2p1d] for N and Cl, [2s1p] for C, and [1s] for H. Triple-ζ quality (ANO-RCC-VTZP) basis sets were also used for Co, Cu, N, and Cl atoms and double- ζ basis sets (ANO-RCC-VDZP) were also used for C and H atoms. The follow contractions: [6s5p3d2f1g] for metals, [4s3p2d1f] for N, [5s4p2d1f] for Cl, [3s2p1d] for C, and [2s1p] for H. Reduction of four center 2-electron integrals to effective three center integrals via auxiliary basis sets was accomplished with the RICD approximation.[125] For RASPT2 calculations, an imaginary level shift of 0.2 a.u. was used to prevent the occurrence of intruder states.[126] Effective bond order (EBO)[27,127] was calculated for the ground state of each complex by taking the difference of the sum of the bonding orbital occupations.

2.5 Results and discussion

2.5.1 Synthesis

The dark purple $(CoCu)^{4+}$ heterobimetallic, $(py_3tren)CoCuCl$ (**1**-Cl), was generated by reacting the monocobalt precursor, K[Co(py_3tren)], with $CuCl_2$. The synthesis **1**-Cl is not trivial as metal scrambling to the dicobalt analogue, $(py_3tren)Co_2Cl$, occurs readily. The preference for dicobalt over the Co-Cu heterobimetallic can be rationalized by the 10^3-fold faster H_2O-exchange rate of the Cu(II) aqua ion relative to Co(II).[158] We have found that the best reaction conditions to produce **1**-Cl cleanly is to add K[Co(py_3tren)] to a stirring, dilute solution of $CuCl_2$ (~4 μM in THF) at −78 °C for a short period of time, ca. 5 min, prior to filtering the reaction mixture (Scheme 1). Since **1**-Cl is practically insoluble in THF or CH_3CN, and only sparingly soluble in CH_2Cl_2, we also investigated a more soluble analogue, **1**-OTf, by exchanging the chloride ligand for triflate with AgOTf.

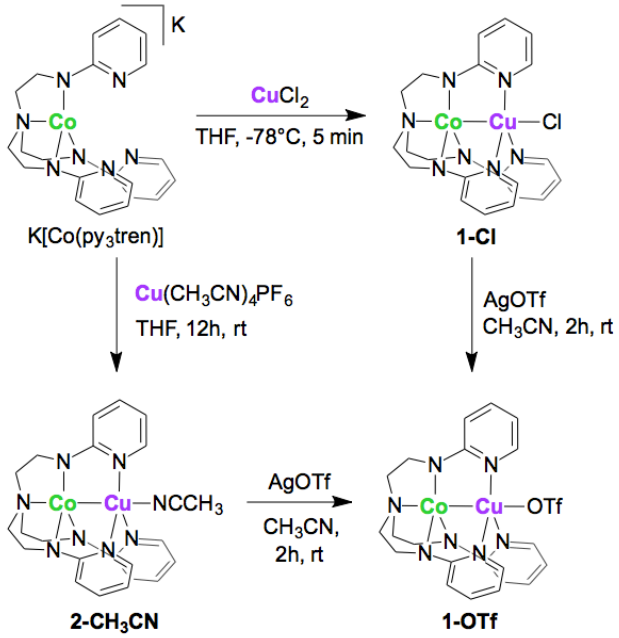

Figure 2.1. Synthesis of Co-Cu complexes in two oxidation states, $(CoCu)^{4+}$ and $(CoCu)^{3+}$. Two viable routes to **1**-OTf are shown.

The green $(CoCu)^{+3}$ species, (py_3tren)CoCu(CH_3CN) (**2**-CH_3CN), was isolated from a rt metallation of K[Co(py_3tren)] and [Cu(CH_3CN)$_4$]PF_6 (Figure 2.1). Unlike **1**-Cl, the reaction to make the reduced counterpart, **2**-CH_3CN, showed no dicobalt impurity. The outcome is consistent with the notion that chloride ions facilitate metal scrambling via a bridging chloride intermediate, M(μ-Cl)M'. Recently, metal scrambling was studied using a triiron system that undergoes step-wise exchange of iron sites for cobalt upon addition of different equivalents of $CoCl_2$.[113] Complex **2**-CH_3CN is unstable to vacuum, and loss of acetonitrile forms a solvent-free species that has a molecular formula consistent with "(py_3tren)CoCu" (**2**). In an alternative synthesis, **1**-OTf was prepared by oxidation of **2** with AgOTf (Fig 2.1). This reaction is the preferred route to **1**-OTf because it avoids the use of fairly insoluble **1**-Cl.

2.5.2 NMR Spectroscopy

The paramagnetic ^{1}H NMR spectra of the $(CoCu)^{4+}$ heterobimetallics, **1**-Cl and **1**-OTf, in CD_2Cl_2 are similar; and, each contains 6 unique resonances, consistent with C_{3v} symmetry in solution. By contrast, the paramagnetic ^{1}H NMR spectrum of $(CoCu)^{3+}$ **2** in CD_2Cl_2 is more complex with 14 discernible peaks. However, by switching to CD_3CN, the NMR spectrum of **2** simplifies to 6 peaks, which is consistent with the C_{3v} symmetry of the acetonitrile adduct, **2**-CH_3CN.

Figure 2.2 is a stacked ^{1}H NMR plot of **1**-OTf and **2**-CD_3CN, and the corresponding proton assignments are listed in Table 2.1. The proton assignments are based on relative integrations and spin-lattice relaxation times, as described previously.[20] Of note, the relaxation time is significantly faster for **2**-CD_3CN (0.82−9.9 ms) compared

to **1**-OTf (12.5−61 ms), presumably because of more unpaired spins in the former (*vide infra*).

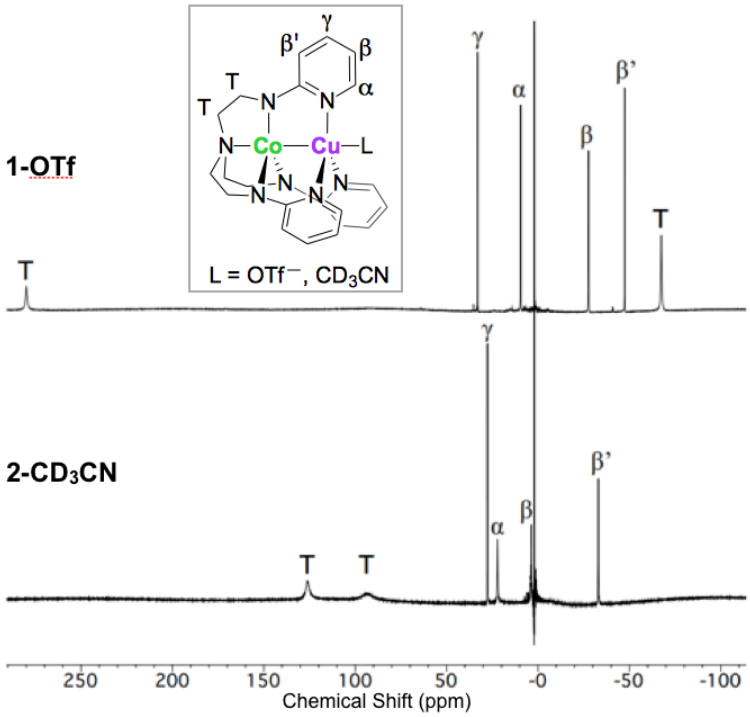

Figure 2.2. Stacked ^{1}H NMR spectra of **1**-OTf and **2**-CD_3CN (300 MHz, CD_3CN).

Table 2.1. Proton NMR chemical shifts (ppm) of **1**-OTf and **2**-CD_3CN with corresponding spin-lattice relaxation times (ms) in parentheses.

	Complex	
	1-OTf	**2**-CD_3CN
α	9.5 (12.5)	21.2 (0.82)
γ	33.0 (61)	27.5 (9.9)
β	−27.7 (22.0)	5.1 (4.1)
β′	−47.5 (14.2)	−33.4 (1.8)
T	280, −67.6[a]	125, 99.5[a]

[a] Peak was too broad to measure relaxation time.

The ^{1}H NMR pattern of **2**-CD_3CN closely resembles that of the monocobalt precursor, K[Co(py$_3$tren)]. Their similitude suggests that the $(CoCu)^{3+}$ core of **2**-CH_3CN comprises d^{10} Cu(I) and d^{7} Co(II) centers, which is loosely isoelectronic to a single d^{7}

Co(II) center in K[Co(py$_3$tren)]. The largest difference in their ^{1}H NMR spectra is the chemical shift of the pyridyl α proton, from 0.3 ppm in K[Co(py$_3$tren)] to 21.2 ppm in **2**-CD_3CN. The sensitivity of the α-proton to the substitution of K^+ for Cu^+ is reasonable considering its proximity to the metal-binding site.

2.5.3 X-ray Diffraction Study

Single crystals of **1**-Cl, **2**-CH_3CN, and **2** were examined by X-ray diffraction. Complex **1**-Cl crystallized in the monoclinic space group $P2_1/n$. From concentrated acetonitrile, **2**-CH_3CN crystallized in the monoclinic space group $P2_1/c$ with three lattice acetonitriles. However, by switching to a less coordinating solution of hexane and dichloromethane, **2** crystallized as a polymeric one-dimensional helical chain in the hexagonal space group $P6_1$. In the coordination polymer **2**, each Cu site is bound to three pyridyl donors, two that are intramolecular and one intermolecular (vide infra).

In **1**-Cl and **2**-CH_3CN, the Co centers are trigonal bipyramidal (tbp) (Figure 2.3). The Cu site in **2**-CH_3CN is also tbp, with a tau value (τ_5) of 0.94, where 1 is the theoretical value for ideal tbp geometry. By contrast, the Cu site in **1**-Cl is severely distorted from three-fold symmetry with N_{py}−Cu−N_{py} bond angles of 146.67, 107.01, and 101.15(5) degrees, and one relatively longer Cu−N_{py} bond of 2.169(1) Å. The τ_5 value of the Cu site in **1**-Cl is 0.48, indicating a distorted geometry that lies between tbp and square pyramidal.

In common, **1**-Cl and **2**-CH_3CN have relatively short Cu−Co bond lengths of 2.3963(3) and 2.4707(4) Å, respectively (Table 2.2). The formal shortness ratio (FSR), which is the quotient of metal-metal bond length to the sum of the metals' single-bond

radii, is 1.03 and 1.06 for **1**-Cl and **2**-CH_3CN, respectively. FSR values near 1 typically indicate a significant metal-metal interaction, such as a single covalent or dative metal-metal bond. A search of the Cambridge Structural Database for *heterometallic* interactions involving copper showed a wide range of Cu−M distances from 2.31 to 3.5 Å, where the average is 2.72 Å (standard deviation of 0.15 Å). The structures with short Cu−M bonds (≤ 2.4 Å) are almost exclusively low-spin Cu-Co and Cu-Fe bimetallics containing a bridging, or semi-bridging, carbonyl ligand. Hence, **1**-Cl is an atypical coordination complex with a short Cu−M bond.

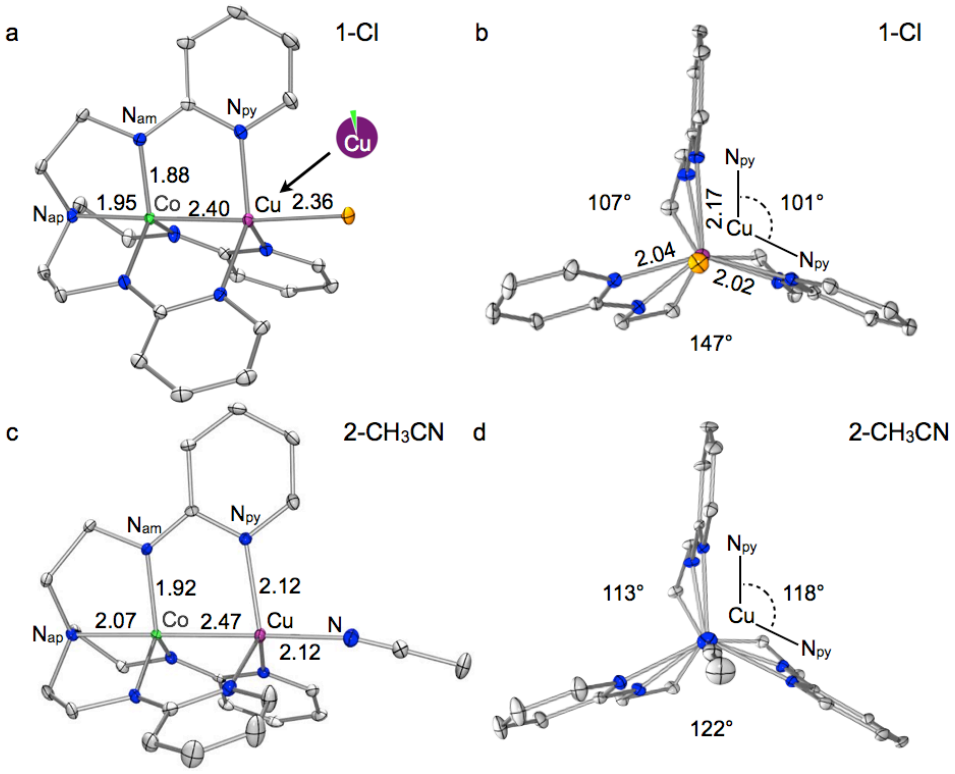

Figure 2.3. Solid-state structures of **1**-Cl (a – side view, b – top view) and **2**-CH_3CN (c – side view, d – top view). Bond distances (Å) and N_{py}−Cu−N_{py} angles are provided. Thermal ellipsoids are shown at 50% probability, and protons were omitted for clarity. The pie chart indicates the metal composition in the pyridyl site as determined by X-ray anomalous scattering.

Table 2.2. Geometrical Parameters, Including Bond Lengths (Å) and Angles (deg), for Complexes **1**-Cl, **2**-CH_3CN, and **2**.[a]

	1-Cl	**2**-CH_3CN	**2**
Co−Cu	2.3963(3)	2.4707(4)	2.6492(8)
FSR[b]	1.03	1.06	1.14
Co−N_{ap}	1.946(1)	2.067(2)	2.094(4)
Co−N_{am}	1.873(1)	1.919(2)	1.942(4)
	1.884(1)	1.911(2)	1.945(4)
	1.894(1)	1.925(2)	1.965(4)
avg Co−N_{am}	1.884	1.918	1.951
Cu−N_{py}	2.021(1)	2.101(2)	1.957(4)
	2.032(1)	2.121(2)	1.960(3)
	2.169(1)	2.131(2)	2.244(4)[c]
avg Cu−N_{py}	2.075	2.118	1.959
Cu−X (X = Cl, $NCCH_3$)	2.3548(4)	2.120(2)	—
$\sum(N_{am}-Co-N_{am})$	359.3	358.9	357.5
N_{py}−Cu−N_{py}	146.67(5)	118.34(7)	157.3(2)
	101.15(5)	122.38(7)	102.7(2)[c]
	107.01(5)	112.85(7)	98.28(1)[c]
N_{ap}−Co−Cu	178.07(4)	179.44(6)	156.9(1)
Co−Cu−X	175.69(1)	178.50(6)	—
Co to $(N_{am})_3$-plane	0.0886(7)	0.118(1)	0.180(2)
Cu to $(N_{py})_3$-plane	0.2491(7)	0.312(1)	0.123(1)[c]

[a] Estimated standard deviations (esd's) are provided in parenthesis. [b] formal shortness ratio (FSR) = (Cu−Co bond distance) / (sum of the Cu and Co single-bond radii). [c] Involving an intermolecular N_{py} donor.

Scrutiny of the metal sites in **1**-Cl and **2**-CH_3CN shows that all metal-ligand bonds expand upon reduction. On average, the equatorial M−L bond lengths, Co−N_{am} and Cu−N_{py}, elongate by ~0.04 Å from **1**-Cl to **2**-CH_3CN. More substantial increases are observed in the apical Co−N_{ap} (by 0.12 Å) and the Cu−Co (by 0.07 Å) bond distances. Though the structural changes at both metal sites would hint that the reducing equivalent is delocalized over both metals, we know that this is not the case. Spectroscopic and theoretical evidence (*vide infra*) support a Co(II)Cu(II) core in **1**-Cl and a Co(II)Cu(I)

core in **2**-CH_3CN, where the redox change is localized at Cu. To further investigate the changes at the Cu site, comparisons to mononuclear Cu complexes with a trigonal set of pyridyl donors, e.g. $[Cu^{II}Cl(TMPA)]^+$ and $[Cu^{I}(NCCH_3)(TMPA)]^+$, may be useful. Several crystal structures have been reported for both monocopper species with different counterions.[159–161] Notably, both $[Cu^{II}Cl(TMPA)]^+$ and $[Cu^{I}(NCCH_3)(TMPA)]^+$ have structures that vary from ideal to distorted tbp, with τ_5 as low as 0.84.[162] By comparison, the Cu site in **1**-Cl is significantly more distorted. Unfortunately, the Cu−N_{py} bond lengths in both $[Cu^{II}Cl(TMPA)]^+$ and $[Cu^{I}(NCCH_3)(TMPA)]^+$ overlap, and do not uniquely identify the Cu oxidation state. The only instructive comparisons are the Cu−X bond distances, specifically the Cu−Cl bond length between **1**-Cl and $[Cu^{II}Cl(TMPA)]^+$, as well as Cu−N_{CH_3CN} between **2**-CH_3CN and $[Cu^{I}(NCCH_3)(TMPA)]^+$. On average, the Cu−X bonds are longer by 0.12 to 0.15 Å, respectively, in **1**-Cl and **2**-CH_3CN. We propose that the stronger *trans* effect of an ancillary Co center versus the tertiary amine in TMPA results in the longer Cu−X bonds, though the difference in molecular charge would also contribute.

When **2** crystallizes in absence of donor solvents, an infinite one-dimensional helix is formed (Figure 2.4). The helix is right-handed, and one complete turn comprises six (py_3tren)CoCu molecules with a pitch of 11.2024(5) Å and a pore diameter of ~8 Å. The py_3tren ligand rearranges by rotating one of the pyridyl rings by nearly 180 degrees such that a single pyridyl *N*-donor forms an intermolecular bond to a Cu center in an adjacent molecule. The Co−Cu distance is 2.6492(8) Å (FSR 1.14), which is likely too long to be interacting. The Co site is trigonal monopyramidal, and the geometry at Cu is

close to T-shaped with N_{py}–Cu–N_{py} angles of 157.3(2), 102.7(2), and 98.28(1) deg. The intramolecular Cu–N_{py} bonds are contracted compared to **2**-CH_3CN with lengths of 1.96 Å while the intermolecular Cu–N_{py} is elongated to 2.244(4) Å.

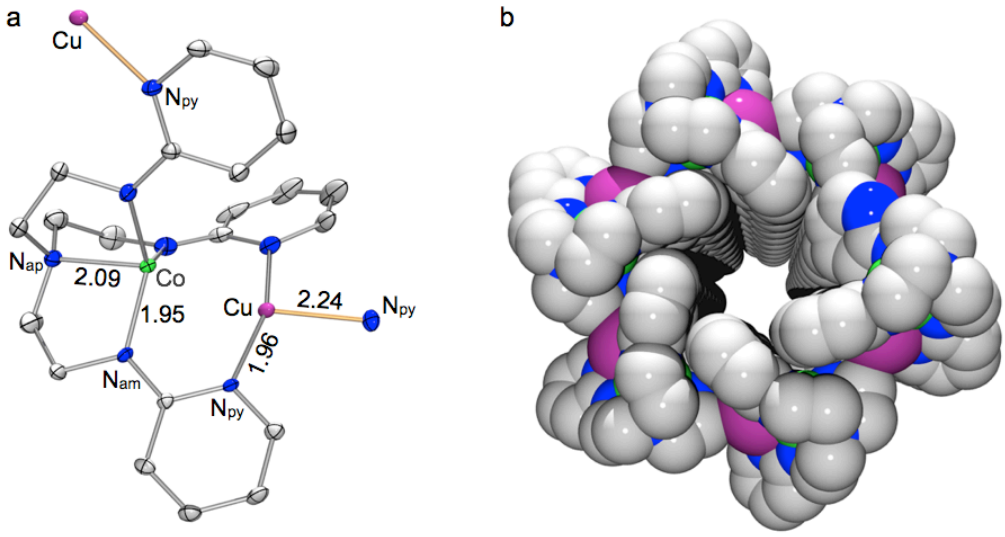

Figure 2.4. (a) Molecular structure of **2** with thermal ellipsoids at 50% probability. Protons omitted for clarity. Intermolecular bonds are shown in gold. (b) Space filling model of the macromolecular **2** showing its hexagonal polymeric structure.

Finally, complex **1**-Cl was studied by anomalous X-ray scattering to assess the purity of each metal binding site. This technique exploits the uniqueness of metal K-edge energies to differentiate between metals with similar electron counts. The occupancies of Co versus Cu can be extracted for each binding site, and are depicted by the pie chart in Figure 2.3. In the triamido(amine) pocket, Co has an occupancy percentage of 1.000(9), and Cu of 0.000(9). Slightly more metal disorder is found in the tripyridyl binding pocket, 0.953(7) for the Cu occupancy and 0.047(7) for Co. Hence, the purity of the Co-Cu bimetallic is 95.3%, with a minor (4.7%) impurity of the dicobalt species. Previously, other heterometallic pairings, such as Co-Fe, Fe-Mn, and Co-Mn, showed heterometallic

purity ranges in the range of 88 to 97%. The relative metal compositions was also investigated on bulk material by ICP-OES, which is consistent with a Co:Cu ratio of 0.98:1.02.

2.5.4 EPR Spectroscopy and Magnetic Susceptibility

The EPR spectra of **2**-CH_3CN (Figure 2.5) is consistent with an $S = 3/2$ system. The signal is axial with $g = (2.163, 2.16, 2.002)$. The eight-line splitting in g_z arises from hyperfine interactions with the ^{59}Co ($I = 7/2$) nucleus. The EPR spectrum looks quite similar to that of the monocobalt precursor, K[Co(py_3tren)], where the Co(II) center is $S = 3/2$ (SI Figure S5). The absence of any hyperfine coupling to $^{65,63}Cu$ ($I = 3/2$) nuclei further supports the interpretation that all unpaired spin are localized at cobalt. It then follows that the copper center is $S = 0$, d^{10} Cu(I).

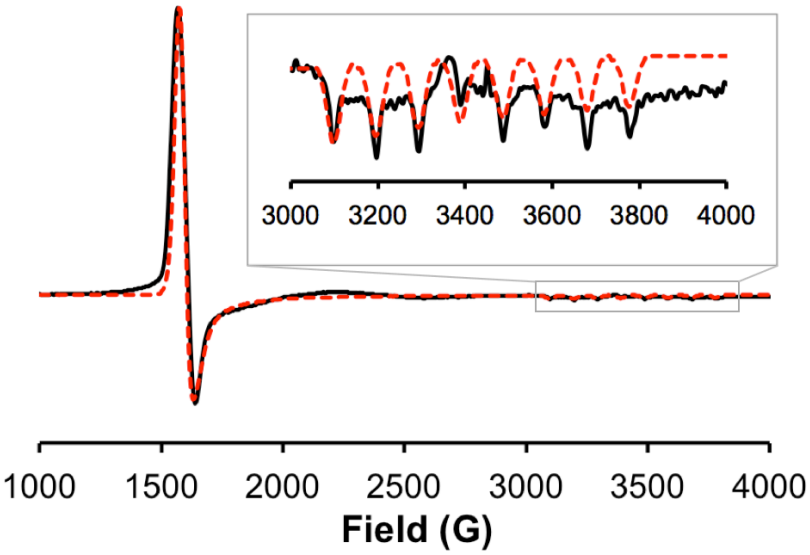

Figure 2.5. X-band EPR spectra (9.65 MHz) of **2** in frozen THF (1 mM, 20 K). Experimental spectra is shown as a solid, black line, and the corresponding simulation in a red dashed line. Simulation parameters for **2**: $D = 0$, $E/D = 0.1$, $g = (4.33, 4.3, 2.002)$, W = (24.1, 38.5, 18 G), $A_z = 206$ MHz (real g-values: 2.163, 2.16, 2.002)

The magnetic susceptibility of **1**-OTf was determined by Evans method and SQUID magnetometry. The solution-state magnetic moment of **1**-OTf is 2.96 ± 0.17 μ_B (average of three measurements), which is consistent with $S = 1$ with a spin-only value of 2.83 μ_B. The temperature dependence of the magnetic moment (Figure 2.6) is also consistent with a triplet ground state that is energetically isolated. The overall spin state presumably arises from strong antiferromagnetic coupling between the $S = 3/2$ Co(II) and $S = 1/2$ Cu(II) centers. Of note, a large zero-field splitting (D) of 64 cm^{-1} was observed for **1**-OTf, which was validated by variable temperature and variable field measurements. Zero-field splitting values in the range of 50-70 cm^{-1} have been observed previously in high-spin pentacoordinate Co(II) complexes.[163]

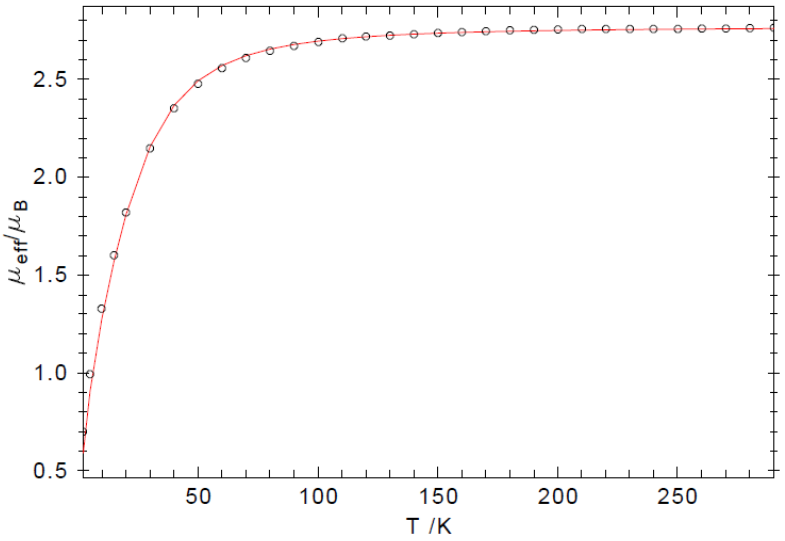

Figure 2.6. Temperature dependence of the magnetic susceptibility of **1-Cl** plotted as μ_{eff} versus T (2 to 290 K, 1 T). The data, represented by open circles, was corrected for temperature independent paramagnetism of 350 x 10^{-6} emu). The red line shows the simulation with the following parameters: $S = 1$, $g = 1.956$, $D = 64.584$ cm^{-1}.

2.5.5 Electrochemistry

The redox behavior of **1**-OTf and **2**-CH_3CN should be complementary, and indeed, their cyclic voltammograms (CVs) are similar with a total of two one-electron transfer processes (Figure 2.7). In the CV of **1**-OTf, the reductive event at −0.56 V is fully reversible ($E_{pc} - E_{pa} = 0.072$ V, $i_{pc}/i_{pa} = 0.97$), and is assigned to the Cu(II)/Cu(I) redox couple. In contrast, the oxidative process at 0.03V is quasi-reversible, with increasing reversibility up to 1 V/s. The oxidation most likely is Co(II)/Co(III) as monocobalt K[Co(py_3tren)] shows an oxidation at 0.02 V. Finally, we note that the CV of **1**-Cl is quite similar to **1**-OTf with a reversible reduction at −0.55 V and an irreversible oxidation near 0 V.

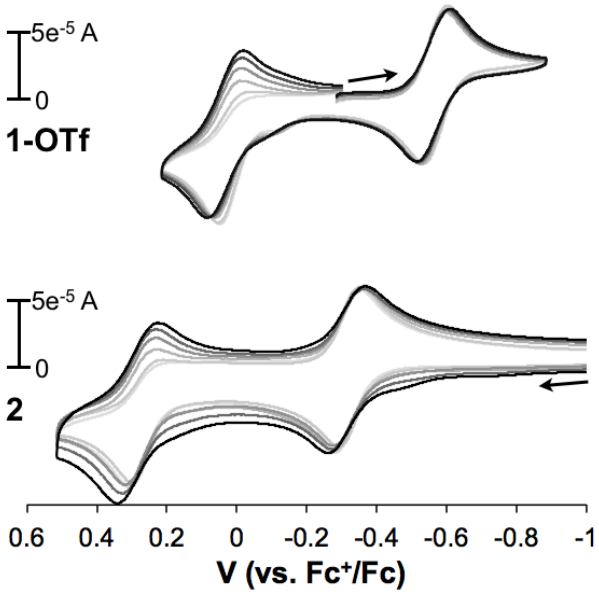

Figure 2.7. Cyclic voltammagrams of **1**-OTf (top) and **2**-CH_3CN (bottom) in 0.1 M [nBu$_4$N]PF_6/CH_3CN at varying scan speeds: 2 (in black), 1, 0.5, 0.25, 0.1, 0.05 V/s (in light grey). Currents were corrected for scan speed.

The CV of **2**-CH_3CN contains two oxidative events at −0.33 V and 0.28 V. The first oxidation, which is fully reversible, corresponds to the Cu(II)/Cu(I) redox potential. The redox potential is shifted positively by 0.2 V with respect to the corresponding

potential in **1**-OTf and **1**-Cl. The second oxidation is quasi-reversible and is also shifted positively by 0.25 V with respect to **1**-OTf. The anodic shift of both redox processes in **2** versus **1**-OTf suggests that the triflate ligand remains bound to the Co center in acetonitrile. Also, the shift in the Co(III)/Co(II) and Cu(II)/Cu(I) reduction potentials is consistent with the differences in charge between the acetonitrile and triflate ligand, where the presence of an anionic triflate makes both metal-based reductions more difficult. Finally, the corresponding Cu(II)/Cu(I) redox potential in (TMPA)Cu(CH_3CN) is −0.40 V,[164] suggesting the trialkylamine donor in TMPA donates more electron density to the Cu(I) center than the weakly interacting Co(II) center in **2**.

2.5.6 Electronic absorption spectroscopy

The UV-vis-NIR spectra of the **1**-Cl and **2**-CH_3CN complexes were measured in CH_2Cl_2 (Figure 2.8). Both complexes show intense bands peaks around 300−350 nm, which is typical for py_3tren coordination complexes, including K[Co(py_3tren)].

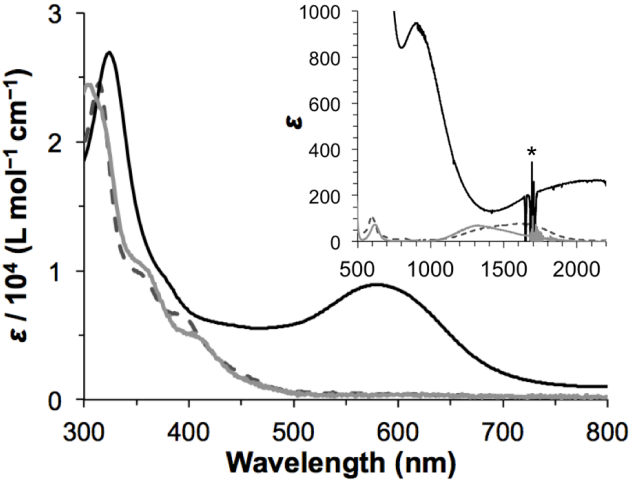

Figure 2.8. UV-Vis plots of **1**-Cl (black), **2**-CH_3CN (solid grey), and K[Co(py_3tren)] (dashed grey). Inset shows the Vis-NIR region. Spectra were collected as solutions in CH_2Cl_2. The asterisk denotes artifacts from solvent subtraction.

Of interest, **1**-Cl has a visible band at 580 nm (ε = 890 L mol^{-1} cm^{-1}) that is notably absent for **2**-CH_3CN and K[Co(py_3tren)]. This peak has been assigned as a intermetal charge transfer, or Co→Cu, in analogy to previously reported MCoCl(py_3tren) species. The striking similarity in the overall electronic absorption spectra of **2**-CH_3CN and K[Co(py_3tren)] is fully consistent with the presence of a d^{10} Cu(I) center in the former, such that all the observed energy transitions can be attributed to the Co(II) center.

2.5.7 Theory

Theoretical calculations were performed to investigate the electronic structures of **1**-Cl and **2**-CH_3CN. Previously, we employed a large active space of 20 orbitals, comprising all 3d and 4d orbitals, to correctly predict the spin states of related metal-metal complexes.[165] Using the full experimental structures, RASSCF and RASPT2 calculations were conducted with 16 and 17 total d-electrons in 20 orbitals for **1**-Cl and **2**-CH_3CN, respectively. In both cases, the calculated ground spin states matched that found experimentally (Tables 2.3).

Table 2.3. Relative energies (kcal/mol) for **1** and **2** for accessible spin states

		RASSCF	RASPT2
CoCuCl (**1**)	singlet	44.6	31.9
	triplet	0.0	0.0
	quintet	1.8	5.5
CoCuCH_3CN (**2**)	doublet	51.0	46.5
	quartet	0.0	0.0

The qualitative MO diagram for **1**-Cl is shown in Figure 2.9 with the corresponding natural orbitals. The only delocalized MO is consistent with Co−Cu σ-

bonding. The main electronic configuration, which represents 42% of the ground state, is (Cu $d_{xz,}d_{yx}$)^4(Cu d_x^2-$_y^2$,d_{xy})^4(Co d_{xz},d_{yz})^4(σ)^2(Co d_x^2-$_y^2$,d_{xy})^2, and it corresponds to a single Co−Cu bond. However, the total ground state, represented by (Cu $d_{xz,}d_{yx}$)$^{3.98}$(Cu d_x^2-$_y^2$,d_{xy})$^{3.98}$(Co d_{xz},d_{yz})$^{3.92}$(σ)$^{1.20}$(Co d_x^2-$_y^2$,d_{xy})$^{2.06}$(σ*)$^{0.79}$, has substantial multiconfigurational character with significant population of the Co−Cu anti-bonding MO, or σ*. The net effect is weakening of the metal-metal bond, and a decrease in the effective Co−Cu bond order to 0.21.

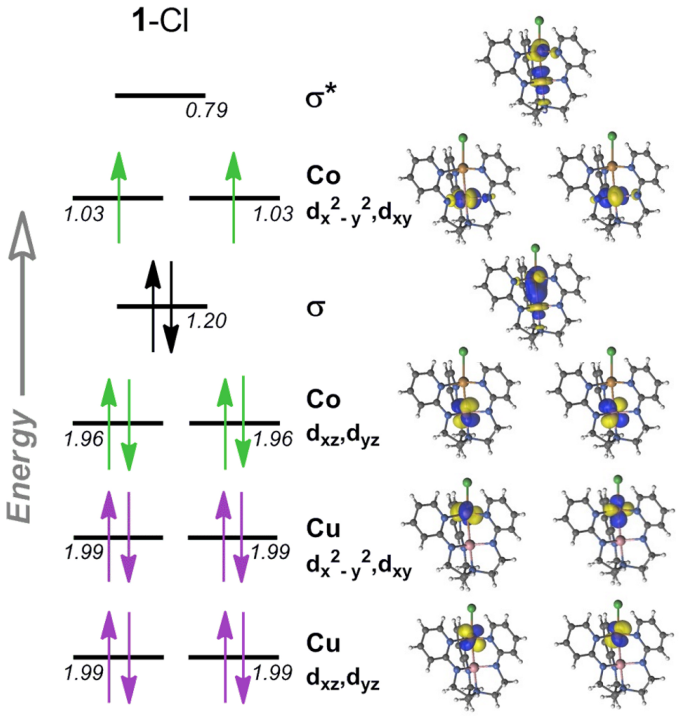

Figure 2.9. Qualitative MO diagram and natural orbitals of **1**-Cl. Electron filling corresponds to the main configuration (42%), while the numerical value of each natural orbital is the population summed over all contributing configurations.

The qualitative MO diagram for **2**-CH_3CN, which is shown in Figure 2.10, is completely localized in contrast to **1**-Cl. No Co−Cu covalent bonding was predicted, though the possibility of a Cu→Co dative interaction should be entertained because of

the reasonably short intermetal distance in the solid-state structure. The electronic structure of **2**-CH_3CN is represented essentially by a single configuration, (Cu $d_{xz,}d_{yx})^4$(Cu $d_x{}^2$-$_y{}^2$,$d_{xy})^4$(Cu $d_z{}^2)^2$(Co d_{xz},$d_{yz})^4$(Co $d_x{}^2$-$_y{}^2$,$d_{xy})^2$(Cu $d_z{}^2)^1$, which accounts for 91% of the total ground state. The predicted electronic structure is consistent with the EPR finding that $S = 3/2$ is localized at a high-spin Co(II) center, with no spin density at d^{10} Cu(I).

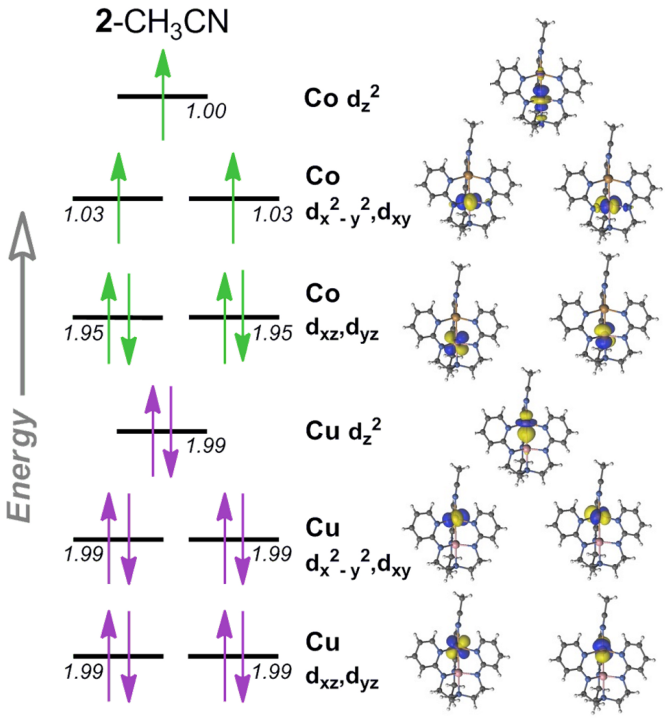

Figure 2.10. Qualitative MO diagram and natural orbitals of **2**-CH_3CN. Electron filling corresponds to the main configuration (91%), while the numerical value of each natural orbital is the population summed over all contributing configurations.

2.6 Conclusions

The heterobimetallic $(CoCu)^{4+}$ and $(CoCu)^{3+}$ complexes were isolated and characterized. Though two one-electron processes appear viable by CV, thus far, we have only been able to isolate these two redox states. The triplet $(Co\text{-}Cu)^{4+}$ core is overall S =

1. Its electronic structure comprises high-spin Co(II) and d^9 Cu(II) centers, which interact via a Co−Cu sigma bond. The multiconfigurationality in the ground-state substantially weakens the Co-Cu bond (effective bond order of 0.2), which seems consistent with a slightly elevated FSR of 1.03. Notably, a metal-to-metal (Co→Cu) charge transfer band is observed for **1**-Cl in the visible region at 580 nm.

The electronic structure of the $(CoCu)^{3+}$ species, **2**-CH_3CN, is localized with a high-spin Co(II) and d^{10} Cu(I) sites. No Co-Cu covalent bonding was predicted, though a dative interaction is possible considering the intermetal distance is less than 2.5 Å. Of interest, the Cu coordination site can toggle between 5-coordinate distorted trigonal bipyramidal to 3-coordinate T-shaped geometries, forming a heterobimetallic coordination polymer.

Author Contributions

Experiment: Reed J. Eisenhart, Laura J. Clouston, Victor G. Young Jr, Yu-Sheng Chen, Eckhard Bill, Connie C. Lu.

Theory: Rebecca K. Carlson, Laura Gagliardi

Chapter 3

Synthesis and Redox Reactivity of a Phosphine-ligated Dichromium Paddlewheel

Reprinted in part from

Inorganica Chimica Acta, vol. 424, Reed J. Eisenhart, Rebecca K. Carlson, Kelsey M. Boyle, Laura Gagliardi, Connie C. Lu, Synthesis and Redox Reactivity of a Phosphine-ligated Dichromium Paddlewheel, 336-344, Copyright 2015, with permission from Elsevier.

3.1 Overview

A pentadentate ligand platform, bis[2-(diispropylphosphino-methylamino)phenyl]ether (**1**), abbreviated as H_2(PNONP), is introduced that enables the isolation of homodinuclear chromium complexes. In a one-step metalation using Cr(III) and Cr(II) chloride reagents, the bimetallic compounds, [Cr(μ−Cl)(PNONP)]$_2$ (**2**) and [Cr(PNONP)]$_2$ (**3**), respectively, were synthesized. These complexes have been characterized by X-ray diffraction, NMR spectroscopy, cyclic voltammetry, magnetometry, UV−vis−NIR spectroscopy, combustion analysis, and computational methods. Complex **3** has a reasonably short Cr−Cr bond length of 2.1342(5) Å. Theoretical calculations support a diradical singlet ground-state with a formal triple bond between the chromium centers. By cyclic voltammetry, **3** exhibits two reversible oxidations at $E_{½}$ = −472 and −753 mV versus $FeCp_2^{0/+}$. The one- and two-electron oxidized analogues, $\mathbf{3}^{+}$ and $\mathbf{3}^{2+}$, were generated *in situ* via chemical oxidation using ferrocenium. Based on *in situ* characterization of $\mathbf{3}^{+}$ and $\mathbf{3}^{2+}$, we hypothesize the oxidations are metal-based to yield Cr_2^{5+} and Cr_2^{6+} cores, respectively.

3.2 Introduction

Dichromium paddlewheels feature prominently in the history of metal-metal multiple bonds.[5,6,11,166] Despite the vast number of multiply bonded Cr_2^{4+} paddlewheels, only one species, a dichromium tetraguanidinate complex, $Cr_2(DPPC)_4$ (where DPPC is $(PhN)_2CN(CH_2)_4$; Figure 3.1, **a**), was reported to exhibit reversible oxidation processes by cyclic voltammetry (CV), with two redox couples at $E_{1/2}$ of 0.02 and 1.10 V (vs. Ag/AgCl).[167] The Cr_2^{5+} analogue was subsequently isolated and characterized by X-ray diffraction.[168] A high-field (W-band) EPR spectroscopic study proved definitively that the unpaired spin resided at chromium, thus supporting the formation of an oxidized Cr_2^{5+} core. The unique redox behavior was attributed to the extreme σ and π basicity of the guanidinate ligands. Recently, an Cr_2^{6+} species was isolated via oxidation of a Cr_2^{4+} paddlewheel, $Cr_2(dpa)_4$ (where dpa is dipyridylamide) using two equiv. of AgOTf.[169] The solid-state structure revealed a complete rupture of the Cr−Cr bond with a long Cr···Cr

distance of 3.197(3) Å, attesting to the challenge in isolating higher valent Cr_2^{5+} and Cr_2^{6+} paddlewheels (Figure 3.1, **b**).

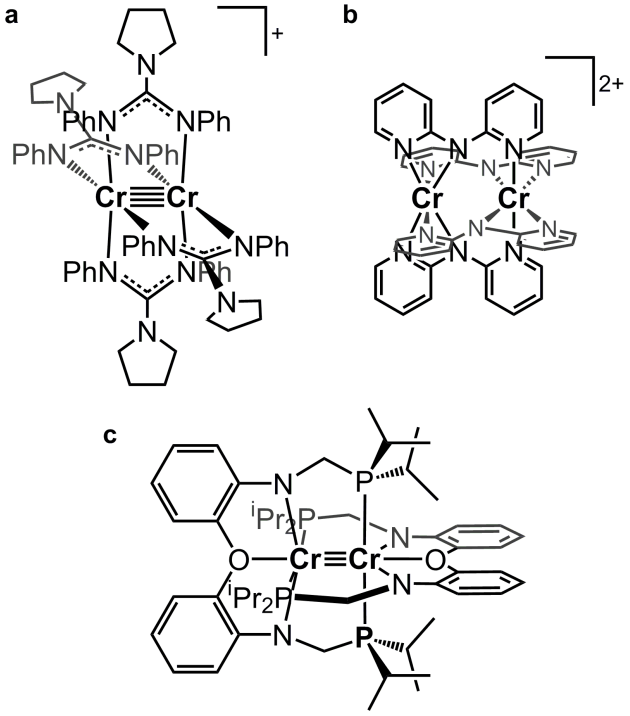

Figure 3.1. Dichromium paddlewheels

Herein, we report a Cr_2^{4+} paddlewheel supported by new pentadentate ligand that comprises mixed phosphine, amide, and ether donors. The ligand binds dichromium in a 2:1 ratio, thus saturating all the available coordination sites of the Cr_4^{2+} unit (Figure 3.1, **c**). Phosphine ligands are rare in the coordination chemistry of multiply-bonded dichromium. To our knowledge, the only structurally characterized complex is $Li_2[Cr_2(CH_2PMe_2)_6]$.[170] This is in contrast to the heavier Group 6 metals, Mo and W, for which numerous examples of phosphine-supported multiply bonded cores have been isolated, including a family of $M_2(PR_3)_4X_4$ complexes, where M is either Mo or W, and X is a halide.[171,172] The Cr_2^{4+} paddlewheel with the mixed *P*,*N*,*O*-donor set was

characterized by a suite of physical methods, including X-ray diffraction, cyclic voltammetry, and magnetic susceptibility measurements. Theoretical studies were also conducted to elucidate its electronic structure and bonding. The combined physical and theoretical data support a triply bonded dichromium core that is capable of undergoing two one-electron oxidations. The oxidized counterparts were generated *in situ*, and preliminary characterization suggests metal-based oxidations to Cr_2^{5+} and Cr_2^{6+} species.

3.3 Experimental Section

Details about the experimental synthesis and characterization protocol and calibration, including X-Ray crystallography, anomalous diffraction, UV-Vis-NIR spectroscopy, NMR, and SQUID magnetometry can be found in Appendix 3.

3.4 Computational Methods

The full molecule **3** was optimized by constraining the Cr-Cr bond distance to 2.13 Å, while allowing the ligand atoms to relax. Kohn–Sham density functional theory (KS-DFT) calculations were performed using the Gaussian 09 program package.[129] The M06-L[173] functional was used with def2-TZVP[174] basis set on Cr, N, O, and P atoms and def2-SVP[174] on C and H atoms. No symmetry constraints were imposed on the structure and once the SCF convergence was achieved, a stability check was performed using the 'stable=opt' keyword.

In addition to KS-DFT calculations, the electronic structure was further investigated using complete active space self-consistent field (CASSCF)[34] calculations on the M06-L optimized structure using the Molcas 7.8 package.[120] The relativistic all-electron ANO-RCC basis sets were used for all elements.[121,122] In all of these

calculations, the ANO-RCC-VDZP basis set was used for N, O, P, and Cr, and the ANO-RCC-MB basis set was used for C and H atoms. The following contractions were used: [5s4p2d1f] for metals, [4s3p1d] for P, [3s2p1d] for N and O, [2s1p] for C, and [1s] for H. Additionally, the Cholesky decomposition technique was used combined with local exchange screening to reduce the computational costs involved in generating the two-electron integrals.[125]

The chosen active spaces used for **3** consisted of eight valence 3d-electrons in ten 3d-orbitals plus the empty correlating 4d-shell, ranging from zero (8,10) to ten 4d-orbitals (8,20). The natural orbital occupation numbers were used for the evaluations of the effective bond order (EBO), which was calculated as the difference between the total occupancies of the bonding and antibonding molecular orbitals of the metal–metal bond divided by 2.[27,127]

3.5 Results and discussion

3.5.1 Synthesis

The ligand bis(2-((diispropylphosphino)methylamino)phenyl)ether (**1**), abbreviated as H_2(PNONP), was obtained in one step by heating bis(2-amino-phenyl)ether and 1.95 equiv $^{i}Pr_2PCH_2OH$ in THF at 65°C for 12 h (Figure 3.2). The amount of $^{i}Pr_2PCH_2OH$ used in the reaction was slightly less than stoichiometric to prevent the formation of the tris-substituted byproduct. The crude product was purified by eluting through a silica plug, giving clean H_2(PNONP) as a clear viscous oil in good yield (3.1 g, 78%).

In the metallation reactions, H_2(PNONP) was deprotonated with 2 equiv. of ^{n}BuLi, followed by metathesis with either $CrCl_3$ or $CrCl_2$. In both reactions, dinuclear chromium complexes were generated, as shown in Fig 3.2. Using $CrCl_3(THF)_3$ as the metal precursor, the orange-red bis(μ-chloride)dichromium(III) complex, [Cr(μ-Cl)(PNONP)]$_2$ (**2**), was isolated in moderate yield (55%). Switching to $CrCl_2$, the green-yellow dichromium(II) complex, [Cr(PNONP)]$_2$ (**3**), was produced featuring multiple bonds between the metal atoms (70% yield). Complex **3** can also be cleanly formed by reducing **2** with two equiv. KC_8.

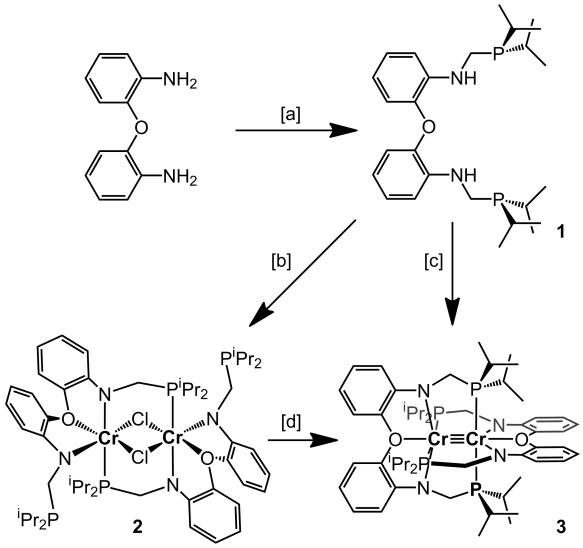

Figure 3.2. Synthesis of the ligand, H_2(PNONP) (**1**), and the dinuclear Cr complexes, **2** and **3**. [a] 1.95 ^{i}Pr$_2$PCH$_2$OH, THF, 65 °C, 12 h; [b] *i*) 2 ^{n}BuLi, Et$_2$O, −196 °C to rt, 2 h; *ii*) $CrCl_3(THF)_3$, THF, −50 °C to rt, 12 h; [c] *i*) 2 ^{n}BuLi, Et$_2$O, −196 °C to rt, 2 h; *ii*) $CrCl_2$, THF, −50°C to rt, 12 h; [d] 2 KC_8, THF, −78°C, 3 h.

3.5.2 Molecular Structures

X-ray diffraction studies were conducted on single crystals of **2** and **3** to determine their molecular structures. The structure of **2** is C_i symmetric where the (PNONP)$^{2-}$ ligands, the chromium centers, and the bridging chlorides are related by an

inversion center in the $Cr_2(\mu\text{-}Cl)_2$ core (Fig. 3.3). Each chromium center is octahedral with a facial coordination of the *N*,*O*,*N'*-donors in the ligand backbone. The remaining three donors are the two bridging chlorides and a single phosphine. The other phosphine is unligated and is disordered in the crystal lattice.

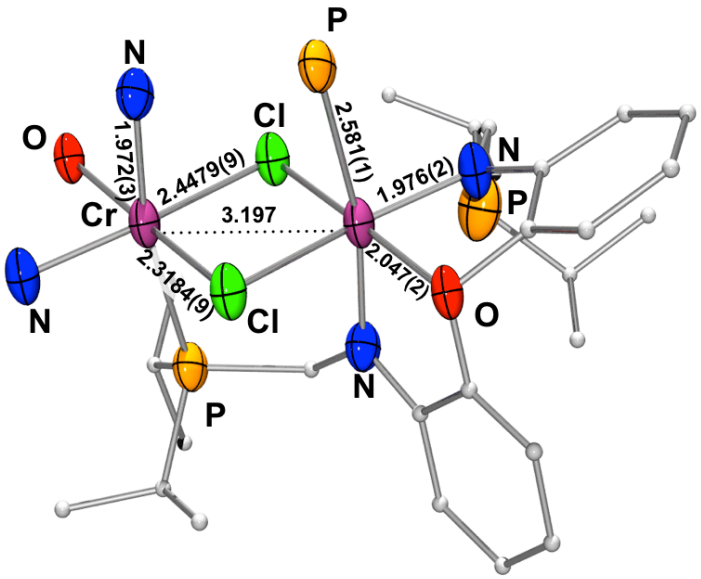

Figure 3.3. Solid−state structure of the core of dinuclear **2** by X−ray crystallography at 173 K. Thermal ellipsoids are shown at 50% probability for atoms in the first coordination sphere only. For clarity, only one of the two ligands is shown, and hydrogen atoms are omitted.

The structure of **2** is not particularly remarkable, except that the Cr−P bond distance of 2.581(1) Å is quite long (Table 3.1). A search of the Cambridge Structural Database (CSD) for $Cr_2(\mu\text{-}Cl)_2$ cores with a phosphine ligand reveals that the average Cr−P bond distance is 2.47 Å.[157] Only one other complex, $[Cr(\mu\text{-}Cl)Cl_2(Ph_2PNPhPPh_2)]_2$, has a similarly long Cr−P bond distance of 2.578(2) Å.[175] Considering that other $Cr_2(\mu\text{-}Cl)_2$ complexes are equally split between being 6- or 5-coordinate, the weak Cr−P interaction in **2** is reasonable, especially since the phosphine donor is *trans* to an amide donor. The

trans influence of the other amide donor is also observed in the elongation of the Cr−Cl bond by 0.13 Å when *trans* to the amide versus ether donor. Finally, no metal-metal interactions are present in **2** as the Cr···Cr distance of 3.197 Å is far too long.

Table 3.1. Selected bond lengths and angles for **2** and **3**

	2	**3**
Cr···Cr	3.197(2)	2.1342(5)
FSR[a]	1.36	0.91
Cr−N	1.972(3), 1.976(2)	2.026(1), 2.045(1)
Cr−O	2.047(2)	2.239(1)
Cr−P	2.581(1)	2.5568(5), 2.5742(5)
Cr−Cl	2.3184(9), 2.4479(9)	—
N−Cr−N (°)	99.3(1)	148.20(5)
P−Cr−P (°)	—	173.24(2)

[a]Formal shortness ratio (FSR) is the ratio of the Cr···Cr distance to the sum of their single-bond radii.[176]

The molecular structure of **3** is shown in Fig. 3.4. The molecule has approximate D_{2d} symmetry, with two perpendicular C_2 axes that bisect the Cr−Cr bond and cut between the paddlewheels (Fig. 3.4 b).

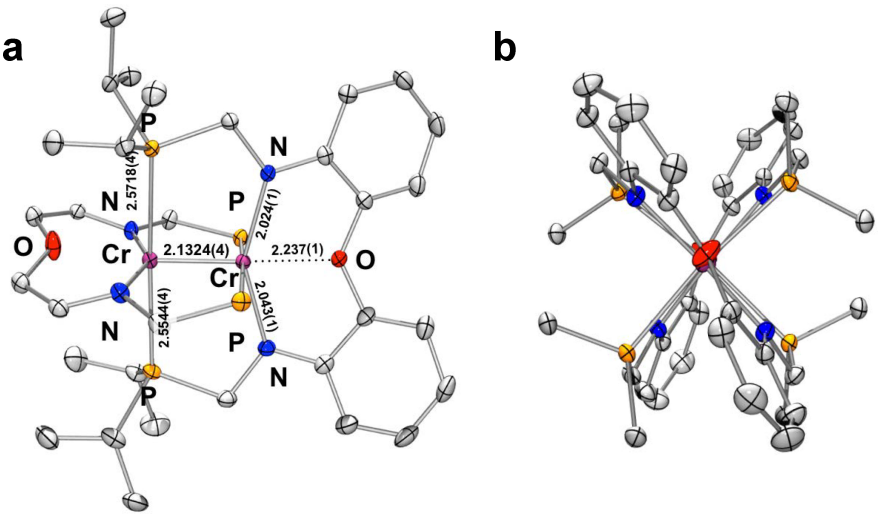

Figure 3.4. Two views of the solid-state structure of $[PNONPCr]_2$ **3** (50% probability level). View **a** is perpendicular to the Cr−Cr bond axis, and view **b** looks down the bond axis. For clarity, only one of the two ligands is fully shown. Hydrogen atoms are omitted for clarity.

The chromium atoms are closely bonded to one another with an apical ether donor *trans* to the metal-metal bond. The *N*,*O*,*N*′-donors in the ligand backbone coordinate meridionally. Both ligand arms span across the metal-metal bond, so that the phosphine donors of one ligand coordinate the other Cr center in a *trans* manner with P−Cr−P bond angles of 173.24(2)°. By contrast, the amide donors deviate from linearity, with an N−Cr−N angle of 148.20(5)°.

The Cr−Cr bond distance of 2.1324(4) Å has a formal shortness ratio (FSR) of 0.91 (Table 3.1).[11] Dichromium paddlewheels show a wide range of Cr−Cr bond distances (1.8 to 2.7 Å), but typically, < 2.0 Å is considered the safe limit for quadruple bonds.[11] Indeed, the Cr−Cr bond in **3** is longer than other dichromium paddlewheels with similar *N*- or *P*-donors. For example, the Cr-Cr bond length in $Cr_2(map)_4$, where map is 2-amino-6-methylpyridine, and in $Li_2Cr_2(Me_2PCH_2)_6$ are 1.870(3) and 1.950(2) Å, respectively.[170,177] The long Cr−Cr bond in **3** is most likely attributed to the *trans* ether donors, as Cr−Cr bonds in paddlewheel geometries are well known to elongate in the presence of axial donors. Not surprisingly, the Cr−Cr bond in **3** is quite close to the Cr_2 paddlewheel, Cr_2(*N,N*′-bis(2-methoxyphenyl)formamidinate)$_4$ (2.140(2) Å), wherein two of the tethered methoxy groups can coordinate the Cr center in the apical positions.[178] The Cr···O distances in this paddlewheel are 2.4 and 2.6 Å, which are significantly longer than the Cr−O bond length of 2.237(1) Å in **3**. The strong dative interactions in **3** likely disrupt quadruple bonding between the metal centers. Finally, the Cr−P bond lengths (2.5544(4) and 2.5718(4) Å) in **3** are considerably longer than those found in $Li_2Cr_2(Me_2PCH_2)_6$ (2.395(1) Å), but is similar to those in **2**, suggesting weak Cr−P

interactions.

3.5.3 NMR Studies

The ^{1}H NMR spectrum of the ligand **1** in C_6D_6 displays 11 resonances, which is unusual because only 8 unique protons were expected: 4 aryl protons, 1 N*H*, 1 methylene, 1 methine, and 1 methyl group. The additional resonances result from the presence of four methyl peaks, suggesting that the isopropyl groups are locked on the NMR timescale and consistent with a solution-state structure that has C_{2v} symmetry. We speculate that intramolecular hydrogen bonds between the phosphine donors and the amine protons may restrict the movement and/or rotation of the P−C bonds. The ^{31}P NMR spectrum of **1** consists of a single sharp peak at 2.4 ppm.

The ^{1}H NMR spectrum of **2** in C_6D_6 is paramagnetic with 8 broad resonances between 68 and −27 ppm, which corresponds to either two-fold or mirror symmetry of the ligand. Compared to the C_i symmetry of **2** in the solid state, the solution-state structure has higher symmetry, suggesting that the bound and dangling phosphine donors are undergoing fast exchange relative to the NMR timescale. The fluxional process would also have to invert the two aryl rings in the ligand backbone. Deligation of the bound phosphine could allow the ligand backbone to twist in a turnstile manner, so that the aryl rings exchange, prior to coordination of the other phosphine.

The ^{1}H NMR spectrum of **3** in C_6D_6 is diamagnetic with 8 sharp resonances, which is consistent with D_{2d} symmetry in the solid-state and in solution. The methylene peak is notably shifted downfield to 2.19 ppm (compared to 1.60 ppm in **1**), which is likely due to deshielding by the ring current of the Cr−Cr multiple bond (*vide infra*). To

determine if the phosphine can dissociate in **3** as in **2** (both have similarly long Cr-P bond lengths), complex **3** was further investigated by variable temperature NMR spectroscopy. Over a wide temperature range from −80° to 80°C, the phosphorus peak shifts upfield from 24.2 to 16 ppm and shows significant peak broadening with increasing temperature (Fig. 3.5).

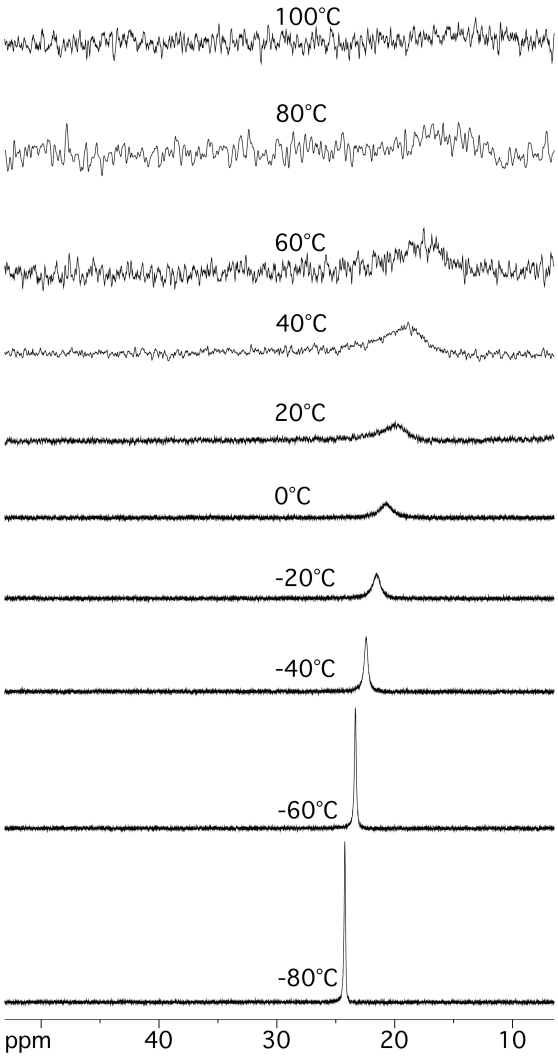

Figure 3.5. Stacked ^{31}P VT−NMR plot of **3** (THF-d_8, −80° to 100°C). At each temperature, the position and integration of the peak was determined against an internal reference of 85% H_3PO_4 at temperatures above 0°C and PPh_3 in toluene at temperatures below 0°C.

In this same temperature window, the changes in the ^{1}H NMR spectra are minimal, with only slight broadening of peaks above 80°C. Similar ^{31}P NMR observations (broadening and upfield shifting ^{31}P peaks at elevated temperatures) have been made in a series of $M_2X_4(PP)_2$ (M = Mo, W) complexes, the cause of which was thought to be observation of a singlet-triplet gap, though no magnetic measurements were reported for these complexes.[171]

Dichromium paddlewheels can exhibit weak paramagnetism at rt as a result of a small energy gap between the singlet and triplet states. The singlet-triplet energy gaps have even been estimated by analyzing ^{1}H NMR shifts as a function of temperature.[179] To determine if the triplet excited state is thermally accessible for **3**, the magnetic susceptibility was measured from 4 to 290 K. At 290 K, a minute magnetic moment of 0.68 μ_B was measured, which could arise from a low-lying paramagnetic excited state. However, diamagnetic compounds can exhibit weak paramagnetism under an applied magnetic field; and indeed, the magnetic susceptibility plot of **3** was well modeled by using only a temperature-independent paramagnetism term (TIP = 180 x 10^{-6} emu). Moreover, in the case of **3**, the ^{1}H NMR peak shifts are invariant with temperature, discounting an energetically low-lying paramagnetic state.

Metal-metal multiple bonds are known to exhibit diamagnetic anisotropy ($\Delta\chi$),[180] and indeed, the methylene resonances for **3** are notably shifted downfield. The diamagnetic anisotropy can be calculated using[181]

$$\Delta\sigma_i = \left(\frac{1}{3r^3}\right)\frac{(\Delta\chi)\left(1-3cos^2(\theta)\right)}{4\pi}$$

where $\Delta\sigma_i$ is the difference in chemical shifts of the methylene protons in **3** (4.30 ppm)

versus a suitable reference, such as the deprotonated ligand Li_2(PNONP) (3.46 ppm). The remaining variables were extracted from the solid-state structure, where *r* is the average distance and θ is the average acute angle of the protons relative to the center and axis of the metal-metal bond, respectively. Compared to other dichromium paddlewheel complexes (Table 3.2), the diamagnetic anisotropy of **3** is quite low. Notably, its $\Delta\chi$ is half the value reported for the tetraformamidinate dichromium complex, $Cr_2((p\text{-}CH_3C_6H_4N)_2CH)_4$.[182] The low diamagnetic anisotropy of **3** probably arises from the fewer number of Cr−Cr bonding electrons, which is consistent with its longer Cr−Cr bond length and lower than quadruple bond order. On the other hand, the diamagnetic anisotropies reported for a family of dichromium tetraformamidinates appear to depend more on the electronics of the aryl rings rather than Cr−Cr bond distances, which all fall within a tight range between 1.90 and 1.92 Å.[183]

Table 3.2. Diamagnetic anisotropy ($\Delta\chi$) values for selected dichromium paddlewheels.

	$\Delta\chi$[a]	ref
3	−2536	this work
$Cr_2((p\text{-}CH_3C_6H_4N)_2CH)_4$	−5230	182
$Cr_2((p\text{-}ClC_6H_4N)_2CH)_4$	−4313	183
$Cr_2((3,5\text{-}Cl_2C_6H_3N)_2CH)_4$	−2341	183
$Cr_2((m\text{-}CF_3C_6H_4N)_2CH)_4$	−3407	183
$Cr_2((m\text{-}OCH_3C_6H_4N)_2CH)_4$	−4522	183

[a] Unit of 10^{-36} m^3 $molecule^{-1}$

In particular, the complex $Cr_2((3,5\text{-}Cl_2C_6H_3N)_2CH)_4$, which contains electron-withdrawing substituents, has a similarly low $\Delta\chi$ as **3** despite having a significantly shorter Cr-Cr bond (1.916(1) Å). The small $\Delta\chi$ value of $Cr_2((3,5\text{-}Cl_2C_6H_3N)_2CH)_4$ could be rationalized by considering the effect of the aromatic ring current on the shift of

backbone proton. For instance, the backbone proton could possibly be shielded by interacting with the π-system of the aryl rings, thus countering the deshielding effect of the metal-metal multiple bond. In the case of **3**, the methylene protons are sufficiently removed from the aryl rings in the ligand backbone, so to eschew this alternative explanation.

3.5.4 Cyclic Voltammetry

Complex **3** shows two reversible redox couples at $E_{½}$ = −472 and −753 mV versus $FeCp_2^{0/+}$. The reversibility of these processes ($E_{pa}-E_{pc}$ = 98 mV for both processes; i_{pa}/i_{pc} = 1.14, 1.00 for $\mathbf{3}^{0/+}$ and $\mathbf{3}^{+/2+}$, respectively) suggests the complex may undergo two successive one-electron transfers with minimal structural rearrangement or decomposition. In general, the redox processes of dichromium paddlewheels are irreversible, and attempts to chemically oxidize the Cr_2^{4+} core result in decomposition, presumably via rupture of the Cr−Cr bond.[167] As mentioned above, the X-ray structure of a dinuclear Cr(III)Cr(III) complex, made from oxidizing $Cr_2(dpa)_4$ with 2 equiv. AgOTf, revealed a long Cr···Cr distance of 3.197(3) Å.[169] To our knowledge, the only dichromium paddlewheel that displays any reversible redox processes is the tetraguanidinate complex, $Cr_2(DPPC)_4$. In **3**, the two redox couples are separated by 281 mV, which is small compared to the 1.08 V separation for $Cr_2(DPPC)_4$.[167] The comproportionation constant (K_c) for **3** is 5.66×10^4, which is 14 magnitudes smaller than $Cr_2(DPPC)_4$ ($K_c = 1.85\times10^{18}$), meaning that the electronic delocalization in **3** is substantially less than in $Cr_2(DPPC)_4$. Nonetheless, the K_c value for **3** is sufficiently large that isolation of the mixed-valent Cr(II)Cr(III) complex should be feasible.

Unfortunately, attempts to isolate the monocation or dication by chemical oxidation have not yielded any well-characterized compounds to date. Addition of 1 and 2 equiv. $[FeCp_2][BAr^F{}_4]$ did generate new species that were sufficiently stable in solution to allow for *in situ* characterization. For instance, CV scans were performed on an electrochemical solution of **3** after adding 1 and 2 equiv. ferrocenium (Fig. 3.6). As expected, each equivalent of oxidant shifted the open circuit potential in the positive direction. The general invariance of the redox potentials for the redox trio, $[Cr_2(PNONP)_2]^{0/+1/+2}$, indicates that the dinuclear molecule remains intact on the CV timescale upon both one-electron oxidations.

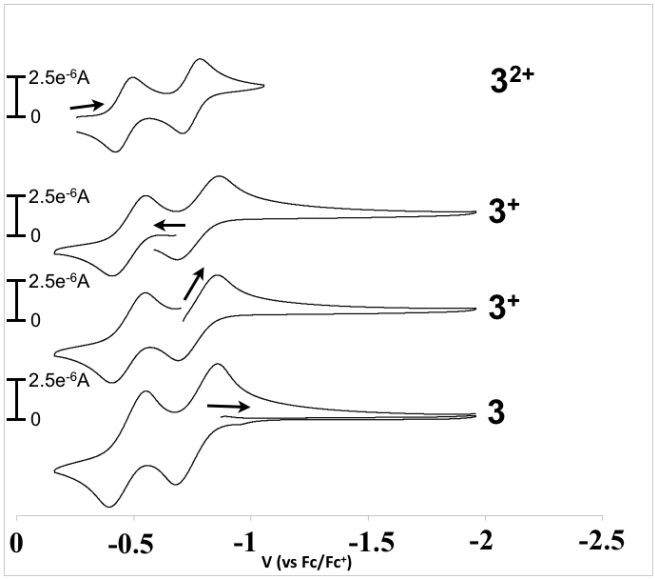

Figure 3.6. CV of $[Cr_2(PNONP)_2]^{0/+1/+2}$ (**3**, $\mathbf{3}^+$, and $\mathbf{3}^{2+}$) in 0.1 M $[N^nBu_4]PF_6$ with a scan rate of 200 mV/s. Complexes $\mathbf{3}^+$ and $\mathbf{3}^{2+}$ were generated *in situ* by adding $[FeCp_2][BAr^F{}_4]$. Potentials were referenced to $FeCp_2^{0/+}$.

The oxidative processes could be metal and/or ligand centered. As mentioned previously, reversible oxidation(s) for dichromium paddlewheels are rare. To our knowledge, only one Cr_2^{5+} and no Cr_2^{6+} paddlewheel has been structurally

characterized.[167,168] Thus, we considered the possibility of ligand-based redox reactivity, where each $PNONP^{2-}$ ligand in the dimer is oxidized by one electron to the monoanionic radical state, $PNONP^{\bullet-}$. To investigate the redox non-innocence of the $PNONP^{2-}$ ligand, we performed CV on Zn(PNONP), which was made by mixing Li_2PNONP to $ZnCl_2$ and doing a simple work up. Proton and phosphorous NMR of the crude showed a diamagnetic product that is neither the neutral or deprotonated ligand. No oxidative events were observed below 1 V vs. $FeCp_2^{0/+}$, suggesting that the ligand is redox innocent below 1 V. In addition, $\mathbf{3}^+$ was further characterized by X-band EPR spectroscopy. An isotropic S = ½ signal was observed at g = 1.98, which is typical for a chromium-based spin, as a ligand-based spin would have g = 2.00. Higher frequency EPR experiments would be needed to definitively assign the metal-character of the spin, as these g-values are close to 2.0.[168] Thus, we tentatively assign the redox processes as metal-based oxidations of the Cr_2^{4+} core to Cr_2^{5+} and Cr_2^{6+}.

3.5.5 Electronic Absorption Spectroscopy

The electronic absorption spectra of **3**, $\mathbf{3}^+$, and $\mathbf{3}^{2+}$, are shown in Figure 3.7, with the spectral data listed in Table 3.3. Complex **3** has multiple absorptions in the visible range. Of note, two of the spectral features for **3** show temperature dependence. As the THF solution of **3** is cooled from 0°C to −80 °C, the shoulder at 500 nm decreases while the band at 619 nm increases in intensity. Thus, the yellow-green solution at rt turns more intensely green upon cooling. We hypothesize that the color change and the VT ^{31}P NMR behavior are related, resulting from a fluxional process where the phosphine arms are labile. We expect the δ→δ* transition energy to be sensitive to the binding of phosphine

donors, as the ligand field energies are directly affected by their interaction with the Cr_2 unit. Hence, the band at 619 nm may be interpreted as the δ→δ* transition energy of the fully ligated dichromium paddlewheel.

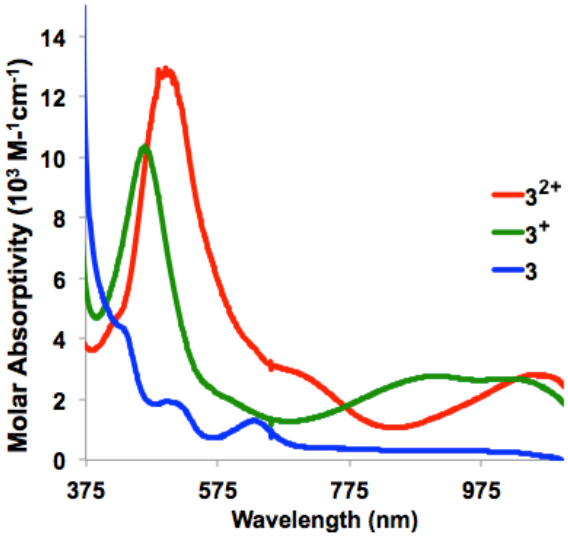

Figure 3.7. *In situ* oxidation of **3** with $[FeCp_2][BAr^F{}_4]$ in THF at −80°C, to produce $\mathbf{3}^+$, and $\mathbf{3}^{2+}$. The ferrocene byproduct (one and two equivalents, respectively) has a weak absorption at 440 nm, but its intensity (100 M^{-1} cm^{-1}) is very low.

This transition energy for **3** (16,155 cm^{-1}) is low relative to other Cr_2^{4+} paddlewheel complexes, which are typically yellow and have δ→δ* bands near 450 nm (~22,000 cm^{-1}). The comparison is unsettling because a small δ→δ* gap would imply an accessible triplet excited state, which would contradict the ^{1}H VT NMR data and the magnetic susceptibility measurements. We thus propose an alternative explanation where because of the longer Cr−Cr bond, δ-bonding becomes suppressed and the d_{xy} orbitals are more localized giving a singlet diradical ground state, i.e. (Cr d_{xy})^1(Cr' d_{xy})^1. Thus, the low energy band may be more aptly described as a intermetal *d-d* charge transfer, e.g. (Cr d_{xy})^1(Cr' d_{xy})^1 → (Cr d_{xy})^2(Cr' d_{xy})^0.

To the best of our knowledge, Cr_2^{4+} paddlewheel complexes with short Cr-Cr bond lengths (≤ 2.0 Å) only exhibit δ→δ* transitions between 445 and 490 nm (22500-20800 cm^{-1}).[167,182,184–186] A few exception exist, such as the trimetallic complexes, $Cr_2Fe(dpa)_4Cl_2$ and $Cr_2Zn(dpa)_4Cl_2$.[187,188] The latter complexes are characterized by low energy transitions at 700 and 697 nm (14300 and 14600 cm^{-1}), respectively, which is similar to **3**. These transitions were assigned to the Cr_2^{4+} unit. Though the Cr-Cr bond lengths are quite short 2.0 Å, the N-Cr-Cr-N torsion angles are atypically large at ~20 degrees. As large torsions angles should also disrupt δ-bonding, we proposed that the low-energy bands are the transitions of localized d_{xy} electrons in the Cr_2^{4+} core.

Table 3.3. Visible electronic absorption data (λ_{max}, nm; molar absorptivity in parenthesis, $M^{-1}\,cm^{-1}$) for **3**, $\mathbf{3}^+$, and $\mathbf{3}^{2+}$ and selected dichromium paddlewheels.

Complex	**λ_{max}**, nm (**ε**, L $mol^{-1}cm^{-1}$)	ref
3	428 (4590), 500 (1900), 619 (845), 762 (110)	this work
$\mathbf{3}^+$	464 (10000), 580 (2000), 899 (2780), 1020 (2690)	this work
$\mathbf{3}^{2+}$	489 (12700), 690 (2900), 1058 (2800)	this work
$Li_4[Cr_2(CH_3)_8]$	454 (700)	189
$Cr_2(mhp)_4$ [a]	445 (320)	185,190
$Cr_2(DPPC)_4$ [a]	454 (980)	167
$[Cr_2(DPPC)_4]PF_6$ [a]	435 (2200), 580 (3200), 752 (6800)	167

[a] mhp = deprotonated 2-hydroxy-6-methylpyridine; DPPC = $[(PhN)_2CN(CH_2)_4]^-$ (guanidinate)

The spectral changes between **3** and its oxidized cogeners, $\mathbf{3}^+$ and $\mathbf{3}^{2+}$, confirm the formation of new species upon *in situ* oxidation with $[FeCp_2][BAr^F{}_4]$ at −80 °C. The most notable change from **3** to $\mathbf{3}^+$ is the appearance of an intense band at 464 nm (21,550 cm^{-1}), as the solution turns a red-brown color. This band shifts to lower energy (489 nm, 20,450 cm^{-1}) in $\mathbf{3}^{2+}$. Because of the similarity of this band in both oxidized species, we speculate this is a π → δ transition, specifically $\pi^4\delta^1 \rightarrow \pi^3\delta^2$ in $\mathbf{3}^+$ and $\pi^4\delta^0 \rightarrow \pi^3\delta^1$ in $\mathbf{3}^{2+}$.

The additional energy needed to overcome electron-electron repulsion in $\mathbf{3}^{+}$ could account for its higher energy transition relative to $\mathbf{3}^{2+}$.

3.5.6 Theory

To gain insight into the electronic structure and bonding nature of **3**, KS-DFT and CASSCF studies were conducted. All the calculations were performed on the full molecule, using the X-ray structure of **3**, where only the Cr-Cr bond distance was constrained to the experimental vale. To address whether diamagnetic **3** is truly a closed-shell singlet or a singlet diradical, ground state energies were computed for both the restricted and unrestricted singlet. The singlet diradical state was found to be lower in energy, by ~36 kcal/mol using the M06-L functional. The Kohn-Sham molecular orbitals (MOs) of the singlet diradical ground state (Fig. 3.8) are consistent with the electronic configuration, $(\pi)^2(\pi)^2(\sigma)^2(\text{Cr } d_{xy})^1(\text{Cr' } d_{xy})^1$, where the chromium atoms are formally triply bonded.[11]

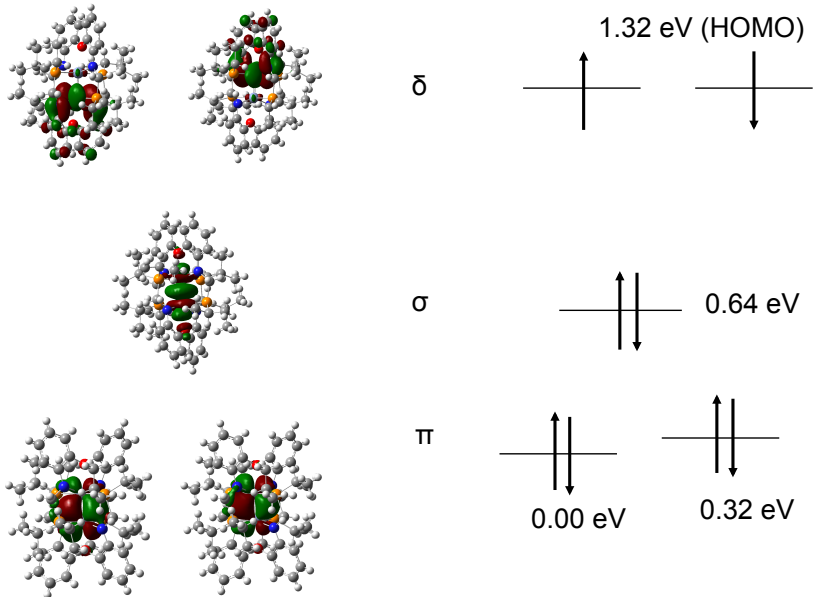

Figure 3.8. M06-L molecular orbitals for singlet diradical **3**.

For the CASSCF calculations on **3**, two active spaces were investigated, each containing 8 valence electrons in either ten 3*d* orbitals (10 total orbitals) or in ten 3*d* plus ten 4*d* orbitals (20 total). Both calculations yielded similar results. The ground-state wave function is highly multiconfigurational, as the Hartree–Fock configuration, which is the dominant configuration, accounts for only 23% of the total wave function. The natural orbitals that arise from the CASSCF calculations are shown in Fig 3.9. They are similar to the DFT orbitals, but one key difference is that the d_{xy} orbitals form linear combinations in CASSCF. The resultant MOs, however, show little to no overlap between the atomic orbitals, making them non-bonding, and they are best described as (Cr d_{xy} + Cr' d_{xy}) and (Cr d_{xy} - Cr' d_{xy}), rather than δ and δ*, respectively.

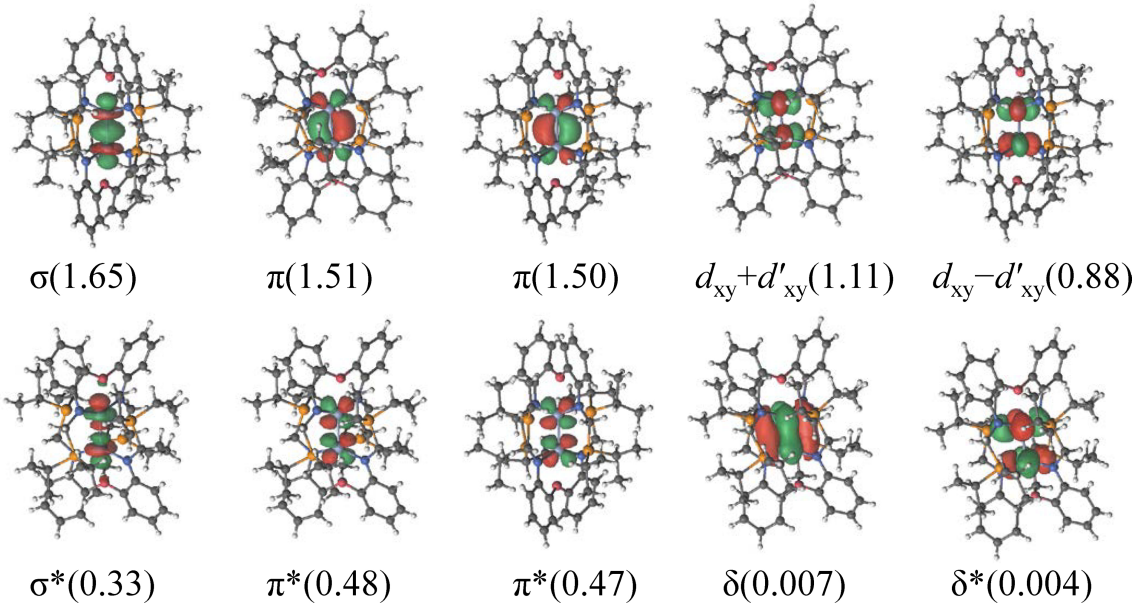

Figure 3.9. Natural orbitals of **3** and their electron occupation numbers.

For the total ground-state wave function, the natural orbital occupation numbers are: $(\sigma)^{1.66}\,(\pi)^{1.53}(\pi)^{1.53}\,(\text{Cr } d_{xy} + \text{Cr' } d_{xy})^{1.12}(\text{Cr } d_{xy} - \text{Cr' } d_{xy})^{0.86}(\pi^*)^{0.46}(\pi^*)^{0.45}(\sigma^*)^{0.32}$. The

partial occupation of anti-bonding orbitals decreases the effective metal-metal bond order to 1.8, which is consistent with the long Cr-Cr bond in **3**. Moreover, the absence of delta-bonding in **3** explains the atypical spectroscopic properties of **3** relative to other quadruply bonded dichromium paddlewheels in the literature.[191]

3.5.7 Initial Reactivity Studies

Preliminary reactivity studies were conducted to determine if the multiply bonded Cr_2^{4+} core of **3** could mediate redox reactions. Indeed, the pair of **2** and **3** was attractive for proton-to-H_2 reduction, whereby the $Cr(II)_2$ core in **3** reacts with two equiv HCl to generate H_2 and in turn becomes oxidized to **3** ($Cr(III)_2Cl_2$). Alas, none of these anticipated products were observed, and instead, HCl merely protonates the ligand to form H_2(PNONP). We also investigated whether **2** could be photolyzed to release Cl• (or Cl_2) to generate **3**, but that was also unsuccessful.

Under a CO_2 atmosphere, **3** reacts cleanly to generate a product that by ESI-MS is consistent with a 4:1 ratio of CO_2 to **3**. With $^{13}CO_2$, the *m/z* of the parent peak increases by 4. ^{13}C NMR studies suggest that the product of this reaction is a chromium paddlewheel complex with bridging carbamate ligands, which are formed by insertion of the anionic amide ligand groups into CO_2. Indeed, the product of this reaction can be independently synthesized by reacting the deprotonated ligand with CO_2 followed by reaction with $CrCl_2$.

3.6 Conclusions

Dinuclear chromium complexes self-assemble in the metallation reactions of the

mixed phosphine-amide-ether donor ligand, $PNONP^{2-}$, with either Cr(II) or Cr(III) chloride reagents. In the case of Cr(II), the Cr_2^{4+} paddlewheel complex, Cr_2(PNONP) (**3**), was generated that contains a formal triple Cr≡Cr bond. The computed electronic structure supports this bonding description, and reveals that two *d*-electrons are non-bonding and are localized at the individual chromium sites. The electronic structure is consistent with the relative long Cr-Cr bond length (> 2.0 Å), which would preclude delta-bonding, and thus, rationalizes the unusually rich electronic absorption spectra of **3** relative to other quadruply bonded Cr_2^{4+} species. In addition, Cr_2(PNONP) shows two intriguing redox couples that are reversible on the CV timescale. We propose that the oxidized members are the mixed-valent Cr_2^{5+} and the Cr_2^{6+} species, but further characterization will be needed to definitively assign their oxidation states.

Author Contributions

Experimental: Reed J. Eisenhart, Kelsey Boyle, Connie C. Lu.

Theoretical: Rebecca K. Carlson, Laura Gagliardi

Chapter 4

Pushing the limits of delta bonding in metal-chromium complexes with redox changes and metal swapping

4.1 Overview

Into the metalloligand Cr[N(*o*-(NCH$_2$P(^{i}Pr)$_2$)C$_6$H$_4$)$_3$] (**1**, CrL), a second chromium atom was installed to generate the dichromium complex, Cr$_2$L (**2**), which is a homobimetallic analogue of the known MCrL complexes, where M is manganese (**3**) or iron (**4**). The cationic and anionic counterparts, [MCrL]$^+$ and [MCrL]$^-$, were targeted, and each MCr pair was isolated in at least one other redox state. The solid-state structures of the [MCrL]$^{+,0,-}$ redox members are essentially the same, with ultra-short metal-metal bonds be- tween 1.97 – 1.74 Å. The formal shortness ratios (*r*) of these interactions are between 0.84 and 0.74 and are interpreted as triple to quintuple metal-metal bonds with the aid of theory. The trio of $(d\text{-}d)^{10}$ species, [Cr2L]$^-$ (**2^{red}**), MnCrL (**3**), and [FeCrL]$^+$ (**4^{ox}**), are *S*= 0 diamagnets. On the basis of M−Cr bond distances and theoretical calculations, the strength of the metal-metal bond across the $(d\text{-}d)^{10}$ series increases for M = Fe < Mn < Cr. The methylene protons in the ligand are shifted downfield in the ^{1}H NMR spectra, and the diamagnetic anisotropy of the metal-metal bond was calculated as −3500, −3900, and −5800 x 10^{-36}m^3 molecule^{-1} for **2^{red}**,**3**, and **4^{ox}** respectively. The magnitude of diamagnetic anisotropy is, thus, affected more by bond polarity than by bond order. A comparative Vis-NIR study of quintuply bonded **2^{red}**, and **3** revealed a large red-shift in the $\delta^4 \rightarrow \delta^3\delta^*$ transition energy upon swap- ping from the Cr$_2$ to the MnCr core. Complex **2^{red}** was further investigated by resonance Raman spectroscopy, and a band at 434 cm^{-1} was assigned as the Cr-Cr bond vibration. Finally, **4^{ox}** exhibited a Mössbauer doublet with an isomer shift of 0.18 mm/s that suggests a primarily Fe-based oxidation to Fe(I).

4.2 Introduction

The chemical bond is arguably the most fundamental yet evolving concept in chemistry.[1] Although the notation of the delta bond was developed in 1929,[192,193] the first structural evidence of the delta bond came in 1964 when a quadruple bond ($\sigma + 2\pi + \delta$) was invoked to explain the short Re-Re distance and eclipsed conformation in [Re$_2$Cl$_8$]$^{2-}$.[2] Since this seminal discovery, studies of metal-metal multiple bonds have flourished and traversed a number of disciplines. Physical chemists coupled new methodologies to generate and interrogate bare, or unligated, dinuclear metal clusters, so to understand the bonding, electronic structures, and spectroscopic properties of metal-metal bonds across the periodic table.[194,195] These efforts were heavily aided by theorists,

who improved the accuracy of their predictions by developing new electronic structure theories to address the problems of electron correlation.[27,40,127]

In a momentous discovery, a complex with a quintuply bonded ($\sigma + 2\pi + 2\delta$) dichromium unit was isolated using bulky terphenyl ligands.[5] Today, the coordination chemistry of the quintuple bond comprises several dichromium, a few dimolybdenum, and a single MnCr heterobimetallic.[6] The reactivity of these quintuply bonded species are currently being explored, and initial studies show promise as inorganic counterparts to the wider reactivity of unsaturated carbon-carbon bonds.[6,8,166,196]

Heterometallic multiple bonds involving exclusively first-row transition metals have been reported by Thomas and coworkers[197,198] and by some of us.[21,22] Starting from the monochromium complex, Cr[N(*o*-($NCH_2P(^iPr)_2$)C_6H_4)$_3$] (abbreviated as CrL, **1**), which acts as a metalloligand to bind a second transition metal, a series of MCr binuclear compounds was isolated for M = Mn, Fe, Co, and Ni. The series culminated in a quintuply bonded MnCr heterometallic, which opened the possibility of investigating metal substitution effects on delta bonding. In addition, the rich electrochemistry of the neutral MCr bimetallics gave us hope that redox counterparts with high bond multiplicity could be isolated and probed to understand the redox properties associated with delta bonding. To this end, we report four additional members of the MCr series, including the homobimetallic dichromium complex, Cr_2L (**2**), and the MCr cationic and/or anionic counterparts, $[MCrL]^{+/-}$ for M = Cr, Mn, and Fe (Figure 4.1). In particular, a trio of (d-d)^{10} species, comprising $[Cr_2L]^-$ (**2**$^{\mathbf{red}}$), MnCrL (**3**), and $[FeCrL]^+$ (**4**$^{\mathbf{ox}}$), form a unique group of isostructural and potentially isoelectronic bimetallics with multiple metal-metal

bonds. These bimetallics of the mid first-row transition metals have been investigated through spectroscopic studies (NMR, EPR, Raman, and Mössbauer) that are complemented with quantum chemical calculations.

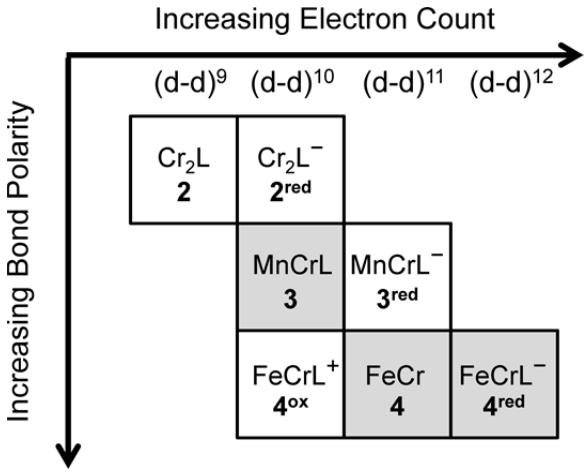

Figure 4.1. Metal-chromium complexes and their $(d\text{-}d)^n$ counts, where the polarity of the M-Cr bonds increases as M = Cr > Mn > Fe. White boxes represent new compounds. Previously reported complexes are shown in light gray boxes.

4.3 Experimental Section

Details about the experimental synthesis and characterization protocol and calibration, including X-Ray crystallography, UV-Vis-NIR spectroscopy, and NMR, can be found in Appendix 4.

4.4 Computational Methods

A quantum chemical study of the model complexes, **2'**, $\mathbf{2^{red\prime}}$, $\mathbf{3^{red\prime}}$ and $\mathbf{4^{ox\prime}}$, was performed, where the isopropyl groups were truncated to methyls. Analogous studies for **3', 4',** and $\mathbf{4^{red\prime}}$ were reported previously.[21,22] Gas-phase geometry optimizations were performed with density functional theory (DFT) using the Perdew−Burke−Ernzerhof (PBE)[199] exchange-correlation functional as implemented in

the TURBOMOLE 6.4 package.[200] Initial starting structures for geometry optimizations were derived from experimentally determined X-ray structures. No symmetry constraints were used. For C and H atoms, the double-ζ quality basis sets def-SV(P) was used. The triple-ζ quality basis set def-TZVP was employed for N and P. Additional polarized functions were introduced for Fe, Mn, and Cr by using def-TZVPP.[135] The DFT calculations were performed using an unrestricted, broken symmetry formalism, and the resolution of the identity (RI) approximation was used for the Coulomb integrals.[125] All stationary points were confirmed as minima by computing vibrational frequencies using the harmonic approximation. For $\mathbf{2}^{\mathbf{red'}}$, Raman intensities were computed from polarizabilities as implemented in TURBOMOLE. To increase the accuracy of computed vibrational frequencies, a scale factor is commonly employed.[201,202] In the computed Raman spectra for $\mathbf{2}^{\mathbf{red'}}$, the computed frequencies (391, 473, 503, 597 cm^{-1}) were scaled by a factor of 0.88 to obtain the shown frequencies (344, 416, 443, 524 cm^{-1}), whose intensities were plotted as a convolutions of Lorentzian functions with half height widths of 10 cm^{-1}.

In addition to DFT calculations, the electronic structure was further investigated using complete active space and restricted active space self-consistent field (CASSCF/RASSCF) followed by second-order perturbation theory (CASPT2/ RASPT2) calculations on the DFT/PBE optimized geometries using the Molcas 7.8 package.[120] Relativistic effects were included through the use of the scalar Douglas−Kroll−Hess (DKH) Hamiltonian.[123,124] The relativistic all-electron ANO-RCC basis sets were used for all elements.[121,122] In all of these calculations, the ANO-RCC-VTZP basis set was

used for the Fe, Mn, and Cr, ANO-RCC-VDZP basis set was used for N and P, and the ANO-RCC-MB basis set was used for C and H. Additionally, the Cholesky decomposition technique was used combined with local exchange screening to reduce the computational costs involved in generating the two-electron integrals significantly.[125] Atomic charges were computed at the CASSCF level for the ground state using the LoProp procedure.[203]

Previously, the CASSCF active space for **3', 4',** and **4$^{red'}$** was constrained to the valence 3*d*-electrons in 15 orbitals, which include all the 3d orbitals from the two metals and five empty correlating 4*d*-orbitals of Mn or Fe.[21,22] A larger active space was used here for **2'**, **2$^{red'}$**, **3$^{red'}$** and **4$^{ox'}$** consisting of the valence 3*d*-electrons in 20 orbitals, which include all the 3*d* orbitals and the empty correlating 4d-orbitals of both metals. For consistency, **3', 4',** and **4$^{red'}$** were recomputed with the larger active space, and the results were consistent with the earlier studies. To account for the double shell effect, RASSCF calculations incorporating a large configuration interaction space were performed for all species and spin multiplicities, denoted by (*n*,20)/(*n*,10)/2, where *n* = 9, 10 or 11 for the $(d\text{-}d)^{9}$, $(d\text{-}d)^{10}$ and $(d\text{-}d)^{11}$ species respectively.[40] In this notation, the first set of parentheses corresponds to the total number of electrons (*n*) and the total number of orbitals (20) in all of the RAS spaces. The second set of parentheses corresponds to the number of active electrons and orbitals in the primary space, containing the 3*d* orbitals of both metals; the final value of 2 refers to the maximum number of electrons allowed into the secondary space. The natural orbital occupation numbers were used for the evaluation of the effective bond order (EBO), which was calculated as the difference

between the total occupancies of the bonding and antibonding molecular orbitals of the metal–metal bond divided by 2.[27,127]

State Averaged-Complete Active Space Self Consistent Field (SA-CASSCF) calculations were performed for the $(d\text{-}d)^{10}$ complexes. Due to the computational cost of calculating multiple electronic states, the active spaces for SA-CASSCF calculations were truncated from the aforementioned RASSCF choices to a (10,10) active space. For each $(d\text{-}d)^{10}$ complex, a 6 root calculation was performed. The complete active space state interaction (CASSI) method was applied to compute the transition probabilities.[204,205] CASSI results served to obtain a qualitative orbital ordering based on the analysis of the energies and the nature of the orbitals involved in the electronic excitations of the various roots and to characterize the low energy vis-NIR spectroscopic transitions.

4.5 Results and Discussion

4.5.1 Synthesis and cyclic voltammetry (CV)

The neutral MCr complexes for M = Mn and Fe were generated previously by mixing the metal dibromide precursors, MBr_2, with the monometallic chromium complex (**1**, CrL), and two equiv. of reductant, KC_8 (Figure 4.2).[21,22] A similar procedure was used to generate the chromium homobimetallic. Mixing **1**, chromium(III) chloride, and three equiv. of KC_8 produced the red-brown di-chromium complex (**2**, Cr_2L). As previously reported, neutral MCr complexes where M = Mn, Fe, Co and Ni, exhibit multiple one- electron transfer processes by cyclic voltammetry (CV).

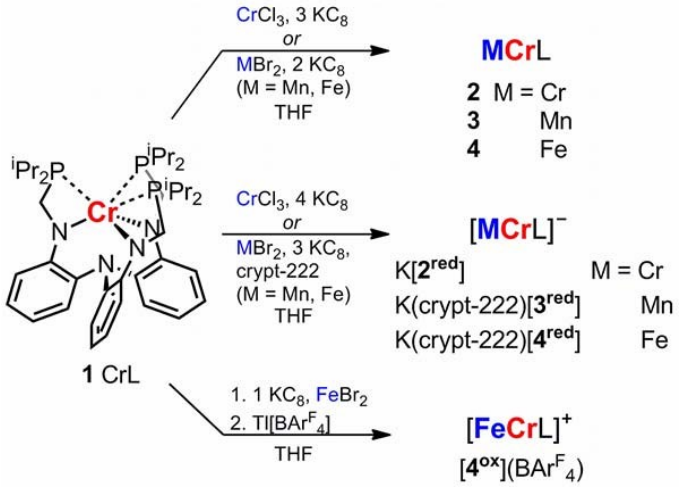

Figure 4.2. From complex **1** (*left*), the syntheses of: neutral metal-chromium complexes **2** – **4** and their one-electron reduced and/or oxidized counterparts.

The CV of **2** is shown in Figure 4.3, along with the CVs of the manganese−chromium (**3**, MnCrL) and iron−chromium (**4**, FeCrL) complexes, and the redox potentials are listed in Table 4.1.

Table 4.1. Redox Potentials (V)[a] of **2** – **4**

Complex	Reduction ($E°'$)	Oxidation ($E°'$)
2	−2.26	−1.66
3	−2.21, −2.55[b]	−1.18[c]
4	−2.33	−1.32, −0.62

[a] vs. $FeCp_2^{0/+}$ [b] quasi-reversible [c] irreversible, E_{pa} reported

Complex **2** exhibits two reversible, one-electron transfer processes: an oxidation at −1.66 V and a reduction at −2.26 V (vs. $FeCp_2/FeCp_2^+$). Presumably, reduction of **2** generates a $\{Cr_2\}^{10}$ species that would be isoelectronic to diamagnetic **3**. Collectively, the CVs suggest the possibility of characterizing several redox members (Figure 4.1), including an isoelectronic $(d\text{-}d)^{10}$ subset that comprises $[Cr_2L]^-$, MnCrL, and $[FeCrL]^+$.

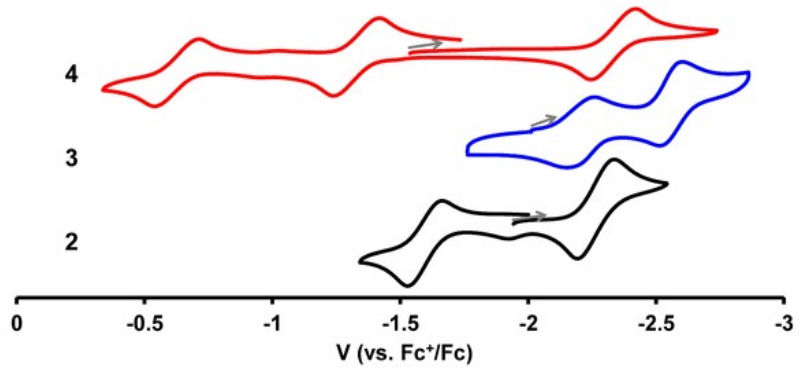

Figure 4.3. Cyclic voltammograms of **2** – **4** with [*n*Bu$_4$N]PF$_6$ (0.1 to 0.4 M) in THF (vs. FeCp$_2^{0/+}$). Scan rates and electrolyte concentrations for: **2** (black), 25 mV/s, 0.4 M; **3** (blue), 250 mV/s, 0.4 M; and **4** (red), 10 mV/s, 0.1 M.

The reduction of **4** to [FeCrL]$^-$ (**4^{red}**) was previously achieved using one equiv. KC$_8$ in THF.[21] The monoanionic counterparts of **2** and **3**, [Cr$_2$L]$^-$ (**2^{red}**) and [MnCrL]$^-$ (**3^{red}**), respectively, were generated from **1** using CrCl$_3$ and MnBr$_2$, respectively, and the appropriate equivalents of KC$_8$ (Fig 4.2). In THF, the color of **2^{red}** is forest green, while **3^{red}** and **4^{red}** are red-brown. One equivalent of 2.2.2-cryptand (crypt-222) was added to solutions of **3^{red}** or **4^{red}** to improve the crystallinity of the product. Chemical oxidation of **4** to [FeCrL]$^+$ (**4^{ox}**) can be performed with [FeCp$_2$](B(Ar$_F$)$_4$). However, an alternative, cleaner synthesis of [**4^{ox}**](B(Ar$_F$)$_4$) avoids neutral **4** altogether. Complex **1** was stirred with FeBr$_2$ and one equiv. KC$_8$ to generate a green intermediate which is presumably (Br)FeCrL. Abstraction of the halide with Tl(B(Ar$_F$)$_4$) gave [**4^{ox}**](B(Ar$_F$)$_4$) in moderate yield. The presence of the B(Ar$_F$)$_4$ counter-ion renders [**4^{ox}**](B(Ar$_F$)$_4$) highly soluble even in hydrocarbon solvents such as benzene. So far, efforts to isolate the dicationic (*d*-*d*)[9] [FeCrL]$^{2+}$ or the dianionic (*d*-*d*)[12] [MnCrL]$^{2-}$ have not been fruitful.

4.5.2 NMR and EPR spectroscopy

The three $(d\text{-}d)^{10}$ species, $\mathbf{2^{red}}$, **3**, and $\mathbf{4^{ox}}$ are all diamagnetic, allowing for detailed comparisons by ^{1}H NMR spectroscopy. These complexes all display fluxional behavior, as shown in Figure 4.4 for $\mathbf{2^{red}}$. At high temperature, each complex exhibits C_{3V} symmetry (total of 7 unique protons) with equivalent methyl, methylene, and methine protons. As the temperature is lowered, the solution structures of the MCrL species adopt a C_3-propeller configuration (total of 12 unique protons), where the methylene protons are diastereotopic, and the two methine protons and four methyl groups are also distinct.

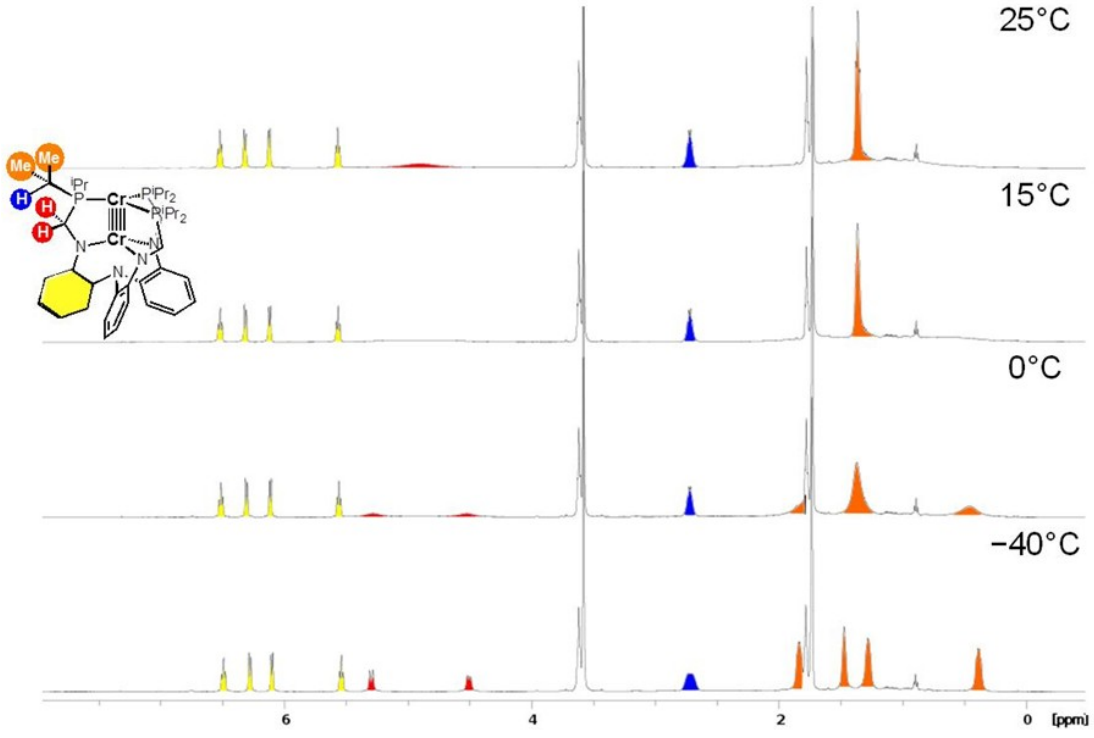

Figure 4.4. Stacked plot of variable temperature ^{1}H NMR spectra for K[$\mathbf{2^{red}}$] (THF−d_8, 500 MHz). Protons are color-matched to by the inset color figure. For clarity, only one ligand arm is labeled.

The energy barrier ($\Delta G^{\ddagger}$) for the fluxional process can be estimated from the coalescence temperature of the methylene peaks for the trio of (d-d)[10] complexes, $\mathbf{2^{red}}$, **3**, and $\mathbf{4^{ox}}$.[206] For example, the coalescence of the methylene resonances of $\mathbf{2^{red}}$ occurs at 15°C, as shown in Figure 4.4. The energy barriers for $\mathbf{2^{red}}$, **3**, and $\mathbf{4^{ox}}$ are 13.0, 14.6, and 16.6 kcal mol^{-1}, respectively. Two possible mechanisms could account for the observed fluxionality: (1) dissociation of one phosphine donor followed by rotation and re-association,[207] or (2) a simple twisting of the methylene backbone while the phosphine arms remain associated. Unfortunately, the variable temperature (VT) ^{31}P-NMR behavior of these species was inconclusive. Notably, the aryl protons of the ligand backbone stay sharp and coupled throughout the VT NMR studies of $\mathbf{2^{red}}$, **3**, and $\mathbf{4^{ox}}$ (up to 60 °C), which rules out the presence of a low-lying triplet state.

The ^{1}H NMR spectrum of **2** is paramagnetic and displays 12 resonances, suggesting that it is locked in a C_3 environment on the NMR timescale. The S = ½ spin state was confirmed by X-band EPR spectroscopy (Figure 4.5, top). The S = ½ EPR signal is isotropic with g = 1.99, which is typical for a Cr-based spin.[208,209] The spectral splitting arises from coupling to three I =½ ^{31}P nuclei with an isotropic coupling constant (A) of 10 x 10^{-4} cm^{-1}, suggesting that spin density resides at the Cr center in the phosphine-binding pocket. Notably, the hyperfine coupling is lower than that reported for octahedral, phosphine-ligated Cr(I) carbonyls, e.g. $[Cr(CO)_3(PMe_3)_3]^+$, which feature hyperfine coupling constants in the range of 57 to 96 MHz, or 19 to 36 x 10^{-4} cm^{-1}.[210] This may suggest some delocalization of the unpaired spin in the

dichromium unit. Complex **3**$^{\mathbf{red}}$ is also paramagnetic, and the 12 observed resonances by ^{1}H NMR spectroscopy are consistent with C_3 symmetry. The solution-state magnetic moment of **3**$^{\mathbf{red}}$ is 1.87 μB, indicating $S = ½$.[211]

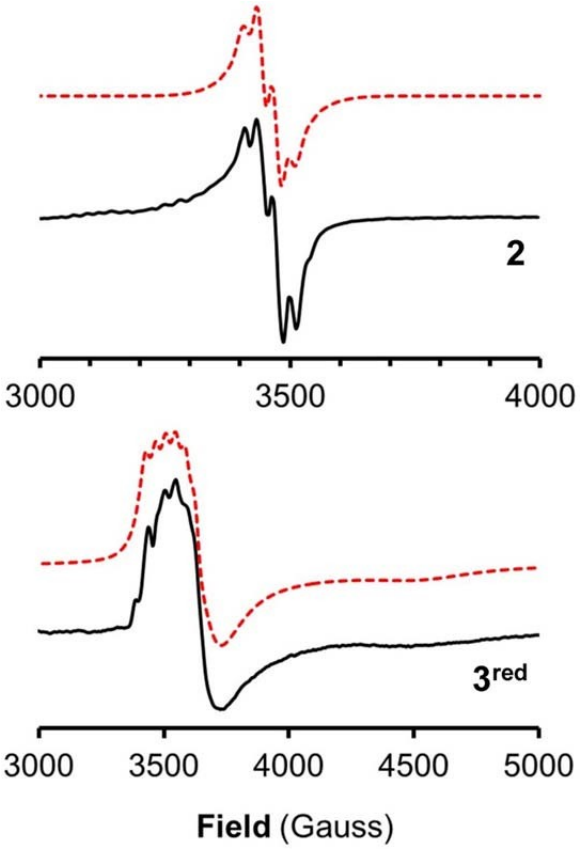

Figure 4.5. X-band EPR spectra (9.65 MHz) of **2** (top, 20 K) and **3**$^{\mathbf{red}}$ (bottom, 34 K) in frozen THF (1 mM). Experimental spectra are shown as black, solid lines with corresponding simulations in red, dashed lines. Simulation parameters: for **2**, $g_x = g_y = g_z = 1.99$; W=(11, 16, 11 G), A(3 x ^{31}P) = 10 x 10^{-4} cm^{-1} and for **3**$^{\mathbf{red}}$, $g_{ave} = 1.79$, g = (1.95, 1.88, 1.52), W = (30, 200, *620*) G, A_x(^{55}Mn) = 36 x 10^{-4} cm^{-1}

The X-band EPR spectrum of **3**$^{\mathbf{red}}$ (Figure 4.5, bottom) is roughly axial with g = (1.95, 1.88, 1.52), where *g*ave is 1.79. Hyperfine coupling to the ^{55}Mn nucleus (I = 5/2) can be discerned in g_x where A_x = 36 x 10^{-4} cm^{-1}. Complex **4** with a $(d\text{-}d)^{11}$ electron count was

previously characterized as $S = ½$ by EPR spectroscopy. The reported *g*ave of 1.88 for complex **4** is consistent with a Cr-based spin.

4.5.3 Solid−state structures

Single crystal X−ray diffraction studies of complexes **1**, **2**, $\mathbf{2^{red}}$, $\mathbf{3^{red}}$, and $\mathbf{4^{ox}}$ provided the solid−state structures shown in Figure 4.6, with the relevant geometric parameters in Table 4.2. For comparison, the previously reported compounds **3** and **4** are also included. All complexes are essentially three−fold symmetric and have a highly conserved coordination geometry.

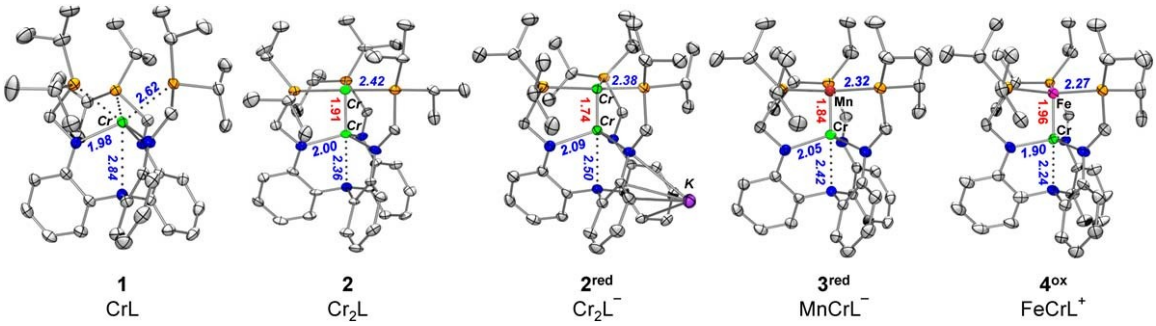

Figure 4.6. Solid−state structures of **1**, **2**, $\mathbf{2^{red}}$, $\mathbf{3^{red}}$, and $\mathbf{4^{ox}}$ by X−ray crystallography at 123 K for $\mathbf{4^{ox}}$ and at 173 K for the remaining compounds. Thermal ellipsoids are shown at 50% probability. Hydrogen atoms, counterions, and lattice solvent molecules have been omitted for clarity. Green, chromium; red, manganese; pink, iron; blue, nitrogen; orange, phosphorus. M−Cr bond distances are given in red, and average M-P and Cr-N bond distances are given in blue.

As anticipated based on previous work, **2**, $\mathbf{2^{red}}$, $\mathbf{3^{red}}$, and $\mathbf{4^{ox}}$ all have ultra-short metal-metal bonds (<2.0 Å), suggesting multiply bonded metal atoms. The dichromium complex $\mathbf{2^{red}}$ has the shortest metal-metal bond distance in the series of 1.7407(6) Å and possesses one of the shortest dichromium distances in the literature (Table 4.3).[5,212–217] Among heterometallic complexes, the shortest metal-metal bonds are currently found in **3**

and **3**$^{\mathbf{red}}$, followed FeCr complexes **4**$^{\mathbf{ox}}$, **4**, and **4**$^{\mathbf{red}}$,[21] and the FeV complexes, V(^{i}PrNPPh$_2$)$_3$FeI and V(^{i}PrNPPh$_2$)$_3$FePMe$_3$.[197]

As an aside, all the examples cited above use bridging ligand(s) to stabilize the bimetallic cores. A long-standing critique has been that the bridging ligands may be ultimately responsible for short metal-metal distances, in lieu of any true metal-metal bonding. It then follows that the diamagnetic (or low-spin) nature of the bimetallic species arises from antiferromagnetic coupling of the two metal spins. We would argue that this critique is invalid here. The present ligand is highly flexible and has supported a wide range of metal-metal distances, not all of which are short. For example, the isostructural CoCrL and NiCrL complexes have longer M-Cr bond distances of 2.14 and 2.41 Å, respectively. Indeed, the M-Cr bond lengths change by 0.7 Å from [Cr$_2$L]$^-$ (**2**$^{\mathbf{red}}$) to NiCrL, which is substantially larger than any intrinsic differences in the metals' single-bond metallic radii (Cr, 1.172; Ni, 1.149 Å) or covalent radii (Cr, 1.39; Ni, 1.24 Å). Also, despite a constant ligand and supporting Cr metal, the Cr-N$_{apical}$ bond length changes by 0.4 Å (2.50 Å in **2**$^{\mathbf{red}}$, 2.09 Å in NiCrL). Finally, an absence of metal-metal interaction would require the two metal-based spins to couple antiferromagnetically, either through the ligand or through space. The former cannot account for singlet-triplet splitting more than 10 – 100 cm^{-1} because the ligand backbone is saturated, where fully diamagnetic behavior at room temperature requires excited spin states to be higher than 1000 cm^{-1} in energy. Spin-spin interactions through space are even weaker (ca. 1 cm^{-1}), even at a short distance of 1.5 Å.[218] Thus, the argument for through space spin-spin

coupling is highly inconsistent with the fully diamagnetic behavior of **2**^{red}, **3**, and **4**^{ox} in the VT-NMR studies described above.

Table 4.2. Geometrical parameters, including bond lengths (Å) and angles (°) for **2**-**4**.[a]

	2	**2**^{red}	**3**	**3**^{red}	**4**	**4**^{ox}
M−Cr (Å)	1.913(1)	1.7407(6)	1.819(2)	1.8389(6)	1.944(1)	1.955(7)
r [b]	0.82	0.74	0.77	0.81	0.83	0.84
M–P (Å)	2.421(2)	2.3844(9) ± 0.004	2.379(1)	2.3167(5)	2.265(2) ± 0.004	2.268(8) ± 0.014
Cr−N_{eq} (Å)	1.997(5)	2.094(2) ± 0.014	2.021(3)	2.0472(15)	1.960(3) ± 0.019	1.889(8) ± 0.011
Cr−N_{ap} (Å)	2.359(5)	2.499	2.366(6)	2.416(2)	2.284(3)	2.240(9)
M to P_3−plane (Å)	−0.132	−0.203	−0.188	−0.174	−0.192	−0.270
Cr to N_3−plane (Å)	+0.447	+0.654	+0.498	+0.558	+ 0.412	+0.329
Σ (P−M−P) (°)	359.07	357.84	358.14	358.32	359.89(6)	355.79
Σ (N−Cr−N) (°)	345.33	331.58	342.42	338.49	349.1(2)	351.11
M−Cr−N_{ap} (°)	179.96	179.85	180	180	177.53(7)	178.08

[a] Complexes **2**^{red}, **4**, **4**^{ox}, crystallized with approximate three-fold symmetry, so several parameters, (e.g. M-P bond lengths) represent the average of three (**2**^{red}) or six (**4**) distinct values. Estimated standard deviations (esd) are provided in parentheses, and standard deviations of averages are shown with ± after the values. [b] r = ratio of M-Cr bond distance to the sum of M and Cr single bond metallic radii[176]

Table 4.3. Ultra-short Cr-Cr bond distances in selected Cr_2 systems

Cr_2 Complex	d(Cr-Cr) (Å)	r	ref
$Cr_2(2,6\text{-}(2,6\text{-}^{i}Pr_2C_6H_3)_2C_6H_3)_2$	1.8351(4)	0.78	5
$Cr_2(2,6\text{-}(2,6\text{-}^{i}Pr_2C_6H_3)_2\text{-}4\text{-}SiMe_3(C_6H_2))_2$	1.8077(7)	0.76	212
Cr_2(*N*,*N*'-bis(2,6-diisopropylphenyl)-1,4-diazadiene)$_2$	1.8028(9)	0.76	214
K[Cr_2L] (**2**^{red})	1.7407(6)	0.74	this work
$Cr_2(HC(N(2,4,6\text{-}(CH_3)_3C_6H_2)_2)_2$	1.7404(8)	0.74	216
$Cr_2(HC(N(2,6\text{-}(CH_3)_2C_6H_3)_2)_3$	1.7397(9)	0.74	217
$Cr_2(Me_2NC(N(2,6\text{-}^{i}Pr_2C_6H_3)_2)_2$	1.7293(12)	0.74	215
$Cr_2((2,6\text{-}(CH_3)_2C_5H_8N)C(2,6\text{-}^{i}Pr_2C_6H_3)_2)_2$	1.7056(12)	0.73	213
Cr_2^- [a]	1.705(10) [b]	0.73	219
Cr_2 [a]	1.68(1) [b]	0.72	220

[a] gas phase [b] based on a Morse fit of the vibrational frequency of rotational analysis

A useful metric to compare metal-metal bonding across different metals is the formal shortness ratio (*r*),[11] which is defined as the ratio of the metal-metal bond distance to the sum of their single-bond metallic radii.[176] By accounting for the sizes of different metals, the *r* value allows for a more fair comparison between homo- and heterobimetallic bonds. As defined, values close to unity represent single bonds, and values significantly below unity indicate multiple bonds. The *r* values for all complexes here are well below unity (0.74 to 0.84). The isoelectronic species, $\{Cr_2\}^{10}$ $\mathbf{2^{red}}$ and $\{MnCr\}^{10}$ **3**, have the lowest *r* values of 0.74 and 0.77, respectively. We propose these low *r* values are indicative of delta-bonding, and theoretical studies support these molecules as being formally quintuply bonded ($\sigma + 2\,\pi + 2\,\delta$).[22] We have also shown that the δ-symmetry *d*-orbitals at iron and chromium in $\{FeCr\}^{11}$ **4** do not interact because of their poor energy overlap, and hence, the formal bond order decreases to 3 ($\sigma + 2\,\pi$). Since $\mathbf{4^{ox}}$ has an *r* value that is close to that of **4**, $\mathbf{4^{ox}}$ is also interpreted as triply bonded. Indeed, $\mathbf{4^{ox}}$ is characterized by the largest *r* of 0.84 in this series, consistent with its lower bond order. By the *r* values, $\{Cr_2\}^{9}$ **2** and $\{MnCr\}^{11}$ $\mathbf{3^{red}}$ are in the middle of this series, suggesting an intermediate bond order between 3 and 5. For $(d\text{-}d)^9$ and $(d\text{-}d)^{11}$ systems, the expected dominant electronic configurations of $(\sigma)^2(\pi)^4(\delta)^3$ and $(\sigma)^2(\pi)^4(\delta)^4(\delta^*)^1$, respectively, would both predict a bond order of 4.5. However, the *r* values for **2** and $\mathbf{3^{red}}$ are only slightly lower than those for the Fe-Cr triply bonded complexes, **4** and $\mathbf{4^{ox}}$. A possible explanation is that the two δ-bonds are not fully formed in the cases of **2** and $\mathbf{3^{red}}$, resulting in a bond order less than 4.5 (*vide infra*). The

Cr-Cr bond distance of 1.913(1) Å in **2** is consistent with a wide range of dichromium complexes with formal quadruple bonds.[11] Also, δ-bonds are weak by nature, so their effects on bond lengths (and *r*) are often unclear.[11]

X-ray crystallography can sometimes be useful to reveal changes in the metal's oxidation states through corresponding changes in metal-ligand bond lengths. Structural comparison between various redox states may give insight into the redox site(s), though these are preliminary assignments, as *d*-electrons can easily delocalize across the two metals, and they should be validated with complementary spectroscopic and theoretical studies. The metal-metal bond contracts substantially between $\{Cr_2\}^9$ **2** and $\{Cr_2\}^{10}$ $\mathbf{2^{red}}$ ($\Delta = -0.17$ Å), which is about double the change observed in an analogous redox pair, $[Cr_2(ArNC(H)NAr)_3]^{0/1-}$ ($\Delta = -0.08$ Å, Ar = 2,6-$(CH_3)_2C_6H_3$).[221] One possible explanation for the relatively long Cr-Cr interaction in **2** versus $\mathbf{2^{red}}$ is the variable strength of the Cr-N_{apical} interaction, which lengthens appreciably upon reduction (Δ = 0.15 Å). The presence of axial donors is well known to elongate Cr-Cr multiple bonds, and σ donors can account for changes up to 0.1 Å.[11,222] Reduction of **2** to $\mathbf{2^{red}}$ also induces contraction of Cr−P and elongation of Cr−N_{eq} bond distances by 0.036 and 0.097 Å, respectively. The greater change in the Cr−N_{eq} bond distances may suggest a more localized reduction at the Cr residing in the amide-binding pocket.

Upon reduction of the formally quintuply bonded $\{MnCr\}^{10}$ **3** to $\{MnCr\}^{11}$ $\mathbf{3^{red}}$, the metal-metal bond lengthens slightly from 1.819(2) to 1.8389(6) Å, which is expected as the additional electron should populate an anti-bonding orbital. Upon reduction, the

Mn−P bond distances decrease (Δ = −0.062 Å) while the Cr-N distances increase (Δ(Cr-N_{eq}) = 0.026 Å, Δ(Cr-N_{ap}) = 0.050 Å), which can be interpreted as stronger Mn-phosphine backbonding and increased Cr-N_{eq} repulsion upon reduction of the MnCr core. In contrast, the oxidation of **4** did not produce any statistically significant changes in the Fe-Cr and Fe-P bond metrics, but alterations in the Cr-N_{eq} bond are statistically significant (Δ = 0.07(2) Å). These structure changes possibly suggest oxidation at Cr, but we note that the esds in $\mathbf{4^{ox}}$ (up to 0.009 Å) are large enough to mask moderate changes.

4.5.4 Diamagnetic anisotropy

In analogy to unsaturated organic molecules with π-bonds, complexes with multiple metal-metal bonds can have large diamagnetic anisotropies, Δχ, that impact NMR chemical shifts.[180] In axially symmetric molecules, the circulating electrons in the multiple bond can either shield (+) or deshield (-) nearby protons, depending on the proton's position within the spatial zones demarcated by the double cone, as shown in Figure 4.7. Protons in the equatorial region, e.g. methylene resonances, are expected to shift downfield if multiple bonds are present. Indeed, the methylene protons in all three $(d\text{-}d)^{10}$ complexes (**3**, $\mathbf{2^{red}}$, and $\mathbf{4^{ox}}$) are significantly deshielded appearing 2 to 3 ppm downfield relative to the methylene protons in the free ligand. The diamagnetic anisotropy ($\chi_{\parallel} - \chi_{\perp}\ or\ \Delta\chi$) can be calculated using the equation[223]

$$\Delta\sigma_i = \left(\frac{1}{3r^3}\right)\frac{(\Delta\chi)\left(1 - 3cos^2(\theta)\right)}{4\pi}$$

where $\Delta\sigma_i$ is the difference in chemical shift (in ppm) of methylene protons in the multiply bonded bimetallic complex versus that of a reference complex without any metal-metal bonds. For the reference complex, we chose the isostructural Ni-Al complex featuring a Ni→Al dative bond.[118] The distance of the proton to the center of the metal-metal bond is *r*, and the acute angle between the methylenes proton and the metal-metal axis is θ. By assimilating data from NMR and X-ray crystallographic studies, we implicitly assume that the solution and solid-state structures are similar. In addition, we discount an energetically low-lying triplet state as the cause of the dramatic NMR shifts. The VT-NMR profiles of $\mathbf{2^{red}}$, **3**, and $\mathbf{4^{ox}}$ are inconsistent with paramagnetic contributions. Moreover, in the dichromium species that have thermally accessible singlet-triplet gaps, the Cr-Cr bond distances are dramatically longer, ≥ 2.25 Å.[224]

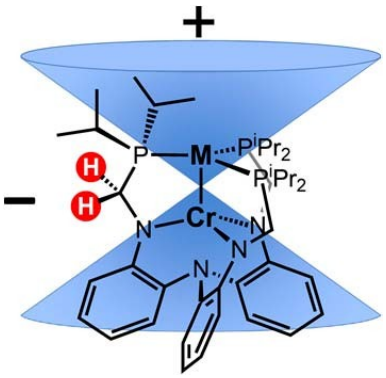

Figure 4.7. Spatial zones of shielded (+) and deshielded (-) chemical shifts that arise from the diamagnetic anisotropy of the multiply bonded $[MCr]^{3+}$ cores.

While diamagnetic anisotropies are known for several homobimetallic species, such data is limited for heterobimetallic pairings (Table 4.4).[172,182,225,226] Cotton and co-workers systematically studied a series of quadruply bonded complexes, $M_2X_4(\mu\text{-}PP)_2$, where M_2 = Mo_2, MoW, and W_2.[172,227,228] The average $\Delta\chi$ values increase across the

pairings, Mo_2 < MoW < W_2, where each substitution of a Mo center for W increases $\Delta\chi$ by approximately -640×10^{-36} m^3 $molecule^{-1}$ (13%). The calculated $\Delta\chi$ values for $\{Cr_2\}^{10}$ **2^{red}**, $\{MnCr\}^{10}$ **3**, and $\{FeCr\}^{10}$ **4^{ox}** are −3500, −3900, and −5800 (x 10^{-36} m^3 $molecule^{-1}$). The diamagnetic susceptibility increases with respect to effective bond order and with the polarization of the metal-metal bond. Substituting Mn for Cr results in an 11% gain in $\Delta\chi$, while swapping Fe for Cr produces a dramatic 66% increase. This trend is well known in organic molecules, whereby heteronuclear π-bonds, e.g. C=O (+420) and N=O (+1300), exhibit larger diamagnetic anisotropies than their homonuclear analogues e.g. C=C (+150) and C≡C (−340).[181] Finally, we note that the diamagnetic anisotropy for **2^{red}** is similar in value to another trigonal dichromium complex, $[Cr_2(ArNC(H)NAr)_3]^-$, where Ar = 2,6-$Me_2(C_6H_3)$.[221]

Table 4.4. Diamagnetic anisotropies ($\Delta\chi$) for multiply bonded bimetallic complexes.

Complex[a]	$\Delta\chi$ (10^{-36} m^3 $molecule^{-1}$)	ref
2^{red}	-3500	this work
3	-3900	this work
4^{ox}	-5800	this work
$Cr_2(ArNC(H)NAr)_3$	-3030	221
$Cr_2(DFM)_4$	-5230	182
$Mo_2(DFM)_4$	-5020	182
$W_2(DFM)_4$	-5480	182
$Re_2(DFM)_4$	-4430	182
$Ru_2(DFM)_4$	-3780	182
$Mo_2X_4(PP)_2$	-4450[b]	228
$MoWCl_4(PP)_2$	-5082[b]	227
$W_2X_4(PP)_2$	-5728[b]	172

[a]DFM = di-*p*-tolylformamidinate; PP = dppe, dppm, dmpm, dmpe [b]average value

4.5.5 Theory

Quantum chemical studies were conducted on the bimetallic models, **2′, 2$^{red′}$**, **3$^{red′}$**, and **4$^{ox′}$**, where the isopropyl groups were truncated to methyls. Computational studies of **3′** and **4′** were reported previously.[21,22] Geometry optimizations were performed using density functional theory (DFT) for several possible spin states. For all the complexes, the computed spin state with the lowest energy corresponded to the proposed ground state backed by experimental evidence. To address the strong correlation effects known for complexes with metal-metal bonds, we performed complete active space self−consistent field (CASSCF) followed by second−order perturbation theory (CASPT2) calculations. These methods give a more accurate description of bimetallic systems that are characterized by a heavy multireference character, large dynamic correlation energy, and/or significant relativistic effects.[127,191] For many of the systems here, a single electronic configuration represents the majority (55 to 64%) of the ground-state wave function. The exception is **2$^{red′}$**, where the contribution of the main configuration is slightly lower at 42% (Table 4.5).

Table 4.5. Main electronic configuration of metal-chromium complexes and the formal versus effective bond orders (FBO vs. EBO).

	MCr Complex	Dominant config.	%[a]	r^b	FBO	EBO
$(d\text{-}d)^9$	CrCr (**2′**)	$\sigma^2\pi^4\delta^2(\text{Cr } d_{xy})^1$	42	0.82	4	2.71
$(d\text{-}d)^{10}$	CrCr (**2$^{red′}$**)	$\sigma^2\pi^4\delta^4$	60	0.74	5	3.99
	MnCr (**3′**)	$\sigma^2\pi^4\delta^4$	55	0.77	5	3.85
	FeCr (**4$^{ox′}$**)	$\sigma^2\pi^4(\text{Fe } d_{xy}, d_{x^2-y^2})^4$	55	0.84	3	2.21
$(d\text{-}d)^{11}$	MnCr (**3$^{red′}$**)	$\sigma^2\pi^4(\text{Mn } d_{xy}, d_{x^2-y^2})^4(\text{Cr } d_{xy})^1$	64	0.81	3	2.39
	FeCr (**4′**)	$\sigma^2\pi^4(\text{Fe } d_{xy}, d_{x^2-y^2})^4(\text{Cr } d_{xy})^1$	58	0.83	3	2.15
$(d\text{-}d)^{12}$	FeCr (**4$^{red′}$**)	$\sigma^2\pi^4(\text{Fe } d_{xy}, d_{x^2-y^2})^4(\text{Cr } d_{xy})^2$	60	0.84	3	2.35

[a] Percentage of the ground-state wave function described by main configuration. [b] formal shortness ratio

Because of the weak ligand field associated with trigonal coordination geometries, all five *d*−orbitals in these bimetallic species have the potential to participate in metal−metal bonding. The *d*−orbitals can combine maximally to form quintuple bonds comprising one σ (d_z^2), two π (d_{xz}, d_{yz}), and two δ (d_{xy}, $d_x^2 - d_y^2$) bonds. Indeed, all five of these interactions are observed in $\mathbf{2^{red\prime}}$ and **3′,** where the $(d\text{-}d)^{10}$ electron count fills all the metal-metal bonding molecular orbitals (MOs), as shown in Figure 4.8 for $\mathbf{2^{red\prime}}$. Such a high bond order is consistent with the exceedingly low *r* values of 0.74 and 0.77 determined from experiment for $\mathbf{2^{red}}$ and **3**, respectively.

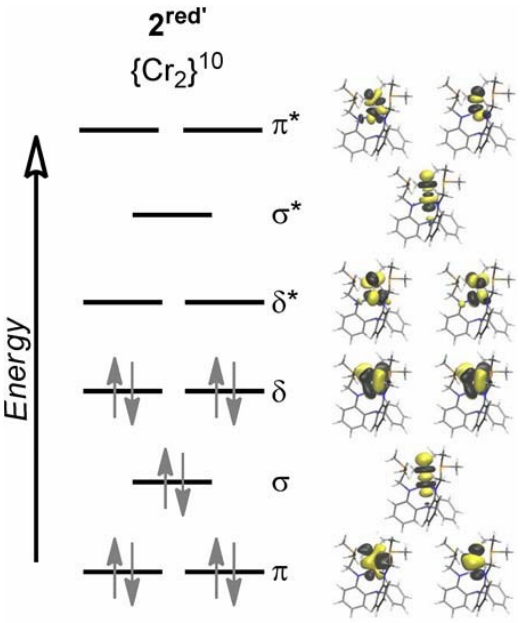

Figure 4.8. Qualitative MO diagram of $\mathbf{2^{red\prime}}$ showing the natural orbitals of σ (d_z^2), two π (d_{xz}, d_{yz}), and two δ (d_{xy}, $d_x^2 - d_y^2$) symmetry for main configuration (60%) from RASSCF calculations.

However, this simple MO picture does not hold for the other members. In complexes where the two metal partners are increasingly different, *e.g.* Fe and Cr in $\mathbf{4^{ox\prime}}$, **4′**, and $\mathbf{4^{red\prime}}$, the metal-metal bonds are increasingly polarized, resulting in localization of

the δ-symmetric d-orbitals so that only delocalized σ and π-bonds remain (Table 4.5). Indeed, an *r* value of 0.84 for $(d\text{-}d)^{10}$ $\mathbf{4^{ox}}$ is more congruous with three-fold rather than five-fold bonding. Five-fold interactions also break down when the electron count deviates from $(d\text{-}d)^{10}$. In $(d\text{-}d)^{9}$ $\mathbf{2'}$ and $(d\text{-}d)^{11}$ $\mathbf{3^{red\prime}}$ and $\mathbf{4'}$, one would predict FBOs of 4.5 for these complexes based on the simple MO pictures. However, as one or both pairs of δ-symmetric d-orbitals become increasingly localized (Table 4.6), the formal bond orders drop to 4, 3, and 3 for $\mathbf{2'}$, $\mathbf{3^{red\prime}}$, and $\mathbf{4'}$, respectively.

An analysis that parses the natural population of the active orbitals into weighted contributions from each metal partner, can provide the *d*-electron count at each metal center, which may be useful in contemplating oxidation states (Tables A4.2-7). In a first approximation of the neutral bimetallics, the asymmetric charge distribution in the ligand would favor a trivalent metal in the triamido pocket, e.g. M_N(III), while stabilizing a zero-valent metal in the triphosphine site, e.g. M_P(0). However, because of covalent metal-metal bonding, the electronic charges can be further distributed between the two metal centers. For neutral di-chromium $\mathbf{2'}$ and MnCr $\mathbf{3'}$, the calculated oxidation states are consistent with M_P(I)M_N(II), specifically Cr_P(1.0)Cr_N(2.0) and Mn(0.9)Cr(2.1). Their one-electron reduced counterparts, $\mathbf{2^{red\prime}}$ and $\mathbf{3^{red\prime}}$ have core oxidation states of Cr_P(0.5)Cr_N(1.5) and Mn(0.3)Cr(1.7), respectively, where the additional electron is delocalized on the two metal partners nearly equally. The neutral FeCr complex, $\mathbf{4'}$, which has core oxidation states of Fe(0.6)Cr(2.4), is half-way between the two extremes of M_P(0)M_N(III) and M_P(I)M_N(II). Its redox analogues $\mathbf{4^{ox\prime}}$, Fe(1.2)Cr(2.8), and $\mathbf{4^{red\prime}}$,

Fe(0)Cr(2.0), are interpreted as possessing Fe(I) and Fe(0), respectively. Thus, the computations predict that reduction of the $(FeCr)^n$ core is equally shared by the two metals, whereas oxidation is primarily localized at the iron site.

Table 4.6. Percentage of Metal Character (% Cr, % M) in metal-chromium bonding orbitals of σ-, π-, and δ-symmetry from CASSCF calculations.

	MCr Complex	σ		π		δ	
		% Cr	%M	% Cr	%M	% Cr	%M
$(d\text{-}d)^9$	CrCr (**2′**)	46	54	52	48	50	50
				52	48	*0*	*100*
$(d\text{-}d)^{10}$	CrCr (**2^{red}′**)	48	54	48	52	39	61
				48	52	39	61
	MnCr (**3′**)	40	60	38	62	33	67
				38	62	33	67
	FeCr (**4^{ox}′**)	33	67	45	55	*13*	*87*
				44	56	*12*	*88*
$(d\text{-}d)^{11}$	MnCr (**3^{red}′**)	44	56	47	53	*14*	*86*
				53	47	*3*	*97*
	FeCr (**4′**)	31	69	45	55	*8*	*92*
				49	51	*18*	*82*
$(d\text{-}d)^{12}$	FeCr (**4^{red}′**)	36	64	27	73	*0*	*100*
				27	73	*0*	*100*

[a] Italicized values are percentages below 75/25% and represent *δ*-bonding MOs that are more aptly described as localized, e.g., d_{xy}.

With the calculated structures in hand, we were also able to gauge the *predicted* structural perturbations upon changing the redox state (Table 4.7). By comparing the

neutral bimetallics against their charged analogues, it became clear that the predicted bond changes are all consistent with increased Cr−N repulsion (elongation) and increased M−P π-back-bonding (contraction) upon reduction. Notably, the $Cr-N_{eq}$ and $Cr-N_{ap}$ bonds are extremely sensitive, elongating by (0.05 to 0.07 Å) and (0.03 to 0.09 Å), respectively, per additional electron. In contrast, the M−P bonds were fairly insensitive, decreasing by ≤ 0.02 Å per additional electron. For example, the differences between **4′** and **4^{ox}′,** which was predicted to be primarily Fe-based, include a 0.05 Å change in the $Cr-N_{eq}$ bond length, but as little as a 0.007 Å perturbation in the Fe−P bond.

Table 4.7. DFT bond lengths for MCrL series (Å)

	2′	**2^{red}′**	**3′** [a]	**3^{red}′**	**4^{ox}′**	**4′** [b]	**4^{red}′** [b]
M-Cr	1.844	1.745	1.811	1.846	1.890	1.935	2.021
$Cr-N_{ap}$	2.399	2.484	2.368	2.401	2.273	2.308	2.353
	1.955	2.027	1.950	2.043	1.907	1.944	2.009
$Cr-N_{eq}$	1.954	2.027	1.950	2.002	1.907	1.941	2.009
	1.967	2.027	1.950	2.000	1.907	1.996	2.009

[a] ref. 22 [b] ref. 21

4.5.6 Mössbauer spectroscopy

To elucidate the redox changes at the iron site, **4^{ox}** was further investigated by ^{57}Fe Mössbauer spectroscopy (Figure 4.9). The Mössbauer doublet is characterized by an isomer shift of 0.18 mm/s and a quadrupole splitting (ΔE_Q) of +5.85 mm/s. Previously, **4** and two variants of **4^{red}** (with K(crypt-222) and K(18-c-6) counterions)

were analyzed by Mössbauer spectroscopy. Akin to **4** and $\mathbf{4^{red}}$, $\mathbf{4^{ox}}$ has an excessively large ΔE_Q value (>5.0 mm/s), which was attributed to large charge anisotropy in the iron valence shell that arises from the strong covalent bonds within the $[FeCr]^{3+}$ core.

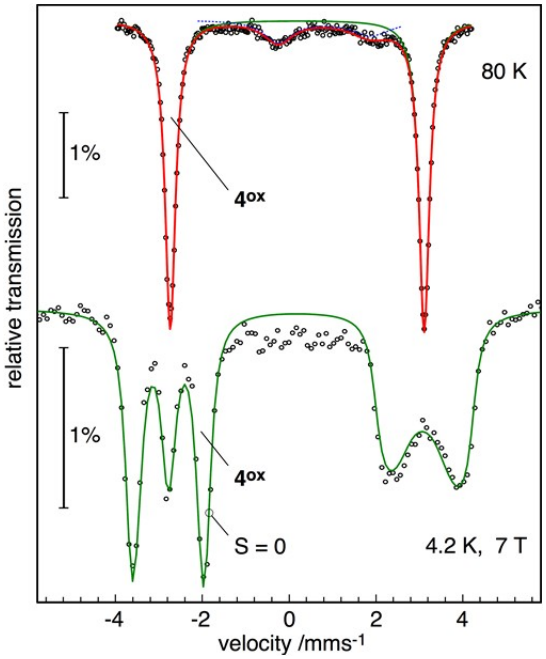

Figure 4.9. Zero-field ^{57}Fe Mössbauer spectra of $\mathbf{4^{ox}}$ recorded at 80 K (top) and magnetic spectrum recorded at 4.2 K with a field of 7 Tesla applied perpendicular to the γ –rays (bottom). The green line represents the best fit with $\delta = 0.18$ mm s^{-1} and $\Delta E_Q =$ +5.85 mm s^{-1} , $\eta = 0$ (85% purity) and with $S = 0$. There is also a high-spin Fe(II) impurity with $\delta = 0.83$ mm s^{-1} and $\Delta E_Q = 2.15$ mm s^{-1} (dotted blue line in top panel).

While **4** and $\mathbf{4^{red}}$ showed essentially identical isomer shifts of 0.25 and 0.26/0.29 mm/s, respectively,[21] $\mathbf{4^{ox}}$ has a notably lower isomer shift by approximately 0.1 mm/s. Isomer shifts owes their differences essentially to the degree of 4*s*-electron population at the Mössbauer atom, which arises from covalent bond formation with *σ*-type ligand orbitals.[229] Higher oxidation states, at least for Werner-type complexes in the mid-to-high valent regime, cause shorter iron ligand bonds, and hence, lower isomer shifts.[230]

Hence, the oxidation state of the iron nucleus remains Fe(0) in **4** and $\mathbf{4^{red}}$, but increases to Fe(I) in $\mathbf{4^{ox}}$.

However, one has to note that in the low-valent regime (e.g, Fe(0), Fe(I)), the negative correlation of the isomer shift with the oxidation state typically fades, and even the opposite scenario can be observed, namely that *lower* oxidation states result in *lower* isomer shifts.[197,231–233] This has been explained by the onset of Fe(3*d*)→π-back donation for low-valent iron,[234] which by shortening of the iron ligand bonds leads to increased the *s*-electron density at the Mössbauer nucleus, giving lower isomer shifts. In two representative redox series, $[(SiP_3)FeN_2]^n$ and $[(SiP_3)FeCO]^n$,[231,232] the Fe-P bond lengths contract by ca. 0.1 Å per unit oxidation state decrease from Fe(II) to Fe(0), which lends support to increased π-back-bonding from low-valent iron. In contrast, the FeCr series does not fit with other low-valent iron complexes. The average Fe-P bond distances in $\mathbf{4^{ox}}$, **4**, and $\mathbf{4^{red}}$ are all similar at 2.268(8), 2.265(2), and 2.2444(8) Å, respectively, and no Fe-P back-bonding is observed. The isomer shifts of **4** and $\mathbf{4^{ox}}$ behave as expected (for no Fe-L back-donation) and are consistent with the proposed oxidation states of Fe(0) and Fe(I), respectively.

4.5.7 Vis-NIR and resonance Raman (rR) Spectroscopy

The electronic absorption spectra of the bimetallic complexes, as shown in Figure 4.10 and summarized in Table 4.8, were recorded in THF at rt. Except for a common UV peak at ~310 nm, which is ascribed to a ligand-based transition, the MCr bimetallics show sufficiently different vis-NIR transitions to justify substantial metal-based character in them. Generally, in the electronic spectra of multiply bonded bimetallic complexes,

the most interesting feature is the δ→δ*-type transition.[182,184,235] A seminal study of quadruply bonded M^{4+} cores in tetragonal $M_2X_4P_4$ complexes revealed dramatic red-shifts in the $\delta^2 \rightarrow \delta\delta^*$ energies upon metal substitution of W for Mo: Mo_2^{4+} (ave. 608 nm; 16,460 cm^{-1}) > MoW^{4+} (658 nm; 15,200 cm^{-1}) > W_2^{4+} (682 nm, 14,660 cm^{-1}).[172] The first heavy-metal substitution, i.e. Mo^{4+} to MoW^{4+}, perturbs the $\delta^2 \rightarrow \delta\delta^*$ excitation significantly more than the second substitution, i.e. MoW^{4+} to W_2^{4+}. Similar effects of metal substitution were also observed in a trio of homobimetallic $M_2(mhp)_4$ compounds (M_2 = Cr_2, Mo_2 ,W_2; mhp = deprotonated 6-methyl-2-hydroxypyridine), where the δ →δδ* energies decrease down the group (22,500 cm for M_2 = Cr_2 to 18,700 cm^{-1} for M_2 = W_2).[235] To our knowledge, electronic absorption data are limited for trigonal M_2^{n+} systems and especially so for quintuply bonded species.[5,212,214,216,236] Thus, we were keen to determine the $\delta^4 \rightarrow \delta^3\delta^*$ transition energy in the isoelectronic, quintuply bonded complexes, **2red** and **3**, which would allow quantitative comparison between homo- versus heterobimetallic quintuple bonds.

The lowest energy band observed for **2red** has a λmax of 675 nm, or 14,815 cm^{-1}. This band is assigned as the $\delta^4 \rightarrow \delta^3\delta^*$ excitation, and a resonance Raman (rR) study of **2red** corroborates the assignment (vide infra). For **3**, the lowest energy band is signifi- cantly shifted to lower energy by ~5,000 cm^{-1} to 1025 nm (9,756 cm^{-1}). The dramatic decrease in the $\delta^4 \rightarrow \delta^3\delta^*$ transition energy upon formal substitution of Cr(I) with Mn(I) is unprecedented, and may be a consequence of a smaller δ/δ*-splitting and/or

larger exchange stabilization of the excited state in the case of heterobimetallic **3** versus homobimetallic $\mathbf{2}^{red}$.

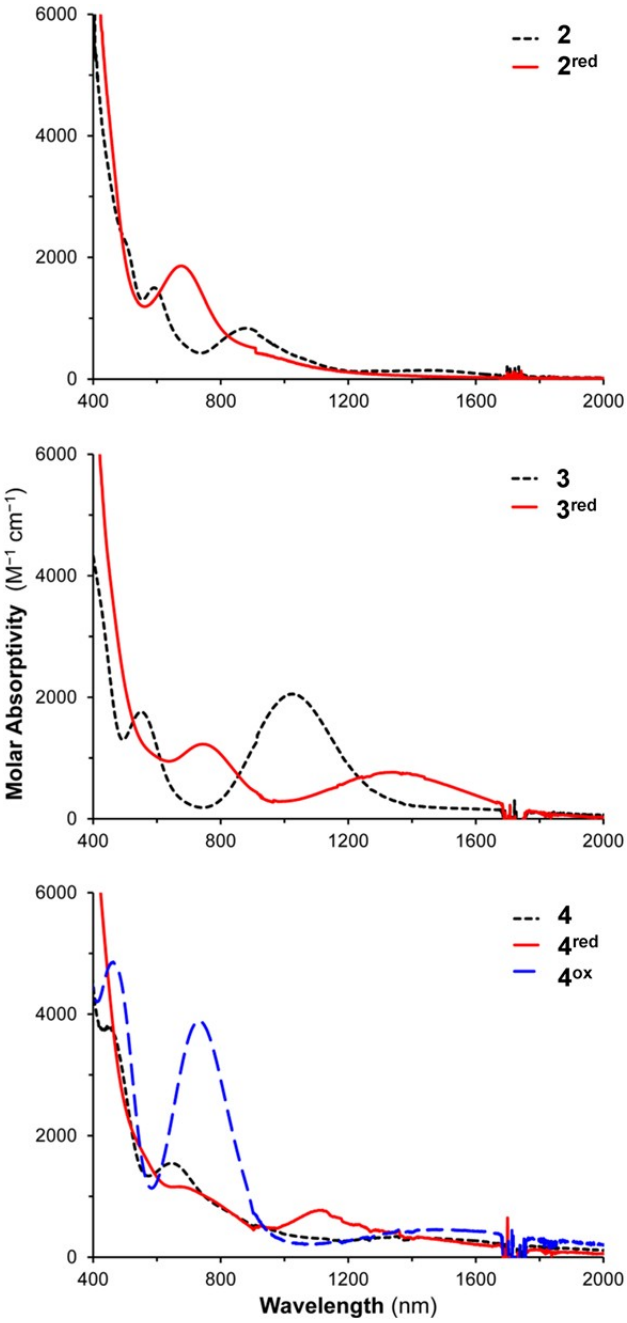

Figure 4.10. Vis-NIR plots for **2** and $\mathbf{2}^{red}$ (top), **3** and $\mathbf{3}^{red}$ (middle), and $\mathbf{4}^{ox}$, **4**, and $\mathbf{4}^{red}$ (bottom) in THF at rt. Artifacts from solvent subtraction or light source changes appear at ~1750 nm.

Table 4.8. Visible-NIR electronic absorbance data for **2**, $\mathbf{2^{red}}$, **3**, $\mathbf{3^{red}}$, **4**, $\mathbf{4^{red}}$, and $\mathbf{4^{ox}}$.

Complex	λ_{max}, nm	ε, M^{-1} cm^{-1}
2	495	2300
	600	1480
	880	930
	1460	140
$\mathbf{2^{red}}$	675 (14815)[a]	1880
3	400	4400
	550	1850
	1025(9756)[a]	2160
$\mathbf{3^{red}}$	745	1230
	1350	760
4	448	3640
	645	1440
	1344	220
$\mathbf{4^{red}}$	680	1200
	1110	7400
$\mathbf{4^{ox}}$	463	4860
	730	3890
	1495	490

[a] in wavenumbers (cm^{-1})

To comprehend the electronic absorption spectra of the $(d\text{-}d)^{10}$ species, state-averaged CASSCF/PT2 and CASSI calculations were performed for $\mathbf{2^{red\prime}}$, $\mathbf{3'}$, and $\mathbf{4^{ox\prime}}$. Since these calculations are expensive, only the first six excitations were computed. Gratifyingly, $\delta^4 \rightarrow \delta^3\delta^*$ transitions were predicted for both $\mathbf{2^{red\prime}}$ and $\mathbf{3'}$, and the transition energy for $\mathbf{3'}$ (673 nm) was correctly calculated to be lower than that for $\mathbf{2^{red\prime}}$ (545 nm). Although the absolute energies do not correspond well to the experimental values, the computed energy difference of 3,500 cm^{-1} is in good agreement. For $\mathbf{4^{ox\prime}}$, $\delta \rightarrow \delta^*$ type transitions were notably absent, and the two low-lying transitions at 1006 and 1021 nm, which may correspond to the experimental band at 1495 nm, were $d\text{Fe}^4 \rightarrow d\text{Fe}^3\ \pi^*$

transitions. These findings validate the quintuple bonding in $\mathbf{2^{red}}$ and **3** as well as the lower bond order in $\mathbf{4^{ox}}$.

Ground-state metal-metal vibrational frequencies are known for a handful of dichromium species,[185,235,237] but to our knowledge, such data is lacking for any quintuply bonded complexes. To obtain MCr vibrational frequencies of quintuply bonded species, $\mathbf{2^{red}}$ and **3** were probed by resonance Raman (rR) spectroscopy. Excitation into the $\delta^4 \rightarrow \delta^3\delta^*$ band should selectively enhance the νMCr vibration. Indeed, irradiating a frozen sample of $\mathbf{2^{red}}$ at 647.1 nm afforded a series of low frequency bands between 350-550 cm^{-1} (Figure 4.11), specifically at 363, 413, 434, and 495 cm^{-1}. The resonance enhancement of these modes was confirmed by the resultant depletion in their intensity when using a different wavelength (λ_{ex}: 514.5 nm) that is off-resonance with the $\delta^4 \rightarrow \delta^3\delta^*$ transition.

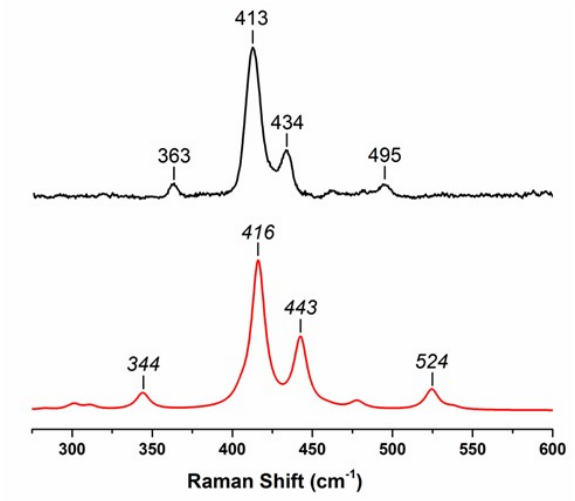

Figure 4.11. A stack plot of the resonance Raman spectrum of $\mathbf{2^{red}}$ (10.4 mM in THF, λex: 647.1 nm, 77 K) (top, in black) and the DFT calculated Raman spectrum of $\mathbf{2^{red}}$, (bottom, in red).

The observation of multiple vibrations by rR spectroscopy can result from coupling of the νMM vibration with various ligand normal modes.[238] Thus, we turned to DFT to elucidate the origin of the observed peaks. The DFT-calculated Raman spectrum of $\mathbf{2}^{\mathbf{red'}}$ revealed four intense vibrations in the low frequency region, whose spectral pattern and relative intensities are in good agreement with experiment. The calculated frequencies were 8-20% higher than the experimental ones, which is reasonable at the DFT level of theory.[35] To increase the accuracy of computed vibrational frequencies, a scale factor is commonly employed.[201,202] Hence, a scale factor of 0.88 was applied, giving the predicted Raman spectrum shown in Figure 4.11. The two most intense DFT-calculated vibrations at 416 and 443 cm^{-1} are the asymmetric Cr-Cr-N_{ap} stretch and a relatively pure Cr-Cr vibration, respectively. Thus, we assign the dichromium stretching frequency νCrCr at 434 cm^{-1} (corresponding to the calculated νCrCr value of 443 cm^{-1}). Of note, νCrCr for quadruply bonded dichromium complexes are greater at 556 and 570 cm^{-1} despite having longer Cr-Cr distances (1.89, 2.11 Å vs. 1.74 Å in $\mathbf{2}^{\mathbf{red}}$).[185,237] On the other hand, the naked dichromium molecule, which has a formal sextuple bond, also exhibits a relatively low νCrCr at 481 cm^{-1}.[231,232] The lack of correspondence between bond order and νCrCr may be due, in part, to the distorted potential energy surface of Cr_2, which has a minimum at 1.68 Å as well as a flat, shoulder region at 2.5 Å.[219,239,240]

Finally, in contrast to $\mathbf{2}^{\mathbf{red}}$, the isoelectronic manganese-chromium species **3** did not exhibit any enhanced non-solvent features, precluding any determination of νMnCr. However, the absence of νMnCr band(s) is reasonable considering that the $\delta^4 \rightarrow \delta^3\delta^*$

transition in **3** occurs at a longer wavelength that is currently beyond our visible laser set up.

4.6 Conclusions

To better understand the nature of δ-bonding, complexes with interactions between chromium and another mid first-row transition metal (Cr, Mn, and Fe) were investigated. Specifically, bimetallics with $(d\text{-}d)^9$ to $(d\text{-}d)^{11}$ configurations were targeted to maximize the multiplicity of their metal-metal bond. The quintuply bonded complexes, $[Cr_2L]^-$ (**2**$^{\mathbf{red}}$) and MnCrL (**3**), have ultra- short M-Cr bonds, at 1.74 (r = 0.74) and 1.82 Å (r = 0.77), respectively. The remaining complexes (**2**, **3**$^{\mathbf{red}}$, **4**, **4**$^{\mathbf{ox}}$, **4**$^{\mathbf{red}}$) have r values from 0.81 to 0.84, which are in the range of triple to quadruple bonds. A $(d\text{-}d)^{10}$ configuration does not necessitate the formation of delta bond(s), as the FeCr complex **4**$^{\mathbf{ox}}$ lacks any. Another lesson is that deviations from the $(d\text{-}d)^{10}$ count can destroy δ bonds completely. The prototype MO picture of five-fold bonding would predict a formal bond order of 4.5 for both $(d\text{-}d)^9$ and $(d\text{-}d)^{11}$, but the experimental r values clearly show lower bond orders that are closer to 3. Finally, in contrast to the sensitive nature of δ bonds, σ and π bonds are quite robust in this series.

The spectroscopic characterization of this series also yielded some interesting findings. For instance, the diamagnetic anisotropy of metal-metal multiple bonds appear to be primarily affected by the polarity of the M-Cr bond, rather than the multiplicity. The $\delta^4 \rightarrow \delta^3\delta^*$ transition energy was red-shifted by over 5000 cm^{-1} by a simple metal atom substitution, from $[Cr_2L]^-$ to MnCrL. The νCrCr for quintuply bonded $[Cr_2L]^-$ was

unexpectedly lower than quadruply bonded analogues from the literature. In the $[FeCrL]^{+,0,-}$ redox series, the Mössbauer isomer shifts are consistent with $[Fe(I)Cr(III)L]^{+} \xrightarrow{e^-} [Fe(0)Cr(III)L]^{0} \xrightarrow{e^-} [Fe(0)Cr(II)L]^{-}$. The redox changes from $[Fe(I)CrL]^{+}$ to Fe(0)CrL, however, does not manifest in significant bond changes in the first coordination sphere of iron, but at chromium. Thus, assigning oxidation states based on changes in metal-ligand bond lengths, as revealed by X-ray crystallography, may be misleading in bimetallic systems with covalent metal-metal bonds and/or mixed amide-phosphine ligands.

Author Contributions:

Experimental: Reed J. Eisenhart **,** P. Alex Rudd **,** David W. Boyce **,** William B. Tolman **,** Eckhard Bill **,** Connie C. Lu

Theoretical: Nora Planas contributed the to the DFT, ground state CASSCF, and state average CASSCF calculations, Rebecca K. Carlson contributed to the ground state CASSCF calculations for Table 4.6 and oxidation state analysis, Laura Gagliardi

Chapter 5

Bimetallic cobalt-dinitrogen complexes: impact of the supporting metal on N_2 activation

Reproduced in part from

Bimetallic Cobalt–Dinitrogen Complexes: Impact of the Supporting Metal on N_2 Activation, Laura J. Clouston, Varinia Bernales, Rebecca K. Carlson, Laura Gagliardi, and Connie C. Lu**,** *Inorganic Chemistry*,**2015,** *54* (19), 9263-9270.

5.1 Overview

To expand a family of cobalt bimetallic complexes, we report the synthesis of the Ti(III) metalloligand, Ti[N(*o*-(NCH$_2$P(^{i}Pr)$_2$)C$_6$H$_4$)$_3$] (abbreviated as TiL), and three heterobimetallics, CoTiL (**1**), K(crypt-222)[(N$_2$)CoVL] (**2**), and K(crypt-222)[(N$_2$)CoCrL] (**3**). The latter two complexes, along with previously reported K(crypt-222)[(N$_2$)CoAlL] and K(crypt-222)[(N$_2$)Co$_2$L], constitute an isostructural series of cobalt-dinitrogen bimetallics, [(N$_2$)CoML]$^-$. The characterization of **1**−**3** includes cyclic voltammetry, X-ray crystallography, and infrared spectroscopy. The [CoTiL]$^{0/-}$ reduction potential is extremely negative at −3.20 V versus Fc$^+$/Fc. In the CoML series, the reduction potentials shift anodically as M is varied across the first-row period. Among the [(N$_2$)CoML]$^-$ compounds, the bound dinitrogen is weakly activated, as evidenced by N−N bond lengths between 1.110(8) and 1.135(4) Å, and by N−N stretching frequencies between 1971 and 1995 cm^{-1}. Though changes in ν_{N2} are subtle, the N$_2$ activation decreases across the period in the [(N$_2$)CoML]$^-$ series. A correlation is found between the [CoML]$^{0/-}$ reduction potentials and N$_2$ activation, where the more cathodic potentials correspond to lower N−N frequencies. Theoretical calculations on [(N$_2$)CoML]$^-$ models reveal important variations in the electronic structure and Co−M interactions, which depend on the exact nature of the supporting metal ion, M.

5.2 Introduction

Cobalt is generally surpassed by iron as the choice metal for N$_2$ activation. In synthetic systems where both cobalt-dinitrogen and iron-dinitrogen adducts are known, the cobalt counterparts typically activate N$_2$ more weakly.[118,233,241–252] This has been attributed to the energetically lower Co *d*-orbitals being worse at π-back-bonding to the N$_2$ substrate.[253] There are, however, a few exceptional cases where cobalt site(s) reduce N$_2$ by two or more electrons. Cobalt, supported by the triphosphine ligand, [PhBP$^{iPr}_3$]$^-$, effected an overall two-electron transformation of N$_2$ to the diazenido species, Co−N=NR.[247] Cobalt diketiminate compounds, when subjected to alkali metals, capture N$_2$ within a Co−N=N−Co linkage, which is a formal two-electron reduction.[245] Finally, monocobalt and dicobalt complexes have been discovered to catalyze the silylation of N$_2$ to two N(SiMe$_3$)$_3$ molecules in a six-electron redox reaction.[24]

A hallmark of the dicobalt system is the presence of a metal-metal interaction in the precatalyst. Using hemi-labile interactions between a catalytic metal center and an ancillary main group ion is a powerful strategy in small-molecule activation.[250,251] An enlightening example is the iron-boratrane system that mediates the reduction of N_2 to NH_3.[252] Of relevance, a ZrCo heterobimetallic complex harnesses early-late metal cooperativity to completely rupture strong C=O bonds in CO_2 and benzophenone.[254,255] Cleavage of C=O bonds is inherent in the reactivity of a related TiCo complex, which reductively couples aryl ketones to alkenes in a stoichiometric manner.[256] Metal cooperativity also operates in triiron platforms that mediate the multi-electron reduction and N=N cleavage of azobenzene.[257]

We have been targeting a family of CoM bimetallics to understand how an ancillary metal tunes Co−M interactions and overall redox properties.[22,118,233,258] Reduction of the CoM bimetallics provided access to cobalt-dinitrogen complexes, which are isostructural and allow tunability of the supporting metal ion. Through synthesis, physical/spectroscopic characterization, and theoretical calculations, we unravel the impact of the ancillary metal on N_2 activation in cobalt bimetallics.

5.3 Experimental Section

Details about the synthesis and characterization techniques, including NMR and X-ray crystallography can be found in Appendix 5.

5.4 Computational Methods

5.4.1 DFT Calculations

DFT calculations were performed on the model species, CoTiLMe and $[(N_2)CoMLMe]^-$ (where M = Al, Ti, V, Cr, Co), wherein LMe represents the truncated ligand (P^iPr_2 to PMe_2). Gas-phase optimizations of all possible spin states were carried out using the M06-L[173] functional and def2-TZVP (for N, P, Al, Ti, V, Cr and Co atoms) / def2-SVP (for C, H atoms) basis sets.[174] The experimental structures were used as initial geometries. In one case, CoTiLMe, the optimized Co−Ti distance did not match well with experiment (M06-L underestimated by ~0.14 Å), so the Co−Ti bond distance was kept fixed, while the rest of the molecule was allowed to relax. Vibrational frequencies were calculated at the optimized geometries to characterize the nature of the stationary points. Solvation effects were also considered by performing single-point calculations for all intermediates using the SMD[259] solvation model with the diffuse basis set, def2-TZVPD[260] (for N, P, Al, Ti, V, Cr and Co)(def2-SVP for C and H) and THF as the solvent. In summary, the energies of all calculated structures were determined at the M06-L/def2-TZVP and M06-L/def2-TZVPD/SMD levels of theory, where the former is used for geometry optimizations, and the latter for single-point energy calculations. The Gaussian09[129] suite of programs was used for all DFT calculations.

5.4.2 CASSCF/CASPT2 calculations

Four species, CoTiLMe and $[(N_2)CoMLMe]^-$ (where M = Ti, V, Cr), were further investigated by multi-reference calculations using the DFT-optimized geometries in the MOLCAS-7.8 program.[120] The complete active space self-consistent field (CASSCF)[34] method was used, followed by multi-configurational second order perturbation theory, CASPT2.[37] The following relativistic all-electron basis sets were used: ANO-RCC-VTZP

for Co, Cr, V, and Ti, ANO-RCC-VDZP for P and N, and ANO-RCC-MB for C and H atoms.[121,122] Scalar relativistic effects were included by using the Douglas–Kroll–Hess Hamiltonian.[123,124] The two-electron integral evaluation was simplified by using the resolution-of-identity (RI) and the Cholesky decomposition technique.[125] To avoid intruder states, an imaginary level shift of 0.2 au was used in the CASPT2 calculations.[126]

5.5 Results and Discussion

5.5.1 Synthesis and characterization of CoTiL (1)

The cobalt-titanium complex, CoTiL (**1**), is the latest addition to a growing family of isostructural cobalt bimetallics, where L = $[N(o\text{-}(NCH_2P(^iPr)_2)C_6H_4)_3]^{3-}$. Previously, we reported CoVL,[258] CoCrL,[22] Co_2L[24] and (N_2)CoAlL,[118] where the latter is the only $(CoM)^{3+}$ example in this ligand scaffold to bind N_2 in the apical pocket. Complex **1** was synthesized by mixing $CoBr_2$ and the metalloligand TiL, followed by reduction with two equiv. KC_8 (Figure 5.1).

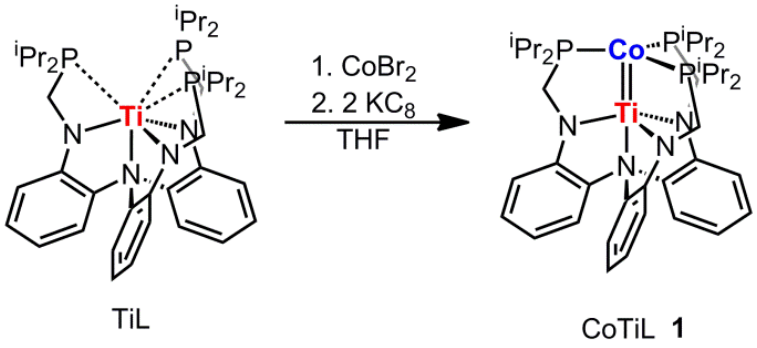

Figure 5.1. Synthesis of compound **1**.

As complex **1** is (*d*-*d*)[10] and diamagnetic, it was characterized by multi-nuclear NMR spectroscopy. A single ^{31}P signal is observed at 17.1 ppm, suggesting three-fold symmetry. The ^1H NMR spectrum is consistent with a locked C_3 conformation, where

the methylene protons in the ligand arms are diastereotopic, and the diisopropyl phosphine groups are split into two methine and four methyl peaks.

The molecular structure of CoTiL contains a short Co−Ti bond distance of 2.1979(8) Å, which is significantly smaller than the sum of two metals' single-bond radii at 2.48 Å (Figure 5.2, Table 5.1).[176] The formal shortness ratio (FSR), a quotient of the metal-metal bond length and the sum of the metals' single-bond radii, is 0.89 for **1**.

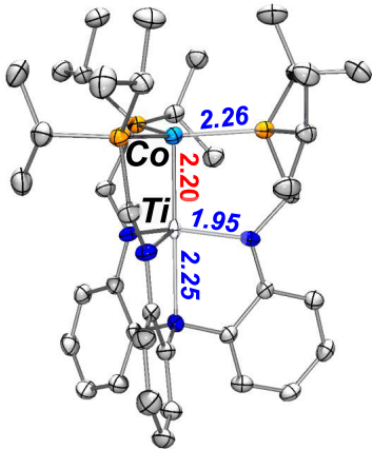

Figure 5.2. Molecular structure of **1** shown at 50% thermal ellipsoid probability. Hydrogen atoms were omitted for clarity. Average bond lengths (Å) are shown.

Of note, it is strikingly longer than the Co−Ti bond length of 2.02 Å in $(PMe_3)Co(^iPr_2PNAr)_2Ti(Cl)$,[256] where the FSR is 0.81 and was interpreted as a Co−Ti triple bond. It is however, similar to the Co−M bond lengths in the isostructural CoVL and CoCrL compounds (2.135 and 2.123 Å, with FSR values of 0.92 and 0.89, respectively), which were formulated as Co−M double bonds. By analogy, **1** likely has a Co−Ti double bond.

Of note, the Co−P bond lengths in CoTiL are similar to those in CoVL, CoCrL, Co_2L and $(N_2)CoAlL$, which all fall between 2.21 to 2.30 Å. For the cobalt-transition metal complexes, the P−Co−P bond angles also adhere to a narrow range of 118 to 121

degrees. Variation of the supporting metal from Ti to Cr in the amide-binding pocket, hence, has little impact on the ligation of the cobalt in the phosphine pocket. Only (N_2)CoAlL shows a significant distortion from three-fold symmetry with P−Co−P bond angles of 105, 112, and 132 degrees. The distortion could arise from a Jahn-Teller distortion of a d^9 Co(0) center in three-fold symmetry.

Table 5.1. Geometrical parameters, including bond lengths (Å), formal shortness ratio (FSR), and angles (deg), for **1** – **3**.

	1	**2**[b]		**3**[b]	
	CoTiL	K(crypt-222)[(N_2)CoVL]		K(crypt-222)[(N_2)CoCrL]	
Co–M	2.1979(8)	2.6466(7)	2.6661(7)	2.5822(11)	2.5377(12)
FSR[a]	0.89	1.11	1.12	1.11	1.09
Co–N		1.796(3)	1.788(3)	1.792(5)	1.813(5)
N–N		1.130(4)	1.135(4)	1.135(6)	1.120(7)
	2.2444(11)	2.2024(9)	2.1859(10)	2.1907(15)	2.1988(14)
Co–P	2.2553(11)	2.2049(10)	2.1968(10)	2.1918(14)	2.2057(14)
	2.2704(11)	2.2121(10)	2.2094(10)	2.1965(14)	2.2188(15)
	1.947(3)	1.952(3)	1.946(3)	1.953(4)	1.975(4)
M–N_{amide}	1.954(3)	1.954(3)	1.949(3)	1.974(4)	1.975(5)
	1.955(3)	1.958(3)	1.957(3)	1.980(4)	1.979(4)
M–N_{amine}	2.251(3)	2.212(2)	2.222(3)	2.202(4)	2.183(4)
Co to P_3-plane	−0.128	0.407	0.428	0.312	0.357
M to N_3-plane	0.298	0.356	0.343	0.34	0.328
	119.63(4)	109.29(4)	107.59(4)	116.36(6)	122.21(6)
P–Co–P	118.16(4)	124.97(4)	121.18(4)	117.64(6)	113.74(6)
	121.25(4)	115.63(4)	120.04(4)	120.01(6)	116.31(6)
	117.50(13)	117.35(11)	116.39(12)	115.07(18)	118.3(2)
N_{amide}–M–N_{amide}	116.68(13)	117.03(11)	118.89(12)	107.07(18)	128.26(19)
	118.93(13)	115.89(11)	115.65(12)	128.88(19)	105.13(19)
Co–M–N_{amine}	178.90(8)	179.03(7)	178.37(8)	179.06(11)	178.91(12)
N–Co–M		171.11(10)	175.52(10)	176.70(15)	176.60(16)

[a] FSR = (M−V bond distance) / (sum of M and V single-bond radii). See text.
[b] Two unique molecules per asymmetric unit.

5.5.2 Electrochemistry of CoML series

Multiple redox processes have been observed in the cyclic voltammograms (CVs) of the cobalt-transition metal complexes (Figure 5.3). The CV of CoTiL (**1**) shows two reversible oxidations at −0.76 and −0.19 V versus Fc^{+}/Fc. Under argon, a quasi-reversible reduction occurs at −3.20 V, which becomes fully irreversible under N_2. Similar electrochemical behavior was observed for CoVL, CoCrL, and Co_2L, in which the first reductive process is irreversible under N_2 but is more reversible under argon.[22,24,258] The behavior is consistent with a rapid chemical reaction, such as N_2 binding, following electron transfer. The (N_2)CoAlL complex has a single, reversible reduction under N_2 at −0.95 V versus Fc^{+}/Fc, which is expected since N_2 is already bound to the Co center in (N_2)CoAlL.[118] Of all the cobalt bimetallics, the (N_2)CoAlL has the mildest reduction potential by over 1 V. For the ancillary transition metals, the $[CoML]^{0/-}$ redox potentials become increasingly mild as the supporting metal is varied across the period, i.e. from early to late: CoTiL < CoVL < CoCrL < Co_2L.

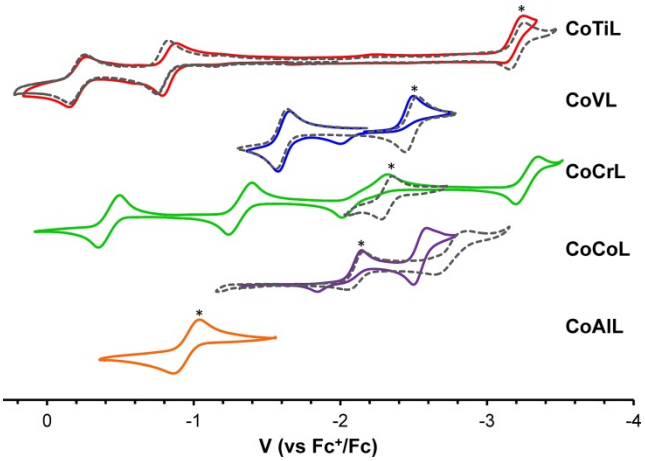

Figure 5.3. Cyclic voltammograms of CoML complexes collected under an atmosphere of N_2 (colored lines) or argon (---) in 0.4 M $[^{n}Bu_4N]PF_6$ in THF at a scan speed of 50 mV/s. Exceptions: 10mV/s for CoCrL and Co_2L, which was dissolved in 0.1 M $[^{n}Bu_4N]PF_6$ in DME. Asterik (*) indicates $[CoML]^{0/-}$ redox couple.

5.5.3 Synthesis and characterization of dinitrogen adducts 2 and 3

To probe N_2 activation, chemical reduction of the CoML species with KC_8 followed by addition of crypt-222 provided the end-on N_2 complexes, $[(N_2)CoML]^-$ (Figure 5.4). Both K(crypt-222)[(N_2)CoVL] (**2**) and K(crypt-222)[(N_2)CoCrL] (**3**) were successfully generated, but we were unable to isolate any reduced CoTi species.

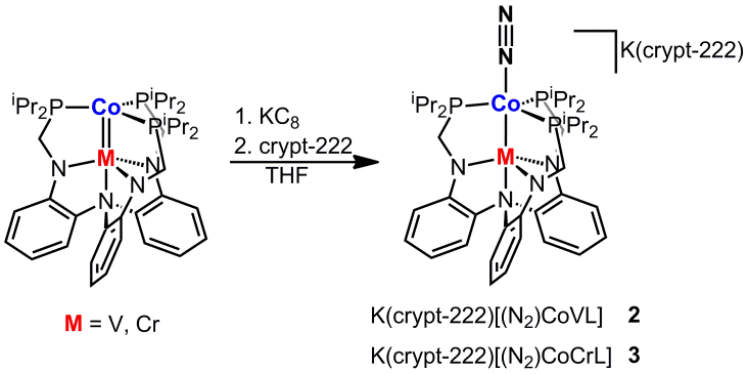

Figure 5.4. Synthesis of compounds **2** and **3**.

The solution-state magnetic moments of **2** and **3** were measured to be 2.68 and 3.58 μ_B, respectively. Hence, the ground states of **2** and **3** are assigned as $S = 1$ and $S = 3/2$, respectively, as they are close to the spin-only moments of 2.83 and 3.87 μ_B, respectively. The remaining anionic members, $[(N_2)Co_2L]^-$[24] and $[(N_2)CoAlL]^-$,[233] have been reported previously.

Figure 5.5 shows the molecular structures of **2** and **3**. The unit cells for **2** and **3** each contain two unique molecules. The N−N bond elongates upon binding, from 1.098 Å in free N_2 to 1.130(4)/1.135(4) Å and 1.120(7)/1.135(6) Å in **2** and **3**, respectively (Table 5.1).[261] By this metric, N_2 is slightly less activated in $[(N_2)Co_2L]^-$ and $[(N_2)CoAlL]^-$, which have N−N bond lengths of 1.114(4) and 1.110(8) Å, respectively. The M−N_2 bond length can be useful to assess metal−N_2 back-bonding. However, the

Co−N bond distances are all the same at 1.80 Å (within error). Cobalt centers are typically poor at π-back-bonding to N_2, and the N−N and Co−N metrics of these cobalt bimetallics are consistent with weak N_2 activation.

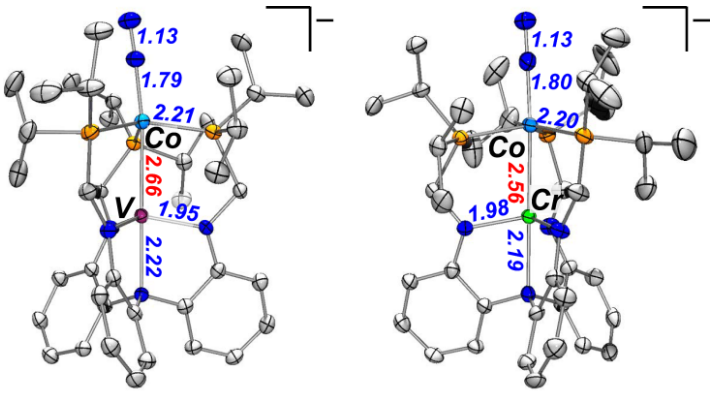

2 3

Figure 5.5. Molecular structures of **2** and **3** shown at 50% thermal ellipsoid probability. Hydrogen atoms, K(crypt-222) counterion, and non-coordinating solvent molecules were omitted for clarity. Average bond lengths (Å) are shown.

Upon reduction, the FSR values of the Co−M bonds in the cobalt-transition metal pairs all increase above unity (1.1 to 1.2). Presumably, elongation of the Co−M bond is a direct consequence of N_2 binding *trans* to the supporting metal, and thereby, weakening the Co−M interaction. Only $[(N_2)CoAlL]^-$ shows a decrease in FSR (1.06 to 1.02) relative to its neutral analogue. Again, N_2 already occupies the apical pocket in the neutral complex, and so, the increase in cobalt electron density (by one electron) is interpreted to increase cobalt back-bonding to the Lewis acidic Al(III) center. Finally, systematic changes in the Co−P bond lengths can be discerned among the K(crypt-222)$[(N_2)CoML]$ compounds. Specifically, the Co−P bond distances increase according to the order: 2.18 Å in $[(N_2)CoAlL]^-$ < 2.19 to 2.21 in **2** and **3** < 2.26 Å in $[(N_2)Co_2L]^-$, where the latter has substantially longer Co−P bonds than the others.

The N−N bond stretching frequency should be a more precise measure of N_2 activation. The N−N frequencies were measured on solid KBr samples of the K(crypt-222)[(N_2)CoML] complexes. In order of increasing N_2 activation, the frequencies are: 1995 cm^{-1}, $[(N_2)CoAlL]^-$ ≈ 1994 cm^{-1}, $[(N_2)Co_2L]^-$ > 1990 cm^{-1}, $[(N_2)CoCrL]^-$ > 1971 cm^{-1}, $[(N_2)CoVL]^-$.[24,233] The N−N frequencies, which span 24 cm^{-1}, are all consistent with a weakly activated N_2 ligand. Except for a general correlation, we could not pinpoint an exact relationship between the N−N frequencies and the $[CoML]^{0/-}$ reduction potentials, nor alternatively, the E_{pa} of $[(N_2)CoML]^-$. However, in terms of N−N frequencies and redox potentials, $[(N_2)CoVL]^-$ and $[(N_2)Co_2L]^-$ represent the different extremes of N_2 activation and reducing capability in this series. Dinitrogen is most activated in $[(N_2)CoVL]^-$, and the $E_{1/2}$ of $[CoVL]^{0/-}$ is highly cathodic. Any precise relationship between reducing ability and N_2 activation, however, deteriorates upon further scrutiny. For instance, N_2 is activated to a similar extent in $[(N_2)CoAlL]^-$ and $[(N_2)Co_2L]^-$, though the corresponding $[CoML]^{0/-}$ redox potentials differ by over 1 volt.

5.5.4 Theory

The $[(N_2)CoML]^-$ series and CoTiL (**1**) were investigated using density functional theory (DFT) and complete active space self-consistent field (CASSCF) calculations. Optimizations were performed at the DFT level on the model species, $[(N_2)CoML^{Me}]^-$, where L^{Me} is the truncated ligand (from P^iPr_2 to PMe_2), and M = Al, Ti, V, Cr, and Co (see Experimental Section for details). The DFT optimized structures were then used as

inputs for multiconfigurational CASSCF calculations with second-order perturbation (CASPT2).

The qualitative molecular orbital (MO) diagram for the model CoTi complex, $CoTiL^{Me}$ (**1'**), is shown in Figure 5.6.

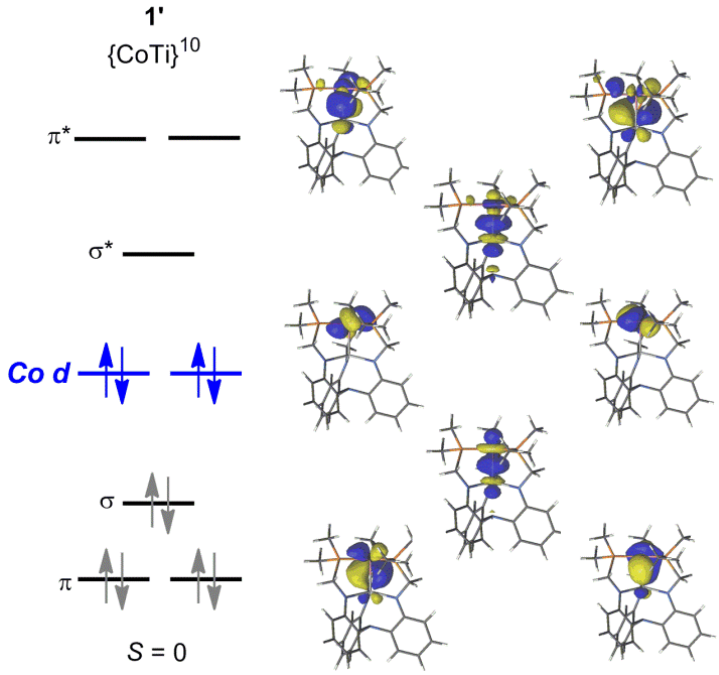

Figure 5.6. Qualitative MO diagram showing the natural orbitals for $CoTiL^{Me}$ (**1'**) that arise from CASSCF calculations. The dominating electronic configuration (83%) is shown.

The main electronic configuration, $\pi^4\sigma^2$(Co $3d_{xy}$,$d_{x^2-y^2}$)^4, which accounts for 83% of the total wave function, predicts a formal Co−Ti triple bond. For the entire ground-state wave function, the occupation numbers were summed over all configurations to give the "total" electronic configuration, $\pi^{3.82}\sigma^{1.89}$(Co $3d_{xy}$,$d_{x^2-y^2}$)$^{3.88}$ $\sigma^{*0.11}$ $\pi^{*0.18}$(Co $4d_{xy}$,$d_{x^2-y^2}$)$^{0.12}$. Partial population of anti-bonding orbitals results in a slight lowering of the bond order to 2.71. Although the calculations predict a Co−Ti triple bond, the FSR of **1** is more consistent with a double bond (*vide supra*). The discrepancy may be explained by the

polarization of the σ (Co/Ti: 86/14%) and π MOs (Co/Ti: 86/14%, 65/35%), which should further decrease the formal bond order.

The qualitative splitting diagram for the $[(N_2)CoML^{Me}]^-$ series is shown in Figure 5.7. The $[(N_2)CoTiL^{Me}]^-$ species is purely hypothetical since its experimental congener has not yet been isolated. The energy ordering of the orbitals were based on the DFT calculations. In common, the N_2 π* molecular orbitals are energetically inaccessible, lying well above the HOMO/SOMO for each species. This is consistent with weak N_2 activation and preservation of the N−N triple bond. Of interest, the energy gap between the N_2 π* MOs and the Co $d_{xy}/d_{x^2-y^2}$ orbitals remain constant for all the different supporting metals, and so, these orbitals were used as a benchmark for comparing Co d-orbital energies across the series.

For the transition metal pairings, one notable difference between the $[(N_2)CoML^{Me}]^-$ anions and their neutral CoML analogues is the greater localization of electrons at the individual metal centers in the anions. Indeed, the only MO with any degree of delocalization is the σ (Co−M). For M = Ti, V, and Cr, the σ (Co−M) is heavily polarized towards cobalt, such that the percentage of the MO on each of the metals, Co and M, is ~80% and ~20%, respectively. Hence, the CoTi, CoV, and CoCr analogues have a similar electronic structure to the CoAl species, where the cobalt center is formally subvalent, d^{10} Co(−I), and the supporting metals are trivalent, d^0 Al(III), d^1 Ti(III), d^2 V(III) and d^3 Cr(III). The natural orbital occupation numbers for each MO and the percentage that each metal contributes to the MO can help to qualitatively assign oxidation states to each metal (Table 5.2) by summing the weighted contributions to get

an effective number of electrons on each metal.[21] The effective oxidation states predicted from CASSCF calculations are in agreement with the formal assignments. The Co d_z^2 electrons are greatly stabilized by the Lewis acidic Al(III) supporting ion. For M = Ti, V, and Cr, the ligand-field splitting of the cobalt-based *d*-orbitals remains fairly constant for M = Ti, V, and Cr, where the Co d_z^2 electrons are intermediate in energy between the non-bonding d_{xz}/d_{yz} and metal-ligand anti-bonding $d_{xy}/d_{x^2-y^2}$ orbitals.

Table 5.2. Effective oxidation state of $[(N_2)CoML^{Me}]^-$ and percent polarization of σ bond on Co.

M	Oxidation State Co	Oxidation State M	% MO on Co
Al	-1.0	3.0	100
Ti	-0.6	2.6	82
V	-0.6	2.6	80
Cr	-0.6	2.6	79
Co	0.0	2.0	37

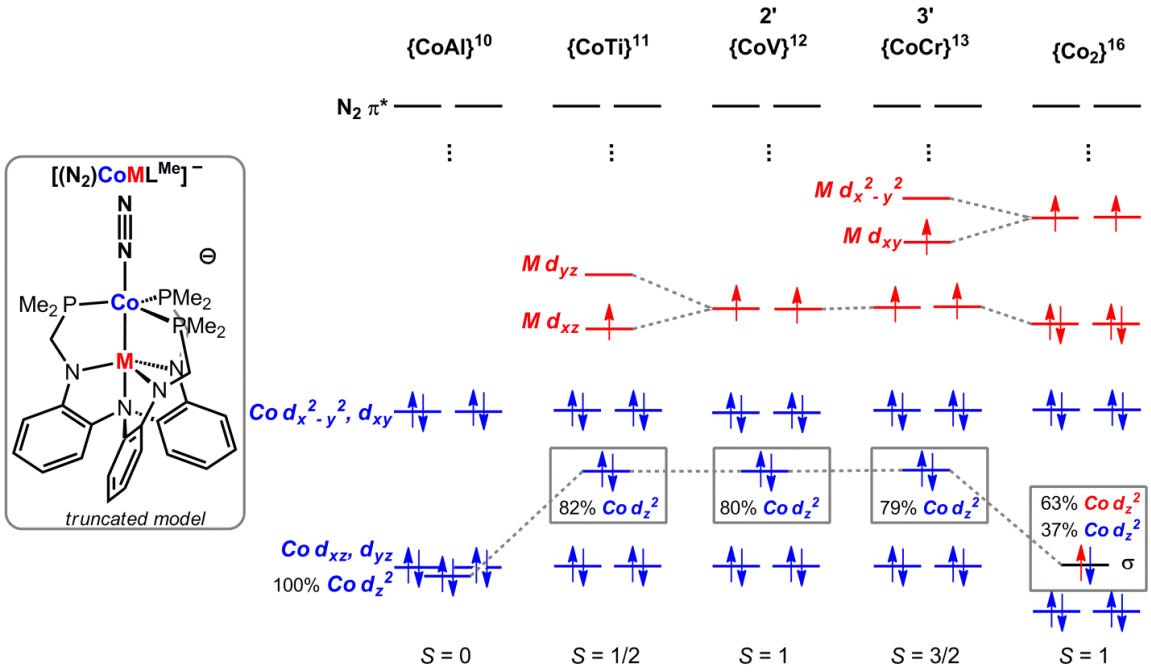

Figure 5.7. Qualitative MO diagrams of the d-orbital manifold for the $[(N_2)CoML^{Me}]^-$ series, where M = Al, Ti, V, Cr, and Co.

The dicobalt analogue, $[(N_2)Co_2L^{Me}]^-$, is the stand-out in this series. Its electronic structure is different, which makes sense, considering it is the only late-late metal combination. Opposed to the Co(−I)M(III) redox states of the other anions, the oxidation state of the dicobalt core is Co(0)Co(II). The key difference is the presence of a well delocalized, Co−Co σ-bonding MO (63/37%). Hence, a formal single bond is predicted between the two metal centers. The better overlap and mixing between the two metals' d-orbitals is likely responsible for the greater ligand-field splitting for the phosphine-ligated cobalt compared to the other anions. Of note, the different oxidation state of Co(0) in the dicobalt anion versus Co(−I) in other $[(N_2)CoML^{Me}]^-$ anions may have observable ramifications. Recall that the Co−P bonds are significantly longer in $[(N_2)Co_2L]^-$ (2.26 Å) compared to the Al, V, and Cr counterparts (2.19 to 2.21 Å). The shorter Co−P bond lengths in the latter complexes are consistent with a more reduced cobalt site, which can better back-bond to the phosphine ligands.

5.6 Conclusions

The neutral CoTiL complex is the fifth member of a $(CoM)^{3+}$ family supported by the triphosphino(triamido)amine scaffold. The Co−Ti bond is short at 2.20 Å. Theory predicts a formal triple Co−Ti bond (σ + 2π). However, polarization of these metal-metal bonding MOs should weaken the Co−Ti bonding. Based on a formal shortness ratio of 0.89, we approximate a Co−Ti double bond. Three one-electron transfers are observed in the CV of CoTiL. The $[CoTiL]^{0/-}$ reduction potential is extremely negative at −3.20 V. Including (N_2)CoAlL, the $(CoM)^{+3/+2}$ redox couples in this family span a large range of 2.25 V. The supporting metal ion has a large impact on the $[CoML]^{0/-}$ redox potentials.

The $[CoML]^{0/-}$ reduction potentials shift anodically as M is varied across the first-row period. Of interest to N_2 activation, four isostructural $[(N_2)CoML]^-$ compounds were isolated and characterized for M = Al, V, Cr, and Co.[24,233] Varying the supporting metal ion has a limited impact on the extent of N_2 activation. For instance, the range of N−N bond lengths in the N_2 adducts, $[(N_2)CoML]^-$, is extremely narrow from 1.110(8) to 1.135(4) Å. Likewise, the stretching frequencies of the N_2 adducts span only 24 cm^{-1}. Though the changes in ν_{N2} are subtle, N_2 activation in the $[(N_2)CoML]^-$ series does decrease across the period. As might be expected, there is a correspondence between the $[CoML]^{0/-}$ reduction potentials ($E^\circ_{1/2}$) and N_2 activation:

$E^\circ_{1/2}$ ($[CoML]^{0/-}$ or $[(N_2)CoAlL]^{0/-}$): Al << Co < Cr < V << Ti

ν_{N2} ($[(N_2)CoAlL]^-$): Al ~ Co > Cr > V

Varying the supporting metal ion changes the electronic structure of the $[(N_2)CoML]^-$ species. As elucidated through theory, the oxidation state of the $(CoM)^{2+}$ core is Co(−I)M(III) for M = Al, Ti, V, and Cr. The dicobalt anion is unique in that the oxidation states are Co(0)Co(II). The Co−M interactions, which are similar for M = Ti, V, and Cr, are potentially significant for Al and Co, albeit in different manifestations. In $[(N_2)CoAlL]^-$, an inverse dative bond (Co→Al) greatly stabilizes the Co d_z^2 electrons, a consequence of pairing cobalt with the Lewis acidic ion, Al(III). In $[(N_2)Co_2L]^-$, the late-late pairing enables better *d*-orbital overlap such that a Co−Co σ-bond is formed.

Author Contributions

Experiment: Laura J. Clouston, Connie C. Lu

Theory: Varinia Bernales contributed to DFT and CASSCF calculations, Rebecca K. Carlson contributed to CASSCF calculations of CoTi, CoV, and CoCr, Laura Gagliardi

Chapter 6

Structure and Bonding of Group 4-Nickel Heterobimetallics Supported by 2-(diphenylphosphino)pyrrolide Ligands

Reproduced in part from

Structure and bonding of group 4-nickel heterobimetallics supported by 2-(diphenylphosphino)pyrrolide ligands, Peter L. Dunn, Rebecca K. Carlson, Laura Gagliardi and Ian A. Tonks,***Dalton Trans.***, 2016, **45**, 9892-9901.

6.1 Overview

The synthesis of a full series of group 4/nickel complexes supported by a 2-(diphenylphosphino)pyrrolide (NP) ligand is reported. Treatment of the homoleptic, 8-coordinate $M(NP)_4$ monometallic precursors with $Ni(COD)_2$ (COD = 1,5-cyclooctadiene) yielded the heterobimetallic complexes (κ^2-NP)M(μ_2-NP)$_3$Ni (M = Ti, Zr, Hf). Although X-ray crystallographic analysis reveals similarly short metal-metal distances in all three complexes, Quantum chemical calculations indicate that ZrNi (**5**) and HfNi (**6**) contain only single Ni→M dative bonds while TiNi (**4**) has an additional covalent Ti-Ni π-bond. All three complexes have quasireversible reductions by cyclic voltammetry, and 1-electron chemical reduction of **4** by Na(Hg) yields the anion, [Na][(κ^2-NP)Ti(μ_2-NP)$_3$Ni.] X-ray and computational analysis indicate that the 1-electron reduction of **4** completely breaks the metal-metal double bond, yielding a formally Ti^{III}-Ni^0 complex. Ti-Ni bonding can also be disrupted by coordination of CO, wherein Ni→CO backbonding effectively outcompetes Ni→Ti dative bonding.

6.2 Introduction

There is significant incentive to utilize first row transition metal catalysts based on Fe, Co or Ni instead of their heavier congeners because of their relative earth abundance, cost, and carbon footprint.[13,14] However, an inherent challenge in utilizing first row transition metals is overcoming (or harnessing) their propensity to undergo 1-electron radical pathways instead of the more easily controlled 2-electron processes that coincide with many fundamental organometallic reactions. Many successful and novel strategies have been developed to address this challenge, including the use of redox non-innocent ligand scaffold[262–271] and metal/ligand or metal/metal cooperative reactivity.[17–19,24,233,272–285]

Within the area of metal/ligand or metal/metal cooperativity, two main strategies have been used. First, various groups have designed systems in which reactivity occurs on both the metal and ligand. For example, Milstein coupled ligand aromatization/dearomatization with H_2 oxidative addition with tridentate Ru and Fe

pincer complexes to successfully hydrogenate a variety of substrates.[17,19] Noyori performed enantioselective catalytic transfer hydrogenation with Ruthenium diamine complexes where heterolytic H_2 cleavage occurs across the Ru-N bond.[18,272,284] Parkin reported Ni-B boratrane complexes where the dative Ni→B bond is the site of reactivity, resulting in oxidative addition across the bond.[273] Building upon this, Peters has recently reported several Ni borane complexes that feature cooperative addition of H-X across the Ni-B bond en route to catalytic olefin hydrogenation,[274] while Thomas has demonstrated diverse cooperative reactivity such as CO_2 activation, hydrosilylation, and E-H and E-E bond activation across trigonally symmetric ZrCo and TiCo heterobimetallics.[275–280]

Second, several research groups have exploited M-M bonding to attenuate the electrophilicity of a reacting metal through retrodative interactions. For example, Lu has studied several Ni-M (M = Al, Ga, In) olefin hydrogenation catalysts and found that the strength of H_2 binding and resulting catalytic TOF was impacted by the nature of the Lewis acidic metal.[25] Additionally, Co-M (M=Al, Co) were shown to be active for silylation of N_2, and the identity of the supporting metal affected catalyst activity.[24] Similarly, Nagashima and Michaelis each have carried out catalytic nucleophilic allylic amination reactions with heterobimetallic PdTi complexes. In these amination reactions, a dative Pd→Ti interaction increases the electrophilicity of Pd(η^3-allyl) complexes such that they can undergo attack by weak amine nucleophiles.[282,283,285]

To further investigate cooperative Lewis acidic effects and to investigate the potential role of covalent M-M bonding on fundamental organometallic reactivity, we are

interested in synthesizing early-late transition metal complexes supported by phosphinopyrrolide group 4 metalloligands.[286] While these ligands should impart σ-electronic properties somewhat similar to existing phosphinoamide ligand frameworks,[23,279,280,287] they are much poorer N π-donors, which should allow for stronger M-M interactions between electron-rich late transition metals and electron-poor group 4 metals. Herein we report the synthesis, characterization and electrochemistry of a series of (κ^2-NP)M(μ_2-NP)$_3$Ni complexes (NP = 2-diphenylphosphinopyrrolide; M = Ti, Zr, Hf) and lend insight into how group trends affect bonding in early-late bimetallic complexes.

6.3 Experimental Methods

See Appendix 6 for details about the synthesis and characterization of the complexes.

6.4 Computational Methods

6.4.1 DFT All density functional theory (DFT) calculations were performed with the Gaussian 09 program package.[129] The structures were optimized with the M06-L[173] functional and 6-311G+(d) basis sets for Ti, Ni, N, and P, 6-31G(d) for C, 6-31G for H[288–295] and Def2-TZVP with effective core potentials for Zr and Hf.[296] Frequency calculations were performed to confirm structures were local minima. Natural bond order analysis was performed on the optimized structures to estimate the Mayer bond order.[297,298]

6.4.2 CASSCF Calculations All the complete active space self-consistent-field (CASSCF)[34] were performed with the MOLCAS 7.8 package.[120] These calculations were

performed on the M06-L optimized structures. The relativistic all-electron ANO-RCC basis sets were used on all atoms in the complexes.[121,122] Specifically, ANO-RCC-VTZP basis sets were used for Hf, Zr, Ti, and Ni atoms, ANO-RCC-VDZP basis sets for N and P atoms, and ANO-RCC minimal basis sets were used for C and H atoms. Scalar-relativistic effects were included with the Douglas-Kroll-Hess Hamiltonian up to the second-order.[123,124] In addition, reduction of the four center 2-electron integrals to effective three center integrals via auxiliary basis sets were accomplished with the RICD[125] approximation as implemented in MOLCAS 7.8. For the anion, the active space choice was 11 3*d* electrons in 12 orbitals, corresponding to the five doubly occupied Ni 3*d* orbitals and one singly occupied Ti 3*d* orbital and a set of corresponding set of correlating orbitals for a total of 12 orbitals. For the neutral species, the active space comprised 10 electrons in 12 orbitals, corresponding to the five doubly occupied Ni 3*d* orbitals, a set of 4*d* correlating orbitals for each doubly occupied orbital, plus two other M=Ti, Zr, or Hf 3*d* orbitals for σ and π bonding.

6.5 Results and Discussion

The homoleptic group 4 complexes $M(NP)_4$ (NP = 2-diphenylphosphinopyrrolide; M = Ti (**1**), Zr (**2**), Hf (**3**)) were synthesized via salt metathesis of $MCl_4(THF)_2$ with 4 eq. LiNP (Fig. 6.1). Complexes **1** and **2** were previously reported via salt metathesis from MCl_4; in this case, utilization of the THF adducts gives significantly improved yields for Zr and Hf.[286] In the solid state, **1**-**3** are all 8-coordinate with κ^2-bound phosphinopyrrolide ligands. However, each of these complexes are fluxional on the NMR timescale: **1** displays only a single sharp ^{31}P NMR resonance indicating fast exchange, while **2** and **3**

both have broad ^{31}P NMR resonances indicative of slower exchange. These exchange processes are a function of phosphine ligand decoordination from the high coordination number metal centers.[286]

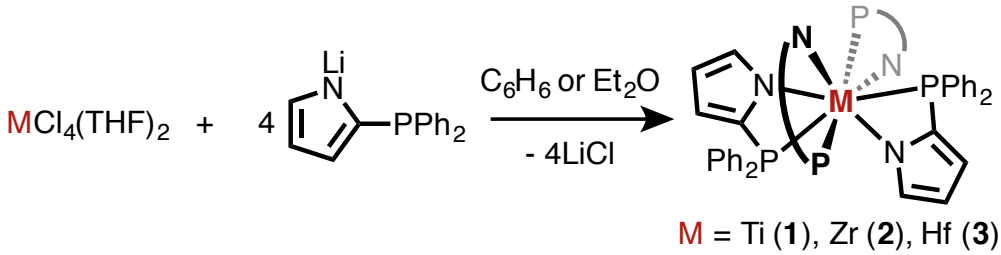

Figure 6.1. Synthesis of mono-metallic **1**, **2**, and **3**.

Treatment of **1-3** with Ni(COD)$_2$ (COD = 1,5-cyclooctadiene) affords the heterobimetallic complexes (κ^2-NP)M(μ_2-NP)$_3$Ni (M = Ti (**4**), Zr (**5**), Hf (**6**)) in relatively high yield (Fig. 6.2). While **4** could be prepared from treatment with 1 equivalent of Ni(COD)$_2$ at room temperature, both **5** and **6** required a large excess of Ni(COD)$_2$ (> 5 equiv) and elevated temperatures (90 °C) in order to react. Presumably, the higher reaction temperature is required because the M-P bonds are significantly less labile (demonstrated by ^{31}P NMR exchange) in the heavier congeners than in Ti, while excess Ni(COD)$_2$ is needed because it decomposes under high temperatures.

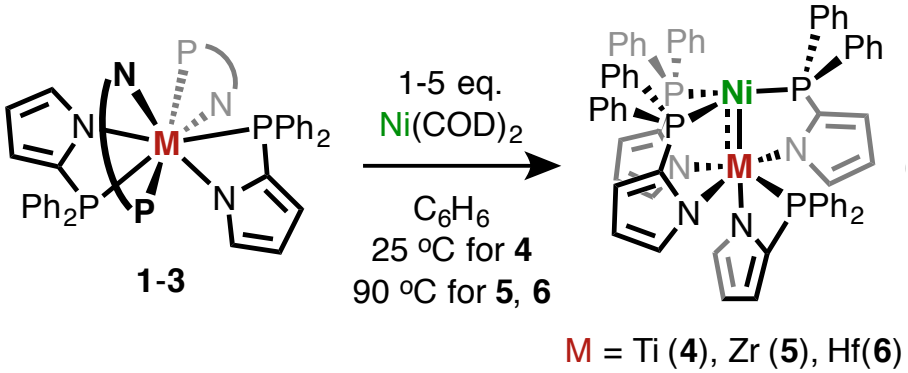

Figure 6.2. Synthesis of bimetallic **4**, **5**, and **6**.

The structures of **4**-**6** are presented in Figure 6.3 and relevant bond lengths and angles can be found in Table 6.1. All three bimetallic compounds are isostructural, containing three phosphinopyrrolide ligands that bridge between the two metals and one phosphinopyrrolide ligand that binds in κ^2-fashion to the group 4 metal center. The geometry about the group 4 metal is pseudooctahedral, while the geometry about Ni is a distorted trigonal pyramidal wherein the group 4 metal occupies the axial site of the pyramid. Interestingly, two of the three bridging phosphinopyrrolide ligands are significantly skewed from the M-Ni vector, although this has no significant effect on M-N or Ni-P bond lengths. The M-P bond of the phosphinopyrrolide that remains κ^2 to the group 4 metal is significantly longer than average for all three complexes, although shorter than the M-P bonds observed in the homoleptic 8-coordinate **1**-**3**.[286]

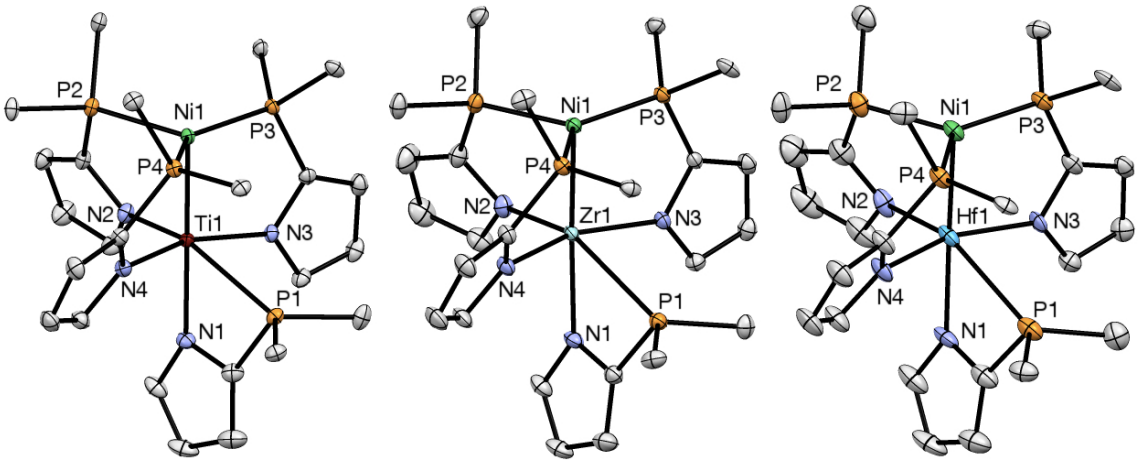

Figure 6.3. Thermal ellipsoid drawings of **4** (left), **5** (center), and **6** (right). Solvent and hydrogen atoms have been removed and phenyl groups have been reduced to the ipso carbon for clarity. Relevant bond distances (Å) and angles (°) are presented in Table 6.1.

Complexes **4**-**6** are all diamagnetic, and at room temperature display two resonances in the ^{31}P NMR: a broad feature (Ti = 2 ppm, Zr = -9 ppm, Hf = -9 ppm) of

integration 3 for the Ni-bound phosphines, and a sharp singlet (Ti = -19.2 ppm, Zr = -29.6 ppm, Hf = -26.6 ppm) that integrates to 1 for the group 4-bound phosphine. Low temperature NMR experiments reveal 3 inequivalent Ni-bound phosphines, as expected based on the solid-state structure: for **4** (TiNi), the broad feature at 2 ppm splits into three distinct resonances (Fig. 6.4). These resonances consist of two sets of doublets of doublets of doublets (J_{PP} = 11.1 Hz, 44.5 Hz, 92 Hz and J_{PP} = 11.1 Hz, 44.5 Hz, 55.6 Hz), which correspond to the two Ni-bound phosphines that are *pseudo-trans* to each other in the distorted trigonal plane; a doublet of doublets (J_{PP} = 55.6 Hz, 92.0 Hz), corresponding to the phosphine *trans* to open space; and a triplet belonging to the titanium bound phosphine (J_{PP} = 11.1 Hz). **5** (ZrNi) and **6** (HfNi) do not fully decoalesce at low temperature, but the same signal pattern emerges in all the complexes. The source of this fluxional behavior is likely twisting of the NP ligands along the M-Ni vector.

Table 6.1. Relevant bond lengths (Å) and angles (°) for **4**-**6**.

	4	**5**	**6**
M-Ni (Å)	2.2665(5)	2.3724(3)	2.4123(6)
FSR[a]	0.91	0.91	0.93
P-Ni (Å)	2.1906(6)	2.1979(5)	2.1849(10)
	2.2181(6)	2.2160(5)	2.2072(10)
	2.2354(6)	2.2257(5)	2.2171(11)
P-Ni-P (°)	135.91(2)	131.631(19)	131.53(4)
	110.19(2)	110.103(19)	110.61(4)
	112.47(2)	117.840(19)	117.68(4)
M-N (Å)	2.0800(17)	2.1747(14)	2.156(3)
	2.1053(17)	2.1926(13)	2.178(3)
	2.0433(17)	2.2234(13)	2.203(3)
	2.1089(17)	2.2283(13)	2.203(3)
M-P (Å)	2.7224(7)	2.8799(4)	2.8543(11)
	24.35(5)	30.78(4)	31.60(9)
Torsional Angle (P-Ni-M-N) (°)	5.83(5)	3.48(4)	23.99(8)
	30.67(5)	24.17(4)	2.73(8)

[a] FSR = $M_D/\sum(M_c)$: M_D = Metal-metal distance, M_c= Covalent Radii

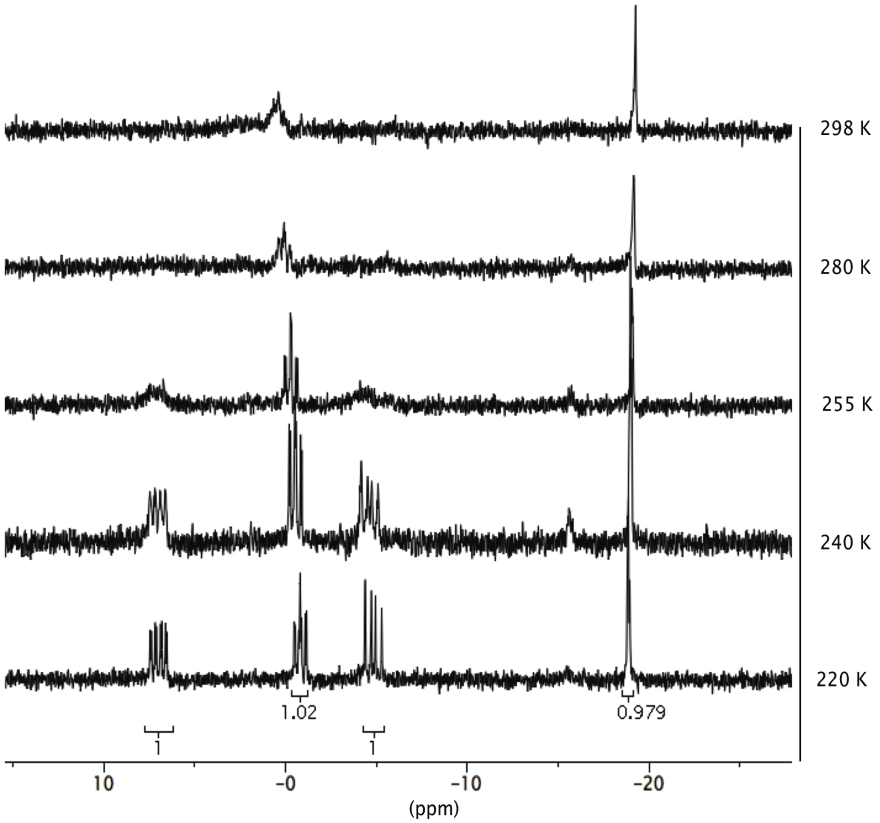

Figure 6.4. Variable temperature ^{31}P NMR spectra of **4** showing decoalescence of the 3 inequivalent Ni-bound phosphines at low temperature**.**

All three heterobimetallics possess remarkably short M-Ni bond distances: Ti-Ni 2.2665(5) Å; Zr-Ni 2.3724(3) Å; Hf-Ni 2.4123(6) Å. Although the bonds become longer as the group 4 atomic radius increases, the formal shortness ratio (FSR) increases only slightly down the series, from 0.91 in **4** (TiNi) to 0.93 in **6** (HfNi) potentially indicating a minor decrease in the strength of M-M bonding down the triad. **4** (TiNi) represents the second discrete TiNi bimetallic complex; Lu recently reported a d^{11} TiNi bimetallic complex with a Ti-Ni bond length of 2.4118(7) Å contained in a double-decker phosphinoamide ligand framework.[23] A CSD search revealed no examples of ZrNi or HfNi complexes containing a metal-metal bond.[299]

In order to develop a better understanding of the M-Ni bonding in **4**-**6**, DFT and CASSCF calculations were performed. Geometry optimization and frequency calculations were performed using the M06-L functional and are in good agreement with crystallographic bond distances. CASSCF calculations performed on **4** show that the wave function is multiconfigurational and dominated by two configurations. The dominant configuration (72%) is $\sigma^2\pi^2(\text{Nid}_{yz})^2(\text{Nid}_{xy})^2(\text{Nid}_{x^2-y^2})^2$, containing two Ti-Ni bonding interactions: a σ-bond between the Ti d_{z^2} and Ni d_{z^2} orbitals, and a π-bond between the Ti d_{xz} and Ni d_{xz} orbitals (Figure 6.5).

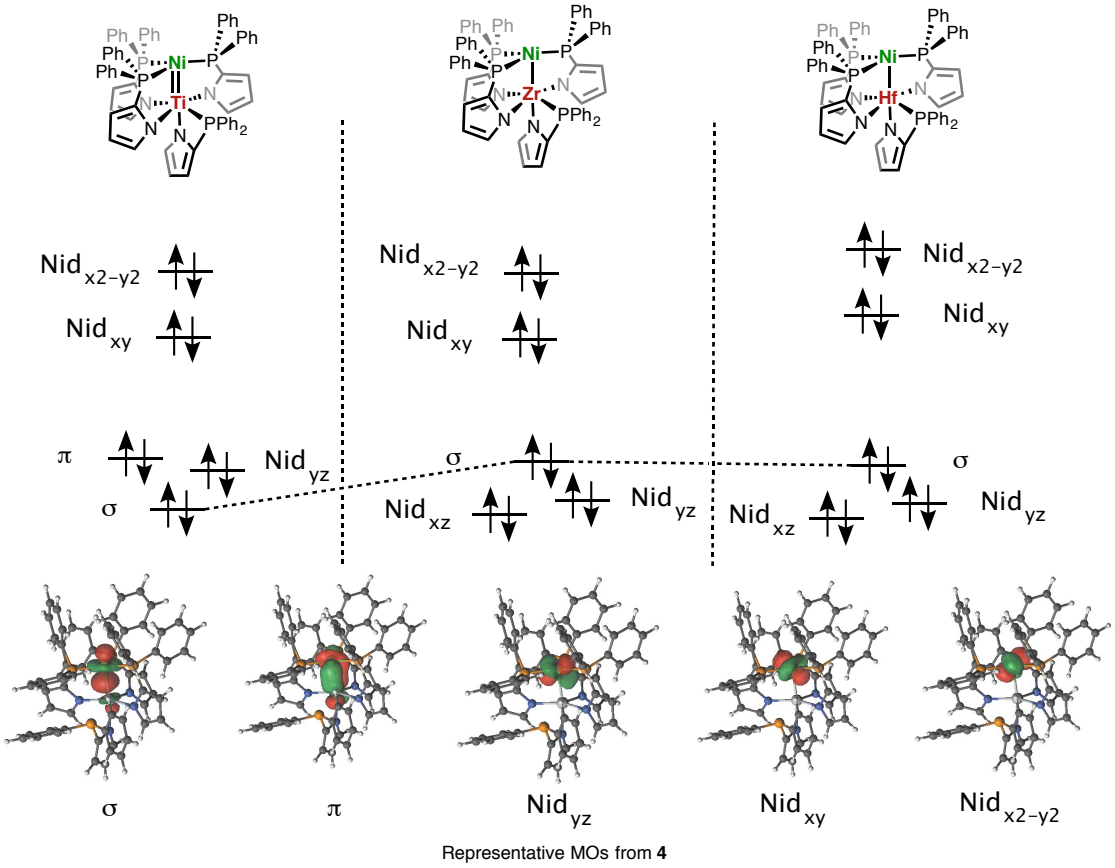

Figure 6.5. Qualitative molecular orbital diagrams taken from M06-L energies for **4**, **5**, and **6**(above) and representative molecular orbitals for **4**(below).

The second major configuration (11.3%) is similar but contains a double excitation from the Ti-Ni π orbital to π*. The σ-bond is predominantly polarized (94%) on Ni, while the π orbital is more covalent, with 71% of the electron density on Ni. Effective oxidation states can be estimated from the natural orbital occupation numbers and the percentage each atomic orbital of the metals contribute to the molecular orbital. From this analysis, Ti has a charge of +3.1 electrons and Ni has a charge of +0.9 electrons, and the system is best described as Ti^{III}/Ni^{I}. From DFT natural bond order (NBO) analysis, the Mayer bond order is calculated to be 0.91, approximately a Ti-Ni single bond.

In contrast, calculations on the Zr and Hf analogues **5** and **6** indicate that there are *no* M-Ni π interactions, most likely due to poor energy overlap between the two participating orbitals.[23,198] For both, the dominant configuration is $\sigma^2(Nid_{xz})^2(Nid_{yz})^2(Nid_{xy})^2(Nid_{x2-y2})^2$, with a σ-bond between the Zr/Hf d_z^2 and Ni d_z^2 orbitals that is predominantly Ni based (94% for Zr; 93% for Hf). Also unlike the Ti case, there is significantly less orbital occupation on the group 4 metal in **5** and **6** (approximately 0.2-0.3 electrons), indicating that these are best described as M^{IV}/Ni^{0} systems. The Mayer bond orders for 5 and 6 are 0.78 and 0.70, respectively, suggesting weaker metal-Ni interactions as the metal period increases. Furthermore, since Ti has better orbital overlap with Ni, there is a larger degree of bonding and covalency in **4** than in **5** or **6**, ultimately yielding a formally Ti^{III}/Ni^{I} bimetallic core in which Ni has effectively reduced the Ti center.[23,198]

To further examine the effects of introducing a late transition metal into the coordination sphere of group 4 metals, cyclic voltammetry experiments were performed

on the monometallic complexes **1**-**3** as well as the corresponding bimetallics **4**-**6** (Figure 6.6). Monometallic **1**-**3** each showed one quasi-reversible reduction, and the reduction potential becomes increasingly more negative down the group 4 triad: -0.6 V for **1** (Ti); -1.8 V for **2** (Zr); - 2.2 V for **3** (Hf) *vs*. Fc/Fc^{+}. This trend follows the Pauling electronegativities of the groul 4 elements, and the large gap between Ti and Zr is expected; for example, electrochemical studies performed by Laviron with Cp_2MCl_2 (M = Ti, Zr, Hf) revealed reduction potentials of -0.6 V for Ti, -1.5 V for Zr, and -1.9 V for Hf.[300,301] Surprisingly, there were no oxidation events observed within the solvent window for **4**-**6**.

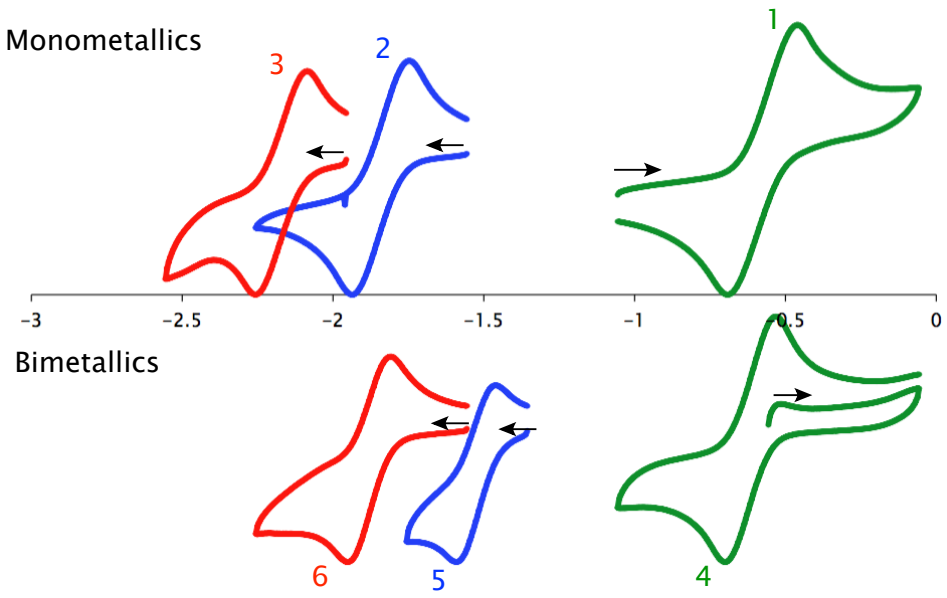

Figure 6.6. Cyclic voltammograms of **1**, **2**, and **3** (top) and **4**, **5**, and **6** (bottom). Potentials are referenced to Fc/Fc^{+}.

Interestingly, addition of a d^{10} Ni center to the coordination environment of Ti, Zr, or Hf has only a small effect on the reduction potential of the bimetallics **4**-**6**. Cyclic voltammetry of **4**-**6** showed a single quasireversible reduction for each compound. Like

the monometallic series, the reduction potentials are increasingly negative down the group 4 triad: -0.6 V for **4** (Ti); -1.3 V for **5** (Zr); -1.7 V for **6** (Hf) *vs.* Fc/Fc^{+}. Because this trend is identical to that observed in the monometallics and because the Ni center is d^{10}, the electrochemical events observed in **4**-**6** are likely the M^{IV}/M^{III} redox couple. The reduction potentials of **5** (ZrNi) and **6** (HfNi) are 0.2 V *higher* than their monometallic counterparts. In this case, the dramatic change in the group 4 metal coordination environment likely makes reduction more facile: the monometallic complexes are 8-coordinate, formally 16-electron species with 4 dative M-P bonds, whereas the bimetallic complexes are 6-coordinate, formally 12-electron species with only 1 dative M-P and 1 dative $M\text{-}Ni^{0}$ bond. Coincidentally, the reduction potential of **4** (TiNi) is virtually unshifted with respect to the monometallic **1**.

Given the facile reduction of **4**, we sought to isolate the reduced species *via* chemical reduction. Reduction of **4** with Na(Hg) in benzene leads to the clean formation of the 1-electron reduced anion, $[Na]^{+}[(\kappa^{2}\text{-NP})Ti(\mu_{2}\text{-NP})_{3}Ni]^{-}$, **7** (Fig. 6.7). The ligand connectivity of **7** is identical to that of **4**; however, the Ti-Ni bond distance has dramatically elongated from 2.2665(5) Å to 2.6892(5) Å, giving an FSR (1.08) indicative of complete breakage of the Ti-Ni bond. While the Ni-P bond distances are roughly unchanged in **7** from **4**, the Ti-N distances are all elongated by 0.02-0.06 Å and the Ti-P distance has elongated by 0.14 Å. The elongated Ti-ligand bond lengths are consistent with a Ti^{III} metal center, yielding a formally Ti^{III}/Ni^{0} bimetallic core with little-to-no interaction between the two metals. Similar phosphine elongation has been observed by Wass in isostructural cationic and neutral (2-(Di-t-butylphosphino)phenol)titanocenes

where the Ti-P bond length increases from 2.785(2) Å to 2.9067(9) Å upon reduction from Ti^{IV} to Ti^{III}.[302,303] While the d^{11} TiNi core in **7** is isoelectronic with Lu's previously-reported TiNi complex NiTi(N(*o*-($NCH_2P^iPr_2$)C_6H_4)$_3$) which contains a formal Ti-Ni single bond, the intermetallic distance in **7** is significantly (> 0.2 Å) longer and thus any bonding interaction is much weaker.[23]

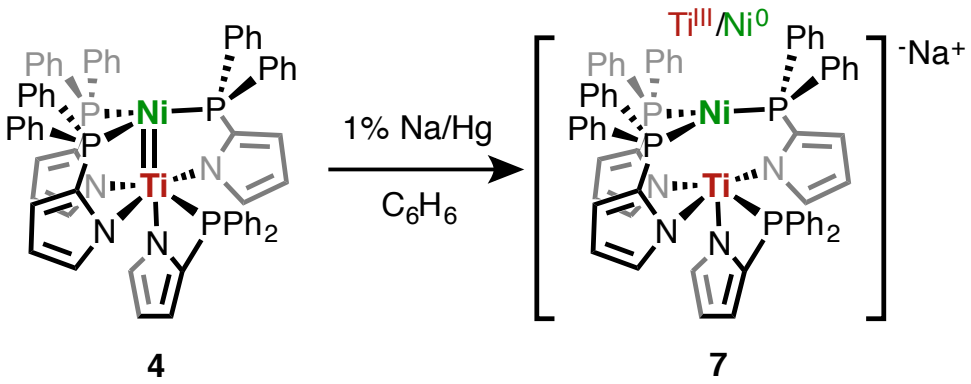

4 **7**

Figure 6.7. Synthesis of **7.**

CASSCF calculations were performed on **7** to confirm the bonding picture. The dominant configuration, $\sigma^2(Nid_{xz})^2(Nid_{yz})^2(Nid_{xy})^2(Nid_{x2-y2})^2(Tid_{xz})^1$, (89%) is consistent with a reduced Ti metal center and a weak σ-bonding interaction between the Ti and Ni d_z^2 orbitals. As predicted by the X-ray structure, the oxidation state of the system based on orbital occupancy is best described as Ti^{III}/Ni^0 with Ti having a +2.8 charge and Ni a +0.3 charge. Unlike in **4**, Nid_{xz} and Tid_{xz} do not form a π-bond and instead have electron density localized on each metal. Consistent with Ti^{III} being a weaker Lewis acid than Ti^{IV}, the Mayer bond order of 0.43 is significantly lower than that observed in **4** (0.91). Remarkably, addition of a single electron into the Ti-Ni bimetallic core has the dual effect of breaking the Ti-Ni π-bond and significantly weakening the dative bond.

Exposure of **4** to 1 atm of H_2, ethylene or CO_2 yielded no reactivity by ^{31}P NMR analysis. However, reaction of **4** with 1 atm of CO resulted in the reversible formation of a Ni-CO adduct **8** (Fig 6.8). The Ni center in **8** is *pseudo*-trigonal bipyramidal with CO and Ti occupying the axial sites. Much like in **7**, the Ni-Ti intermetallic distance has significantly elongated to 2.6136(8) Å (FSR = 1.05), indicating breakage of the Ni-Ti bond. The C-O bond (1.211(5) Å) is also elongated with respect to free CO, demonstrating that Ni→CO backbonding effectively outcompetes Ni→Ti dative bonding. The ^{31}P NMR spectrum also provides evidence for breakage of the Ni-Ti bond: when compared to **4**, **8** shows a significant sharpening and upfield shift of the broad feature in the ^{31}P NMR associated with the Ni-bound phosphines. The more facile coalescence of the three inequivalent Ni-bound phosphines is a consequence of an *increase* in motion/degrees of freedom about the Ni centre that results from breakage of the Ni-Ti bond. Prolonged exposure of **8** to vacuum results in complete reformation of **4**.

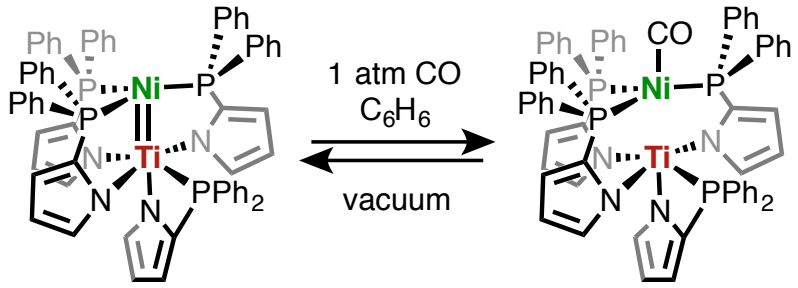

Figure 6.8. Binding of CO to **4** to form a Ni-CO adduct **8**.

Complexes **1-8** are extremely water-sensitive. When crystallizing **4** or **8** in the presence of trace amounts of H_2O (<10 ppm), the oxo-bridged tetrametallic **9** often preferentially crystallizes from solution (Fig. 6.9). In **9**, the geometry around Ti is

trigonal bipyramidal with O and Ni occupying the axial sites, and the geometry around Ni is trigonal pyramidal. The Ti-Ni bond distance is 2.3846(6) Å, indicative of a single bond (FSR = 0.96). This distance is again elongated with respect to **4**, likely due to the presence of a ligand (O) *trans* to Ni and the geometry change about Ti. While we have been unable to intentionally synthesize **9** *via* stoichiometric addition of H_2O, this complex raises the possibility of synthesizing trigonally symmetric structures and molecular wires with the NP framework.

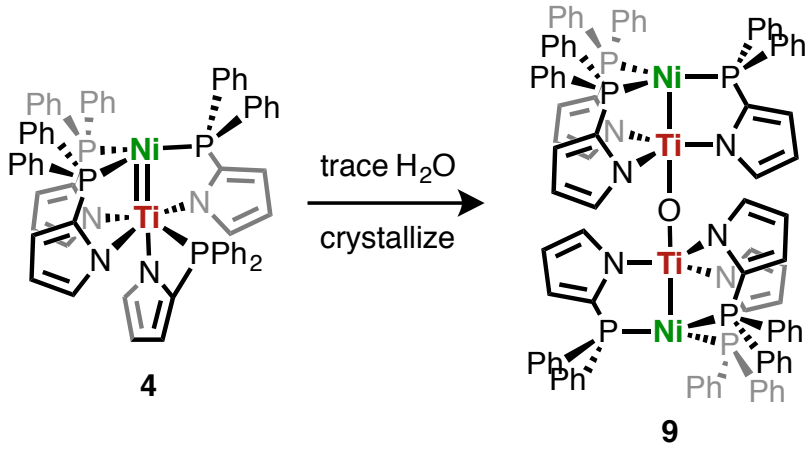

Figure 6.9. Structure of product (**9**) that forms when crystallizing **4** in trace amounts of H_2O.

6.6 Conclusions

A complete series of group 4/Ni heterobimetallic complexes based on a 2-(diphenylphosphino)pyrrole ligand scaffold have been synthesized and characterized. X-ray crystallography and computational analysis has revealed that the extent and type of metal-metal bonding in the complexes is dependent on the nature of the group 4 metal. The heavier congeners Zr and Hf are strictly limited to forming strong dative single bonds with Ni, while Ti can form a Ti-Ni double bond through covalent π-bonding.

Reductions of the heterobimetallic complexes take place at the group 4 metal. In the case of Ti, the reduced $[TiNi]^-$ anion was isolated and characterized. Interestingly, addition of a single electron to the bimetallic core completely disrupts the two bonding interactions present in the neutral species: the resulting Ti^{III}/Ni^0 system has no π bonding and a significantly weakened Ti-Ni dative σ-bond.

Author Contributions
Experimental: Peter L. Dunn, Ian Tonks
Theoretical: Rebecca K. Carlson, Laura Gagliardi

Chapter 7

Multi-Configuration Pair-Density Functional Theory

Reproduced in part from

Multiconfiguration Pair-Density Functional Theory, Giovanni Li Manni, Rebecca K. Carlson, Sijie Luo, Dongxia Ma, Jeppe Olsen, Donald G. Truhlar, and Laura Gagliardi, *Journal of Chemical Theory and Computation,* **2014** ,*10* (9), 3669-3680.

7.1 Overview

We present a new theoretical framework, called Multi-Configuration Pair-Density Functional Theory (MC-PDFT), which combines multi-configurational wave functions with a generalization of density functional theory (DFT). A multi-configurational self-consistent-field (MCSCF) wave function with correct spin and space symmetry is used to compute the total electronic density, its gradient, the on-top pair density, and the kinetic and Coulomb contributions to the total electronic energy. We then use a functional of the total density, its gradient, and the on-top pair density to calculate the remaining part of the energy, which we call the exchange-correlation energy by analogy to the exchange-correlation energy of Kohn–Sham DFT. Because the on-top pair density is an element of the two-particle density matrix, this goes beyond the Hohenberg-Kohn theorem that refers only to the one-particle density. To illustrate the theory, we obtain first approximations to the required new kind of density functionals by translating conventional density functionals of the spin densities using a simple prescription, and we perform post-SCF density functional calculations using the total density, density gradient, and on-top pair density from the MSCSF calculations. Double counting of dynamic correlation or exchange does not occur because the MCSCF energy is not used. The theory is illustrated by applications to the bond energies and potential energy curves of H_2, N_2, F_2, CaO, Cr_2, and NiCl and the electronic excitation energies of Be, C, N, N^+, O, O^+, Sc^+, Mn, Co, Mo, Ru, N_2, HCHO, C_4H_6, c-C_5H_6, and pyrazine. The method presented has a computational cost and scaling similar to MCSCF, but a quantitative accuracy, even with the present first approximations to the new kinds of density functionals, that is comparable to much more expensive multireference perturbation theory methods.

7.2 Introduction

In Kohn-Sham Density Functional Theory, KS-DFT,[42] as extended to spin-polarized electronic systems,[304,305] the electronic energy is expressed as a functional of the electron spin densities (in the local-spin-density approximation, LSDA) and their gradients (in the generalized gradient approximation, GGA), as well as possibly as a functional of orbital-dependent quantities such as exchange energy density or kinetic energy density. The dependence on these quantities, as opposed to a dependence on the full two-particle density matrix,[43] makes the method computationally simpler and more affordable than wave function theory (WFT).[306]

A key concern in the present article is the treatment of inherently multi-configurational systems, that is, systems whose electronic structure cannot be described

to a good approximation by only a single way of distributing the electrons in the orbitals of a single Slater determinant. Such systems are usually labeled as "strongly correlated" systems or "multireference" systems, where the latter reminds us that a converged treatment by most WFT methods requires a multi-configuration reference state or zero-order wave function. In WFT, the special kinds of errors in the energy that arise from using a single-reference treatment of an inherently multi-configurational system are called "static," "nondynamical," "near-degeneracy," or "left–right" correlation energy.[31–33] Examples of inherently multi-configurational systems include many transition metals and molecules and solids containing them, partially broken bonds, most excited states of molecules, and some transition states.

In KS-DFT,[42,304,305] the spin densities are represented by a single Slater determinant, and the spin-orbitals of this determinant are used to evaluate the kinetic energy of the noninteracting electron system with the same density as the real system. The correction to the kinetic energy, the exchange energy, and the correlation energy are then represented by a functional of the spin densities. This functional, called the exchange–correlation functional is so complicated it will probably never be known exactly.[307] In order to obtain correct energetics, a determinant that is not a spin eigenfunction and has the wrong symmetry may be necessary.[43]

Nevertheless, one must be careful: not all broken symmetry solutions are permissible. Because the true density has to respect, e.g., some spatial symmetries the exact KS theory must only lead to solutions whose total density preserves the appropriate symmetries of the density. Note, however, that producing a density with the correct

symmetry is generally less of a constraint on a Slater determinant than producing a wave function with the correct symmetry. Notice also that, in a different approach, it has been proposed to generate true spin-density functionals based on a size-extensive construction of self-interaction correction orbitals.[308]

Moreover, even if a system is inherently multi-configurational, KS-DFT with the exact functional is exact, even with the single-configuration representation of the density, but the accuracy is typically low with existing functionals.[309–311] Furthermore, it is not always clear which of the nearly degenerate states is being approximated, leading to the development of strategies for interpreting broken-symmetry solutions.[35,45,312–317] Therefore, one of the unmet challenges for DFT is the proper treatment of multireference systems and, more generally, the treatment of nearly degenerate states by enforcing their spatial and spin symmetries. Multi-configuration self-consistent-field (MCSCF) methods, such as the complete active space self-consistent field (CASSCF)[34] method, on the other hand, are able to treat near-degeneracies with no ambiguity about which state is being approximated, but they do not include dynamic correlation energy, which is essential for a quantitative treatment of chemical properties like bond energies and electronic excitation energies, nor do they include core-valence correlation, which can also be important. Both of these effects can be added by a post-SCF method, for example multireference perturbation theory [such as complete-active-space second-order perturbation theory (CASPT2)[37]] or multireference configuration interaction (MRCI)[36] methods, using the MCSCF wave function as reference, but these methods are limited in their applicability due to a high computational cost that rises steeply as a function of the

increasing size of the system (unfavorable scaling with system size). Modern extensions of these methods allow the use of larger active spaces with the formulation of restricted active space (RAS),[40] generalized active space (GAS), and SplitGAS wave functions[41,318,319] and with the occupation-restricted-multiple-active-space (ORMAS) SCF method.[320] However, the applicability of methods that add approximations to the full dynamic correlation energy based on these kinds of reference functions (by multireference perturbation theory, multireference configuration interaction, or multireference coupled cluster theory) is still limited to small-to middle-size systems. For large systems in which both static and dynamic correlation energy are crucial, a method that allows a description of both types of correlation with affordable computational costs is needed.

Several attempts to combine multi-configurational WFT with DFT-based methods have been proposed, either based on adding some amount of density functional correlation to a multi-configurational wave function calculation[47–90] or adding some amount of wave function correlation to a density functional calculation. The present paper is concerned with the former. The general goal has been to describe static correlation by the multi-configurational WFT approach, while dynamic correlation is included by DFT. However, two main problems arise in such treatments. The first problem is the double counting of dynamic electron correlation, since any attempt to include static correlation energy by WFT inevitably involves including some dynamic correlation energy. One can try to eliminate that portion of the dynamic correlation from the exchange-correlation functional, but it is very hard to do this in a systematic and

accurate way.[60] The second problem consists in the choice of the input quantities to be used in the density functionals, since existing functionals are not compatible with spin densities of multi-configurational wave functions or in general with any spin and space adapted wave function for which the total spin, *S*, is smaller than half of the number of the singly occupied orbitals (including single-configuration, multi-determinantal wave functions). This has been called the "symmetry dilemma" in the context of KS-DFT,[44] and an analogous symmetry dilemma is well known in Hartree-Fock theory.[321] (The situations are different in that despite having the wrong symmetry for the Slater determinant, KS-DFT would yield the exactly correct 1-particle density if one could use the unknown exact density functional, whereas Hartree-Fock theory does not yield the correct 1-particle density when applied to a system with two or more interacting electrons.)

In the present article we propose a way to circumvent both of these difficulties. To eliminate double counting of correlation energy, we calculate only the Coulomb energy and a multi-configurational portion of the kinetic energy from the MCSCF wave function, with the rest of the energy calculated by a density functional. To overcome the symmetry dilemma, following a suggestion of Becke *et al*.[91] and earlier work by Moscardó and San-Fabián,[322] we express the density functional in terms of the total density ρ and on-top pair density Π defined by[323]

$$\Pi(\mathbf{r}) = \binom{N}{2} \int \left|\Psi\left(x_1, x_2, ..., x_N\right)\right|^2 d\sigma_1 d\sigma_2 ... d\sigma_N d\mathbf{r}_3 d\mathbf{r}_4 ... d\mathbf{r}_N \Big|_{\mathbf{r}_1=\mathbf{r}_2=\mathbf{r}} \qquad (1)$$

where σ_i is a spin variable, and $x_i = (\mathbf{r}_i, \sigma_i)$ is a space-spin variable, and not in terms of the total density and the difference between the spin-up and spin-down densities. The density functional of the new theory will be called the on-top density functional to distinguish it from the exchange-correlation functional of KS-DFT; the new theory is called *multi-configuration pair-density functional theory*, MC-PDFT. To illustrate the theory, we employ multi-configurational wave functions of CASSCF-type and first approximations to the required new kind of density functionals.

We note that another very promising approach to the combination of wave function theory with DFT is provided by range separation.[55,65–67,79] Range separation is a powerful method for improving DFT, and it has been applied in a variety of ways.[132,324–330] There is no reason why the present approach could not be combined with range separation in later work, but it is beyond our scope to discuss it further in the present article. We emphasize that the idea of using the total density and on-top density in DFT is not new. Many others have worked on it, and citations are given at appropriate places in the development below. What is new in this work is that unlike previous "additive" efforts where a mixture of the form E(WF) + ΔE(DFT) was used, we propose evaluating only the classical Coulomb energy and an approximation to the kinetic energy from the reference multi-configuration “wave function” and evaluating all the rest of the energy from a density functional, called an on-top density functional, in terms of the total density ρ and on-top pair density Π, and we suggest a simple but general way to develop this kind of density functional from Kohn-Sham exchange-correlation functionals that depend only on up-spin and down-spin densities and their gradients. This eliminates all double

counting of correlation energy, and it provides a framework in which better on-top density functionals can be developed. To our knowledge this has not been tried before. We should also mention at this point some recent work by Garza et al. who propose to describe electronic correlation without double counting via a combination of spin-projected Hartree-Fock and density functional theories,[331,332]

7.3 Theory

7.3.1. MC-PDFT equations

We make the Born-Oppenheimer approximation, and we consider the fixed-nucleus energy *E.* For a multi-configuration electronic wave function and a spin-free, nonrelativistic Hamiltonian, the WFT energy, obtained as the expectation value of the Hamiltonian operator, is given by

$$E = V_{\mathrm{nn}} + \sum_{pq} h_{pq} D_{pq} + \frac{1}{2} \sum_{pqrs} g_{pqrs} d_{pqrs} \tag{2}$$

where V_{nn} is the sum of the nucleus-nucleus repulsions, the indices *p, q, r*, and *s* refer to generic orbitals, h_{pq} and g_{pqrs} are respectively the one-electron and two-electron integrals, and D_{pq} and d_{pqrs} are respectively the one- and two-body electronic density matrices.

In the CASSCF method, a complete CI expansion in space and spin symmetry-adapted CSFs is generated by all possible excitations within an active space. One set of orbitals, called the inactive orbitals, is doubly occupied in all configurations. This allows the simplification of the energy expression to

$$E = V_{\mathrm{nn}} + 2\sum_{i} h_{ii} + \sum_{ij} \left(2g_{iijj} - g_{ijij}\right) + \sum_{vw} h_{vw} D_{vw} + \sum_{ivw} (2g_{iivw} - g_{iviw}) D_{vw} + \frac{1}{2} \sum_{vwxy} g_{vwxy} d_{vwxy} \tag{3}$$

where indices *i* and *j* denote inactive orbitals, and *v, w, x, y* denote active orbitals.

In contrast to the WFT expression, the new MC-PDFT method calculates the energy by

$$E = V_{\mathrm{nn}} + \langle \Psi | T + V_{ne} | \Psi \rangle + V_c[\rho] + E_{ot}[\rho, \Pi] \tag{4}$$

where $|\Psi\rangle$ is the multi-configurational MC wave function, T is the kinetic energy operator, V_{ne} is the electron-nuclear interaction, and $V_{\mathrm{C}}[\rho]$ and $E_{\mathrm{ot}}[\rho,\Pi]$ are the electronic Coulomb energy and the on-top electronic density functional, respectively. This energy may be written in terms of the one-electron density matrix and the on-top density functional as

$$E = V_{\mathrm{nn}} + \sum_{pq} h_{pq} D_{pq} + \frac{1}{2} \sum_{pqrs} g_{pqrs} D_{pq} D_{rs} + E_{ot}[\rho, \Pi] \tag{5}$$

When we recognize that some orbitals are doubly occupied in all CSFs, this becomes

$$E = V_{\mathrm{nn}} + 2\sum_{i} h_{ii} + 2\sum_{ij} g_{iijj} + \sum_{vw} h_{vw} D_{vw} + 2\sum_{ivw} g_{iivw} D_{vw} + \frac{1}{2} \sum_{vwxy} g_{vwxy} D_{vw} D_{xy} + E_{\mathrm{ot}}[\rho,\Pi] \tag{6}$$

With respect to the WFT energy expression, the two-electron contribution has been replaced by a Coulomb term involving a product of one-particle density matrices and an on-top density functional term.

The generalization to include scalar relativistic effects by using the Douglas–Kroll Hamiltonian[123,124] is straightforward; it simply involves changing the definition of the one-electron terms.[333]

7.3.2 Pair-Density functionals

Next we discuss the choice of on-top density functional. If one approximates an exchange-correlation functional using only local densities and their gradients, an exchange-correlation functional for a spin-polarized system can be written as a functional

of the total density ρ, the spin magnetization density *m* (which may also be called the net spin density), and the magnitudes, $\rho' \equiv |\nabla\rho|$ and $m' \equiv |\nabla m|$, of their gradients, where

$$\rho(\mathbf{r}) = \rho_\alpha(\mathbf{r}) + \rho_\beta(\mathbf{r}) \tag{7}$$

and

$$m(\mathbf{r}) = \rho_\alpha(\mathbf{r}) - \rho_\beta(\mathbf{r}) \tag{8}$$

and where ρ_α is the density of majority-spin electrons, and ρ_β is the density of minority-spin electrons at a point **r**. As previously described,[44,91] the exchange-correlation functionals defined in terms of the net spin density give reasonable energies with broken-symmetry Slater determinants in spin-polarized Kohn–Sham theory, but the net spin densities are not appropriate variables for density functionals if the correct spin symmetry is imposed.

Moscardo and San-Fabián[322] discussed using the on-top density of a multi-configuration wave function to motivate functional forms for including electron correlation in density functionals of the spin densities. Becke *et al*.[91] discussed changing the independent variables of density functional approximations from ρ and *m* to ρ and Π. For a single-determinant wave function, *m* can be related to Π and ρ by the relation[91]

$$m(\mathbf{r}) = \rho(\mathbf{r})\left[1 - R(\mathbf{r})\right]^{1/2} \tag{9}$$

where

$$R(\mathbf{r}) = \frac{4\Pi(\mathbf{r})}{\left[\rho(\mathbf{r})\right]^2} \tag{10}$$

with $R \leq 1$ at all points in space. However, for multi-configuration wave functions, eq 9 is not true, and R can be larger than unity. Later Perdew *et al*.[44,334] discussed the use of the ρ and Π variables for interpreting the symmetry dilemma, and Miehlich *et al*.,[48] McDouall,[57] and Gusarov et al.[58] proposed using functionals of the density and the pair density to recover the difference between the full correlation energy and the MCSCF correlation energy. Tsuchimmochi et al.[335] proposed using a density functional defined in terms of ρ and Π in conjunction with another WFT method, namely constrained-pairing mean-field theory. Here we use ρ and Π to define the on-top density functional for MC-PDFT.

Ultimately we must develop new on-top density functionals specifically for use with MC-PDFT. As a first step, we simply "translate" previously developed exchange-correlation functionals of spin densities. In particular, given $E_{xc}(\rho, m, \rho', m')$, we write the following translation prescription:

$$E_{ot}\left[\rho(\mathbf{r}),\Pi(\mathbf{r})\right] = E_{xc}\left(\rho(\mathbf{r}),\left\{\begin{array}{c}\rho(\mathbf{r})(1-R)^{1/2} \text{ if } R\leq 1\\ 0 \text{ if } R>1\end{array}\right\},\rho'(\mathbf{r}),\left\{\begin{array}{c}\rho'(\mathbf{r})(1-R)^{1/2} \text{ if } R\leq 1\\ 0 \text{ if } R>1\end{array}\right\}\right) \quad (11)$$

where we simplified the equation by just writing R for the functional, $R[\rho(\mathbf{r}),\Pi(\mathbf{r})]$, defined in eq. 10. To summarize, equation 11 is our postulated on-top density functional as obtained by a "translation" protocol from a GGA; it is not derived from eqs 9 and 10; rather its form is motivated in part by their form.

7.4 Test Cases

MC-PDFT was tested for a variety of cases, including some for which KS-DFT fails or performs poorly. There are four kinds of tests: (1) multiplet splittings for selected

main group atoms (Be, C, N, N^+, O, O^+) and transition metals (Co, Mn, Mo, Ru and Sc^+); (2) atomic singlet-singlet excitation energy of Be and vertical singlet-singlet excitation energies for N_2, formaldehyde, butadiene, cyclopentadiene, and pyrazine; and (3, 4) equilibrium dissociation energies (D_e) and potential energy curves of the H_2, N_2, F_2, CaO, Cr_2, and NiCl diatomic molecules.

We do not include spin-orbit coupling in any of the calculations. For atomic excitation energies, we removed spin-orbit coupling from the experimental values in the usual way (weighted average of the multiplet). However, for the molecules we ignore this step since the necessary data is not available for all cases, but this correction should be small for the molecules because they contain no atom heavier than Ni.

Calculations on singlet-singlet excitation energies were performed at fixed geometries obtained with the M06-L[173] exchange-correlation functional and the 6-311+G(d,p)[292,294,336] basis set, except for cyclopentadiene for which we used the 6-31+G(2d,p)[293–295] basis set.

Calculations of bond energies were performed at consistently optimized geometries. For CaO and NiCl, as for the other molecules, the bond energy is defined as the energy of the neutral atoms in their ground states minus the energy of the molecule at its ground-state optimized geometry; but note that the separated-atom ground state of CaO is a triplet (Ca ^{1}S plus O ^{3}P), and therefore Table 7.4 is based on this triplet, whereas Fig. 7.5 shows the singlet potential curve (CaO $^1\Sigma^+$). Similarly the separated-atom limit for NiCl is triplet Ni (^{3}F) + doublet Cl (^{2}P), whereas Fig. 7.6 shows the doublet potential curve (NiCl $^2\Pi$).

7.5 Computational Details

In addition to MC-PDFT results, we report results by CASSCF, CASPT2, and KS-DFT for comparison. The MC-PDFT method was implemented in a locally modified version of the *Molcas* program package.[120] All MC-PDFT, CASSCF, and CASPT2 calculations were performed using *Molcas*. All KS-DFT calculations were performed with the *Gaussian 09* program.[129]

7.5.1 Basis sets. We employed basis sets of multiply polarized triple-zeta and quadruple-zeta quality. In the article itself, we report the triple zeta results, while the quadruple zeta ones are reported in Supporting Information (SI). For the various calculations (CASSCF, CASPT2, MC-PDFT, and KS-DFT) on the same system, we use the same basis set for all the calculations.

For the calculations presented in the article itself, we use the following basis sets. For the multiplicity-changing excitation energies of the main-group atoms and diatomic molecules, CaO, and the singlet-to-singlet excitation energies except for N_2 and butadiene, we used the cc-pVTZ[337] basis set. For excitation energies of N_2 and butadiene we used aug-cc-pVTZ.[338] The Cr_2 calculations employ the cc-pVTZ-DK[339] basis set. For the NiCl and transition metal atom calculations we used the ANO-RCC-VTZP[121,122] basis set. For Cr_2, NiCl, and the transition metal atoms, the second-order Douglas-Kroll-Hess Hamiltonian was used;[123,124] the other calculations are nonrelativistic.

7.5.2 CASSCF. For each system the minimal-size active space that gives qualitatively correct results was employed. The active spaces are specified in footnotes to tables; the same active spaces were used for the figures.

7.5.3 CASPT2. For CASPT2, an imaginary shift is introduced to remove problems with intruder states (states giving small denominators in second-order perturbation, and hence having a spuriously large effect on the energy, even when they are weakly coupled to the ground state), and an ionization-potential-electron-affinity (IPEA) shift is introduced as an empirical adjustment to the energies of the active orbitals to improve agreement with experiment. We employ the standard imaginary shift[126] of 5.44 eV and the *Molcas* default IPEA shift[340] of 6.80 eV. (For Cr_2, one can obtain better CASPT2 results with a molecule-specific IPEA[341] of 12.25 eV, but we do not consider such molecule-specific empirical adjustments in this article.)

7.5.4 KS-DFT. We use collinear spin-orbitals, and we consider three exchange-correlation functionals: one of which is a local-spin-density approximation (LSDA), and the other two of which are generalized gradient approximations (GGAs). The LSDA depends only on ρ and m, not on ρ'; it employs the exchange potential of Gáspár[342] (equal to 2/3 the one used by Slater[343] and the same as used later by Kohn and Sham,[42]) and correlation potential no. 3 of Vosko *et al.*[344] This is labeled GVWN3. The GGAs depend on ρ, m, ρ', and m'; the ones we employ are the popular BLYP[344,345] and PBE[199] functionals.

In KS-DFT, with approximate exchange-correlation functionals, the calculated energy is not independent of the M_S value of the Slater determinant (even though it should be). Therefore one does the calculation with M_S equal to S, where S is the total electronic spin quantum number of the target state. We carried out KS-DFT calculations in two ways,[314] which we call variational (Var.) and weighted-average broken symmetry

(WABS). Both kinds of calculations are based on the stable, broken-symmetry solutions of the Kohn-Sham equations in which the only symmetry enforced is the total electron spin component M_S. Thus when SCF convergence is attained, we do a stability check.[346,347] If the solution is unstable, we break the symmetry and continue optimizing the orbitals until a stable solution is attained. In the Var. method, we take this as the energy of the state; this would be the correct procedure if one had the (unknown and probably unknowable) exact Kohn–Sham functional. In the WABS method,[35,45,312,313,315–317] if M_S equals one half the number of singly occupied orbitals (such a state is called a maximal-M_S state), the result is the same as in the Var. method. However, if M_S is smaller, we also perform a calculation on the state with maximal M_S and use the weighted average formula of Yamaguchi and coworkers[312,313] to calculate the energy of the pure spin state.

The singlet-to-singlet excitation energies considered here all correspond to an excitation that changes the spatial symmetry. We enforce the spatial symmetry in these cases so that we can calculate the KS-DFT excitation energies by the difference of two SCF calculations, without needing to use time-dependent response methods.

7.5.5 MC-PDFT. The CASSCF wave functions generated by the *Molcas* program are computed for a specified total spin, but there is no reference to specific spin projections and hence no ambiguity about which M_S value to use and no spurious dependence on M_S.[333] To illustrate MC-PDFT, we implement it in this article as follows:

(a) Calculate a CASSCF wave function self-consistently;

(b) calculate ρ, Π, and ρ' from the CASSCF wave function;

(c) calculate the on-top density functional by eq 11;

(d) calculate the energy (post-SCF) by eq 6, which involves an integration over all values of **r** of the translated density functionals obtained by eq 11.

The translated on-top density functionals are called tVWN3, tBLYP, and tPBE ("t" for translated).

7.6 Results

Tables 7.1 and 7.2 give multiplicity-changing excitation energies of atoms. Table 7.3 gives singlet-to-singlet excitation energies, and Table 7.4 gives equilibrium bond dissociation energies. All mean errors in tables are computed from unrounded data, not from the rounded data in the tables. Figures 7.1–7.6 show potential energy curves for diatomic molecules that compare the CASSCF, CASPT2, tPBE, PBE variational, and PBE WABS results. To increase clarity we left the tBLYP, tGVWN3, BLYP variational, BLYP WABS, GVWN3 variational, and GVWNM3 WABS results off these figures, but additional figures containing these results are in supporting information. Figures 7.7 and 7.8 show the value of the pair density, total density, and ratio R along the bond axis of H_2 and N_2.

7.7 Discussion

For main-group atomic multiplicity-changing excitation energies, given in Table 7.1, CASSCF has a mean absolute error (MAE) of 0.3 eV. Variational and WABS KS-DFT calculations with GGAs have much larger errors, with MAEs in the range 0.7–1.2 eV respectively; variational GVWN3 calculations also have a large error, 0.9 eV, but WABS GVWN3 does quite well, with an MAE of only 0.12 eV. The MC-PDFT

calculations with tBLYP, tPBE and tGVWN3 all have an MAE of 0.5 eV, much better than the average (0.8 eV) of the six KS-DFT results. The supporting information shows that the transformed functional performance is approximately independent of basis set size and almost independent of active space size, although the MAE can be reduced to 0.3 eV with other active space choices, but in the rest of the main article we concentrate on what is achieved with the smallest reasonable complete active space choices and triple zeta basis sets, rather than search for the lowest possible errors. We conclude that on average the translated functionals perform better (0.5 eV) than their KS-DFT counterparts (0.8 eV). The MC-PDFT calculations perform slightly worse than CASSCF and CASPT2.

Table 7.1. Main group atomic excitation energies (eV).

Transition	AS[a]	CASSCF	CASPT2	tBLYP	tPBE	tGVWN3	BLYP		PBE		GVWN3		Exp.
							Var.	WABS	Var.	WABS	Var.	WABS	
Be $^1S \rightarrow {}^3P$	2,4	2.9	2.8	2.6	2.6	2.6	2.5	2.5	2.3	2.3	2.4	2.4	2.73[b]
C $^3P \rightarrow {}^1D$	4,4	1.6	1.3	1.0	1.1	1.0	0.3	0.7	0.4	0.8	0.6	1.3	1.26[c]
N^+ $^3P \rightarrow {}^1D$	4,4	2.2	1.9	1.5	1.5	1.4	0.6	1.1	0.6	1.2	0.9	1.9	1.89[c]
N $^4S \rightarrow {}^2D$	5,4	2.8	2.5	2.0	2.1	1.9	0.9	1.4	1.1	1.6	1.5	2.3	2.38[c]
O^+ $^4S \rightarrow {}^2D$	5,4	3.7	3.4	2.7	2.8	2.6	1.4	2.1	1.5	2.3	2.1	3.2	3.32[d]
O $^3P \rightarrow {}^1D$	6,4	2.2	2.0	1.3	1.3	1.2	0.7	1.3	0.7	1.4	0.9	1.8	1.96[c]
MAE[e]	*n*,4	0.3	0.07	0.4	0.4	0.5	1.2	0.8	1.2	0.7	0.9	0.12	

[a] The active space (AS) choices are given for each atom with the notation *n/m*, where *n* is the number of active electrons, and *m* is the number of active orbitals. In this table the active spaces include the valence 2*s* and 2*p* orbitals.

[b] Kramida, A.; Martin, W. C. *J. Phys. Chem. Ref. Data*, **1997**, *26*, 1185–1194.

[c] Moore, C. E. *CRC Series in Evaluated Data in Atomic Physics*; Gallager, J. W., Ed.; CRC Press: Boca Raton, FL, 1993.

[d] Martin, W. C.; Kaufman, V.; Musgrove, A. *J. Phys. Chem. Ref. Data* **1993,** *22*, 1179–1212.

[e] MAE denotes mean absolute error, i.e., mean unsigned deviation from the experimental value.

Table 7.2 shows that for transition metal atoms, the excitation energies obtained by the MC-PDFT calculations with the translated functionals are better (MAE: 0.2 eV) than CASSCF (0.4 eV) or CASPT2 (0.3 eV) and comparable to KS-DFT (mean MAE of 0.2 eV when averaged over either the three variational sets of the three WABS sets of results). Averaging over the main group and transition metal results one finds that MC-PDFT is already (that is, even with these first attempts at on-top functionals) better on average than CASSCF or KS-DFT, but not systematically better than the much more expensive and less favorably scaling CASPT2.

Table 7.2. Transition metal atomic excitation energies (eV).

Transition	AS[a]	CASSCF	CASPT2	tBLYP	tPBE	tGVWN3	BLYP		PBE		GVWN3		Exp.
							Var.	WABS	Var.	WABS	Var.	WABS	
Sc^+ $^3D \rightarrow {}^1D$	2,6	0.4	0.3	0.5	0.5	0.4	0.2	0.3	0.2	0.5	0.2	0.5	0.30[b]
Mn $^6S \rightarrow {}^8P$	7,9	2.2	2.3	2.4	2.2	2.4	2.9	2.9	2.3	2.3	2.6	2.6	2.15[b]
Co $^4F \rightarrow {}^2F$	9,6	2.3	0.4	1.1	0.9	0.8	0.7	1.0	0.7	1.0	0.3	0.5	0.89[b]
Mo $^7S \rightarrow {}^5S$	6,6	1.7	1.7	1.8	2.0	1.9	0.9	1.1	1.3	1.6	1.4	1.6	1.34[c]
Ru $^5F \rightarrow {}^3F$	8,6	1.0	1.0	0.9	1.1	0.9	0.6	0.8	0.7	0.9	0.7	0.9	0.78[d]
MAE[e]		0.4	0.3	0.2	0.2	0.2	0.3	0.2	0.11	0.2	0.2	0.3	

[a] The active space choices are given for each atom with the notation *n/m*, where *n* is the number of active electrons, and *m* is the number of active orbitals. For Sc^+ and Co, the active space consists of the 3*d* and 4*s* orbitals. For Mn, the active space includes the 3*d*, 4*s,* and 4*p* orbitals. For Mo and Ru, the active space includes the 4*d* and 5*s* orbitals.

[b] Sugar, J.; Corliss, C. Atomic Energy Levels of the Iron-Period Elements: Potassium through Nickel, *J. Phys. Chem. Ref. Data*, **1985**, *14, Suppl. 2*, 1-664.

[c] Sugar, J.; Musgrove, A. *J. Phys. Chem. Ref. Data*, **1988**, *17*, 155–239.

[d] Moore, C. E. *Ref. Data Ser. 35, Vol. III (Reprint of NBS Circ. 467, Vol. III, 195*8), Nat. Bur. Stand.: 1971; p 245.

[e] MAE denotes mean absolute error, i.e., mean unsigned deviation from the experimental value.

Inspection of Table 7.3 shows that MC-PDFT calculations with the translated functionals succeed in performing much better (average MAE of 0.5 eV) than CASSCF

(MAE: 1.4 eV) in predicting vertical excitation energies. MC-PDFT performs better than KS-DFT for butadiene, pyrazine, and formaldehyde, but not for the other four cases. MC-PDFT is more accurate than CASPT2 for butadiene and has the same accuracy for formaldehyde, but is less accurate than the more expensive method on average. The relatively good results for butadiene are interesting since this molecule is a case in which both the ground and excited states have substantial double excitation character.[348]

Table 7.3. Singlet-to-singlet atomic and vertical electronic excitation energies (eV).

System	AS[a]	CASSCF	CASPT2	tBLYP	tPBE	tGVWN3	BLYP	PBE	GVWN3	Exp.
Be $^1S \rightarrow {}^1P$ ($s \rightarrow p$)	2,4	6.2	5.7	4.2	4.4	4.3	5.0	5.0	5.0	5.28[b]
N_2 $^1\Sigma_g^+ \rightarrow {}^1\Pi_g$ ($\sigma_g \rightarrow \pi_g$)	6,6	11.9	9.4	8.6	8.6	8.6	9.1	9.1	9.1	9.31[c]
N_2 $^1\Sigma_g^+ \rightarrow {}^1\Sigma_u^-$ ($\pi_u \rightarrow \pi_g$)	6,6	10.9	9.8	9.5	9.6	9.6	9.6	9.7	9.7	9.92[c]
s-trans-1,3-butadiene ^1A_g to ^1B_u ($\pi \rightarrow \pi^*$)	4,4	7.6	6.8	5.6	5.7	5.9	5.3	5.5	5.5	5.92[d]
pyrazine ^1A_g to $^1B_{3u}$ ($n \rightarrow \pi^*$)	10,10	5.3	4.1	3.9	3.9	3.8	3.6	3.6	3.5	4.20[e]
cyclopentadiene $^1A_1$ to $^1B_2$ ($\pi \rightarrow \pi^*$)	4,4	7.3	5.5	4.1	4.1	4.1	4.9	5.0	5.0	5.26[f,g]
formaldehyde $^1A_1$ to $^1A_2$ ($I \rightarrow \pi^*$)	8,6	4.4	4.0	4.0	4.0	4.0	4.0	3.9	3.8	4.00[h]
MAE[i]		1.4	0.3	0.6	0.5	0.5	0.3	0.3	0.3	

[a] For Be and N_2, the active space (AS) in each case is the full valence active space. For *s-trans*-1,3-butadiene, cyclopentadiene, and pyrazine the AS includes the π electrons, π bonding and antibonding orbitals, and additional nitrogen lone pairs/orbitals for pyrazine. For formaldehyde, the AS includes all the electrons, lone pair orbitals, and bonding and antibonding orbitals of the carbonyl.

[b] Kramida, A.; Martin, W. C. *J. Phys. Chem. Ref. Data*, **1997**, *26*, 1185–1194.

[c] Nielsen, E.S.; Jorgensen, P.; Oddershede, J. *J. Chem. Phys.* **1980,** 73, 6238.

[d] Doering, J. P.; McDiarmid, R. *J. Chem. Phys.* **1980**, *73*, 3617.

[e] Bolovinos, A.; Tsekeris, P.; Anditopoulos, G. *J. Mol. Spectrosc.* **1984**, *103*, 240.

[f] Frueholz, R. D.; Flicker, W. M.; Mosher, O. A.; Kuppermann, A. *J. Chem. Phys*. **1979**, *70*, 2003.

[g] McDiarmid, R.; Sabljić, A.; Doering, J. P. *J. Chem. Phys.* **1985**, *83*, 2147.

[h] Wiberg, K. B.; de Oliveira, A. E.; Trucks, G. *J. Phys. Chem.* **2002**, *106*, 4192-4199. For N_2, an equilibrium geometry of 1.098 Å was used. All other geometries were optimized according to specifications in Table S5 with M06-L.

[i] MAE denotes mean absolute error, i.e., mean unsigned deviation from the experimental value.

Figures 7.1–7.6 show that MC-PDFT fulfills one of its major goals, namely the calculation of reasonable potential energy curves for bond breaking. The results for Cr_2 in Fig. 7.5 are particularly striking because the CASSCF curve does not even have a minimum, and the CASPT2 curve has a minimum energy at a qualitatively wrong geometry. The tPBE curve has a minimum at a reasonable geometry. By changing the IPEA shift in CASPT2 the curve has much better agreement with the experimental result,[341] but here we prefer to compare with only the standard CASPT2 method.

For bond energies of the diatomic molecules considered in Table 7.4, the translated GGAs, with MAEs of 0.3 and 0.4 eV, perform better than KS-DFT for the BLYP and PBE functionals (MAE: 0.5–0.6 eV), and the translated GVWN3 performs better (MAE: 0.9 eV) than GVWN3 (MAE: 1.4-1.5 eV). MC-PDFT also improves upon CASSCF (MAE: 0.8 eV). The results for bond energies are especially encouraging because of the diversity of cases involved: a closed-shell single bond with no static correlation error (H_2), a closed-shell single bond with large static correlation error if treated by Hartree-Fock (F_2), a triple bond (N_2), singlet and doublet polar molecules involving metal atoms (CaO and NiCl), and the notoriously difficult Cr_2 molecule.

One of the main reasons we developed MC-PDFT is to avoid the ambiguity and resulting inaccuracy of using broken-symmetry solutions for inherently multi-configurations systems. Molecules with partly broken bonds (that is, highly stretched bonds) are the most commonly encountered class of such multireference systems. In order to study how well the present method does for such cases, the figures show magnified views of the intermediate-bond-distance regions of the potential as part b of

five of the six figures. The results are generally encouraging. See especially Figs. 7.2b-7.4b, and 7.6b where the MC-PDFT results with tPBE functionals follow the CASPT2 curves better than either the Var. KS-DFT or the WABS KS-DFT results.

Table 7.4. Dissociation energies (eV) of diatomic molecules

Transition	AS[a]	CASSCF	CASPT2	tBLYP	tPBE	tGVWN3	BLYP		PBE		GVWN3		Exp.
							Var.	WABS	Var.	WABS	Var.	WABS	
H_2	2,2	4.1	4.6	4.9	4.7	5.0	4.8	4.8[b]	4.5	4.5[b]	4.9	4.9[b]	4.75[c]
N_2	6,6	8.8	9.4	9.4	9.8	11.1	10.4	10.4[b]	10.6	10.6[b]	11.9	11.9[b]	9.74[d]
F_2	2,2	0.9	1.5	1.9	2.1	2.8	2.2	2.2[b]	2.4	2.4[b]	3.5	3.5[b]	1.66[e]
Cr_2	12,12	0[f]	1.0	0.5	0.6	2.3	2.1	2.5	1.6	2.1	3.5	3.7	1.47[g]
CaO	8,8	3.9	3.5	4.0	4.2	5.2	4.7	4.7[h]	5.0	5.0[h]	6.1	6.1[h]	4.22[i]
NiCl	11,12	2.7	3.9	3.7	4.1	4.9	3.4	3.7	3.7	3.7	4.5	4.6	3.97[j,k]
MAE[l]		0.8	0.3	0.4	0.3	0.9	0.5	0.5	0.5	0.6	1.4	1.5	

[a] The active space (AS) choice for H_2 and N_2 includes the bonding electrons and bonding/antibonding orbitals. For F_2, the active space includes one 2*p* electron and orbital on each atom contributing to the ^{2}P configuration of the neutral atom. For Cr_2, the active space includes the *d* and 4*s* electrons and orbitals on each atom. The AS for CaO includes the 4*s* electrons on Ca and the 2*s* and 2*p* electrons on O. In addition to these orbitals, there is a correlating 4*p* shell on Ca. For NiCl, the active space includes the 4*s* and 3*d* electrons on Ni and one 2*p* electron and orbital on Cl that contributes to the ^{2}P configuration of the neutral atom.

[b] WABS dissociation energy is the same as variational one because this case has no spin contamination at the equilibrium geometry.

[c] Huber, K. P.; Herzberg, G. *Molecular Spectra and Molecular Structure: Constants of Diatomic Molecules*; Van Nostrand Reinhold: New York, 1979.

[d] Lofthus, A.; Krupenie, P. H. *J. Phys. Chem. Ref. Data* **1977**, 6, 113.

[e] L. Bytautas and K. Ruedenberg, *J. Chem. Phys.* **2005,** *122*, 154110.

[f] The potential curve has no minimum in this case; see Fig. 7.5.

[g] Casey, S. M.; Leopold, D. G. *J. Phys. Chem*. **1993**, *97*, 816.

[h] The WABS dissociation energy is the same as the variational dissociation energy in this case because there is negligible spin contamination in the ground-state triplet asymptote that is used to compute the dissociation energy from the singlet equilibrium ground state, whereas the Var. and WABS curves in Fig. 7.4 differ because they are relative to the singlet asymptote.

[i] Vasiliu, M.; Feller, D.; Gole, J. L.; Dixon, D. A. *J. Phys. Chem. A* **2010**, *114*, 9349–9358.

[j] Jiang, W.; DeYonker, N. J.; Determan, J. J.; Wilson, A. K. *J. Phys. Chem. A* **2011**, *116*, 870−885.

[k] Zhang, W.; Truhlar, D. G.; Tang, M. *J. Chem. Theory Comput.* **2013**, *9*, 3965-3977.

[l] MAE denotes mean absolute error, i.e., mean unsigned deviation from the experimental value.

The good results obtained for N_2 and Cr_2 dissociation are especially noteworthy because these are both difficult cases. They both involve dissociation to highly open-shell atoms with three or more unpaired electrons. While KS-DFT can properly describe N_2 at equilibrium because it is a closed-shell singlet, KS-DFT can only obtain reasonable results for Cr_2 at equilibrium by treating it as two antiferromagnetically coupled high-spin atoms in a broken-symmetry solution. The ability of the new theory to treat these most difficult cases shows that the on-top pair density is successful not just for breaking a single bond in systems like H_2 and F_2, but also in providing a qualitatively correct description for more complicated bond-breaking processes requiring the spin recoupling of more than one electron pair.

For both H_2 and N_2, the success of the on-top pair density in describing molecular dissociations is shown in Fig. 7.7 and Fig. 7.8. In the limit of a closed shell singlet at equilibrium, $R(z) = 1$. Figures 7.7 and 7.8 show the densities, on-top pair densities, and the ratio R of eq. 11 as functions of location z along the internuclear axis for dissociating H_2 and N_2. In the limit of infinite separation for H_2 in Fig. 7.7b, $R(z) = 0$ because the value of the on-top pair density is zero (corresponding to one electron on each center). In Fig 7.8b we show how the on-top pair density behaves for an intermediate distance along the potential energy curve.

Just as CASPT2 and other WFT methods for including dynamical correlation energy are employed as post-SCF steps, the present version of MC-PDFT is employed as a post-SCF procedure. If the density functional were to depend only on the one-particle density matrix, the equations for the self-consistent CASSCF wave function (in which the

wave function is optimized to minimize the MC-PDFT energy rather than the expectation value of the Hamiltonian) would be an indeterminate system of equations because a one-electron operator does not couple configurations differing by two orbitals, and there would be no unique solution. However, our on-top density functional also depends on part of the two-particle density matrix; nevertheless we include the energy contribution of the on-top density functional as a post-SCF step.

Another topic for future work would be to develop foundational theorems, if possible, about the existence and uniqueness of an exact on-top density functional for use with MC-PDFT. We note, however, that the immediate goal of the present new kind of density functional theory is not to extend Kohn-Sham theory to classes of systems where the density does not belong to the representability class for which Kohn-Sham theory is applicable and exact,[349–353] but rather to develop a practical framework for obtaining less ambiguous and/or more accurate densities and energies for systems where Kohn-Sham theory with approximate exchange-correlation functionals does not do well.

7.8 Concluding Remarks

We have presented a theory called *multi-configuration pair-density functional theory*, MC-PDFT. The kinetic and Coulomb contributions to the total electronic energy are computed from an optimized MCSCF wave function, and the exchange and correlation contributions are computed from a functional of the total density and the on-top pair density; this functional is called the on-top density functional. Just as for exchange-correlation functionals in Kohn-Sham density functional theory, the on-top density functional can also be a function of functionals of the density. For example, it

could depend on the density gradient or the orbital-dependent kinetic energy density. For a first set of approximate on-top density functionals, we use functionals of the density, the density gradient, and the on-top density that we obtain by translating Kohn-Sham exchange-correlation functionals according to a simple prescription. Also, we would like to eventually include dependence on the pair-density gradient and the kinetic energy density.

The presented theory has been used in combination with the tBLYP, tPBE, and tGVWN3 on-top density functionals generated from the BLYP, PBE, and GVWN3 exchange-correlation functionals. Results with the translated functionals have been generated for a variety of systems and compared with the corresponding results at the CASSCF, CASPT2, and Kohn-Sham DFT levels. This method is promising. To provide a better overview of the results, Table 7.5 provides survey of the average mean absolute errors in Tables 7.1-7.4.

Table 7.5. Averaged mean absolute errors (eV).

Quantity	CASSCF	CASPT2	tGGA[a]	GGA[b]
main group atomic excitation energies	0.29	0.07	0.40	1.01
transition metal atomic excitation energies	0.41	0.26	0.24	0.21
singlet-to-singlet molecular excitation energies	1.39	0.26	0.55	0.33
bond dissociation energies	0.89	0.32	0.32	0.51
average	0.75	0.23	0.38	0.52

[a] averaged over tBLYP and tPBE

[b] averaged over BLYP var., BLYP WABS, PBE var., and PBE WABS

We see that the first results with the new theory, using simply translated GGA functionals, reduce the error in CASSCF by an average of almost a factor of 2 and are about 20% more accurate than Kohn-Sham theory based on the same GGAs. This theory

even produces results of similar quality to the much more expensive CASPT2 method for two of the four databases. The basis set dependence is smaller than for CASPT2, and the troublesome problem of intruder states does not arise. In the future we plan to develop new functionals of the total density and on-top pair density, which will be optimized for use with multi-configurational wave functions. We will also employ RASSCF, GASSCF, and SplitGAS wave functions to be able to deal with larger active spaces and CI problems than those that are currently affordable with CASSCF.

The advantages of the new theory may be summarized as follows:

i) It can correctly describe inherently multi-configurational systems, including described by the chosen MCSCF wave function.

ii) Because all states have the correct spin and spatial symmetry, there are no ambiguities about which state is being approximated.

iii) There is no spurious dependence on the spin projection quantum number.

iv) Its computational cost scales with system size in the same way as CASSCF (the cost depends on the choice of active space) but produces results closer to and sometimes better than CASPT2 quality.

v) Unlike prior attempts to combine CASSCF and DFT, which combine a portion of the energy calculated by wave function methods with another portion calculated from a density functional, the present method avoids any possibility of double counting the electron correlation energy.

vi) The new method has a moderate dependence on the active space choice, or at least a smaller dependence than CASPT2. This is a promising feature, since ideally one

would like to work with a small active space.

Author Contributions

Giovanni Li Manni contributed to the method development and CASSCF, CASPT2, and MC-PDFT calculations, Rebecca K. Carlson contributed to the method development and CASSCF, CASPT2, and MC-PDFT calculations, Sijie Luo contributed to the KS-DFT calculations, Dongxia Ma contributed to the method development. These four authors (GLM, RKC, SL, DM) contributed equally.

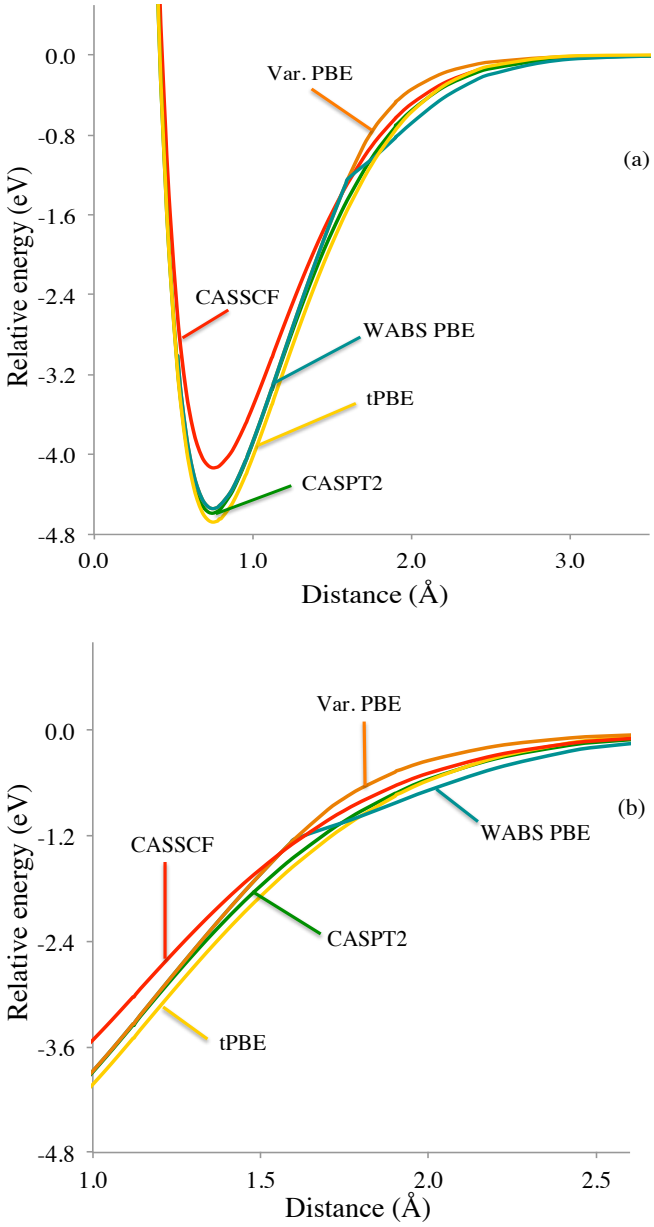

Figure 7.1. Potential energy curves for H_2. (a) Part a shows the whole range of distances. At equilibrium, the Var. and WABS curves for each functional are the same, but they are different at intermediate distances. The CASPT2 minimum is just below the WABS PBE minimum. (b) Part b is a blowup of the region from 1 to 3 Å. The WABS curves are lower in energy than the Var. counterparts at intermediate distances.

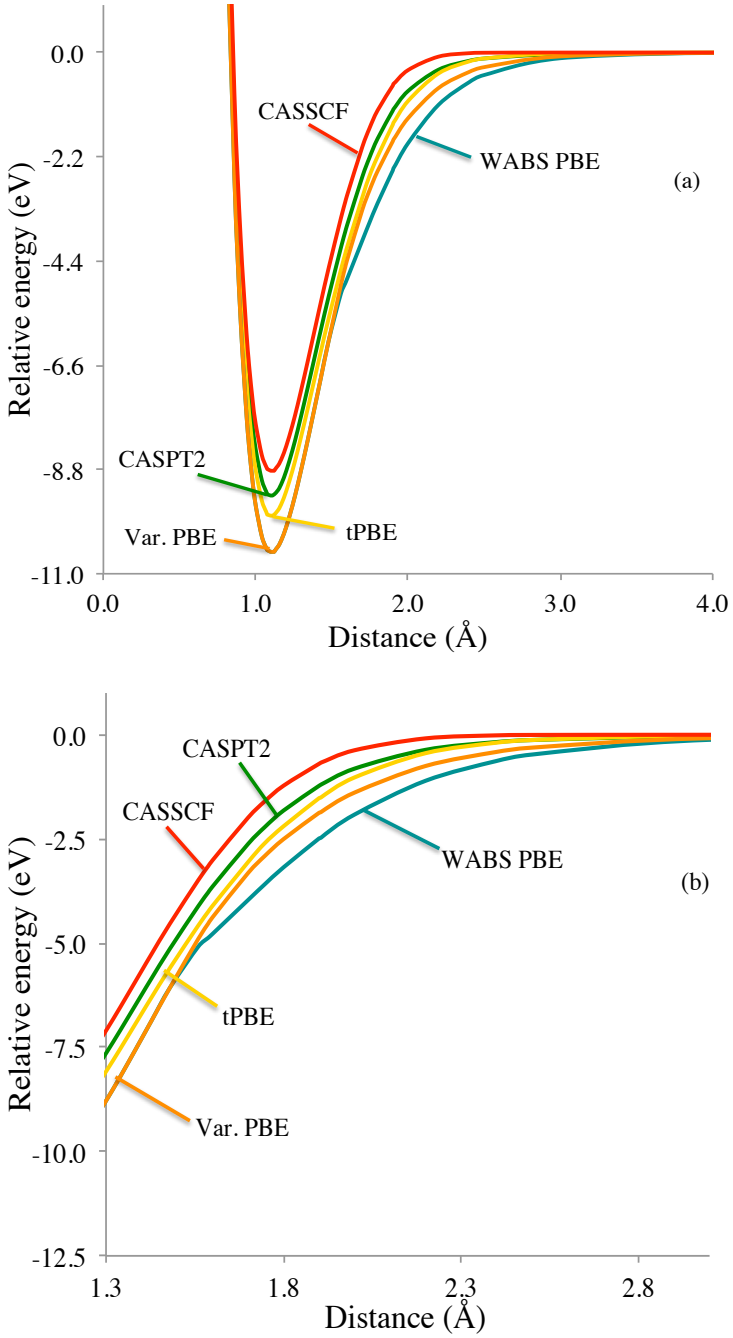

Figure 7.2. Potential energy curves for N_2. (a) Part a shows the whole range of distances. At equilibrium, the Var. and WABS curves for each functional are the same, but they are different at intermediate distances. (b) Part b is a blowup of the region from 1.3 to 2.8 Å.

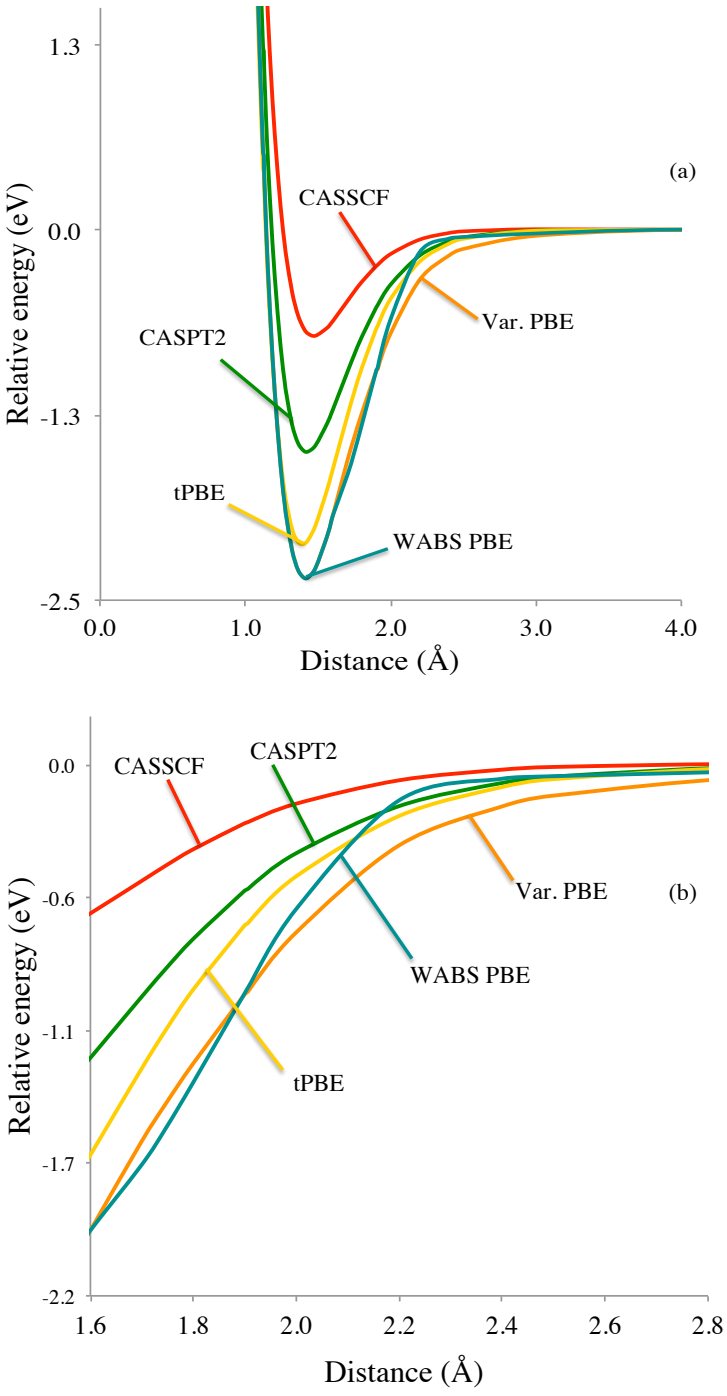

Figure 7.3. Potential energy curves for F_2. a) Part a shows the whole range of distances. At equilibrium, the Var. and WABS curves for each functional are the same, but they are different at intermediate distances. b) Part b is a blowup of the region from 1.6 to 2.8 Å.

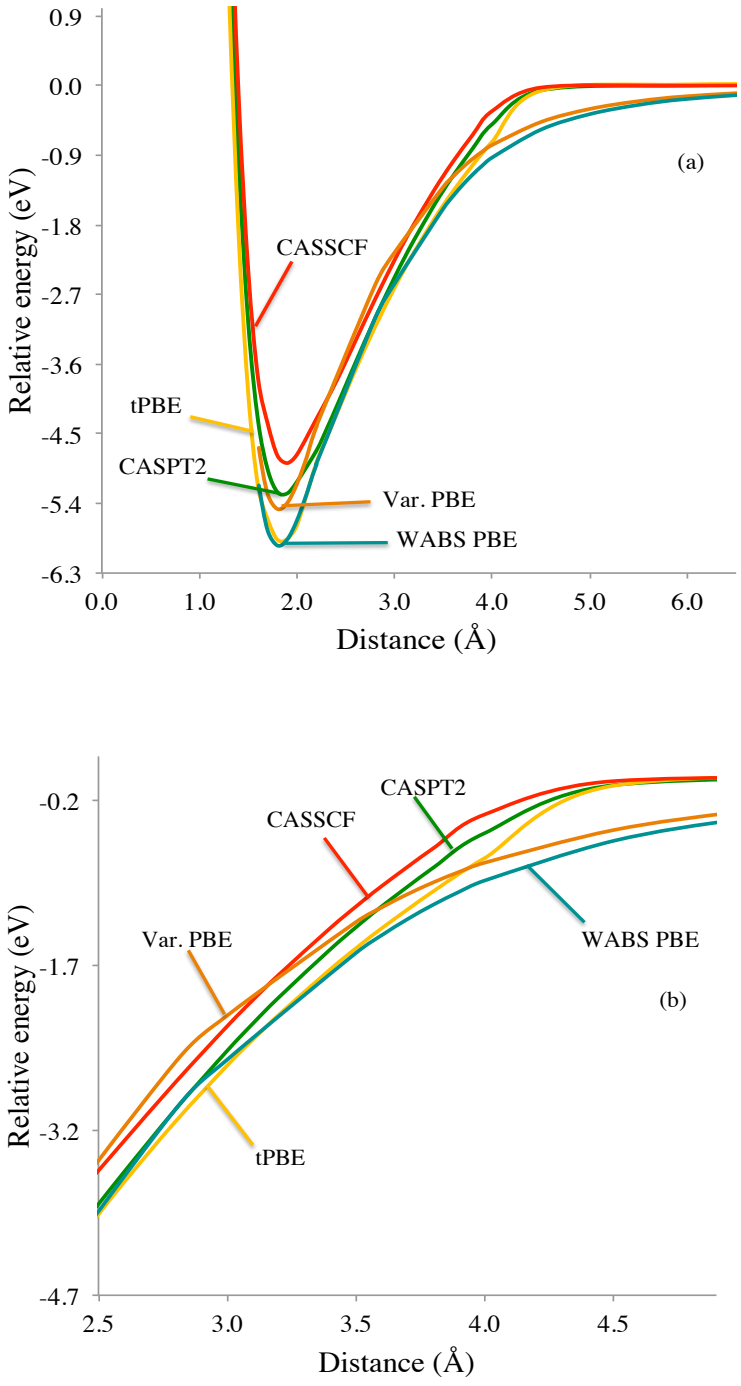

Figure 7.4. Potential energy curves for the $^1\Sigma^+$ state of CaO. a) Part a shows the whole range of distances. The CASPT2 and tPBE curves are very close at equilibrium and so are hard to distinguish in the figure. b) Part b is a blowup of the region from 2.5 to 5.5Å.

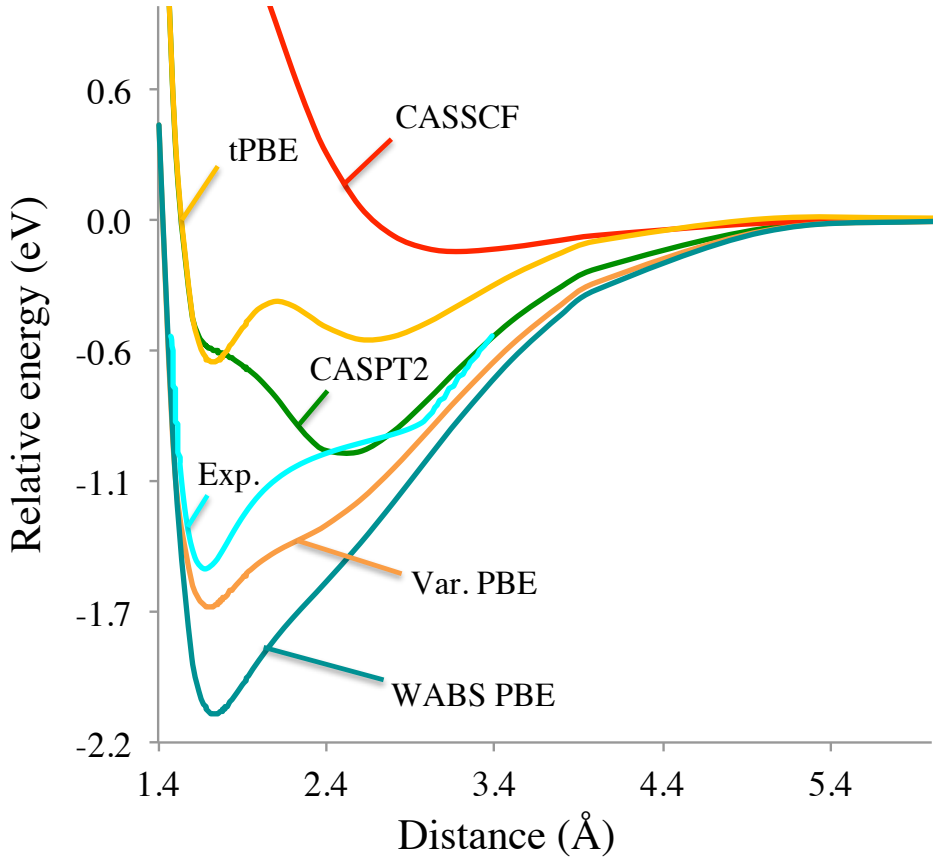

Figure 7.5. Potential energy curves for Cr_2. The experimental curve (Casey and Leopold, Ref. 219) is shown for experimentally measurable distances and is shifted to a common asymptote by the experimentally determined dissociation energy.

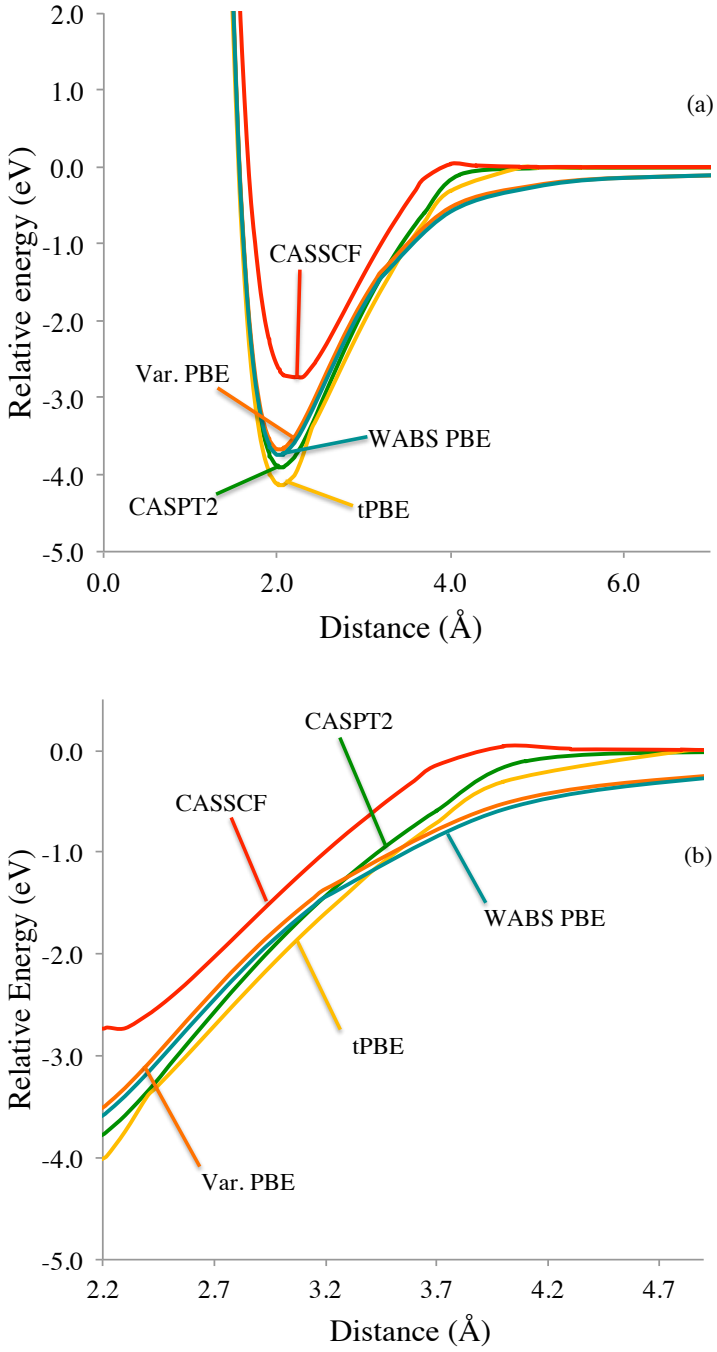

Figure 7.6. Potential energy curves for the $^2\Pi$ state of NiCl. a) Part a shows the whole range of distances. At equilibrium, the electronic structure is ionic, with Ni^+ having a $3d^9$ configuration. At dissociation, Ni is in its $3d^8 4s^2$ ground state. b) Part b is a blowup of the region from 2.5 to 5.5 Å.

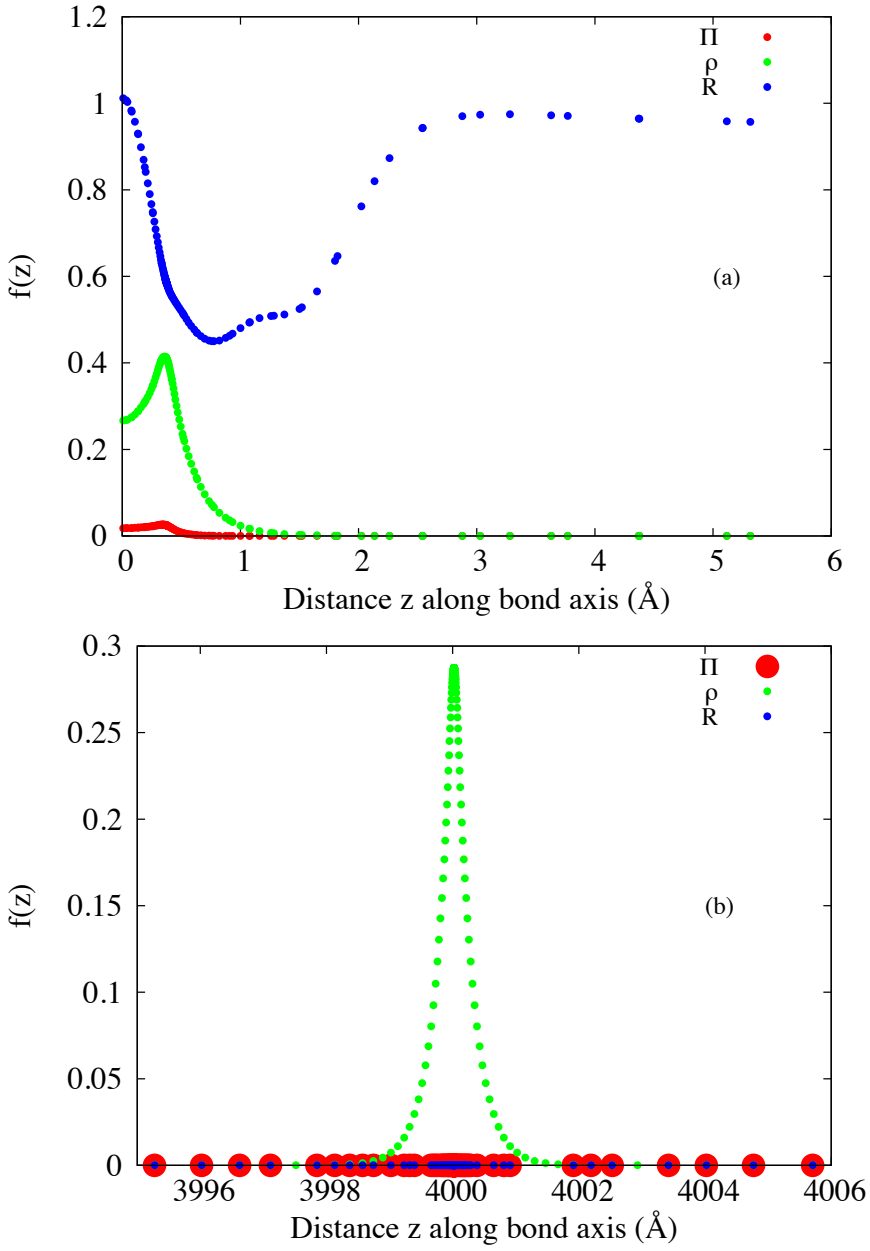

Figure 7.7. Plot of the pair density, total density, and the ratio for H_2 along the bond axis. In the plot, 0 Å is the middle of the bond between the atoms. a) Part a represents these quantities, f(z), at equilibrium. Only one atom of the dimer is represented in the plot, centered at about 0.35 Å. b) Part b represents these quantities at dissociation.

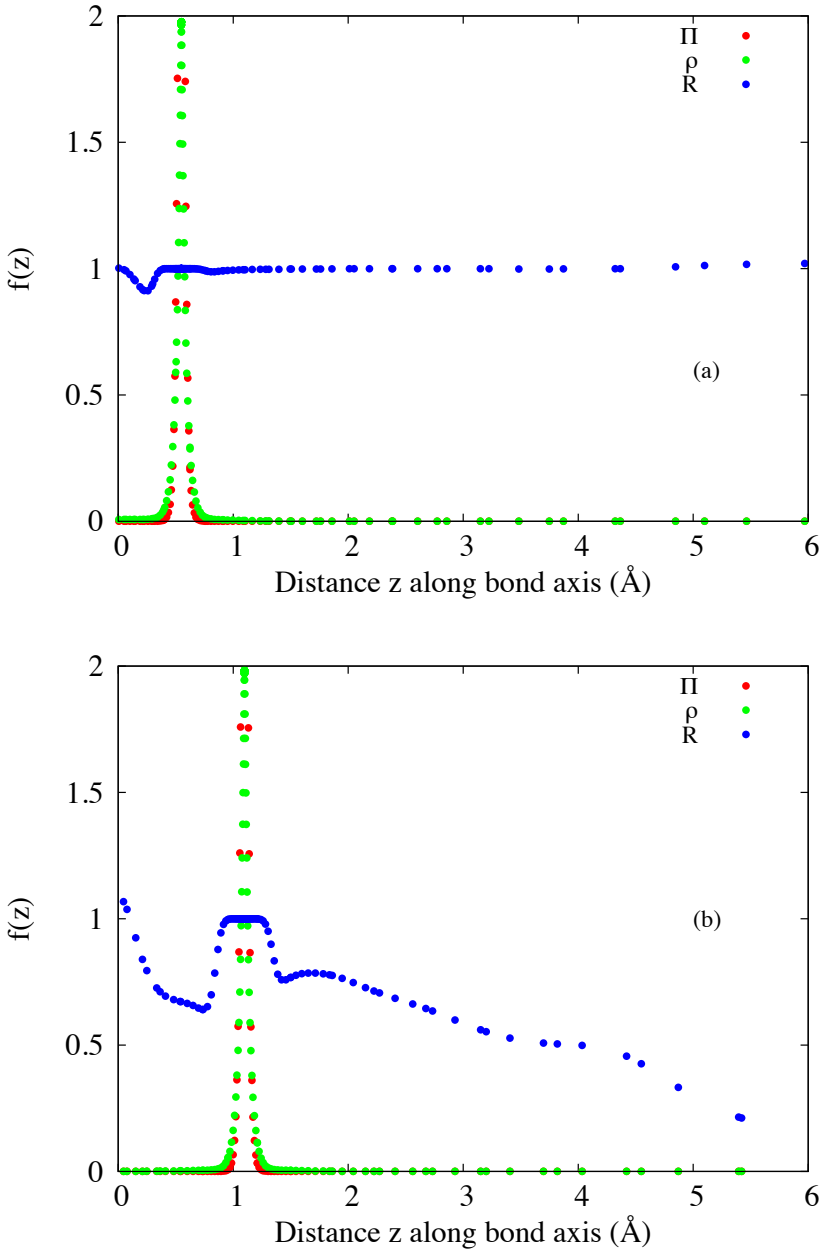

Figure 7.8. Plot of the pair density, total density, and the ratio for N_2 along the bond axis. In the plot, 0 Å is the middle of the bond between the atoms. The pair density and total density have been scaled in this figure by a factor of 1000 and 100, respectively. a) Part a represents these quantities, f(z), at equilibrium. Only one atom of the dimer is represented in the plot, centered at about 0.55 Å. b) Part b represents these quantities at 2Re.

Chapter 8

Multiconfiguration Pair-Density Functional Theory: Barrier Heights and Main Group and Transition Metal Energetics

Reproduced in part from

Multiconfiguration Pair-Density Functional Theory: Barrier Heights and Main Group and Transition Metal Energetics, Rebecca K. Carlson, Giovanni Li Manni, Andrew L. Sonnenberger, Donald G. Truhlar, and Laura Gagliardi**,** *Journal of Chemical Theory and Computation,* **2015,** *11* (1), 82-90.

8.1 Overview

Kohn–Sham density functional theory, resting on the representation of the electronic density and kinetic energy by a single Slater determinant, has revolutionized chemistry, but for open-shell systems the Kohn–Sham Slater determinant has the wrong symmetry properties as compared to an accurate wave function. We have recently proposed a theory, called multiconfiguration pair-density functional theory (MC-PDFT), in which the electronic kinetic energy and classical Coulomb energy are calculated from a multiconfiguration wave function with the correct symmetry properties, and the rest of the energy is calculated from a density functional, called the on-top density functional, that depends on the density and the on-top pair density calculated from this wave function. We also proposed a simple way to approximate the on-top density functional by translation of Kohn–Sham exchange-correlation functionals. The method is much less expensive than other post-SCF methods for calculating the dynamical correlation energy starting with a multiconfiguration self-consistent-field wave function as the reference wave function, and initial tests of the theory were quite encouraging. Here we provide a broader test of the theory by applying it to bond energies of main-group molecules and transition metal complexes, barrier, heights and reaction energies for diverse chemical reactions, proton affinities, and the water dimerization energy. Averaged over 56 data, the mean unsigned error is 3.2 kcal/mol for MC-PDFT, as compared to 6.9 kcal/mol for Kohn-Sham theory with a comparable density functional. MC-PDFT is more accurate on average than complete active space second-order perturbation theory (CASPT2) for main-group small-molecule bond energies, alkyl bond dissociation energies, transition-metal–ligand bond energies, proton affinities, and the water dimerization energy.

8.2 Introduction

Wave function theory (WFT) and density functional theory (DFT) have complementary strengths for electronic structure problems. Great progress has been made in the ability of theory to make useful predictions of barrier heights, bond energies, complexation energies, and other quantities important for mechanistic, analytical, and synthetic chemistry.[306,354] However, problem areas remain, one of which is the treatment of strongly correlated systems, which may also be described as inherently multiconfiguration systems. Such systems, sometimes called multi-reference systems (in contrast to weakly correlated systems, which may also be called single-reference systems and which are described qualitatively correctly by a single electronic configuration)

include many transition metal complexes, some transition states, systems with partially broken bonds, and most electronically excited states.

For treating inherently multiconfigurational systems, WFT methods such as complete active space self-consistent field theory (CASSCF)[34] or other multiconfiguration self-consistent-field (MCSCF) methods[355] have the advantage of explicitly describing the dominant electron configurations, but they do not include enough dynamical correlation energy to be quantitatively accurate. More quantitative results for dissociation energies, barrier heights, and excitation energies of both main group and transition-metal containing systems can be produced when wave functions obtained by these methods are used as reference wave functions for post-SCF dynamical correlation treatments like complete active space second order perturbation theory (CASPT2)[37] or multi-reference configuration interaction (MRCI).[356] MCSCF methods with smaller configuration spaces, such as generalized valence bond,[357] restricted active space self consistent field theory (RASSCF),[40,358] occupation-restricted-multiple-active space (ORMAS) SCF method,[320] generalized active space self consistent field theory (GASSCF),[41] and SplitGAS,[318,319] have also been used successfully to model multireference systems. However, adding the rest of the correlation energy to an MCSCF calculation by post-SCF wave function methods has the major drawback that computational cost rises rapidly as system size increases.

Because the electron-electron interaction is a two-body operator, the electronic energy can be written exactly in terms of the one-particle and two-particle density matrices. The Hohenberg-Kohn theorem shows that the energy is also a functional of the

one-particle density, which leads to DFT.[359] Density functional theory in the Kohn-Sham formulation (KS-DFT)[42] can treat much larger systems than dynamically correlated WFT. Although KS-DFT uses a single configurational representation of the density, it would be an exact theory if the exact exchange-correlation functional were used. However, the exact functional is unknown and probably unknowable. With the use of existing functionals, the treatment of strongly correlated systems is much less satisfactory than the treatment of weakly correlated ones.[309] First of all, one must used spin-polarized (spin-unrestricted) density functional theory in which the energy is a functional of the spin densities (spin-up and spin-down densities) rather than the total density, which is their sum. Not only are the energies less accurate but the theory becomes ambiguous as to which state is being approximated because the stationary solutions of the Kohn-Sham equation do not have the correct symmetry properties.[305]

Recently, we published a new method that combines the strengths of WFT and DFT in a new theory, called multiconfigurational pair-density functional theory (MC–PDFT).[46] This theory is not covered by the Hohenberg-Kohn theorem since it involves the diagonal element of the two-particle density matrix (but not the whole two-particle density matrix); we call the diagonal element of the two-particle density matrix the on-top density. The on-top density offers a way to treat inherently multiconfigurational systems with the correct symmetry,[44,91,322,334] and MC-PDFT uses new on-top density functionals to create a systematic new density functional method. The first step in this theory is a correlated WFT calculation, which we have so far taken to be an MCSCF calculation and in particular a CASSCF calculation. There have been many previous

attempts to combine MCSCF theory with DFT, but these have been plagued with the problem of double counting portions of the correlation energy.[60] We eliminated this problem by calculating only the kinetic energy from the CASSCF wave function; all other components of the energy are calculated in a post-SCF step by a functional of the (one-particle) density and the on-top pair density calculated from the CASSCF wave function. Because the MC-PDFT method is systematic, it offers a clear path forward for improvements. Another appealing aspect of MC-PDFT is that its computational cost scales with system size in the same way as CASSCF (the cost depends on the choice of active space), but we are aiming at producing results similar to (and eventually better than) CASPT2 quality.

As already mentioned, MC-PDFT requires a new kind of density functional, called the on-top density functional, which is a function of the total density and the on-top density rather than of the spin densities on which the exchange-correlation functionals of spin-polarized Kohn-Sham theory depend. For our first applications, we developed on-top density functionals by a simple translation protocol that we postulated for converting a generalized-gradient-approximation (GGA) exchange-correlation functional to an on-top density functional; we calculated 19 atomic and molecular excitation energies (the molecules have 2–11 atoms) and six diatomic potential energy curves and dissociation energies (four for main-group diatomics and two for diatomics containing a transition metal), and we obtained encouraging results.[46] For example, MC-PDFT provided a realistic description of the potential energy curve of the dissociating N_2 molecule, which transforms upon dissociation from a closed-shell singlet to a system with six unpaired

electrons.

To further develop the theory we need improvements in two regards: (i) We need to understand the performance of MC-PDFT for a broader class of problems, including barrier heights and a more representative set of transition metal bond energies. (ii) We need to identify or develop less expensive methods than CASSCF for determining the kinetic energy, density, and on-top density. CASSCF, although much less expensive than CASPT2 or MRCI, is still prohibitively expensive when large active spaces are required to model the chemical problem of interest. (iii) We need to develop more accurate on-top density functionals.

We need to carry out step i before we can carry out step ii because we need to establish more broadly than was done in our initial paper, how well the theory works with CASSCF wave functions. They provide a systematic standard when they are affordable, so that we can see how much accuracy, if any, is lost when using simpler methods to generate the kinetic energy, density, and on-top density. That is the goal of the present paper, in which we continue to use CASSCF with one of our simple translated functionals, in particular tPBE[46] (which is a translation of the PBE[199] functional for the MC–PDFT method). We report the results of MC–PDFT over a broader set of data than in the original paper, in particular, we consider six main-group atomization energies for systems with 2–12 atoms, ten transition-metal atomization energies for systems with 2–6 atoms, three proton affinities of triatomic and tetra-atomic molecules, two alkyl bond dissociation energies for systems with 17 and 18 atoms, the complexation energy of the water dimer, 24 barrier heights for reactions with 3-7 atoms, and 10 energies of reaction

for the subset of these reactions where the energy of reaction is not zero. This makes a total of 56 data, and the database may be called CE56 (denoting 56 chemical energies).

In addition to comparing the MC-PDFT results to reference data derived mainly from experiment, we also compare to conventional Kohn-Sham calculations with three standard exchange-correlation functionals, namely the PBE[199] GGA and two hybrid functionals, B3LYP[345,360–362] and M06-2X.[363] We note that the M06-2X functional, when originally published,[363] was recommended only for systems that do not contain transition metals, but it is applied here to the entire database just to illustrate the difficulty in Kohn-Sham theory of obtaining excellent performance for transition metals with one of the best functionals for the main group.

The theory was presented in the original paper[46] and is summarized in section 2. Section 3 explains the CE56 database.

8.3 Theory

See Chapter 7, section 3.

8.4 CE56 Database and its Subdatabases

All data in the energetic databases are non-relativistic electronic energies (including nuclear repulsion for molecules). For values derived from experiment, the rotational-vibrational and zero-point energies and the spin-orbit energy have been removed from experimental values as described in detail in previous work.[364] For databases based on atomization energies, we divide the atomization energy by the number of bonds in the molecule to produce the average bond energy for that molecules; in counting bonds, a double bond counts as one bond, i.e., we add bonds, not bond orders.

The reason for this is so that the large atomization energies of large molecules do not have an excessive effect on the mean errors. The seven subdatabases that compose the CE56 database are all based on previous work[81,173,309,364–372] and are explained in Table 8.1. The actual data in each database will be shown in Tables 8.2-8.8 later in the article.

8.5 Computational Details

One goal in developing the MC–PDFT method was to create a general method that describes a state with a well defined wave function for any single-reference or multireference system and derives an energy from that wave function as a post-SCF step. By using a CASSCF wave function, a state with the correct symmetry of the wave function is unambiguously defined and is used to provide the kinetic energy, density, and on-top density for the post-SCF on-top density functional. For multireference systems, there is no longer a need to describe a state with a broken symmetry approach[35,45,312,314] which is commonly used in KS–DFT.

All MC–PDFT, CASSCF, and CASPT2 calculations were performed with a locally modified version of the Molcas electronic structure package;[120] these methods will soon be available in an update to version 8. All calculations are non-relativistic except when the Ag atom is present (see below), and geometries were obtained from the respective databases specified in Table 8.1. The basis sets used for the database containing transition metals were def2-TZVP[174] for metals and ma-TZVP[373] for other atoms. For Ag, the def2-TZVP relativistic effective core potential was used. Calculations for all other databases used the MG3S[374] basis set. Atomization energies are computed as the difference between the sum of the energies of the atoms and the energy of molecule.

Table 8.1. Descriptions of Subdatabases

Subdatabase	Description
MGABE6	6 main-group average bond energies. This database is obtained from an older database (AE6, from Ref. 365) of six atomization energies by dividing each datum by the number of bonds in the molecule.
TMABE10	10 average bond energies of molecules containing transition metals: reference data and geometry for AgH and FeH from Ref. 309, for CoH from Ref. [372], and for the other 7 from Zhang et al. (Ref. 364)
PA3	proton affinities of 3 small molecules from Ref. 367
ABDE2	two alkyl Bond dissociation energies from Refs. 173,365,368
WDCE1	water dimer complexation energy from Ref. 375
DBH24/08	24 diverse barrier heights from Refs. 365, 376, 370, and 371 (the "/08" denotes that we use the database as updated in 200837)
DRE10	10 diverse reaction energies from DBH24/10
MGE46	union of MGABE6, PA3, ABDE2, WDCE1, DBH24/08, and DRE10

Reasonable CASSCF active spaces were selected for each system. The active spaces are specified in footnotes to tables. In all cases we use the same active space for CASSCF, CASPT2, and MC-PDFT.

All CASPT2 calculations were performed with standard imaginary shift[126] value of 5.44 eV and the Molcas default IPEA shift[340] of 6.80 eV. The imaginary shift serves to remediate the problem of intruder states, and the ionization-potential-electron-affinity (IPEA) shift is a parameter modifying the zeroth-order Hamiltonian that adjusts the energies of the active orbitals to be in better agreement with experiment. In the CASPT2 calculations, we did not correlate the core orbitals. For the main group we froze 1s orbitals; for the second period, we froze 1s, 2s, and 2p orbitals, except for Si for which

we only froze 1s and 2s; for 3d transition metals we froze 1s, 2s, 2p, and 3s orbitals; and for Ag we froze 1s, 2s, 2p, 3s, 3p, 3d, and 4s orbitals.

The KS–DFT results presented for comparison were obtained from previous work.[372]

8.6 Multireference Diagnostics

In order to better understand the results, it is useful to have a quantitative measure of the multireference nature of each system in the database. While there are many diagnostics that have been used to define the extent of multireference character in a system[309,377–394] we limit ourselves here to just two. In particular we report both (i) the M diagnostic,[381] called M, which is derived from natural orbital occupation numbers of a CASSCF wave function, and (ii) the percentage weight of the dominant configuration from a CASSCF wave function, which is the absolute square of the largest coefficient in the configuration interaction expansion expressed as a percentage and is called P.

A rough rule of thumb is that a state is considered to have multireference character if $M \geq 0.04$ and/or $P < 95$. For atomization energies and bond dissociation energies, we use the full molecule to determine the M diagnostic (thus the diagnostics shown do not take account of the fact that the multireference character could be larger in the fragments produced by breaking bonds than in the parent molecule). For proton affinities and the hydrogen-bonded water dimer, we use the protonated species and the hydrogen-bonded complex as the measure of multireference character. Finally, for barrier heights and reaction energies, we use the transition state as the multireference measure.

8.7 Results

Tables 8.2-8.8 give the results obtained with three standard KS–DFT functionals and with CASSCF, CASPT2, and MC–PDT. These tables also give the active space specifications, using the notation *n/m*, where *n* is the number of active electrons, and *m* is the number of active orbitals. The bottom row of each table is the mean unsigned error averaged over the values in the table. Tables 8.2-8.8 also include the *M* and *P* diagnostics explained in Section 4. Table 8.9 contains the mean unsigned errors averaged over all 56 data, and it compares these to separate averages for the 10 data involving transition metals and the 46 data that do not involve transition metals. All mean errors in the tables are computed from unrounded data, not from the rounded data in the tables. The atomization energies underlying the data in Tables 8.2 and 8.3 are first converted to average bond energies, as listed in the tables, and the errors for each molecule and the mean errors are computed using the average bond energies.

8.8 Discussion

CASPT2 is sensitive to the active space choice, in particular, to the size of the correlating space. The present active spaces are large enough to remove the major static correlation error in most cases, but the dynamical correlation, even the portion due only to the valence space, is very slowly convergent with respect to the size of the active space (the dynamical correlation energy is even more slowly convergent at the CASSCF level, such that CASSCF is not a practically useful method to recover dynamical correlation energy). Chief among the questions that the present tests are designed to answer is: Are

these reasonable active spaces large enough to yield accurate bond energies and barrier heights energies by MC-PDFT?

Table 8.2 shows that CASSCF has a mean absolute error (MAE) of 17 kcal/mol for main group bond energies. This is by far the largest error of the methods tested, as expected since it is the only method that does not attempt to recover the full or full valence dynamical correlation energy.

Table 8.2. Main-Group Average Bond Energies (kcal/mol)

			WFT		MC-PDFT	KS-DFT			
	M^a	P^b	CASSCF	CASPT2	tPBE	PBE	M06-2X	B3LYP	Exp.
SiH_4[c]	0.02	96.3	72.4	78.0	78.9	78.4	80.4	80.9	81.2
S_2[d]	0.07	94.8	76.9	100.8	109.2	114.7	104.2	102.9	104.3
SiO[e]	0.04	94.2	191.0	188.0	187.0	196.3	190.2	188.0	193.1
C_3H_4[f]	0.06	92.8	95.2	113.8	117.5	120.2	117.5	117.1	117.5
HC(O)CHO[g]	0.07	90.6	110.5	123.1	127.1	132.7	126.7	126.2	126.8
C_4H_8[h]	0.03	95.6	73.7	92.4	95.5	97.3	95.7	95.1	95.8
MUE[i]			16.5	3.8	2.3	4.4	0.7	1.4	

[a] The M diagnostic values are computed according to reference 381.

[b] The percent dominant configuration is of the CASSCF wave function.

[c] The active space is 8/8, where the eight electrons are the sigma bonding electrons and the eight orbitals are the sigma bonding and antibonding orbitals.

[d] The AS is 12/8, the full valence space, where the electrons and orbitals are the valence 3s and 3p choices.

[e] The AS is 10/8, the full valence space, where the electrons and orbitals are the valence s and p choices for each atom.

[f] The AS is 8/8 and excludes all carbon-hydrogen bonds. The eight electrons are those of the carbon-carbon triple bond and the carbon-carbon single bond. The orbitals are the corresponding bonding and antibonding pairs.

[g] The AS is 12/12 and includes the carbon atomic 2p electrons and orbitals and the oxygen 2p electrons and orbitals.

[h] The AS is 8/8, where the electrons and orbitals are bonding electrons of the carbon-carbon single bonds and the orbitals are the corresponding bonding/antibonding pairs.

Recovering more dynamical correlation energy with CASPT2 reduces the errors by more than a factor of four, but only to 3.8 kcal/mol. In fact, for this test set, the errors for

CASPT2 are almost as big as those for standard KS–DFT with the PBE functional (4.4 kcal/mol). The two hybrid functionals, M06-2X and B3LYP, have the lowest errors for the main group atomization energies at 0.7 kcal/mol and 1.4 kcal/mol, respectively. While MC–PDFT does not perform as well as these standard hybrid functionals; tPBE does improve by factors of 1.9 and 1.7 over PBE and CASPT2.

The *M* and *P* diagnostic values show that four of the systems in Table 8.1 (all except SiH_4 and C_4H_8) are multireference systems. The tPBE results are quite accurate for the two cases with the most multireference character, which is very encouraging for the ability of MC-PDFT to treat multireference systems.

Table 8.3 gives average bond energies of molecules containing transition metals, where the average bond energy is the atomization energy per bond (atomization energy divided by the number of bonds in the molecules). Table 8.3 shows that CASSCF tends to underestimate the atomization energy and has a mean unsigned error of 22.2 kcal/mol per bond. As for the main group atomization energies, CASPT2 reduces the average error as compared to CASSCF, in this case to to 5.5 kcal/mol per bond. M06-2X is included in this table only for completeness since the original article[363] presenting it said it was not designed for treating transition metals; it has a mean unsigned error of 7.2 kcal/mol per bond The other hybrid functional, B3LYP, has an average error of 6.1 kcal/mol, and PBE and tPBE have an average error of 7.6 and 4.5 kcal/mol, respectively.

For the three transition metal hydrides in Table 8.3 (rows 1–3), tPBE performs better than CASPT2. All three of these cases are considered to be multireference systems

by the M and P diagnostics, but the weight of the dominant configuration is high for AgH.

Table 8.3 Transition-Metal-Ligand Average Bond Energies (kcal/mol)

			WFT		MC-PDFT	KS-DFT			
	M^a	P^b	CASSCF	CASPT2	tPBE	PBE	M06-2X	B3LYP	Exp.
AgH[c]	0.05	97.7	38.2	52.2	52.9	55.9	48.1	54.5	54.0
FeH[d]	0.65	53.2	19.2	28.9	31.8	49.3	57.4	57.2	36.8
CoH[e]	0.98	34.4	18.2	42.9	39.6	60.5	56.5	60.1	45.2
TiCl[f]	0.05	50	92.3	104.2	103.6	116.6	97.9	103.8	102.3
CrCl[g]	0.01	99.4	64.0	86.4	82.3	89.8	99.1	86.7	91.0
VF_5[h]	0.06	89.7	74.2	107.6	116.9	126.5	103.1	111.8	113.4
$CrCl_2$[i]	0.006	99.5	72.5	80.7	78.2	88.8	96.6	85.3	91.4
MnF_2[j]	0.01	99.4	87.3	118.2	120.7	127.6	113.8	117.2	116.5
$FeCl_2$[k]	0.008	99.4	78.3	94.2	95.7	99.5	94.7	93.3	96.6
$CoCl_2$[l]	0.01	99.5	74.4	77.7	91.3	94.0	94.9	86	93.5
MUE			22.2	5.5	4.6	7.6	7.2	6.1	

[a] The M diagnostic values are computed according to reference 381.

[b] The percent dominant configuration is of the CASSCF wave function.

[c] The active space is 12/7, where the electrons and orbitals are those from the 4d and 5s orbitals of Ag and the 1s of hydrogen. The spin state is a singlet.

[d] The AS is 9/7, where the electrons and orbitals are those from the 3d and 4s orbitals of Fe and the 1s orbital of hydrogen. The spin state is a quartet.

[e] The AS is 10/7, where the electrons and orbitals are those from the 3d and 4s orbitals of Co and the 1s orbital of hydrogen. The spin state is triplet.

[f] The AS is 5/7, where the electrons and orbitals are those from the 3d and 4s orbitals of Ti and the bonding 3p electron and orbital of Cl. The spin state is a quartet.

[g] The AS is 7/7, where the electrons and orbitals are those from the 3d and 4s orbitals of Cr and the bonding 3p electron and orbital of Cl. The spin state is a sextet.

[h] The AS is 10/11, where the electrons and orbitals are those from the 3d and 4s orbitals of V and the bonding 2p electron and orbital of each F. The spin state is a singlet.

[i] The AS is 8/8, where the electrons and orbitals are those from the 3d and 4s orbitals of Cr and the bonding 3p electron and orbital of Cl. The spin state is a quartet.

[j] The AS is 9/8, where the electrons and orbitals are those from the 3d and 4s orbitals of Mn and the bonding 2p electron and orbital of F. The spin state is a sextet.

[k] The AS is 10/8, where the electrons and orbitals are those from the 3d and 4s orbitals of Fe and the bonding 3p electron and orbital of Cl. The spin state is a quintet.

[l] The AS is 11/8, where the electrons and orbitals are those from the 3d and 4s orbitals of Co and the bonding 3p electron and orbital of Cl. The spin state is a quartet.

The metal halides (rows 4–10 of Table 8.3) are not characterized as having significant multireference character by either diagnostic, except for VF_5 and TiCl. In

some cases, such as $FeCl_2$ and $CoCl_2$, tPBE improves upon CASPT2 and does about as well as standard KS–DFT. In other cases like CrCl and $CrCl_2$, tPBE substantially underestimates the atomization energy.

Table 8.3 shows that for cases with a high M value and low dominant-configuration reference weight, tPBE generally does well. A particular success of tPBE compared with PBE is VF_5. With PBE, the atomization energy is about 66 kcal/mol too high (13 kcal/mol per bond), and tPBE reduces this error by almost a factor of four.

In Table 8.4, we report proton affinities for three small molecules. All methods have lower average errors than CASSCF (5.5 kcal/mol). For this test set, tPBE has the lowest average error of 0.3 kcal/mol, followed by CASPT2 (0.6 kcal/mol). Standard KS–DFT has errors that are approximately much higher (1.0-1.4 kcal/mol for the functionals tested here and about 2 kcal/mol for a typical exchange-correlation functional[372]). This is a very significant success for the new formalism since proton affinity is a direct test of the effect of changing the external potential in which the electrons move without changing the number of electrons or their spin state.

Table 8.4. Proton Affinities of Small Molecules (kcal/mol)

	M^a	P^b	CASSCF	CASPT2	tPBE	PBE	M06-2X	B3LYP	Exp.
NH_3[c]	0.02	96.3	212.9	212.3	212.1	210.9	209.9	211.3	211.9
H_2O[d]	0.02	97.4	171.0	171.5	172.3	170.4	170.7	170.5	171.8
H_2S[e]	0.03	96.2	188.6	174.9	174.0	174.4	172.4	174.8	173.7
MUE			5.5	0.6	0.3	1.03	1.4	1.03	

[a] The M diagnostic values are computed according to reference 381.
[b] The percent dominant configuration is of the CASSCF wave function.
[c] The AS is 6/6
[d] The AS is 4/4
[e] The AS is 8/7, which includes the 3s and 3p electrons and orbitals from S and the 1s electrons and orbitals from each H, plus the orbital from the proton.

Alkyl bond dissociation energies are well known to be a difficult problem for Kohn-Sham DFT.[368,395–397] For alkyl bond dissociation energies, given in Table 8.5, tPBE has the lowest error of 0.5 kcal/mol, followed by M06-2X with and average error of 0.8 kcal/mol. The CASPT2 error is much smaller than CASSCF (2.6 vs. 19.1 kcal/mol, respectively) and the popular B3LYP functional has an error of 12.6 kcal/mol.

Table 8.5. Alkyl Bond Dissociation Energies (kcal/mol)

	M^a	P^b	CASSCF	CASPT2	tPBE	PBE	M06-2X	B3LYP	Exp.
tBu-CH_3[c]	0.02	96.2	74.5	95.1	90.6	86.2	92.7	81.6	93.7
tBu-OCH_3[d]	0.03	98.9	70.3	93.0	89.6	80.1	89.9	76.2	89.3
MUE			19.1	2.6	1.7	8.3	0.8	12.6	

[a] The M diagnostic values are computed according to reference 381.

[b] The percent dominant configuration is of the CASSCF wave function.

[c] The AS is 8/8 for the molecule, which includes all carbon-carbon electrons and corresponding bonding/antibonding orbital pairs. For the methyl radical, the AS was 1/1. For the butyl radical, the AS was 7/7 for the butyl radical, which includes the carbon-carbon electrons and corresponding bonding/antibonding orbital pairs plus the radical electron and orbital.

[d] The AS is 2/2 for the molecule, which includes all carbon-carbon electrons and corresponding bonding/antibonding orbital pairs. For each radical, the AS was 1/1.

For the noncovalent energy of hydrogen bonding in a water dimer, given in Table 8.6, B3LYP is the best method tested with an error of 0.01 kcal/mol, followed by tPBE with an error of 0.2 kcal/mol. The other functionals and CASPT2 give a much higher error of 0.5 kcal/mol.

Table 8.6. Non-covalent energy of hydrogen bonding (kcal/mol)

	M^a	P^b	CASSCF	CASPT2	tPBE	PBE	M06-2X	B3LYP	Exp.
$(H_2O)_2$[c]	0.02	96.0	4.0	5.5	4.8	5.4	5.5	4.96	4.97
unsigned error			0.96	0.5	0.2	0.5	0.5	0.01	

[a] The M diagnostic values are computed according to reference 381.

[b] The percent dominant configuration is of the CASSCF wave function.

[c] The AS is 16/8 for the dimer, and 8/4 for each water molecule.

Table 8.7. Forward and reverse barrier heights for small molecules (kcal/mol)

	M^a	P^b	CAS	CASPT2	tPBE	PBE	M06-2X	B3LYP	Exp
$OH+CH_4 \rightarrow H_2O+CH_3$	0.03	93.1	18.9	6.9	5.5	-5.2	5.4	2.3	6.5
reverse[c]			24.4	17.9	21.0	8.8	17.5	13.9	19.6
$H+HO \rightarrow H_2+O$	0.04	96.5	17.1	12.0	10.5	3.6	9.6	4.0	10.5
reverse[d]			27.0	13.8	8.1	-1.3	11.8	6.3	12.9
$H+H_2S \rightarrow H_2+HS$	0.04	96.0	11.3	5.5	4.3	-1.1	4.4	-0.5	3.5
reverse[e]			24.6	18.1	15.1	9.5	18.2	15.9	16.8
$H+N_2O \rightarrow OH+N_2$	0.08	87.6	29.8	20.4	17.3	10.5	17.6	11.8	17.1
reverse[f]			96.2	80.2	71.2	52.8	82.1	73.1	82.3
$H+ClH \rightarrow HCl+H$	0.05	95.8	29.9	20.4	16.7	10.4	18.6	13.1	18.0
reverse[g]			29.9	20.4	16.7	10.4	18.6	13.1	18.0
$CH_3+FCl \rightarrow CH_3F+Cl$	0.09	91.7	8.3	8.9	6.3	-6.4	4.7	-1.5	6.8
reverse[h]			86.5	51.1	45.5	42.0	59.7	51.2	59.2
$Cl^-\cdots CH_3Cl \rightarrow ClCH_3\cdots Cl^-$	0.03	99.1	20.2	12.2	7.9	6.9	13.5	9.0	13.4
reverse[i]			20.2	12.2	7.9	6.9	13.5	9.0	13.4
$F^-\cdots CH_3Cl \rightarrow FCH_3\cdots Cl^-$	0.03	95.6	6.4	2.4	0.2	-1.0	3.2	0.1	3.4
reverse[j]			46.5	26.5	26.2	21.0	33.5	26.2	29.4
$OH^-+CH_3F \rightarrow HOCH_3+F^-$	0.04	95.1	10.3	-3.6	-6.7	-10.7	-2.9	-5.9	-2.4
reverse[k]			30.6	17.2	14.1	9.6	17.5	14.6	17.7
$H+N_2 \rightarrow HN_2$	0.07	91.1	26.5	16.6	13.0	5.6	14.1	7.8	14.4
reverse[l]			-0.5	10.9	14.5	9.2	11.3	11.0	10.6
$H+C_2H_4 \rightarrow CH_3CH_2$	0.08	90.0	-9.6	1.7	3.4	0.0	2.9	-0.1	1.7
reverse[m]			34.5	41.3	42.8	40.4	43.7	41.9	41.8
$HCN \rightarrow HNC$	0.06	92.7	53.9	48.2	46.7	46.0	46.2	47.7	48.1
reverse[n]			37.5	33.9	32.8	41.0	33.3	33.8	32.8
MUE			10.2	1.7	2.9	8.5	0.98	4.2	

a) The M diagnostic values are computed according to reference 381. *b)* The percent dominant config. is of the CASSCF wave function. *c)* The AS for the transition state (TS) is 15/13. *d)* The AS for the TS is 8/6. *e)* The AS for the TS is 9/7. *f)* The AS for TS is 17/13. *g)* The AS for HCl is 8/5 which includes the valence electrons and orbitals on Cl and the 1s electron and orbital from H, 1/1 for H, and 9/6 for the TS which includes the aforementioned electrons and orbitals. *h)* The AS for CH_3 is 7/7 which includes the carbon-hydrogen sigma electrons and corresponding bonding/antibonding orbitals and the electron and orbitals of the radical. The AS for FCl is 10/6 which includes the valence p electrons and orbitals of the halogens. The AS for the TS is 17/13, the sum of the reactant active spaces. The AS for CH_3F is 12/10 which includes the carbon 2s and 2p electrons and orbitals, the F 2p electrons and orbitals, and the H 1s electrons and orbitals. Finally, for Cl, the AS is 5/3 which includes the 3p electrons and orbitals. *i)* The AS is 10/9 for all molecules, and includes the carbon-hydrogen sigma bonds and corresponding bonding/antibonding orbitals, the bonding lone pair and orbital on the coordinating Cl, and the bonding electrons and corresponding bonding/antibonding orbitals of the bonded Cl. *j)* The AS is 10/9 for all molecules, and is analogous to Cl-···CH3Cl → ClCH3···Cl-. *k)* The AS is 2/1 for the anions, corresponding to the electrons that will form the bond in the reaction. For the neutral species, the AS is 8/8 and includes all electrons and their corresponding bonding/antibonding orbitals that are associated with the central C atom. For the TS, the AS is analogous to Cl-···CH3Cl → ClCH3···Cl- and F-···CH3Cl → FCH3···Cl-. *l)* The AS is 1/1 for hydrogen and 10/8 for N_2 corresponding to the valence electrons and orbitals. The TS and HN_2 were described with an AS of 11/9, the sum of the active spaces used for the products. *m)* The AS is 1/1 for hydrogen and 12/13 for C_2H_4. The TS and product both used an AS of 13/14. *n)* The AS is 10/9 for all species, corresponding to the 1s electron and orbital of H and the valence 2s and 2p electrons and orbitals from C and N.

In Table 8.7, we test the new theory against a diverse set of forward and reverse barrier heights for chemical reactions.[371] M06-2X has the lowest mean unsigned error (1.0 kcal/mol), followed by CASPT2 (1.7 kcal/mol). Comparing tPBE to PBE, the average error is reduced by a factor of 2.7 (3.2 vs. 8.5 kcal/mol). As is typical of CASSCF, the average error is the highest (10.2 kcal/mol) of any of the methods tested, and B3LYP has an average error of about 4 kcal/mol, which is typical behavior for this functional.[370,371] Comparing PBE and tPBE, we see that when PBE predicts an incorrect sign of either the forward or reverse barrier height (which is the case for the first, second, sixth and eighth reactions in the table), tPBE instead gets the correct sign. For the sixth reaction, whose transition structure has the highest multireference character of any reaction considered, PBE underestimates the barrier height by 13.2 kcal/mol for the forward barrier, while tPBE predicts the correct sign and only underestimates the barrier by 0.5 kcal/mol. The fourth and eleventh reactions are the next highest in multireference character by both diagnostics. For the former, tPBE outperforms PBE and is better than CASPT2 for describing the forward barrier. For the latter, CASPT2 is very accurate; the performance of tPBE is very similar to M06-2X for this reaction although the forward barrier height is overestimated. In general, for the reactions in Table 8.7, tPBE performs more similarly to the hybrid functionals (which are well known[364,371] to be better for barrier heights than are local functionals) than to the local PBE functional.

The last set of data is composed of reaction energies and is given in Table 8.8. The lowest average error for this set is provided by M06-2X (1.4 kcal/mol) followed by B3LYP (2.0 kcal/mol) and CASPT2 (2.5 kcal/mol). The tPBE calculations have a lower

average error, 4.1 kcal/mol, than CASSCF or PBE. There are two cases where PBE has the wrong sign for the energy of reaction; although tPBE also has the incorrect sign in these cases, the improvement is in the correct direction. For the H + N_2O reaction, which has the most multireference character by either the M or P diagnostic, tPBE improves upon PBE by about 8 kcal/mol, but it still underperforms compared to the other methods.

Table 8.8. Reaction energies for small molecules (kcal/mol) [a]

	CASSCF	CASPT2	tPBE	PBE	M06-2X	B3LYP	Exp.
$OH+CH_4 \rightarrow H_2O+CH_3$	-5.5	-11.0	-15.5	-14.0	-12.1	-11.5	-13.1
$H+HO \rightarrow H_2+O$	-10.0	-1.8	2.5	4.9	-2.2	-2.3	-2.4
$H+H_2S \rightarrow H_2+HS$	-13.3	-12.6	-10.8	-10.6	-13.7	-16.4	-13.3
$H+N_2O \rightarrow OH+N_2$	-66.4	-59.8	-53.9	-42.4	-64.5	-61.3	-65.1
$CH_3+FCl \rightarrow CH_3F+Cl$	-78.2	-42.2	-39.2	-48.4	-55.0	-52.8	-52.4
$F^-\cdots CH_3Cl \rightarrow FCH_3\cdots Cl^-$	-40.1	-24.1	-26.0	-22.0	-30.3	-26.1	-26.0
$OH^-+CH_3F \rightarrow HOCH_3+F^-$	-20.3	-20.8	-20.8	-20.3	-20.4	-20.5	-20.1
$H+N_2 \rightarrow HN_2$	26.9	5.7	-1.5	-3.7	2.8	-3.1	3.8
$H+C_2H_4 \rightarrow CH_3CH_2$	-44.1	-39.6	-39.4	-40.4	-40.7	-41.9	-40.0
$HCN \rightarrow HNC$	16.4	14.3	13.9	5.0	12.8	13.9	15.3
MUE	8.5	2.5	4.2	6.0	1.4	2.0	

[a] See Table 8.7 for active space descriptions.

The average errors over all the test data are given in Table 8.9. The first row of Table 8.9 is averaged over all 56 data of the earlier tables. In the next row, we average over only the 10 transition metal data in the TMABE10 subdatabase, and in the third row we average over the other 46 data, which are labeled MGE46 for 46 main-group energies. The first row shows that, on average, CASPT2 and tPBE have similar errors (2.7 and 3.2 kcal/mol, respectively) and both outperform standard KS–DFT, with the exception of M06-2X. Of the three KS functionals, M06-2X has the lowest average error of 2.1 kcal/mol, then B3LYP with an average error of 3.9 kcal/mol, and finally PBE with an average error of 6.9 kcal/mol. The second row of Table 9 shows that tPBE is the best of

all six methods tested for transition metal–ligand bond energies. The third row of Table 9 shows that tPBE is better than either PBE or B3LYP for main group energetics, although not quite as good as CASPT2. It will be interesting to see how the performance improves after we optimize a density functional, but the present performance is already very encouraging for an unoptimized first-generation on-top density functional.

Table 8.9. Average mean unsigned errors (kcal/mol)

	CASSCF	CASPT2	tPBE	PBE	M06-2X	B3LYP
MUE(CE56)[a]	12.5	2.7	3.2	6.9	2.1	3.9
MUE(TMABE10)[b]	22.2	5.5	4.6	7.6	7.2	6.1
MUE(MGE46)[c]	10.5	2.1	2.9	6.7	1.0	3.4

[a] The mean unsigned errors averaged over all data in Tables 8.2-8.8

[b] The mean unsigned errors from the last row of Table 8.3.

[c] The mean unsigned errors averaged over all data in Tables 8.2 and 8.4-8.8.

8.9 Conclusions

We tested the performance of MC–PDFT across a wide variety of cases. A main purpose of this work was to create a test suite against which further improvements of MC-PDFT (especially the use of more economical wave functions and better density functionals, which are not yet developed) could be tested and measured, but the results are of great interest in their own right. The results show that tPBE reduces the average error in CASSCF by a factor of three and that of PBE by a factor of two. Averaging errors over al 56 data, we find that the performance of MC–PDFT is a good on the average as the much more expensive CASPT2. This indicates that the using a qualitatively correct wave function to represent the density and on-top density and calculate the kinetic energy already goes a long way toward improving density functional

theory over the Kohn-Sham formulation, even without optimizing new density functionals.

For main group atomization energies, MC–PDFT is better than CASPT2. For transition metal atomization energies, many of which are highly multireference in character, MC–PDFT is the best of all six methods tested here. While the test sets are smaller for proton affinities and alkyl bond dissociation energies, previous work has shown that these are still representative of larger databases; for these two subdatabases, MC–PDFT again has the best performance of all the methods tested. MC-PDFT also gives a reasonably accurate energy for the dimerization energy of water. Finally, for energies of reactions and barrier heights, MC–PDFT has a performance quality between that of the most (CASPT2 and M06-2X) and least (CASSCF and PBE) accurate methods that are tested here.

Author Contributions

Rebecca K. Carlson contributed all calculations, Giovanni Li Manni contributed to main group and barrier heights, Andrew L. Sonnenberger contributed to proton affinities, alkyl bond dissociations energies, and barrier heights.

Chapter 9

Multiconfiguration Pair-Density Functional Theory: a Fully Translated Gradient Approximation and its Performance for Transition Metal Dimers and the Spectroscopy of $Re_2Cl_8^{2-}$

Reproduced in part from

Multiconfiguration Pair-Density Functional Theory: A Fully Translated Gradient Approximation and Its Performance for Transition Metal Dimers and the Spectroscopy of $Re_2Cl_8^{2-}$, Rebecca K. Carlson, Donald G. Truhlar, and Laura Gagliardi**,** *Journal of Chemical Theory and Computation,* **2015,** *11* (9), 4077-4085.

9.1 Overview

We extend the on-top density functional of multi-configuration pair-density functional theory (MC-PDFT) to include the gradient of the on-top density as well as the gradient of the density. We find that the theory is reasonably stable to this extension, and furthermore it provides improved accuracy for molecules containing transition metals. We illustrate the extended on-top density functionals by applying them to Cr_2, Cu_2, Ag_2, Os_2, and $Re_2Cl_8^{2-}$ as well as to our previous database of 56 data for bond dissociation energies, barrier heights, reaction energies, proton affinities, and the water dimer. The performance of MC-PDFT is comparable to or better than that of CASPT2.

9.2 Introduction

Properly describing the dissociation of diatomic molecules can be problematic for both wave function theory (WFT) and Kohn–Sham density functional theory (KS-DFT).[42] To keep the spin and space symmetry of even simple dissociating diatomics such as H_2 or N_2, a multi-determinant wave function is necessary; for a single determinant, symmetry breaking is needed.[35,45,312,313] In Kohn-Sham theory, a broken-symmetry solution may yield accurate energetics at the equilibrium geometry and dissociation limit, but a Slater determinant of the noninteracting reference system is nonphysical at the dissociation limit.[44,398] If the exact exchange-correlation functional were known, the single Slater determinant obtained by minimizing its energy would yield correct energetics despite the inherently multi-determinantal character of dissociation.[42,399] However, currently available density functionals are limited in their ability to model systems with intrinsically multi-determinantal character[309–311,364] (such systems are called multireference systems or systems with high static correlation). When the symmetry of the Slater determinant is severely broken, the state being modeled may be ambiguous.

Transition metal dimers with a high level of multireference character are also challenging for WFT. For example, the ground state of Cr_2 is a $^1\Sigma_g^+$ state, where – at the

equilibrium geometry – there is a formal bond order of six;[219] the molecule dissociates to atoms in the ^7S configuration, coupled to make an overall spin singlet. There is significant multireference character such that the Hartree–Fock configuration is only about 47% of the wave function at equilibrium.[341] The most accurate WFT potential energy curves for the Cr_2 system have been obtained using complete active space self consistent field[34] (CASSCF) theory, followed by a complete active space second order perturbation[37] (CASPT2) or the split generalized active space[318] (SplitGAS) methods. Such calculations, like the one by Ruipérez et al.[341] that uses a molecule-specific Ionization Potential–Electron Affinity (IPEA) shift (an empirical parameter introduced in the zeroth-order Hamiltonian in the CASPT2 method) – can yield a potential energy curve that mimics the features of the experimental curve[219], i.e. a minimum around 1.678 Å and a shoulder around 2.6 Å, but those CASPT2 calculations overestimate the dissociation energy which should be around 1.47 eV.[318,341] When one uses the standard value for the empirical IPEA shift, the results are worse. Coupled cluster theory needs higher than the connected triple excitations of the so called "gold standard" CCSD(T) method to accurately reproduce experiment, and this makes the cost prohibitively expensive for typical Cr-containing molecules.[400] For KS-DFT, the bond length and dissociation energy of Cr_2 may be over or underestimated, depending on the functional.[127,401–403]

Not only are transition metal dimers with a large amount of static correlation a challenge for quantum chemistry, but challenges are also presented by those dimers for which dynamic correlation dominates at equilibrium. For Cu_2 and Ag_2, there is a single

bond between the atoms of the 4s or 5s σ_g orbitals, respectively, with the 3*d* subshell (for Cu_2) and the 4d subshell (for Ag_2) being completely full. Both molecules have a $^1\Sigma_g^+$ ground state and dissociate to atoms in the ^2S configuration. As with Cr_2, depending on the choice of the exchange-correlation functional and basis set, KS-DFT may predict the correct geometry or dissociation energy, but not both.[401–404] For Cu_2, CASPT2 has been found to reproduce the experimental geometry, but to underestimate the dissociation energy by 0.01 to 0.24 eV, depending on the basis set, relativistic corrections, and type of Fock matrix employed in the calculation.[405]

We have recently presented a new form of density functional theory, namely multiconfiguration pair-density functional theory (MC-PDFT), a post-SCF method that is able to treat intrinsically multi-determinantal systems in a physical way.[46,406] MC-PDFT combines multiconfigurational self-consistent field (MCSCF) wave functions with a new kind of density functional called the on-top density functional to distinguish it from the exchange-correlation functional of KS-DFT. The MCSCF wave function is used to compute kinetic energy and classical Coulomb contributions to the electronic energy as well as the total density ρ, on-top pair density Π, and their gradients, which are variables in the on-top density functional that is used to compute the remaining contributions to the energy. KS-DFT involves only the one-particle density, as justified by the Hohenberg-Kohn theorem,[399] but MC-PDFT goes beyond that as the on-top pair density is a two-particle quantity. MC-PDFT can treat intrinsically multi-determinantal systems with the correct spin and space symmetry, and it approximates the sum of the static and dynamic correlation energy without attempting to separate them. The use of the on-top density as

an ingredient in combining multi-configurational WFT with DFT is not new (see previous discussions and methods[48,52,57,58,60,74,91,199,322,407–410]), but the present approach of calculating the correlation energy from the on-top density, without using the CASSCF wave function to estimate the correlation energy, avoids the double counting of the portion of the correlation energy that is contained in the MCSCF energy estimate. This double counting problem has been one of the chief drawbacks of previous attempts to combine density functional theory with a multi-determinantal representation of the density.

In previous work we obtained first approximations to the on-top density functional by a translation prescription starting with the local-spin-density approximation or a gradient approximation (GA) to the exchange-correlation functionals. For example we obtained the translated PBE functional called tPBE by translating the PBE[199] exchange-correlation functional. In the translation prescription, we did not translate the gradient of the on-top density. The first goal of the present article is to show that we can include the gradient of the on-top density (resulting in a functional we call fully translated PBE or ftPBE) in a stable way, and we illustrate the fully translated functional by results on the CE56 database that we presented in a previous paper.[406] The second goal of the present paper is to present calculated potential energy curves for Cr_2, Cu_2, and Ag_2 with MC-PDFT using both the tPBE and ftPBE functionals.

9.3 Theory

See Chapter 7, section 3

9.4 Translated and Fully Translated Functionals

A gradient approximation to the exchange-correlation energy can be written in terms of the total density ρ, the spin magnetization density m, and the magnitudes ρ´ and of their gradients, where

$$\rho(\mathbf{r}) = \rho_\alpha(\mathbf{r}) + \rho_\beta(\mathbf{r}) \tag{1}$$

and

$$m(\mathbf{r}) = \rho_\alpha(\mathbf{r}) - \rho_\beta(\mathbf{r}) \tag{2}$$

and where ρ_α is the density of spin-up electrons, and ρ_β is the density of spin-down electrons at a point **r**. We then write the functional dependence of a gradient approximation as

$$E_{\mathrm{xc}} = E_{\mathrm{xc}}\,(\rho, m, \rho', m') \tag{3a}$$

where

$$\rho' = \nabla\rho \tag{3b}$$

$$m' = \nabla m \tag{3c}$$

To enable the treatment of open-shell states with a proper representation of the symmetry, the spin-free quantities ρ and Π, are used, where Π is the on-top pair density defined by[91]

$$\Pi(\mathbf{r}) = \binom{N}{2} \int |\Psi(x_1, x_2, \ldots, x_N)|^2 d\sigma_1\, d\sigma_2 \ldots d\sigma_N d\mathbf{r}_3 d\mathbf{r}_4 \ldots d\mathbf{r}_N \Big|_{\mathbf{r}_1=\mathbf{r}_2=\mathbf{r}} \tag{4a}$$

In eq 4a, N is the number of electrons, Ψ is the wave function, and x_i denotes the spatial ($\mathbf{r}_i$) and spin (σ_i) coordinates of electron i. Note that our definition of Π differs from that in Ref. [91] by a factor of 2 (we use the definition of Ref. [58]). If a wave function is a single Slater determinant, one can show that[91]

$$m(\mathbf{r}) = \rho(\mathbf{r})\chi(R(\mathbf{r})) \tag{4b}$$

where

$$\chi\left(R\right) = \left[1 - R\right]^{1/2} \tag{4c}$$

and

$$R(\mathbf{r}) = \frac{4\Pi(\mathbf{r})}{\left[\rho(\mathbf{r})\right]^2} \tag{4d}$$

For a single Slater determinant, $R \leq 1$ at all points in space. However, for wave functions that are multiconfigurational, eq 4b is not true, and R can be larger than unity.[91]

In MC-PDFT we use ρ and Π to define the on-top density functional. Although eventually new on-top functionals should be developed directly in terms of ρ and Π, in our work so far we obtain the on-top functional by "translating" existing exchange-correlation functionals. In our original translation,[46] we used the following prescription for translation:

$$E_{\text{ot}}\left[\rho(\mathbf{r}),\Pi(\mathbf{r})\right] = E_{\text{xc}}\left(\rho(\mathbf{r}),\left\{\begin{array}{c}\rho(\mathbf{r})(1-R)^{1/2} \text{ if } R \leq 1 \\ 0 \text{ if } R > 1\end{array}\right\},\rho'(\mathbf{r}),\left\{\begin{array}{c}\rho'(\mathbf{r})(1-R)^{1/2} \text{ if } R \leq 1 \\ 0 \text{ if } R > 1\end{array}\right\}\right) \tag{5}$$

where $E_{\text{xc}}(\rho, m, p', m')$ was introduced in eq 3a. We call this translation of a GA functional, "tGA", where "t" denotes "translated". We have tested tPBE and tBLYP in previous work.[46,406] In eq.5, only the gradient of the total density is used and we did not include the gradient of the on-top pair density due to the discontinuity when $R > 1$.

There are two reasons to go beyond the above translation. First of all, we want to include the gradient of the on-top density to be able to take advantage of the physics contained in this quantity when we design new density functionals. Second, we want the

functional to have continuous first and second derivatives to facilitate the later incorporation of the on-top density functional into the SCF procedure. In order to include the gradient of the on-top pair density in a continuous way, we first make a new translation that is continuous with continuous first and second derivatives. After systematic testing, we chose the following translation prescription for a "fully translated" gradient approximation or "ftGA":

$$E_{\mathrm{ot}}^{\mathrm{ftGA}}[\rho(\boldsymbol{r}),\Pi(\mathbf{r})] = E_{xc}\left(\rho(\boldsymbol{r}),\begin{cases}\rho(\boldsymbol{r})\chi_t(R) & \text{for } R < R_0\\ \rho(\boldsymbol{r})\chi_{ft}(R) & \text{for } R_0 \le R \le R_1\\ 0 & \text{for } R > R_1\end{cases},\right.$$
$$\left.\rho'(\boldsymbol{r}),\begin{cases}\rho'(\boldsymbol{r})\chi_t(R) + \rho(\boldsymbol{r})\chi_t'(R) & \text{for } R < R_0\\ \rho'(\boldsymbol{r})\chi_{ft}(R) + \rho(\boldsymbol{r})\chi_{ft}'(R) & \text{for } R_0 \le R \le R_1\\ 0 & \text{for } R > R_1\end{cases}\right) \quad (6)$$

where $\chi_t(R)$, $\chi_{ft}(R)$, $\chi_t'(R)$, and $\chi_{ft}'(R)$ are defined as

$$\chi_t(R) = (1-R)^{\frac{1}{2}}$$

$$\chi_{ft}(R) = A(R-R_1)^5 + B(R-R_1)^4 + C(R-R_1)^3$$

$$\chi_t'(R) = -\frac{1}{2}R'(1-R)^{\frac{-1}{2}}$$

and

$$\chi_{ft}'(R) = R'[5A(R-R_1)^4 + 4B(R-R_1)^3 + 3C(R-R_1)^2]$$

where A, B, and C are determined such that E_{ot} is continuous with continuous first and second derivatives, and where R_0 and R_1 are unitless parameters. Based on a combination of smoothness and accuracy considerations in our preliminary trials, we set $R_0 = 0.9$ and $R_1 = 1.15$. The continuity conditions then yield

A = -475.60656009
B = -379.47331922
C = -85.38149682

Equation 6 has no discontinuity and utilizes the entirety of the gradient. Moreover, we can interpret this procedure as a redefinition of $\chi(R)$, namely

$$\chi(R) = \begin{cases} \chi_t(R) & \text{for } R < R_0 \\ \chi_{ft}(R) & \text{for } R_0 \leq R \leq R_1 \\ 0 & \text{for } R > R_1 \end{cases} \quad (7a)$$

so that

$$\chi'(R) = \begin{cases} \chi'_t(R) & \text{for } R < R_0 \\ \chi'_{ft}(R) & \text{for } R_0 \leq R \leq R_1 \\ 0 & \text{for } R > R_1 \end{cases} \quad (7b)$$

If R_0 and R_1 were equal to 1.0, then $E_{\text{ot}}^{\text{ftGA}}$ would equal $E_{\text{ot}}^{\text{tGA}}$. We plot $\chi(R)$ as a function of R, eq. 7a, in Fig. 9.1.

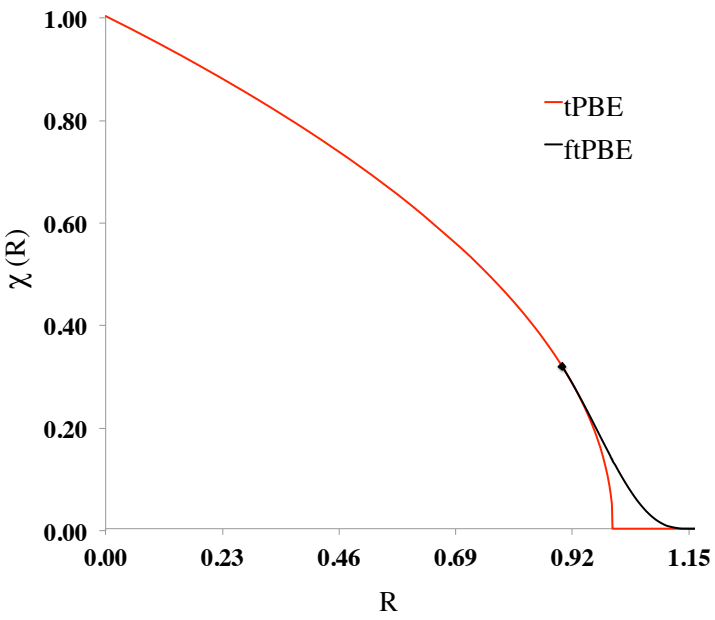

Figure 9.1. Plot of tPBE and ftPBE approximations to χ as a function of R. In the original translation (as used in tPBE), the red curve is followed for $0 < R \leq 1.0$, and χ is zero beyond that. In the full translation (as used in ftPBE), the red curve is followed when $0 < R < 0.9$, the black curve is followed when $0.9 \leq R \leq 1.15$, and χ is zero beyond that; this piecewise curve is continuous with continuous first and second derivatives.

9.5 Test systems

9.5.1 CE56 Database and its Subdatabases

The CE56 database was presented in an earlier paper.[406] It contains 18 bond energies (6 main-group non-alkyl, 2 alkyl, and 8 transition-metal), 24 diverse barrier heights, 10 diverse reaction energies, 3 proton affinities, and the complexation energy of the water dimer. Except for AgH, all data in the CE56 database are non-relativistic electronic energies (including nuclear repulsion for molecules). For values derived from experiment, the rotational-vibrational and zero-point energies and the spin-orbit energy have been removed from experimental values as described in detail in previous work.[364] For atomization energies, we divide the atomization energy by the number of bonds in the molecule to produce the average bond energy for that molecule (thus we call these results bond energies or atomization energies per bond; the reason for this division is so that the large atomization energies of large molecules do not have an excessive effect on the mean errors). The seven subdatabases that compose the CE56 database are all based on previous work[81,173,309,364,365,368,370–372,375,411] and are explained in Table 8.1.

9.5.2 Transition Metal Dimers and a Dinuclear Complex

We chose to study Ag_2, Cu_2, and Cr_2 because they represent some difficult cases for which accurate experimental results are available. We selected Os_2 for study because a recent study identified it as a difficult system for KS-DFT. Finally will study excitation energies in $Re_2Cl_8^{2-}$ ion.

9.6 Computational Details

For the CE56 database, all MC–PDFT, CASSCF, and CASPT2 calculations were performed with a locally modified version of the *Molcas 8.1* electronic structure package.[120] All calculations for this database are non-relativistic except when the Ag atom is present (see below). Geometries were obtained from the respective databases specified in Table 8.1. The basis sets used for the database containing transition metals were def2-TZVP[174] for metals and ma-TZVP[373] for other atoms. For Ag, the def2-TZVP relativistic effective core potential was used. Calculations for all databases not containing transition metals used the MG3S[374] basis set. Atomization energies are computed as the difference between the sum of the energies of the atoms and the energy of molecule.

Reasonable CASSCF active spaces were selected for each system to appropriately describe the chemistry in each case. The active spaces for the transition metal dimers are specified in footnotes to tables; active spaces used for CE56 are the same as used previously. In all cases we use the same active space for CASSCF, CASPT2, and MC-PDFT.

All CASPT2 calculations in this article were performed with the standard imaginary shift[126] value of 5.44 eV that serves to remediate the issue of intruder states. We also follow the usual convention of employing an "IPEA shift" in the zeroth order Hamiltonian of CASPT2. Except where specified otherwise (for Cr_2) we employ the *Molcas* default IPEA shift of 6.80 eV that was determined empirically[340] by considering the calculated dissociation energies of a database of 49 diatomic molecules. Note that the imaginary shift and the IPEA shift have no effect on the CASSCF or MC-PDFT results

(MC-PDFT does not have the intruder state problem, and it does not require an empirical shift parameter.)

In the CASPT2 calculations, we did not correlate the core orbitals. In particular, for the main group we did not correlate 1s orbitals; for the second period, we did not correlate 1s, 2s, and 2p orbitals, except for Si for which we only did not correlate 1s and 2s; for 3d transition metals we did not correlate 1s, 2s, 2p, and 3s orbitals; and for Ag we did not correlate 1s, 2s, 2p, 3s, 3p, 3d, and 4s orbitals.

For Os_2, we did not correlate 1s, 2s, 2p, 3s, 3p, 3d, 4s, 4p, and 4d orbitals. For $Re_2Cl_8^{2-}$, we correlate only the 5p and 5d orbitals of Re and only the 3s and 3p orbitals of Cl. KS–DFT results (PBE) for CE56 are presented for comparison and were obtained from previous work.[372]

For the three potential curves of transition metal dimers presented in this paper, we used individually selected basis sets. For Cr_2, the cc-pVTZ-DK basis sets was used.[339] For Cu_2, def2-TZVP[174] with the Douglas-Kroll-Hess (DKH) Hamiltonian[412] was used. For Ag_2 we used the def2-TZVP basis set with a effective core potential replacing 28 electrons.[174]

For calculating the equilibrium internuclear distance and excitation energy of Os_2, we used the ANO-RCC basis set with the [9s8p6d4f3g][47] contraction and with the DKH Hamiltonian. For $Re_2Cl_8^{2-}$, we used the ANO-RCC-VTZP[47,48] basis set with DKH Hamiltonian.

9.7 Results

We tested the new ftPBE functional using the same representative CE56 database that was used to benchmark our tPBE functional – see Table 8.1. The average errors are shown in Tables 9.1 and 9.2, and the complete data can be found in Appendix 7.

After testing the stability of the ftPBE functional against the dataset and finding improved performance for transition metal systems, we tested our ftPBE functional on some transition metal dimers that are a challenge for quantum chemistry, as discussed in the introduction. The results for equilibrium geometries and dissociation energies are shown in Tables 9.3-9.5. We also show the potential energy curves in Figs. 9.2-9.4.

9.8 Discussion

9.8.1 CE56 Dataset

The overall performance of the ftPBE functional, which includes the gradient of both ρ and Π, is similar to that of tPBE for the CE56 database, 3.2 kcal/mol for tPBE and 3.3 kcal/mol for ftPBE as shown in Table 9.1. For the main group energetics, the average errors are slightly lower for tPBE compared to ftPBE and the performance is still better than PBE by about a factor of 2 and worse than CASPT2 by about 1 kcal/mol. For transition metal atomization energies, ftPBE improves upon the performance of tPBE and has about 1.5 kcal/mol smaller error than CASPT2. The errors are approximately cut in half with ftPBE when compared to PBE. In all the datasets, ftPBE lowers the errors relative to CASSCF, a method that is missing substantial dynamic correlation in its energies.

Table 9.1. Average mean unsigned errors (kcal/mol) for entire database and breakdown into subdatabase containing transition metals and the rest.

	CASSCF	CASPT2	ftPBE[a]	tPBE[b]	PBE
MUE(CE56)[c]	12.4	2.7	3.3	3.2	6.9
MUE(TMABE10)[d]	22.2	5.5	3.9	4.6	7.6
MUE(MGE46)[e]	10.3	2.0	3.1	2.9	6.7

[a] $R_0 = 0.90$; $R_1 = 1.15$ in eq. 9

[b] $R_0 = 1$; $R_1 = 1$ in eq. 9

[c] The mean unsigned errors averaged over all data in the database

[d] The mean unsigned errors from the transition metal subdatabase

[e] The mean unsigned errors averaged over all data except those for molecules containing transition metals

The performance of ftPBE for the subdatabases that make up the CE56 dataset is shown in Table 9.2. For main group atomization energies, ftPBE is similar to tPBE and halves the errors relative to PBE and CASPT2. For reaction barrier heights, ftPBE gives slightly higher errors by around 0.2 kcal/mol than tPBE, but still outperforms PBE. For these types of energetics, despite the addition of the gradient of the on-top pair density, CASPT2 still outperforms ftPBE, as well as tPBE, but that performance comes at the cost of greatly increased computation time and memory. Comparing the reaction energies of the various methods, ftPBE does about the same as tPBE and falls between the performance of CASPT2 and PBE. In the case of proton affinities, the errors for ftPBE have increased relative to tPBE, but are no worse than PBE and similar to CASPT2. Alkyl bond dissociation energies are another case where ftPBE has about doubled the errors that were found with tPBE, but are still over a factor of 3 times smaller than PBE. Lastly, the energy of hydrogen bonding for a water dimer has the largest increase in errors by a factor of 6.5 for ftPBE relative to tPBE. Even in this case, it is no worse than CASPT2. In all cases in Table 9.2, ftPBE lowers the average errors relative to CASSCF.

Table 9.2. Average mean unsigned errors (kcal/mol) for subdatabases

	CASSCF	CASPT2	ftPBE	tPBE	PBE
MGABE6	16.5	3.8	2.2	2.3	4.4
TMABE10	22.2	5.5	3.9	4.5	7.6
DBH24/08	10.0	1.6	3.3	3.1	8.5
DRE10	8.5	2.5	4.4	4.1	6.0
PA3	5.5	0.6	1.0	0.3	1.0
ABDE2	19.1	2.6	2.5	0.5	8.3
WDCE1	0.96	0.5	1.3	0.2	0.5

Although the fully translated functional does not result in a decrease in the average error, we consider the incorporation of the gradient of the on-top pair density a success for the following reasons. First of all, we have now shown that the results are not sensitive to full translation of an existing GA functional, which is physically satisfying. Second we want to be able to take advantage of the gradient of the on-top density when we design improved functionals, so it is important that we have established a stable starting point for such optimization.

Finally, results presented in the supporting information show that ftPBE is not as sensitive to basis set as CASPT2, which is another attractive feature of this method.

9.8.2 Ag_2

Experimentally, the silver dimer has an equilibrium bond length of 2.530 Å.[413] Most computational methods tend to overestimate the equilibrium bond length of Ag_2 and as shown in Table 9.3, our results also show an elongated equilibrium geometry compared to experiment. It is well known that CASSCF does not recover all the dynamic correlation, and post-SCF methods such as CASPT2 are necessary to account for this correlation. The ground state geometry shortens in length from 2.767 Å by CASSCF to

2.548 Å by CASPT2. The ground state geometries obtained by both MC-PDFT functionals are more similar to KS-PBE than to CASPT2, but are within 0.05 Å of experiment. Comparing tPBE with ftPBE, i.e., adding the gradient of Π and smoothing the translation, decreases the equilibrium bond length, although only modestly.

Table 9.3. Silver dimer geometries and dissociation energies with the def2-TZVP basis set

	R_e (Å)	D_e (eV)
CASSCF[a]	2.767	0.74
CASPT2[a]	2.548	1.58
tPBE[a]	2.580	1.50
ftPBE[a]	2.575	1.64
PBE	2.574	1.77
Exp.	2.530[b]	1.65±0.03[c]

[a] The active space was 2/2, corresponding to the 4*s* electrons and orbitals. [b] Ref. [413] [c] Ref. [414]

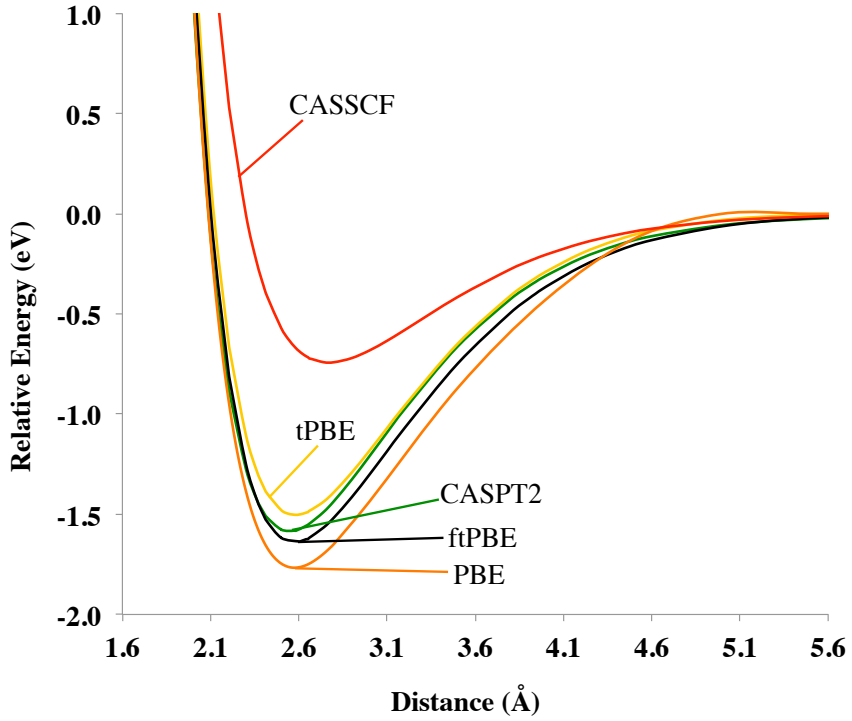

Figure 9.2. Silver dimer potential energy curves with def2-TZVP basis set

For the dissociation energy, ftPBE is the most accurate of the methods tested in Table 9.3; and the improvement over tPBE is substantial. The dissociation energy increases from 0.74 eV for CASSCF to 1.64 eV for ftPBE, which shows that the effect of dynamic correlation is very large. The potential energy curves for Ag_2 are shown in Fig. 9.2, which shows that ftPBE potential energy curve is very reasonable.

9.8.3 Cr_2

The chromium dimer is a well known example where accounting for intrinsically multi-determinantal character is essential. The potential energy curves are shown in Figure 9.3 for the various methods tested in this work.

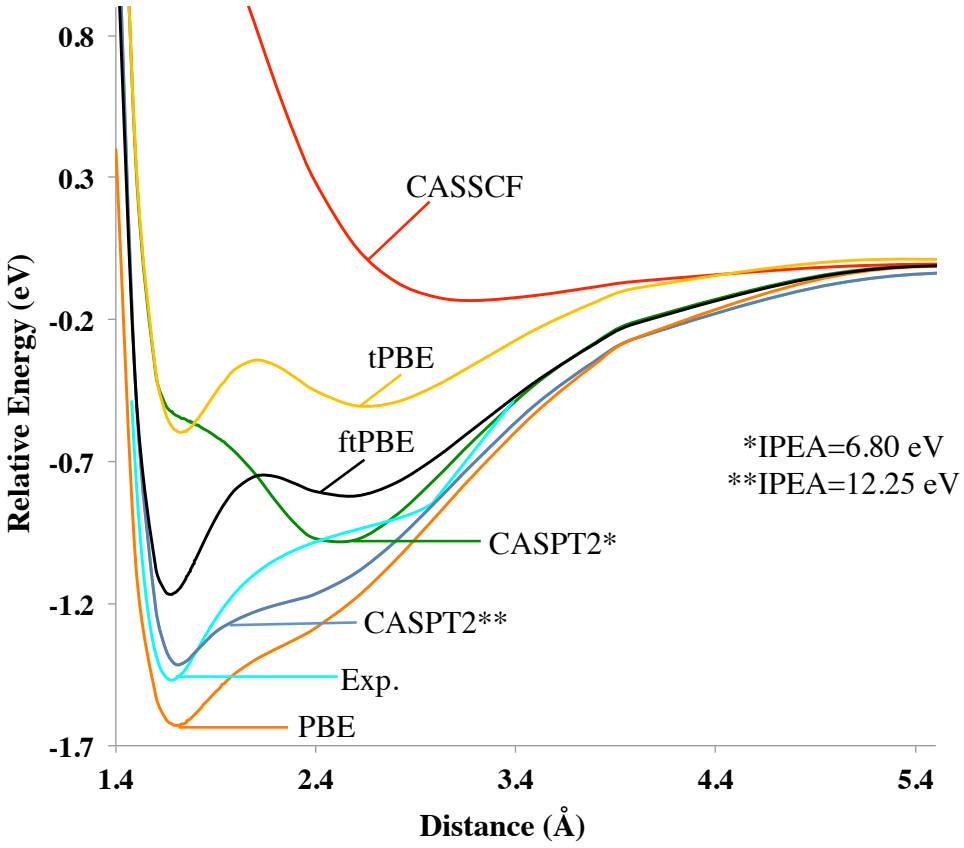

Figure 9.3. Chromium dimer potential energy curves with cc-pVTZ-DK basis set.

Experimentally, the equilibrium bond distance is 1.680 Å with a small shoulder in the potential energy curve around 2.6 Å.[219] At the CASSCF level, the molecule is not bound. In Fig. 9.3, we show the two different CASPT2 curves, corresponding to two different values of the empirical IPEA shift, and these curves are qualitatively different. One curve, obtained with the standard empirical IPEA shift parameter of 6.80 eV that is the default in MOLCAS, has a qualitatively incorrect minimum around 2.5 Å. For Cr_2, Ruipérez et al found that an molecule-specific value of 12.25 eV;[341] this molecule-specific value changes the equilibrium geometry to 1.713 Å with a small shoulder between 2.5 and 2.6 Å. Using the same CASSCF reference wave function as CASPT2, ftPBE correctly describes the dissociation of Cr_2 and, unlike CASPT2, one does not encounter the problem of intruder states or the necessity of fine-tuning empirical parameters. The equilibrium bond distance for ftPBE is only 0.006 Å shorter than experiment, and there is a small minimum around 2.6 Å. Compared to tPBE, which has two minima of approximately equal depth, the ground state geometry is shortened by adding the gradient of Π and smoothing the translation in the functional. The shape of the PBE curve is qualitatively correct but has an elongated equilibrium geometry.

The experimental dissociation energy of Cr_2 is 1.47 eV (Table 9.4). As with Ag_2, PBE overestimates the dissociation energy – in this case by 0.16 eV. For CASPT2 with the default IPEA value of 6.80 eV, the dissociation energy is 0.99 eV, but the potential energy curve has the wrong shape. For CASPT2 with an IPEA value of 12.25 eV, the dissociation energy is 1.42 eV. The effect of adding the gradient of Π and having a smooth translation in the functional is shown clearly by the ftPBE potential energy curve.

The shape of the ftPBE potential energy curve approaches experiment, and the dissociation energy is nearly double that of tPBE.

Table 9.4. Chromium dimer geometries and dissociation energies with the cc-pVTZ-DK basis set

	R_e (Å)	D_e (eV)
CASSCF[a]	-	0.00
CASPT2[a]	2.506	0.99[*]
CASPT2[a]	1.713	1.42[**]
tPBE[a]	1.727	0.60
ftPBE[a]	1.674	1.17
PBE	1.703	1.63
Exp.	1.680[b]	1.47[b]

[a] The active space for the CASSCF, tPBE, and ftPBE calculations is 12/12, corresponding to the 3*s* and 3*d* electrons and orbitals. For CASPT2, [*] denotes IPEA= 6.80 eV, and [**] denotes IPEA= 12.25 eV.[415] With CASSCF, the molecule is not bound.
[b] Ref. [219]

9.8.4 Cu_2

Experimentally, the copper dimer has an equilibrium bond length of 2.219 Å.[416] As for Ag_2, the tendency of theoretical methods is to overestimate the equilibrium bond length. In Table 9.5, all methods tested overestimate the equilibrium geometry, with PBE being the closest to experiment. Both tPBE and ftPBE shorten the geometry compared to CASSCF by about 0.2 Å, but both are longer than CASPT2 and PBE. For ftPBE, there is a slight decrease of bond length compared to tPBE.

The potential energy curves for the copper dimer are shown in Fig. 9.4. PBE overestimates the dissociation energy by 0.15 eV, and CASSCF substantially underestimates it – by about 1.1 eV. The CASPT2 and tPBE curves are similar in shape and have dissociation energies of 1.86 and 1.85 eV, respectively. Similarly to the other

two dimers, adding the gradient of Π and having a smooth translation in the functional results in an increase in the dissociation energy for ftPBE. Compared to experiment, the ftPBE dissociation energy is 0.1 eV below the measured dissociation energy.

Table 9.5. Copper dimer geometries and dissociation energies with the def2-TZVP basis set with DKH

	R_e (Å)	D_e (eV)
CASSCF[a]	2.456	0.87
CASPT2[a]	2.246	1.86
tPBE[a]	2.258	1.85
ftPBE[a]	2.255	1.98
PBE	2.235	2.23
Exp.	2.219[b]	2.08 ± 0.02[c]

[a] The active space was 2/2, corresponding to the 3*s* electrons and orbitals. [b] Ref. [414] [c] Ref. [416]

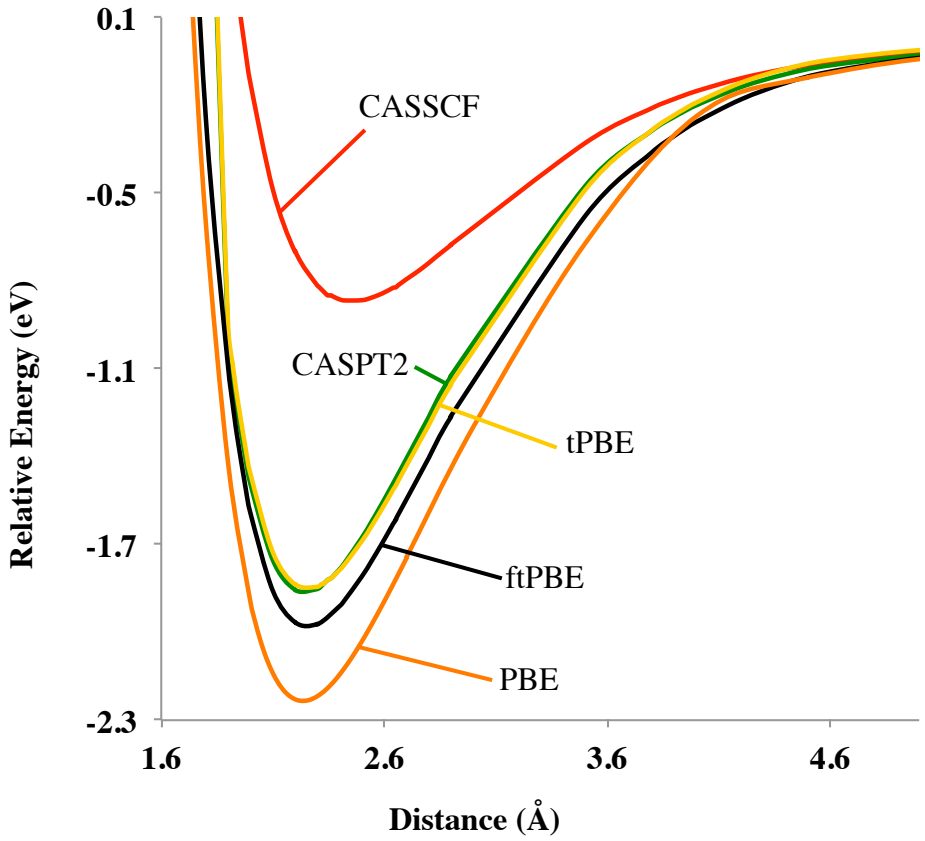

Figure 9.4. Copper dimer potential energy curves with def2-TZVP basis set and DKH relativistic Hamiltonian.

9.8.5 Os_2

Compared to other transition metal dimers, there are fewer theoretical studies on Os_2. Due to its multiconfigurational character, the predictions depend strongly on the choice of functional and basis set, with the calculated ground state being either $^7\Delta_u$ or a $^5\Pi_u$.[417–420] In addition to a KS-DFT study, Kim et al[420] reported CASSCF, CASPT2, MRMP2, and MRCI wave function results for Os_2, and they predicted that the ground state is the $^5\Pi_u$ state. In Table 9.6, we report our calculated values for the dissociation energy and equilibrium geometry of Os_2 and in Table 9.7 we compare the energetics of the $^7\Delta_u$ and $^5\Pi_u$ states. To compare the experimental ground-state dissociation energy, D_0, we subtracted the zero-point vibrational energy, which was calculated to be 0.02 eV by using the VIBROT module in MOLCAS. The resulting D_0 values are in Table 9.6.

Table 9.6. Osmium dimer geometries and dissociation energies of the $^5\Pi_u$ state

	R_e (Å)	D_o (eV)
CASSCF[a]	2.163	1.36
CASPT2[a]	2.103	4.56
tPBE[a]	2.122	4.33
ftPBE[a]	2.121	4.25
PBE[b]	2.122	4.64
Exp.	N/A	4.3 ± 0.8[c]

[a] The active space was 16/12, corresponding to the 5*d* and 6*s* electrons and orbitals. The basis set is ANO-RCC [9s8p6d4f3g] basis set, and scalar relativistic effects are included by the DKH method.
[b] For Os_2, PBE results were obtained with the def2-TZVP basis set and a scalar-relativistic ECP.
[c] Ref. [195]

Table 9.7 shows that both tPBE and ftPBE predict a $^5\Pi_u$ ground state. While there is a large range of experimental values for the dissociation energy, many of the functionals tested by Kim and Kim[420] predict a dissociation energy (in a range form 1.83

to 5.47 eV) that does not fall with within the experimental range. The underestimation of many functionals is due, in part, because they predict the $^7\Delta_u$ state as the ground state. The high-level MRCI+Q/dhf-QVPP and MRMP2/def2-QZVPP also (apparently incorrectly) predict a septet ground state – by 0.36 and 0.17 eV respectively, and the calculated dissociation energies of these methods are 3.29 and 4.51 eV, respectively.[420] Considering the difficulty of the problem (the wide range of previous results) and the uncertainty in the experimental results, the tPBE and ftPBE results are both considered satisfactory.

Table 9.7. Osmium dimer geometries and relative energies of the $^7\Delta_u$ and $^5\Pi_u$ states

	R_e (Å)	ΔE^a (eV)
CASSCF[b]	2.306	0.25
CASPT2[b]	2.202	0.24
tPBE[b]	2.231	0.35
ftPBE[b]	2.235	0.37
PBE[c]	2.245	0.18

[a] $\Delta E = E(^7\Delta_u) - E(^5\Pi_u)$

[b] The active space was 16/12, corresponding to the 5*d* and 6*s* electrons and orbitals. The basis set is RCC [9s8p6d4f3g], and the DKH treatment of scalar relativistic effects is used.

[c] For Os_2, PBE results are obtained with the def2-TZVP basis set and a scalar-relativistic ECP.

9.8.6 $Re_2Cl_8^{2-}$

The $Re_2Cl_8^{2-}$ ion, like Cr_2, presents an example of metal-metal multiple bonding. The CASSCF calculations yield a significantly multiconfigurational $^1A_{1g}$ ground state (the weights of the two most important configurations are 66% and 15%) that has natural orbital occupation numbers of 1.54 and 0.46 in the δ and δ* orbitals, respectively.[421] The lowest-energy excitation is an intra-d-band transition, in particular, a δ to δ* transition ($^1A_{1g}$ to $^1A_{2u}$). The excited state is also significantly multiconfigurational (the weight of

the dominant configuration is 74%); it is an open-shell singlet and is a good test case for MC-PDFT. The excitations in this ion were examined with CASPT2, and those calculations reproduced the experimental electronic spectrum well.[422]

The excitation energies are shown in Table 9.8, calculated using the experimental geometry of Cotton et al.[3] With CASPT2, the $^1A_{1g}$ to $^1A_{2u}$ excitation energy is 2.03 eV compared to the experimental value of 1.82 eV.[422] PBE underestimates the excitation energy by 1.1 eV, and tPBE and ftPBE underestimate it by 0.6-0.8 eV, which is not useful accuracy. As usual for comparing the energies of states of different symmetry, the results in Table 9.8 correspond to carrying out separate CASSCF and CASPT2 calculations for each symmetry. Curiously, if we use the ground-state orbitals for both states (i.e., treat the excited state by CASCI with ground-state orbitals), the calculated excitation energies increase to 2.02 eV for tPBE and 1.89 eV for ftPBE, in better agreement with experiment but probably fortuitously. The sensitivity of the results to the way the orbitals are optimized will be an interesting subject for further study.

Table 9.8. $Re_2Cl_8^{2-}$ excitation energies for the δ to δ* transition ($^1A_{1g}$ to $^1A_{2u}$) with the ANO-RCC-VTZP basis set with DKH

	ΔE (eV)
CASSCF[a]	3.08
CASPT2[a]	2.03
tPBE[a]	1.18
ftPBE[a]	1.03
PBE[b]	0.69
Exp.[c]	1.82 ± 0.02

[a] The active space was 12/12 corresponding to eight Re-Re 5*d* bonding/anti-bonding orbitals and four Re-Cl bonding/anti-bonding orbitals
[b] ΔSCF energies
[c] Ref. [422]

9.9 Conclusions

We have presented a full-translation prescription for deriving on-top density functionals for MC-PDFT. The resulting functionals include the gradient of the on-top pair density as well as the total one-particle density, and they have continuous first and second derivatives. We find that MC-PDFT is stable with respect to including the gradient of the on-top density. Furthermore, we find that the new ftPBE on-top density functional performs about as well as the original tPBE translation for overall energetics of the CE56 database, but it provides an improvement for system with transition metal–transition metal bonds. To examine this further we present full potential curve calculations for Cr_2, Cu_2, and Ag_2., and these calculations show that our new ftPBE functional improves over the original tPBE functional in these cases. In the case of the transition metal dimers presented here, ftPBE has more accurate dissociation energies and bond lengths than tPBE and is more accurate than CASPT2 for dissociation energies. Although the bond lengths of the silver and copper dimers are elongated compared to experiment, consideration of the energetics and potential energy curves, particularly of the chromium dimer, seems to indicate that including the gradient of the on-top density accounts for important physics that is missing in the tGA translation.

We also present calculations on the difficult Os2 system and obtain satisfactory results for both bond lengths and quintet-septet splittings; the latter appear to be more accurate than values calculated by MRCI. Finally we present results for the $\delta \rightarrow \delta^*$ excitation of $Re_2Cl_8^{2-,}$ where the method is less successful.

We hope it will be possible to build on the present results in designing new

functionals. The good accuracy obtained so far with MC-PDFT is encouraging. One can obtain results comparable in quality to CASPT2 but at much lower cost and with lower basis-set dependence, as well as having the spatial and spin symmetries of the approximated states represented explicitly and correctly. The method is very promising for treating systems that are intrinsically multi-determinantal in character.

Chapter 10

Separated-Pair Approximation and Separated-Pair Pair-Density Functional Theory

Reproduced in part from

Separated-Pair Approximation and Separated-pair Pair-Density Functional Theory, S. O. Odoh, G. L. Manni, R. K. Carlson, D. G. Truhlar and L. Gagliardi, *Chem. Sci.*, 2016, **7**, 2399. Published by the PCCP Owner Society.

10.1 Overview

Multi-configuration pair-density functional theory (MC-PDFT) has proved to be a powerful way to combine the capabilities of multi-configuration self-consistent-field theory to represent the electronic wave function with a highly efficient way to include dynamic correlation energy by density functional theory. All applications reported previously involved complete active space self-consistent-field (CASSCF) theory for the reference wave function. For treating large systems efficiently, it is necessary to ask whether good accuracy is retained when using less complete configuration interaction spaces. To answer this question, we present here calculations employing MC-PDFT with the separated pair (SP) approximation, which is a special case (defined in this article) of generalized active space self-consistent-field (GASSCF) theory in which no more than two orbitals are included in any GAS subspace and in which inter-subspace excitations are excluded. This special case of MC-PDFT will be called SP-PDFT. In SP-PDFT, the electronic kinetic energy and the classical Coulomb energy, the electronic density and its gradient, and the on-top pair density and its gradient are obtained from an SP approximation wave function; the electronic energy is then calculated from the first two of these quantities and an on-top density functional of the last four. The accuracy of the SP-PDFT method for predicting the structural properties and bond dissociation energies of twelve diatomic molecules and two triatomic molecules is compared to the SP approximation itself and to CASSCF, MC-PDFT based on CASSCF, CASSCF followed by second order perturbation theory, CASPT2, and Kohn-Sham density functional theory with the PBE exchange–correlation potential. We show that SP-PDFT reproduces the accuracy of MC-PDFT based on the corresponding CASSCF wave function for predicting C-H bond dissociation energies, the reaction barriers of pericyclic reactions and the properties of open-shell singlet systems, all at only a small fraction of the computational cost.

10.2 Introduction

There is strong interest in the development of quantum chemical methods for accurately treating large systems with inherently multiconfigurational electronic structures at affordable computational cost.[423–425] Such systems are also called multireference systems or strongly correlated systems, and they are usually treated, at least as a first-order approximation, by multiconfigurational self-consistent field (MCSCF) methods.[355] This approach includes static electron correlation that would be neglected if a single electronic configuration were employed. In MCSCF methods, one

simultaneously variationally optimizes all the orbitals and the coefficients of the various configurations in a configuration interaction (CI) expansion of the electronic wave function. There are several possible ways to select the configurations that are included. In the complete active space self-consistent field (CASSCF) method, a Full Configuration Interaction (FCI) expansion of the wave function is constructed over an active space of n electrons in N orbitals, with other orbitals double occupied (inactive) or vacant.[34,36] The size of the FCI expansion grows exponentially as the active space is enlarged, such that an active space with n = 18 and N = 18, labeled as CAS(18,18), is already at the limit of what is affordable. For medium-to-large systems, the active space limit, CAS(18,18), is typically not large enough to describe bond-breaking, electronic excitations, and other chemical properties in a balanced fashion. Thus well-balanced CASSCF calculations are in practice limited to the study of small-to-medium systems.

Generally, most of the configurations in the FCI expansion of the active space in CASSCF computations make only small contributions to the total wave function. As a result, Ruedenberg and coworkers suggested that these configuration state functions (CSFs) are "deadwood" that can be excluded without significantly affecting the accuracy of the results.[39,426,427] The generalized active space (GAS)[41] restricted active space (RAS)[40,358] occupation restricted multiple active spaces (ORMAS)[320] and Split-GAS[318,428] approaches are some of the frameworks that attempt to remove deadwood CSFs by partitioning the active space into subspaces. We have previously shown that active spaces larger than the CAS(18,18) limit can be attained with the generalized active space self-consistent-field theory, GASSCF.[41,318,428]

These MCSCF-type wave functions (CASSCF, GASSCF, etc.) can recover static correlation effects well, but are impractically slowly convergent (with respect to active space size) for the dynamic correlation energy, which is necessary for chemically accurate energetic calculations. For higher accuracy they can be used as zeroth-order reference functions in post-SCF perturbative, multireference coupled-cluster (CC), or multireference configuration interaction (CI) calculations to obtain a good approximation to the dynamic correlation energy. CASPT2 is a popular example that applies second-order perturbation theory to a CASSCF zero-order wave function.[37,429] Such approaches, while capable of high accuracy,[415,430,431] are however not suited for studying large systems because their computational costs rise rapidly with system size.

We have recently proposed an approach for treating strongly correlated systems at much lower computational costs than CASPT2, by combining CASSCF with density functional theory (DFT). This approach is called multiconfigurational pair-density functional theory (MC-PDFT).[46] It may be considered to be a multiconfigurational analog of Kohn-Sham[42] density functional theory[305] (KS-DFT). In KS-DFT, the energy is computed as the kinetic energy and classical Coulomb energy of a Slater determinant (which is a single-configuration reference wave function) and a one-electron integral over an exchange-correlation functional of the one-electron density of the Slater determinant. The classical Coulomb energy includes the nuclear attraction of the electrons, the classical interelectronic repulsion of the electronic charge density, and the nuclear repulsion. The exchange-correlation density functional includes electron exchange, electron correlation, and the difference between the exact kinetic energy and that

computed from the Slater determinant. The exact exchange-correlation density functional is unknown, so one uses approximations. In MC-PDFT, the energy is computed as the kinetic energy and classical Coulomb energy of an MCSCF reference wave function and a one-electron integral over an on-top density functional of the one-electron density and the on-top pair density of the reference wave function. The on-top density functional includes electron exchange, electron correlation, and the difference between the exact kinetic energy and that computed from the reference wave function. The MC-PDFT energy may be written as

$$E = 2\sum h_{ii} + 2\sum g_{iijj} + \sum h_{vw}D_{vw} + 2\sum g_{iivw}D_{vw} + \frac{1}{2}\sum g_{vwxy}D_{vw}\,D_{xy} + V_{\mathrm{N}} + E_{\mathrm{ot}}[\rho,\Pi] \quad (1)$$

where orbital indices refer to the spatial molecular orbitals, *i* and *j* are the doubly occupied inactive orbitals, *v, w, x,* and *y* are the active orbitals, h_{vw} and g_{pqrs} are respectively, one-electron and two-electron integrals, D_{pq} is the one-electron reduced density matrix, V_N is the nuclear repulsion, and E_{ot} [ρ,Π] is an on-top density functional of the total density, ρ, and the on-top pair density, Π. Functional expressions for E_{ot} [ρ,Π] when using ρ and Π obtained from an MCSCF solution have been provided in references [46] and [406].

KS-DFT is usually applied full self-consistently; that is, the exchange-correlation functional is included during the SCF step. MC-PDFT can also in principle be applied fully self-consistently, but in all work reported so far and in the present article, we carry out the MCSCF calculation by CASSCF without the on-top density functional, and then calculate the final energy post-SCF from eq 1. In this post-SCF mode, MC-PDFT is like the perturbation theory, multireference CC, and multireference CI wave function methods

in that it attempts to use an MCSCF method to obtain a balanced reference wave function in an SCF step and to calculate an accurate energy in a post-SCF step. However, in the case of MC-PDFT, the cost of the post-SCF density functional step is negligible compared to the cost of the SCF step, whereas in the wave function methods like CASPT2, the post-SCF step is more expensive than the SCF step. The cost of the SCF step though is still prohibitive for large systems if one uses CASSCF as the MCSCF method. In the present article we test whether MC-PDFT can yield accurate results when based on a GASSCF wave function. In particular, we present a systematic way to choose the active space in GASSCF theory. This new way of choosing the active space is called the separated-pair (SP) approximation. The method is intermediate between generalized valence bond (GVB) theory and complete active space self-consistent-field (CASSCF) theory. We then use SP and CASSCF as reference wave functions for MC-PDFT. The MC-PDFT method based on a CASSCF and a SP reference wave function will be labeled as CAS-PDFT and SP-PDFT, respectively, when it is desired to distinguish the kind of MCSCF wave function being used as the reference.

The next section presents the relevant theory and defines the separated pair (SP) approximation. We then provide computational details, test sets, results, and discussion.

10.3 Theory

10.3.1 On-top density functionals. We have previously presented a prescription for translating existing exchange-correlation functionals of KS-DFT to on-top functionals.[46] As an example, tPBE is an on-top pair density functional developed by translating the PBE functional;[46] tPBE is a function of the electron density, its gradient, and the on-top

pair density. We have also described a "fully" translated functional called ftPBE that also depends on the gradient of the on-top pair density.[432]

10.3.2 Separated pair approximation. The first step in building a GASSCF wave function is to choose the number *m* of GAS subspaces and the number and type of orbitals in each GAS subspace. Note that not only in equation 1 but also in the whole rest of the article, when we talk about orbitals, we are referring to spatial orbitals, not spin-orbitals. We use the notation GAS-*m*(*n,N*) for *n* electrons in *N* orbitals divided into m subspaces. But this is not a complete specification; in addition, for each irreducible representation, one specifies the accumulated minimum and maximum electron occupations after each GAS subspace is added. For a GAS-*m*(*n,N*) calculation, the number of electrons in each space, the number and nature of orbitals in each space, and the number of inter-subspace excitations can significantly affect the number of CSFs in the CI expansion, and – by extension – the quality of the results obtained. A GAS wave function includes all configurations that can be defined within the restrictions imposed by the accumulated minimum and maximum electron occupations and by the restriction, if any, on inter-subspace excitations. The effects of these specifications on the computed properties of various molecules have been previously reported.[41,428,433]

In the present work, we only use GAS subspaces in which each subspace contains at most two orbitals, and interspace excitations are not allowed. A GASSCF calculation with these restrictions will be called the separated pair (SP) approximation, and when the number of subspaces is *m*, it will be abbreviated SP-*m*. If each subspace contains two electrons in two orbitals, this would be specified in the language of GASSCF as GAS-

$m(2m,2m)$ with the additional specification that no inter-subspace excitations are allowed. For singlet systems with an even number of electrons, we typically do have two electrons in two orbitals in each subspace, and the two orbitals in a given subspace are usually a bonding orbital and the corresponding antibonding orbital. This is reminiscent of the generalized valence bond perfect pairing (GVB-PP) algorithm,[434] but it is more general. The GVB-PP approximation has subspaces of two electrons in two orbitals coupled to a singlet; this involves two or three configurations, depending on symmetry. In the SP approximation, when there are two electrons in two orbitals, they may be coupled into either a singlet or a triplet, and the various triplet pairs may be coupled in all possible ways to obtain CSFs with the desired overall spin symmetry of the system (for example, if the overall wave function is a singlet, one may have CSFs where four of the pairs are triplets and all the others are singlets, and the four triplet pairs may be coupled to each other in a variety of ways to obtain an overall singlet); thus the SP approximation involves more possible configurations than does the GVB-PP approximation. Nevertheless, the SP approximation greatly reduces the number of CSFs in the CI expansion as compared to CASSCF. It is also important to note that we carry out a FCI expansion in each GAS subspace. This is because we allow both singles and double excitations in each subspace containing just two orbitals. The SP approximation is more similar to the generalized valence bond restricted pairing (GVB-RP) approximation[435] than to GVB-PP. A key advantage of SP and GVB-RP is that, unlike GVB-PP, they allow dissociation to high-spin fragments.[434,435]

In the SP approximation, every GAS subspace contains one electron in one or two

orbitals or two or three electrons in two orbitals, depending on the system. Intersubspace excitations are always excluded. For closed-shell systems (and for open-shell singlets that can be made by breaking a bond in a closed-shell system) an SP-*m* approximation always corresponds to GAS *m*(2*m* ,2*m*). But the value of *m* depends on which pairs are included in the active space and which are treated as inactive (doubly occupied in all CSFs), and that is an individual choice. For example, we treat the molecular orbitals with parentage in the 2s atomic orbitals as active for C_2 but inactive for N_2, O_2, and F_2. Moss and coworkers,[436] in their GVB-CI calculations on O_2, also removed the fully occupied $1\sigma_g$,$1\sigma_u$, $2\sigma_g$ and $2\sigma_u$ molecular orbitals from the active space. For F_2, we also treat the molecular orbitals with parentage in the $2p_x$ and $2p_y$ orbitals as inactive.

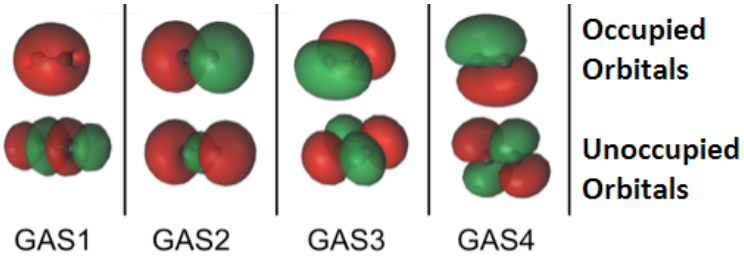

Figure 10.1. The four GAS subspaces used in the SP-4 approximation for the carbon dimer, C_2. In this scheme, the 2s, $2p_z$, $2p_x$, and $2p_y$ atomic orbitals form σ_g, σ_u, $\pi(p_x)$, and $\pi(p_y)$ (which are bonding or in the case of $2\sigma_u$, GAS2, antibonding) orbitals respectively as well as their antibonding (or in the case of $2\sigma_u$, GAS2, bonding) counterparts. These pairs are shown from left to right. The orbitals with an occupation close to two are placed at the *top*, while those that are nearly empty are placed at the *bottom*. Two electrons are placed in each GAS subspace. Intra-space excitations (up to double excitations) between a bonding orbital and its antibonding pair are allowed. Inter-subspace excitations between GAS subspaces are not allowed.

The SP approximation we used for the carbon dimer, C_2, is shown in Figure 10.1. This molecule has a closed-shell singlet ground state, and the orbitals shown in Figure 10.1 correspond formally (at equilibrium) to a double bond and a ground state

configuration of $2\sigma_g^2,2\sigma_u^2,1\pi_{ux}^2,1\pi_{uy}^2$. This corresponds to a double bond as the occupied $2\sigma_u$ orbital is actually of antibonding character. Within C_1 symmetry, there are 150 CSFs in this reference for the closed-shell singlet, as compared to 1764 CSFs in the analogous CAS(8,8) reference. (The analogous GVB-PP wave function would have only 16 CSFs). We note that the SP-4 reference correctly dissociates to two high-spin (3P) carbon atoms, just like the CAS(8,8) reference.

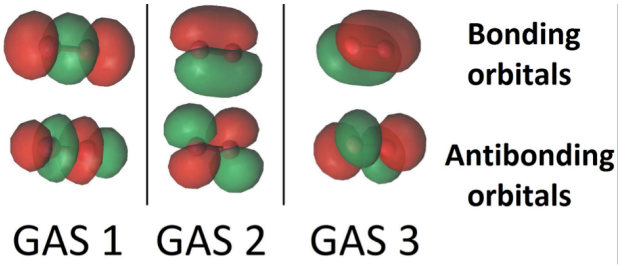

Figure 10.2. The three GAS subspaces used in SP calculations on triplet dioxygen, O_2. In this scheme, the $2p_z$ atomic orbitals form 3σ and 3σ* orbitals, and the $2p_x$ and $2p_y$ atomic orbitals form bonding $\pi(p_x)$, and $\pi(p_y)$ orbitals and correlating antibonding $\pi^*(px)$, and $\pi^*(py)$ orbitals. These are shown from left to right. GAS 1 contains two electrons while GAS 2 and GAS 3 each contain 3 electrons. Inter-subspace excitations between GAS spaces are not allowed.

The SP scheme for open-shell systems depends on the type of open-shell character. The SP-3 approximation that we used for O_2 is shown in Figure 10.2. O_2 differs from C_2 in that the σ bonding combination of 2p orbitals lies higher in energy than the π bonding combination for C_2 but lower for O_2. In O_2, as already mentioned, the 2σ and 2σ* molecular orbitals (which are predominantly formed from the 2s atomic orbitals) are kept inactive. Therefore the SP-3 approximation that we used for O_2 has GAS1 containing two electrons in the 3σg and 3σu orbitals (which are predominantly formed from the 2pz atomic orbitals), GAS2 containing three electrons in the $1\pi(p_x)$ and $1\pi^*(p_x)$ orbitals, and GAS3 containing three electrons in the $1\pi(p_y)$ and $1\pi^*(p_y)$ orbitals. This is a

GAS-3(8,6) reference. It contains 20 CSFs in comparison to 378 CSFs for the full valence CAS(12,8) and 105 CSFs for CAS(8,6). This GAS-3(8,6) reference also correctly dissociates into two ^{3}P oxygen atoms. The SP approximations we used for SO and S_2 are isoelectronic to that for O_2.

For the Cr dimer, Cr_2, we calculated the potential energy curve with an SP-6 approximation, equivalent to GAS-6(12,12), with the twelve valence orbitals coupled in six GAS subspaces and two active electrons in each GAS subspace. Within D_{2h} symmetry, there are 1516 CSFs in the SP-6 CI expansion, as compared to 28784 CSFs in the analogous CAS(12,12) CI expansion. The SP-6 approximation is sufficiently complete that the dimer correctly dissociates to two high-spin (^{7}S Cr) atoms.

For methylene triplet or methylene open-shell singlet, a full valence CAS is (6,6). We can think of CH_2 as derived from methane by dissociating two C-H bonds, and the antibonding orbitals associated with those bonds have left with the hydrogens. Thus these systems each have two singly occupied orbitals, which are taken as their own GAS subspaces with one electron in one orbital in each. In addition, they have two GAS spaces that each have two electrons in two orbitals. Thus, the separated pair approximation we use is SP-4, which is shorthand for GAS-4(6,6).

There are two important points to note. First, the SP approximation allows one to design GAS subspaces that contain only the bonding and antibonding orbitals necessary to describe a particular process. For example to compute the C-H dissociation energies of acetylene, ethylene and ethane, we included only orbitals relevant to C-H bonding in the SP active space. This formally leads to a SP-3 active space for both acetylene and

ethynyl, an SP-4 active space for both ethylene and vinyl, and an SP-6 active space for both ethane and ethyl. We illustrate this feature with several examples. For the ethyl radical, a full valence CAS space would be (13,13) with seven bonds. We think of this as derived from ethane by removing a hydrogen atom, and the antibonding orbital accompanies it. Constructing GAS subspaces with the same logic as explained above for methylene then yields an SP-7 approximation that is equivalent to GAS-7(13,13). However, when we study C-H bond dissociation in this paper, we treat the C-C bonding orbital as inactive and use an SP-6 approximation corresponding to GAS-6(11,11). Ethynyl has a full-valence CAS of size (9,9). Since we are interested in C-H bond dissociation, we made the four electrons in π 3(5,5) reference. Vinyl has a full valence CAS of size (11,11). Since we are interested in C-H bond dissociation in, and because we are interested in seeing the effect of aggressively reducing the size of the active space, we removed the four electrons in the C=C bond and the associated σ, σ^*, π, and π^* orbitals from the active space, which yields an SP-4 approximation, equivalent to GAS-4(7,7).

Second, the SP-1 approximation is equivalent to CASSCF(2,2), a case which applies to lithium hydride (LiH), as an example. In addition, as we are performing a full CI for each subspace, SP and SP-PDFT are size consistent in so far as the active space is chosen correctly. For all other molecules, the SP approximation used here involves an active pair for all or some of the bonds, as specified in each case. Nonbonding valence orbitals and core orbitals are always doubly occupied.

10.4 Computational Details

10.4.1 Basis sets

The aug-cc-pVTZ basis set is used to describe all the H, Li, B, C, N, O, F and S atoms in the molecules studied in this work.[337,338,437] For the Cr dimer we used the ANO-RCC basis set[121] containing [21s15p10d6f4g2h] primitive functions contracted to (10s10p8d6f4g2h).

10.4.2 Symmetry

For the Cr dimer, a D_{2h} point group was adopted. All other calculations in this work were carried out without symmetry. This is because the method is designed for large molecules that usually have no symmetry so we want to test it in that context. CASSCF calculations. We used full valence active spaces in CASSCF calculations on all the molecules studied in this work. The exceptions are ozone, for which we used CAS(12,9), α-3-didehydrotoluene and 1,4-didehydrobenzene, for which we used CAS(8,8), and the compounds involved in pericyclic reactions for which we included only the subset of π, π*, σ, and σ* orbitals of the carbon ring systems that are transformed during the reaction.

10.4.3 CASPT2 and CAS-PDFT

To include dynamic correlation, the CASSCF solutions are used as references in MC-PDFT and CASPT2 calculations. For MC-PDFT, we used the CAS-tPBE and CAS-ftPBE functionals.[46,432] These are our translated and fully translated functionals that use CASSCF solutions as references. For CASPT2, an empirical ionization-potential – electron-affinity (IPEA) shift of 0.25 atomic units (6.80 eV) is added to improve agreement with experiment.[340] To illustrate the dependence of CASPT2 on this empirical

parameter and to allow for a more standard comparison with MC-PDFT, we performed analogous calculations without the IPEA shift. These calculations are labeled as CASPT2-0. For the Cr dimer we also employed an IPEA value of 0.45 atomic units, as suggested for this specific system in previous work.8 All CASPT2 and CASPT2-0 computations used a standard imaginary shift of 0.2 atomic units (5.44 eV) to prevent intruder states.[126]

10.4.4 SP calculations

As in CASSCF and GASSCF in general, the CI coefficients are optimized via a Direct-CI procedure[438–440] while the orbital parameters are optimized through the Super-CI approach.[441] Intra-space rotations (inactive-inactive, virtual-virtual, gas1-gas1, gas2-gas2, ...) are redundant and are not included in the optimization step; only inter-subspace rotations are included in the orbital optimization procedure. SP-PDFT calculations are just like CAS-PDFT calculations, except that the reference wave function is a separated pairs approximation.

10.4.5 KS-DFT calculations

The results of calculations with CASPT2, CASPT2-0, CAS-tPBE, CAS-ftPBE, SP-tPBE and SP-ftPBE are compared with those obtained from KS-DFT calculations with the PBE[199] exchange-correlation functional.

10.4.6 Geometries

We used the experimental geometries of acetylene and ethylene as well as those of the ethynyl and vinyl radicals.[442] We optimized the structures of ethane and the ethyl

radical by M06-2X[363]/6-31G(d). For the pericyclic reactions, the geometries and zero point energies of the reactants and transition states were obtained at the B3LYP/6-31G(d) level by Houk and coworkers.[443] The geometries of methylene and ozone were optimized by scanning the bond lengths at various bond angles. The geometries of planar and twisted ethylene were obtained with the MR-CISD/SA-3-RDP/aug-cc-pVTZ method by Lischka and coworkers.[444] For α-3-didehydrotoluene and 1,4-didehydrobenzene, we use geometries optimized at the M06-2X/6-31G(d) level while using unrestricted Kohn-Sham DFT (abbreviated as UDFT).

10.4.7 Bond energies and atomization energies

All bond energies and atomization energies in this paper are potential energy differences excluding vibrational energies. Usually these are obtained from the literature, but for CH_2 the thermal correction to the enthalpy at 298 K obtained by KS-PBE/aug-cc-pVTZ is added to the empirical ΔH_{298} of CH_2. The frequency component of this correction was scaled using the scaling factor obtained from ref. [202] for this model chemistry.

10.4.8 Software

All the CASSCF, CASPT2, CASPT2-0, SP, and SP-PDFT calculations in this work were carried out with a locally modified version of the Molcas 7.9 program suite.[120] All KS-DFT calculations were carried out with the Gaussian 09 program.[129]

10.4.9 Systems Studied

In order to provide a broad test of the performance of SP-PDFT, we have

computed the structural properties and bond energies of twelve diatomic molecules (LiH, HF, B_2, C_2, CO, S_2, SO, NH, N_2, O_2, F_2, and Cr_2) and two triatomic molecules (CH_2 and O_3). We also studied C-H bond dissociation in three prototypical organic compounds (acetylene, ethylene and ethane) and the barrier heights of five pericyclic reactions. The pericyclic reactions are the electrocyclic ring opening of cyclobutene, the ring closing of cis-1,3,5-hexatriene and ortho-xylylene, and the sigmatropic shift reactions of 1,3-pentadiene and 1,3-cyclopentadiene. Finally, we examined the performance of SP-PDFT for describing the properties of open-shell singlet (OSS) systems, specifically the relative energies of planar and twisted ethylene, and the singlet-triplet separations in α-3-didehydrotoluene and 1,4-didehydrobenzene.

10.5 Results and Discussion

10.5.1 Diatomic molecules

The ability of an electronic structure method to provide potential energy surfaces or potential energy curves that accurately describe the formation and cleavage of chemical bonds is a very important test of its capabilities. This task is challenging for methods based on a single-configuration reference state; for example, coupled cluster theory with full inclusion of single, double, and triple excitations (CCSDT) fails to properly describe the dissociation of N_2 into two N atoms.[445] The spectroscopic constants (the equilibrium distances, R_e, and dissociation energies, D_e) of diatomic molecules have been computed with many theoretical methods (see refs.[446–448] for examples), and they are good test cases to compare the results obtained from SP-PDFT to those obtained with CAS-PDFT and CASPT2 as well as to accurate experimental data.

10.5.2 Equilibrium bond distances of diatomic molecules

In Figure 10.3, we show the performance of SP-PDFT and other methods for predicting the equilibrium bond distances of eleven diverse main-group diatomic molecules, LiH, HF, B_2, C_2, CO, S_2, SO, NH, N_2, O_2, and F_2, and one transition-metal diatomic molecule, Cr_2. The dominant configurations in the CASSCF wave functions when using full-valence complete active spaces have percentage weights of 98.0, 99.9, 78.5, 70.9, 94.3, 94.8, 95.0, 98.3, 92.8, 94.0, 93.2, and 44.3, respectively. Since molecules in which the dominant configuration has a weight of less than or equal to 95% are usually considered to be multireference, we see that nine of the twelve molecules are multireference ones, the Cr_2 case being the one least dominated by a single configuration, followed by B_2 and C_2.

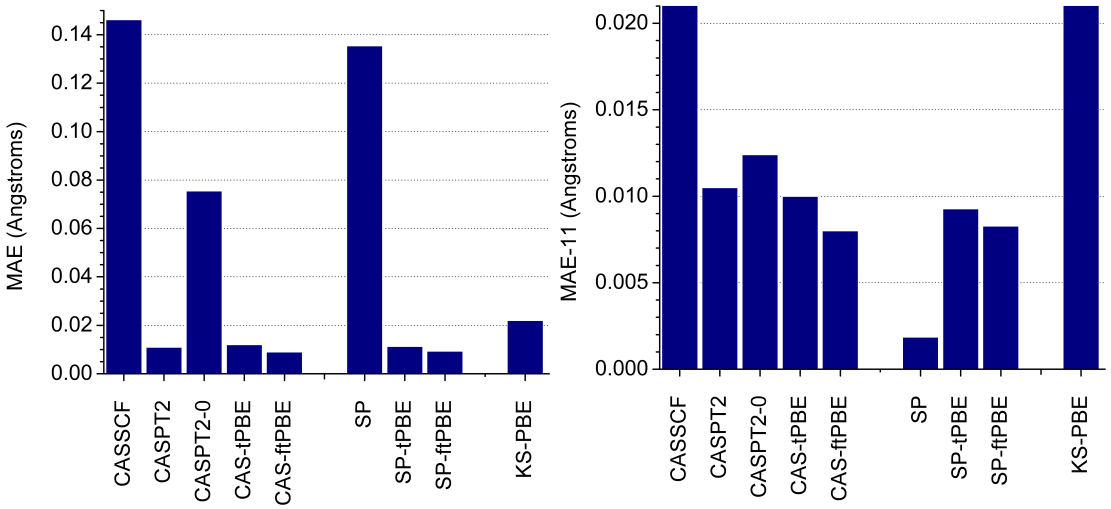

Figure 10.3. Mean absolute errors (MAE) with respect to experimental values of the calculated bond distances of eleven main-group diatomic molecules and Cr_2, obtained with several approaches (left). The MAE obtained without the results for Cr_2 (labeled as MAE-11) is shown on the right. The methods are grouped into three classes. The first are based on CASSCF (CASSCF, CASPT2, CASPT2-0, CAS-tPBE, CAS-ftPBE). The second are based on the SP approximation (SP, SP-tPBE, SP-ftPBE). The third is Kohn-Sham DFT with the PBE exchange-correlation functional. All experimental data were obtained from ref. 449.

It has previously been recognized that CASSCF solutions generally lead to equilibrium bond lengths that are too long,[450] and our results are consistent with this. CASSCF has a mean absolute error (MAE) of 0.146 Å when compared to experimental data. This statistic is however dominated by the result obtained for Cr_2, for which CASSCF overestimates the equilibrium bond length by 1.52 Å. Without the results obtained for Cr_2, the MAE of CASSCF (labeled as MAE-11) is 0.021 Å. This is similar to previous results.[450] The MAE-11 of KS-PBE (0.022 Å) is similar to that of CASSCF. However, we find that the CAS-tPBE and CAS-ftPBE methods reduce the MAEs of both CASSCF and KS-PBE by in excess of 50%. As shown in Figure 10.3, CAS-tPBE (MAE of 0.012 Å and MAE-11 of 0.010 Å) and CAS-ftPBE (MAE of 0.009 Å and MAE of 0.008 Å) perform as well as the much more expensive CASPT2 method (MAE of 0.011 Å and MAE-11 of 0.011 Å), with CAS-ftPBE being the best of the three approaches for bond distances. Without the IPEA shift, CASPT2 (labelled as CASPT2-0), performs poorly for Cr_2, resulting in a MAE of 0.076 Å. Even without the data for Cr_2, CASPT2-0 (MAE-11 of 0.012 Å) is not as good as CAS-tPBE and CAS-ftPBE.

CASPT2 and CASPT2-0 significantly outperform CAS-PDFT and SP-PDFT only for the bond length of the fluorine molecular dimer, F_2. CAS-tPBE and CAS-ftPBE underestimate the bond-length of F_2 by 0.021–0.023 Å, while CASPT2 and CASPT2-0 overestimate it by 0.011–0.014 Å. For the highly multireference systems (B_2, C_2, and Cr_2), CAS-tPBE and CAS-ftPBE perform better than CASPT2 and CASPT2-0 for B_2 and C_2, while CAS-ftPBE gives a similar error as CASPT2 for Cr_2.

When comparing SP and CASSCF, we see that restricting the active space with

the SP approximation only marginally alters the MAE and MAE-11 of the calculated bond distances of these diatomic molecules. The largest difference between the results obtained with CASSCF and SP was found for B_2 and Cr_2. In all other cases, the difference between these methods is in the range 0.002–0.007 Å. More importantly, there is no noticeable difference in the MAE obtained for SP-PDFT (SP-tPBE and SP-ftPBE) and MC-PDFT (CAS-tPBE and CAS-ftPBE), as shown in Figure 10.3. Indeed, SP-PDFT performs equally as well as CAS-PDFT in all the cases that were tested.

10.5.3 Dissociation energies of diatomic molecules

The calculated bond dissociation energies of these twelve diatomic molecules are presented in Table 10.1. The dissociation energies are calculated as the difference between the potential energy of the molecule at 12 Å and the energy of the molecule at equilibrium. With CASSCF, the dissociation energies of these diatomic molecules are generally underestimated, and the MAE with respect to experimental values is 19.3 kcal/mol. Without the results obtained for Cr_2, for which it underestimates the experimental dissociation energy by 30.8 kcal/mol, CASSCF has an MAE (labeled as MAE-11) of 18.2 kcal/mol. This underestimation of the dissociation energy is associated with an underestimation of the force constant and is related to the excessive antibonding character of CASSCF solutions.[450] Imposition of restrictions on the CI expansion by enforcing the SP approximation raises the MAE to 21.7 kcal/mol and the MAE to 20.8 kcal/mol, corresponding to differences of 3.4 and 2.6 kcal/mol, respectively, or about 11-13%. Of the methods that were tested, SP has the largest error. This is not surprising since the SP calculations use smaller active spaces than the CASSCF calculations. As

discussed above, we use full valence active spaces in the CASSCF calculations, whereas the SP calculations contain only selected pairs of orbitals with no interpair excitations. KS-PBE calculations perform much better than either CASSCF or SP in nearly all cases, as expected since neither CASSCF nor SP include dynamic correlation. However KS-PBE also has a rather large MAE (11.8 kcal/mol) as well as a large MAE-11 (12.0 kcal/mol). The only system for which KS-PBE approaches chemical accuracy is hydrogen fluoride (HF), a system in which the dominant configuration has a weight of 99.9%. This is by all measures a single-reference system.

The importance of including dynamic correlation for correctly computing the dissociation energies of these diatomic molecules is seen by comparing CASSCF with CAS-tPBE, CAS-ftPBE, CASPT2, and CASPT2-0 as well as by comparing SP with SP-tPBE and SP-ftPBE. The CAS- PDFT and SP-PDFT methods both perform very well for B_2 and C_2, which are two systems with strong multireference character (the dominant configuration has a weight of less than 80%).[451–453] They reduce the MAEs and MAE-11s of CASSCF and SP by factors of about 4 and 6 respectively. For the systems presented in Table 10.1, the MAEs and MAE-11s of CAS-PDFT and SP-PDFT are close to those of CASPT2. When comparing CAS-PDFT and SP-PDFT to CASPT2, one has to bear in mind that the latter incorporates an empirical IPEA shift, specifically designed to improve agreement with experimental results; 2.2 (2.3) kcal/mol separates the MAE (MAE-11) of CASPT2 and CASPT2-0, indicating the importance of the empirical IPEA shift.[340]

The CAS-PDFT and SP-PDFT results are almost as good as CASPT2 and

CASPT2-0. Table 10.1 shows that the worst results for CAS-PDFT and SP-PDFT are obtained for F_2 (and Cr_2 in the case of CAS-tPBE and SP-tPBE). It is encouraging that SP-PDFT match CAS-PDFT, which are based on full-valence CASSCF; this is a key finding, and it shows SP-PDFT can treat much larger systems than CAS-PDFT.

Table 10.1 The experimental dissociation energies (in parentheses below molecule) of eleven main-group diatomic molecules and the chromium dimer, Cr_2, are compared with the calculated results obtained with several levels of theory. The MAE obtained without the results for Cr_2 is labeled as MAE-11. For each theoretical method, the deviation of the calculated results from experimental values is given. A negative sign denotes underestimation of the bond energy, while a positive sign indicates overestimation (kcal/mol). All experimental data are taken from ref. 261,449,454,455

	CAS CSFs[b]	CAS	PT2[c]	PT2-0[c]	CAS-tPBE	CAS-ftPBE	SP-CSFs[b]	SP	SP-tPBE	SP-ftPBE	PBE
LiH (57.7)	3	-13.3	-3.9	-3.5	-3.4	-2.7	3	-13.3	-3.4	-2.7	-4.2
HF (141.3)	15	-26.8	-1.5	-2.2	4.8	5.7	3	-26.8	4.8	5.7	0.7
B_2 (70.0)	1512	-11	-3.7	-4.0	-2.5	-2.3	100	-15.9	0.7	-1.2	7.0
C_2 (146.0)	1764	-1.3	0.1	-3.6	-1.3	3.8	150	-7.1	-1.2	3.6	10.2
CO (256.2)	1176	-4.4	-4.0	-9.6	0.4	-0.5	37	-8.1	0.2	0.5	11.9
S_2 (100.8)	378	-26.3	-1.1	-4.4	6.6	1.9	20	-26.8	6.3	1.7	12
SO (123.5)	378	36.5	1.5	3.2	4.8	0.3	20	37.1	4.4	0.6	14.6
NH (78.5)	45	-13.7	1.4	-0.3	4.5	9.4	4	-15.2	5.0	9.5	18.4
N_2 (228.5)	1176	-16	-7.1	-16.5	-1.6	4.0	37	-24.7	-3.2	2.5	14.9
O_2 (120.3)	378	-31.9	-0.1	-1.0	8.6	1.0	20	-32.6	8.1	0.6	22.9
F_2 (38.2)	36	-19.1	-0.5	-1.8	12.6	10.8	3	-21.6	10.2	9.0	14.8
Cr_2 (33.9)	28784	-30.8	-5.8	-7.8	-18.5	-5.1	1516	-31.2	-19.4	-6.1	10.5
MAE		19.3	2.6	4.8	5.8	4.0		21.7	5.6	3.6	11.8
MAE-11		18.2	2.3	4.6	4.6	3.9		20.8	4.3	3.4	12.0

[a] MAE = mean absolute error and MAE-11 = mean absolute error without the data for Cr_2

[b] These rows give the numbers of CSFs in the CASSCF and SP calculations

[c] PT2 refers to CASPT2 and PT2-0 refers to CASPT2-0

In principle, as CASSCF is affordable to upwards of 35 million CSFs, it should be possible to create SP solutions that approach that limit as well. As such one can envisage using SP and SP-PDFT for systems that are unaffordable for CASSCF and CAS-PDFT. As examples, SP and SP-PDFT can be used to describe the full π/π^* manifold of chrysene ($C_{18}H_{12}$) as well as the full valence space of benzene-tetracyanoethylene complexes.

Two other interesting points are (1) that the results are stable as far as replacing tPBE by ftPBE or vice versa and (2) that ftPBE results in significant improvements in the results obtained for Cr_2, suggesting that it might be particularly well suited for transition metal systems.

10.5.4 Potential energy curves of diatomic molecules.

The ground-state potential energy curves of these twelve diatomic molecules were also scanned from near equilibrium to dissociation. Static correlation effects are generally more dominant at dissociation, and it is therefore important to test the ability of SP-PDFT to predict potential curves all the way out to this limit. CASSCF, SP, CASPT2, CAS-PDFT, and SP-PDFT all give smooth curves. The potential curves obtained with SP are similar to those obtained with CASSCF, the energies obtained with SP-tPBE are similar to those obtained with CAS-tPBE, and those obtained with SP-ftPBE are similar to those obtained with CAS-ftPBE. Thus we find that the restrictions in going from CAS to SP do not degrade the potential energy curves.

For O_2 and N_2 in the bonding regions (~ 0.9-1.2 Å), the total electronic energy obtained with SP deviates from the CASSCF energy by about 3-10 kcal/mol as shown in

Table 10.2. This is because some of the CSFs deleted in going from the complete active space to the separated-pair active space contribute nonnegligible amounts of dynamic correlation in these cases. At greater internuclear separations (2.5 and 5.0 Å), the differences between the total energies obtained with CASSCF and SP become small, as also shown in Table 10.2.

Table 10.2. Effect of imposing restrictions on the active space with the GAS scheme on the total electronic energies of N_2, O_2 and Cr_2 as functions of inter-nuclear distance R(Å). The differences in the total electronic energies obtained with CASSCF and SP, CAS-tPBE and SP-tPBE as well as CAS-ftPBE and SP-ftPBE are reported in kcal/mol, where A:B denotes the absolute value of the energy difference between A and B.

	R (Å)	% Weight of dominant configuration CASSCF : SP	CASSCF: SP	CAS-tPBE: SP-tPBE	CAS-ftPBE: SP-ftPBE
N_2	0.9	96.0 : 96.6	7.1	1.4	1.2
	1.2	90.6 : 91.2	9.4	1.6	1.7
	2.5	12.4 : 12.1	0.54	0.26	0.27
	5.0	6.3 : 8.3	0.002	0.001	0.001
O_2	1.1	96.0 : 96.3	3.6	0.28	0.29
	1.2	94.2 : 94.6	4.0	0.033	0.046
	2.5	34.2 : 33.8	0.26	0.21	0.20
	5.0	25.0 : 33.3	0.044	0.030	0.038
Cr_2	1.6	57.6 : 56.4	8.8	1.0	1.1
	1.8	28.8 : 25.9	3.7	1.5	1.8
	2.6	< 2 : < 2	0.3	0.03	0.004
	5.0	< 2 : < 2	< 0.001	0.002	0.002

In contrast, the total energies obtained with SP-tPBE and SP-ftPBE are much closer to those of CAS-tPBE and CAS-ftPBE respectively. In Table 10.2, we see that the largest difference between the total energies obtained with the SP-PDFT and CAS-PDFT approaches are about 1.7 kcal/mol, which shows that the PDFT approach recovers the static and dynamic correlation energy that were neglected by using the approximate SP approximation in a variational wave function calculation. This is extremely encouraging.

The ability of PDFT to recover these electron correlation effects is the reason why the potential energy curves obtained with SP-PDFT are closer to those obtained with CAS-PDFT than SP is to CASSCF.

We emphasize that the SP-PDFT and CAS-PDFT agree well both in the bonding regions of N_2 and O_2, where there are dominant configurations with greater than 90% weight, and in the limit of dissociation, where there are many configurations with appreciable weights. We see similar effects in Cr_2. These results are shown in Table 10.2. It is also interesting to probe the origins of the agreement between SP-PDFT and CAS-PDFT by examining the approximate occupation numbers of the correlated orbitals in the SP and CASSCF solutions on which they are based, respectively. If we examine C_2 at equilibrium, the CASSCF solution has occupation numbers of (1.9840:0.0136); ;(1.5960:0.3997);(1.8913:0.1121);(1.8911:0.1123), in order, for the pairs shown in Figure 10.1. The SP solution has very similar occupation numbers of (1.9892:0.0108); (1.6051:0.3949);(1.8924:0.1074);(1.8924:0.1074). This suggests that the CASSCF and SP solutions result in comparable density and on-top pair density, a fact that is sufficient for quantitatively accurate SP-PDFT calculations, even though the parent SP solution is higher in energy than the analogous CASSCF solution by 0.0116 Hartrees (11.6 mH).

10.5.5 Triatomic molecules

In this section, the calculated bond lengths, bond angles, and atomization energies of the two lowest energy states of methylene (CH_2) are presented, along with the calculated adiabatic $^3B_1$ - $^1A_1$ gaps. The calculated geometry and atomization energy of ground-electronic-state ozone (O_3) are also presented.

For CH_2, a full valence CASSCF(6,6) wave function is used for subsequent CASPT2, CASPT2-0, and CAS-PDFT calculations. In C_1 symmetry, this active space choice results in 189 and 175 CSFs for the $^3B_1$ and $^1A_1$ states, respectively. For SP and SP-PDFT calculations, we used the SP-4 active space, as described above. This leads to a total of 25 and 17 CSFs for the $^3B_1$ and $^1A_1$ states, respectively.

For ozone, we used a CAS(12,9) reference for CASSCF and an SP-3 reference for the SP approximation, with the latter resulting in the reduction of the number of CSFs from 2520 to 37. In essence 98.5% of the CSFs in the CASSCF(12,9) solution are completely neglected in the SP-3 approximate wave function. These active space schemes are illustrated in Figure 10.4.

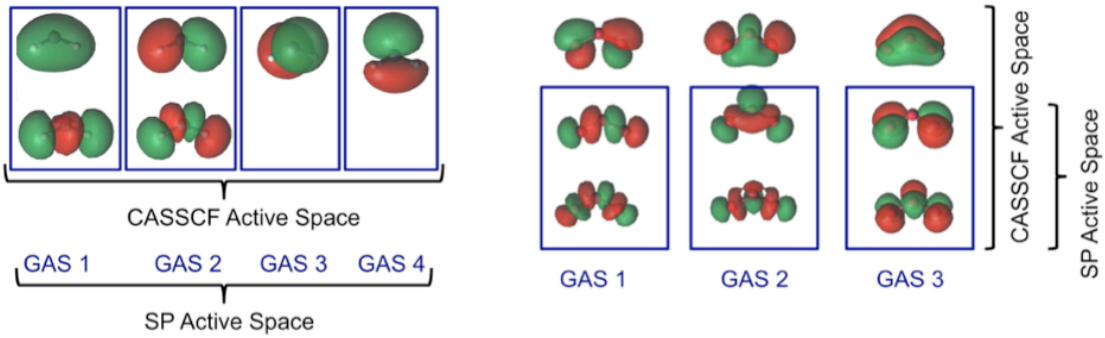

Figure 10.4. Illustrative descriptions of the CAS and SP active spaces used in CASSCF and SP calculations on $^3B_1$ CH_2 (*left*) and O_3 (*right*). Refer to the text for the full descriptions of the active spaces used in the CASSCF and SP calculations.

10.5.6 Methylene

The structural parameters that we obtained with CASSCF are in good agreement with the CASSCF results of Apeloig et al.[456] The calculated C-H bond lengths and bond angles of the $^3B_1$ and $^1A_1$ states of CH_2 are compared with experimental data in Table 10.3. The experimental values of the C-H bond length and bond angle of the $^3B_1$ state of

CH_2 are 1.085 Å and 135.5° respectively. For the $^1A_1$ state, the C-H bonds are longer (1.107 Å) and the bond angle is significantly smaller (102.4°).[457,458] Similarly to what was seen for the diatomic molecules, CASSCF and SP overestimate the C-H bond lengths in the $^3B_1$ and $^1A_1$ states of CH_2. The calculated bond angles are also too large, as seen in Table 10.3.

Table 10.3 Comparison of the calculated equilibrium bond distances (R_e), bond angles (<), and atomization energies (AE) of CH_2 and O_3 obtained at different levels of theory with experimental data. For each theoretical method, the deviation of the calculated results from experimental values is given. A negative sign denotes underestimation and a positive sign indicates overestimation of the experimental data. The calculated adiabatic singlet-triplet (S-T) gaps of CH_2 are also presented.

	CAS	PT2[a]	PT2-0[a]	CAS-tPBE	CAS-ftPBE	SP	SP-tPBE	SP-ftPBE	PBE	Exp[b]
Methylene										
R_e (Å)										
$^3B_1$	0.005	-0.006	-0.005	-0.002	-0.003	0.005	-0.003	-0.004	0.000	1.085
$^1A_1$	0.017	0.005	0.005	0.011	0.010	0.023	0.012	0.006	0.015	1.107
<HCH (°)										
$^3B_1$	-4.2	-1.9	-1.3	0.7	1.2	-4.1	2.0	3.4	0.0	135.5
$^1A_1$	-1.1	-0.5	-0.7	0.1	1.0	-1.5	0.5	2.6	-1.6	102.4
AE of $^3B_1$ (kcal/mol)	-19.5	0.9	-0.8	2.5	8.1	-22.4	2.4	7.1	8.2	186.2
S-T gap (kcal/mol)	1.5	2.7	4.8	-1.2	-2.3	4.5	-0.8	-2.7	6.9	8.6
Ozone										
R_e (Å)	0.005	0.007	0.007	-0.006	-0.005	0.002	-0.009	-0.012	-0.003	1.278
<OOO (°)	-0.6	-0.2	-0.4	0.6	0.4	-2.2	1.8	1.6	1.4	116.8
AE (kcal/mol)	-46.2	+2.2	-4.8	27.7	21.4	-81.0	29.9	27.5	41.9	142.5

[a] PT2 refers to CASPT2 and PT2-0 refers to CASPT2-0

[b] To obtain these values, the thermal correction to the enthalpy at 298 K obtained by KS-PBE/aug-cc-pVTZ is added to the empirical atomization ΔH_{298} of CH_2. The frequency component of this correction was scaled using a scaling factor obtained from ref. 202 for this model chemistry. Exp values from Ref 457,458, 459,460

CAS-PDFT reduces the errors in the calculated structural properties of CH_2 to within the margins provided by CASPT2 and CASPT2-0. In general, the C-H bond

lengths obtained with CAS-PDFT are within 0.004-0.007 Å of the values obtained with CASPT2 and CASPT2-0. This is the case for the $^3B_1$ and $^1A_1$ states.

For the $^3B_1$ state, CAS-PDFT overestimates bond angles by about 0.7-1.5° while CASPT2 underestimates them by about 1.9°. Compared with CAS-PDFT, SP-PDFT gives almost the same C-H bond lengths, and the bond angles are about 2° larger. We note that Jensen and Bunker obtained a bond angle of 133.9° for the $^3B_1$ state.[461] This is 1.6° below the experimental value shown in Table 10.3, and indicates that the results obtained with CASPT2, CASPT2-0, CAS-PDFT and SP-PDFT are within the range of available experimental data.

For the $^1A_1$ state, CAS-PDFT overestimates the bond angle by up to 1.0°, while CASPT2 and CASPT2-0 underestimate by 0.5 and 0.7°, respectively. Similar to the situation for the $^3B_1$ state, SP-PDFT results in slightly larger bond angles.

An earlier approach for combining MCSCF-type methods with DFT has been described by Cremer and coworkers.[49,52,60] This method, which they call CAS-DFT, does not perform as well as CAS-PDFT and SP-PDFT for predicting the structural properties of CH_2.[462] It overestimates the C-H bond length of the $^3B_1$ state by 0.017 Å. For the $^1A_1$ state of CH_2, it overestimates the C-H bond length by 0.031 Å.

To calculate the atomization energy of CH_2 and O_3, the C-H and O-O bond lengths are stretched to 12 Å, while keeping the equilibrium bond angle fixed at the value obtained with each method. (Our general conclusions remain unchanged if we use the experimental value of the bond angle.) CASSCF and SP underestimate the atomization energy of the $^3B_1$ state of CH_2 by about 20 kcal/mol while PBE overestimates by about

8.5 kcal/mol, as shown in Table 10.3. Calculations with CAS-tPBE and SP-tPBE bring the error down to below 3.0 kcal/mol, which is similar to CASPT2, which overestimates the bond energy by 1.2 kcal/mol. Inclusion of the gradient of the on-top pair density, results in errors of 8.4 and 7.4 kcal/mol for CAS-ftPBE and SP-ftPBE, respectively, still better than KS-PBE but much worse than tPBE.

10.5.7 Ozone

The ozone molecule has been studied with a large number of quantum-mechanical methods.[428,463–468] We highlight the work of Vogiatzis and coworkers in which they showed that a GAS-2(12,9)-1e active space provides the same MAE as CASSCF(12,9) for the computed vertical excitation energies, ionization potential, and electron affinity of O_3.[428] The GAS-2(12,9)-1e notation corresponds to two subspaces containing 12 electrons in 9 orbitals with one excitation allowed between the subspaces.

In the present work, we have used an even more restrictive framework, namely SP-3, which becomes GASSCF-3(6,6)-0e in the general notation. The first two subspaces each contain a coupled pair of σ and σ* orbitals while the third space contains a coupled pair of π and π* orbitals. In contrast, we placed 12 electrons in 9 orbitals for the CASSCF calculations. The nine orbitals are those formed by combination of the $2p_x$, $2p_y$, and $2p_z$ orbitals of the three oxygen atoms, as shown in Figure 10.4. The dominant configuration in the CASSCF(12,9) wave function has a weight of only 84%, showing that this system has significant multi-reference character.

Table 10.3 shows that the optimized geometry of O_3 obtained with CASSCF is in good agreement with the results of Tsuneda et al.[464] who used a similar active space with

the cc-pVTZ basis sets augmented with s, p, and d diffuse functions. Also, the structural parameters obtained with CASPT2 are in agreement with the reports of Ljubic and Sabljic, who used the same active space.[463] The bond lengths and angles obtained with SP-PDFT are similar to those obtained with CAS-PDFT, despite the fact that the SP wave function contains only about 1.4% of the number of CSFs in the CASSCF solution. CAS-PDFT slightly underestimates the O-O distances and slightly overestimates the bond angle, while CASPT2 and CASPT2-0 have opposite behaviors.

Krishna and Jordan have previously reported that CASSCF underestimates the atomization energy of O_3 by about 57.7 kcal/mol.[469] Table 10.3 shows that CASSCF and the SP approximation are both poor for calculating the atomization energy of O_3. These are the two methods that do not attempt to include most of the dynamic electron correlation. On the other hand, PBE overestimates the atomization energy by about 42 kcal/mol but CAS-tPBE and CAS-ftPBE reduce the error of PBE by 14 and 20 kcal/mol, respectively. SP-tPBE and SP-ftPBE behave similarly to CAS-tPBE and CAS-ftPBE respectively. However, CASPT2 and CASPT2-0 perform best for predicting the atomization energy of O_3.

10.5.8 C-H Bond dissociation energies in organic compounds

In this section we study C-H bond dissociation in acetylene, ethylene, and ethane, that is:

$$C_2H_2 \rightarrow C_2H^{\cdot} + H^{\cdot}$$

$$C_2H_4 \rightarrow C_2H_3^{\cdot} + H^{\cdot}$$

$$C_2H_6 \rightarrow C_2H_5^{\cdot} + H^{\cdot}$$

The calculated energies for these reactions are compiled in Table 10.4, where they are compared to experimental values estimated by adding the thermal correction to the enthalpy at 298 K obtained by KS-PBE/aug-cc-pVTZ to the empirical ΔH_{298} reported by Blanskby and Ellison.[470] The frequency component of this correction was scaled using scaling factors obtained from ref. [202] for this model chemistry. We used full valence active spaces for the CASSCF calculations in this table: CAS(10,10), CAS(9,9), CAS(12,12), CAS(11,11), CAS(14,14) and CAS(13,13) for acetylene, ethynyl, ethylene, vinyl, ethane and ethyl respectively. With C_1 symmetry, these active spaces result in 19404, 8820, 226512, 104544, 2760615 and 1288287 CSFs respectively. In Table 10.4 we report the number of CSFs only for the parent compound and not for the dissociation radical species.

Table 10.4. The calculated C-H dissociation energies (kcal/mol) of three organic compounds obtained with different levels of theory are compared with experimental data. For each theoretical method, the deviations of the calculated results from experimental values are given. A negative sign denotes underestimation and a positive sign indicates overestimation of the experimental data.

	CAS	CAS CSFs[a]	PT2[b]	PT2-0[b]	CAS-tPBE	CAS-ftPBE	SP	SP CSFs[a]	SP-tPBE	SP-ftPBE	PBE	Exp.[c]
Acetylene	123.7	19404	136.1	134.8	140.7	141.4	115.7	37	141.5	141.3	138.2	140.9
Error	-17.2		-4.8	-6.1	-0.2	0.5	-25.2		0.6	0.4	-2.7	
Ethylene	106.3	226512	114.9	113.7	116.7	116.9	93.8	150	117.4	116.0	113.6	119.5
Error	-13.2		-4.6	-5.8	-2.8	-2.6	-25.7		-2.1	-3.5	-5.9	
Ethane	99.7	2760615	106.4	105.1	106.1	105.7	68.8	3012	112.3	111.3	104.6	110.4
Error	-10.7		-4.0	-5.3	-4.3	-4.7	-41.6		1.9	0.9	-5.8	
MSE	-13.7		-4.5	-5.7	-2.4	-2.3	-30.8		0.1	-0.7	-4.8	
MAE	13.7		4.5	5.7	2.4	2.6	30.8		1.5	1.6	4.8	

[a] These columns give the numbers of CSFs in the CASSCF and SP calculations for the compound.

[b] PT2 refers to CASPT2 and PT2-0 refers to CASPT2-0

[c] Thermal correction to the enthalpy at 298 K obtained by KS-PBE/aug-cc-pVTZ are added to empirical enthalpy ΔH_{298} data. [470]

The active spaces used in SP and SP-PDFT calculations are presented in the computational details section and are illustrated for ethane and the ethyl radical in Figure 10.5. Only orbitals with significant C-H character are included in the SP active spaces. As previously noted, we used SP-3, SP-3, SP-4, SP-4, SP-6 and SP-6 active spaces for the acetylene, ethynyl, ethylene, vinyl, ethane and ethyl, respectively. These result in 37, 17, 150, 76, 3012 and 1704 CSFs respectively, a significant reduction compared with the full CASSCF calculation.

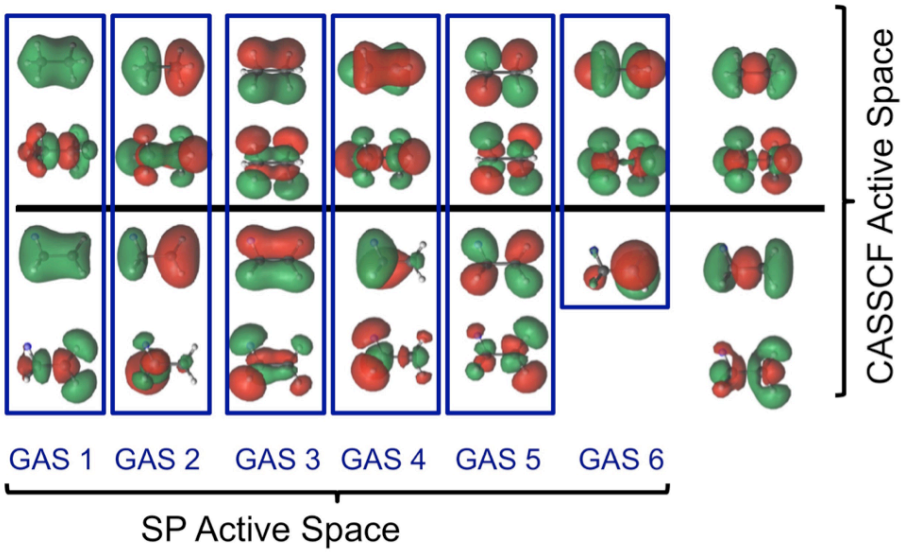

Figure 10.5. Illustrative descriptions of the CAS and SP active spaces used in CASSCF and SP calculations on: ethane (top) and the ethyl radical (bottom). Notice that the C-C orbitals are not included in SP sub spaces as we are concerned only with C-H bond dissociation.

In all the three cases presented in Table 10.4, CAS-PDFT performs much better than CASPT2, CASPT2-0, or PBE, and SP-tPBE and SP-ftPBE do even better with MAEs of only 1.6 and 1.7 kcal/mol, respectively. This is another demonstration that PDFT effectively recovers correlation that is left behind by the active space restrictions

of the SP approximation, even though we were very aggressive in including only a small number of pairs.

In general we are presenting the SP-PDFT results for just one small active space, as previously indicated. We did do some testing to see the effect of using different choices of which pair of orbitals to include, and we found that the effect of adding or removing spectator pairs was small. For example we used SP-5 for ethylene and vinyl and found a difference in the calculated C-H dissociation energy of only 0.2 kcal/mol as compared to the SP-4 results presented in the table.

10.5.9 Barrier heights for pericyclic reactions

We have previously shown that CAS-tPBE reduces the average error of PBE by a factor of 2.7 for predicting the forward and reverse barrier heights for chemical reactions involving small molecules.[432] CASPT2 however was found to have a lower MAE than CAS-tPBE. Houk and coworkers have collected datasets of the barrier heights of pericyclic reactions.[443,471] These datasets can be used to benchmark computational approaches. In Table 10.5, we compare the calculated barriers for five pericyclic reactions with experimental data taken from the dataset of Houk and coworkers.[443,471] These reactions are shown in Figure 10.6.

SP and CASSCF overestimate the reaction barriers by 15 kcal/mol or more, in nearly all cases. Table 10.5 shows that the only exception is for reaction 1, for which they overestimate it by only 2.4 and 3.0 kcal/mol respectively. SP-PDFT and CAS-PDFT greatly improve on CASSCF and SP, reducing the MAEs by factors of 3-6. This is similar to the situation found for reactions involving small molecules.[432] The MAEs of

SP-PDFT and CAS-PDFT are still somewhat large, at least when compared to CASPT2. However, regarding the central topic of this manuscript, we find that the calculated reaction barriers are stable to the use of a restricted SP wave function; that is, SP-PDFT and CAS-PDFT yield similar results for each reaction and overall have similar MAEs.

Table 10.5 The calculated barriers (kcal/mol) of five pericyclic reactions computed with different methods are compared with experimental data. For each method, the deviations of the calculated results from experimental values are also given. A negative sign denotes underestimation and a positive sign indicates overestimation of the experimental data.

	CAS	CAS CSFs[a]	PT2[b]	PT2-0[b]	CAS-tPBE	CAS-ftPBE	SP	SP CSFs[a]	SP-tPBE	SP-ftPBE	PBE	Exp.[c]
1	36.0	20	34.0	32.5	36.0	36.2	36.6	10	36.2	36.3	32.1	33.6
Error	2.4		0.4	-1.1	2.4	2.6	3.0		2.6	2.7	-1.5	
2	45.3	175	28.8	27.7	30.0	30.0	58.3	37	30.3	30.8	25.5	30.2
Error	15.1		-1.4	-2.5	-0.2	-0.2	28.1		0.1	0.6	-4.7	
3	39.1	1764	25.5	24.4	25.8	25.8	52.1	150	25.5	25.9	23.2	29.5
Error	9.6		-4.0	-5.2	-3.7	-3.7	22.0		-4.0	-3.6	-6.3	
4	50.8	20	36.4	35.4	31.9	33.1	60.1	10	32.0	32.9	31.3	38.8
Error	12.0		-2.4	-3.4	-6.9	-5.7	21.3		-6.8	-5.9	-7.5	
5	43.9	20	25.5	25.4	21.0	22.3	40.7	10	20.9	21.9	22.8	25.8
Error	18.1		-0.3	-0.4	-4.8	-3.5	14.9		-4.8	-3.8	-3.0	
MSE	11.4		-1.5	-2.5	-2.6	-2.1	17.9		-2.6	-2.0	-4.6	
MAE	11.4		1.7	2.5	3.6	3.1	17.9		3.7	3.2	4.6	

[a] These columns give the numbers of CSFs in the CASSCF and SP calculations

[b] PT2 refers to CASPT2 and PT2-0 refers to CASPT2-0

[c] Scaled zero point energy corrections obtained at the B3LYP/6-31G(d) level are added to experimental $\Delta H_{0K}^{\ddagger}$ data to obtain the last column.[443,471]

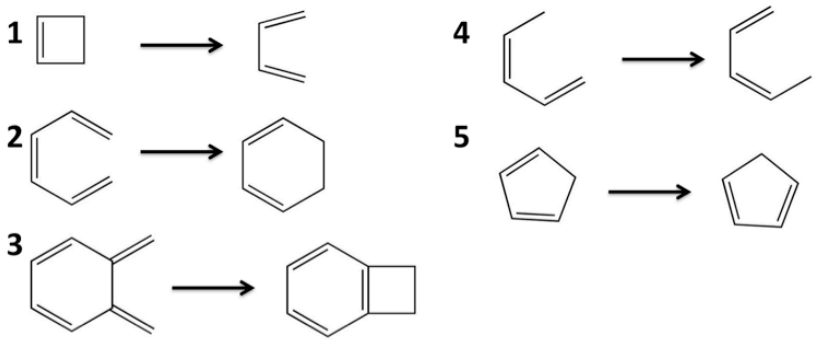

Figure 10.6. The barriers for these pericyclic reactions were calculated with SP-PDFT and other theoretical methods.

10.5.10 Open-shell singlet systems

Cremer and coworkers have previously used UDFT, broken-symmetry UDFT, and CAS-DFT[49,52,60] to study open-shell singlet diradicals.[462] Specifically, they studied the energy of the $^1\boldsymbol{B_1}$ state of twisted ethylene relative to planar ethylene. In addition, they also studied the singlet–triplet gaps of 1,4-didehydrobenzene and α,3-didehydrotoluene, which are shown in Figure 10.7. They found that CAS-DFT predicts the $^1\boldsymbol{A}''$ state of α,3-didehydrotoluene to be lower in energy than the $^3\boldsymbol{A}''$ state. Also the $^1\boldsymbol{A_g}$ state of 4-didehydrobenzene is predicted to be lower in energy than the $^3\boldsymbol{B_{1u}}$ state. These state orderings are in agreement with experimental data.[472,473] In Table 10.6, we compare the results obtained when PBE, CASSCF, SP, SP-PDFT, CAS-PDFT and CASPT2 are used to carry out similar computations to those performed by Cremer and coworkers.[462] We used CAS(8,8) and SP-4 active spaces in the calculations on the singlet and triplet states of 1,4-dide hydrobenzene and α-3-dide-hydrotoluene. For the KS-DFT computations, the singlet states were treated as unrestricted broken-symmetry solutions. For planar and twisted ethylene, we used CAS(12,12) and SP-1 active spaces, respectively.

For the gap between twisted and planar ethylene, SP-tPBE and SP-ftPBE provide similar results that are 2-3 kcal/mol above those obtained with CAS-tPBE and CAS-ftPBE respectively, as shown in Table 10.6. The results obtained with CAS-ftPBE and CASPT2 are the same. The results obtain for the fully translated functionals improve upon CAS-tPBE and SP-tPBE. Lischka and coworkers obtained a value of 69.2 kcal/mol

at the MR-CISD+Q/SA-3-RDP level while using similar basis sets.[444] This is close to the values obtained by CAS-ftPBE and CASPT2.

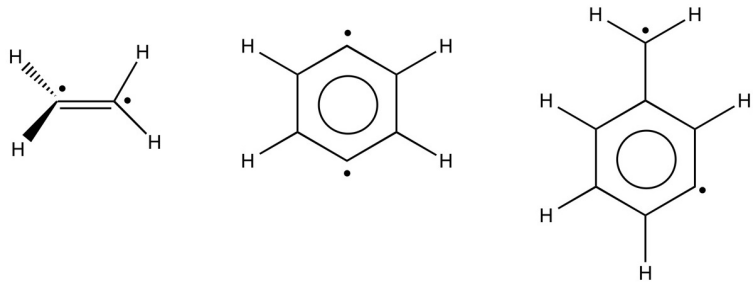

Figure 10.7. Illustrations of the structures of twisted ethylene, 1,4-didehydrobenzene and α,3-didehydrotoluene.

Table 10.6 The calculated energy separation (kcal/mol) of twisted and planar ethylene (**A**) and the singlet-triplet gaps of 1,4-didehydrobenzene (**B**) and α,3-didehydrotoluene (**C**).

	CAS	CAS CSFs[a]	PT2[d]	PT2-0[d]	CAS-tPBE	CAS-ftPBE	SP	SP CSFs[a]	SP-tPBE	SP-ftPBE	PBE[b]	Exp.
A[c]	73.1	226512	69.7	67.6	72.6	69.5	72.0	3	74.3	72.5	65.8	
B[c]	-2.6	2352;1764	-4.7	-4.5	-3.9	-4.0	-3.7	204;200	-3.9	-4.0	-3.6	-3.5±0.5[e]
C[c]	-2.9	2352;1764	-1.9	-1.7	-0.3	-0.4	+0.7	204;200	-0.3	-0.3	-0.7	-2.5±2.5[f]

[a] These columns give the numbers of CSFs in the CASSCF and SP calculations. For **B** and **C**, we give the number of CSFs in the triplet state first.

[b] We compare the variational energies obtained at the PBE level.

[c] For **A**, we give the energy of twisted ethylene relative to planar ethylene. For **B** and **C**, we give the energies of the singlet states relative to the triplet state.

[d] PT2 refers to CASPT2 and PT2-0 refers to CASPT2-0

[e] Ref 472,473

[f] Ref 474

For 1,4-didehydrobenzene, the results obtained with CAS-tPBE, CAS-ftPBE, SP-tPBE and SP-ftPBE fall within the error bar of the experiment, which is -3.5±0.5 kcal/mol. In contrast, CASPT2 and CASPT2-0 fall outside this range; they overestimate even as compared to the high end of the experimental results[472,473] by 0.7 and 0.5 kcal/mol, respectively. CAS-DFT predicted an energy separation of -2.6 kcal/mol

between the ^1A_g and $^3B_{1u}$ states of 1,4-didehydrobenzene.47 For α,3-didehydro toluene, CAS-tPBE, CAS-ftPBE, SP-tPBE and SP-ftPBE correctly predict that the $^1A''$ state is more stable than the $^3A''$ state. The separations provided by all these methods are similar and fall within the range of available experimental data. They are however about 1.5 kcal/mol smaller than the separations predicted by CASPT2 and CASPT2-0. Unfortunately, available experimental reports only indicate that the splitting should be lesser than 5.0 kcal/mol.

10.6 Concluding remarks

The present paper contains new methods for both wave function theory and density functional theory. Starting with wave function theory, we have presented a systematic way to choose the active space in generalized-active-space self-consistent-field (GASSCF) theory. This new way of choosing the active space is called the separated-pair (SP) approximation. The method is intermediate between generalized valence bond (GVB) theory and complete active space self-consistent-field (CASSCF) theory. The SP wave function is a truncation of CASSCF, obtained by partitioning the CAS active space into an arbitrary number of generalized-active-space (GAS) subspaces that each contain at most two orbitals, and inter-subspace excitations are excluded. In the examples, only pairs required to describe a particular bond-breaking process are included in the GAS subspaces; all other orbitals are treated at the Hartree-Fock level. With such a choice, the SP methods can be used for large systems for which conventional CASSCF calculations are unaffordable. Just as for GVB and CASSCF, the precise choice of active space in the SP approximation is not completely unambiguous because in all three

methods one must decide which orbitals to correlate. The orbitals to be correlated are an individual choice, although we expect that the most useful choice will usually be a bonding orbital and the corresponding antibonding orbital. In the present paper we include the orbitals involved in bond breaking and in some cases also additional orbitals closely close coupled to the bond breaking. A general objective might be to include the orbitals responsible for nondynamic correlation, which is also called static correlation, strong correlation, and near-degeneracy correlation. Although dynamic correlation tends to be very similar across systems, nondynamic correlation is usually system-specific. Therefore, a practical multi-configuration approach may well have to be applied in a case-by-case manner, sometimes requiring chemical insight. But the examples presented here show that simple considerations lead to reasonably accurate results for a set of diverse cases and significantly reduce the computational cost of specific problems. The definition and exploration of SP may be useful for all methods that need to start from a strongly correlated reference wave function.

We subsequently considered whether the SP approximation is useful for multi-configuration pair-density functional theory (MC-PDFT), and to put this in context we first contrast MC-PDFT to Kohn-Sham density functional theory (KS-DFT). In KS-DFT, ones represents the density by a Slater determinant, and one writes the total energy as the sum of the kinetic energy computed from the Slater determinant by standard wave function methods, the Coulomb energy computed classically from the density, and a remainder. The remainder is a functional of the density and is called the exchange-correlation energy, and it includes not just the deviation of the true potential energy from

the Coulomb energy computed classically from the density, but also the deviation of the true kinetic energy from the Slater-determinant kinetic energy. In MC-PDFT, we represent the density and the on-top pair density by a multi-configurational wave function, and we write the total energy as the sum of the kinetic energy computed from the multi-configurational wave function by standard wave function methods, the Coulomb energy computed classically from the density, and a remainder. The remainder is a functional of the density and the on-top pair density and is called the on-top energy, and it includes both the deviation of the true potential energy from the Coulomb energy computed classically from the density and the deviation of the true kinetic energy from the multi-configurational-wave-function kinetic energy. In most previous attempts to combine multi-configurational wave functions with density functional theory, one writes the total energy as the sum of the energy computed by wave function theory from the multi-configurational wave function plus a remainder. Because the energy computed by wave function theory from the multi-configurational wave function includes some of the effect of electron correlation on the true potential energy, one must be careful not to include this portion of the correlation energy in the remainder; this can be called the double counting problem. Because we use only the kinetic energy of the multi-configurational wave function, we avoid this double counting problem. Note though that we do not know an exact on-top functional, just as an exact exchange-correlation functional is not known in KS-DFT, so our treatment is not exact. A major goal of both KS-DFT and MC-PDFT is to find a better approximation to the corresponding exact functional. One motivation for MC-PDFT is that it might be “easier" to find a good on-

top functional than to find a good exchange-correlation functional for two reasons: (1) our kinetic energy is based on a representation that better conforms to the true wave function when (as is often the case) the system is inherently multi-configurational (as, for example, for describing the breaking of a covalent bond), and (2) our functional is allowed to depend on the on-top pair density, which brings in extra information. Many years of development have gone into modern exchange-correlation functionals,[372] whereas for on-top functionals we are still using first-generation approximations. The present paper, however, is not about improving the functional but rather about testing how many and what kind of configurations need be present in the multi-configurational wave function in order obtain reasonable results with simple density functionals. We found that the new SP approximation, discussed in the previous paragraph for wave function theory, provides an economical multi-configurational wave function that yields good accuracy with MC-PDFT. Thus we have presented a version of MC-PDFT called separated-pair pair-density functional theory, abbreviated SP-PDFT. The SP-PDFT method uses a separated-pair (SP) wave function to generate the kinetic and classical Coulomb contributions to the total electronic energy, and the remainder of the total electronic energy is computed from a functional of the total density and the on-top pair density taken from the SP wave function. The SP-PDFT methods can therefore be used for large systems for which conventional CASSCF calculations, CASPT2, and CAS-PDFT are unaffordable.

Sometimes the SP approximation wave function calculations agree well with the CASSCF ones; in other cases they are less accurate, as would be expected. But even in

cases where the energetic results obtained by wave function theory from the SP approximation are less accurate than those obtained by CASSCF, we show that the SP approximation is able to produce an accurate enough kinetic energy and on-top pair density that the SP-PDFT results are in generally good agreement with the CAS-PDFT results. The tests included in this article include structural properties and bond dissociation energies of eleven diatomic and two triatomic molecules, the C-H dissociation energies of prototypical organic systems, the reaction barriers of pericyclic reactions, and the description of open-shell singlet species. In all the cases that were tested, SP-PDFT provides approximately the same accuracy as CAS-PDFT. In most cases, both SP-PDFT and CAS-PDFT provide similar levels of accuracy as the much more expensive CASPT2 approach; the only exception to this is for the reaction barriers of pericyclic reactions.

The key result for wave function theory is that SP often agrees quite well with CASSCF, at greatly reduced cost, and this extends the usefulness of the method to bigger systems. The key result for density functional theory is that the quality of results obtained from MC-PDFT calculations remains largely unchanged even with drastic reductions in the number of included CSFs, as we have in made in the SP-PDFT variant of the method. In addition the SP-PDFT approach, just as is the more general MC-PDFT framework, is free of double-counting of electron correlation energies. This double-counting problem plagues nearly all other hybrid approaches for combining CASSCF and KS-DFT.

Future work that one can anticipate includes testing the performance of the SP and SP-PDFT methods for transition metal complexes, developing better on-top

functionals of the MCSCF density and on-top pair density, and developing an orbital optimization algorithm that includes the on-top functional in the self-consistent-field step.

Author Contributions

Samuel O. Odoh contributed to all calculations except Cr_2 and developed SP method, Giovanni Li Manni contributed to CASSCF, CASPT2 and CAS-tPBE calculations of Cr_2 and developed GASSCF method, Rebecca K. Carlson contributed to SP, SP-tPBE, SP-ftPBE, and CAS-ftPBE, and CASSCF calculations of Cr_2 and developed ft method.

Chapter 11

On-Top Pair Density as a Measure of Left-Right Correlation in Bond Breaking

Reproduced in part from

On-Top Pair Density as a Measure of Left-Right Correlation in Bond Breaking, Rebecca K. Carlson, Donald G. Truhlar, and Laura Gagliardi, *The Journal of Physical Chemistry A,* 2017, DOI: 10.1021/acs.jpca.7b04259.

11.1 Overview

In order to better understand left-right electron correlation and the effect of bond breaking on the on-top pair density, analytic expressions for the total density, the on-top pair density, and the ratio of the on-top pair density to the square of the total density were derived for H_2 for both a restricted Hartree-Fock wave function and a complete active space self-consistent-field wave function with two electrons in two active orbitals. These quantities are compared for the two wave functions for various points in space around the molecule as a function of internuclear distance. At some points in space, in the CASSCF(2,2) wave function, electron correlation, perhaps counterintuitively, increases the probability that two electrons are at the same point in space. At the Coulson-Fischer point, the on-top pair density for the CAS wave function starts to rapidly approach zero, and this can be taken as an indicator of bond breaking.

11.2 Introduction

The electronic structure of the dissociating H_2 molecule is an archetypal example of an inherently multiconfigurational problem. The wave function at equilibrium can be well described by a single determinant, but as the molecule dissociates, the wave function becomes increasingly multiconfigurational. A restricted Hartree Fock (RHF)[475–477] wave function that uses a single Slater determinant cannot properly describe the dissociation of H_2 in a singlet state. One can achieve the correct dissociation limit of two neutral hydrogen atoms by an unrestricted Hartree-Fock (UHF)[478] wave function, but such a wave function has the wrong spatial and spin symmetry. An example of a wave function that can describe the ground ${}^1\Sigma_g^+$ state of H_2 along the entire potential energy curve is a complete active space self-consistent field (CASSCF)[34] wave function using two electrons in two orbitals (CASSCF(2,2)); for H_2, this is also called an optimized double configurations wave function[447] or a perfect-pairing generalized valence bond wave function.[434] Such a wave function corresponds to configuration interaction theory in which one optimizes not just the coefficients of configuration state functions (CSFs), but also the orbitals used to construct the CSFs.

An early treatment of the dissociation of H_2 that provided insight into the problem of breaking a bond was the method of asymmetric molecular orbitals introduced by Coulson and Fischer.[479] Their wave function involved a variational parameter λ in the molecular orbitals that weighted the contribution from each atom; their treatment yields the same result as valence bond theory when $\lambda = 0$ and the same result as RHF theory when $\lambda = 1$, and they showed that the effect of configuration interaction can be included in the wave function by using these asymmetric orbitals. This provides insight into the UHF wave function. By finding the value of λ that minimizes the total energy of a single determinantal wave function using asymmetric molecular orbitals, Coulson and Fischer showed that at internuclear distances larger than 2.27 a_0, λ is no longer equal to 1, and it approaches a value of 0 as the molecule dissociates. This point at 2.27 a_0 is called the Coulson-Fischer (CF) point, and it indicates the distance at which antiferromagnetic coupling of the two atomic orbitals of interacting hydrogen atoms begins to break down, and the atoms start to become an uncoupled diradical. If $\lambda = 1$ for all internuclear distances, this wave function includes too much ionic character (an equal mixture of H^+H^- and H^-H^+) at the expense of diradical character, resulting in a calculated dissociation energy that is too high.

The incorrect dissociation of the H_2 bond in RHF theory may be attributed to a lack of multi-center correlation, which lowers the energy by separating the two electrons onto different centers, and it is a special case of what is sometimes called static or near-degeneracy correlation.[31–33] A CASSCF(2,2) wave function provides a way to treat this problem and has the correct spatial and spin symmetry. This is achieved by mixing the

$|\sigma_g^2\rangle$ configuration of RHF theory with a $|\sigma_u^2\rangle$ configuration. At the equilibrium internuclear distance, this lowers the energy of the wave function by 12 kcal/mol, but the contribution slowly increases to 21 kcal/mol at the CF point,[447] and eventually to 157 kcal/mol at infinite separation of the atoms. Because H_2 needs more than one CSF for a correct description at infinite separation, H_2 is called a multireference system. It is also sometimes called or a strongly correlated system. The dominant contribution to the difference between the RHF solution and a CASSCF(2,2) solution for dissociation of a single bond is sometimes called left-right correlation energy.[32]

The present article analyzes the H_2 dissociation problem, which is the simplest case of left-right correlation energy, in terms of the total electron density, the on-top pair density, and ratio of the on-top pair density to the square of the total density. The electron density ρ is the probability of finding an electron at a given point is space. The on-top density Π is the probability of finding two electrons at a given point in space. The motivation for anticipating that looking at these two quantities together provides a way to characterize left-right correlation energy is that Π equals $(\rho/2)^2$ for an RHF wave function but not for the CASSCF wave function; thus the deviation of this ratio from unity for a small CASSCF calculation on H_2 is one measure of left-right correlation. We analyze an RHF wave function and a CASSCF wave function by deriving analytic expressions with a minimal basis set. Just as the deviation of the total density from the sum of atomic densities has been used to analyze bonding character,[480] the deviation of the CASSCF(2,2) on-top pair density for a bond-breaking process from the RHF on-top pair density for that process should be able to teach us about left-right correlation energy.

Analysis of systems using 2-electron quantities is not new,[480–482] and the present study is complementary to previous studies that have focused on understanding 2-electron properties in molecules as they relate to the Coulomb hole.[483–485] It has also been previously suggested by looking at the Coulomb hole that electron correlation may bring electrons closer together[486] and we hope this work may add to the discussion about this behavior.

11.3 Theoretical Foundations

A CASSCF wave function for H_2 with two electrons in two orbitals, denoted as (2,2), can be written as a linear combination of two CSFs:

$$\Psi(x_1, x_2) = C_1\left|{\sigma_g}^2(x_1, x_2)\right\rangle + C_2|{\sigma_u}^2(x_1, x_2)\rangle \quad (1)$$

where C_1 and C_2 are the expansion coefficients, x_1 denotes the general spatial and spin coordinates of electron 1, i.e., $\mathbf{r}_1$ and σ_1, and x_2 denotes the general spatial and spin coordinates of electron 2. For the analytical derivation we write the wave functions for the $\left|{\sigma_g}^2\right\rangle$ and $|{\sigma_u}^2\rangle$ states in eq 1 in terms of a minimal basis of Slater-type orbitals

$$\left|{\sigma_g}^2(x_1, x_2)\right\rangle = \frac{Z^3}{2\pi(1+S)}(e^{-Zr_{1a}} + e^{-Zr_{1b}})(e^{-Zr_{2a}} + e^{-Zr_{2b}})\frac{\alpha(1)\beta(2)-\alpha(2)\beta(1)}{\sqrt{2}} \quad (2)$$

$$|{\sigma_u}^2(x_1, x_2)\rangle = \frac{Z^3}{2\pi(1-S)}(e^{-Zr_{1a}} - e^{-Zr_{1b}})(e^{-Zr_{2a}} - e^{-Zr_{2b}})\frac{\alpha(1)\beta(2)-\alpha(2)\beta(1)}{\sqrt{2}} \quad (3)$$

where Z is a parameter optimized at each internuclear distance by fitting the energies as a function of Z to a parabola and finding the Z that minimizes the total energy; S is the overlap integral of the basis functions, r_{1a} and r_{1b} are the distances from nuclei a and b to electron 1 (see the Supporting Information for a discussion of coordinates), r_{2a} and r_{2b} are

the distances from nuclei *a* and *b* to electron 2, and the last factors in eqs 2 and 3 are the spin components of the CSFs. A single-determinant RHF wave function corresponds to setting C_2 equal to 0 in eq 1 and setting Z equal to a value that was optimized for this case in eq 2.

For a diatomic molecule, a point in space can be characterized by the distances r_a and r_b from the two nuclei. The on-top pair density defined for H_2 is

$$\Pi(r_a, r_b) = \int |\psi(x_1, x_2)|^2 \, d\sigma_1 d\sigma_2 |_{r_{1a}=r_{2a}=r_a, r_{1b}=r_{2b}=r_b} \tag{4}$$

For the CASSCF(2,2) wave function of eqs 1-3, this yields.

$$\Pi_{\mathrm{CASSCF}}(r_a, r_b) = \frac{Z^6 e^{-4Z(r_a+r_b)} \left(C_1 \left(e^{Zr_a}+e^{Zr_b}\right)^2 (-1+S) - C_2 \left(e^{Zr_a}-e^{Zr_b}\right)^2 (1+S) \right)^2}{4\pi^2 (-1+S^2)^2} \tag{5}$$

and for the RHF wave function of eq 2 it yields

$$\Pi_{HF}(r_a, r_b) = \frac{Z^6 e^{-4Z(r_a+r_b)} \left(e^{Zr_a}+e^{Zr_b}\right)^4}{4\pi^2 (1+S)^2} \tag{6}$$

The electron density ρ of H_2 is

$$\rho(r_a, r_b) = 2 \int |\psi(x_1, x_2)|^2 \, d\sigma_1 d\sigma_2 dr_1 d\boldsymbol{r_2} |_{r_{1a}=r_a, r_{1b}=r_b} \tag{7}$$

For the CASSCF(2,2) wave function, we get

$$\rho_{\mathrm{CASSCF}}(r_a, r_b) = \frac{Z^3 e^{-2Z(r_a+r_b)} \left(C_1^2 \left(e^{Zr_a}+e^{Zr_b}\right)^2 (-1+S) - C_2^2 \left(e^{Zr_a}-e^{Zr_b}\right)^2 (1+S) \right)}{\pi(-1+S)(1+S)} \tag{8}$$

and for the RHF wave function we get

$$\rho_{HF}(r_a, r_b) = \frac{Z^3 e^{-2Z(r_a+r_b)} \left(e^{Zr_a}+e^{Zr_b}\right)^2}{\pi(1+S)} \tag{9}$$

For H_2, the ratio of the on-top pair density to the product of the up-spin and down-spin densities (which are always equal for singlet H_2) is

$$R(r_a, r_b) = \frac{4\Pi(r_a,r_b)}{\rho^2(r_a,r_b)} \tag{10}$$

Equations 6 and 9 show that $R = 1$ for the single-determinant wave function of eq 2. This is not the case for our CASSCF(2,2) wave function where the expression for R is

$$R_{\mathrm{CASSCF}}(r_a, r_b) = \frac{\left(C_1\left(e^{Zr_a}+e^{Zr_b}\right)^2(-1+S)-C_2\left(e^{Zr_a}-e^{Zr_b}\right)^2(1+S)\right)^2}{\left(C_1^2\left(e^{Zr_a}+e^{Zr_b}\right)^2(-1+S)-C_2^2\left(e^{Zr_a}-e^{Zr_b}\right)^2(1+S)\right)^2} \tag{11}$$

The ratio R will be called the on-top ratio. In order to achieve a more general understanding of R and Π and how they are related to electron correlation in wave functions, we use their analytic expressions and examine their behavior as functions of internuclear distance.

11.4 Computational Details

All the results presented below were evaluated by employing the analytical expressions of Π and ρ derived using *Mathematica* version 10.4.1.[487] In the following we will report values of Π in a_0^{-6} and of ρ in a_0^{-3} that we computed using the 'ListContourPlot' option in *Mathematica*.

11.5 Results and Discussion

Specific values of ρ, Π, and R for both wave functions are tabulated in Appendix 8 at various geometries for the bond midpoint (Table A8.1), a point 0.5 a_0 from an atom

along the bond axis and inside the bond (Table A8.2), a point 0.5 a_0 from an atom along the bond axis and outside the bond (Table A8.3), a point 0.5 a_0 from an atom perpendicular to the bond (Table A8.4), and a point 0.5 a_0 perpendicular to the bond from the point in Table A8.2 (Table A8.5) to supplement the contour plots discussed below. To keep the number of figures manageable, most of the figures for ρ can be found in the Supporting Information and are labeled throughout the discussion. Many of these tables and figures are mentioned throughout the discussion to alert readers who wish to consult them for more detailed study.

11.5.1 Density and on-top density for H_2 near equilibrium

The equilibrium internuclear distance r_{ab} of H_2 is 1.4 a_0. Since H_2 at its equilibrium geometry can be reasonably well described by a single determinant, the CI coefficient for the $|\sigma_u{}^2\rangle$ configuration is small, but not zero. In fact, we find $C_2 = -0.1122$. Nevertheless, Figs. 11.1 and 11.2 show that at 1.4 a_0, Π has a noticeably different distribution for the CASSCF(2,2) wave function than for the RHF one; in particular, at the nuclei, RHF has larger values of Π than does CASSCF(2,2). From the contour plots, it is clear that there is a smaller probability density for finding two electrons in the same space near the center of the bond than for two electrons to occupy the same space near the nuclei and both wave functions have similar values of Π near the center of the bond. Both wave functions have smaller values of Π outside the bond than inside, which is not unexpected, since the density is smaller there. The difference in Π for the two wave functions (CASSCF(2,2) minus RHF) is shown in Fig. 11.3; since the differences in Π are small and are not all positive, Fig 11.3 is a plot of the natural logarithm of the absolute

value of difference. The only region where CASSCF(2,2) has a value of Π larger than RHF is the central oval from about -0.7 to 0.7 a_0 along the x-axis. At all other points the RHF wave function has larger values of Π.

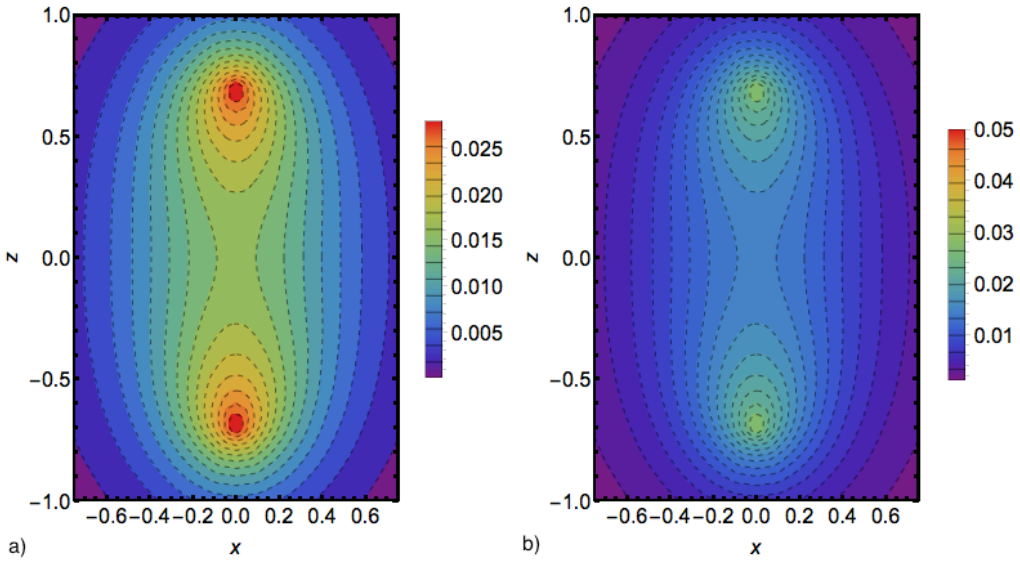

Figure 11.1. Contour plot of on-top pair density for CASSCF(2,2) at 1.4 a_0 where the bond is along the z-axis. Part (a) has a color scale that illustrates the structure as well as possible. Part (b) uses the same color scale as Fig. 2 so that one can see the difference clearly.

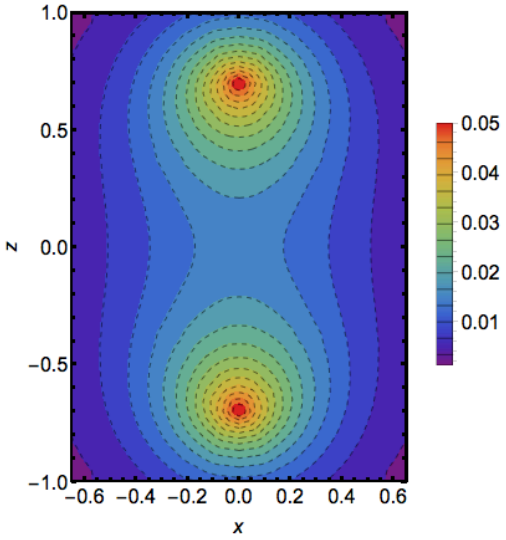

Figure 11.2. Contour plot of on-top pair density for RHF at 1.4 a_0 where the bond is along the z-axis

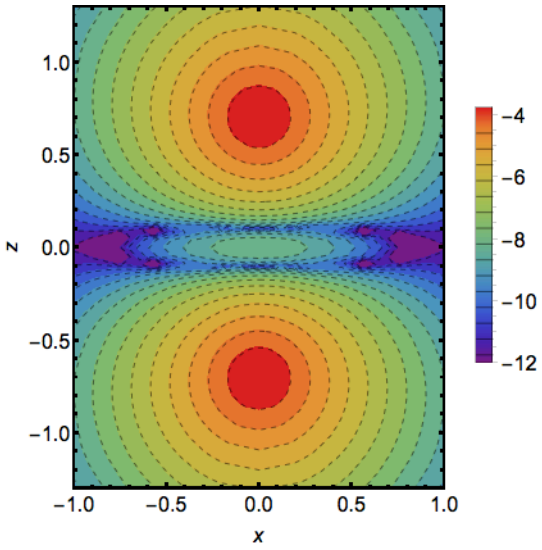

Figure 11.3. Natural logarithm of the absolute value of the difference of the RHF on-top pair density from the CASSCF(2,2) on-top pair density at 1.4 a_0. The RHF wave function has larger values of Π everywhere except for the oval in the center of the contour plot from -0.7 to 0.7 a_0 along the x-axis.

We see that adding the $|{\sigma_u}^2\rangle$ configuration to the wave function has a significant effect on Π even when the overall contribution from $|{\sigma_u}^2\rangle$ to the wave function is small. In order to understand this we partitioned Π for both wave functions into contributions from the ionic and covalent terms; ionic terms are defined as those terms that only depend on r_a or r_b when the numerators of eqs 5 and 6 are expanded, and covalent terms are those that contain both r_a and r_b. Figure 11.4 shows the contributions to Π in eqs 5 and 6 from the ionic and covalent terms. For RHF, the magnitude of the ionic (Fig. 11.4a) and covalent terms (Fig. 11.4b) are about the same, and as expected, the on-top pair density for the ionic terms is located around the atoms. The sum of Fig. 11.4a and Fig. 11.4b yields the result shown in Fig. 11.2. Figure 11.4 elucidates a point illustrated by Coulson and Fischer, in particular that the ionic terms are overemphasized in a single determinantal wave function in molecular orbital theory. Without the ionic terms, the

remaining contribution to Π for RHF is much more similar to that of a CASSCF(2,2) wave function (Fig. 11.1). The effect of configuration interaction is a reduction of the ionic configurations in the CASSCF(2,2) wave function (Fig. 11.4c) such that there is less of a build up in the on-top pair density around the nucleus (Fig. 11.1).

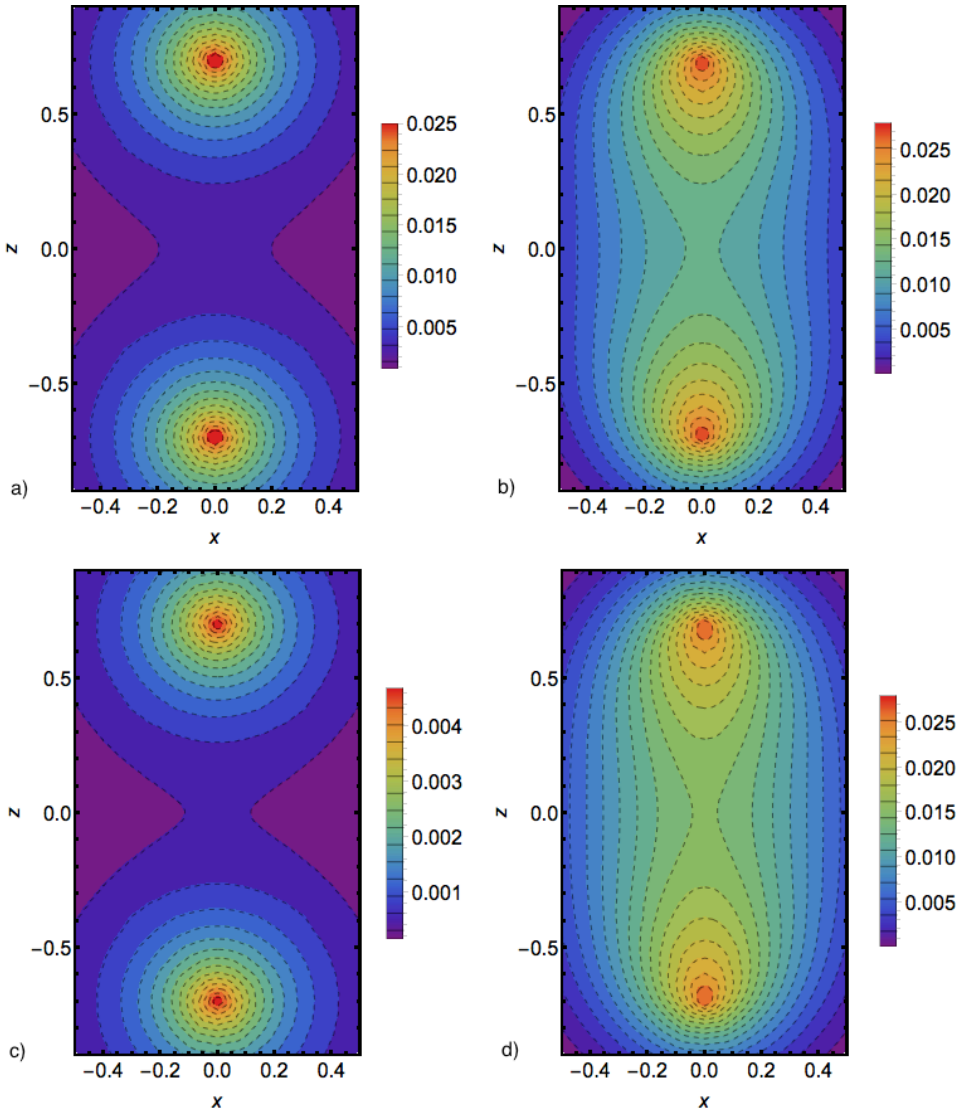

Figure 11.4. Contour plots of contributions to the on-top pair density for H_2 at 1.4 a_0 for (a) RHF ionic terms, (b) RHF covalent terms (c) CASSCF(2,2) ionic terms, and (d) CASSCF(2,2) covalent terms.

At the bond midpoint the terms involving the $|\sigma_u{}^2\rangle$ configuration are zero, leaving the CASSCF(2,2) expression for Π the same as RHF, except for the CI coefficient, normalization constant, and value of the screening parameter *Z*. Table A8.1 shows that at the midpoint of the bond, the value of Π differs by only 1.7% for the RHF and CASSCF(2,2) wave functions when the internuclear distance is 1.4 a_0.

Unlike Π, the density ρ is qualitatively similar for both RHF and CASSCF(2,2) when the internuclear distance is 1.4 a_0 (Fig A8.2 and A8.3). This corresponds well to the usual expectation that one-electron properties are more accurate than two-electron properties for an HF wave function. For CASSCF(2,2) near equilibrium, ρ will largely be described the $|\sigma_g{}^2\rangle$ configuration since C_2^2 will be small and unlike Π, there are no surviving cross terms, resulting an expression for ρ that is qualitatively similar to that for RHF near equilibrium. In general, the distribution of ρ and Π is similar for the geometries near equilibrium and out to the CF point.

11.5.2 Density and on-top density at the Coulson-Fischer point

The CF point occurs around 2.3 a_0. Just as the CF point was found to be a critical point in the behavior of the wave function with respect to total energies, the CF point also signals a region where the behavior of Π begins to change rapidly. Beyond the CF point at 2.5 a_0, the RHF wave function now has larger values of Π everywhere in space (Fig 11.5), in contrast to the situation at shorter internuclear distances. Table A8.1 shows that the ratio of Π_{CASSCF} at the bond midpoint to Π_{HF} at the bond midpoint is close to unity (it is 1.01) at the CF point, but then it drops precipitously, for example to 0.93 at 3 a_0, to

0.68 at 4 a_0, to 0.43 at 5 a_0, and to 0.06 at 10 a_0, although Π is approaching 0 for both wave functions.

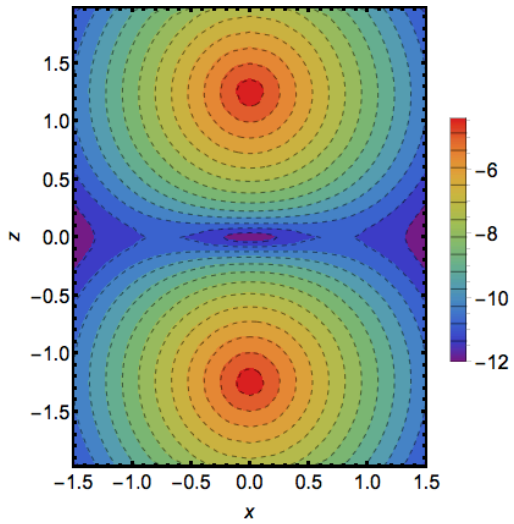

Figure 11.5. Natural logarithm of the difference (RHF minus CASSCF(2,2)) in values of the on-top pair density at 2.5 a_0. RHF has larger values of Π everywhere.

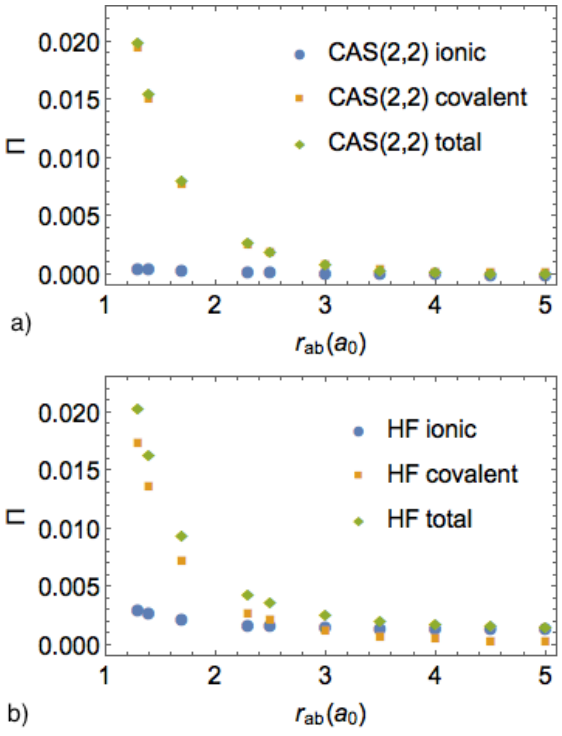

Figure 11.6. Contributions to the on-top pair density at a point 0.5 a_0 from one hydrogen atom inside the bond along the internuclear axis for (a) CASSCF(2,2) and (b) RHF.

Figure 11.6 shows the contribution to Π from the ionic and covalent terms at a representative point 0.5 a_0 from one hydrogen atom inside the bond for various internuclear distances. This partitioning helps illustrate why the RHF and CASSCF(2,2) wave functions start to differ as they dissociate. The total contribution to Π for the CASSCF(2,2) wave function is mostly from the covalent terms (Fig. 11.6a), whereas both the ionic and covalent terms have a substantial contribution for RHF (Fig. 11.6b). Around the CF point, the ionic terms begin to have a greater contribution to Π for RHF than the covalent terms. Plotting both wave functions together and focusing on the region from 2.0-3.5 a_0 shows that the RHF covalent terms are actually close to the covalent Π and total Π for the CASSCF(2,2) wave function (Fig. 11.7). However, as these terms are approaching zero, the RHF ionic terms become the dominant part of the RHF Π after the CF point because there is not enough flexibility in the wave function to properly cancel these terms.

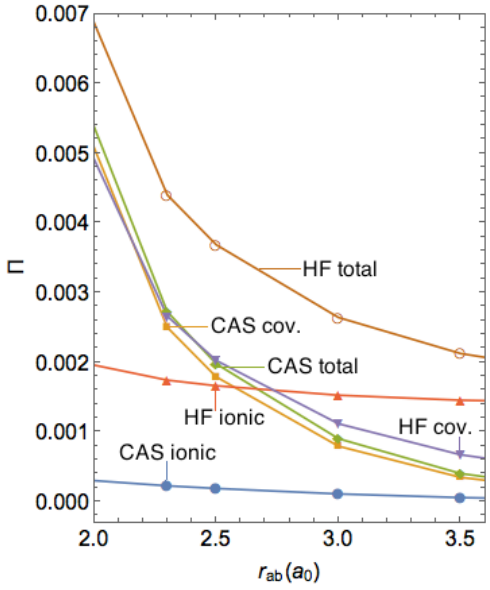

Figure 11.7. Contributions to the on-top pair density at a point 0.5 a_0 from one H atom inside the bond along the internuclear axis for CASSCF(2,2) and RHF near the CF point.

11.5.3 Density and on-top density at the asymptotic dissociation limit

The CASSCF(2,2) wave function has larger values (than RHF) of ρ near the center of the bond when the internuclear distance is 1.4 a_0., but just after the CF point, ρ is now larger in the center region of the bond (Fig. A8.7) for RHF. Moving toward infinite separation, ρ remains larger at the bond midpoint for RHF (Table A8.1), while ρ remains larger near the nuclei for CASSCF(2,2) (Tables A8.2-A8.5). Comparing eqs 8 and 9, at the bond midpoint where the difference in the exponential terms from the $|{\sigma_u}^2\rangle$ configuration is 0, C_1^2 starts to become significantly smaller than unity after 2.5 a_0, reducing the density of the CASSCF(2,2) wave function compared to RHF. After the CF point, the RHF orbitals start to become more diffuse (Table A8.7) to accommodate the ionic character of the wave function, and this decreases ρ around the nuclei compared to CASSCF(2,2).

At infinite separation, Π should go to zero for a wave function that properly predicts a diradical; this is the case for a CASSCF(2,2). The RHF wave function has a nonzero value of Π at infinite separation of the nuclei due to its single determinantal nature, which has a 50% contribution from terms that put two electrons on one atom. For a point 0.5 a_0 from the nuclei at r_{ab} =100 a_0, Π has a value of 0.0017 atomic units for RHF (Tables A8.2-A8.4).

When the nuclei are infinitely separated, points near nucleus *a* have $r_b = \infty$. The limit of eq 6 is

$$\lim_{r_b\to\infty} \frac{Z^6 e^{-4Z(r_a+r_b)}\left(e^{Zr_a}+e^{Zr_b}\right)^4}{4\pi^2(1+S)^2} = \left(\frac{Z^3}{2\pi}\right)^2 \frac{1}{(1+S)^2} e^{-4Z(r_a)} \qquad (12)$$

For RHF, the only non-zero term in this limit is the ionic term where both electrons are on the same nucleus. In the CASSCF(2,2), the only non-zero terms that survive in this limit are a few ionic terms from both the $|\sigma_g{}^2\rangle$ and $|\sigma_u{}^2\rangle$ configurations which cancel with the cross terms at infinite separation, resulting in an on-top pair density value of 0. The triplet state of H_2 is degenerate with the singlet of a CASSCF(2,2) wave function at infinite separation, and Π is identically zero for triplet stats of H_2 as it must to be in accordance with the Pauli exclusion principle.

11.5.4 The on-top ratio R

The on-top ratio *R* provides useful information about the nature of the wave function in the following sense: If $R = 1$, the system can be described as a single determinant. If $R > 1$ or $R < 1$, the electronic motion is correlated to a greater extent than that simply required by antisymmetry, and the wave function cannot be described by a single determinant.

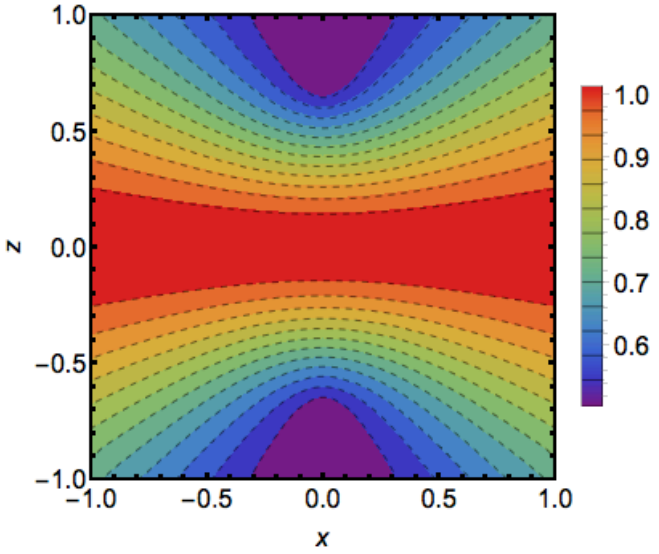

Figure 11.8. Contour plot of on-top ratio *R* at r_{ab} = 1.4 a_0

For RHF, the on-top *R* of eq 10 is always unity, but for CASSCF(2,2) this is not the case as shown in Fig 11.8 for 1.4 a_0 . At the bond midpoint for all internuclear distances, $R > 1$ (Table 11.1); *R* also has this value for all points when the electrons are equidistant from the nuclei because the orbital part of the $|\sigma_u{}^2\rangle$ configuration in eq 11 will be 0. Moving from the bond midpoint toward the nuclei, *R* decreases.

Table 11.1. On-top ratio at the bond midpoint

$r_{ab}(a_0)$	Ratio
0.6	1.002
0.7	1.003
1.3	1.011
1.4	1.013
1.7	1.022
2.5	1.073
3.0	1.138
3.5	1.235
4.0	1.359
4.5	1.491
5.0	1.615
10.0	1.991
100.0	2.000

The distribution of the on-top ratio *R* at all internuclear distances is qualitatively similar to that shown in Fig 8, but this distribution looks notably different than either that of Π or ρ alone (Figs 11.1-11.2, A8.2-A8.3).

Looking at the expression for *R*, there are terms containing $e^{r_a} \pm e^{r_b}$ that are reminiscent of the molecular orbitals: $(e^{-\boldsymbol{r}_{1a}} \pm e^{-\boldsymbol{r}_{1b}}) = \sigma_g$ or σ_u. These exponentials can be expressed in terms of hyperbolic functions of the elliptic and hyperbolic coordinates (see Appendix 8) and in the expression for *R,* the elliptical part of the orbitals

cancels, leaving an expression in terms of the hyperbolic part of the orbitals, resulting in a distribution of R values along hyperboloids in 3D space.

While one can see from Fig. 11.8 that R deviates from the RHF value in most regions of space, it is especially enlightening to look at the quantity

$$R - 1 = \frac{(A+B)^2 C_1^2 C_2^2 - 2ABC_1C_2}{\left(C_1^2 A - C_2^2 B\right)^2} \tag{12}$$

where, for simplicity, $A = (e^{Zr_a} + e^{Zr_b})^2(S-1)$, and $B = (e^{Zr_a} - e^{Zr_b})^2(S+1)$ and C_1 and C_2 are the CI coefficients. The largest deviations from the RHF value of 1 occur around the nuclei, where the ionic cross terms in Π have their largest contribution. We can use $C_1^2 = 1 - C_2^2$ to eliminate C_1 from eq 12 and expand eq 12 as Maclaurin series expansion to fourth order; this is useful to understand where the approximation that C_2 is small is valid and to understand when the $|\sigma_u{}^2\rangle$ configuration begins to change the character of the wave function. Plotting both functions (eq 12 and the series expansion) along the z axis for various internuclear distances shows that the curves overlap exactly at equilibrium (Fig. 11.9a). At 1.7 a_0 and 2.5 a_0 the functions differ by about 0.02 at the nuclei (Fig. 11.9b and 11.9c), so C_2may be considered small in these regions. At 3.5 a_0 there starts to be a large difference at the nuclei, about 0.05, and the point of differentiation between the two functions begins about 0.7 a_0 from the atoms (Fig 11.9d). At 3.5 a_0, the agreement between the functions in the center of the bond also starts to differ by 0.01. It is clear that the two functions no longer have good agreement after 3.5 a_0 (Fig 11.9e and 11.9f). One can consider 3.5 a_0 to approximately be the point where left-right correlation starts to drastically change the character of the wave function. The

difference in the functions at the bond midpoint, a point where $R = \frac{1}{C_1^2}$ or $R - 1 = \frac{C_2^2}{C_1^2}$, is significant as it shows that the CI expansion is no longer dominated by a single configuration. In fact, $C_2^2 = 0.19$ at 3.5 a_0, whereas it is 0.07 at 2.5 a_0.

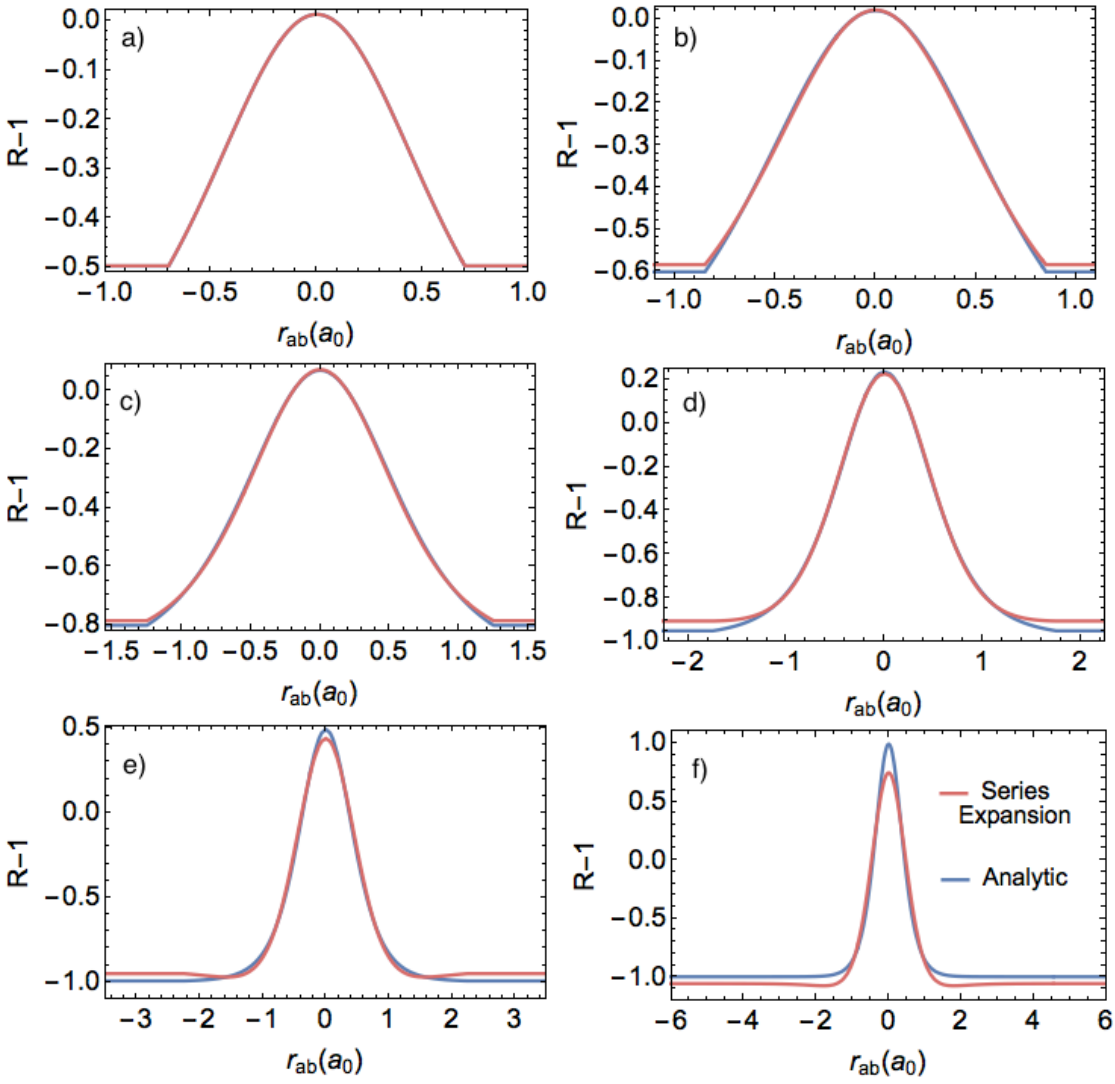

Figure 11.9. Plots of eq 12 and a series expansion along z-axis for a) r_{ab} = 1.4 a_0 b) r_{ab} = 1.7 a_0 c) r_{ab} = 2.5 a_0 d) r_{ab} = 3.5 a_0 e) r_{ab} = 4.5 a_0 f) r_{ab} = 10 a_0

As previously mentioned, the on-top ratio R for a correlated wave function is the ratio of the probability of finding two electrons in the same place to the probability of finding two

electrons in the same place for an uncorrelated wave function that has the same density as the correlated one. Where R is less than 1, the electrons avoid each other more and one can say that electron correlation decreases the probability of the electrons being in the same place relative to an uncorrelated wave function with the same density; we see this, particularly near the nuclei for a CASSCF(2,2) wave function.

Looking at 1.4 a_0 as an example, we see that $R > 1$ at the bond midpoint (Fig. 11.8) and so correlation increases the probability of finding the electrons in the same place relative to an uncorrelated wave function, although this probability is small. At the bond midpoint, integrating the expressions for Π and $\frac{\rho}{2}$ over a very small interval results in probabilities of 8.184×10^{-7} and 8.990×10^{-4}, respectively. Dividing these values according to eq 9 results in the value in Table 11.1 of 1.013. The distribution of R in Fig 11.8, can be used to understand in a general sense, the relative probabilities of finding two electrons in one place for a multideterminantal wave function versus a single determinantal wave function with the same density.

Approaching the dissociation limit, left-right correlation is increasing in the wave function as the $|\sigma_g{}^2\rangle$ and $|\sigma_u{}^2\rangle$ configurations become degenerate in energy. Figure 11.10 shows the on-top ratio R as a function of internuclear separation at the bond midpoint. Once H_2 reaches the CF point, R begins to rapidly approach its limit of 2.0. After 5 a_0, the on-top ratio R is about 2.0, which means that a correlated wave function is twice as likely to place two electrons in the same place as an uncorrelated wave function with the same density; at equilibrium they are approximately equally as likely to place two electrons in the same place since $R \approx 1.0$.

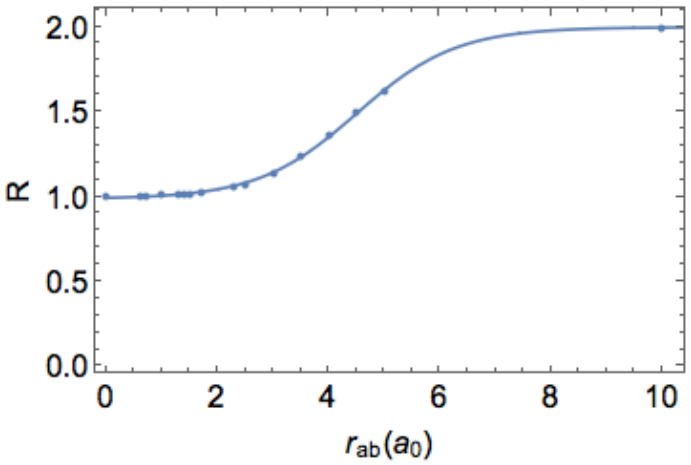

Figure 11.10. On-top ratio at the bond midpoint for various internuclear distances.

11.5.5 On-top pair density and bond breaking

The previous sections discussed the behavior of Π, ρ and R at different points in space around the molecule for different internuclear distances. We shall now discuss more generally the changes in Π as the bond breaks. A convenient way to characterize the bonding in a molecule using a CASSCF wave function is by calculating the effective bond order (EBO),[27] which only depends on the natural orbital occupation numbers of the orbitals. The EBO values for the CASSCF(2,2) are plotted as a function of internuclear distance in Fig 11.11; the inflection point is at 3.9 a_0. The sigmoidal segment from 2 to 6 a_0 can be considered to be the bond breaking region. At 1.9 a_0, the change in the 'acceleration' (using the illustrative terminology of physics) of the EBO values toward 0.0 is a local minimum and after this point, the EBO values rapidly start decreasing from 0.93 at 1.9 a_0 . It is around this point that the single bond starts to break. At 5.9 a_0, the bond is almost completely broken, as the EBO values rapidly approach zero after this point. At the inflection point around 3.9 a_0, the EBO is 0.51 and represents the point

where the magnitude of the change in EBO is the greatest as the $|\sigma_u{}^2\rangle$ configuration is low enough in energy to be substantially populated. This is around the point predicted from the series expansion of eq 12 where the character of the wave function begins to drastically change.

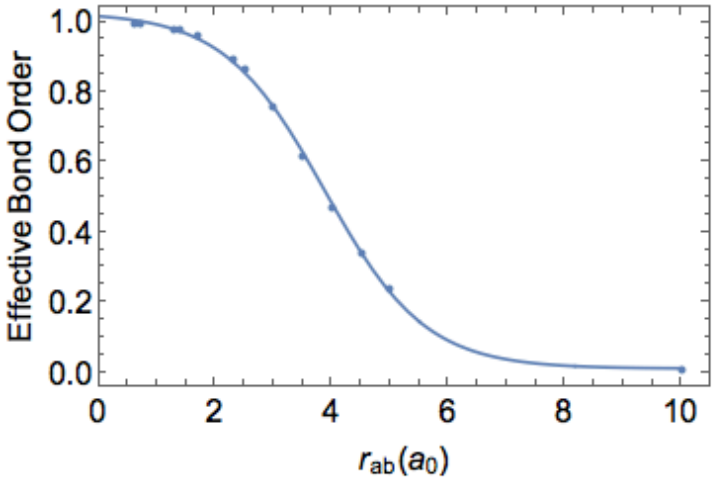

Figure 11.11. Effective bond order calculated by CASSCF(2,2)

The behavior of *R* at the bond midpoint is very similar to that of the EBO. Looking at the critical points of Fig. 11.10, they are similar to those in Fig. 11.11 with the most important one corresponding to the inflection point at 4.5 a_0. At 2.5 a_0, close to the CF point, *R* has a value of 1.08. As the bond starts to break, *R* begins to deviate from the RHF value and at 4.5 a_0 *R* increases to 1.49 and finally 1.91 at 6.6 a_0, the point where the bond is essentially completely broken. The on-top pair density therefore offers another way to quantify bond breaking in molecules. As previously mentioned, the bond midpoint for this CASSCF(2,2) wave function, *R* reduces to $\frac{1}{C_1^2}$, which is close to the natural orbital occupation numbers.

11.6 Conclusions

We have derived analytic expressions for $\Pi, \rho,$ and R for the RHF and CASSCF(2,2) wave functions for H_2 in a minimal basis set in order to better understand how these quantities are related to left-right electron correlation. Accurate prediction of Π requires the correct balance between covalent and ionic terms, which cannot be achieved with a single determinantal wave function. At the CF point, the relative magnitude of Π for RHF and CASSCF(2,2) begins to change rapidly as RHF dissociates to the incorrect limit with a non-zero value of Π and CASSCF(2,2) dissociates H_2 correctly because the covalent and ionic terms are properly canceled in Π. R deviates from unity for CASSCF(2,2) at all internuclear distances due to the cross terms in Π resulting from the CI treatment of the wave function. After the CF point, around 3.5 a_0, the $|{\sigma_u}^2\rangle$ configuration begins to contribute substantially to the wave function, resulting in significant changes in R from the RHF value at the bond midpoint, where the behavior of R may be a way to quantify bond breaking in molecules.

Chapter 12

Can Multiconfigurational Self-Consistent Field Theory and Density Functional Theory Correctly Predict the Ground State of Metal-Metal Bonded Complexes?

Reproduced in part from

Can Multiconfigurational Self-Consistent Field Theory and Density Functional Theory Correctly Predict the Ground State of Metal–Metal-Bonded Complexes?, Rebecca K. Carlson, Samuel O. Odoh, Stephen J. Tereniak, Connie C. Lu, and Laura Gagliardi, *Journal of Chemical Theory and Computation,* **2015,** *11* (9), 4093-4101.

12.1 Overview

The electronic structure of a diiron (FeFe) complex with strong metal-metal interaction and those of analogous complexes (CoCo, CoMn, CoFe, and FeMn) with much weaker metal-metal bonding are investigated with wave function-based methods and density functional theory. The delocalization and bonding between the metal centers in the diiron complex is only fully captured after inclusion of the complete set of 3*d* and 4*d* orbitals in the active space, a situation best suited for restricted active space (RAS) approaches. Truncation of the included set of 4*d* orbitals result in inappropriate localization of some 3*d* orbitals, incorrect description of the ground spin state as well as wrong spin state energetics, as compared to experiment. Using density functional theory, some local functionals are able to predict the correct ground spin states, and describe the chemical bonding and structural properties of all the metal-metal complexes considered in this work. In contrast, the introduction of some exact exchange results in increased localization of 3*d* orbitals and wrong spin state energetics, a situation that is particularly troublesome for the diiron complex.

12.2 Introduction

One of the outstanding challenges for quantum mechanical methods relates to the accurate treatment of multireference systems to fully account for electron correlation effects. In general, multireference systems are those that cannot be qualitatively correctly described by a single electronic configuration. Electronic correlation energy, according to Löwdin, is defined as the difference between the exact energy of a Hamiltonian and the Hartree–Fock (HF) energy using the same Hamiltonian.[488] The special types of errors that occur in a single-reference formalism, where one Slater determinant (SD) or configuration state function (CSF) is used, are called “static” or “non-dynamical” correlation errors.[31–33] Particularly, systems containing transition metals are often multiconfigurational and in order to accurately describe their structural properties, electronic structure and catalytic properties, a proper treatment of static electron correlation is needed.

Kohn–Sham density functional theory (KS-DFT)[42] is a very popular method. It has been applied to a large number and variety of systems and is particularly amenable for studying large molecules that are often intractable with wave function based methods. However, as KS-DFT is a single determinantal method, the accuracy achievable with existing functionals is typically low for inherently multiconfigurational systems.[309–311] In addition, there have been many cases in which various exchange-correlation functionals give conflicting results for multiconfigurational systems. This problem often occurs in the prediction of the ground spin states of transition metal complexes. In general, hybrid functionals favor high-spin states, while generalized gradient approximation (GGA) functionals favor low-spin states.[489,490] Truhlar et al.,[28] Swart,[29] and Reiher et al.[30] have shown that the relative spin state energies of various iron-containing systems depend on the type of functional and the amount of exact HF exchange used. Another complication that arises in KS-DFT is the existence of broken symmetry[491,492] solutions. While breaking symmetry constraints allows for a variationally lower energy solution that may be more accurate in energy[28], ambiguous spin states may result from optimizing a wave function for a non-physical state.

As an alternative to KS-DFT, multiconfiguration self-consistent-field (MCSCF) approaches, such as the complete active space self-consistent field (CASSCF)[34] method, are used to study the properties of inherently multiconfigurational systems. These methods can account for static electron correlation effects. Dynamic correlation effects can then be added by multireference perturbation theory [such as complete-active-space second-order perturbation theory (CASPT2)[429]] or multireference configuration

interaction (MRCI)[36] methods, using the MCSCF wave function as a reference, to achieve quantitative accuracy. Such methods are generally considered as the standards to which to compare results obtained with different exchange-correlation density functionals.[493,494]

CASSCF/CASPT2 is a popular multireference method. However, in CASSCF the major drawback is that the number CSFs or SDs scales exponentially with the number of active orbitals. CASSCF/CASPT2 calculations with more than eighteen electrons in eighteen active orbitals are not currently feasible, and this limits the type of chemical problem that can be addressed with such a method. One can employ larger active spaces and still reduce the computational cost associated with CASSCF/CASPT2 by imposing constraints on the active space using the restricted active space (RASSCF)[438] and generalized active space (GASSCF)[41] self consistent field methods. Other wave function methods aimed at reducing the size of the CI expansion include SplitGAS,[318] occupation-restricted-multiple-active-space (ORMAS) SCF methods,[38,320] and DMRG.[495–499] We have also recently developed a method, multiconfiguration pair-density functional theory (MC-PDFT)[46], that incorporates multiconfigurational character into the density, avoiding the need for the broken-symmetry solutions that exist in KS-DFT.

Most studies on metallic systems with multiconfigurational character have focused on monometallic complexes[29,500], particularly heme complexes[494,501] with much fewer studies performed on bimetallic, multiply bonded metal-metal complexes. In the present work we are interested in examining the electronic structures of bimetallic complexes that contain first-row transition metals in a trigonal ligand scaffold, as

synthesized by Lu and co-workers, Figure 12.1.[20,22] In particular, we are interested in the electronic structure properties of the diiron chloride analogue of the M_1-M_2-Cl series with the pyridine scaffold, where M_1 and M_2 represent the identity of a transition metal in Figure 12.1.[20] The interest in this particular complex arises from the fact that, while the electronic structures of the various Co-M_2-Cl (Co-Co-Cl, Co-Mn-Cl, and Co-Fe-Cl) and Fe-Mn-Cl species were well described by various theoretical methods, it was found that attaining the correct electronic structure properties for the Fe-Fe-Cl analogue was more challenging. The Fe-Fe-Cl complex is all the more interesting as it was empirically found to be an outlier from the available series of M_1-M_2-Cl complexes as it possesses a high spin ground state with ferromagnetic

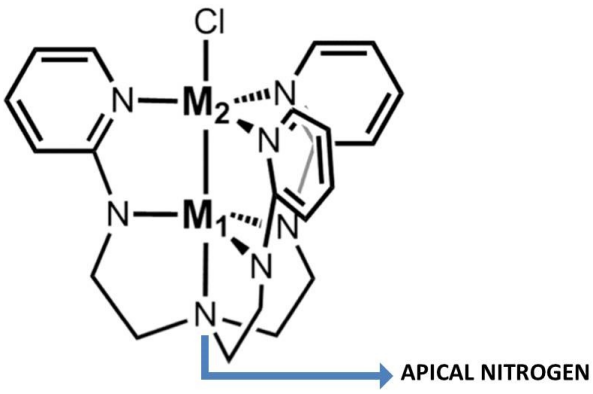

Figure 12.1. Structure of the M_1-M_2-Cl series of complexes. These complexes possess a N,N,N-tri(2-(2-pyridylamino)ethyl)amine ligand scaffold and two 1st row transition metals that are labeled as M_1 (bottom metal) and M_2 (top metal). There are three nitrogen atoms in the equatorial regions of the metal atoms while M_1 also has a apical nitrogen.

coupling of the two iron centers, in stark contrast to all other complexes in this series which were found to possess low spin ground states with antiferromagnetic coupling of the metal sites.[20] In this paper, we present an in-depth theoretical study of the Fe-Fe-Cl

complex and attempt to explain the differences between this particular complex and other members of the M_1-M_2-Cl series.

12.3 Computational Details

12.3.1 Wave Function Calculations All the CASSCF/CASPT2 and RASSCF/RASPT2[40] (RASPT2 is a second order perturbation on a RASSCF wave function) calculations were performed using the MOLCAS 7.8 package[120] on the experimental X-ray structures. The active space choices, denoted (*n*, *m*) for the CASSCF calculations, included all 3*d* electrons *n* of the transition metals in *m* 3*d* and 4*d* orbitals. For Fe-Fe-Cl, the CASSCF active spaces used were (12,12), (12,14), and (12,15) which include all the 3*d* electrons and orbitals and an additional two, four, five, or ten 4*d* orbitals, respectively. The active space choice for the RASSCF calculations is denoted by (12,20)/(12,10)/2. The first set of parentheses corresponds to the total number of electrons in RAS1 and RAS2 and the total number of orbitals in all of the RAS spaces. The second set of parentheses corresponds to the number of active electrons and orbitals in RAS2; the final value of 2 indicates the number of particles allowed into RAS3. In addition, we also performed RAS-CI calculations with the (12,20)/(12,10)/2 active space for the Fe-Fe-Cl complex, optimizing the CI expansion for each spin state without optimizing the orbitals for each spin state. For these RAS-CI calculations, the orbitals used were obtained from the septet RASSCF (12,20)/(12,10)/2 calculation and used for all spin states and we only re-optimized the CI coefficients for each state.

The relativistic all-electron ANO-RCC basis sets were used on all atoms in the complexes. Specifically, double-ζ quality (ANO-RCC-VDZP)[121,502] basis sets were used

for Co, Fe, N, and Cl atoms and minimal basis sets (ANO-RCC-MB)[502] were used for C and H atoms. The following contractions were employed: [5s4p2d1f] for all the metal atoms, [3s2p1d] for the nitrogen and chlorine, [2s1p] for the carbon atoms, and [1s] for the hydrogen atoms. Reduction of the four center 2-electron integrals to effective three center integrals via auxiliary basis sets was accomplished with the RICD approximation.[125] For the CASPT2/RASPT2 calculations, an imaginary level shift of 0.2 a.u. was used to prevent the occurrence of intruder states.[126] The effective bond orders (EBO)[27] between the atoms in these complexes were calculated at the electronic ground state. The EBO is defined as the difference of the sum of the bonding orbital occupations and the sum of the antibonding orbital occupation numbers divided by two.

12.3.2 DFT Calculations All the DFT calculations were performed using the ADF 2013 package.[503] The scalar-relativistic Zeroth Order Regular Approximation (ZORA) was employed to include relativistic effects.[504,505] In all DFT calculations, all-electron Slater type orbitals of triple-ζ quality with two polarization functions (TZ2P) were used to describe all atoms. Three classes of functionals were used to calculate the relative energies of the various spin states of the M_1-M_2-Cl complexes at the structures obtained from X-ray crystallography experiments.[20] The first are local functionals, namely LDA,[344] PBE[199,506] and the Minnesota M06-L[173,363] functional. The effect of exact exchange was investigated by considering the PBE0-12%, PBE0-25% and PBE0-50% functionals. For these hybrid functionals, the notation -*x*% denotes the fraction of Hartree-Fock exchange included in a PBE0-type functional. As an example, PBE0-12% contains 12% exact exchange, instead of 25% as used in the original PBE0 (here labeled

as PBE0-25%) functional.[506] The last class of functionals contain two of the Minnesota 06 metahybrid functionals, M06 and M06-2X.[173,363] All these calculations were carried out within the unrestricted DFT formalism.

To examine the performance of the various density functionals for predicting the structures of the metal-metal complexes, geometry optimizations were carried out in the gas phase without symmetry constraints. In these geometry optimizations, we have used only the LDA, PBE, PBE0-12%, PBE0 and M06 functionals. The geometry optimizations were followed by vibrational frequency analyses to confirm that the optimized structures were local minima. More details about the calculations are presented in the supporting information section.

12.4 Results and Discussion

12.4.1 Multiconfigurational Calculations. All the metals in the bimetallic complexes considered in this work are formally in the +2 oxidation state. A minimal active space includes the 3*d* electrons from each of the metals in an orbital space of all ten 3*d* orbitals. Based on previous experience with similar complexes, we found that including some, but not all of the correlating 4*d* shell is enough to accurately describe the wave function of these M_1-M_2-Cl complexes.[20,22,507]

A suitable active space for the three Co-M_2-Cl and Fe-Mn-Cl complexes in our calculations included all the 3*d* electrons in all the 3*d* orbitals as well as two additional 4*d* correlating orbitals, for a total of 12 orbitals. However, this active space was found to be insufficient for capturing the septet state as the correct ground state, based on experimental studies, of the Fe-Fe-Cl complex. We explored larger active spaces, in order

to see if we could accurately predict the correct ground state and capture the electronic structure properties of Fe-Fe-Cl. The following active spaces were attempted for all spin states: (12,12), (12,14), (12,15). For the singlet and triplet spin states, CASSCF calculations with the (12,15) active space were not feasible due to the large number of configurations state functions and the slow convergence of the CI expansion with concomitant orbital relaxation. However, to qualitatively describe all the spin states of Fe-Fe-Cl while using larger active spaces, we carried out RAS-CI calculations for the different spin states while using the orbitals obtained from the septet electronic state of the (12,20)/(12,10)/2 calculation and only re-optimized the CI coefficients for each state. For the (12,12), (12,14), and (12,20)/(12,10)/2 active spaces, the relative spin state energies of Fe-Fe-Cl are presented in Table 12.1.

Table 12.1. Relative spin state energies (kcal/mol) of the Fe-Fe-Cl complex for various active spaces with respect to the energy of the septet state.

	(12,12)		(12,14)		(12,20)/(12,10)/2	
	CASSCF	CASPT2	CASSCF	CASPT2	RASCI	RASPT2
Singlet	-5.1	-8.7	-6.3	-3.1	-1.6	1.5
Triplet	-4.7	-4.3	-5.5	-1.2	-1.3	1.6
Quintet	-2.7	-4.4	-3.9	0.6	-1.2	-0.1
Septet	0.0	0.0	0.0	0.0	0.0	0.0
Nonet	11.8	0.7	-1.1	-5.3	3.9	2.0

There are several important things to note. First, the singlet state is always predicted to be the lowest in energy for the Fe-Fe-Cl complex at the CASSCF and RASCI levels. Second, as the π/π^* pairs of orbitals are not present when the active space contains less than 20 orbitals, the inclusion of the full 20 orbitals has a significant effect on the calculated relative energies, as well as on the bonding between the two iron centers. To

illustrate, the EBO between the metal centers as well as the weights of the d_{xz} and d_{yz} orbitals in the π molecular orbital are shown in Table 12.2 for the septet wave function for different active space sizes. For the (12,12) and (12,14) active spaces, the d_{xz} and d_{yz} orbitals in the π molecular orbital are largely localized, with little mixing or delocalization, and have an EBO of about 0.2. Only once the active space is sufficiently increased to (12,20)/(12,10)/2 does a delocalized bonding scheme (25.6% & 74.4% weight of the d_{xz} and d_{yz} orbitals in the π molecular orbital between the two metals) between the metals appear, consistent with a much larger EBO of 0.73.

Table 12.2. EBO, weight of dominant configuration (DC) and percent distribution of d_{xz} and d_{yz} components between the Fe centers of the π symmetry molecular orbitals for the septet spin state of Fe-Fe-Cl.

Active Space	EBO	Weight of DC	% of d_{xz} and d_{yz} in the π symmetry MO
(12,12)	0.18	27.3%	Completely localized
(12,14)	0.22	28.6%	1.5% & 98.5%
(12,20)/(12,10)/2	0.73	28.0%	25.6% & 74.4%

Second, the expansion of the active space size alters the relative energies of the various spin states. For the calculations employing 12 electrons in 12 active orbitals, the nonet state is about 17 kcal/mol higher in energy than the singlet state with CASPT2. Such calculations include only σ/σ^* pairs. As the active space is enlarged to include more 4*d* orbitals of the metals, the bonding orbital becomes more delocalized and the nonet state becomes lower in energy. Once the active space is increased to include all ten 3*d* in RAS2 and all ten 4*d* in RAS3 results in spin states that are much closer in energy at the SCF level, Table 12.1.

Third, with perturbation methods, it appears that there is a large effect from dynamic correlation, Table 12.1. For the (12,12) active space, the singlet is still predicted to be the ground state, although the nonet is lowered in energy and is predicted to be only about 1 kcal/mol higher than the septet. Expansion of the active space to (12,14), results in a nonet ground state with the quintet and triplet states also slightly higher in energy than the septet. Neither the CASSCF nor CASPT2 are converged with respect to these smaller active space sizes. However, the relative energies of the spin states obtained at the RASPT2 level are all within 2 kcal/mol. It should be noted that since only the CI coefficients were optimized in an orbital space of septet orbitals from a RASSCF (12,20)/(12,10)/2 calculation, these spin state energy spacing represent a maximum spacing since the orbitals are only fully optimized for the septet state. Indeed, examination of the septet-nonet splitting as the active space is increased, suggests that the true energy splitting between the states, best represented by the (12,20)/(12,10)/2 RASCF/RASPT2 calculation using the SCF orbitals for each spin state, will be smaller, Table 12.3.

Table 12.3. Relative spin state energies (kcal/mol) of the septet and nonet spin states of Fe-Fe-Cl obtained at the CASPT2 and RASPT2 levels of theory.

	(12,12)[a]	(12,14)[a]	(12,15)[a]	(12,20)/(12,10)/2[b]	(12,20)/(12,10)/2[c]
Septet	0.0	0.0	0.0	0.0	0.0
Nonet	0.7	-5.3	-3.7	-0.02	2.0

[a] (12,12), (12,14), (12,15) active spaces for CASSCF/CASPT2 calculations using SCF orbitals for each spin state.
[b] (12,20)/(12,10)/2 active space for a RASSCF/RASPT2 calculation using SCF orbitals for each spin state.
[c] (12,20)/(12,10)/2 active space for a RASCI/RASPT2 calculation using orbitals obtained for the septet state.

A full RASSCF calculation with 20 orbitals was feasible only for the septet and nonet states. As shown in Table 12.3, as more 4*d* orbitals are added up to the full 4*d* shell, the splitting between the septet and nonet states decreases until these are nearly degenerate. While the (12,12) active space was sufficient[20] for Co-Co-Cl, Co-Fe-Cl, Co-Mn-Cl, and Fe-Mn-Cl it is evident from Table 12.2 that the active space is not converged as the total energy splitting for the Fe-Fe-Cl complex decreases dramatically from (12,12) to (12,20), with the relative energies between the septet and nonet states fluctuating.

The dominant configuration of the CASSCF (12,14) and (12,15) septet states is $(\sigma)^2(Fe_1\ d_{xz})^2(Fe_1\ d_{yz})^1(Fe_2\ d_{xz})^1(Fe_2\ d_{yz})^2\ (\delta)^2(\delta^*)^2(\sigma^*)^0$, similar to what was obtained for Co-Co-Cl. In contrast, for the RASSCF (12,20)/(12,10)/2 active space, the wave function is $(\sigma)^2(\pi)^4(\pi^*)^2(\delta)^2(\delta^*)^2(\sigma^*)^0$ and is delocalized. The weights of the DC are listed in Table 12.2. The EBO obtained from the RASSCF (12,20)/(12,10)/2 calculation is much higher than those obtained from the CASSCF calculations and also stands in contrast to those obtained for the other complexes in the series (Co_1-M-Cl = 0.22, Fe-Mn-Cl=0.31).[20] All these results illustrate that for Fe-Fe-Cl, only active spaces with a full 4*d* shell are sufficient to capture the stronger metal-metal interactions and electron delocalization across the metal-metal distance.

The Mulliken 3*d* and 4*d* spin densities for the (12,15) and (12,20)/(12,10)/2 active spaces are shown in Figure 12.2. Overall, the spin densities of the 3*d* orbitals obtained from the calculation employing the (12,15) active space are unevenly distributed between the two metals within each 3*d* AO type. As an example, the $3d^0$ spin densities are 0.70 for Fe_1 and 0.35 for Fe_2. In contrast, the 3*d* spin density distribution is more evenly

distributed between the two Fe centers for the (12,20)/(12,10)/2 active space. For example, the $3d^0$ orbital spin density is 0.55 and 0.49 for Fe_1 (bottom Fe) and Fe_2 (top Fe) respectively, Figure 12.2a. This more even distribution of spin density reflects the increased delocalized nature of the *d*-orbital electron density that is expected for a shorter M-M distance compared to the other M_1-M_2-Cl complexes in the series.

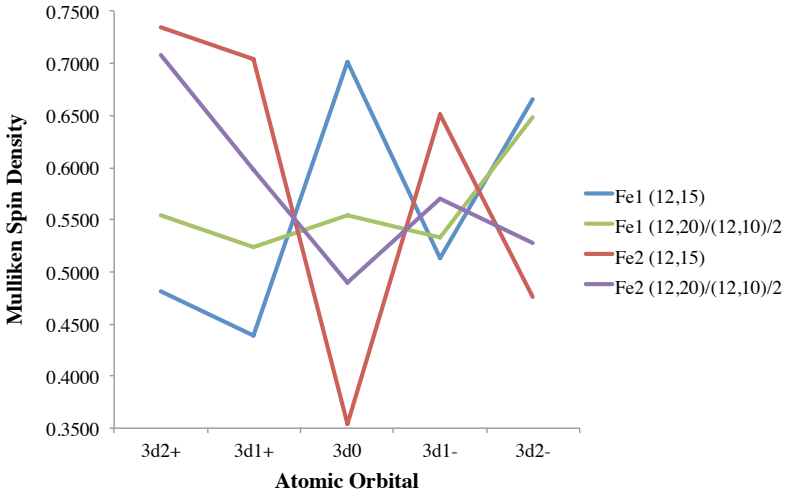

Figure 12.2a. Mulliken spin density plot of 3*d* orbitals for Fe-Fe-Cl for the (12,15) and (12,20)/(12,10)/2 active spaces.

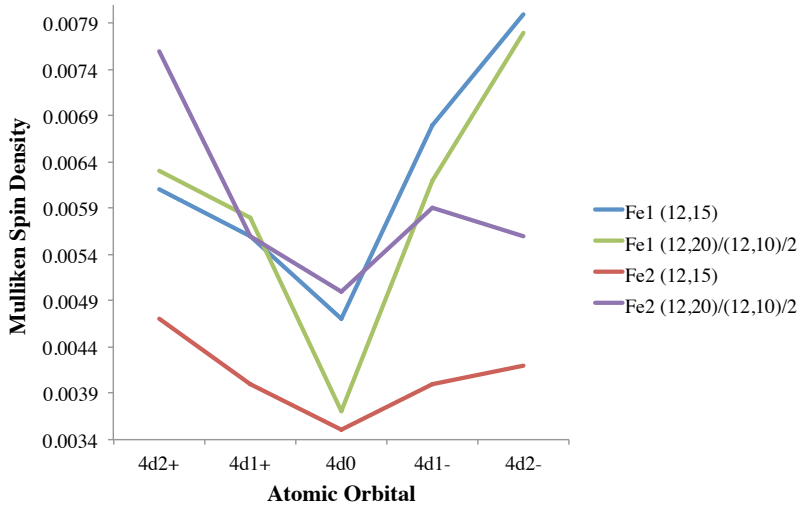

Figure 12.2b. Mulliken spin density plot of 4*d* orbitals for Fe-Fe-Cl for the (12,15) and (12,20)/(12,10)/2 active spaces.

For the 4*d* orbitals, the spin density on Fe_1 for both active spaces is relatively unchanged, but increases slightly for Fe_2 with a full 4*d* shell. For $4d^{2+}$ on Fe_2, the spin density increases from 0.0047 to 0.0076 with the (12,20)/(12,10)/2 active space. This occurs despite the fact that the addition of the full 4*d* set of orbitals is primarily responsible for the more even distribution of spin density (greater delocalized picture) between the metals, as well as the nearly degenerate spin state spectrum, Table 12.1. In Figure 12.2a, the spin density shifts between the two metals for the (12,15) active space and becomes more evenly distributed for the (12,20)/(12,10)/2 active space. In Figure 12.2b, the spin density for the correlating shell is shown. For the (12,15) active space, most of the spin density is on the bottom metal. Once the full *4d* shell is added, the red curve in Figure 12.2b shifts up to the purple curve.

In Figure 12.3, we show that the (12,20)/(12,10)/2 active space contains a 4*d* orbital of σ-character, two of π/ π* -character, and two δ/ δ*-type orbitals, while there are no π bonding orbitals for the (12,15) active space.

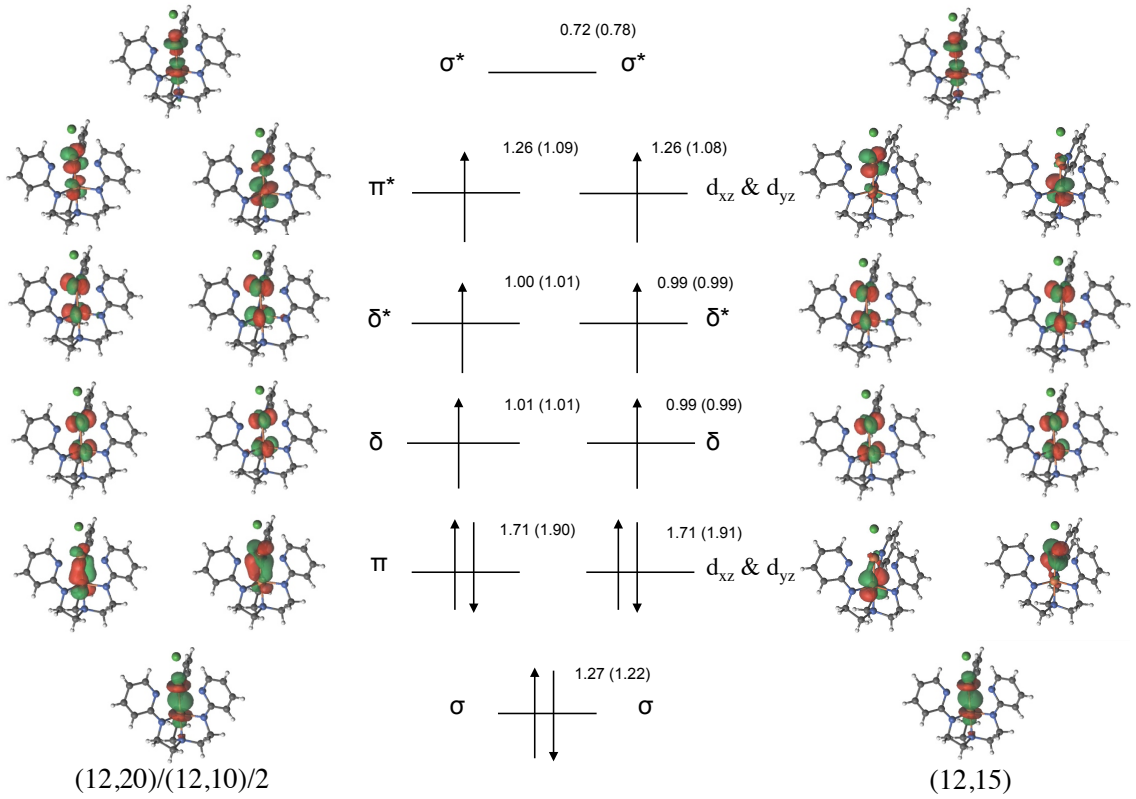

Figure 12.3. Qualitative orbital diagrams for the 3*d* orbitals computed with the (12,20)/(12,10)/2 and (12,15) active spaces. The natural orbital occupation numbers obtained for these orbitals in the (12,20)/(12,10)/2 calculation are shown while those corresponding to the (12,15) active space are given in parentheses. Note that the (12,15) MO diagram shows a more localized bonding manifold, similar to the other M-M-Cl complexes, especially for the π and π* orbitals. This is in contrast to the larger (12,20)/(12,10)/2 active space which shows significant delocalization in these particular orbitals.

12.4.2 Isostructural Co-Co-Cl Complex. It is important to determine why the inclusion of the full 4*d*-shell results in the alteration of the relative energies of the various spin states of Fe-Fe-Cl complex, Tables 12.1 and 12.3. Insights into the effect of the *4d*-shell can be obtained by comparing Fe-Fe-Cl to other members of the M_1-M_2-Cl series. To this end, similar calculations were performed for the analogous Co-Co-Cl complex. The relative energies between the singlet, triplet, quintet and septet states of Co-Co-Cl

obtained with the (14,12) and (14,20)/(14,10)/2 active spaces are presented in Table 4. To summarize, the singlet state remains the ground state of Co-Co-Cl, which is consistent with experiment, regardless of active space size. Additionally, the relative energies of the higher spin states obtained with the (14,12) active space are generally within 2 kcal/mol of those obtained with the (14,20)/(14,10)/2 active space, suggesting that additional 4d orbitals play little role in the ordering of these spin states of Co-Co-Cl.

Table 12.4. Relative spin state energies (kcal/mol) of the Co-Co-Cl complex obtained with active spaces containing various amounts of the 4*d* shell.

	(14,12)		(14,20)/(14,10)/2	
	CASSCF	CASPT2	RASSCF	RASPT2
Singlet	0.0	0.0	0.0	0.0
Triplet	0.8	2.0	0.9	1.6
Quintet	2.4	5.6	2.8	4.5
Septet	4.8	10.7	5.7	9.2

As we did for Fe-Fe-Cl, we now examine the electronic configuration of Co-Co-Cl. It was found that the dominant configuration obtained from calculations with (14,12), (14,14), and (14,20)/(14,10)/2 active spaces for the singlet ground state of Co-Co-Cl is $(\sigma)^2(Co_2\ 3d_{yz})^2(Co_2\ 3d_{xz})^2(Co_1\ 3d_{yz})^2(Co_1\ 3d_{xz})^2(Co_1\ 3d_{xy})^1(Co_1\ 3d_{x^2-y^2})^1(Co_2\ 3d_{xy})^1(Co_2\ 3d_{x^2-y^2})^1\ (\sigma^*)^0$. The weight of this configuration and the EBO obtained for the different active space sizes are shown in Table 12.5. Although, the weight of the dominant configuration decreases slightly after addition of a full 4*d* shell to the active space, the EBO and the average occupation numbers are relatively unchanged. Overall, these results suggest that the 4*d* shell has a minimal impact on the electronic structure and bonding in Co-Co-Cl, in stark contrast to the situation obtained for Fe-Fe-Cl.

Table 12.5. Effect of active space size on the weights of the dominant configuration (DC) and estimated EBO for the singlet spin state of the Co-Co-Cl complex.

	(14,12)	(14,14)	(14,20)/(14,10)/2
Weight of DC	19%	17%	14%
EBO	0.22	0.22	0.25

12.4.3 Density Functional Theory Approaches. Given the significant multiconfigurational characters of the wave functions of the M_1-M_2-Cl complexes, it is reasonable to expect that the suitability of DFT for studying their electronic, structural and chemical reaction properties will be limited. DFT however offers significant computational savings over correlated wave function approaches. For this reason, it is important to determine the performance of various exchange-correlation functionals for capturing the properties of these complexes.

Relative energies of various spin states. The relative energies of the various spin states of the Fe-Fe-Cl complex were calculated with the LDA, PBE, M06-L, PBE0-12%, PBE0-25%, PBE0-50%, M06 and M06-2X functionals, at the X-ray crystal structure. LDA predicts Fe-Fe-Cl to have a septet ground state while PBE and BLYP predict the septet and triplet to be degenerate, ground spin states of Fe-Fe-Cl, Figure 12.4. In contrast, although the meta-GGA functionals TPSS and M06-L both also predict the septet and triplet states to be close in energy, Figure 12.4, M06-L in particular appears to favor the high spin Fe(II) nonet and broken-symmetry singlet states by 6.0 and 4.3 kcal/mol relative to the septet state, respectively.

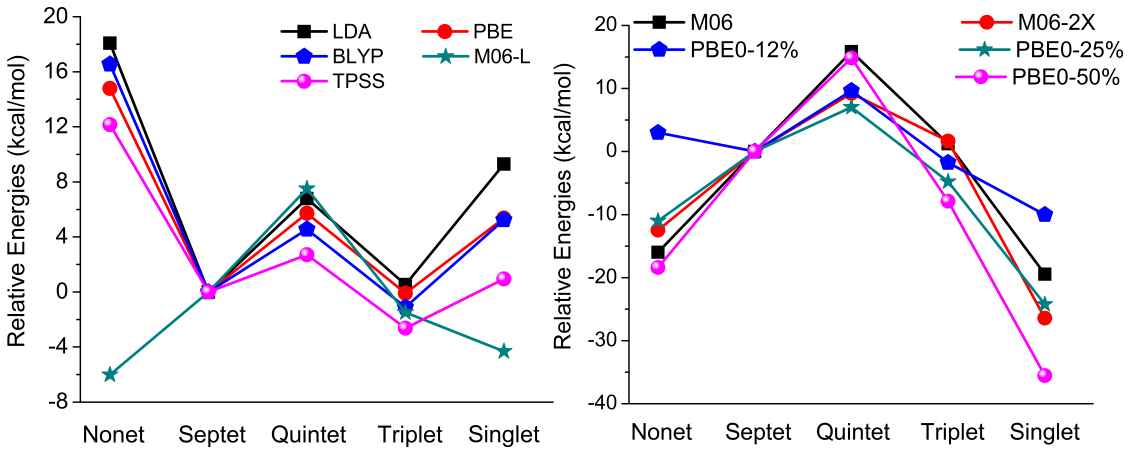

Figure 12.4. Calculated relative energies of various electronic spin states of Fe-Fe-Cl obtained with several (*left*) local and (*right*) hybrid exchange-correlation functionals. The energies of the various states are given relative to the energy of the septet state.

To confirm the suitability of the LDA, BLYP and PBE functionals for correctly predicting the ground spin states of the M_1-M_2-Cl family of complexes, we calculated the relative energies of the various spin states of the Co-Co-Cl, Co-Fe-Cl, Co-Mn-Cl and Fe-Mn-Cl complexes. These functionals predict doublet ground states for Co-Fe-Cl and Fe-Mn-Cl, the broken-symmetry singlet state for Co-Co-Cl and the triplet state for Co-Mn-Cl complex, all in agreement with accurate experimental assignments.

For Fe-Fe-Cl, addition of exact exchange to the PBE functional leads to the stabilization of the nonet and singlet states relative to the septet state, Figure 12.4. To illustrate, with the local PBE functional, the nonet state is about 15 kcal/mol less stable than the septet state. Addition of 12% exact exchange reduces this energy difference to about 3 kcal/mol. As noted previously, the nonet and singlet states have high spin Fe(II) ions. As the amount of exact exchange is increased from 12% in PBE0-12% to 50% in PBE0-50%, these high-spin Fe(II) states become more stable than the septet state. A

similar stabilization of the nonet state is obtained when the meta-hybrid M06 and M06-2X are used, Figure 12.4. The propensity of hybrid functionals towards stabilization of the high-spin states of metal complexes is expected from literature experience.[30,508,509] However, our current results suggest that only the LDA, BLYP and PBE functionals are suitable for describing the Fe-Fe-Cl complex, as addition of more than 12% exact exchange to the PBE functional results in the prediction of an incorrect ground spin state, Figure 12.4.

In contrast to the situation obtained for Fe-Fe-Cl, the hybrid PBE0-(12, 25 and 50%) functionals as well as the metahybrid Minnesota functionals correctly predict the ground spin states of Co-Co-Cl, Co-Mn-Cl, Co-Fe-Cl and Fe-Mn-Cl. The Fe-Fe-Cl species likely features a greater amount of delocalization and bonding across its intermetallic distance than Co-Co-Cl, Co-Mn-Cl, Co-Fe-Cl and Fe-Mn-Cl, consistent with its significantly shorter M_1-M_2 distance (2.29 Å in Fe-Fe-Cl in contrast to 2.49-2.53 Å for the other complexes). It appears that using hybrid density functionals for Fe-Fe-Cl invariably leads to localization of the 3d orbitals involved in the bonding between the metal centers. For example, in Figure 12.5, we see that that the π orbitals in Fe-Fe-Cl are significantly delocalized with the PBE functional. With this GGA functional, the two π orbitals each have about 50% contribution from Fe_1 (bottom metal) and 37% from Fe_2 (top metal). However, when the PBE0 functional is used, the π orbitals become largely localized on the bottom metal (51-71%), with very little contribution from the top metal (only 5-8 %). The increase in the localization of the π orbitals by the hybrid functional is a situation that seems to be associated with incorrect ground states and spin state

energetics, Figure 12.4. The fact the hybrid functionals increase the localization of the π orbitals for the Fe-Fe-Cl complex and that hybrid functionals do not predict the correct relative energetics of the various spin states mimics the effect of not including the correlating 4d orbitals in the active space of the CASSCF and RASSCF calculations, Figure 12.3. The Co-Co-Cl, Co-Mn-Cl, Co-Fe-Cl and Fe-Mn-Cl species present little interaction between the two metal centers. The orbital localization occurs with hybrid functionals in all cases. However in these cases it does not have as severe of an effect as in the Fe-Fe case because the MOs of the other M-M-Cl complexes are inherently more localized, so either GGA or hybrid functionals can correctly predict relative spin state energetics.

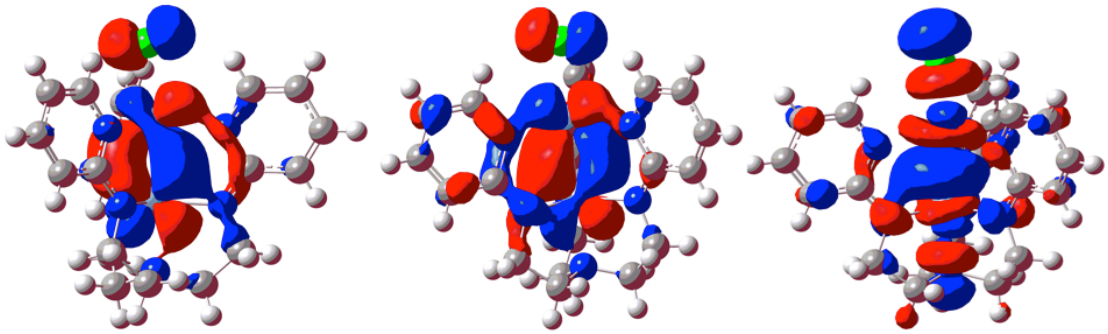

Figure 12.5. A series of π (*left* and *middle*) and σ (*right*) orbitals between the metals of Fe-Fe-Cl obtained at the PBE level of theory. The contributions to the π orbitals are 51%-Fe_1+37%-Fe_2 (*left*) and 49%-Fe_1+37%-Fe_2 (*middle*) with PBE. These orbitals become localized largely on the bottom metal when hybrid functionals are used. For example with PBE0 the contributions to the π orbitals are 56%-Fe_1+5%-Fe_2 and 71%-Fe_1+8%-Fe_2.

12.4.4 Calculated structural properties. The structures of Co-Co-Cl, Co-Mn-Cl, Co-Fe-Cl, Fe-Fe-Cl and Fe-Mn-Cl were optimized with several density functionals. The mean absolute errors (MAEs) are presented in Table 12.6. Two observations can be made.

First, of the tested functionals, PBE appears to perform reasonably well, suggesting that it is a good compromise between accuracy and computational expediency.

Table 12.6. Mean Absolute Errors (MAE) of the structural properties (M-M, M-Cl, M-N bond distances (Å) and N-M-N bond angles (degrees)) obtained at the DFT level compared to experimental structures.

	LDA	BLYP	PBE	M06-L	PBE0-12	PBE0	PBE0-50
M-M	0.18	0.07	0.05	0.06	0.04	0.09	0.14
M-Cl	0.04	0.05	0.01	0.01	0.02	0.02	0.03
M-N	0.07	0.03	0.02	0.01	0.01	0.02	0.02
N-M-N	4.37	2.57	2.04	3.05	3.75	5.17	4.28

Second, the deviation between the calculated and experimental intermetallic M_1-M_2 distance is largest for LDA and hybrid density functionals containing in excess of 20% exact exchange. This situation is observed for the highly delocalized Fe-Fe-Cl complex as well as the cobalt complexes, possessing greater amounts of localization of the metal 3*d* orbitals.

12.4.5 MC-PDFT results for Fe-Fe-Cl. The spin state splittings were computed with tPBE on the CASSCF(12,12) and RASCI(12,20)/(12,10)/2 wave functions and the results are shown in Figure 12.6. The ground spin state at the tPBE (12,12) level is predicted to be the singlet by about 7 kcal/mol, which is very similar to the CASPT2 result (Table 12.1) for the (12,12) active space. For the (12,20)/(12,10)/2 active space, the tPBE results are also very similar to the corresponding RASPT2 results. With tPBE, the quintet is predicted to be lower in energy than the septet by 0.2 kcal/mol, which is within the error of the method. A notable difference between the tPBE results and the

CASPT2/RASPT2 results is that the nonet state is much higher in energy than the other spin states and tPBE is more similar to KS-PBE in this respect (Fig. 12.4).

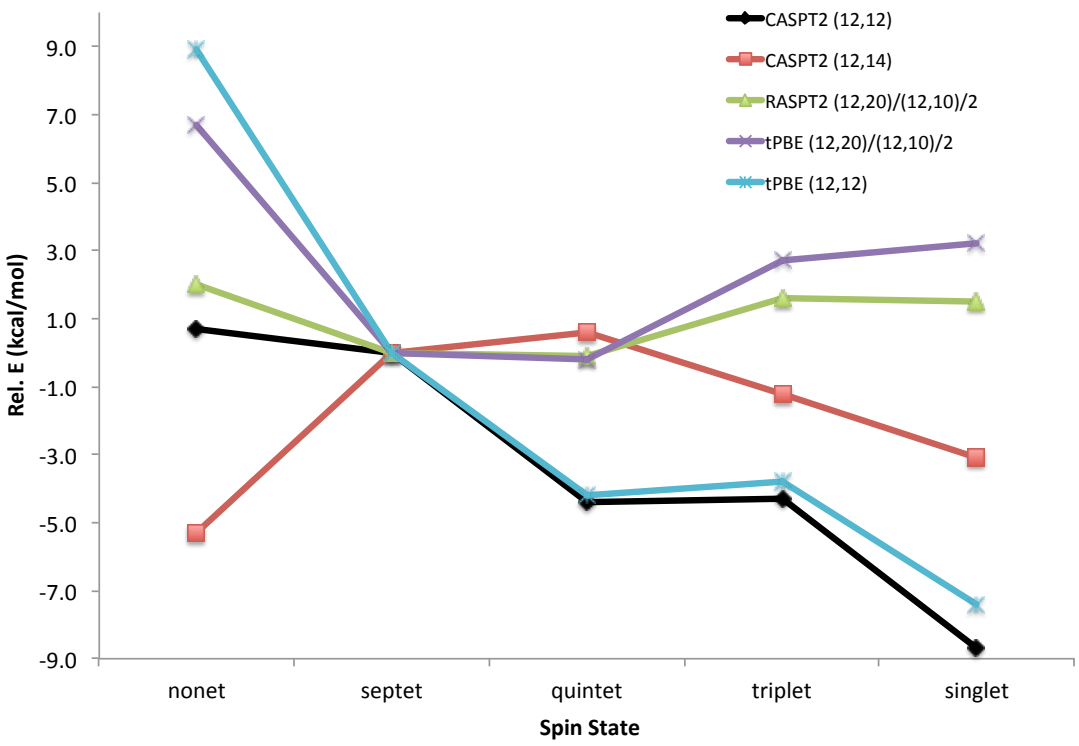

Figure 12.6. Relative spin state energies (kcal/mol) for CASPT2 (12,12), CASPT2 (12,14), RASPT2 (12,20)/(12,10)/2, tPBE (12,12), and tPBE (12,20)/(12,10)/2 for Fe-Fe-Cl.

It is encouraging that MC-PDFT performs similarly to CASPT2 and RASPT2 and it would be interesting in future work to look at how the on-top pair density and on-top ratio change as the active space increases. This could have implications for developing new functionals and understanding electron correlation in these challenging multireference systems.

12.5 Conclusions

In this work, we have employed multiconfigurational wave functions followed by second order perturbation theory, CASPT2 and RASPT2, to correctly determine the ground spin state of a diiron (Fe-Fe-Cl) complex that features significant delocalization of the 3*d* orbitals, consistent with a very short intermetallic distance. We compared the performance of CASPT2 and RASPT2 for Fe-Fe-Cl to their performance for the analogous Co-Co-Cl, Co-Fe-Cl, Co-Mn-Cl and Fe-Mn-Cl, systems that feature longer intermetallic distances and greater degrees of localization of the metal 3d orbitals. Lastly, we examined the performance of different types of exchange-correlation functionals for predicting the correct spin state, and the structural properties of these bimetallic complexes.

Overall for Fe-Fe-Cl, an active space that includes a truncated 4*d* shell, in the complete or restricted formalisms, qualitatively describes the bonding between the metals correctly. However, the inclusion of some portion of the 4*d* orbital manifold still results in the prediction of incorrect ground states as well as the exact nature of the electronic wave function. In contrast, for the analogous Co-Co-Cl, a complex with localized metal centers, we obtain essentially the same result with either inclusion of full 4*d* shell or a truncated 4*d* shell in the active space. On the other hand, for Fe-Fe-Cl, only when the π/π^* pair is added to the active space will the correct electronic structure and ground state be predicted.

The need to capture bonding via delocalization of 3*d* atomic orbitals as π and σ molecular orbitals between the iron centers of Fe-Fe-Cl also extend to density functional

theory methods. Pure exchange correlation functionals are able to correctly predict the ground spin state of Fe-Fe-Cl as well as those of the other members of the M_1-M_2-Cl series. Inclusion of exact exchange however results in greater localization of the 3*d* atomic orbitals, resulting in a failure to properly describe the intermetallic bonding in Fe-Fe-Cl, a situation that is associated with incorrect prediction of the ground spin states as well as poorer agreement of calculated structural properties with available experimental data.

Author Contributions

Experimental: Stephen J. Tereniak, Connie C. Lu

Theoretical: Rebecca K. Carlson contributed to MCSCF calculations, Samuel O. Odoh contributed to DFT calculations, Laura Gagliardi

Bibliography

(1) Pauling, L. *J. Am. Chem. Soc.* **1931**, *53*, 1367.
(2) Cotton, F. A.; Curtis, N. F.; Harris, C. B.; Johnson, B. F. G.; Lippard, S. J.; Mague, J. T.; Robinson, W. R.; Wood, J. S. *Science (80-.).* **1964**, *145*, 1305.
(3) Cotton, F. A.; Harris, C. B. *Inorg. Chem.* **1965**, *4*, 330.
(4) Merino, G.; Donald, K. J.; D'Acchioli, J. S.; Hoffmann, R. *J. Am. Chem. Soc.* **2007**, *125*, 15295.
(5) Nguyen, T.; Sutton, A. D.; Brynda, M.; Fettinger, J. C.; Long, G. J.; Power, P. P. *Science (80-.).* **2005**, *310*, 844.
(6) Nair, A. K.; Harisomayajula, N. V. S.; Tsai, Y.-C. *Dalt. Trans.* **2014**, *43*, 5618.
(7) Eisenhart, R. J.; Rudd, P. A.; Planas, N.; Boyce, D. W.; Carlson, R. K.; Tolman, W. B.; Bill, E.; Gagliardi, L.; Lu, C. C. *Inorg. Chem.* **2015**, *54*, 7579.
(8) Tamne, E. S.; Noor, A.; Qayyum, S.; Bauer, T.; Kempe, R. *Inorg. Chem.* **2012**, *52*, 329.
(9) Shen, J.; Yap, G. P. a; Werner, J.-P.; Theopold, K. H. *Chem. Commun. (Camb).* **2011**, *47*, 12191.
(10) Goodgame, D. M. L.; Hill, N. J.; Marsham, D. F.; Skapski, A. C.; Smart, M. L.; Throughton, P. G. H. *Chem. Comm.* **1969**, *448*, 629.
(11) Cotton, F. A.; Murillo, C. A.; Walton, R. A. *Multiple Bonds Between Metal Atoms*; 3rd ed.; New York, 2005.
(12) Kung, Y.; Drennan, C. L. *Curr. Opin. Chem. Biol.* **2011**, *15*, 276.
(13) Bullock, R. M. *Catalysis without Precious Metals*; Wiley-VCH, 2010.
(14) Bolm, C. *Nat. Chem.* **2009**, *1*, 420.
(15) van der Ham, C. J. M.; Koper, M. T. M.; Hetterscheid, D. G. H. *Chem. Soc. Rev.* **2014**, *43*, 5183.
(16) Collman, J. P.; Wagenknecht, P. S.; Hutchison, J. E. *Angew. Chem. Int. Ed.* **1994**, *33*, 1537.
(17) Feller, M.; Ben-Ari, E.; Diskin-Posner, Y.; Carmieli, R.; Weiner, L.; Milstein, D. *J. Am. Chem. Soc.* **2015**, *53*, 4459.
(18) Noyori, R.; Ohta, M.; Hsiao, Y.; Kitamura, M.; Ohta, T.; Takaya, H. *J. Am. Chem. Soc.* **1986**, *108*, 7117.
(19) Gunanathan, C.; Milstein, D. *Chem. Rev.* **2014**, *114*, 12024.
(20) Tereniak, S. J.; Carlson, R. K.; Clouston, L. J.; Young, Jr., V. G.; Bill, E.; Maurice, R.; Chen, Y.; Kim, H. J.; Gagliardi, L.; Lu, C. C. *J. Am. Chem. Soc.* **2013**, *136*, 1842.
(21) Rudd, P. A.; Liu, S.; Planas, N.; Bill, E.; Gagliardi, L.; Lu, C. C. *Angew. Chemie Int. Ed.* **2013**, *52*, 4449.
(22) Clouston, L. J.; Siedschlag, R. B.; Rudd, P. A.; Planas, N.; Hu, S.; Miller, A. D.; Gagliardi, L.; Lu, C. C. *J. Am. Chem. Soc.* **2013**, *135*, 13142.
(23) Eisenhart, R. J.; Clouston, L. J.; Lu, C. C. *Acc. Chem. Res.* **2015**, *48*, 2885.
(24) Siedschlag, R. B.; Bernales, V.; Vogiatzis, K. D.; Planas, N.; Clouston, L. J.; Bill, E.; Gagliardi, L.; Lu, C. C. *J. Am. Chem. Soc.* **2015**, *137*, 4638.
(25) Cammarota, R. C.; Lu, C. C. *J. Am. Chem. Soc.* **2015**.
(26) Dunn, P. L.; Carlson, R. K.; Gagliardi, L.; Tonks, I. A. *Dalton Trans.* **2016**, *45*, 9892.
(27) Roos, B. O.; Borin, A. C.; Gagliardi, L. *Angew. Chem. Int. Ed. Engl.* **2007**, *46*, 1469.
(28) Sorkin, A.; Iron, M. A.; Truhlar, D. G. *J. Chem. Theory Comput.* **2008**, *4*, 307.
(29) Swart, M. *J. Chem. Theory Comput.* **2008**, *4*, 2057.
(30) Reiher, M.; Salomon, O.; Hess, B. A. *Theor. Chem. Acc.* **2001**, *107*, 48.
(31) Mok, D. K. W.; Neumann, R.; Handy, N. C. *J. Phys. Chem.* **1996**, *100*, 6225.

(32) Handy, N. C.; Cohen, A. J. *Mol. Phys.* **2001**, *99*, 403.
(33) Hollett, J. W.; Gill, P. M. W. *J. Chem. Phys.* **2011**, *134*, 114111.
(34) Roos, B. O.; Taylor, P. R.; Siegbahn, P. E. M. *Chem. Phys.* **1980**, *48*, 157.
(35) Cramer, C. J.; Truhlar, D. G. *Phys. Chem. Chem. Phys.* **2009**, *11*, 10757.
(36) Siegbahn, P. E. M.; Almlof, J.; Heiberg, A.; Roos, B. O. *J. Chem. Phys.* **1981**, *74*, 2384.
(37) Andersson, K.; Malmqvist, P.-A.; Roos, B. O. *J. Chem. Phys.* **1992**, *96*, 1218.
(38) Ivanic, J.; Ruedenberg, K. Identification of deadwood in configuration spaces through general direct configuration interaction. *Theoretical Chemistry Accounts*, 2001, *106*, 339–351.
(39) Ivanic, J.; Ruedenberg, K. *Theor. Chem. Acc.* **2002**, *107*, 220.
(40) Malmqvist, P. A.; Pierloot, K.; Shahi, A. R. M.; Cramer, C. J.; Gagliardi, L. *J. Chem. Phys.* **2008**, *128*, 204109.
(41) Ma, D.; Li Manni, G.; Gagliardi, L. *J. Chem. Phys.* **2011**, *135*, 84108.
(42) Kohn, W.; Sham, L. J. *Phys. Rev.* **1965**, *140*, A1133.
(43) Löwdin, P. O. *Phys. Rev.* **1955**, *97*, 1474.
(44) Perdew, J. P.; Savin, A.; Burke, K. *Phys. Rev. A* **1995**, *51*, 4531.
(45) Noodleman, L. *J. Chem. Phys.* **1981**, *74*, 5737.
(46) Li Manni, G.; Carlson, R. K.; Luo, S.; Ma, D.; Olsen, J.; Truhlar, D. G.; Gagliardi, L. *J. Chem. Theory Comput.* **2014**, *10*, 3669.
(47) Savin, A. In *Density Functional Methods in Chemistry*; Labanowski, J. K.; Andzelm, J. W., Eds.; Springer: Berlin, 1991; pp. 213–230.
(48) Miehlich, B.; Stoll, H.; Savin, A. *Mol. Phys.* **1997**, *91*, 527.
(49) Grafenstein, J.; Kraka, E.; Cremer, D. *Chem. Phys. Lett.* **1998**, *288*, 593.
(50) Malcolm, N. O. J.; McDouall, J. J. W. *Chem. Phys. Lett.* **1998**, *282*, 121.
(51) Wu, W.; Shaik, S. *Chem. Phys. Lett.* **1999**, *301*, 37.
(52) Grafenstein, J.; Cremer, D. *Chem. Phys. Lett.* **2000**, *316*, 569.
(53) He, Y.; Grafenstein, J.; Kraka, E.; Cremer, D. *Mol. Phys.* **2000**, *98*, 1639.
(54) Takeda, R.; Yamanaka, S.; Yamaguchi, K. *Chem. Phys. Lett.* **2002**, *366*, 321.
(55) Pollet, R.; Savin, A.; Leininger, T.; Stoll, H. *J. Chem. Phys.* **2002**, *116*, 1250.
(56) Stoll, H. *Chem. Phys. Lett.* **2003**, *376*, 141.
(57) McDouall, J. J. W. *Mol. Phys.* **2003**, *101*, 361.
(58) Gusarov, S.; Malmqvist *, P.-Å.; Lindh, R. *Mol. Phys.* **2004**, *102*, 2207.
(59) Gusarov, S.; Malmqvist, P.-Å.; Lindh, R.; Roos, B. O. *Theor. Chim. Acta.* **2004**, *112*, 84.
(60) Gräfenstein, J.; Cremer, D. *Mol. Phys.* **2005**, *103*, 279.
(61) Ukai, T.; Nakata, K.; Yamanaka, S.; Kubo, T.; Morita, Y.; Takada, T.; Yamaguchi, K. *Polyhedron* **2007**, *26*, 2313.
(62) Kurzweil, Y.; Lawler, K.; Head-Gordon, M. *Mol. Phys.* **2009**, *107*, 2103.
(63) Sharkas, K.; Savin, A.; Jensen, H. J. A.; Toulouse, J. *J. Chem. Phys.* **2012**, *137*, 44104.
(64) Cagg, B. A.; Rassolov, V. A. *Chem. Phys. Lett.* **2012**, *543*, 205.
(65) Goll, E.; Werner, H.-J.; Stoll, H.; Leininger, T.; Gori-Giorgi, P.; Savin, A. *Chem. Phys.* **2006**, *329*, 276.
(66) Goll, E.; Werner, H. J.; Stoll, H. *Chem. Phys.* **2008**, *346*, 257.
(67) Stoyanova, A.; Teale, A. M.; Toulouse, J.; Helgaker, T.; Fromager, E. *J. Chem. Phys.* **2013**, *139*, 134113.
(68) Grimme, S.; Waletzke, M. *J. Chem. Phys.* **1999**, *111*, 5645.
(69) Filatov, M.; Shaik, S. *J. Phys. Chem. A* **2000**, *104*, 6628.
(70) Khait, Y. G.; Hoffmann, M. R. *J. Chem. Phys.* **2004**, *120*, 5005.
(71) Yamanaka, S.; Nakata, K.; Ukai, T.; Takada, T.; Yamaguchi, K. *Int. J. Quantum Chem.* **2006**, *106*, 3312.

(72) Fromager, E.; Toulouse, J.; Jensen, H. J. A. *J. Chem. Phys.* **2007**, *126*.
(73) Pérez-Jiménez, Á. J.; Pérez-Jordá, J. M. *Phys. Rev. A* **2007**, *75*.
(74) Perez-Jimenez, Á. J.; Perez-Jordá, J. M.; Sancho-García, J. C. *J. Chem. Phys.* **2007**, *127*, 104102.
(75) Perez-Jimenez, Á. J.; Perez-Jordá, J. M.; Moreira, I. D. P. R.; Illas, F. *J. Comput. Chem.* **2007**, *28*, 2559.
(76) Ukai, T.; Nakata, K.; Yamanaka, S.; Takada, T.; Yamaguchi, K. *Mol. Phys.* **2007**, *105*, 2667.
(77) Nishihara, S.; Yamanaka, S.; Ukai, T.; Nakata, K.; Kusakabe, K.; Yonezawa, Y.; Nakamura, H.; Takada, T.; Yamaguchi, K. *Int. J. Quantum Chem.* **2008**, *108*, 2966.
(78) Weimer, M.; Della Sala, F.; Görling, A. *J. Chem. Phys.* **2008**, *128*.
(79) Fromager, E.; Cimiraglia, R.; Jensen, H. J. A. *Phys. Rev. A* **2010**, *81*.
(80) Ying, F.; Su, P.; Chen, Z.; Shaik, S.; Wu, W. *J. Chem. Theory Comput.* **2012**, *8*, 1608.
(81) Zhao, Y.; Lynch, B. J.; Truhlar, D. G. *Phys. Chem. Chem. Phys.* **2005**, *7*, 43.
(82) Zhao, Y.; Lynch, B. J.; Truhlar, D. G. *J. Phys. Chem. A* **2004**, *108*, 4786.
(83) Tarnopolsky, A.; Karton, A.; Sertchook, R.; Vuzman, D.; Martin, J. M. L. *J. Phys. Chem. A* **2008**, *112*, 3.
(84) Zhang, I. Y.; Luo, Y.; Xu, X. *J. Chem. Phys.* **2010**, *132*, 194105.
(85) Sharkas, K.; Toulouse, J.; Savin, A. *J. Chem. Phys.* **2011**, *134*.
(86) Goerigk, L.; Grimme, S. *J. Chem. Theory Comput.* **2011**, *7*, 291.
(87) Zhang, I. Y.; Xu, X.; Jung, Y.; Goddard III, W. A. *Proc. Natl. Acad. Sci.* **2011**, *108*, 19896.
(88) Zhang, I. Y.; Xu, X. *Int. Rev. Phys. Chem.* **2011**, *30*, 115.
(89) Zhang, I. Y.; Su, N. Q.; Brémond, É. A. G.; Adamo, C.; Xu, X. *J. Chem. Phys.* **2012**, *136*, 174103.
(90) Souvi, S. M. O.; Sharkas, K.; Toulouse, J. *J. Chem. Phys.* **2014**, *140*, 84107.
(91) Becke, A. D.; Savin, A.; Stoll, H. *Theor. Chim. Acta* **1995**, *91*, 147.
(92) Odoh, S. O.; Manni, G. L.; Carlson, R. K.; Truhlar, D. G.; Gagliardi, L. *Chem. Sci.* **2016**, *7*, 2399.
(93) Bertini, I.; Gray, H. B.; Stiefel, E. I.; Valentine, J. S. *Biological Inorganic Chemistry: Structure and Reactivity*; 2006.
(94) Fontecilla-Camps, J. C.; Volbeda, A.; Cavazza, C.; Nicolet, Y. *Chem. Rev.* **2007**, *107*, 4273.
(95) Ragsdale, S. W. *J. Inorg. Biochem.* **2007**, *101*, 1657.
(96) Dobbek, H.; Svetlitchnyi, V.; Gremer, L.; Huber, R.; Meyer, O. *Science (80-.).* **2001**, *293*, 1281.
(97) Jiang, W.; Yun, D.; Saleh, L.; Barr, E.; Xing, G.; Hoffart, L. M.; Maslak, M.; Krebs, C.; Bollinger Jr., J. M. *Science (80-.).* **2007**, *316*, 1188.
(98) Jiang, W.; Bollinger, J. M.; Krebs, C. *J. Am. Chem. Soc.* **2007**, *129*, 7504.
(99) Stubbe, J.; Nocera, D. G.; Yee, C. S.; Chang, M. C. Y. *Chem. Rev.* **2003**, *103*, 2167.
(100) Dassama, L. M. K.; Boal, A. K.; Krebs, C.; Rosenzweig, A. C.; Bollinger, J. M. *J. Am. Chem. Soc.* **2012**, *134*, 2520.
(101) Roos, K.; Siegbahn, P. E. M. *Biochemistry* **2009**, *48*, 1878.
(102) Andersson, C. S.; Öhrström, M.; Popović-Bijelić, A.; Gräslund, A.; Stenmark, P.; Högbom, M. *J. Am. Chem. Soc.* **2012**, *134*, 123.
(103) Han, W.-G.; Giammona, D. A.; Bashford, D.; Noodleman, L. *Inorg. Chem.* **2010**, *49*, 7266.
(104) Younker, J. M.; Krest, C. M.; Jiang, W.; Krebs, C.; Bollinger, J. M.; Green, M. T. *J. Am. Chem. Soc.* **2008**, *130*, 15022.

(105) Carboni, M.; Latour, J. M. *Coord. Chem. Rev.* **2011**, *255*, 186.
(106) Carboni, M.; Clemancey, M.; Molton, F.; Pecaut, J.; Lebrun, C.; Dubois, L.; Blondin, G.; Latour, J. M. *Inorg. Chem.* **2012**, *51*, 10447.
(107) Jarenmark, M.; Haukka, M.; Demeshko, S.; Tuczek, F.; Zuppiroli, L.; Meyer, F.; Nordlander, E. *Inorg. Chem.* **2011**, *50*, 3866.
(108) Holman, T. R.; Wang, Z.; Hendrich, M. P.; Que, Jr., L. *Inorg. Chem.* **1995**, *34*, 134.
(109) Hotzelmann, R.; Wieghardt, K. E.; Florke, U.; Haupt, H. J.; Weatherburn, D. C.; Bonvoisin, J.; Blondin, G.; Girerd, J.-J. J. *J. Am. Chem. Soc.* **1992**, *114*, 1681.
(110) Ross, S.; Weyhermuller, T.; Bill, E.; Bothe, E.; Florke, U.; Wieghardt, K.; Chaudhuri, P. *Eur. J. Inorg. Chem.* **2004**, *2004*, 984.
(111) Borovik, A. S.; Que, L.; Papaefthymiou, V.; Muenck, E.; Taylor, L. F.; Anderson, O. P. *J. Am. Chem. Soc.* **1988**, *110*, 1986.
(112) Powers, T. M.; Gu, N. X.; Fout, A. R.; Baldwin, A. M.; Hernández Sánchez, R.; Alfonso, D. M.; Chen, Y. S.; Zheng, S. L.; Betley, T. A. *J. Am. Chem. Soc.* **2013**, *135*, 14448.
(113) Eames, E. V.; Hernandez Sanchez, R.; Betley, T. A. *Inorg. Chem.* **2013**, *52*, 5006.
(114) Eames, E. V.; Harris, T. D.; Betley, T. a. *Chem. Sci.* **2012**, *3*, 407.
(115) Fout, A. R.; Xiao, D. J.; Zhao, Q.; Harris, T. D.; King, E. R.; Eames, E. V; Zheng, S.-L.; Betley, T. a. *Inorg. Chem.* **2012**, *51*, 10290.
(116) Tsui, E. Y.; Agapie, T. *Proc. Natl. Acad. Sci.* **2013**, *110*, 10084.
(117) Tsui, E. Y.; Tran, R.; Yano, J.; Agapie, T. *Nat. Chem.* **2013**, *5*, 293.
(118) Rudd, P. A.; Liu, S.; Gagliardi, L.; Young, V. G.; Lu, C. C. *J. Am. Chem. Soc.* **2011**, 20724.
(119) Zall, C. M.; Clouston, L. J.; Young, V. G.; Ding, K.; Kim, H. J.; Zherebetskyy, D.; Chen, Y. S.; Bill, E.; Gagliardi, L.; Lu, C. C. *Inorg. Chem.* **2013**, *52*, 9216.
(120) F. Aquilante; L. De Vico; N. Ferré; G. Ghigo; P.-Å Malmqvist; P. Neogrády; T.B. Pedersen; M. Pitonak; M. Reiher; B.O. Roos; L. Serrano-Andrés; M. Urban; V. Veryazov; R. Lindh. *J. Comp. Chem.* **2010**, *31*, 224.
(121) Roos, B. O. .; Lindh, R. .; Malmqvist, P.-Å. .; Veryazov, V. .; Widmark, P.-O. *J. Phys. Chem. A.* **2005**, *109*, 6575.
(122) Roos, B. O.; Lindh, R.; Malmqvist, P. Å.; Veryazov, V.; Widmark, P. O. *J. Phys. Chem. A* **2004**, *108*, 2851.
(123) Douglas, M.; Kroll, N. *Ann. Phys.* **1974**, *82*, 89.
(124) Hess, B. A. *Phys. Rev. A* **1986**, *33*, 3742.
(125) Aquilante, F. .; Lindh, R. .; Pedersen, T. B. *J. Chem. Phys.* **2007**, *127*, 114107.
(126) Forsberg, N. .; Malmqvist, P.-Å. *Chem. Phys. Lett.* **1997**, *274*, 196.
(127) Brynda, M.; Gagliardi, L.; Roos, B. O. *Chem. Phys. Lett.* **2009**, *471*, 1.
(128) Yamaguchi, K.; Takahara, Y.; Fueno, T. In *Applied Quantum Chemistry*; Smith, V. H.; Schaefer, H. F.; Morokuma, K., Eds.; Reidel Publishing Co: Boston, 1986; p. 155.
(129) Frisch, M. J. T., G. W.; Schlegel, H. B.; Scuseria, G. E.; Robb, M. A.; Cheeseman, J. R.; Scalmani, G.; Barone, V.; Mennucci, B.; Petersson, G. A.; Nakatsuji, H.; Caricato, M.; Li, X.; Hratchian, H. P.; Izmaylov, A. F.; Bloino, J.; Zheng, G.; Sonnenberg, O. .; Nakai, H.; Vreven, T.; Montgomery, Jr., J. A.; Peralta, J. E.; Ogliaro, F.; Bearpark, M.; Heyd, J. J. .; Brothers, E.; Kudin, K. N.; Staroverov, V. N.; Kobayashi, R.; Normand, J.; Raghavachari, K.; Rendell, A.; Burant, J. C.; Iyengar, S. S.; Tomasi, J.; Cossi, M.; Rega, N.; Millam, J. M.; Klene, M.; Knox, J. E.; Cross, J. B.; Bakken, V.; Adamo, C.; Jaramillo, D. J. *Gaussian, Inc. Wallingford CT* **2009**.
(130) Ernzerhof, M.; Perdew, J. P. *J. Chem. Phys.* **1998**, *109*, 3313.
(131) Perdew, J. P.; Ernzerhof, M.; Burke, K. *J. Chem. Phys.* **1996**, *105*, 9982.
(132) Heyd, J.; Scuseria, G. E.; Ernzerhof, M. *J. Chem. Phys.* **2003**, *118*, 8207.

(133) Heyd, J.; Scuseria, G. E.; Ernzerhof, M. *J. Chem. Phys.* **2006**, *124*, 219906.
(134) Vydrov, O. A.; Scuseria, G. E. *J. Chem. Phys.* **2006**, *125*, 234109.
(135) Schaefer, A. .; Huber, C. .; Ahlrichs, R. *J. Chem. Phys.* **1994**, *100*, 5829.
(136) Schaefer, A. .; Horn, H. .; Ahlrichs, R. *J. Chem. Phys.* **1992**, *97*, 2571.
(137) Fohlmeister, L.; Liu, S.; Schulten, C.; Moubaraki, B.; Stasch, A.; Cashion, J. D.; Murray, K. S.; Gagliardi, L.; Jones, C. *Angew. Chem. Int. Ed.* **2012**, *51*, 8294.
(138) Freedman, D. E.; Han, T. H.; Prodi, A.; Müller, P.; Huang, Q.-Z.; Chen, Y.-S.; Webb, S. M.; Lee, Y. S.; McQueen, T. M.; Nocera, D. G. *J. Am. Chem. Soc.* **2010**, *132*, 16185.
(139) Wulf, R. *Acta Crystallogr., Sect. A Found. Crystallogr* **1990**, *46*, 681.
(140) Toby, B. H.; Von Dreele, R. B. *J. Appl. Crystallogr.* **2013**, *46*, 544.
(141) Zhao, Q.; Betley, T. A. *Angew. Chem. Int. Ed.* **2011**, *50*, 709.
(142) Rivero, P.; Moreira, I. D. P. R.; Illas, F.; Scuseria, G. E. *J. Chem. Phys.* **2008**, *129*, 184110.
(143) Valero, R.; Costa, R.; Moreira, I. D. P. R.; Truhlar, D. G.; Illas, F. *J. Chem. Phys.* **2008**, *128*, 114103.
(144) Solomon, E. I.; Heppner, D. E.; Johnston, E. M.; Ginsbach, J. W.; Cirera, J.; Qayyum, M.; Kieber-Emmons, M. T.; Kjaergaard, C. H.; Hadt, R. G.; Tian, L. *Chem. Rev.* **2014**, *114*, 3659.
(145) Kitajima, N.; Moro-oka, Y. *Chem. Rev.* **1994**, *94*, 737.
(146) Lewis, E. A.; Tolman, W. B. *Chem. Rev.* **2004**, *104*, 1047.
(147) Karlin, K. D.; Tyeklar, Z. *Bioinorganic chemistry of copper*; Chapman & Hall: New York, 1993.
(148) Zhang, C.; Chen, C.; Dong, H.; Shen, J. R.; Dau, H.; Zaho, J. *Science (80-.).* **2015**, *348*, 690.
(149) Powers, T. M.; Fout, A. R.; Zheng, S. L.; Betley, T. A. *J. Am. Chem. Soc.* **2011**, *133*, 3336.
(150) Kanady, J. S.; Tsui, E. Y.; Day, M. W.; Agapie, T. *Science (80-.).* **2011**, *333*, 733.
(151) Collman, J. P.; Devaraj, N. K.; Decréau, R. A.; Yang, Y.; Yan, Y.; Ebina, W.; Eberspacher, T. A.; Chidsey, C. E. D. *Science (80-.).* **2007**, *315*, 1565.
(152) Kornecki, K. P.; Briones, J. F.; Boyarskikh, V.; Fullilove, F.; Autschbach, J.; Schrote, K. E.; Lancaster, K. M.; Davies, H. M. L.; Berry, J. F. *Science (80-.).* **2013**, *342*, 351.
(153) Powers, D. C.; Xiao, D. Y.; Geibel, M. A. L.; Ritter, T. *J. Am. Chem. Soc.* **2010**, *132*, 14530.
(154) Pal, S.; Uyeda, C. *J. Am. Chem. Soc.* **2015**, *137*, 8042.
(155) Cooper, Benjamin G.; Napoline, J. W.; Thomas, C. M. *Catal. Rev. Sci. Eng.* **2012**, *54*, 1.
(156) Che, C. M.; Mao, Z.; Miskowski, V. M.; Tse, M. C.; Chan, C. K.; Cheung, K. K.; Phillips, D. L.; Leung, K. H. *Angew. Chem. Int. Ed.* **2000**, *39*, 4084.
(157) Allen, F. *Acta Crystallogr., Sect B* **2002**, *58*, 380.
(158) Margerum, D. W.; Cayley, G. R.; Weatherburn, D. C.; Pagenkopf, G. K. *Coordination Chemistry*; American Chemical Society: Washington DC, 1978.
(159) Eckenhoff, W. T.; Pintauer, T. *Inorg. Chem.* **2010**, *49*, 10617.
(160) Ward, A. L.; Elbaz, L.; Kerr, J. B.; Arnold, J. *Inorg. Chem.* **2012**, *51*, 4694.
(161) Lim, B. S.; Holm, R. H. *Inorg. Chem.* **1998**, *37*, 4898.
(162) Addison, A. W.; Rao, T. N.; Reedijk, J.; Van Rijn, J.; Verschoor, G. C. *J. Chem. Soc. Dalt. Trans.* **1984**, 1349.
(163) Rajnak, C.; Titis, J.; Salitros, I.; Boca, R.; Fuhr, O.; Ruben, M. *Polyhedron* **2013**, *65*, 122.
(164) Tyeklar, Z.; Jacobson, R. R.; Wei, N.; Murthy, N. N.; Zubieta, J.; Karlin, K. D. *J. Am. Chem. Soc.* **1993**, *115*, 2677.
(165) Carlson, R. K.; Odoh, S. O.; Tereniak, S. J.; Lu, C. C.; Gagliardi, L. *J. Chem. Theory*

Comput. **2015**, *11*, 4093.
(166) Wagner, F. R.; Noor, A.; Kempe, R. *Nat. Chem.* **2009**, *1*, 529.
(167) Cotton, F.; Daniels, L.; Huang, P.; Murillo, C. *Inorg. Chem.* **2002**, *41*, 317.
(168) Cotton, F. A.; Dalal, N. S.; Hillard, E. A.; Huang, P.; Murillo, C. A.; Ramsey, C. M. *Inorg. Chem.* **2003**, *42*, 1388.
(169) Brogden, D. W.; Turov, Y.; Nippe, M.; Li Manni, G.; Hillard, E. A.; Clérac, R.; Gagliardi, L.; Berry, J. F. *Inorg. Chem.* **2014**, *43*, 4777.
(170) Steinborn, D.; Neumann, O.; Bruhn, C.; Ruffer, T.; Boese, R.; Heinemann, F. W. *Chem. Eur. J.* **1998**, *4*, 2204.
(171) Cotton, F. A.; Eglin, J, L.; Hong, B.; James, C. A. *Inorg Chem* **1993**, *32*, 2104.
(172) Cotton, F. A.; Eglin, J, L.; James, C. A. *Inorg. Chem.* **1993**, *32*, 681.
(173) Zhao, Y.; Truhlar, D. G. *J. Chem. Phys.* **2006**, *125*, 194101.
(174) Weigend, F.; Ahlrichs, R. *Phys. Chem. Chem. Phys.* **2005**, *7*, 3297.
(175) Bollmann, A.; Blann, K.; Dixon, J. T.; Hess, F. M.; Killian, E.; Maumela, H.; McGuinness, D. S.; Morgan, D. H.; Neveling, A.; Otto, S.; Overett, M.; Slawin, A. M. Z.; Wasserscheid, P.; Kuhlmann, S. *J. Am. Chem. Soc.* **2004**, *126*, 14712.
(176) Pauling, L. *J. Am. Chem. Soc.* **1947**, *69*, 542.
(177) Cotton, F. A.; Niswander, R. H.; Sekutowski, J. C. *Inorg. Chem.* **1978**, *17*, 3541.
(178) Cotton, F. A.; Daniels, L. M.; Murillo, C. A.; Schooler, P. *J. Chem. Soc. Dalt. Trans.* **2000**, 2007.
(179) Cotton, F. a.; Chen, H.; Daniels, L. M.; Feng, X. *J. Am. Chem. Soc.* **1992**, *114*, 8980.
(180) San Filippo, J. *Inorg. Chem.* **1972**, *11*, 3140.
(181) Harris, R. K. *Nuclear Magnetic Resonance Spectroscopy*; Pittman, London, 1983.
(182) Cotton, F. A.; Ren, T. *J. Amer. Chem. Soc.* **1992**, *114*, 2237.
(183) Carlson-Day, K. M.; Eglin, J. L.; Lin, C.; Smith, L. T.; Staples, R. J.; Wipf, D. O. *Polyhedron* **1999**, *18*, 817.
(184) Belforte, A.; Dell'Amico, D. B.; Calderazzo, F.; Devillers, M.; Englert, U. *Inorg. Chem.* **1993**, *32*, 2282.
(185) Cotton, F. A.; Fanwick, P. E.; Niswander, R. H.; Sekutowski, J. C. *J. Am. Chem. Soc.* **1978**, *100*, 4725.
(186) Clerac, R.; Cotton, F. A.; Jeffery, S. P.; Murillo, C. A.; Wang, X. P. *Dalt. Trans.* **2003**, 3022.
(187) Nippe, M.; Bill, E.; Berry, J. F. *Inorg. Chem.* **2011**, *50*, 7650.
(188) Nippe, M.; Berry, J. F. *J. Am. Chem. Soc.* **2007**, *129*, 12684.
(189) Krausse, J.; Marx, G.; Schödl, G. *J. Organomet. Chem.* **1970**, *21*, 159.
(190) Fanwick, P. E.; Bursten, B. E.; Kaufmann, G. B. *Inorg. Chem.* **1985**, *24*, 1165.
(191) La Macchia, G.; Li Manni, G.; Todorova, T. K.; Brynda, M.; Aquilante, F.; Roos, B. O.; Gagliardi, L. *Inorg. Chem.* **2010**, *49*, 5216.
(192) Mulliken, R. S. *Chem. Rev.* **1931**, *9*, 347.
(193) Mulliken, R. S. *Chem. Rev.* **1930**, *6*, 503.
(194) Spain, E. M.; Morse, M. D. *J. Phys. Chem.* **1992**, 2479.
(195) Morse, M. D. *Chem. Rev.* **1986**, *86*, 1049.
(196) Shen, J.; Yap, G. P. A.; Theopold, K. H. *J. Am. Chem. Soc.* **2014**, *136*, 3382.
(197) Kuppuswamy, S.; Powers, T. M.; Krogman, J. P.; Bezpalko, M. W.; Foxman, B. M.; Thomas, C. M. *Chem. Sci.* **2013**, *4*, 3557.
(198) Krogman, J. P.; Thomas, C. M. *Chem. Commun.* **2014**, *50*, 5115.
(199) Perdew, J. P.; Burke, K.; Ernzerhof, M. *Phys. Rev. Lett.* **1996**, *77*, 3865.
(200) Ahlrichs, R.; Bäcker, S.; Ehrig, M.; Eichkorn, K.; Elliott, S.; Haase, F.; Hoser, M.; Horn, H.; Huber, C.; Huniar, U.; Kattannek, M.; Kolmel, C.; Kollwitz, M.; Ochsenfeld, C.; Öhm,

H.; Schäfer, A.; Schneider, U.; Treutler, O.; von Arnim, M.; Weigend, F.; Weis, P.; Weiss, H. TURBOMOLE V6.2 2010, a development of University of Karlsruhe and Forschungszentrum Karlsruhe GmbH, 1989-2007, TURBOMOLE GmbH, since 2007; available from http://www.turbomole.com. *Turbomole*, 2008.
(201) Laury, M. L.; Carlson, M. J.; Wilson, A. K. *J. Comput. Chem.* **2012**, *33*, 2380.
(202) Alecu, I. M.; Zheng, J.; Zhao, Y.; Truhlar, D. G. *J. Chem. Theory Comput.* **2010**, *6*, 2872.
(203) Gagliardi, L.; Lindh, R.; Karlström, G. *J. Chem. Phys.* **2004**, *121*, 4494.
(204) Malmqvist, P.-Å.; Roos, B. O. *Chem. Phys. Lett.* **1989**, *155*, 189.
(205) Malmqvist, P.-Å. *Int. J. Quantum Chem.* **1986**, *30*, 479.
(206) Pregosin, P. S. *NMR in Organometallic Chemistry*; John Wiley & Sons: Somerset, NJ, 2012.
(207) Sircoglou, M.; Bontemps, S.; Bouhadir, G.; Saffon, N.; Miqueu, K.; Gu, W.; Mercy, M.; Chen, C. H.; Foxman, B. M.; Maron, L.; Ozerov, O. V.; Bourissou, D. *J. Am. Chem. Soc.* **2008**, *130*, 16729.
(208) Casey, A. T.; Mitra, S. In *Theory and Applications of Molecular Paramagnetism*; Boudreaux, E. A.; Mulay, L. N., Eds.; John Wiley & Sons: New York, 1976; p. 135.
(209) Dalal, N. S.; Murillo, C. A. *Dalt. Trans.* **2014**, *43*, 8565.
(210) Cummings, D. A.; McMaster, J.; Rieger, A. L.; Rieger, P. H. *Organometallics* **1997**, *16*, 4362.
(211) Evans, D. F. *J. Chem. Soc.* **1959**, 2003.
(212) Wolf, R.; Ni, C.; Nguyen, T.; Brynda, M.; Long, G. J.; Sutton, A. D.; Fischer, R. C.; Fettinger, J. C.; Hellman, M.; Pu, L.; Power, P. P. *Inorg. Chem.* **2007**, *46*, 11277.
(213) Noor, A.; Bauer, T.; Todorova, T. K.; Weber, B.; Gagliardi, L.; Kempe, R. *Chem. - A Eur. J.* **2013**, *19*, 9825.
(214) Kreisel, K. A.; Yap, G. P. A.; Dmitrenko, O.; Landis, C. R.; Theopold, K. H. *J. Am. Chem. Soc.* **2007**, *129*, 14162.
(215) Noor, A.; Glatz, G.; Müller, R.; Kaupp, M.; Demeshko, S.; Kempe, R. *Zeitschrift fur Anorg. und Allg. Chemie* **2009**, *635*, 1149.
(216) Hsu, C. W.; Yu, J. S. K.; Yen, C. H.; Lee, G. H.; Wang, Y.; Tasi, Y. C. *Angew. Chem. Int. Ed.* **2008**, *47*, 9933.
(217) Wu, L. C.; Hsu, C. W.; Chuang, Y. C.; Lee, G. H.; Tsai, Y.-C.; Wang, Y. *J. Chem. Phys. A* **2011**, *115*, 12602.
(218) Chasteen, N. D.; Belford, R. L. *Inorg. Chem.* **1970**, *9*, 169.
(219) Casey, S. M.; Leopold, D. G. *J. Phys. Chem.* **1993**, *97*, 816.
(220) Bondybey, V. E.; English, J. H. *Chem. Phys. Lett.* **1983**, *94*, 443.
(221) Tsai, Y.-C.; Hsu, C. W.; Yu, J. S. K.; Lee, G. H.; Wang, Y.; Kuo, T. S. *Angew. Chem. Int. Ed.* **2008**, *47*, 7250.
(222) Cotton, F. A.; Daniels, L. M.; Murillo, C. A.; Pascual, I.; Zhou, H. C. *J. Am. Chem. Soc.* **1999**, *121*, 6856.
(223) McConnell, H. M.; Holm, C. H. *J. Chem. Phys.* **1957**, *27*, 314.
(224) Balazs, G.; Cloke, F. G. N.; Gagliardi, L.; Green, J. C.; Harrison, A.; Hitchcock, P. B.; Shahi, A. R. M.; Summerscales, O. T. *Organometallics* **2008**, *27*, 2013.
(225) Agaskar, P. A.; Cotton, F. A. *Polyhedron* **1986**, *5*, 899.
(226) McGlinchey, M. J. *Inorg. Chem.* **1980**, *19*, 1392.
(227) Cotton, F. A.; James, C. A. *Inorg. Chem.* **1992**, *31*, 5298.
(228) Cotton, F. A.; Dunbar, K. R.; Hong, B.; James, C. A.; Matonic, J. H.; Thomas, J. L. C. *Inorg. Chem.* **1993**, *32*, 5183.
(229) Neese, F. *Inorg. Chim. Acta* **2002**, *337*, 181.
(230) Berry, J. F.; Bill, E.; Bothe, E.; George, S. D.; Mienert, B.; Neese, F.; Wieghardt, K.

Science (80-.). **2006**, *312*, 1937.
(231) Rittle, J.; Peters, J. C. *Proc. Natl. Acad. Sci.* **2013**, *110*, 15898.
(232) Lee, Y.; Mankad, N. P.; Peters, J. C. *Nat. Chem.* **2010**, *2*, 558.
(233) Alex Rudd, P.; Planas, N.; Bill, E.; Gagliardi, L.; Lu, C. C. *Eur. J. Inorg. Chem.* **2013**, *2013*, 3898.
(234) Gütlich, P.; Bill, E.; Trautwein, A. X. In *Mössbauer Spectroscopy and Transition Metal Chemistry*; Springer-Verlag: Berlin Heidelberg, 2011.
(235) Manning, M. C.; Trogler, W. C. *J. Am. Chem. Soc.* **1983**, *105*, 5311.
(236) Zall, C. M.; Zherebetskyy, D.; Dzubak, A. L.; Bill, E.; Gagliardi, L.; Lu, C. C. *Inorg. Chem.* **2012**, *51*, 728.
(237) Hsiao, C. J.; Lai, S. H.; Chen, I. C.; Wang, W. Z.; Peng, S. M. *J. Phys. Chem. A* **2008**, *112*, 13528.
(238) John, K. D.; Miskowski, V. M.; Vance, M. A.; Dallinger, R. F.; Wang, L. C.; Geib, S. J.; Hopkins, M. D. *Inorg.Chem.* **1998**, *37*, 6858.
(239) Moskovits, M.; Limm, W.; Mejean, T. *J. Phys. Chem.* **1985**, *89*, 3886.
(240) Dachsel, H.; Harrison, R. J.; Dixon, D. A. *J. Phys. Chem. A* **1998**, *103*, 152.
(241) Rozenel, S. S.; Padilla, R.; Arnold, J. *Inorg. Chem.* **2013**, *52*, 11544.
(242) Chomitz, W. A.; Arnold, J. *Chem. Commun.* **2007**, *45*, 4797.
(243) Bowman, A. C.; Milsmann, C.; Atienza, C. C. H.; Lobkovsky, E.; Wieghardt, K.; Chirik, P. J. *J. Am. Chem. Soc.* **2010**, *132*, 1676.
(244) Archer, A. M.; Bouwkamp, M. W.; Cortez, M. P.; Lobkovsky, E.; Chirik, P. J. *Organometallics* **2006**, *25*, 4269.
(245) Ding, K.; Pierpont, A. W.; Brennessel, W. W.; Lukat-Rodgers, G.; Rodgers, K. R.; Cundari, T. R.; Bill, E.; Holland, P. L. *J. Am. Chem. Soc.* **2009**, *131*, 9471.
(246) Smith, J. M.; Lachicotte, R. J.; Pittard, K. A.; Cundari, T. R.; Lukat-Rodgers, G.; Rodgers, K. R.; Holland, P. L. *J. Am. Chem. Soc.* **2001**, *123*, 9222.
(247) Betley, T. A.; Peters, J. C. *J. Am. Chem. Soc.* **2003**, *125*, 10782.
(248) Yu, R. P.; Darmon, J. M.; Milsmann, C.; Margulieux, G. W.; Stieber, S. C. E.; Debeer, S.; Chirik, P. J. *J. Am. Chem. Soc.* **2013**, *135*, 13168.
(249) Whited, M. T.; Mankad, N. P.; Lee, Y.; Oblad, P. F.; Peters, J. C. *Inorg. Chem.* **2009**, *48*, 2507.
(250) Lin, T. P.; Peters, J. C. *J. Am. Chem. Soc.* **2013**, *135*.
(251) Lin, T. P.; Peters, J. C. *J. Am. Chem. Soc.* **2014**, *136*.
(252) Anderson, J. S.; Rittle, J.; Peters, J. C. *Nature* **2013**, *501*, 84.
(253) Holland, P. L. *Dalt. Trans.* **2010**, *39*, 5415.
(254) Marquard, S. L.; Bezpalko, M. W.; Foxman, B. M.; Thomas, C. M. *J. Am. Chem. Soc.* **2013**, *135*, 6018.
(255) Krogman, J. P.; Bezpalko, M. W.; Foxman, B. M.; Thomas, C. M. *Inorg. Chem.* **2013**, *52*, 3022.
(256) Wu, B.; Bezpalko, M. W.; Foxman, B. M.; Thomas, C. M. *Chem. Sci.* **2015**, *6*, 2044.
(257) Powers, T. M.; Betley, T. A. *J. Am. Chem. Soc.* **2013**, *135*, 12289.
(258) Clouston, L. J.; Bernales, V.; Cammarota, R. C.; Carlson, R. K.; Bill, E.; Gagliardi, L.; Lu, C. C. *Inorg. Chem.* **2015**, *54*, 11669.
(259) Marenich, A. V.; Cramer, C. J.; Truhlar, D. G. *J. Phys. Chem. B* **2009**, *113*, 6378.
(260) Rappoport, D.; Furche, F. *J. Chem. Phys.* **2010**, *133*, 134105.
(261) Huber, K. P.; Herzberg, G. *Constants of Diatomic Molecules*; Von Nostrand Reinhold, 1979.
(262) Chirik, P. J.; Wieghardt, K. *Science (80-.).* **2010**, *327*, 794.
(263) Blackmore, K. J.; Ziller, J. W.; Heyduk, A. F. *Inorg. Chem.* **2005**, *44*, 5559.

(264) Haneline, M. R.; Heyduk, A. F. *J. Am. Chem. Soc.* **2006**, *128*, 8410.
(265) Small, B. L.; Brookhart, M.; Bennett, A. M. A. *J. Am. Chem. Soc.* **1998**, *120*, 4049.
(266) Bart, S. C.; Chłopek, K.; Bill, E.; Bouwkamp, M. W.; Lobkovsky, E.; Neese, F.; Wieghardt, K.; Chirik, P. J. *J. Am. Chem. Soc.* **2006**, *128*, 13901.
(267) Smith, A. L.; Hardcastle, K. I.; Soper, J. D. *J. Am. Chem. Soc.* **2010**, *132*, 14358.
(268) Chaudhuri, P.; Hess, M.; Müller, J.; Hildenbrand, K.; Bill, E.; Weyhermüller, T.; Wieghardt, K. *J. Am. Chem. Soc.* **1999**, *121*, 9599.
(269) Frazier, B. A.; Wolczanski, P. T.; Keresztes, I.; DeBeer, S.; Lobkovsky, E. B.; Pierpont, A. W.; Cundari, T. R. *Inorg. Chem.* **2012**, *51*, 8177.
(270) Williams, V. A.; Hulley, E. B.; Wolczanski, P. T.; Lancaster, K. M.; Lobkovsky, E. B. *Chem. Sci.* **2013**, *4*, 3636.
(271) Williams, V. A.; Wolczanski, P. T.; Sutter, J.; Meyer, K.; Lobkovsky, E. B.; Cundari, T. R. *Inorg. Chem.* **2014**, *53*, 4459.
(272) Casey, C. P.; Singer, S. W.; Powell, D. R.; Hayashi, R. K.; Kavana, M. *J. Am. Chem. Soc.* **2001**, *123*, 1090.
(273) Pang, K.; Tanski, J. M.; Parkin, G. *Chem. Commun.* **2008**, *1008*.
(274) Harman, W. H.; Peters, J. C. *J. Am. Chem. Soc.* **2012**, *134*, 5080.
(275) Thomas, C. M.; Napoline, J. W.; Rowea, G. T.; Foxman, B. M. *Chem. Commun.* **2010**, *46*, 5790.
(276) Zhou, W.; Napoline, J. W.; Thomas, C. M. *Eur. J. Inorg. Chem.* **2011**, *2011*, 2029.
(277) Krogman, J. P.; Foxman, B. M.; Thomas, C. M. *J. Am. Chem. Soc.* **2011**, *133*, 14582.
(278) Wesley Napoline, J.; Krogman, J. P.; Shi, R.; Kuppuswamy, S.; Bezpalko, M. W.; Foxman, B. M.; Thomas, C. M. *Eur. J. Inorg. Chem.* **2013**, 3874.
(279) Greenwood, B. P.; Forman, S. I.; Rowe, G. T.; Chen, C. H.; Foxman, B. M.; Thomas, C. M. *Inorg. Chem.* **2009**, *48*, 6251.
(280) Cooper, B. G.; Fafard, C. M.; Foxman, B. M.; Thomas, C. M. *Organometallics* **2010**, *29*, 5179.
(281) Clouston, L. J.; Bernales, V.; Carlson, R. K.; Gagliardi, L.; Lu, C. C. *Inorg. Chem.* **2015**, *54*, 9263.
(282) Sunada, Y.; Sue, T.; Matsumoto, T.; Nagashima, H. *J. Organomet. Chem.* **2006**, *691*, 3176.
(283) Walker, W. K.; Kay, B. M.; Michaelis, S. A.; Anderson, D. L.; Smith, S. J.; Ess, D. H.; Michaelis, D. J. *J. Am. Chem. Soc.* **2015**, *137*, 7371.
(284) Ohkuma, T.; Koizumi, M.; Doucet, H.; Pham, T.; Kozawa, M.; Murata, K.; Katayama, E.; Yokozawa, T.; Ikariya, T.; Noyori, R. *J. Am. Chem. Soc.* **1998**, *120*, 13529.
(285) Nagashima, H.; Sue, T.; Oda, A.; Kanemitsu, A.; Matsumoto, T.; Motoyama, Y.; Sunada, Y. *Organometallics* **2006**, *25*, 1987.
(286) Dunn, P. L.; Reath, A. H.; Clouston, L. J.; Young, V. G.; Tonks, I. A. *Polyhedron* **2014**, *84*, 111.
(287) Setty, V. N.; Zhou, W.; Foxman, B. M.; Thomas, C. M. *Inorg. Chem.* **2011**, *50*, 4647.
(288) McLean, A. D.; Chandler, G. S. *J. Chem. Phys.* **1980**, *72*, 5639.
(289) Raghavachari, K.; Binkley, J. S.; Seeger, R.; Pople, J. A. *J. Chem. Phys.* **1980**, *72*, 650.
(290) Wachters, A. J. H. *J. Chem. Phys.* **1970**, *52*, 1033.
(291) Hay, P. J. *J. Chem. Phys.* **1977**, *66*, 4377.
(292) Clark, T.; Chandrasekhar, J.; Spitznagel, G. W.; Schleyer, G. W. *J. Comp. Chem.* **1983**, *4*, 294.
(293) Frisch, M. J.; Pople, J. A.; Binkley, J. S. *J. Chem. Phys.* **1984**, *80*, 3265.
(294) Hariharan, P. C.; Pople, J. A. *Theor. Chem. Acc.* **1973**, *28*, 213.
(295) Hehre, W. J.; Ditchfield, R.; Pople, J. A. *J. Chem. Phys.* **1972**, *56*, 2257.

(296) Andrae, D.; Haeussermann, U.; Dolg, M.; Stoll, H.; Preuss, H. *Theor. Chim. Acta.* **1990**, *77*, 213.
(297) Mayer, I. *Chem. Phys. Lett.* **1983**, *97*, 270.
(298) Mayer, I. *Int. J. Quantum Chem.* **1984**, *26*, 151.
(299) Bruno, I. J.; Cole, J. C.; Edgington, P. R.; Kessler, M.; Macrae, C. F.; McCabe, P.; Pearson, J.; Taylor, R. *Acta Crystallogr., Sect B* **2002**, *58*, 389.
(300) Mugnier, Y.; Moise, C.; Laviron, E. *J. Organomet. Chem.* **1981**, 204.
(301) Fakhr, A.; Mugnier, Y.; Gautheron, B.; Laviron, E. *J. Organomet. Chem.* **1986**, *3*, C7.
(302) Chapman, A. M.; Wass, D. R. *Dalt. Trans.* **2012**, *41*, 9067.
(303) Chapman, A. M.; Haddow, M. F.; Wass, D. R. *Eur. J. Inorg. Chem.* **2012**, *2012*, 1546.
(304) Engel, E.; Dreizler, R. M. *Density Functional Theory*; Springer-Verlag: Berlin, 2011.
(305) Jacob, C.; Reiher, M. *Int. J. Quantum Chem.* **2012**, *112*, 3661.
(306) Kohn, W. *Rev. Mod. Phys.* **1999**, *71*, 1253.
(307) Schuch, N.; Verstaete, F. *Nat. Phys.* **2009**, *5*, 732.
(308) Pederson, M. R.; Ruzsinszky, A.; Perdew, J. P. *J. Chem. Phys.* **2014**, *140*, 121103.
(309) Schultz, N. E.; Zhao, Y.; Truhlar, D. G. *J. Phys. Chem. A* **2005**, *109*, 11127.
(310) Harvey, J. N. On the accuracy of density functional theory in transition metal chemistry. *Annual Reports Section "C" (Physical Chemistry)*, 2006, *102*, 203–226.
(311) Cohen, A. J.; Mori-Sánchez, P.; Yang, W. *Science* **2008**, *321*, 792.
(312) Yamaguchi, K.; Jensen, F.; Dorigo, A. .; Houk, K. N. *Chem. Phys. Lett.* **1988**, *149*, 537.
(313) Yamaguchi, K.; Tsunekawa, T.; Toyoda, Y.; Fueno, T. *Chem. Phys. Lett.* **1988**, *143*, 371.
(314) Luo, S. J.; Averkiev, B.; Yang, K. R.; Xu, X. F.; Truhlar, D. G. *J. Chem. Theory Comput.* **2014**, *10*, 102.
(315) Nishino, M.; Yamanaka, S.; Yoshioka, Y.; Yamaguchi, K. *J. Chem. Phys.* **1997**, *101*, 705.
(316) Lovell, T.; Liu, T. Q.; Case, D. A.; Noodleman, L. *J. Am. Chem. Soc.* **2003**, *125*, 8377.
(317) Noodleman, L.; Han, W. G. *J. Biol. Inorg. Chem.* **2006**, *11*, 674.
(318) Li Manni, G.; Ma, D.; Aquilante, F.; Olsen, J.; Gagliardi, L. *J. Chem. Theory Comput.* **2013**, *9*, 3375.
(319) Li Manni, G.; Aquilante, F.; Gagliardi, L. *J. Chem. Phys.* **2011**, *134*, 34114.
(320) Ivanic, J. *J. Chem. Phys.* **2003**, *119*, 9377.
(321) Lowdin, P. O. *Rev. Mod. Phys.* **1981**, *35*, 496.
(322) Moscarda, F.; San-Fabian, E. *Phys. Rev. A* **1991**, *44*, 1549.
(323) Staroverov, V. N.; Davidson, E. R. *Int. J. Quantum Chem.* **2000**, *77*, 651.
(324) Henderson, T. M.; Izmaylov, A. F.; Scuseria, G. E.; Savin, A. *J. Chem. Theory Comput.* **2008**, *4*, 1254.
(325) Chai, J.-D.; Head-Gordon, M. *Phys. Chem. Chem. Phys.* **2008**, *10*, 6615.
(326) Chai, J. Da; Head-Gordon, M. *J. Chem. Phys.* **2008**, *128*, 84106.
(327) Peverati, R.; Truhlar, D. G. *Phys. Chem. Chem. Phys.* **2012**, *14*, 13171.
(328) Peverati, R.; Truhlar, D. G. *J. Phys. Chem. Lett.* **2012**, *3*, 117.
(329) Peverati, R.; Truhlar, D. G. *J. Phys. Chem. Lett.* **2011**, *2*, 2810.
(330) Tsai, C. W.; Su, Y. C.; Li, G. D.; Chai, J.-D. *Phys. Chem. Chem. Phys.* **2013**, *15*, 8352.
(331) Garza, A. J.; Jiménez-Hoyos, C. A.; Scuseria, G. E. *J. Chem. Phys.* **2013**, *138*, 134102.
(332) Garza, A. J.; Jiménez-Hoyos, C. A.; Scuseria, G. E. *J. Chem. Phys.* **2014**, *140*, 244102.
(333) Roos, B. O.; Malmqvist, P. A. *Phys. Chem. Chem. Phys.* **2004**, *6*, 2919.
(334) Perdew, J. P.; Ernzerhof, M.; Burke, K.; Savin, A. *Int. J. Quantum Chem.* **1995**, *61*, 197.
(335) Tsuchimochi, T.; Scuseria, G. E.; Savin, A. *J. Chem. Phys.* **2010**, *132*, 24111.
(336) Krishnan, R.; Binkley, J. S.; Seeger, R.; Pople, J. A. *J. Chem. Phys.* **1980**, *72*, 650.
(337) Dunning, T. H. *J. Chem. Phys.* **1989**, *90*, 1007.
(338) Kendall, R. A.; Dunning, T. H.; Harrison, R. J. *J. Chem. Phys.* **1992**, *96*, 6796.

(339) Balabanov, N. B.; Peterson, K. A. *J. Chem. Phys.* **2005**, *123*, 64107.
(340) Ghigo, G.; Roos, B. O.; Malmqvist, P. Å. *Chem. Phys. Lett.* **2004**, *396*, 142.
(341) Ruiperez, F.; Aquilante, F.; Ugalde, J. M.; Infante, I. *J. Chem. Theory Comput.* **2011**, *7*, 1640.
(342) Gáspár, R. *Acta Phys. Acad. Sci. Hungaricae* **1974**, *35*, 213.
(343) Slater, J. C. *Phys. Rev.* **1951**, *81*, 385.
(344) Vosko, S. H.; Wilk, L.; Nusair, M. *Can. J. Phys.* **1980**, *58*, 1200.
(345) Becke, A. D. *Phys. Rev. A* **1988**, *38*, 3098.
(346) Seeger, R.; Pople, J. A. *J. Chem. Phys.* **1977**, *66*, 3045.
(347) Bauernschmitt, R.; Ahlrichs, R. *J. Chem. Phys.* **1996**, *104*, 9047.
(348) Starcke, J. H.; Wormit, M.; Schirmer, J.; Dreuw, A. *Chem. Phys.* **2006**, *329*, 39.
(349) Levy, M. *Phys. Rev. A* **1982**, *26*, 1200.
(350) Lieb, E. H. *Int. J. Quantum Chem.* **1983**, *24*, 243.
(351) Morrison, R. C. *J. Chem. Phys.* **2002**, *117*, 10506.
(352) Kraisler, E.; Makov, G.; Argaman, N.; Kelson, I. *Phys. Rev. A* **2009**, *80*.
(353) Chai, J. Da. *J. Chem. Phys.* **2012**, *136*, 154104.
(354) Szabo, A.; Ostlund, N. S. *Modern Quantum Chemistry: Introduction to Advanced Electronic Structure Theory*; Macmillan: New York, 1982.
(355) Schmidt, M. W.; Gordon, M. S. *Annu. Rev. Phys. Chem.* **1998**, *49*, 233.
(356) Shavitt, I. *Methods of Electronic Structure Theory*; Schaefer, H. F. I., Ed.; Plenum: New York, 1977.
(357) Goddard, W. A. I.; Dunning, T. H.; Hunt, W. J.; Hay, P. J. *Acc. Chem. Res.* **1973**, *6*, 368.
(358) Malmqvist, P.; Rendell, A.; Roos, B. *J. Chem. Phys.* **1990**, *94*, 5477.
(359) Hohenberg, P.; W., K. *Phys. Rev.* **1964**, *136*.
(360) Lee, C.; Yang, W.; Parr, R. G. *Phys. Rev. B* **1988**, *37*, 785.
(361) Becke, A. D. *J. Chem. Phys.* **1993**, *98*, 5648.
(362) Stephens, P.; Devlin, F. J.; Chabalowski, C. F.; Frisch, M. J. *J. Phys. Chem.* **1994**, *98*, 11623.
(363) Zhao, Y.; Truhlar, D. G. *Theor. Chem. Acc.* **2008**, *120*, 215.
(364) Zhang, W.; Truhlar, D. G.; Tang, M. *J. Chem. Theory Comput.* **2013**, *9*, 3965.
(365) Zhao, Y.; Schultz, N. E.; Truhlar, D. G. *J. Chem. Theory Comput.* **2006**, *2*, 364.
(366) Zhang, W.; Truhlar, D. G.; Tang, M. *J. Chem. Theory Comput.* **2014**, *10*, 2399.
(367) Zhao, Y.; Truhlar, D. G. *J. Phys. Chem. A.* **2006**, *110*, 10478.
(368) Izgorodina, E. I.; Coote, M. L.; Radom, L. *J. Phys. Chem. A* **2005**, *109*, 7558.
(369) Zhao, Y.; Truhlar, D. G. *J. Chem. Theory Comput.* **2005**, *1*, 415.
(370) Zhao, Y.; González-Garda, N.; Truhlar, D. G. *J. Phys. Chem. A* **2005**, *109*, 2012.
(371) Zheng, J.; Zhao, Y.; Truhlar, D. G. *J. Chem. Theory Comput.* **2009**, *5*, 808.
(372) Peverati, R.; Truhlar, D. G. *Philos. Trans. A. Math. Phys. Eng. Sci.* **2014**, *372*, 20120476.
(373) Zheng, J.; Xu, X.; Truhlar, D. G. *Theor. Chem. Acc.* **2011**, *128*, 295.
(374) Lynch, B. J.; Zhao, Y.; Truhlar, D. G. *J. Phys. Chem. A* **2003**, *107*, 1384.
(375) Zhao, Y.; Truhlar, D. G. *J. Chem. Theory Comput.* **2005**, *1*, 415.
(376) Zhao, Y.; Lynch, B. J.; Truhlar, D. G. *Phys. Chem. Chem. Phys.* **2005**, *7*, 43.
(377) Lee, T. J.; Taylor, P. R. *Int. J. Quantum Chem. Symp.* **1989**, *23*, 199.
(378) Lee, T. J.; Rendell, A. P.; Taylor, P. R. *J. Chem. Phys.* **1990**, *94*, 5463.
(379) Heard, G. L.; Marsden, C. J.; Scuseria, G. E. *J. Phys. Chem.* **1992**, *96*, 4359.
(380) Gordon, M. S.; Schmidt, M. W.; Chaban, G. M.; Glaesemann, K. R.; Stevens, W. J.; Gonzalez, C. *J. Chem. Phys.* **1999**, *110*, 4199.
(381) Tishchenko, O.; Zheng, J.; Truhlar, D. G. *J. Chem. Theory Comput.* **2008**, *4*, 1208.
(382) Zheng, J.; Zhao, Y.; Truhlar, D. G. *J. Phys. Chem. A* **2007**, *111*, 4632.

(383) Timerghazin, Q. K.; Peslherbe, G. H.; English, A. M. *Phys. Chem. Chem. Phys.* **2008**, *10*, 1532.
(384) Zhao, Y.; Tishchenko, O.; Gour, J. R.; Li, W.; Lutz, J. J.; Piecuch, P.; Truhlar, D. G. *J. Phys. Chem. A* **2009**, *113*, 5786.
(385) Mintz, B.; Chan, B.; Sullivan, M. B.; Buesgen, T.; Scott, A. P.; Kass, S. R.; Radom, L.; Wilson, A. K. *J. Phys. Chem. A* **2009**, *113*, 9501.
(386) Hajgató, B.; Szieberth, D.; Geerlings, P.; De Proft, F.; Deleuze, M. S. *J. Chem. Phys.* **2009**, *131*, 224321.
(387) Oyedepo, G. A.; Peterson, C.; Wilson, A. K. *J. Chem. Phys.* **2011**, *135*, 94103.
(388) Jiang, W.; Deyonker, N. J.; Wilson, A. K. *J. Chem. Theory Comput.* **2012**, *8*, 460.
(389) Jiang, W.; DeYonker, N. J.; Determan, J. J.; Wilson, A. K. *J. Phys. Chem. A* **2012**, *116*, 870.
(390) Law, M. M.; Fraser-Smith, J. T.; Perotto, C. U. *Phys. Chem. Chem. Phys.* **2012**, *14*, 6922.
(391) Boguslawski, K.; Tecmer, P.; Barcza, G.; Legeza, O.; Reiher, M. *J. Chem. Theory Comput.* **2013**, *9*, 2959.
(392) Fogueri, U. R.; Kozuch, S.; Karton, A.; Martin, J. M. L. *Theor. Chem. Acc.* **2013**, *132*, 1.
(393) Torres, A. E.; Guadarrama, P.; Fomine, S. *J. Mol. Model.* **2014**, *20*, 2208.
(394) Hill, J. G.; Bucher, G. J. *J. Phys. Chem. A* **2014**, *118*, 2332.
(395) Zhao, Y.; Truhlar, D. G. *J. Chem. Phys. A* **2008**, *112*, 1095.
(396) Yang, K.; Zheng, J.; Zhao, Y.; Truhlar, D. G. *J. Chem. Phys.* **2010**, *132*, 164117.
(397) Steinmann, S. N.; Wodrich, M. D.; Corminboeuf, C. *Theor. Chem. Acc.* **2010**, *127*, 429.
(398) Ruzsinszky, A.; Perdew, J. P.; Csonka, G. I. *J. Phys. Chem. A* **2005**, *109*, 11006.
(399) Hohenberg, P.; Kohn, W. *Phys. Rev.* **1964**, *136*, 864.
(400) Scuseria, G. E. *J. Chem. Phys.* **1991**, *94*, 442.
(401) Gutsev, G. L.; Bauschlicher, C. W. *J. Phys. Chem. A* **2003**, *107*, 4755.
(402) Barden, C. J.; Rienstra-Kiracofe, J. C.; Schaefer, H. F. *J. Chem. Phys.* **2000**, *113*, 690.
(403) Schultz, N. E.; Zhao, Y.; Truhlar, D. G. *J. Phys. Chem. A* **2005**, *109*, 4388.
(404) Yanagisawa, S.; Tsuneda, T.; Hirao, K. *J. Chem. Phys.* **2000**, *112*, 545.
(405) Pou-Amérigo, R.; Merchán, M.; Nebot-Gil, I.; Malmqvist, P.-Å.; Roos, B. O. *J. Chem. Phys.* **1994**, *101*, 4893.
(406) Carlson, R. K.; Li Manni, G.; Sonnenberger, A. L.; Truhlar, D. G.; Gagliardi, L. *J. Chem. Theory Comput.* **2015**, *11*, 82.
(407) Colle, R.; Salvetti, O. *Theor. Chim. Acta.* **1975**, *37*, 329.
(408) Colle, R.; Salvetti, O. *Theor. Chim. Acta.* **1979**, *53*, 55.
(409) Grafenstein, J.; Cremer, D. *Phys. Chem. Chem. Phys.* **2000**, *2*, 2091.
(410) Takeda, R.; Yamanaka, S.; Yamaguchi, K. *Int. J. Quantum Chem.* **2004**, *96*, 463.
(411) Zhao, Y.; Truhlar, D. G. *J. Phys. Chem. A* **2006**, *110*, 10478.
(412) Reiher, M. *Wiley Interdiscip. Rev. Comput. Mol. Sci.* **2012**, *2*, 139.
(413) Simard, B.; Hackett, P. A.; James, A. M.; Langridge-Smith, P. R. R. The bond length of silver dimer. *Chemical Physics Letters*, 1991, *186*, 415–422.
(414) Lombardi, J. R.; Davis, B. *Chem. Rev.* **2002**, *102*, 2431.
(415) Ruipérez, F.; Aquilante, F.; Ugalde, J. M.; Infante, I. *J. Chem. Theory Comput.* **2011**, *7*, 1640.
(416) Rohlfing, E. A.; Valentini, J. J. *J. Chem. Phys.* **1986**, *84*, 6560.
(417) Wu, Z. J.; Han, B.; Dai, Z. W.; Jin, P. C. *Chem. Phys. Lett.* **2005**, *403*, 367.
(418) Du, J.; Sun, X.; Wang, H. *Int. J. Quantum Chem.* **2008**, *108*, 1505.
(419) Takahashi, K.; Isobe, S.; Ohnuki, S. *Chem. Phys. Lett.* **2013**, *555*, 26.
(420) Kim, J.; Kim, J. *Int. J. Quantum Chem.* **2014**, *114*, 1466.
(421) Gagliardi, L.; Roos, B. O. *Inorg. Chem.* **2003**, *42*, 1599.

(422) Trogler, W. C.; Gray, H. B. *Acc. Chem. Res.* **1978**, *11*, 232.
(423) Fromager, E. *Mol. Phys.* **2015**, *113*, 419.
(424) Malet, F.; Gori-Giorgi, P. *Phys. Rev. Lett.* **2012**, *109*, 246402.
(425) Tew, D. P.; Klopper, W.; Helgaker, T. *J. Comput. Chem.* **2007**, *28*, 1307.
(426) Bytautas, L.; Ruedenberg, K. *Chem. Phys.* **2009**, *356*, 64.
(427) Ivanic, J.; Ruedenberg, K. *Theor. Chem. Acc.* **2001**, *106*, 339.
(428) Vogiatzis, K. D.; Li Manni, G.; Stoneburner, S. J.; Ma, D.; Gagliardi, L. *J. Chem. Theory Comput.* **2015**, *11*, 3010.
(429) Andersson, K.; Malmqvist, P. A.; Roos, B. O.; Sadlej, A. J.; Wolinski, K. *J. Phys. Chem.* **1990**, *94*, 5483.
(430) Sauri, V.; Serrano-Andrés, L.; Shahi, A. R. M.; Gagliardi, L.; Vancoillie, S.; Pierloot, K. *J. Chem. Theory Comput.* **2011**, *7*, 153.
(431) Shahi, A. R. M.; Cramer, C. J.; Gagliardi, L. *Phys. Chem. Chem. Phys.* **2009**, *11*, 10964.
(432) Carlson, R. K.; Truhlar, D. G.; Gagliardi, L. *J. Chem. Theory Comput.* **2015**, *11*, 4077.
(433) Vlaisavljevich, B.; Mirõ, P.; Ma, D.; Sigmon, G. E.; Burns, P. C.; Cramer, C. J.; Gagliardi, L. *Chem. - A Eur. J.* **2013**, *19*, 2937.
(434) Hunt, W. J.; Hay, P. J.; Goddard III, W. A. *J. Chem. Phys.* **1972**, *57*, 738.
(435) Faglioni, F.; Goddard, W. A. *Int. J. Quantum Chem.* **1999**, *73*, 1.
(436) Moss, B. J.; Bobrowicz, F. W.; Goddard, W. A. *J. Chem. Phys.* **1975**, *63*, 4632.
(437) Woon, D. E.; Dunning, T. H. *J. Chem. Phys.* **1993**, *98*, 1358.
(438) Olsen, J.; Roos, B. O.; Jo/rgensen, P.; Jensen, H. J. A. *J. Chem. Phys.* **1988**, *89*, 2185.
(439) Handy, N. C. *Chem. Phys. Lett.* **1980**, *74*, 280.
(440) Knowles, P. J.; Handy, N. C. *Chem. Phys. Lett.* **1984**, *111*, 315.
(441) Banerjee, A.; Grein, F. *Int. J. Quantum Chem.* **1976**, *10*, 123.
(442) NIST Chemistry Webbook www.nist.gov/chemistry.
(443) Guner, V.; Khuong, K.; Leach, A.; Lee, P.; Bartberger, M. D.; Houk, K. N. *J. Phys. Chem.* **2003**, *107*, 11445.
(444) Barbatti, M.; Paier, J.; Lischka, H. *J. Chem. Phys.* **2004**, *121*, 11614.
(445) Piecuch, P.; Kucharski, S. A.; Kowalski, K. *Chem. Phys. Lett.* **2001**, *344*, 176.
(446) Azizi, Z.; Roos, B. O.; Veryazov, V. *Phys. Chem. Chem. Phys.* **2006**, *8*, 2727.
(447) Das, G.; Wahl, A. C. *J. Chem. Phys.* **1966**, *44*, 87.
(448) Chattopadhyay, S.; Chaudhuri, R. K.; Mahapatra, U. S. *J. Comput. Chem.* **2015**, *36*, 907.
(449) NIST Computational Chemistry Comparison and Benchmark Database. http://cccbdb.nist.gov/.
(450) Andersson, K.; Roos, B. O. *Int. J. Quantum Chem.* **1993**, *45*, 591.
(451) Abrams, M. L.; Sherrill, C. D. *J. Chem. Phys.* **2004**, *121*, 9211.
(452) Boschen, J. S.; Theis, D.; Ruedenberg, K.; Windus, T. L. *Theor. Chem. Acc.* **2014**, *133*, 1425.
(453) Su, P.; Wu, J.; Gu, J.; Wu, W.; Shaik, S.; Hiberty, P. C. *J. Chem. Theory Comput.* **2011**, *7*, 121.
(454) Herzberg, G. *Spectra of Diatomic Molecules*; Von Nostrand Reinhold: New York, 1950.
(455) Gaydon, A. G. *Dissociation Energies and Spectra of Diatomic Molecules*; Chapman & Hall: London, 1968.
(456) Apeloig, Y.; Pauncz, R.; Karni, M.; West, R.; Steiner, W.; Chapman, D. *Organometallics* **2003**, *22*, 3250.
(457) Petek, H.; Nesbitt, D. J.; Darwin, D. C.; Ogilby, P. R.; Moore, C. B.; Ramsay, D. a. *J. Chem. Phys.* **1989**, *91*, 6566.
(458) Shavitt, I. *Tetrahedron* **1985**, *41*, 1531.
(459) Mikhailenko, S.; Barbe, A.; Plateaux, J. J.; Tyuterev, V. G. *J. Mol. Spectrosc.* **1999**, *196*.

(460) Trambarulo, R.; Ghosh, S, N.; Barrus Jr., C. A.; Gordy, W. *J. Chem. Phys.* **1953**, *21*, 851.
(461) Jensen, P.; Bunker, P. R. *J. Chem. Phys.* **1988**, *89*, 1327.
(462) Gräfenstein, J.; Kraka, E.; Filatov, M.; Cremer, D. *Int. J. Mol. Sci.* **2002**, *3*, 360.
(463) Ljubić, I.; Sabljić, A. *Chem. Phys. Lett.* **2004**, *385*, 214.
(464) Tsuneda, T.; Nakano, H.; Hirao, K. *J. Chem. Phys.* **1995**, *103*, 6520.
(465) Watts, J. D.; Stanton, J. F.; Bartlett, R. J. *Chem. Phys. Lett.* **1991**, *178*, 471.
(466) Shiozaki, T.; Knizia, G.; Werner, H. J. *J. Chem. Phys.* **2011**, *134*, 34113.
(467) Stanton, J. F.; Bartlett, R. J.; Magers, D. H.; Lipscomb, W. N. *Chem. Phys. Lett.* **1989**, *163*, 333.
(468) Yamashita, K.; Morokuma, K.; Le Quéré, F.; Leforestier, C. *Chem. Phys. Lett.* **1992**, *191*, 515.
(469) Krishna, M. V. R.; Jordan, K. D. *Chem. Phys. Lett.* **1987**, *115*, 423.
(470) Blanksby, S. J.; Ellison, G. B. *Acc. Chem. Res.* **2003**, *36*, 255.
(471) Ess, D. H.; Houk, K. N. *J. Chem. Phys. A* **2005**, *109*, 9542.
(472) Wenthold, P. G.; Squires, R. R.; Lineberger, W. C. *J. Am. Chem. Soc.* **1998**, *120*, 5279.
(473) Gräfenstein, J.; Hjerpe, A. M.; Kraka, E.; Cremer, D. *J. Phys. Chem. A* **2000**, *104*, 1748.
(474) Wenthold, P. G.; Wierschke, S. G.; Nash, J. J.; Squires, R. R. *J. Am. Chem. Soc.* **1993**, *115*, 12611.
(475) Lennard-Jones, J. *Proc. Roy. Soc.* **1949**, *A198*, 1.
(476) Roothaan, C. C. J. *Rev. Mod. Phys.* **1951**, *23*, 69.
(477) Hall, G. G. *Proc. Roy. Soc.* **1951**, *A205*, 541.
(478) Pople, J. A.; Nesbet, R. K. *J. Chem. Phys.* **1954**, *22*.
(479) Coulson, C. A.; Fischer, I. *Phil. Mag.* **1949**, *40*, 386.
(480) Ruedenberg, K. *Rev. Mod. Phys.* **1962**, *34*, 326.
(481) Coulson, C. A.; Neilson, A. H. *Proc. Phys. Soc.* **1961**, *78*, 831.
(482) Ugalde, J. M.; Sarasola, C.; Domínguez, L.; Boyd, R. J. *J. Math. Chem.* **1991**, *6*, 51.
(483) Boyd, R. J.; Sarasola, C.; Ugalde, J. M. *J. Phys. B.* **1988**, *21*, 2555.
(484) Sanders, J.; Banyard, K. E. *J. Chem. Phys.* **1992**, *96*, 4536.
(485) Thakker, A. J.; Tripathi, A. N.; Smith Jr., V. H. *Int. J. Quantum Chem.* **1984**, *26*, 157.
(486) Pearson, J. K.; Gill, P. M. W.; Ugalde, J. M.; Boyd, R. J. *Mol. Phys.* **2009**, *107*, 1089.
(487) Mathematica. Version 10.4.1, 2016.
(488) Löwdin, P. O. *Phys. Rev.* **1955**, *97*, 1509.
(489) Rong, C.; Lian, S.; Yin, D.; Shen, B.; Zhong, A.; Bartolotti, L.; Liu, S. *J. Chem. Phys.* **2006**, *125*, 174102.
(490) Rong, C.; Lian, S.; Yin, D.; Zhong, A.; Zhang, R.; Liu, S. *Chem. Phys. Lett.* **2007**, *434*, 149.
(491) Lovell, T.; Han, W. G.; Liu, T.; Noodleman, L. *J. Am. Chem. Soc.* **2002**, *124*, 5890.
(492) Lovell, T.; Liu, T. Q.; Case, D.; Noodleman, L. *J. Am. Chem. Soc.* **1985**, *107*, 3418.
(493) Isley, W. C.; Zarra, S.; Carlson, R. K.; Bilbeisi, R. a; Ronson, T. K.; Nitschke, J. R.; Gagliardi, L.; Cramer, C. J. *Phys. Chem. Chem. Phys.* **2014**, *16*, 10620.
(494) Vancoillie, S.; Zhao, H.; Radoń, M.; Pierloot, K. *J. Chem. Theory Comput.* **2010**, *6*, 576.
(495) Chan, G. K.-L.; Sharma, S. *Annu. Rev. Phys. Chem.* **2011**, *62*, 465.
(496) Marti, K. H.; Ondík, I. M.; Moritz, G.; Reiher, M. *J. Chem. Phys.* **2008**, *128*.
(497) Neuscamman, E.; Yanai, T.; Chan, G. K. L. *J. Chem. Phys.* **2009**, *130*.
(498) Yanai, T.; Kurashige, Y.; Ghosh, D.; Chan, G. K. L. *Int. J. Quantum Chem.* **2009**, *109*, 2178.
(499) Ghosh, D.; Hachmann, J.; Yanai, T.; Chan, G. K. L. *J. Chem. Phys.* **2008**, *128*, 144117.
(500) Ghosh, A. *J. Biol. Inorg. Chem.* **2006**, *11*, 712.
(501) Neese, F.; Zaleski, J. M.; Zaleski, K. L.; Solomon, E. I. *J. Am. Chem. Soc.* **2000**, *122*,

11703.
(502) Roos, B. O. .; Veryazov, V. .; Widmark, P.-O. *Theor. Chim. Acta.* **2004**, *111*, 345.
(503) te Velde, G.; Bickelhaupt, F. M.; van Gisbergen, S. J.; Fonseca Guerra, C.; Baerends, E. J.; Snijders, J. G.; Ziegler, T. *J. Comput. Chem.* **2001**, *22*, 931.
(504) van Lenthe, E. *J. Comp. Chem.* **1999**, *20*, 51.
(505) van Lenthe, E.; Baerends, E. J.; Snijders, J. G. *J. Chem. Phys.* **1993**, *99*, 4597.
(506) Adamo, C.; Barone, V. *J. Chem. Phys.* **1999**, *110*, 6158.
(507) Zall, C. M.; Zherebetskyy, D.; Dzubak, A. L.; Bill, E.; Gagliardi, L.; Lu, C. C. *Inorg. Chem.* **2012**, *51*, 728.
(508) Kim, J.; Kim, J. *Chem. Phys. Lett.* **2014**, *592*, 24.
(509) Lawson Daku, L. M.; Vargas, A.; Hauser, A.; Fouqueau, A.; Casida, M. E. *ChemPhysChem* **2005**, *6*, 1393.

Appendix 1

Experimental Section

General Considerations

Unless otherwise stated, all manipulations were performed under an N_2 atmosphere in a VAC glovebox. Standard solvents were deoxygenated by sparging with dinitrogen and dried by passing through activated alumina columns of a SG Water solvent purification system. Benzylpotassium (KBn) was prepared according to literature methods.[31]Deuterated solvents were purchased from Cambridge Isotope Laboratories, Inc., degassed via freeze-pump-thaw cycles, dried over activated alumina, and stored over activated 4 Å molecular sieves. Tris(2-aminoethyl)amine (tren) was purchased from Pressure Chemical Co. All other reagents were purchased from Aldrich or Strem and used without further purification. Elemental analyses were performed by Complete Analysis Laboratories, Inc. (Parsippany, NJ). Inductively coupled plasma optical emission spectrometry (ICP-OES) data were collected at the University of Minnesota Earth Sciences Analytical Geochemistry Lab using a Thermo Scientific iCAP 6500 dual view instrument, with the addition of cesium as a matrix modifier and yttrium as an internal standard. The weight percent is an average of three or four measurements is reported with standard deviations.

Synthesis of tris(2-(2-pyridylamino)ethyl)amine (H_3[py_3tren]). Tren (9.77 g, 0.0668 mol), 2-bromopyridine (20.0 mL, 0.210 mol), and K_2CO_3 (47.0 g, 0.268 mol) were heated at 180C in 200 mL DMSO for 3 days. After cooling to rt, the crude reaction mixture was extracted in $CHCl_3$, and washed with NaOH (1X) and brine (4X). After removing the volatiles from the organic layer, the crude product was warmed to 50C in toluene and loaded onto a silica gel column. The crude product was purified by silica gel chromatography (3:1:0.12 hexanes:EtOAc:7 N NH_3 in CH_3OH). The product fractions were combined, and the solvents removed *in vacuo*. The product was dried overnight *in vacuo* at 60C. The product was brought into the glovebox, extracted with THF, and dried *in vacuo* again, first at rt, then at 50C overnight. This workup provided the product as a tan solid (14.2 g, 56%). ^{1}H NMR (500 MHz, $CDCl_3$): 8.05 (dd, $^3J_{HH}$ = 6 Hz, $^4J_{HH}$ = 1 Hz, 1H), 7.31 (ddd, $^3J_{HH}$ = 8 Hz, $^3J_{HH}$ = 6 Hz , $^4J_{HH}$ = 1 Hz,1H), 6.52 (t, $^3J_{HH}$ = 6 Hz, 1H), 6.32 (d, $^3J_{HH}$ = 8 Hz, 1H), 5.61 (br, 1H, N*H*), 3.30 (dt, $^3J_{HH}$ = 6 Hz), 2.78 (t, $^3J_{HH}$ = 6Hz). ^{13}C NMR (126 MHz, $CDCl_3$): 159.0, 148.2, 137.4, 113.0, 108.0, 53.5, 40.0. ESI-MS-TOF *m/z*: $[M + H]^+$calc'd for $C_{21}H_{28}N_7$, 378.2406; found 378.2426.

Synthesis of K[Co(py_3tren)]. A solution of H_3[py_3tren] (0.995 g, 0.00264 mol) in 30 mL THF was cooled to −50C. Then, a cold solution of KBn (1.06 g, 0.00814 mol) in 60 mL THF was added dropwise. After stirring for 30 min, $CoCl_2$ (0.361 g, 0.00278 mol) was added. The green reaction was removed from the cold and warmed to rt with stirring overnight. After stirring for 15 h, the reaction solution was filtered through Celite and dried *in vacuo*. The green powder was stirred in 3x10 mL Et_2O, 10 mL pentane, and dried *in vacuo* for several hours, yielding K[Co(py_3tren)] as a green powder (1.10 g, 88% yield). ^{1}H NMR (300 MHz, d_8-THF): 140, 88, 34, 0.3, -36. UV- Vis-NIR (CH_2Cl_2) $_{max}$ (, L mol^{-1} cm^{-1}): 314 (24,500), 347 sh (10,100), 386 sh (6,700), 595 (110), 820 (10), 1620

(80). Anal. Calcd for $C_{21}H_{24}N_7CoK$: C, 53.38; H, 5.12; N, 20.75. Found: C, 53.31; H, 5.19; N, 20.69.

Synthesis of K[Fe(py$_3$tren)]. A solution of H_3[py$_3$tren] (0.392 g, 0.00104 mol) in 10 mL THF was deprotonated with a solution of KBn (0.407 g, 0.00313 mol) in 10 mL THF at rt. After stirring for several hours, $FeCl_2$ (0.132 g, 0.00104 mol) was added. The red-colored reaction was stirred overnight. The reaction was then filtered through Celite and dried *in vacuo*. The orange-red powder was stirred in 2x10 mL Et_2O, 10 mL pentane, and dried *in vacuo*. The resulting powder was transferred to a frit and washed with 2x5 mL toluene, 1x5 mL Et_2O, and 2x5 mL hexanes. The powder was dried *in vacuo* for several hours, yielding K[Fe(py$_3$tren)] as an orange powder (0.215 g, 44% yield).^{1}H NMR (300 MHz, d_8-THF): 183, 82.4, 30.9, 14.3, −23.6, −33.7. UV-Vis-NIR (THF) $_{max}$ (, L mol^{-1} cm^{-1}): 311 (14,100), 489 (2,000), 1650(40). Anal. Calcd for $C_{21}H_{24}N_7FeK$: C, 53.73; H, 5.15; N, 20.89. Found: C, 53.68; H,5.08; N, 20.81.

Synthesis of CoCoCl(py$_3$tren) (1). To K[Co(py$_3$tren)] (639 mg, 1.36 mmol) in 100 mL THF was added $CoCl_2$ (176 mg, 1.36 mmol) at rt. The green solution rapidly turned into a dark green suspension. After stirring for 11 h, the volatiles were removed *in vacuo*. The solids were then extracted repeatedly with CH_2Cl_2 and filtered through Celite. The filtrate was dried *in vacuo*. Compound 1 was purified by recrystallizing this residue using hexanes layered on a CH_2Cl_2 solution to give 312 mg (0.591 mmol, 43% yield) of a dark green-brown solid. X-ray quality crystals were grown from layering Et_2O onto a THF solution. ^{1}H NMR (300 MHz, CD_2Cl_2): 21.7, 20.9, 11.5, 7.7, 6.7, −1.6. UV- Vis-NIR (CH_2Cl_2) $_{max}$ (, L mol^{-1} cm^{-1}): 317 (28,700), 340 sh (17,900), 450 (8,500), 572 (620), 650 (680), 1027 (130), 1650 (40). Anal. Calcd for $C_{21}H_{24}N_7Co_2Cl$: C, 47.79; H, 4.58; N, 18.58. Found: C, 47.77; H, 4.52; N, 18.61.

Synthesis of CoFeCl(py$_3$tren) (2). A THF slurry of $FeCl_2(THF)_{1.5}$ (171 mg, 0.728 mmol) was added to a solution of K[Co(py$_3$tren)] (340 mg, 0.720 mmol) at −50C. The reaction slowly turned red. After stirring overnight, the reaction was filtered through Celite, and the filter cake was washed with 100 mL CH_2Cl_2. The filtrate was dried *in vacuo* to give 352 mg (0.671 mmol, 93% yield) of a dark red-orange solid. X-ray quality crystals were grown from Et_2O layered on a CH_2Cl_2 solution. UV-Vis-NIR (CH_2Cl_2) $_{max}$ (, L mol^{-1} cm^{-1}): 317 (25,000), 356 sh (11,500), 448 (7,500), 574 sh (420), 1258 (90). ^{1}H NMR (300 MHz, CD_2Cl_2): 32.5, 26.6, 16.8, 1.7, −3.6, −20.3. Anal. Calcd for $C_{21}H_{24}N_7CoFeCl$: C, 48.07; H, 4.61; N, 18.69. Found: C, 48.13; H, 4.56; N, 18.78. ICP-OES (wt %): Fe, 10.96(3); Co, 11.83(2), which is consistent with $Co_{1.01}Fe_{0.99}$.

Synthesis of CoMnCl(py$_3$tren) (3). A THF solution of K[Co(py$_3$tren)] (203 mg, 0.430 mmol) was added to a THF slurry of $MnCl_2(THF)_2$ (116 mg, 0.431 mmol) at −50C. The reaction rapidly turned green-yellow. After stirring overnight, the reaction was dried *in vacuo*, reconstituted in 60 mL CH_2Cl_2, filtered through Celite, and the filtrate dried *in vacuo*. X-ray quality crystals were grown from Et_2O layered on a CH_2Cl_2 solution (141 mg, 0.269 mmol, 63% crystalline yield). ^{1}H NMR (500 MHz, CD_2Cl_2): 40, 31.1, 28.6, −9.2, −24.4, −39.4. UV-Vis-NIR (CH_2Cl_2)$_{max}$ (, L mol^{-1} cm^{-1}): 317 (22,600), 349 sh (9,800), 397 sh (6,800), 435 (9,000), 608 (140), 1240 (90). Anal. Calcd for $C_{21}H_{24}N_7CoMnCl$: C, 48.15; H, 4.62; N, 18.72. Found: C, 48.09; H, 4.69; N, 18.71. ICP-OES (wt %): Mn, 12.21(7); Co, 12.80(2), which is consistent with $Co_{0.99}Mn_{1.01}$.

Synthesis of FeFeCl(py$_3$tren) (4). A THF solution of K[Fe(py$_3$tren)] (300 mg, 0.639 mmol) was added to a THF slurry of $FeCl_2(THF)_{1.5}$ (163 mg, 0.690 mmol) at rt. The reaction rapidly turned dark red. After stirring overnight, the filtrate was pumped down, reconstituted in 80 mL CH_2Cl_2, filtered through Celite, and the filtrate was dried *in vacuo*. Dark red crystals were grown from Et_2O layered on a CH_2Cl_2 solution (94 mg, 0.180 mmol, 28% crystalline yield). ^{1}H NMR (500 MHz, CD_2Cl_2): 168, 77.5, 42.1, 9.5, 0.8, −15.7. UV-Vis-NIR (CH_2Cl_2) $_{max}$ (, L mol^{-1} cm^{-1}): 315 (18,000), 530 (5,600), 997 (190). Anal. Calcd for $C_{21}H_{24}N_7Fe_2Cl$: C, 48.36; H, 4.64; N, 18.80. Found: C, 48.32; H, 4.69; N, 18.73.

Synthesis of FeMnCl(py$_3$tren) (5). A THF solution of K[Fe(py$_3$tren)] (101 mg, 0.215 mmol) was added to a THF slurry of $MnCl_2(THF)_2$ (58 mg, 0.215 mmol) at −50C. The reaction rapidly turned orange. After stirring overnight, the reaction was pumped down, reconstituted in 80 mL CH_2Cl_2, and filtered through Celite. The filtrate was dried *in vacuo* to a bright orange solid. Orange crystals (49 mg, 0.094 mmol, 44% crystalline yield) were obtained from Et_2O layered on a CH_2Cl_2 solution. ^{1}H NMR (500 MHz, CD_2Cl_2): 43.7, 16.8, 12.6, 6.5, 2.0, −0.3. UV-Vis-NIR (CH_2Cl_2) $_{max}$ (, L mol^{-1} cm^{-1}): 310 (14,400), 498 (2,600), 1019 (40), 1555 (60). Anal. Calcd for $C_{21}H_{24}N_7FeMnCl$: C, 48.44; H, 4.65; N, 18.83. Found: C, 48.33; H, 4.63; N, 18.88. ICP-OES (wt %): Mn, 12.13(2); Fe, 10.6(1), which is consistent with $Fe_{0.92}Mn_{1.08.}$

X-Ray Crystallographic Data Collection and Refinement of the Structures

Single crystals of K[Co(py$_3$tren)] were grown from a mixture of pentane, Et_2O, and THF (see SI Table 1 for crystallographic data). Single crystals of CoCoCl(py$_3$tren) (**1**) were grown from Et_2O layered on a THF solution. Single crystals of CoFeCl(py$_3$tren) (**2**), CoMnCl(py$_3$tren) (**3**), FeFeCl(py$_3$tren) (**4**), and FeMnCl(py$_3$tren) (**5**) were grown from Et_2O layered on a CH_2Cl_2 solution. A green plate of K[Co(py$_3$tren)], red blocks of **2** (0.40 x 0.20 x 0.20 mm^3) and **4** (0.50 x 0.20 x 0.20 mm^3), a green block of **3** (0.60 x 0.40 x 0.20 mm^3), and an orange block of **5** (0.40 x 0.40 x 0.20 mm^3) were placed on the tip of a glass capillary and mounted on a Bruker APEX II Platform CCD diffractometer for data collection at 173(2) K, and a green block of **1** (0.40 x 0.40 x 0.20 mm^3) was collected at 123(2) K. The data collection was carried out using Mo-Kα radiation (graphite monochromator). The data intensity was corrected for absorption and decay (SADABS). Final cell constants were obtained from least squares fits of all measured reflections. The structure was solved using SHELXS-97 and refined using SHELXL-97. A direct-methods solution was calculated which provided most non-hydrogen atoms from the E-map. Full-matrix least squares / difference Fourier cycles were performed to locate the remaining non-hydrogen atoms. All non-hydrogen atoms were refined with anisotropic displacement parameters. Hydrogen atoms were placed in ideally and refined as riding atoms with relative isotropic displacement parameters. Crystallographic data for **1** − **5** are summarized in Table A1.1

Table A1.1 Crystallographic details for the MM'Cl(py3tren) series, where MM' = CoCo **1**, CoFe **2**, CoMn **3**, FeFe **4**, FeMn **5**.

	1	**2**	**3**	**4**	**5**
chemical formula	$C_{21}H_{24}N_7Co_2Cl$	$C_{21}H_{24}N_7CoFeCl$	$C_{21}H_{24}N_7CoMnCl$	$C_{21}H_{24}N_7Fe_2Cl$	$C_{21}H_{24}N_7FeMnCl$
formula weight	527.78	524.70	523.79	521.62	520.71
crystal system	orthorhombic	monoclinic	monoclinic	monoclinic	monoclinic
space group	$P2_12_12_1$	$P2_1/n$	$P2_1/n$	$P2_1/n$	$P2_1/n$
a (Å)	9.5717(14)	9.2450(6)	9.3125(7)	9.206(3)	9.3535(4)
b (Å)	14.824(2)	12.5597(8)	12.5159(9)	12.673(3)	12.5109(5)
c (Å)	14.934(2)	18.475(1)	18.574(1)	18.423(5)	18.5566(8)
α (deg)	90	90	90	90	90
β (deg)	90	98.724(1)	98.631(1)	100.544(3)	98.5002(4)
γ (deg)	90	90	90	90	90
V (Å3)	2119.0(5)	2120.4(2)	2140.4(3)	2113(1)	2147.7(2)
Z	4	4	4	4	4
Dcalcd (g cm−3)	1.654	1.644	1.625	1.640	1.610
l (Å), μ (mm−1)	0.71073, 1.716	0.71073, 1.617	0.71073, 1.514	0.71073, 1.524	0.71073, 1.412
TK	123(2)	173(2)	173(2)	173(2)	173(2)
range (deg)	1.94 to 27.42	1.97 to 27.42	1.97 to 27.48	1.96 to 27.48	1.97 to 27.48
reflns collected	4812	23646	24156	23676	24203
unique reflns	2945	4801	4900	4831	4918
data/restraints/parameters	2945 / 0 / 280	4801 / 0 / 281	4900 / 0 / 280	4831 / 0 / 281	4918 / 0 / 280
$R1$, $wR2$ ($I > 2\sigma(I)$)	0.0187, 0.0491	0.0226, 0.0607	0.0297, 0.0695	0.0234, 0.0689	0.0265, 0.0659

Anomalous Diffraction Data Collection and Refinement of Metal Occupancies

Single crystals of the heterobimetallic compounds, **2**, **3**, and **5**, were mounted on a glass fiber and cooled to 100 K using an Oxford Instruments Cryojet cryostat. The Bruker D8 diffractometer, integrated with an APEX-II CCD detector, was modified for synchrotron use at the ChemMatCARS 15-ID-B beam line at the Advanced Photon Source (Argonne National Laboratory). For each crystal, diffraction data were collected at seven different energies with 0.3 second frames while manually attenuating the beam to minimize overages of individual pixels. The scan at 30.0 keV (λ=0.41328 Å), which is energetically far from any atomic absorption energies, gave a least-squares refinement of all model positional- and displacement parameters to 0.5 Å resolution. In addition, six anomalous diffraction data sets were collected to span the absorption K-edges of both M_1 and M_2 (at the two metals' K-edges (λ_{edge}) and ± 50 eV) per complex. The specific energies (keV) [wavelengths (Å)] that were used are: for iron, 7.062 [1.7557], 7.112 [1.7433], and 7.162 [1.7312]; for cobalt, 7.659 [1.6188], 7.709 [1.6083], 7.759 [1.5980]; and for manganese, 6.489 [1.9107], 6.539 [1.8961], and 6.589 [1.8817]. The

anomalous diffraction can distinguish Mn/Fe/Co compositions at the two metal sites because of the expected differences in the anomalous scattering factors ($\Delta f'$ and $\Delta f''$) for these elements, as shown in Figure A1.1. Basically, $\Delta f'$ and $\Delta f''$ values of an element change dramatically near the element's absorption edge, but, for other element(s), they remain relatively constant. Each anomalous diffraction data sets thus provides a different view of the electrons present at both sites. Of the 6 anomalous data sets collected per compound, only two sets ($\lambda > \lambda_{edge}$) were used to solve for metal occupancies. The others were excluded for the following reasons. For $\lambda = \lambda_{edge}$, the data is less reliable because of inaccuracies in the metal K-edge energies, which shift for coordination compounds. For $\lambda < \lambda_{edge}$, the data is also less reliable due to potential problems with adsorption and/or fluorescence.[32] For each complex, the two anomalous datasets were simultaneously used in a least-squares refinement to determine the Mn/Fe/Co occupancies at the two metal sites (M_1, M_2). GSAS-II was employed because it allows multiple diffraction data sets as an input with subsequent refinement using a common crystallographic model.[33] The 30 keV data was refined using structural models of **2**, **3**, and **5** that had been previously determined at 173 K. The converged positional- and displacement parameters were than frozen, so that only the metal occupancies were refined.

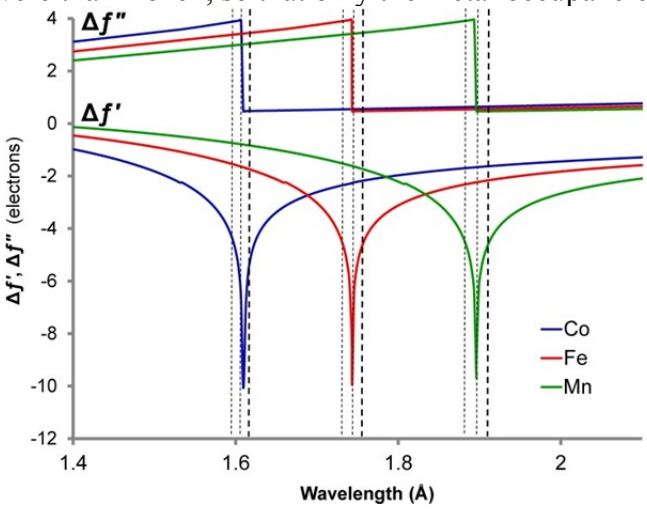

Figure A1.1 Theoretical anomalous dispersion corrections, including the real ($\Delta f'$) and imaginary ($\Delta f''$) scattering factors, for Co(blue), Fe(red) and Mn (green), as a function of wavelength (Å). The dotted lines represent the experimental wavelengths (λ) for the anomalous data collections, which were selected to span the Co, Fe, and Mn absorption edge energies. The datasets collected at $\lambda > \lambda_{edge}$ were used to determine the metal occupancies (bold, dotted lines).

Physical Measurements

NMR spectra were collected on Varian Inova 300 and 500 MHz spectrophotometers. UV-Vis-NIR absorption data were collected on a Cary-14 spectrophotometer. Cyclic voltammetry was conducted using a CH Instruments 600 electrochemical analyzer. The one-cell setup utilized a platinum working electrode, Pt wire counter electrode, and

$Ag/AgNO_3$ reference electrode in CH_3CN. Analyte solutions were prepared in a THF solution of NBu_4PF_6 (0.4 M) and referenced internally to the $FeCp_2/FeCp_2^+$ redox couple. Mössbauer data were recorded on an alternating constant acceleration spectrometer. The minimum experimental line width was 0.24 mm s^{-1} (full width at half-height). The $^{57}Co/Rh$ source (1.8 GBq) was positioned at rt inside the gap of the magnet system at a zero-field position. Isomer shifts are quoted relative to iron metal at 300 K.

Magnetic susceptibility data were measured from powder samples of solid material in the temperature range 2 - 300 K by using a SQUID susceptometer with a field of 1.0 T (MPMS-7, Quantum Design, calibrated with standard palladium reference sample, error <2%). The experimental data were corrected for underlying diamagnetism by use of tabulated Pascal's constants ($\chi_{dia} < 0$),[34,35] as well as for temperature-independent paramagnetism ($\chi_{TIP} > 0$).[36] Specifically, χ_{TIP} (units of 10^{-6} emu) = 630 for **1**, 860 for **2**, 550 for **4**, and 350 for **5**. Also, in the simulation of **1**, a very small (0.4 %) $S = 3/2$ impurity, e.g. monocobalt(II), was accounted for. The susceptibility and magnetization data were simulated with the program julX for exchange coupled systems.[37] The simulations are based on the usual spin-Hamiltonian operator for mononuclear complexes with spin *S:*

$$\widehat{H}_e = g\beta\widehat{\boldsymbol{S}}\cdot\boldsymbol{B} + D[\hat{S}_z^2 - \tfrac{1}{3}S(S+1) + \tfrac{E}{D}(\hat{S}_x^2 - \hat{S}_y^2)]$$

where g is the average electronic g value, and D and E/D are the axial zero-field splitting and rhombicity parameters. Magnetic moments are calculated after diagonalization of the Hamiltonian from the eigenfunctions using the Hellman-Feynman theorem: $\boldsymbol{\mu}_i(B) = \left\langle \psi_i \middle| \partial\widehat{H}/\partial\boldsymbol{B} \middle| \psi_i \right\rangle$. Intermolecular interactions were considered using the Weiss temperature, Θ_W, as a perturbation of the temperature scale for the calculation: $k_B T' = k_B(T - \Theta_W)$. Powder summations were performed using a 16-point Lebedev grid. For the bimetallic complexes, we adopted two subspins $\boldsymbol{S_1}$ and $\boldsymbol{S_2}$ (one per metal) with an exchange coupling constant J, as defined by

$$\widehat{H} = -2J\widehat{S}_1\widehat{S}_2 + \widehat{H}_{e,1} + \widehat{H}_{e,2}$$

Appendix 2

Experimental Section

General Considerations. Unless otherwise stated, manipulations were performed under a dinitrogen atmosphere inside a glovebox. Standard solvents were deoxygenated by sparging with N_2 and dried by passing them through activated alumina columns of an SG Water solvent purification system. Benzylpotassium (KBn) and K[Co(py_3tren)] were prepared according to literature methods.[15,16] Deuterated solvents were purchased from Cambridge Isotope Laboratories, degassed via freeze−pump−thaw cycles, dried over activated alumina, and stored over activated 4 Å molecular sieves. All reagents were purchased from Aldrich or Strem and used without further purification. Elemental analyses were performed by Complete Analysis Laboratories (Parsippany, NJ).

Synthesis of (py_3tren)CoCuCl (1-Cl). To a stirring solution of $CuCl_2$ (28.4 mg, 0.211 mmol) in 50 mL of THF at −78 °C was added a rt solution of K[Co(py_3tren)] (100 mg, 0.211 mmol) in 10 mL of THF. The reaction quickly turned into a dark purple suspension. This suspension was stirred vigorously at −78 °C for 5 min before filtering through a glass frit. The isolated purple solid was dried in vacuo, then stirred in 60 mL CH_2Cl_2 for 30 min. After filtering through Celite, the filtrate was dried in vacuo to yield a dark purple solid. Purple crystals (80 mg, 0.150 mmol) were obtained from layering Et_2O on a CH_2Cl_2 solution (70% crystalline yield). ^{1}H NMR (300 MHz, CD_2Cl_2, 294 K) δ 282 (6H), 29.3 (3H), 0.6 (3H), −38.4 (3H), −55.0 (3H), −58.7 (6H). UV-vis-NIR (CH_2Cl_2) λ_{max}/nm (ε/L mol^{-1} cm^{-1}): 324 (26900), 580 (890), 884 (1090), 2145 (270). Anal. Calcd for $C_{21}H_{24}N_7CoCuCl$: C, 47.38; H, 4.54; N, 18.42. Found C, 47.13; H, 4.51; N, 17.72. ICP-OES (wt %): 10.47(7) Co; 11.87(6) Cu; this relative ratio is consistent with $Co_{0.98}Cu_{1.02}$.

Synthesis of (py_3tren)CoCuOTf (1-OTf). A CH_3CN solution of CoCu(py_3tren) (100 mg, 0.186 mmol) in 15 mL was added to a stirring solution of AgOTf (47.8 mg, 0.186 mmol) in 15 mL CH_3CN at rt. The mixture quickly turned dark purple. After stirring 2 h, a metallic precipitate was observed, and the reaction was filtered through Celite. The filtrate was dried in vacuo to yield a dark purple powder (115 mg, 0.178 mmol, 95% yield). ^{1}H NMR (300 MHz, CD_3CN, 294 K) δ 280 (6H), 33.0 (3H), 9.5 (3H), −27.7 (3H), −47.5 (3H), −67.6 (6H). Calcd for $C_{22}H_{24}CoCuF_3N_7O_3S$: C, 40.90; H, 3.74; N, 15.18. Found C, 42.68; H, 3.90; N, 15.78.

Synthesis of (py_3tren)CoCu (2). To a stirring solution of K[Co(py_3tren)] (200 mg, 0.422 mmol) in 30 mL of THF at −78 °C was added a slurry of $[Cu(CH_3CN)_4]PF_6$ in 10 mL THF. After the reaction mixture was stirred at rt overnight, it was concentrated in vacuo to a 5 mL slurry, and then stirred for 30 min prior to filtering. The resulting solid residue was dissolved in 10 mL CH_2Cl_2 and filtered through a glass filter pipette. The filtrate was dried in vacuo, and then redissolved in 15 mL of CH_3CN at 60 °C. Slow evaporation of this solution to 5 mL yields green crystalline needles comprising CoCu(CH_3CN)(py_3tren) (or **2**-CH_3CN), as determined by X-ray crystallography. These crystals lose solvent under vacuum to yield the solvent-free complex, (py_3tren)CoCu (**2**) (138 mg, 0.278mmol, 65% yield). Single crystals of **2** suitable for X-ray diffraction were obtained by slow diffusion of hexane into a concentrated CH_2Cl_2 solution. ^{1}H NMR (300 MHz, THF-d_8, 294 K) δ 125 (6H), 99.5 (6H), 27.5 (3H), 21.2 (3H), 5.1 (3H), −33.4 (3H). UV-vis-NIR (CH_2Cl_2) λ_{max}/nm (ε/L mol^{-1} cm^{-1}): 263 (32700), 348 sh (10800), 400 sh (5130), 616 (75), 1304 (70). Anal. Calcd for $C_{21}H_{24}N_7CoCu$: C, 50.76; H, 4.87; N, 19.73. Found

C, 50.51; H, 4.84; N, 19.98. ICP-OES (wt %): 10.70(5) Co; 11.81(6) Cu; this relative ratio is consistent with $Co_{0.99}Cu_{1.01}$.

Anomalous X-ray Diffraction Data Collection and Refinement of the Structures and Metal Occupancies. A purple needle of **1**-Cl (0.10 x 0.02 x 0.02 mm), green needle of **2**-CH_3CN (0.10 × 0.04 × 0.04 mm), and block of **2** (0.10 × 0.10 × 0.10 mm), were mounted on a glass fiber and cooled to 100 K using an Oxford Instruments Cryojet cryostat. The Bruker D8 diffractometer, integrated with an APEX-II CCD detector, was modified for synchrotron use at the ChemMatCARS 15-ID-B beamline at the Advanced Photon Source (Argonne National Laboratory). For each crystal, diffraction data were collected at 30.0 keV (λ = 0.41328 Å). This is energetically far from any atomic absorption energies and gives a least-squares refinement of all model positional and displacement parameters to 0.5 Å resolution. For **1**-Cl, two additional sets of data at 25 eV below the K edge (keV[wavelengths (Å)]) of cobalt 7.684[1.614], and copper 8.954[1.385] with 0.3 s frames were collected while manually attenuating the beam to minimize overages of individual pixels.

The anomalous diffraction can distinguish Co/Cu compositions at the two metal sites because of the expected differences in the anomalous scattering factors (Δf′ and Δf″) for these elements. Basically, the Δf′ and Δf″ values of an element change dramatically near the element's absorption edge, while for the other element(s) they remain relatively constant. Each anomalous diffraction data set thus provides a different view of the electrons present at the two sites. Two sets ($\lambda > \lambda_{edge}$) were used to solve for the metal occupancies. These wavelengths were chosen for the following reasons. For $\lambda = \lambda_{edge}$, the data is less reliable because of inaccuracies in the metal K-edge energies, which shift for coordination compounds. For $\lambda < \lambda_{edge}$, the data were also less reliable because of potential problems with adsorption and/or fluorescence.[17] The two anomalous data sets were simultaneously used in a least-squares refinement to determine the Co/Cu occupancies at the two metal sites (M_1 and M_2). GSAS-II was employed because it allows multiple diffraction data sets as input with subsequent refinement using a common crystallographic model.[18]

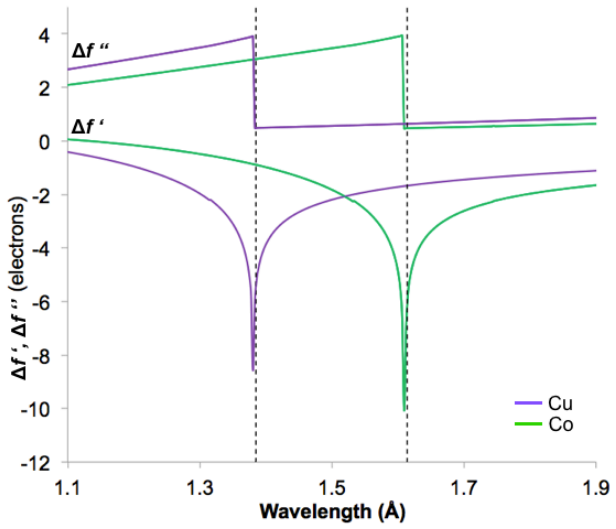

Figure A2.1. Theoretical anomalous dispersion corrections, including the real ($\Delta f'$) and imaginary ($\Delta f''$) scattering factors, for Co(green) and Cu (purple), as a function of wavelength (Å). The dotted lines represent the experimental wavelengths (λ) for the anomalous data

collections, which were selected to span the Co and Cu absorption edge energies. The datasets collected at $\lambda > \lambda_{edge}$ were used to determine the metal occupancies (bold, dotted lines).

Table A2.1. Crystallographic details for **1**-Cl, **2**-CH_3CN, and **2**.

	1-Cl	(**2**-CH_3CN)·$3CH_3CN$	**2**
chemical formula	$C_{21}H_{24}N_7CoCuCl$	$C_{23}H_{27}N_8CoCu$ ·$3CH_3CN$	$C_{21}H_{24}N_7CoCu$
formula weight	532.39	661.16	496.95
crystal system	$P2_1/n$	$P2_1/c$	$P6_1$
space group	monoclinic	monoclinic	hexagonal
a (Å)	14.6118(9)	10.9831(5)	18.891(1)
b (Å)	9.9196(6)	29.329(1)	18.891(1)
c (Å)	14.6848(9)	10.0176(3)	11.1884(9)
α (deg)	90	90	90
β (deg)	101.347(1)	109.533(1)	90
γ (deg)	90	90	120
V (Å^3)	2086.9(2)	3041.2(2)	3457.9(5)
Z	4	4	6
D_{calcd} (g cm^{-3})	1.695	1.440	1.432
λ (Å), μ (mm^{-1})	0.41328	0.41328	0.41328
T (K)	100	100	100
θ range (deg)	1.450 to 17.190	1.389 to 45.384	1.25 to 18.59
reflns collected	56001	13589	8788
unique reflns	6361	7735	6200
data/restraints/parameters	6361/0/280	7735/0/383	6200/0/271
R_1, wR_2 [$I > 2\sigma(I)$]	0.0290, 0.0680	0.0506, 0.1083	0.0552, 0.1014

Physical Measurements. NMR spectra were collected on Varian Inova 300 and 500 MHz spectrometers. UV−vis−NIR absorption data were collected on a Cary-14 spectrophotometer. Cyclic voltammetry was conducted using a CH Instruments 600 electrochemical analyzer. The one-cell setup utilized a glassy carbon working electrode, Ag wire counter electrode, and $Ag/AgNO_3$ reference electrode in CH_3CN. Analyte solutions were prepared in a 0.1M NBu_4PF_6/CH_3CN solution and referenced externally to the $FeCp_2/FeCp_2^+$ redox couple. ICP-OES data were collected at the University of Minnesota Earth Sciences Analytical Geochemistry Lab using a Thermo Scientific iCAP 6500 dual-view instrument with the addition of cesium as a matrix modifier and yttrium as an internal standard. The weight percents are averages of three measurements and are reported with standard deviations. Perpendicular-mode X-band EPR spectra were recorded on a Bruker EPP 300 spectrometer equipped with an Oxford ESR 910 liquid helium cryostat and an Oxford temperature controller.

Magnetic susceptibility data were measured from powder samples of solid material over the temperature range 2−300 K using a SQUID susceptometer with a variable field of 1.0, 4.0 and 7.0 T (MPMS-7, Quantum Design, calibrated with a standard palladium reference sample, error <2%). The experimental data were corrected for underlying diamagnetism using tabulated Pascal's constants ($\chi_{dia} < 0$)[19,20] as well as for temperature-independent paramagnetism ($\chi_{TIP} >$

0).[21] Specifically, χ_{TIP} (units of 10^{-6} emu) was 350 for **1**-Cl. The susceptibility and magnetization data were simulated with the program julX for exchange-coupled systems.[22] The simulations were based on the usual spin Hamiltonian operator for mononuclear complexes with spin S:

$$\hat{H}_e = g\beta \hat{\vec{S}} \cdot \vec{B} + D[\hat{S}_z^{\,2} - 1/3S(S+1) + E/D(\hat{S}_x^{\,2} - \hat{S}_y^{\,2})]$$

where *g* is the average electronic *g* value, and *D* and *E/D* are the axial zero-field splitting and rhombicity parameters. Magnetic moments are calculated after diagonalization of the Hamiltonian from the eigenfunctions using the Hellman-Feyman theorem $\vec{\mu}_i(\vec{B}) = \langle \psi_i | dH/d\vec{B} | \psi_i \rangle$. Intermolecular interactions were considered by using a Weiss temperature, Θ_W, as perturbation of the temperature scale, $kT' = k(T-\Theta_W)$ for the calculation. Powder summations were done by using a 16-point Lebedev grid.

Appendix 3

Experimental Section

General Procedures

All manipulations were performed under a dinitrogen atmosphere inside a glovebox. Standard solvents were deoxygenated by sparging with N_2 and dried by passing them through activated alumina columns of an SG Water solvent purification system. Bis(2-amino-phenyl)ether was prepared according to literature methods.[12] ^{13}Deuterated solvents were purchased from Cambridge Isotope Laboratories, degassed via freeze−pump− thaw cycles, dried over activated alumina, and stored over activated 4 Å molecular sieves. All reagents were purchased from Aldrich or Strem and used without further purification. Elemental analyses were performed by Complete Analysis Laboratories (Parsippany, NJ) and Robertson Microlit Laboratories (Ledgewood, NJ). ^{1}H NMR spectra were recorded on a Bruker 500 MHz, or a Varian 300 or 500 MHz spectrometer at rt unless otherwise stated. All ^{1}H and ^{13}C NMR spectra are referenced to the internal solvent residual. Variable temperature NMR experiments were performed on a Varian 300 MHz spectrometer. The temperature of the NMR probe was calibrated against an external methanol standard. UV−vis−NIR spectra were collected on a HP8453 (190−1000 nm) diode array spectrophotometer. Low temperature UV−vis−NIR experiments were performed using an Unisoku low temperature UV−vis cell holder. Cyclic voltammetry was conducted using a CH Instruments 600 electrochemical analyzer. The one−cell setup utilized a glassy carbon working electrode, Pt wire counter electrode, and $Ag/AgNO_3$ reference electrode in CH_3CN. Analyte solutions were prepared in a THF solution of 0.4 M $[^nBu_4N][PF_6]$ and referenced internally to the $FeCp_2^{0/+}$ redox couple. Perpendicular-mode X-band EPR spectra were recorded at 20 K with a Bruker ESP 300 spectrometer equipped with an Oxford ESR 910 liquid helium cryostat and an Oxford temperature controller. X-band EPR spectra were simulated by using EPR program (version W95) written by Professor Frank Neese (MPI−CEC, Mülheim, Germany). Magnetic susceptibility data were measured from powder samples of solid material over the temperature range 2-290 K using a SQUID susceptometer with a field of 1.0 T (MPMS-7, Quantum Design, calibrated with a standard palladium reference sample, error <2%). The experimental data were corrected for underlying diamagnetism using tabulated Pascal's constants ($\chi_{dia} < 0$) as well as for temperature –independent paramagnetism ($\chi_{TIP} > 0$). Specifically, the value of χ_{TIP} used for **3** was 180 x 10^{-6} emu.

Preparation of bis[2-(diispropylphosphino-methylamino)phenyl]ether, H_2PNONP (**1**)

A mixture of paraformaldehyde (0.512 g, 16.9 mmol), ^{i}Pr$_2$PH (2.00 g, 16.9 mmol) and 15 mL *n*-hexane was stirred at 55°C for 3 h. The solvent was removed in vacuo and to the resulting oil was added 15 mL THF and bis(2-amino-phenyl)ether (1.74 g, 8.67 mmol). This reaction mixture was stirred for 12 h at 65° C, and then the solvent was removed in vacuo. The crude product was dissolved in 20 mL pentane, filtered, and added to the top of a short silica plug. The plug was washed with 60 mL hexane, and the product eluted with 60 mL of a 9:1 hexane/THF mixture. Evaporation of the eluent in vacuo yielded a colorless oil (3.12 g, 6.77 mmol, 78% yield). ^{1}H NMR (500 MHz, C_6D_6) ∂ 7.03 (t, *J*=11 Hz, 2H), 6.84 (d, *J*=13 Hz, 2H), 6.77 (d, *J*=13 Hz, 2H), 6.57 (t, *J*=11 Hz, 2H), 4.45 (br, 2H, N*H*), 3.13 (d, *J*=8.5 Hz, 4H), 1.60 (septet of d, *J*=3 & 7 Hz, 4H), 1.00 (d, *J*=7 Hz, 6H), 0.97 (d, *J*=7 Hz, 6H), 0.96 (d, J=7, 6H), 0.94 (d, *J*=7 Hz, 6H); ^{31}P (282 MHz, C_6D_6) ∂ 2.4; ^{13}C NMR (125 MHz, C_6D_6) ∂ 143.5, 140.3, 124.4, 117.5, 116.7, 111.3, 37.8

(d, *J*=18 Hz), 22.6 (d, *J*=14 Hz), 20.1, 20.0, 18.9, 18.8. ESI-MS-TOF *m/z*: $[M + Na]^+$ calcd for $C_{26}H_{42}N_2OP_2Na$ 483.2665; found, 483.2718.

Preparation of [Cr(μ-Cl)(PNONP)]$_2$ (**2**)

To a frozen Et_2O solution of **1** (92.0 mg, 0.20 mmol), ^{n}BuLi (2.50*M* in hexanes, 0.160 mL, 0.40 mmol) was added dropwise. The stirring reaction was allowed to warm to rt immediately and was stirred for an additional 2 h. After removing the solvent in vacuo, the crude residue was dissolved in 10 mL THF and added to a stirring THF slurry of $CrCl_3(THF)_3$ (0.075 g, 0.200 mmol) at −50°C. Upon warming to rt and stirring overnight the solvent was removed in vacuo. The crude was washed with 10 ml pentane, dissolved in 15 mL benzene, and filtered through a pipette containing a plug of glass filter paper. The filtrate was reduced in vacuo to yield a salmon-colored solid (53.8 mg, 0.107 mmol, 55% yield). ^{1}H NMR (500 MHz, C_6D_6) ∂ 68, 20, 16.7, 1.9, −4.7, −8.4, −17.9, −26.6. UV−vis−NIR (THF) λ_{max}, nm (ε, M^{-1} cm^{-1}): 430 (1,100); 680 sh (150); 850 sh (80). Anal. Calcd for **2**, $C_{52}H_{80}N_4O_2P_4Cr_2Cl_2$: C 57.19, H 7.38, N 5.13. Found: C 56.07, H 7.09, N 4.89.

Preparation of [Cr(PNONP)]$_2$ (**3**)

To a frozen Et_2O solution of **1** (230 mg, 0.50 mmol), ^{n}BuLi (2.50*M* in hexanes, 0.400 mL) was added dropwise. The stirring reaction was allowed to warm to rt immediately and was stirred for an additional 2 h. After removing the solvent in vacuo, the crude residue was dissolved in 10 mL THF and added to a stirring THF slurry of $CrCl_2$ (61.5 mg, 0.500 mmol) at −50°C. Upon warming to rt and stirring overnight the solvent was removed in vacuo. The resulting solid was washed with 20 mL pentane, dissolved in 15 mL benzene, filtered and dried in vacuo to yield a bronze-colored crystalline solid (107 mg, 0.105 mmol, 62% yield). ^{1}H NMR (500 MHz, C_6D_6) ∂ 7.43 (d, *J*=8 Hz, 2H), 7.07 (t, *J*=8 Hz, 2H), 6.65 (d, *J*=8 Hz, 2H), 6.36 (t, *J*=8 Hz, 2H), 4.28 (s, 4H), 2.19 (septet, *J*=7 Hz), 1.05 (d, *J*=6 Hz, 12H), 0.77 (d, *J*=5 Hz, 12H). ^{31}P(282 MHz, C_6D_6) ∂ 19.8; ^{13}C NMR (125 MHz, C_6D_6) ∂ 151.6, 144.6, 124.2, 113.2, 111.5 109.6, 54.4, 26.4, 20.2, 20.0. UV−vis−NIR (THF) λ_{max}, nm (ε, M^{-1} cm^{-1}): 290 (37,000); 331 (41600); 428 sh (4590); 500 sh (1900); 619 (845); 762 sh (110). Anal. Calcd for **3**, $C_{52}H_{80}N_4O_2P_4Cr_2$: C 61.16, H 7.90, N 5.49. Found: C 61.02, H 8.01, N 5.46.

Structural determinations

Single crystals of **2** were grown from the diffusion of ether into a concentrated THF solution. Single crystals of **3** were grown from pentane layered on a concentrated THF solution. A red block of **2** (0.40 × 0.40 × 0.40 mm) and a brown block of **3** (0.20 × 0.20 × 0.20 mm) were placed on the tip of a glass capillary and mounted on a Bruker APEX II Platform CCD diffractometer for data collection at 173(2) K. The data collection was carried out using Mo Kα radiation (graphite monochromator). The data intensities were corrected for absorption and decay (SADABS).[14] Final cell constants were obtained from least-squares fits of all measured reflections. The structures were solved using SHELXS-97 and refined using SHELXL-97.[15,16] In each case, a direct-methods solution was calculated that provided most of the non-hydrogen atoms from the E-map. Full-matrix least-squares/ difference Fourier cycles were performed to locate the remaining non-hydrogen atoms. All of the non-hydrogen atoms were refined with anisotropic displacement parameters. Hydrogen atoms were placed in ideal positions and refined as riding atoms with relative isotropic displacement parameters. Crystallographic data are summarized in Table A3.1.

Table A3.1. Crystallographic data for **2** and **3**

	2	**3**
empirical formula	$C_{26}H_{40}ClCrN_2OP_2$	$C_{26}H_{40}CrN_2OP_2$
formula weight	545.99	510.54
temperature	173(2) K	173(2) K
wavelength	0.71073 Å	0.71073 Å
crystal system	trigonal	monoclinic
space group	R-3	C2/c
a (Å)	21.6460(14)	21.9632(13)
b (Å)	21.6460(14)	10.9312(7)
c (Å)	37.995(3)	22.4127(14)
α (°)	90	90
β (°)	90	109.9460(10)
γ (°)	120	90
V(Å^3)	15417(2)	5058.2(5)
Z	9	8
D_{calcd} (g cm^{-3})	1.059	1.341
θ range (°)	1.882 to 25.052	1.93 to 27.45
reflections collected	47661	28127
independent reflections	6084 [*R*(int) = 0.0228]	5762 [*R*(int) = 0.0224]
data / restraints / parameters	6084/ 25 / 317	5762 / 0 / 297
goodness-of-fit on F^2	1.132	1.046
R_1, wR_2 ($I > 2\sigma(I)$)	0.0499, 0.1543	0.0273, 0.0746

Appendix 4

General Considerations

Unless otherwise stated, all manipulations were performed inside a glovebox under an N_2 atmosphere or using standard Schlenk techniques. Standard solvents were deoxygenated by sparging with N_2 and dried by passing through activated alumina columns of a SG Water solvent purification system. Deuterated solvents were purchased from Cambridge Isotope Laboratories, Inc., degassed via freeze−pump−thaw cycles, and stored over activated 4 Å molecular sieves. The ligand N(*o*−($NHCH_2P\ Pr_2$)C_6H_4)$_3$ (abbreviated as H_3L), CrL (**1**), MnCrL (**3**), FeCrL (**4**), Tl[B(3,5-$(CF_3)_2C_6H_3)_4$], and [$FeCp_2$][B(3,5-$(CF_3)_2C_6H_3)_4$] were synthesized according to literature procedures. Elemental analyses were performed by Complete Analysis Laboratories, Inc. (Parsippany, NJ).

Synthesis of 2, $Cr_2(N(o-(NHCH_2P\ ^iPr_2)C_6H_4)_3)$.

A solution of **1** (0.115 g, 0.157 mmol) was dissolved in THF (c. 4 mL) and mixed with a stirred slurry of $CrCl_3$ (0.026 g, 0.16 mmol) in THF (c. 4 mL) for 15 min, forming a homogenous green solution. The solution was then added to KC_8 (0.064 g, 0.47mmol). Within minutes, the solution turned dark brown with precipitate. After removal of solvent *in vacuo*, the sample was dis- solved in toluene and filtered through a Celite plug. The brown solution was dried *in vacuo*, yielding a brown powder (0.093 g, 76%), which was used without further purification. Single crystals of **2** were grown by diffusion of *n*−pentane into a concentrated solution of **2** in THF. ^{1}H NMR (ppm, C_6D_6, 500 MHz): 34.1, 10.8, 9.1, 5.0, 4.1, 3.4, 1.3, 1.1, 1.0, −0.5, −2.4, −15.1. UV−vis−NIR (THF) λ_{max}, nm (ε, $M^{-1}\ cm^{-1}$): 495 (sh, 2330), 600 (1480), 880 (930), 1460 (140). Anal. Calcd for **2**, $C_{39}H_{60}N_4P_3Cr_2$: 59.91 C, 7.74 H, 7.17 N. Found: 59.79 C, 7.69 H, 7.09 N.

Synthesis of $K[2^{red}]$, $K[Cr_2(N(o-(NHCH_2P\ ^iPr_2)C_6H_4)_3)]$.

A solution of **1** (0.11 g, 0.15 mmol) was dissolved in THF (c. 4 mL) and mixed with a stirred slurry of $CrCl_3$ (0.024 g, 0.15 mmol) in THF (c. 4 mL) for 15 min, forming a homogenous green solution. The solution was then added to KC_8 (0.084 g, 0.62 mmol), forming a dark green solution with precipitate. The sample was filtered through a Celite plug and dried *in vacuo*, yielding a crude, green powder (0.12 g, 98%). Single crystals of $\mathbf{2^{red}}$ were grown by diffusion of *n*−pentane into a concentrated THF solution of $\mathbf{2^{red}}$. The ^{1}H NMR spectrum had extremely broad peaks at rt indicative of fluxional behavior. ^{1}H NMR (ppm, THF−d_8, 500 MHz, −80°C):

6.39 (t, J = 7 Hz, 1H), 6.15 (d, J = 7 Hz, 1H), 6.06(d, J = 7 Hz, 1H), 5.45 (t, J = 7 Hz, 1H), 5.28 (d, J = 12 Hz, 1H), 4.47 (d, J =12 Hz, 1H), 2.73 (br, 1H), 2.63 (br, 1H), 1.85 (br, 3H), 1.54 (br, 3H), 1.21 (br, 3H), 0.27 (br, 3H). ^{13}C NMR (ppm, THF−d8, 126MHz, −80 °C): 157.6, 136.5, 126.5, 124.9, 106.4, 106.1, 67 (overlapping with solvent), 34.1, 29.1, 23.5, 21.2, 21.0, 19.0. ^{31}P NMR (ppm, THF−d8, 200 MHz, −80 °C): 42.4. UV−vis−NIR (THF) λ_{max}, nm (ε, M^{-1} cm^{-1}): 315 (18300); 675 (1880). Anal. Calcd for K(**2**$^{\mathbf{red}}$), $C_{39}H_{60}N_4P_3Cr_2K$: 57.06 C, 7.37 H, 6.82 N. Found: 56.97 C, 7.28 H, 6.69 N.

Synthesis of K(crypt−222)[3$^{\mathbf{red}}$], [K(crypt−222)][MnCr(N(*o*−(NHCH$_2$P $^{\mathbf{i}}$Pr$_2$)C$_6$H$_4$)$_3$)]

A solution of **1** (0.12 g, 0.16 mmol) was dissolved in THF (c. 4 mL) and mixed with a stirred slurry of $MnBr_2$ (0.027 g, 0.17 mmol) in THF (c. 4 mL) for 15 min, forming a homogenous green solution. Solid KC8 (0.057 g, 0.51 mmol) was then added. Within minutes, the solution turned dark red−brown with precipitate. After removal of solvent *in vacuo*, the sample was washed with tolu- ene (c. 1 mL), reconstituted in THF (c. mL) and filtered through a Celite plug onto crypt−222 (0.049 g, 0.16 mmol) in THF (c. 2 mL). The solution was dried *in vacuo* and washed with Et_2O (c. 4 mL). (Alternative synthesis) To a solution of **3** (0.038 g, 0.048 mmol) dissolved in THF (c. 4 mL) was added solid KC_8 (0.0065 g, 0.048 mmol). Within minutes, the initial red−brown color of the solution turned yellow brown. After filtering through a glass filter, the filtrate was mixed with 2.2.2-cryptand (0.018g, 0.0477 mmol) and stirred for 10 min, the solvent was then removed *in vacuo* to yield 54 mg of **3**$^{\mathbf{red}}$ (0.045 mmol, 94% crude yield). Single crystals of **3** (18 mg, 11% crystalline yield) were grown by diffusion of *n*−pentane into a concentrated THF solution of **3**. ^{1}H NMR (ppm, THF−d8, 500 MHz): 26.1, 22.9, 9.6, 7.7, 6.3, 4.8, 3.7, 3.4, 2.5, 0.6, −0.1, −11.8. UV−vis−NIR (THF) λ_{max}, nm (ε, M^{-1} cm^{-1}): 745 (1230); 1350 (762). Anal. Calcd for K(crypt−222)[**3**$^{\mathbf{red}}$], $[K(C_{18}H_{36}N_2O_6)][C_{39}H_{60}N_4P_3CrMn]$: 57.03 C, 8.06 H, 7.00 N. Found: 57.06 C, 8.14 H, 6.97 N.

***Synthesis of* 4$^{\mathbf{ox}}$[B(Ar$_{\mathbf{F}}$)$_4$], [FeCr(N(*o*−(NHCH$_2$P $^{\mathbf{i}}$Pr$_2$)C$_6$H$_4$)$_3$)][B(3,5−(CF$_3$)$_2$C$_6$H$_3$)$_4$]**

A THF slurry (c. 6 mL) of KC_8 (22.2 mg, 0.164 mmol) was added to a stirring solution of **1** (120 mg, 0.164 mmol) in 12 ml THF at −78 °C. The mixture was warmed to rt, stirred for 5 min, and filtered. Solid $FeBr_2$ (20.8 mg, 0.164 mmol) was added to the stirring filtrate at −78 °C. The reaction mixture was warmed to rt and stirred until all $FeBr_2$ solid was reacted, ~20 min. The

reaction was filtered, and the solvent removed *in vacuo*. The crude residue was taken up in 4 mL of toluene, diluted with 10 mL pentane, cooled to −20 °C , and filtered to remove a brown solid. This was repeated two more times, and then the solution was cooled to −20 °C overnight, from which a green crystalline powder, presumably (Br)FeCr(N(o−($NCH_2P^iPr_2$)C_6H_4)$_3$) (33.2 mg, 23% yield), was iso- lated. These crystals were dissolved in 4 ml THF, and to this stirring solution was added dropwise Tl[$B(Ar_F)_4$] (40.9 mg, 0.038 mmol). in 4 mL Et_2O. After stirring 20 min at rt, a grey solid was filtered off and the filtrate was dried *in vacuo*, to yield 55 mg (0.033 mmol, 87% yield) of $\mathbf{4^{ox}}$[$B(Ar_F)_4$]. Single crystals of $\mathbf{4^{ox}}$ were grown by diffusion of *n*−pentane into a concentrated THF solu- tion of $\mathbf{4^{ox}}$. ^{1}H NMR (ppm, THF-d8, 500 MHz, −20 °C): 7.77 (s, 8H), 7.56 (s, 4H), 7.13 (t, *J* = 8 Hz, 3H),7.07 (d, *J* = 8 Hz, 3H), 6.59 (d, *J* = 8 Hz, 3H), 6.45 (t, *J* = 8 Hz, 3H), 6.32 (s, 6H), 3.11 (br, 3H), 2.82 (br, 3H), 1.48 (m, 9H), 1.40 (m, 9H), 1.31 (m, 9H), 0.65 (m, 9H). ^{13}C NMR (ppm, THF−d8, 126 MHz, −20 °C): (Note: quarternary carbons were not observed) 135.4 (aryl, $B(Ar_F)_4$), 128.6 (aryl); 126.6 (aryl), 120.9 (aryl), 118.1 (aryl, $B(Ar_F)_4$), 111 (aryl); 75.6 (C*H*2), 32.8 (C*H*), 28.0 (C*H*), 22.4 (C*H*3), 20.3 (C*H*3), 19.4 (C*H*3), 18.0 (C*H*3). ^{31}P NMR (ppm, THF-d8, 126 MHz, −20 °C): 26.2. UV−vis−NIR (THF) λ_{max}, nm (ε, M^{-1} cm^{-1}): 463 (4860), 730 (3890), 1495 (490), Anal. Calcd for $\mathbf{4^{ox}}$ [$B(Ar_F)_4$], [$C_{39}H_{60}N_4P_3FeCr$][$C_{32}H_{12}F_{24}B$]: 51.72 C, 4.40 H, #.40 N. Found: 51.67 C, 4.40 H, 3.26 N.

Physical Methods

^{1}H NMR spectra were recorded on a Bruker 500 MHz spectrometer at rt unless otherwise stated. All ^{1}H and ^{13}C NMR spectra are referenced to the internal solvent residual. Variable temperature NMR experiments were performed on a Bruker 500 MHz spec- trometer. The temperature of the NMR probe was calibrated against an external methanol standard. Diamagnetic anisotropy is calculated as

$$\Delta\sigma_i = \left(\frac{1}{3r^3}\right)\frac{(\Delta\chi)\left(1-3cos^2(\theta)\right)}{4\pi}$$

where $\Delta\sigma_i$ is the difference in chemical shift (in ppm) between the resonance in a bimetallic complex versus a reference complex, which is the isostructural Ni-Al complex featuring a Ni→Al dative bond. The distance of the proton to the center of the metal-metal bond is *r*, and the acute angle between the proton and the metal-metal axis is θ. The units are 10^{-36} m^3 $molecule^{-1}$. The barrier to inversion, $\Delta G^{\ddagger}$, is calculated

$$\Delta G^{\ddagger} = RT_c \left[23.760 + \ln\left(\frac{T_c}{k_c}\right)\right]$$

where the coalescence temperature T_C is in K, R is the ideal gas constant, and $k_c = [\pi(\Delta\upsilon_0)]/\sqrt{2}$ where $\Delta\upsilon_0$ is the difference in frequency (Hz) between the exchange protons. UV−vis−NIR spectra were collected at rt on a Cary−14 spectrometer. Cyclic voltammetry was conducted using a CH Instruments 600 electrochemical analyzer. The one−cell setup utilized a glassy carbon working electrode, Pt wire counter electrode, and $Ag/AgNO_3$ reference electrode in CH_3CN. Analyte solutions were prepared in a THF solution of 0.4 M $[^nBu_4N][PF_6]$ and referenced internally to the $FeCp2^{0/+}$ redox couple. IR spectra were collected using a Bruker Tensor−37 FTIR instrument with the OPUS 6.5 software. Perpendicular-mode X-band EPR spectra were recorded at 20 K with a Bruker ESP 300 spectrometer equipped with an Oxford ESR 910 liquid helium cryostat and an Oxford temperature controller, X-band EPR spectra were simulated by using EPR program (version W95) written by Frank Neese (MPI-CEC, Mülheim, Ger- many). Mössbauer data were recorded on an alternating constant acceleration spectrometer. The minimum experimental line width was 0.24 mm s^{-1} (full width at half-height). The sample temperature was maintained constant in an Oxford Instruments Variox or an Oxford Instruments Mössbauer-Spectromag 2000 cryostat, which is a split-pair superconducting magnet system for applied fields (up to 8 T). The field at the sample is oriented perpendicular to the γ-beam. The $^{57}Co/Rh$ source (1.8 GBq) was positioned at room temperature inside the gap of the magnet system at a zero-field position. Isomer shifts are quoted relative to iron metal at 300 K. Resonance Raman samples were prepared in a nitrogen-filled glovebox in dry THF and were immediately frozen in quartz tubes at -196 °C. Resonance Raman spectra were recorded on an Acton 506M3 spectrometer using a Princeton Instruments ACTON PyLoN LN/CCD-1340 x 400 detector. The spectra were obtained at -196 °C using backscattering geometry. Excitation at 647.1 nm was provided by a Spectra-Physics BeamLok 2060-KR-V Krypton ion laser. Excitation at 514.5 nm was provided by a Spectra Physics BeamLok 2065-7S Argon ion laser. Raman shifts were externally referenced to indene and internally referenced to solvent (THF).

X−Ray Crystallographic and Structure Refinement Details

Single crystals of **1** were grown by adding hexamethyldisiloxane to a concentrated solution of **1** in Et_2O and storing at −30 °C. Brown plates of **1**, **2**, K(crypt-222)[$\mathbf{3^{red}}$], and $\mathbf{4^{ox}}[B(Ar_F)_4]$, and a green plate of K[$\mathbf{2^{red}}$] were placed onto the tip of a 0.1 mm diameter glass capillary and mounted on a Bruker APEX II CCD diffractometer for data collection at 173(2) for **1**, **2**,

K[$\mathbf{2}^{\mathbf{red}}$], and K(crypt-222))[$\mathbf{3}^{\mathbf{red}}$], and 123(2) K for $\mathbf{4}^{\mathbf{ox}}$[$B(Ar_F)_4$]. The data collection was carried out using Mo Kα radiation (graphite monochromator). The data intensity was corrected for absorption and decay (SADABS). Final cell constants were obtained from least squares fits of all measured reflections. The structure was solved using SHELXS−97 and refined using SHELXL−97. A direct−methods solution was calculated which provided most non−hydrogen atoms from the E−map. Full−matrix least squares / difference Fourier cycles were performed to locate the remaining non−hydrogen atoms. All non−hydrogen atoms were refined with anisotropic displacement parameters. Hydrogen atoms were placed in ideal positions and refined as riding atoms with relative isotropic displacement parameters. Complex **2** solved in the space group P321 and contained channels along the crystallographic *c* axis; although substantial electron density was observed, no solvent molecules could be located. The SQUEEZE function of the PLATON program was used to remove solvent molecules within the void space. The SQUEEZE function removed 839 electrons from a void space volume of 396 $Å^3$. These values are consistent with the presence of approximately 21 THF molecules within the channel. Independent crystals of $\mathbf{4}^{\mathbf{ox}}$[$B(Ar_F)_4$] displayed substantial disorder at 173 and 123 K. At 123 K, the entire cationic component is disordered over two sites with a 57:43 occupancy. The anionic component exhibits rotational disorder of the CF_3 groups, which were treated as ideal rotors. One aryl ring of the counteranion appears to exhibit a rotational disorder, precluding anisotropic refinement of the respective CF_3 group. The presumed minor component of this disorder was not located during refinement. The data for $\mathbf{3}^{\mathbf{red}}$ was twinned, and the appropriate twin law was applied. Crystallographic data are summarized in Table A4.1.

Table A4.1. Crystallographic Details for Complexes of **1**, **2**, K[$\mathbf{2}^{\mathbf{red}}$], K(crypt-222)[$\mathbf{3}^{\mathbf{red}}$], and $\mathbf{4}^{\mathbf{ox}}$[BAr^F].

	1	**2**	K[$\mathbf{2}^{\mathbf{red}}$]·THF	K(crypt-222)[$\mathbf{3}^{\mathbf{red}}$]	$\mathbf{4}^{\mathbf{ox}}$[$B(Ar_F)_4$]
chemical formula	$C_{39}H_{60}CrN_4P_3$	$C_{39}H_{60}N_4P_3Cr_2$	$C_{39}H_{60}N_4Cr_2P_3K{\cdot}C_4H_8O$	$C_{39}H_{60}N_4P_3MnCr{\cdot}C_{18}H_{36}N_2O_6K$	$C_{39}H_{60}N_4P_3FeCr{\cdot}C_{32}H_{12}F_{24}B$
formula weight	729.82	781.82	893.02	1200.35	1648.90
crystal system	monoclinic	trigonal	monoclinic	trigonal	triclinic
space group	$P2_1/n$	$P321$	Cc	$P\bar{3}$	$P\bar{1}$
a (Å)	11.1248(7)	16.067(3)	12.9903(19)	11.3119(7)	10.5449(8)
b (Å)	20.166(1)	16.067(3)	27.035(4)	11.3119(7)	18.5182(14)
c (Å)	17.373(1)	11.673(2)	14.055(2)	28.5164(18)	20.4402(16)
α (deg)	90	90	90	90	71.0960(10)
β (deg)	92.293(1)	90	93.906(2)	90	78.6720(10)
γ (deg)	90	120	90	120	87.5320(10)
V (Å^3)	3894.4(4)	2609.7(9)	4924.6(12)	3160.1(4)	3701.7(5)
Z	4	2	4	2	2
D_{calcd} (g cm^{-3})	1.245	0.995	1.204	1.262	1.479
λ (Å), μ (mm^{-1})	0.71073, 0.449	0.71073, 0.805	0.71073, 0.853	0.71073, 0.564	0.71073, 0.512
T (K)	173(2)	173(2)	173(2)	173(2)	123(2)
θ range (deg)	2.20–27.42	2.260–24.640	2.1945–24.658	2.184–27.486	2.207–27.2555
reflns collected	33608	6896	25827	33862	43571
unique reflns	6647	2958	9412	4397	10885
data/restraint/parameters	8993/0/436	6896/0/145	11248/0/487	4850/0/226	16967/762/1030
R1, wR2 [$I > 2\sigma(I)$]	0.0418, 0.0993	0.0466, 0.0903	0.0422, 0.0873	0.0296, 0.0689	0.1116, 0.3043

Table A4.2. CASSCF orbital analysis of Cr_2L

Cr-Cr	Orbital type	%Cr_P	%Cr_N	total electrons	electron Cr_P	electron Cr_N
orbital 156	sigma	45.6	1.76	0.96	0.80	54.4
orbital 157	delta	49.6	1.39	0.70	0.69	50.4
orbital 158	pi	51.8	1.77	0.85	0.92	48.2
orbital 159	pi	52.0	1.77	0.85	0.92	48.0
orbital 160	3d Cr (P)	0.0	0.98	0.98	0.00	100.0
orbital 161	pi*	48.4	0.22	0.11	0.11	51.6
orbital 162	delta*	55.6	0.60	0.26	0.33	44.4
orbital 163	4d delta*	6.4	0.02	0.02	0.00	93.6
orbital 164	sigma*	53.2	0.23	0.11	0.12	46.8
orbital 165	pi*	49.6	0.21	0.11	0.11	50.4
orbital 166	correlating	13.3	0.01	0.01	0.00	86.7
orbital 167	correlating	32.3	0.01	0.01	0.00	67.7
orbital 168	correlating	88.8	0.00	0.00	0.00	11.2
orbital 169	correlating	4.3	0.02	0.02	0.00	95.7
orbital 170	correlating	31.8	0.01	0.01	0.00	68.2
orbital 171	correlating	45.9	0.01	0.00	0.00	54.1
orbital 172	correlating	40.2	0.00	0.00	0.00	59.8
orbital 173	correlating	39.5	0.00	0.00	0.00	60.5
orbital 174	correlating	31.1	0.00	0.00	0.00	68.9
orbital 175	correlating	29.9	0.00	0.00	0.00	70.1
			totals=	9.00	4.99	4.01

Table A4.3. CASSCF orbital analysis of $[Cr_2L]^-$

CrCr(-)	Orbital type	$\%Cr_P$	$\%Cr_N$	total electrons	electron Cr_P	electron Cr_N
orbital 156	pi	52.1	47.9	1.84	0.96	0.88
orbital 157	pi	52.2	47.8	1.84	0.96	0.88
orbital 158	sigma*	54.6	45.4	1.80	0.98	0.82
orbital 159	delta	61.3	38.7	1.74	1.07	0.68
orbital 160	delta	61.0	39.0	1.74	1.06	0.68
orbital 161	delta*	38.0	62.0	0.23	0.09	0.15
orbital 162	delta*	38.0	62.0	0.24	0.09	0.15
orbital 163	sigma*	46.0	54.0	0.18	0.08	0.10
orbital 164	pi*	48.9	51.1	0.15	0.07	0.08
orbital 165	pi*	49.0	51.0	0.15	0.07	0.08
orbital 166	correlating	68.6	31.4	0.01	0.01	0.00
orbital 167	correlating	68.6	31.4	0.01	0.01	0.00
orbital 168	correlating	84.3	15.7	0.03	0.02	0.00
orbital 169	correlating	88.9	11.1	0.03	0.02	0.00
orbital 170	correlating	84.7	15.3	0.01	0.01	0.00
orbital 171	correlating	54.4	45.6	0.00	0.00	0.00
orbital 172	correlating	53.1	46.9	0.00	0.00	0.00
orbital 173	correlating	54.4	45.6	0.00	0.00	0.00
orbital 174	correlating	53.8	46.2	0.00	0.00	0.00
orbital 175	correlating	52.7	47.3	0.00	0.00	0.00
			totals=	10.00	5.51	4.49

Table A4.4. CASSCF orbital analysis of $[FeCrL]^+$

FeCr+	orbital type	%Fe	%Cr	total electron	electron-Fe	electron-Cr
orbital 156	pi	56.3	43.7	1.69	0.95	0.74
orbital 157	pi	54.4	45.6	1.70	0.92	0.77
orbital 158	delta	87.8	12.2	1.85	1.62	0.22
orbital 159	pi*	45.3	54.7	0.29	0.13	0.16
orbital 160	sigma	67.2	32.8	1.80	1.21	0.59
orbital 161	delta*	27.9	72.1	0.14	0.04	0.10
orbital 162	delta*	27.3	72.7	0.13	0.04	0.10
orbital 163	sigma*	38.4	61.6	0.20	0.07	0.12
orbital 164	delta	87.0	13.0	1.84	1.60	0.24
orbital 165	pi*	44.9	55.1	0.30	0.13	0.16
orbital 166	correlating	88.8	11.2	0.00	0.00	0.00
orbital 167	correlating	100.0	0.0	0.00	0.00	0.00
orbital 168	correlating	83.0	17.0	0.02	0.01	0.00
orbital 169	correlating	88.0	12.0	0.02	0.01	0.00
orbital 170	correlating	100.0	0.0	0.00	0.00	0.00
orbital 171	correlating	96.4	3.6	0.00	0.00	0.00
orbital 172	correlating	100.0	0.0	0.00	0.00	0.00
orbital 173	correlating	80.3	19.7	0.01	0.01	0.00
orbital 174	correlating	78.4	21.6	0.01	0.01	0.00
orbital 175	correlating	61.1	38.9	0.01	0.00	0.00
			totals=	10.00	6.78	3.22

Table A4.5. CASSCF orbital analysis of $[FeCrL]^-$

FeCr (-)	orbital type	%Fe	%Cr	total electron	electron-Fe	electron-Cr
orbital 156	3d Cr	4.8	95.2	1.00	0.05	0.95
orbital 157	sigma	63.6	36.4	1.75	1.11	0.64
orbital 158	pi	72.6	27.4	1.79	1.30	0.49
orbital 159	3d Cr	3.4	96.6	1.00	0.03	0.97
orbital 160	pi	73.1	26.9	1.79	1.31	0.48
orbital 161	pi*	46.7	53.3	0.19	0.09	0.10
orbital 162	pi*	45.5	54.5	0.19	0.09	0.10
orbital 163	sigma*	42.8	57.2	0.24	0.10	0.14
orbital 164	3d Fe	100.0	0.0	1.93	1.93	0.00
orbital 165	3d Fe	100.0	0.0	1.93	1.93	0.00
orbital 166	correlating	93.1	6.9	0.00	0.00	0.00
orbital 167	correlating	42.6	57.4	0.00	0.00	0.00
orbital 168	correlating	12.8	87.2	0.00	0.00	0.00
orbital 169	correlating	13.0	87.0	0.00	0.00	0.00
orbital 170	correlating	66.1	33.9	0.01	0.01	0.00
orbital 171	correlating	90.4	9.6	0.06	0.05	0.01
orbital 172	correlating	87.2	12.8	0.06	0.05	0.01
orbital 173	correlating	92.4	7.6	0.00	0.00	0.00
orbital 174	correlating	65.2	34.8	0.02	0.01	0.01
orbital 175	correlating	64.2	35.8	0.02	0.01	0.01
			totals=	12.00	8.09	3.91

Table A4.6. CASSCF orbital analysis of $[MnCrL]^-$

CrMn (-)	orbital type	%Mn	%Cr	total electron	electron-Mn	electron-Cr
orbital 156	pi	52.7	47.3	1.78	0.94	0.84
orbital 157	pi	47.2	52.8	1.80	0.85	0.95
orbital 158	delta	85.6	14.4	1.88	1.61	0.27
orbital 159	delta	97.5	2.5	1.92	1.88	0.05
orbital 160	sigma	55.7	44.3	1.79	1.00	0.79
orbital 161	sigma*	44.8	55.2	0.20	0.09	0.11
orbital 162	delta*	3.6	96.4	1.00	0.04	0.97
orbital 163	delta*	70.3	29.7	0.10	0.07	0.03
orbital 164	pi*	50.1	49.9	0.21	0.11	0.11
orbital 165	pi*	50.0	50.0	0.19	0.10	0.10
orbital 166	correlating	27.3	72.7	0.03	0.01	0.02
orbital 167	correlating	100.0	0.0	0.06	0.06	0.00
orbital 168	correlating	59.9	40.1	0.01	0.00	0.00
orbital 169	correlating	66.6	33.4	0.01	0.01	0.00
orbital 170	correlating	70.0	30.0	0.01	0.01	0.00
orbital 171	correlating	79.1	20.9	0.00	0.00	0.00
orbital 172	correlating	0.0	0.0	0.01	0.00	0.00
orbital 173	correlating	0.0	0.0	0.00	0.00	0.00
orbital 174	correlating	0.0	0.0	0.00	0.00	0.00
orbital 175	correlating	0.0	0.0	0.00	0.00	0.00
			totals=	11.00	6.75	4.24

Table A4.7. CASSCF orbital analysis of [MnCrL]

CrMn	orbital type	%Mn	%Cr	total electron	electron-Mn	electron-Cr
orbital 156	sigma	59.8	40.2	1.79	1.07	0.72
orbital 157	pi	61.7	38.3	1.80	1.11	0.69
orbital 158	pi	62.0	38.0	1.80	1.12	0.69
orbital 159	delta	66.7	33.3	1.71	1.14	0.57
orbital 160	delta	66.7	33.3	1.71	1.14	0.57
orbital 161	delta*	35.7	64.3	0.27	0.10	0.18
orbital 162	delta*	35.5	64.5	0.27	0.10	0.18
orbital 163	pi*	41.3	58.7	0.18	0.08	0.11
orbital 164	pi*	40.9	59.1	0.18	0.08	0.11
orbital 165	sigma*	42.1	57.9	0.20	0.08	0.11
orbital 166	correlating	87.0	13.0	0.02	0.02	0.00
orbital 167	correlating	72.0	28.0	0.01	0.01	0.00
orbital 168	correlating	87.0	13.0	0.02	0.02	0.00
orbital 169	correlating	72.0	28.0	0.01	0.01	0.00
orbital 170	correlating	64.2	35.8	0.01	0.00	0.00
orbital 171	correlating	65.2	34.8	0.00	0.00	0.00
orbital 172	correlating	91.4	8.6	0.00	0.00	0.00
orbital 173	correlating	93.3	6.7	0.00	0.00	0.00
orbital 174	correlating	92.2	7.8	0.00	0.00	0.00
orbital 175	correlating	91.0	9.0	0.00	0.00	0.00
			totals=	10.00	6.07	3.93

Appendix 5

Experimental Section

General Considerations

Unless otherwise stated, all manipulations were performed under an inert atmosphere in a glovebox or using standard Schlenk techniques. Standard solvents were deoxygenated by sparging with inert gas and dried by passing through activated alumina columns of a SG Water solvent purification system. Deuterated solvents were purchased from Cambridge Isotope Laboratories, Inc. or Sigma Aldrich, degassed via freeze-pump-thaw cycles, and stored over activated 4 Å molecular sieves. Elemental analyses were performed by Complete Analysis Laboratories,Inc. (Parsippany, NJ) or Robertson Microlit Laboraties, Inc. (Ledgewood, NJ). ^{1}H NMR spectra were recorded on Varian 300 MHz or a Bruker 500 MHz spectrometer at ambient temperature unless otherwise stated. Solution magnetic moments were determined using Evans' method. Cyclic voltammetry was performed using a CH instruments 600 electrochemical analyzer. The one-cell setup used a glassy carbon working electrode, Pt wire counter electrode, and $Ag/AgNO_3$ reference electrode in CH_3CN. Analyte solutions consisted of 0.4 M $[^nBu_4N]PF_6$ and the voltammograms were referenced internally to the $FeCp_2^{0/+}$ (abbreviated as Fc^+/Fc) redox couple. The ligand $N(o\text{-}(NHCH_2P^iPr_2)C_6H_4)_3$ (abbreviated as H_3L) was synthesized according to literature procedures.

Synthesis of $Ti(N(o\text{-}(NCH_2P^iPr_2)C_6H_4)_3)$

A solution of neutral ligand $(N(o\text{-}(NHCH_2P^iPr_2)C_6H_4)_3$ (0.308 g, 0.453 mmol) in Et_2O (5 mL) was frozen in a LN_2 coldwell. The solid was layered with nBuLi (0.560 mL, 1.40 mmol), and the mixture was allowed to thaw overnight. The volatiles of the resulting yellow solution were removed in vacuo. The resulting yellow oil was taken up in THF (5 mL) and frozen in a LN_2 cold well along with a solution of $TiCl_3(THF)_3$ (0.168 g, 0.454 mmol) in THF (5 mL). The thawing yellow solution of deprotonated ligand was layered on top of the frozen solution of $TiCl_3(THF)_3$, and allowed to warm to rt. The solution was allowed to stir for 3 h to yield a brown solution. The reaction was dried in vacuo, and reconstituted in benzene. The benzene solution was filtered through a Celite pad and dried in vacuo, resulting in a brown powder (0.320 g, 97% yield). ^{1}H NMR (ppm, C_6D_6, 500 mHz): 8.5, 6.2, 5.0, 1.9, 1.0, −2.7. Anal. Calcd. for TiL, $C_{39}H_{60}N_4P_3Ti$: 64.55 C, 8.33 H, 7.72 N. Found: 64.09 C, 8.12 H, 7.44 N.

Synthesis of 1 $CoTi(N(o\text{-}(NCH_2P^iPr_2)C_6H_4)_3)$

A solution of TiL (0.174 g, 0.238 mmol) in THF (4 mL) was added to a slurry of $CoBr_2$ (0.0522 g, 0.237 mmol) in THF (2 mL) while stirring. After 15 min, a homogeneous, dark green brown solution formed, and the solution was added to KC_8 (0.0658 g, 0.487 mmol). The green color disappeared within minutes, and the reaction was stirred for an additional 4 hours. The reaction solution was filtered through a Celite pad, and the

volatiles were removed in vacuo. The brown powder was reconstituted in benzene and filtered through a Celite pad to remove salts. The resulting brown solution was dried in vacuo to give a brown powder (0.175 g, 93% yield). Single crystals were grown through the slow dissipation of pentane into a concentrated toluene solution. ^{1}H NMR (ppm, THF-d8, 500 MHz): 6.80 (t, J = 7.7 Hz, 3H), 6.71 (d, J = 7.7 Hz, 3H), 6.16 (d, J = 7.7 Hz, 3H), 6.12 (t, J = 7.2 Hz, 3H), 5.28 (d, J = 11.5 Hz, 3H), 4.53 (d, J = 11.4, 3H), 2.96 (s, 3H), 2.77 (s, 3H), 1.60 (s, 9H), 1.46 (s, 9H), 1.34 (s, 9H), 0.53 (s, 9H). 31P NMR (ppm, THF-d_8, 200 MHz): 17.1. 13C NMR (ppm, THF-d_8, 126 MHz): 156.2, 138.2, 128.4, 126.9, 114.4, 108.0, 68.9, 33.35, 28.53, 23.16, 20.26, 19.53, 17.84. Anal. Calcd. for 1 $C_{39}H_{60}N_4P_3TiCo$: 59.70 C, 7.71 H, 7.14 N. Found: 59.82 C, 8.04 H, 6.74 N.

Synthesis of 2 K(crypt-222)[(N_2)CoVL], K($C_{18}H_{36}N_2O_6$)[(N_2)CoV(N(o-($NCH_2P^iPr_2$)C_6H_4)$_3$)]

A solution of 2 (0.0817 g, 0.104 mmol) in THF (8 mL) was added to a vial containing KC_8 (0.0293 g, 0.217 mmol). A solution of crypt-222 (0.402 g, 0.107 mmol) in THF (4 mL) was added to the stirring reaction mixture, and was allowed to stir for 16 h. The resulting brown solution was filtered through a celite plug to remove graphite and the volatiles were removed in vacuo. The resulting brown powder was washed with 5 x 5 mL portions of benzene and then dried to obtain a brown powder (0.113 g, 89 % yield). Single crystals were grown through the layering of a THF solution with hexane. 1H NMR (ppm, THF-d_8, 500 MHz): 27.1, 12.3, 8.7, 5.5, 3.4, 2.4, 1.3, 0.9, -27.5. Evans' Method (THF-d_8): μeff = 2.68 B.M. IR (νN−N, cm–1, KBr pellet): 1971. Anal. Calcd. for 2 $C_{57}H_{96}CoVKN_8O_6P_3$: 55.60 C, 7.86 H, 9.1 N. Found: 55.99 C, 8.51 H, 7.41 N and 55.67 C, 7.88 H, 7.64 N for two independent samples.

Synthesis of 3 K(crypt-222)[(N_2)CoCrL], K($C_{18}H_{36}N_2O_6$)[(N_2)CoCr(N(o-($NCH_2P^iPr_2$)C_6H_4)$_3$)]

THF (6 mL) was added to 3 (0.104 g, 0.132 mmol), and the solution was transferred to a slurry of KC_8 (0.019 g, 0.138 mmol). The mixture was allowed to stir for 4 hours, and the remaining graphite was filtered off through a celite plug. The remaining red-brown solution was dried in vacuo. The solid was taken up in THF (2 mL) and added to a stirring solution of crypt-222 in THF (6 mL) and allowed to stir for one hour. The solution was dried in vacuo to give a dark powder (0.140 g, 88 % yield). Single crystals were grown via the slow diffusion of pentane into a concentrated THF solution. 1H NMR (ppm, THF-d_8, 300 MHz): 15.8, 8.3, 6.5, −21.3. Evans' Method (THF-d_8): μeff = 3.58 B.M. IR (νN−N, cm–1, KBr pellet): 1991. Anal. Calcd. for 3 $C_{57}H_{96}CoCrKN_8O_6P_3$: 55.55 C, 7.85 H, 9.09 N. Found: 56.86 C, 8.11 H, 6.89 N, which is consistent with K(crypt-222)[CoCrL], $C_{57}H_{96}CoCrKN_6O_6P_3$: 56.84 C, 8.03 H, 6.98 N.

X-ray crystallography and structure refinement details

A brown block of 1, a brown needle of 2, and a brown needle of 3 were placed on the tip of a 0.1 mm diameter glass capillary and mounted on a Bruker APEX II CCD diffractometer or a Bruker Photon 100 CMOS diffractometer for data collection at 173(2) K or 123(2) K. The data collection was carried out using Mo Kα radiation (graphite monochromator) or Cu Kα radiation (normal parabolic mirrors). The data intensity was corrected for absorption and decay (SADABS). Final cell constants were obtained from least-squares fits of all measured reflections and the structure was solved using SHELXS-08 and refined using SHELXL-08. A direct-methods solution was calculated which provided most non-hydrogen atoms from the E-map. Full-matrix least-squares/difference Fourier cycles were performed to locate the remaining non-hydrogen atoms and all non-hydrogen atoms were refined with anisotropic displacement parameters with the exception of a disordered THF molecule in 2 is refined isotropically. Hydrogen atoms were placed in ideal positions and refined as riding atoms with relative isotropic displacement parameters. Complex 3 was refined as an inversion twin with the main component contributing 54 %. A disordered isopropyl group in 3 was modeled using SHELXTL EADP constraints, and the geometrical restraints SAME and SADI. Electron density attributed to two disordered molecules of pentane in the asymmetric unit was removed using Platon SQUEEZE. Crystallographic details are summarized in Table A5.1.

Table A5.1. Crystallographic Details for compounds **1**−**3**.

	1	**2**	**3**
chemical formula	$C_{39}H_{60}N_4P_3TiCo$	$C_{39}H_{60}N_6P_3VCo \cdot KC_{18}H_{36}N_2O_6 \cdot C_4H_8O$	$2(C_{39}H_{60}N_6P_3CrCo) \cdot 2(KC_{18}H_{36}N_2O_6)$
fw	784.65	1303.4	2464.7
cryst syst	monoclinic	orthorhombic	monoclinic
space group	$P2_1/n$	$Pna2_1$	$P2_1$
a (Å)	13.5781(18)	63.552(2)	11.2453(3)
b (Å)	13.9450(18)	11.0817(4)	31.9918(7)
c (Å)	20.821(3)	18.9917(7)	18.9780(4)
α (deg)	90	90	90
β (deg)	94.250(2)	90	95.0420(10)
γ (deg)	90	90	90
V (Å^3)	3931.5(9)	13375.2(8)	6801.1(3)
Z	4	8	2
D_{calcd} (g cm^{-3})	1.326	1.295	1.204
λ (Å), μ (mm^{-1})	0.71073, 0.780	1.54178, 4.785	1.54178, 4.831
T (K)	173(2)	123(2)	173(2)
θ range (deg)	1.73−27.50	2.71−74.71	2.337−74.662
reflns collected	9018	25425	27151
unique reflns	5711	22340	23744
data/restraint/params	9018/0/445	25425/1/1476	27151/8/1428
R1, wR2 ($I > 2\sigma(I)$)	0.0527, 0.1170	0.0440, 0.1054	0.0470, 0.1130

Appendix 6

Materials and Methods

General Considerations and Instrumentation. All air- and moisture-sensitive compounds were manipulated in a glovebox under a nitrogen atmosphere. Solvents for air- and moisture-sensitive reactions were vacuum transferred from sodium benzophenone ketyl (THF, Et_2O, pentane, d_6-benzene and d_8-toluene) or predried by passing through activated alumina columns of a SG Water solvent purification system. $Ni(COD)_2$, $ZrCl_4(THF)_2$ and $HfCl_4(THF)_2$ were prepared according to literature procedure. Cyclic volammetry was conducted using Pine Instruments WaveNow. Analyte solutions were prepared in a THF solution of tetra-n-butylammonium hexafluorophosphate (0.1 M) and referenced to the $FeCp_2/FeCp_2^+$ redox couple. ^{1}H, ^{13}C and ^{31}P spectra were recorded on Varian INOVA 500 MHz or Bruker Avance III 400 MHz spectrometers. Chemical shifts are reported with respect to residual protio-solvent impurity for ^{1}H (*s*, 7.16 ppm for C_6D_5H), solvent carbons for ^{13}C (*t*, 128.39 ppm for C_6D_6), and PPh_3 for ^{31}P (*s*, -6 ppm for C_6D_6).

X-ray Crystal Data: General Procedure. Crystals were removed quickly from a scintillation vial to a microscope slide coated with oil. Samples were selected and mounted on the tip of a 0.1 mm diameter glass capillary. Data collection was carried out on a Bruker APEX II CCD diffractometer with a 0.71073 Å Mo Kα source or on a Bruker-AXS D8 Venture diffractometer with a 1.54178 Å Cu Kα source. The structures were solved by direct methods. All non-hydrogen atoms were refined anisotropically. Details regarding refined data and cell parameters are available in Tables A6.1 and A6.2.

Synthesis of $Hf(2\text{-}PPh_2)C_4H_3N)_4$, $Hf(NP)_4$ (3). Solid Li(NP) (325 mg, 1.26 mmol, 4.5 equiv) was dissolved in 5 mL Et_2O and cooled in a glovebox cold well. Solid $HfCl_4(THF)_2$ (130.37 mg, 0.28 mmol, 1 equiv) was added to the solution and warmed to room temperature while stirring, resulting in a colorless solution with significant white precipitate. Solvent was removed *in vacuo* and the remaining solid redissolved in benzene. Following filtration over celite and removal of solvent, 245 mg of **3** was obtained as a white powder in 74 % yield. X-ray quality crystals were obtained by slow diffusion of pentane into a concentrated benzene solution of **3**. Complexes **1** and **2** were prepared in similar fashion and NMR spectra matched reported values [45]. ^{1}H NMR (400MHz, C_6D_6) δ, ppm: 6.2–6.6 (*br*, 10H). 6.7–6.82 (*br*, 17H), 6.96–7.03 (*br*, 14H), 7.15–7.25 (*br*, 5H), 7.35 (*br*, 1H), 7.55 (br 1H). ^{13}C NMR (125 MHz, C_6D_6) δ, ppm: 114.0-114.4 (*br*), 117.4-117.6 (*s*), 126.6 (*d*, *br*), 129.1 (*d*), 129.1-129.3 (*br*), 133.2-134.2 (*br*), 135.1 (*d*, *br*), 135.65 (*d*, *br*). ^{31}P NMR (121 MHz, C_6D_6) δ, ppm: -30 to -40 (*br*).

Synthesis of (κ^2-NP)Ti(μ_2-NP)$_3$Ni (4). Solid **1** (250 mg, 0.24 mmol, 1 equiv) and Ni(COD)$_2$ (65.6 mg, 24 mmol, 1 equiv) were added to a 20 mL scintillation vial, dissolved in 5 mL of benzene and stirred overnight. The solution turned from dark red to a dark yellow/orange. Filtration through celite and removal of solvent yielded 198 mg of **4** as a dark powder in 75% yield. X-Ray quality crystals were grown from a concentrated benzene solution over the course of days. ^{1}H NMR (400MHz, C_6D_6) δ, ppm: 6.1–6.3 (*br*, 2H). 6.40–7.0 (*br*, 47H), 7.55–7.70 (*br*, 3H), 7.86–7.92 (*br*, 1H), 8.13–8.2 (*br*, 1H). ^{13}C NMR (125 MHz, C_6D_6) δ, ppm: 110.5 (*br*), 111.85 (*d*), 116.5 (*s*), 117.9 (*s*), 118.90 (*s*), 127.85 (*d*), 130.3 (*s*), 131.9 (*br*), 132.2 (*br*) 132.4 (*br*), 133.2 (*br*), 134.0 (*br*), 134.5 (*br*) 135-136.5 (*br*), 137.1 (*s*). ^{31}P NMR (121 MHz, C_6D_6) δ, ppm: 4-0 (*br*, 3P), -19.2 (*s*, 1P).

Synthesis of (κ^2-NP)Zr(μ_2-NP)$_3$Ni (5). Solid **2** (222 mg, 0.20 mmol, 1 equiv) and Ni(COD)$_2$ (523 mg, 0.2 mmol, 10 equiv) were added to a 20 mL scintillation vial and dissolved in toluene, heated to 90 °C and stirred overnight. Filtration through celite and removal of volatiles yielded 145 mg of **5** as a dark red powder in 62% yield. Single crystals were grown from vapor diffusion of pentane into a concentrated benzene solution of **5** over the course of days. ^{1}H NMR (400MHz, C_6D_6) δ, ppm: 6.15–6.4 (*br*, 4H), 6.55–6.6 (*s*, 3H), 6.65–7.15 (*br*, 42H), 7.98–8.02 (*m*, 1H). ^{13}C NMR (125 MHz C_6D_6) δ, ppm: 113 (*s*), 113.45 (*d*), 118.5 (*d*), 119.38(*s*), 128.4 (*d*), 128.88 (*d*), 129.17 (*d*), 129.3 (*br*), 133.0 (*br*), 133.15 (*d*), 134.05 (*d*), 134.6 (*d*), 135.15(*br*). ^{31}P NMR (121 MHz, C_6D_6) δ, ppm: -7 to -13 (*br*, 3P), -29.6 (*s*, 1P).

Synthesis of (κ^2-NP)Hf(μ_2-NP)$_3$Ni (6). Solid **3** (109 mg, 0.0925 mmol, 1 equiv) and Ni(COD)$_2$ (119 mg, 0.463 mmol, 5 equiv) were added to a 20 mL scintillation vial and dissolved in benzene. The reaction mixture was heated to 90 °C and stirred overnight, resulting in a dark red solution. Following filtration, volatiles were removed *in vacuo*, yielding 76 mg of crude **6** in 66% yield. Red crystals of **6** were obtained by slow evaporation of pentane into a concentrated benzene solution of **6**. ^{1}H NMR (400MHz, C_6D_6) δ, ppm: 6.0–6.45 (*br*, 3H), 6.6–7.15 (*br*, 41H), 8.1–8.13 (*br*, 1H). ^{13}C NMR (125 MHz, C_6D_6) δ, ppm: 113.38 (*br*), 113.8 (*d*), 118.75 (*d*), 119.5 (*br*), 125.9 (*s*), 126.3 (*s*), 127.86 (*d*), 128.85 (*s*), 128.87 (*s*), 133.2 (*d*), 133.78 (*s*), 133.87 (*s*), 135.3 (*s*). ^{31}P NMR (121 MHz, C_6D_6) δ, ppm: -8 to -10 (*br*, 2P), -17 to -19 (*br*, 1P), -26.6 (*s*, 1P).

Synthesis of [(κ^2-NP)Ti(μ_2-NP)$_3$Ni]$^-$[Na]$^+$ (7). Solid **4** (330 mg, 0.3 mmol, 1 equiv) and 1% Na(Hg) (35 mg, 1.5 mmol, 5 equiv) were added to a 20 mL scintillation vial and dissolved in 3 mL benzene and stirred overnight. The solution turned from dark yellow to a dark orange. Following filtration through celite and removal of solvent yielded 220 mg of **7** as a powder in 65% yield. X-ray quality crystals were grown from a concentrated benzene solution of **7** over the course of days.

Synthesis of (κ^2-NP)Ti(μ_2-NP)$_3$Ni(CO) (8). Solid **4** (1 eq, 40 mg, 0.036 mmol) was dissolved in 0.7 mL of benzene and added to a J Young NMR tube. The J Young tube was attached to a Schlenk line and freeze-pump-thaw degassed three times, followed by addition of approximately 1 atm of CO. ^{31}P NMR confirmed quantitative conversion of the starting material. Single crystals of **4** were grown from a concentrated benzene solution layered with pentane over the course of days. Prolonged exposure of **8** to vacuum results in regeneration of **4**. ^{1}H NMR (300MHz, C_6D_6) δ, ppm: 5.95 (*s*, 2H), 6.25 (*s*, 3H), 6.37 (*t*, 1H), 6.65 (*t*, 3H), 6.8-7.05 (*br*, 28H), 7.12 (*s*, 2 H), 7.33 (*s*, 10H), 7.62 (*s*, 1H). ^{13}C NMR (125 MHz, C_6D_6) δ, ppm: 109.5 (*s*), 111.85 (*d*), 117.25 (*d*), 118.6 (*s*), 127.73 (*d*), 129.925 (*s*), 120.03 (*br*), 129.21 (*s*), 129.5 (*s*), 129.87(*s*), 132.7 (*s*), 133.75 (*s*), 134.4 (*d*), 134.75 (*d*), 135.05 (*d*), 138.25 (*br*), 139.5 (*br*). ^{31}P NMR (121 MHz, C_6D_6) δ, ppm: 6.6 (*s*, 3P), -26 (*s*, 1P).

Table A6.1. Crystal and refinement data for complexes **3**-**6**.

	3	**4**	**5**	**6**
CCDC Number				
Empirical Formula	$C_{64}H_{52}N_4P_4Hf$	$C_{64}H_{52}N_4P_4TiNi$	$C_{64}H_{52}N_4P_4ZrNi\bullet C_6H_6$	$C_{64}H_{52}N_4P_4HfNi\bullet C_6H_6$
Formula weight	1179.47	1107.59	1229.01	1316.34
T (K)	123(2) K	123(2) K	150(2) K	123(2) K
a, Å	9.7556(11)	12.772(2)	11.2579(5)	11.2134(3)
b, Å	16.9397(19)	14.5023(16)	23.6880(9)	23.6739(5)
c, Å	21.120(3)	14.5023(16)	23.6877(9)	22.8293(5)
a, deg	106.175(2)	93.11	90	90
b, deg	103.058(1)	92.3180(10)	102.7780(10)	103.8260(10)
g, deg	93.195(1)	92.3180(10)	90	90
Volume, Å^3	3290.1(6)	2677.9(6)	5900.5(4)	5884.8(2)
Z	2	2	4	4
Crystal System	Triclinic	Triclinic	Monoclinic	Monoclinic
Space Group	P-1	P-1	P2(1)/c	P2(1)/c
d_{calc}, g/cm^3	1.209	1.374	1.384	1.486
θ Range, deg	2.32 to 28.85	3.05 to 72.64	2.728 to 72.155	2.73 to 72.24
μ, mm^{-1}	1.747	3.186	3.227	4.946
Abs. Correction	Multi-scan	Multi-scan	Multi-scan	Multi-scan
GOF	1.033	1.108	1.020	1.039
R_1,[a]	*R*1 = 0.0384	R1 = 0.0383	R1 = 0.0275	*R*1 = 0.0377
wR_2 [b] [I>2s(I)]	*wR*2 = 0.0947	*w*R2 = 0.0970	*w*R2 = 0.0703	*wR*2 = 0.0891

[a] $R_1 = \sum||F_o| - |F_c||/\sum|F_o|$. [b] $wR_2 = [\sum[w(F_o^2-F_c^2)^2]/\sum[w(F_o^2)^2]]^{1/2}$.

Table A6.2. Crystal and refinement data for complexes **7**, **8**, and **9**.

	7	**8**	**9**
CCDC Number			
Empirical Formula	$NaC_{52}H_{64}N_4P_4TiNi \bullet (OC_4H_8)$	$C_{65}H_{52}N_4O_1P_4TiNi$	$C_{84}H_{78}N_6O_1P_6TiNi \bullet 2(C_6H_6)$
Formula weight	1202.68	1229.01	2043.02
T (K)	123(2)	123(2)	123(2)
a, Å	14.5006(3)	11.6014(16)	20.6085(9)
b, Å	14.7943(3)	12.1966(16)	22.0874(9)
c, Å	16.1167(3)	21.545(3)	22.0874(9)
a, deg	98.340(1)	75.265(6)	90
b, deg	107.470(1)	76.711(6)	90
g, deg	94.600(1)	67.796(6)	90
Volume, $Å^3$	3234.93(11)	2699.0(6)	10053.9(7)
Z	2	2	4
Crystal System	Triclinic	Triclinic	Orthorhombic
Space Group	P-1	P-1	Pbca
d_{calc}, g/cm^3	1.235	1.397	1.350
θ Range, deg	2.92 to 72.190	3.99 to 72.470	2.92 to 73.86
μ, mm^{-1}	2.749	3.190	3.055
Abs. Correction	Multi-scan	Multi-scan	Multi-scan
GOF	1.034	1.053	1.037
R_1 ,[a]	*R*1 = 0.0447	R1 = 0.0627	R1 = 0.0523
wR_2 [b] [I>2s(I)]	*w*R2 = 0.1102	*w*R2 = 0.1220	*w*R2 = 0.1462

[a] $R_1 = \sum||F_o| - |F_c||/\sum|F_o|$. [b] $wR_2 = [\sum[w(F_o^2-F_c^2)^2]/\sum[w(F_o^2)^2]]^{1/2}$.

Appendix 7

Table A7.1. Main-Group Average Bond Energies (kcal/mol)

	CASSCF	CASPT2	ftPBE	tPBE	PBE	Exp.
SiH_4[a]	72.4	78.0	80.2	78.9	78.4	81.2
S_2[b]	76.9	100.8	104.1	109.2	114.7	104.3
SiO[c]	191.0	188.0	184.4	187.0	196.3	193.1
C_3H_4[d]	95.2	113.8	119.2	117.5	120.2	117.5
HC(O)CHO[e]	110.5	123.1	127.2	127.1	132.7	126.8
C_4H_8[f]	73.7	92.4	96.8	95.5	97.3	95.8

[a] The active space is 8/8, where the eight electrons are the sigma bonding electrons and the eight orbitals are the sigma bonding and antibonding orbitals.

[b] The AS is 12/8, the full valence space, where the electrons and orbitals are the valence 3*s* and 3*p* choices.

[c] The AS is 10/8, the full valence space, where the electrons and orbitals are the valence *s* and *p* choices for each atom.

[d] The AS is 8/8 and excludes all carbon-hydrogen bonds. The eight electrons are those of the carbon-carbon triple bond and the carbon-carbon single bond. The orbitals are the corresponding bonding and antibonding pairs.

[e] The AS is 12/12 and includes the carbon atomic 2*p* electrons and orbitals and the oxygen 2*p* electrons and orbitals.

[f] The AS is 8/8, where the electrons and orbitals are bonding electrons of the carbon-carbon single bonds and the orbitals are the corresponding bonding/antibonding pairs.

Table A7.2. Transition-Metal-Ligand Average Bond Energies (kcal/mol)

	CASSCF	CASPT2	ftPBE	tPBE	PBE	Exp.
$CrCl_2$[a]	72.5	80.7	80.9	78.2	88.8	91.4
CrCl[b]	64.0	86.4	85.4	82.3	89.8	91.0
$CoCl_2$[c]	74.4	77.7	91.6	91.3	94.0	93.5
$FeCl_2$[d]	78.3	94.2	96.1	95.7	99.5	96.6
TiCl[e]	92.3	104.2	101.8	103.6	116.6	102.3
MnF_2[f]	87.3	118.2	121.0	120.7	127.6	116.5
VF_5[g]	74.2	107.6	117.5	116.9	126.5	113.4
CoH[h]	18.2	42.9	38.6	39.6	60.5	45.2
FeH[i]	19.2	28.9	32.7	31.8	49.3	36.8
AgH[j]	38.2	52.2	55.2	52.9	55.9	54.0

[a] The AS is 8/8, where the electrons and orbitals are those from the 3*d* and *4s* orbitals of Cr and the bonding 3*p* electron and orbital of Cl. The spin state is a quartet.

[b] The AS is 7/7, where the electrons and orbitals are those from the 3*d* and *4s* orbitals of Cr and the bonding 3*p* electron and orbital of Cl. The spin state is a sextet.

[c] The AS is 11/8, where the electrons and orbitals are those from the 3*d* and *4s* orbitals of Co and the bonding 3*p* electron and orbital of Cl. The spin state is a quartet.

[d] The AS is 10/8, where the electrons and orbitals are those from the 3*d* and *4s* orbitals of Fe and the bonding 3*p* electron and orbital of Cl. The spin state is a quintet.

[e] The AS is 5/7, where the electrons and orbitals are those from the 3*d* and *4s* orbitals of Ti and the bonding 3*p* electron and orbital of Cl. The spin state is a quartet.

[f] The AS is 9/8, where the electrons and orbitals are those from the 3*d* and *4s* orbitals of Mn and the bonding 2*p* electron and orbital of F. The spin state is a sextet.

[g] The AS is 10/11, where the electrons and orbitals are those from the 3*d* and *4s* orbitals of V and the bonding 2*p* electron and orbital of each F. The spin state is a singlet.

[h] The AS is 10/7, where the electrons and orbitals are those from the 3*d* and *4s* orbitals of Co and the *1s* orbital of hydrogen. The spin state is triplet.

[i] The AS is 9/7, where the electrons and orbitals are those from the 3*d* and *4s* orbitals of Fe and the *1s* orbital of hydrogen. The spin state is a quartet.

[j] The active space is 12/7, where the electrons and orbitals are those from the 4*d* and *5s* orbitals of Ag and the *1s* of hydrogen. The spin state is a singlet.

Table A7.3. Proton Affinities of Small Molecules (kcal/mol)

	CASSCF	CASPT2	ftPBE	tPBE	PBE	Exp.
H_2O[a]	171.0	171.5	172.9	172.3	170.4	171.8
NH_3[b]	212.9	212.3	212.7	212.1	210.9	211.9
H_2S[c]	188.6	174.9	174.8	174.0	174.4	173.7

[a] The AS is 4/4

[b] The AS is 6/6

[c] The AS is 8/7, which includes the 3*s* and 3*p* electrons and orbitals from S and the 1*s* electrons and orbitals from each H, plus the orbital from the proton.

Table A7.4. Alkyl Bond Dissociation Energies (kcal/mol)

	CASSCF	CASPT2	ftPBE	tPBE	PBE	Exp
tBU-OCH_3[a]	70.3	93.0	89.1	89.6	80.1	89.3
tBu-CH_3[b]	74.5	95.1	88.9	90.6	86.2	93.7

[a] The AS is 2/2 for the molecule, which includes all carbon-carbon electrons and corresponding bonding/antibonding orbital pairs. For each radical, the AS was 1/1.

[b] The AS is 8/8 for the molecule, which includes all carbon-carbon electrons and corresponding bonding/antibonding orbital pairs. For the methyl radical, the AS was 1/1. For the butyl radical, the AS was 7/7 for the butyl radical, which includes the carbon-carbon electrons and corresponding bonding/antibonding orbital pairs plus the radical electron and orbital.

Table A7.5. Non-covalent energy of hydrogen bonding (kcal/mol)

	CASSCF	CASPT2	ftPBE	tPBE	PBE	Exp
$(H_2O)_2$[a]	4.0	5.5	6.3	4.8	5.4	4.97
MUE	0.96	0.5	1.3	0.2	0.5	

[a] The AS is 16/8 for the dimer, and 8/4 for each water molecule.

Table A7.6. Forward and reverse barrier heights for small molecules (kcal/mol)[a]

	CASSCF	CASPT2	ftPBE	tPBE	PBE	Exp
$Cl^-\cdots CH_3Cl \rightarrow ClCH_3\cdots Cl^-$	20.2	12.2	7.7	7.9	6.9	13.4
rev	20.2	12.2	7.7	7.9	6.9	13.4
$OH+CH_4 \rightarrow H_2O+CH_3$	18.9	6.9	6.8	5.5	-5.2	6.5
rev	24.4	17.9	23.8	21.0	8.8	19.6
$H+HO \rightarrow H_2+O$	17.1	12.0	9.9	10.5	3.6	10.5
rev	27.0	13.8	8.6	8.1	-1.3	12.9
$H+H_2S \rightarrow H_2+HS$	11.3	5.5	3.3	4.3	-1.1	3.5
rev	24.6	18.1	16.3	15.1	9.5	16.8
$H+N_2O \rightarrow OH+N_2$	29.8	20.4	16.3	17.3	10.5	17.1
rev	96.2	80.2	73.8	71.2	52.8	82.3
$CH_3+FCl \rightarrow CH_3F+Cl$	8.3	8.9	8.3	6.3	-6.4	6.8
rev	86.5	51.1	43.5	45.5	42.0	59.2
$HCN \rightarrow HNC$	53.9	48.2	48.2	46.7	46.0	48.1
rev	37.5	33.9	34.5	32.8	41.0	32.8
$H+N_2 \rightarrow HN_2$	26.5	16.6	11.9	13.0	5.6	14.4
rev	-0.5	10.9	14.3	14.5	9.2	10.6
$H+ClH \rightarrow HCl+H$	29.9	20.4	14.6	16.7	10.4	18.0
rev	29.9	20.4	14.6	16.7	10.4	18.0
$F^-\cdots CH_3Cl \rightarrow FCH_3\cdots Cl^-$	6.4	2.4	0.1	0.2	-1.0	3.4
rev	46.5	26.5	25.9	26.2	21.0	29.4
$OH^-+CH_3F \rightarrow HOCH_3+F^-$	8.9	-2.7	-5.5	-5.7	-10.7	-2.4
rev	29.2	18.1	15.6	15.1	9.6	17.7
$H+C_2H_4 \rightarrow CH_3CH_2$	-9.6	1.7	0.9	3.4	0.0	1.7
rev	34.5	41.3	43.2	43.0	40.4	41.8

[a] See Table 8.7 for active space descriptions

Table A7.7 . Reaction energies for small molecules (kcal/mol)

	CASSCF	CASPT2	ftPBE	tPBE	PBE	Exp
$OH+CH_4 \rightarrow H_2O+CH_3$	-5.5	-11.0	-17.0	-15.5	-14.0	-13.1
$H+HO \rightarrow H_2+O$	-10.0	-1.8	1.3	2.5	4.9	-2.4
$H+H_2S \rightarrow H_2+HS$	-13.3	-12.6	-13.0	-10.8	-10.6	-13.3
$H+N_2O \rightarrow OH+N_2$	-66.4	-59.8	-57.5	-53.9	-42.4	-65.1
$CH_3+FCl \rightarrow CH_3F+Cl$	-78.2	-42.2	-35.2	-39.4	-48.4	-52.4
$HCN \rightarrow HNC$	16.4	14.3	13.6	13.9	5.0	15.3
$H+N_2 \rightarrow HN_2$	26.9	5.7	-2.5	-1.5	-3.7	3.8
$F^-\cdots CH_3Cl \rightarrow FCH_3\cdots Cl^-$	-40.1	-24.1	-25.8	-26.0	-22.0	-26.0
$OH^-+CH_3F \rightarrow HOCH_3+F^-$	-20.3	-20.8	-21.1	-20.8	-20.3	-20.1
$H+C_2H_4 \rightarrow CH_3CH_2$	-44.1	-39.6	-42.4	-39.6	-40.4	-40.0

Appendix 8

Table A8.1. Values of Π , ρ, *R* at bond midpoint

$r_{ab}(a_0)$	Π HF	ρ HF	Π CAS(2,2)	ρ CAS (2,2)	Ratio *R*
0.6	1.851×10^{-1}	8.60×10^{-1}	1.86×10^{-1}	8.61×10^{-1}	1.002
0.7	1.27×10^{-1}	7.13×10^{-1}	1.28×10^{-1}	7.14×10^{-1}	1.003
1.3	1.91×10^{-2}	2.76×10^{-1}	1.94×10^{-2}	2.77×10^{-1}	1.011
1.4	1.46×10^{-2}	2.41×10^{-1}	1.48×10^{-2}	2.42×10^{-1}	1.013
1.7	6.91×10^{-3}	1.66×10^{-1}	7.04×10^{-3}	1.66×10^{-1}	1.022
2.26	2.06×10^{-3}	9.09×10^{-1}	2.08×10^{-3}	8.90×10^{-2}	1.052
2.5	1.30×10^{-3}	7.20×10^{-2}	1.29×10^{-3}	6.93×10^{-2}	1.073
3.0	5.29×10^{-4}	4.60×10^{-2}	4.92×10^{-4}	4.16×10^{-2}	1.138
3.5	2.30×10^{-4}	3.03×10^{-2}	1.89×10^{-4}	2.47×10^{-2}	1.235
4.0	1.04×10^{-4}	2.04×10^{-2}	7.09×10^{-5}	1.44×10^{-2}	1.359
4.5	4.80×10^{-5}	1.39×10^{-2}	2.61×10^{-5}	8.37×10^{-3}	1.491
5.0	2.23×10^{-5}	9.45×10^{-3}	9.53×10^{-6}	4.86×10^{-3}	1.615
10.0	6.99×10^{-9}	1.67×10^{-4}	4.18×10^{-10}	2.90×10^{-5}	1.991
100.0	7.48×10^{-75}	1.73×10^{-37}	2.80×10^{-88}	2.37×10^{-44}	2.000

Table A8.2. Values of Π , ρ, *R* 0.5 a_0 from atom inside bond along internuclear axis

$r_{ab}(a_0)$	Π HF	ρ HF	Π CAS(2,2)	ρ CAS (2,2)	Ratio
0.6	2.18×10^{-1}	9.34×10^{-1}	1.92×10^{-1}	9.39×10^{-1}	0.872
0.7	1.39×10^{-1}	7.45×10^{-1}	1.31×10^{-1}	7.48×10^{-1}	0.938
1.3	2.04×10^{-2}	2.85×10^{-1}	1.99×10^{-2}	2.87×10^{-1}	0.968
1.4	1.63×10^{-2}	2.55×10^{-1}	1.56×10^{-2}	2.57×10^{-1}	0.942
1.7	9.35×10^{-3}	1.93×10^{-1}	8.04×10^{-3}	1.96×10^{-1}	0.833
2.26	4.58×10^{-3}	1.35×10^{-1}	2.91×10^{-3}	1.42×10^{-1}	0.575
2.5	3.68×10^{-3}	1.21×10^{-1}	1.98×10^{-3}	1.31×10^{-1}	0.462
3.0	2.64×10^{-3}	1.03×10^{-1}	9.02×10^{-4}	1.18×10^{-1}	0.259
3.5	2.12×10^{-3}	9.22×10^{-2}	4.01×10^{-4}	1.14×10^{-1}	0.123
4.0	1.85×10^{-3}	8.59×10^{-2}	1.68×10^{-4}	1.14×10^{-1}	0.052
4.5	1.69×10^{-3}	8.23×10^{-2}	6.60×10^{-5}	1.15×10^{-1}	0.020
5.0	1.61×10^{-3}	8.03×10^{-2}	2.49×10^{-5}	1.16×10^{-1}	0.007
10.0	1.65×10^{-3}	8.12×10^{-2}	1.06×10^{-9}	1.17×10^{-1}	3.1×10^{-7}
100.0	1.69×10^{-3}	8.22×10^{-2}	0.00	1.17×10^{-1}	0.000

Table A8.3. Values of Π , ρ, R 0.5 a_0 from atom outside bond along internuclear axis

$r_{ab}(a_0)$	Π HF	ρ HF	Π CAS(2,2)	ρ CAS (2,2)	Ratio
0.6	1.47×10^{-2}	2.42×10^{-1}	1.10×10^{-2}	2.44×10^{-1}	0.740
0.7	1.21×10^{-2}	2.20×10^{-1}	8.76×10^{-3}	2.22×10^{-1}	0.711
1.3	5.23×10^{-3}	1.45×10^{-1}	2.94×10^{-3}	1.49×10^{-1}	0.533
1.4	4.72×10^{-3}	1.37×10^{-1}	2.53×10^{-3}	1.42×10^{-1}	0.503
1.7	3.62×10^{-3}	1.20×10^{-1}	1.66×10^{-3}	1.27×10^{-1}	0.414
2.26	2.53×10^{-3}	1.01×10^{-1}	8.05×10^{-4}	1.12×10^{-1}	0.259
2.5	2.26×10^{-3}	9.51×10^{-2}	5.94×10^{-4}	1.09×10^{-1}	0.201
3.0	1.90×10^{-3}	8.72×10^{-2}	3.06×10^{-4}	1.07×10^{-1}	0.107
3.5	1.70×10^{-3}	8.24×10^{-2}	1.45×10^{-4}	1.09×10^{-1}	0.049
4.0	1.58×10^{-3}	7.96×10^{-2}	6.29×10^{-5}	1.11×10^{-1}	0.020
4.5	1.53×10^{-3}	7.81×10^{-2}	2.52×10^{-5}	1.14×10^{-1}	0.008
5.0	1.50×10^{-3}	7.75×10^{-2}	9.55×10^{-6}	1.15×10^{-1}	0.003
10.0	1.65×10^{-3}	8.11×10^{-2}	3.85×10^{-10}	1.17×10^{-1}	1.1×10^{-7}
100.0	1.69×10^{-3}	8.22×10^{-2}	0.00	1.17×10^{-1}	0.000

Table A8.4. Values of Π , ρ, R 0.5 a_0 from side of atom perpendicular to bond axis

$r_{ab}(a_0)$	Π HF	ρ HF	Π CAS(2,2)	ρ CAS (2,2)	Ratio
0.6	2.79×10^{-2}	3.34×10^{-1}	2.62×10^{-2}	3.35×10^{-1}	0.935
0.7	2.25×10^{-2}	3.00×10^{-1}	2.06×10^{-2}	3.01×10^{-1}	0.911
1.3	7.92×10^{-3}	1.78×10^{-1}	5.87×10^{-3}	1.81×10^{-1}	0.719
1.4	6.93×10^{-3}	1.66×10^{-1}	4.92×10^{-3}	1.70×10^{-1}	0.682
1.7	4.92×10^{-3}	1.40×10^{-1}	3.00×10^{-3}	1.45×10^{-1}	0.569
2.26	3.09×10^{-3}	1.11×10^{-1}	1.33×10^{-3}	1.21×10^{-1}	0.364
2.5	2.68×10^{-3}	1.03×10^{-1}	9.53×10^{-4}	1.15×10^{-1}	0.286
3.0	2.13×10^{-3}	9.24×10^{-2}	4.71×10^{-4}	1.11×10^{-1}	0.154
3.5	1.84×10^{-3}	8.58×10^{-2}	2.19×10^{-4}	1.10×10^{-1}	0.072
4.0	1.67×10^{-3}	8.19×10^{-2}	9.37×10^{-5}	1.12×10^{-1}	0.030
4.5	1.59×10^{-3}	7.96×10^{-2}	3.73×10^{-5}	1.14×10^{-1}	0.011
5.0	1.54×10^{-3}	7.85×10^{-2}	1.42×10^{-5}	1.15×10^{-1}	0.004
10.0	1.65×10^{-3}	8.12×10^{-2}	5.92×10^{-10}	1.17×10^{-1}	1.7×10^{-7}
100.0	1.69×10^{-3}	8.22×10^{-2}	0.00	1.17×10^{-1}	0.000

Table A8.5. Values of Π , ρ, R 0.5 a_0 from point in Table 2 perpendicular to bond axis

$r_{ab}(a_0)$	Π HF	ρ HF	Π CAS(2,2)	ρ CAS (2,2)	Ratio
0.6	3.220×10^{-2}	3.589×10^{-1}	3.124×10^{-2}	3.592×10^{-1}	0.968
0.7	2.810×10^{-2}	3.352×10^{-1}	2.762×10^{-2}	3.355×10^{-1}	0.982
1.3	8.477×10^{-3}	1.841×10^{-1}	8.355×10^{-3}	1.843×10^{-1}	0.984
1.4	7.036×10^{-3}	1.678×10^{-1}	6.814×10^{-3}	1.680×10^{-1}	0.966
1.7	4.307×10^{-3}	1.313×10^{-1}	3.840×10^{-3}	1.321×10^{-1}	0.880
2.26	2.207×10^{-3}	9.396×10^{-1}	1.502×10^{-3}	9.682×10^{-2}	0.641
2.5	1.793×10^{-3}	8.468×10^{-2}	1.037×10^{-3}	8.885×10^{-2}	0.525
3.0	1.298×10^{-3}	7.204×10^{-2}	4.833×10^{-4}	7.964×10^{-2}	0.305
3.5	1.049×10^{-3}	6.477×10^{-2}	2.169×10^{-4}	7.635×10^{-2}	0.149
4.0	9.151×10^{-4}	6.050×10^{-2}	9.105×10^{-5}	7.580×10^{-2}	0.063
4.5	8.416×10^{-4}	5.802×10^{-2}	3.596×10^{-5}	7.617×10^{-2}	0.025
5.0	8.019×10^{-4}	5.663×10^{-2}	1.365×10^{-5}	7.664×10^{-2}	0.009
10.0	8.212×10^{-4}	5.731×10^{-2}	5.949×10^{-10}	7.739×10^{-2}	4.0×10^{-7}
100.0	8.406×10^{-4}	5.799×10^{-2}	0.00	7.739×10^{-2}	0.000

II. Total energies for CAS(2,2) and HF wave functions

Table A8.6. CAS(2,2) energies (Rydberg), CI coefficients, and Z parameter values

$r_{ab}(a_0)$	E	C_1	C_2	Z
0.6	-1.4672	0.9989	-0.0473	1.4519
0.7	-1.7751	0.9986	-0.0537	1.4115
1	-2.1873	0.9971	-0.0758	1.3067
1.3	-2.2892	0.9948	-0.1023	1.2239
1.4	-2.2956	0.9937	-0.1122	1.2005
1.5	-2.2944	0.9924	-0.1227	1.1790
1.7	-2.2778	0.9894	-0.1455	1.1411
2.26	-2.1941	0.9750	-0.2222	1.0651
2.3	-2.1878	0.9735	-0.2288	1.0612
2.5	-2.1575	0.9654	-0.2607	1.0437
3	-2.0939	0.9374	-0.3481	1.0151
3.5	-2.0509	0.8997	-0.4366	1.0022
4	-2.0256	0.8578	-0.5140	0.9981
4.5	-2.0121	0.8188	-0.5740	0.9977
5	-2.0056	0.7870	-0.6170	0.9984
7	-2.0002	0.7248	-0.6890	0.9999
10	-2.0000	0.7086	-0.7056	1.0000
100	-2.0000	0.7071	-0.7071	1.0000

Table A8.7. Hartree Fock energies (Rydberg) and Z parameter values

$r_{ab}(a_0)$	E	Z
0.6	-1.4491	1.4494
0.7	-1.7548	1.4084
1	-2.1599	1.3009
1.3	-2.2532	1.2144
1.4	-2.2564	1.1895
1.5	-2.2518	1.1664
1.7	-2.2278	1.1247
2.26	-2.1182	1.0349
2.3	-2.1097	1.0297
2.5	-2.0677	1.0057
3	-1.9695	0.9578
3.5	-1.8851	0.9231
4	-1.8148	0.8978
4.5	-1.7570	0.8794
5	-1.7099	0.8660
10	-1.5278	0.8412
100	-1.4338	0.8438

III. Coordinate System

The equations were derived in spheroidal coordinates λ, μ, ϕ. Contours of constant λ are ellipsoids defined on the interval $1 \leq \lambda \leq \infty$ where $\lambda = \frac{r_a + r_b}{r_{ab}}$, contours of constant μ are hyperbaloids defined on the interval $-1 \leq \mu \leq 1$ where $\mu = \frac{r_a - r_b}{r_{ab}}$, and ϕ is the angle of rotation around the nuclear axis. Inverting the equations for λ, μ, $r_a = \frac{(\lambda+\mu)r_{ab}}{2}$ and $r_b = \frac{(\lambda-\mu)r_{ab}}{2}$ where R is the internuclear distance and r_a is the distance from nucleus H_a to an electron and r_a is the distance from nucleus H_b to an electron (Fig 1). In Cartesian coordinates, $r_a = \sqrt{x^2 + y^2 + \left(z + \frac{r_{ab}}{2}\right)^2}$, $r_b = \sqrt{x^2 + y^2 + \left(z - \frac{r_{ab}}{2}\right)^2}$, $x = \frac{r_{ab} cos\phi}{2}\sqrt{(\lambda^2 - 1)(1 - \mu^2)}$, $y = \frac{r_{ab} sin\phi}{2}\sqrt{(\lambda^2 - 1)(1 - \mu^2)}$, $z = \frac{\lambda \mu r_{ab}}{2}$.

S is the overlap integral $\frac{Z^3}{\pi}\int e^{-Zr_a} e^{-Zr_b} dv$

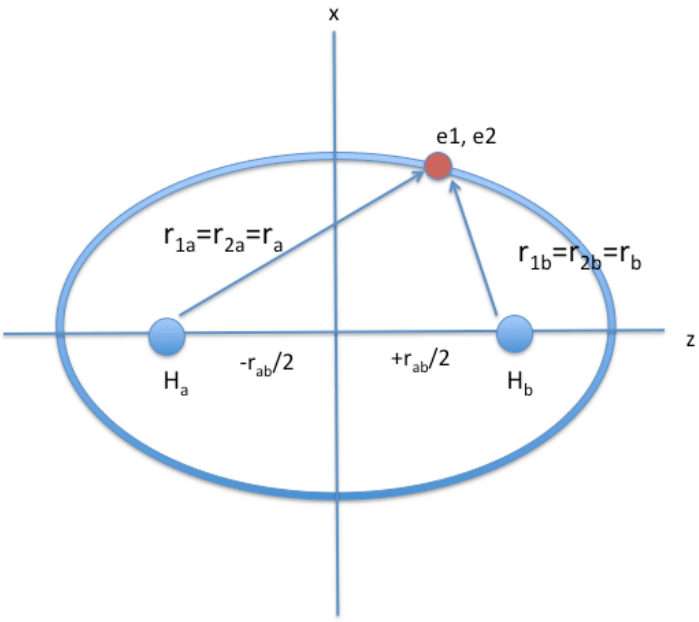

Figure A8.0. H_2 in spheroidal coordinates where both electrons are in the same place.

Looking at the expression for R, there are terms containing $e^{r_{1a}} \pm e^{r_{1b}}$ that are reminiscent of the molecular orbitals: $(e^{-r_{1a}} \pm e^{-r_{1b}}) = \sigma_g$ or σ_u. Expressing these in spheroidal coordinates, $e^{r_{1a}} \pm e^{r_{1b}}$ can be rewritten as $2e^{\left(\frac{\lambda}{2}\right)r_{ab}Z}\cosh(\frac{\mu r_{ab}Z}{2})$ for the upper sign and $2e^{\left(\frac{\lambda}{2}\right)r_{ab}Z}\sinh(\frac{\mu r_{ab}Z}{2})$ for the lower sign, where λ are ellipses and μ are hyperbolas. Similarly, writing $(e^{-r_{1a}} + e^{-r_{1b}}) = \sigma_g$ in terms of hyperbolic functions results in $2e^{\left(\frac{-\lambda}{2}\right)r_{ab}Z}\cosh(\frac{\mu r_{ab}Z}{2})$.

$e^{r_{1a}} + e^{r_{1b}} =$

Using spheroidal coordinates (λ *are ellipses and* μ *are hyperbolas*)
$e^{\left(\frac{\lambda+\mu}{2}\right)r_{ab}Z} + e^{\left(\frac{\lambda-\mu}{2}\right)r_{ab}Z} =$

$e^{\left(\frac{\lambda}{2}\right)r_{ab}Z}e^{\left(\frac{\mu}{2}\right)r_{ab}Z} + e^{\left(\frac{\lambda}{2}\right)r_{ab}Z}e^{\left(\frac{-\mu}{2}\right)r_{ab}Z} =$

$e^{\left(\frac{\lambda}{2}\right)r_{ab}Z}\left(e^{\left(\frac{\mu}{2}\right)r_{ab}Z} + e^{\left(\frac{-\mu}{2}\right)r_{ab}Z}\right) =$

$2e^{\left(\frac{\lambda}{2}\right)r_{ab}Z}cosh(\mu/2)$

Similarly, if you wrote $(e^{-r_{1a}} + e^{-r_{1b}}) = \sigma_g$ in terms of hyperbolic functions you would get

$$2e^{-\left(\frac{\lambda}{2}\right)r_{ab}Z}cosh(\mu)$$

IV. Contour plots for various internuclear distances

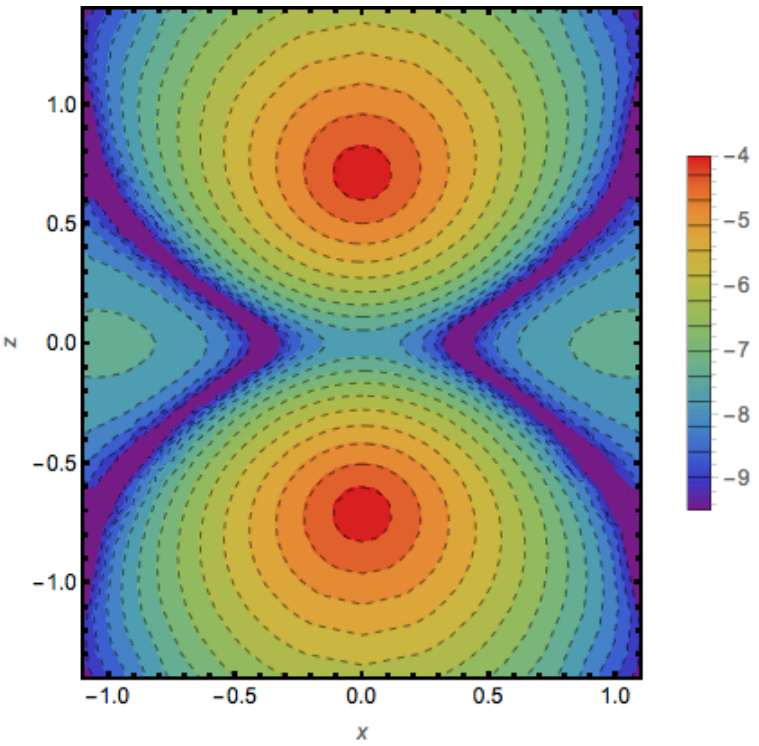

Figure A8.1. Natural logarithm of the difference (CAS(2,2)-HF) of values of rho at 1.4 a_0. CAS(2,2) has larger values of ρ everywhere except for the triangles at the periphery of the bond.

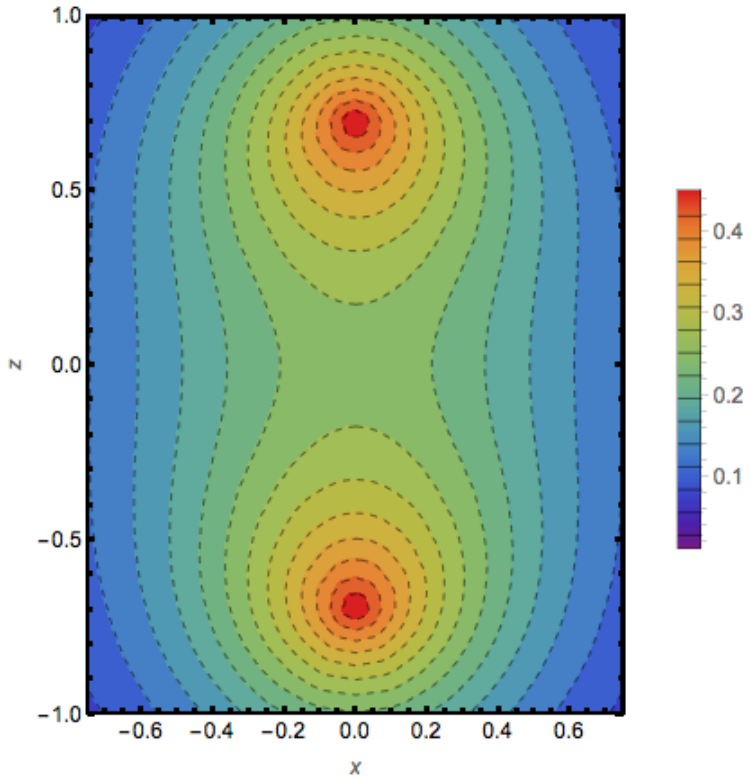

Figure A8.2. Contour plot of the total density for HF at 1.4 a_0 where the bond is along the *z* axis

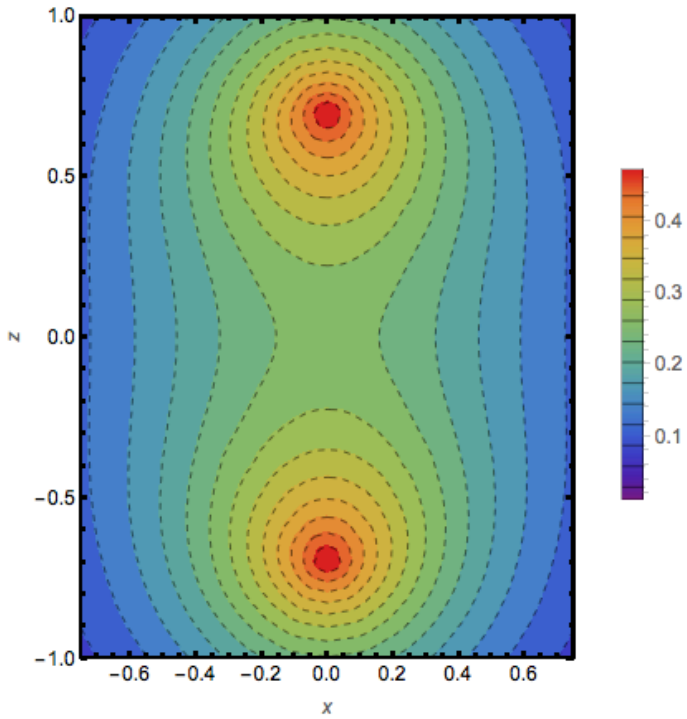

Figure A8.3. Contour plot of the total density for CAS(2,2) at 1.4 a_0 where the bond is along the *z* axis

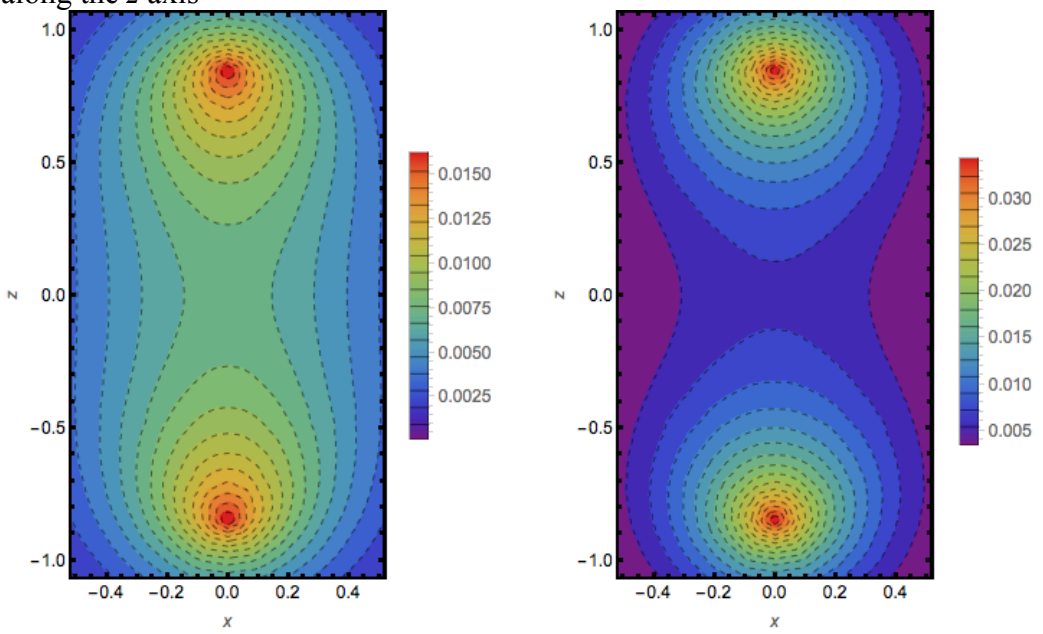

Figure A8.4. Contour plots of on-top pair density for CAS(2,2) and HF (left and right image, respectively) at 1.7 a_0 where the bond is along the *z* axis.

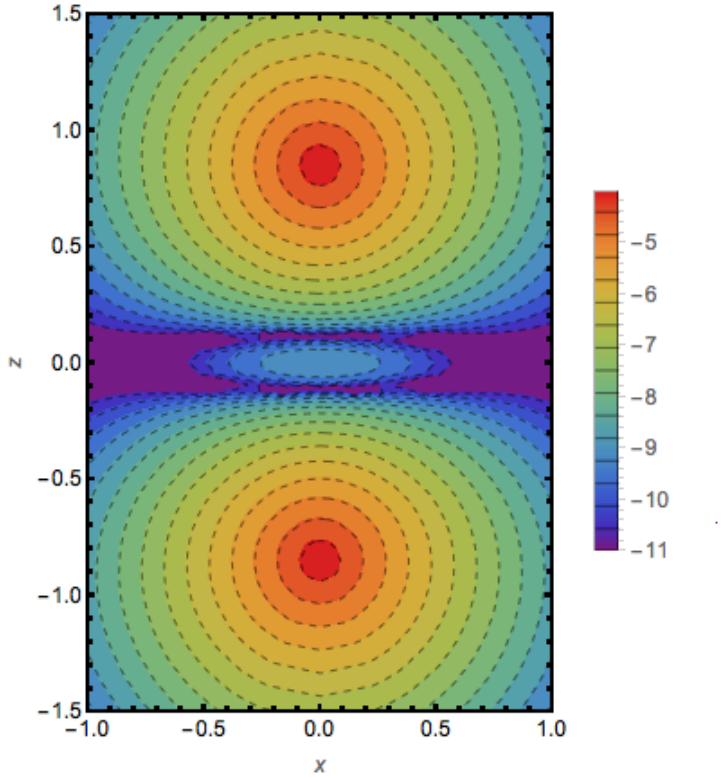

Figure A8.5. Natural logarithm of the difference (CAS(2,2)-HF) of values of the on-top pair density at 1.7 a_0. HF has larger values of Π everywhere except for the oval in the center of the contour plot from -0.6 to 0.6 a_0 along the x-axis.

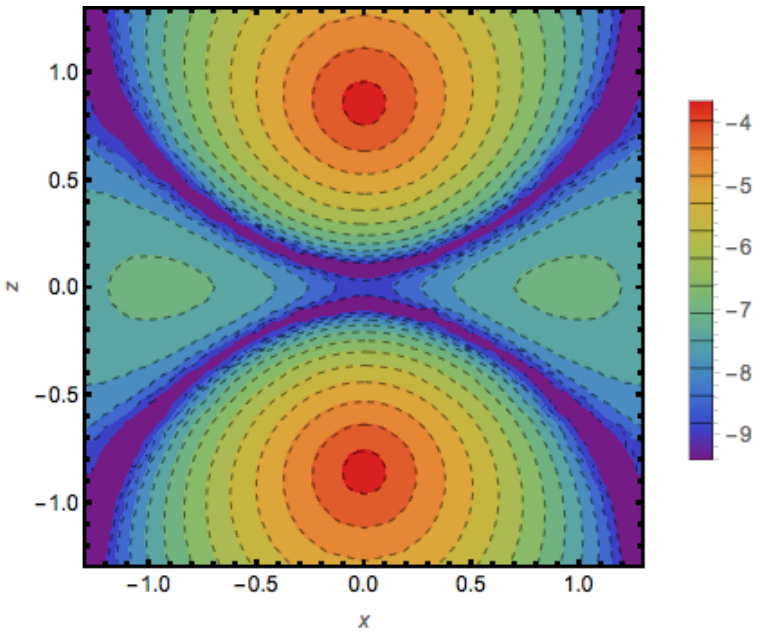

Figure A8.6. Natural logarithm of the difference (CAS(2,2)-HF) of values of rho at 1.7 a_0. CAS(2,2) has larger values of ρ everywhere except for the triangles connected through the midpoint at the periphery of the bond.

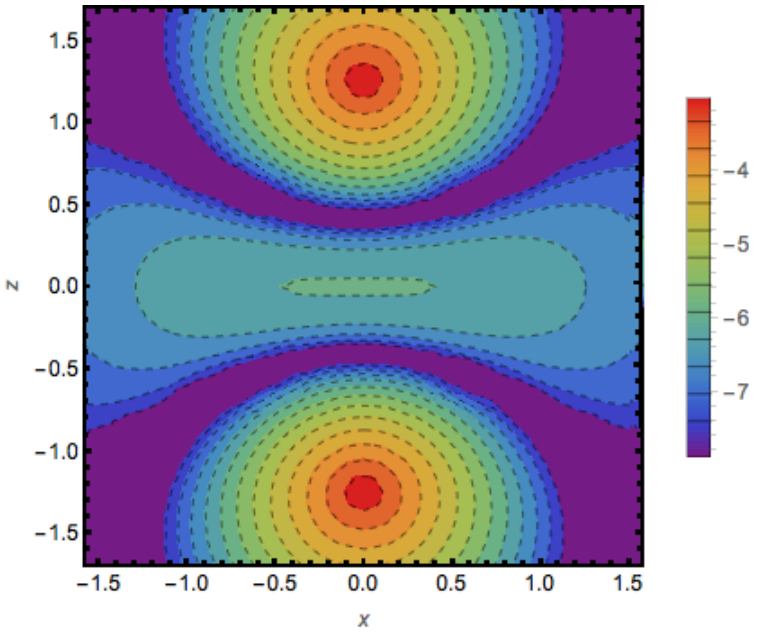

Figure A8.7. Natural logarithm of the difference (CAS(2,2)-HF) in values of the total density at 2.5 a_0. HF has larger values in the center region along the *x* axis.

V. Plots of Π corresponding to tables in section I

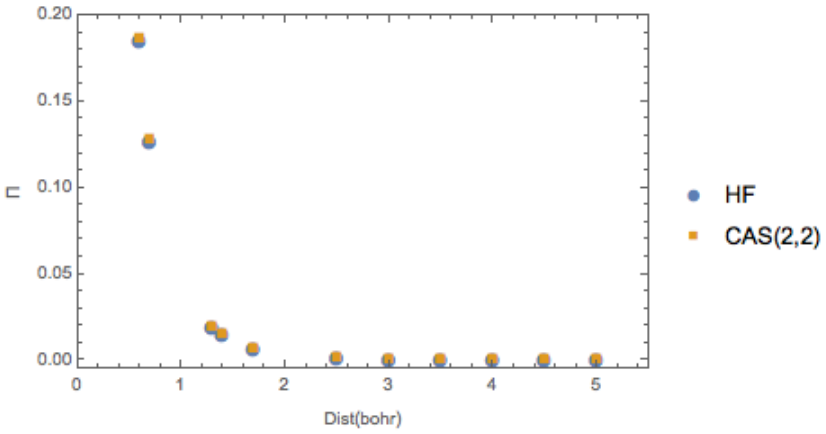

Figure A8.8. On-top pair density at bond midpoint for various internuclear distances

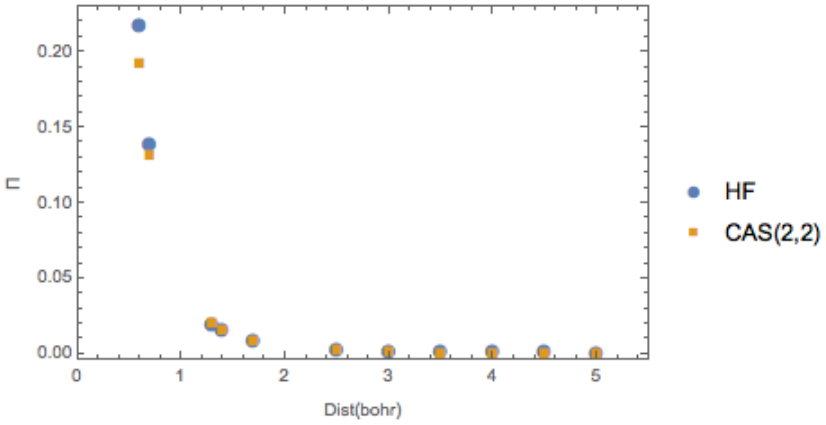

Figure A8.9. On-top pair density for a point 0.5 bohr from atom inside bond.

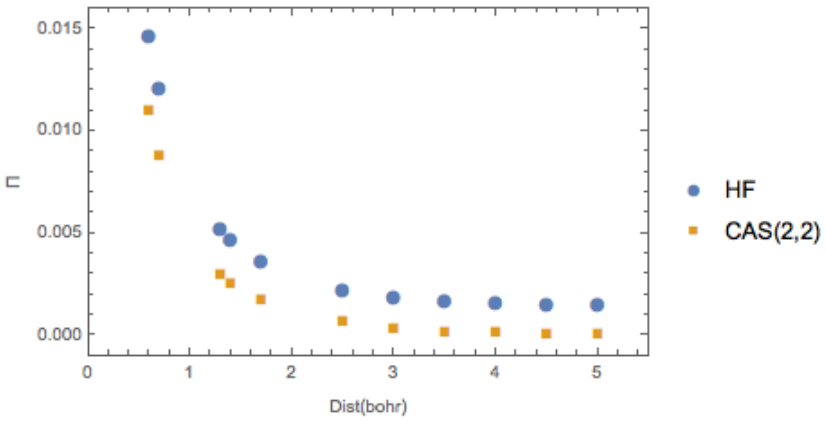

Figure A8.10. On-top pair density values for point 0.5 bohr from atom on internuclear axis outside bond.

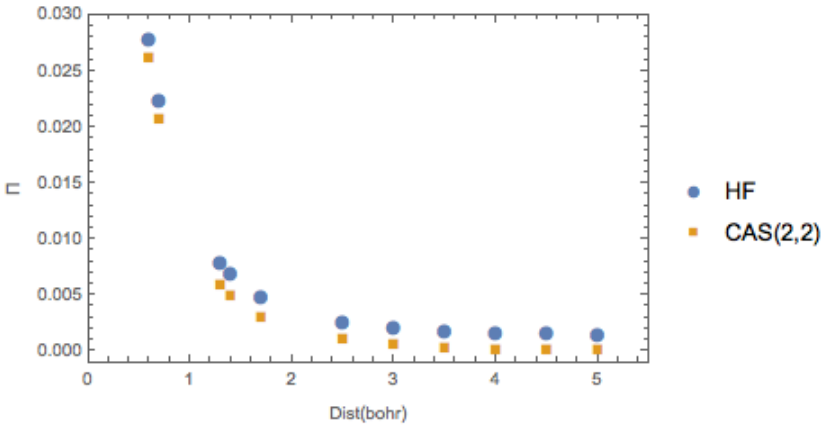

Figure A8.11. On-top pair density values for point 0.5 bohr from atom, perpendicular to the bond axis.

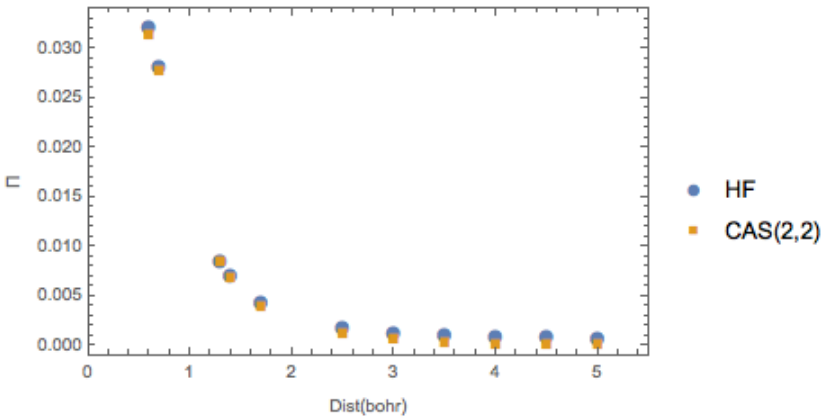

Figure A8.12. On-top pair density values for point 0.5 bohr from point in Fig 16, perpendicular to bond axis.